INVESTIGATION OF FLOW, MIXING AND SUSPENSION DYNAMICS TOWARDS THE OPTIMISATION OF AN iPSC-DERIVED CARDIOMYOCYTE DIFFERENTIATION PROCESS IN DASGIP BIOREACTORS

Jasmin Jade Samaras

A thesis submitted for the degree of Doctor of Philosophy to the University College London

University College London

Department of Biochemical Engineering

2019

I, Jasmin Jade Samaras confirm that the work presented in this thesis is my own. Where information has been derived from other sources, I confirm that this has been indicated in the thesis.

Signed:

To my brother, Maxamillion Dimitrios Samaras

ACKNOWLEDGEMENTS

With the wholly surreal completion of my PhD I saved this section for last; as the saying goes ‘you save the best for last’. This whole 4 years I have put my heart into every bit of work I have performed, my parents taught me this work ethic and it is to them I am firstly so thankful.

I am so proud of them and their strength, when I felt like giving up they got me back up. The words of encouragement, the belief in me, the love and time they have endlessly shown me has directed me down the path in life I took. My biggest fan was my younger brother and it is to him I dedicate my work and every good thing in my life, no day shall erase you from the memory of time little man.

Andrea and Martina, I run out of words to express how grateful and fortunate I feel to have the two of you as my supervisors. You guided and advised me through every problem, you brought out the best in me and in my work – I’m sure it wasn’t always easy! Thank you both so much for bringing me through the most challenging four years, for telling me to not panic and for helping me grow immensely as a researcher. As a mentor, you were the best, as my friends, you kept me smiling.

To my Oma and Opa, you both have also given me so much and helped me more than you know. Your silly messages (essays) always making me smile and your unending belief in me helped me to reach where I now am in life. I love you both very much – never change.

My best friends, I am so fortunate to have all of you in my life, David, Becca, Jessie, Lara and Sophie, thank you for keeping me sane (or as sane as I ever was I suppose)! You helped me through some dark times, you saw me through my panic and when I stopped believing I had it in me, all of you were there to remind me, I got this. You all told me how proud you were of me and it truly meant the world. Thank you.

My research was funded by the Engineering and Physical Sciences Research Council (EPSRC), for whose support I am also most grateful.

There are many more people I am truly indebted to for their help along the last four years - however I may need another chapter! Please know the contributions made were not and never will be forgotten. Thank you all.

ABSTRACT

This thesis describes an experimental investigation of the flow, mixing and suspension dynamics within DASGIP stirred tank bioreactors, including flat and round-bottom geometries, utilising a range of agitation modes to improve understanding of the impact of continuous and intermittent agitation upon an induced pluripotent stem cell-cardiomyocyte (iPSC-CM) cell culture process. Commonly used for cell culture applications, the DASGIP bioreactor has not fully been characterised and the beneficial impact of modifying the agitation mode on cell culture has also not been fully investigated from an engineering perspective.

In the present study, rigorous flow frequency analysis with iPSC differentiation experiments were performed such as to identify and quantify the flow characteristics leading to increased cardiomyocyte differentiation yields with different agitation modes. Intermittent agitation resulted in a pattern of low intensity frequencies at reactor scale that could be controlled by varying three identified time components: rotational speed, interval and dwell time. A proof of concept biological study was undertaken, tuning the hydrodynamic environment through variation of dwell time and a significant improvement in CM yield was obtained.

Ensemble-averaged and phase-resolved Particle Image Velocimetry measurements were carried out in a single-phase flow to evaluate the impact of the changing agitation modes and bioreactor configuration. Suspension and mixing time studies were undertaken to assess the impact of the agitation mode on quality of suspension and mixing time. It was found that the flat bottom geometry of the DASGIP resulted in a strong lower vortical cell below the impeller, resulting in efficient ‘lift’ of various microcarrier types. The application of intermittent agitation resulted in an overall transient amplification of shear stress and turbulence, found to beneficially impact upon the characteristic mixing times, whilst remaining around 100-fold lower to shear stresses found in literature to detrimentally impact upon stem cell culture proliferation and viability.

IMPACT STATEMENT

Regenerative medicine poses a very promising alternative to current treatments for cardiac-related conditions. Current treatment remains primarily symptomatic, using statins or in more severe cases organ transplantation, which do not restore the patient following, for example, myocardial infarction. One of the main challenges to be able to offer regenerative medicine as a plausible alternative, is the vast improvement in process yields and efficiency, with relation to both cost and time. The work presented in this thesis characterised, from a fluid mechanics perspective, various agitation modes within a DASGIP bioreactor configuration and was able to correlate these results with biological outcomes. The methods implemented can be applied to other cell culture processes and presents the possibility of improving both understanding and process efficiencies with other cell types and differentiation pathways. The dissemination of this research, both in published research papers and at conferences, will facilitate the encouragement of multi-disciplinary collaborations such as to improve upon the engineering characterisation and understanding relating to a cell culture process to improve overall yields.

Within academia, this thesis shows how advanced laser-based techniques and flow visualisation can be used to determine flow, mixing and suspension dynamics and quantify their impact upon an induced pluripotent stem cell (iPSC) cardiomyocyte differentiation process. We have introduced the concept of fine-tuning the physical hydrodynamic cues within a three-dimensional flow system to improve cardiomyocyte differentiation yields. This may be applied to other cell culture processes and biological outcomes, not specifically investigated in this work. Performing the same analysis for other bioreactor and impeller configurations will also be of great benefit for other cell culture applications and other vendors to help identify key operating conditions.

Outside of academia, the application of various agitation modes such as to improve the efficiency of a cell culture process, in the absence of expensive growth factors or chemicals, which may also pose a risk for human clinical use at a later stage, is hugely beneficial and cost-effective. The work presented proposes characterisation of the fluid dynamics to be applied towards process optimisation through operational parameters and constraints. Commercialised mass production of iPSC-derived cardiomyocytes for cardiac repair would benefit from this work through reduced costs of additional chemical factor addition, higher process yields and improved process scalability. Characterisation

of the flow, mixing and suspension dynamics of the DASGIP bioreactor operating under different agitation modes would also aid in operational recommendations for other cell culture applications, beyond the scope of this thesis. As the cell and gene therapy industry evolves, such novel insight is becoming increasingly important and critical to ensure improved yields together with process predictability and scalability.

In summary, the work presented in this thesis has both a direct impact, specifically upon the improvement of an iPSC-CM differentiation culture, and a more indirect impact, highlighting the value of flow, suspension and mixing dynamics characterisation to improve cell culture processes. It highlights that multidisciplinary collaborations can collectively improve understanding and optimisation of bioreactor configuration and agitation mode on complex biological systems.

CONTENTS

LIST OF FIGURES

LIST OF TABLES

NOMENCLATURE

Abbreviations

2-D	Two-Dimensional
3-D	Three-Dimensional
BMSC	Bone Marrow Mesenchymal Stem Cells
BSA	Burst Spectrum Analyser
CFD	Computational Fluid Dynamics
CM	Cardiomyocyte
cTnT	Cardiac Troponin T
DISMT	Dual Indicator System for Mixing Time
DO	Dissolved Oxygen
EB	Embryoid Body
ERT	Electrical Resistance Tomography
ESC	Embryonic Stem Cell
FACS	Fluorescence Active Cell Sorting
FBS	Fetal Bovine Serum
FDA	Fluorescin Diacetate
FFT	Fast Fourier Transform
GFP	Green Fluorescent Protein
iPSC	Induced Pluripotent Stem Cell
LDA	Laser Doppler Anemometry
MC	Microcarrier
MSC	Mesenchymal Stem Cell
PBS	Phosphate-Buffered Saline
PBT	Pitched Blade Turbine Impeller
PI	Propidium Iodide
PIV	Particle Image Velocimetry
pLIF	Planar Laser-Induced Fluorescence
PMT	Prochem Maxflo T Impeller
PSC	Pluripotent Stem Cell
r.m.s	Root mean square
RGB	Red Green Blue

Greek Symbols

Φ	Porosity	[%]
$\emptyset$	Roundness	[-]
γ	Shear rate	[s^{-1}]
λ	Wavelength	[nm]
μ	Dynamic viscosity	[m^2/s]
ρ	Density	[g/cm^3]
σG	Standard deviation of the normalised green channel	[-]
τ	Shear stress	[dyn/cm^2]
φ	Phase angle	[°]
ω	Vorticity	[s]

Roman Symbols

AR	Aspect Ratio	[-]
C	Impeller clearance	[m]
D	Impeller diameter	[m]
D_{50}	Median diameter	[m]
$E_i(f)$	kinetic energy per unit of frequency in the *i*th direction	[m^2/s]
f	Frequency	[Hz]
H	Tank height	[m]
$H_{(N)}$	Homogeneity index at speed N	[%]
H_L	Liquid height	[m]
H_t	Homogeneity time constant	[-]
K^*	Missed revolutions ($N.T_{dwell}$)	[-]
$\bar{k}$	Ensemble-averaged kinetic energy	[m^2/s^2]
$\langle k \rangle$	Phase-resolved kinetic energy of periodic motion	[m^2/s^2]
$\langle k' \rangle$	Kinetic energy due to random velocity fluctuations	[m^2/s^2]
N	Rotational speed	[s^{-1}]
N_H	Minimum speed to homogeneity	[s^{-1}]
N_{js}	Just suspended speed	[s^{-1}]
Nt_D	Dispersion number	[-]
Nt_m	Mixing number	[-]
q_x	Metabolic rate of metabolite x	[mol/h]
Re	Reynolds number	[-]
T	Tank diameter	[m]

t_B	Impeller blade thickness	[m]
t_D	Dispersion time	[s]
T_{dwell}	Dwell time of impeller stoppage	[s]
t_H	Time to homogeneity	[s]
T_{inv}	Interval time of impeller motion	[s]
t_m	Mixing time	[s]
t_r	Resuspension time	[s]
u_i	Instantaneous velocity in the *i*th direction	[m/s]
$\overline{U}_i$	Ensemble average of the velocity component in the *i*th direction	[m/s]
$\langle U_i \rangle$	Phase average of the velocity component in the *i*th direction	[m/s]
u'_i	Random velocity fluctuations in the *i*th direction	[m/s]
$\tilde{u}_i$	Periodic oscillatory velocities in the *i*th direction	[m/s]
V_w	Working fluid volume	[L]
V_{tip}	Impeller tip speed	[s^{-1}]

CHAPTER 1 INTRODUCTION

1.1 The context of the research

Globally, cardiovascular disease is the leading cause of death, accounting for approximately 600,000 (40 %) and 4 million (50 %) deaths *per annum* in the United States and Europe, respectively (Roger *et al.*, 2011; Murphy *et al.*, 2013). For 2009, cardiovascular disease was estimated to have directly and indirectly cost the United States $312.6 billion in healthcare costs, medication and loss in productivity (Heidenreich *et al.*, 2011; Doppler *et al.*, 2013). Each year an estimated 720,000 patients in the U.S. suffer from myocardial infarction, one of the most prevalent manifestations of heart disease (Go *et al.*, 2014). Occlusion of the coronary arteries rapidly results in cell death where the loss in oxygen supply ultimately suppresses tissue function. Scar tissue is formed from fibroblasts replacing the dead cardiomyocytes, leading to thinning of the ventricular wall and loss of contractile properties and functionality. This formation of scar tissue is the beginning of a chain of events concluding in extensive cell death and eventual heart failure, statistics suggest that within five years of diagnosis 50 % of patients suffering from heart failure will die (Shimko and Claycomb, 2008; Barad *et al.*, 2014). Although both cardiac stem cells and progenitor cells reside in the myocardium and participate in repair, the inherent regenerative capacity of the myocardium is dramatically reduced as the tissue ages to approximately 1 % *per annum*. As such, large infarcts to the heart cannot be restored and external intervention is needed (Zandstra *et al.*, 2003; Chen *et al.*, 2014).

Currently, all treatments for cardiovascular diseases are predominantly symptomatic, comprising of pharmaceuticals, such as statins, and implantable devices. The last resort is heart transplantation for cases such as end-stage heart failure. These treatments improve the patient's quality of life through management of symptoms however, do little to improve the overall burden, morbidity and mortality rates (Doppler *et al.*, 2013; Tonsho *et al.*, 2014). These treatments do not restore the patient, nor may they be always suitable. Heart transplantation for example may encounter immunological incompatibility and rejection, the demand also far outweighs supply. Left ventricular assist devices are growing in clinical application as a bridge to full transplantation.

Regenerative medicine presents the most plausible treatment to restore and regenerate a patient, offering alternatives such as *de novo* cardiomyocytes for cell replacement

therapies (Pesl, 2013; Acimovic *et al.*, 2014; Tonsho *et al.*, 2014). Studies to cure cardiovascular diseases started with the discovery of human embryonic stem cells (hECSs) in 1998 (Thomson, 1998) and gained momentum with the advance in induced pluripotent stem cells (iPSCs, Takahashi and Yamanaka, 2006; Yu *et al.*, 2007). ESCs were first demonstrated to differentiate into contracting cardiomyocytes, which form the building blocks of the heart muscle tissue (Itskovitz-eldor *et al.*, 2000; Zwi *et al.*, 2009). Research into this field primarily aims to improve the reproducibility and the efficiency of the expansion and differentiation process steps to yield clinically relevant numbers of cardiomyocytes for myocardium repair (Burridge *et al.*, 2012; Pesl, 2013). More recent studies investigating the optimisation of these differentiation protocols have shown promising results using mechanical cues to aid in cardiogenic differentiation (Ting *et al.*, 2012; Correia *et al.*, 2014; Lam *et al.*, 2014).

In the developing embryo, the human heart is one of the first organs to form through hyperplasia of fully differentiated contractile cardiomyocytes (Zandstra *et al.*, 2003). The formation of the heart comprises of four key stages being successively completed. Simplified, mesoderm formation occurs initially which then leads to the specific development of the cardiogenic mesoderm. Cardiac-specific progenitors are then generated, ultimately concluding in cardiomyocyte differentiation to produce the beating myocardium (Chow *et al.*, 2013; Geuss and Suggs, 2013; Acimovic *et al.*, 2014). The heartbeat begins within as little as 3 weeks post-coitum and by 4 weeks typically beats between 105 and 121 times per minute (van Heeswijk *et al.*, 1990). During formation of the heart (perinatal and early postnatal development), the haemodynamic load dramatically increases as the heart assumes its primary role as a circulatory pump. Mechanical stimuli upon the heart muscle are amplified from the pressure increase and pulsatile volume changes. As a result of the increased work load, major changes in phenotype and function of cardiomyocytes occurs. Maturation of cardiomyocytes relies upon both extrinsic and intrinsic mechanical loads, which determine the geometry and pump function of the heart (Zhu *et al.*, 2014). Early studies by Porrello *et al.* (2011) in a murinal model showed cardiac regeneration was possible up to seven days postpartum. Although not wholly translatable to humans, Haubner *et al.* (2018) discuss a clinical case of human perinatal myocardial infarction (heart attack) which, within weeks following treatment, led to cardiac recovery with long-term normal heart development.

Several cell types have been experimentally investigated for cardiac repair, however cardiomyocytes remain the best candidate for donor cells due to their intrinsic

electrophysiological, structural and contractile properties (Zandstra *et al.*, 2003). Cardiogenic differentiation yields three cardiomyocyte phenotypes; nodal-like, atrial-like and ventricular-like, all found within the human heart. A pure population of a single type is required for clinical application, for example, nodal-like cardiomyocytes could be used for the generation of a biological pacemaker, whereas ventricular-like cardiomyocytes can be used for cardiac repair following myocardial infarction (Zhu *et al.*, 2010; Burridge *et al.*, 2012; Barad *et al.*, 2014). The human left ventricle contains approximately 6 x 10^9 ventricular cardiomyocytes. Patients can survive a myocardial infarction when no more than 35 % of the left ventricle is compromised. Regenerative therapies to repair the damaged tissue therefore require around 2 billion fully differentiated cardiomyocytes, capable of full integration into the recipient myocardium without losing the electrical and mechanical properties of the natural muscle (Schroeder *et al.*, 2005; Chen *et al.*, 2014). Successful integration, for example in the form of a cardiac patch, will need to be investigated in larger mammals with suitable/similar heart rates and then in a clinical setting before these therapies can reach globalisation (Chow *et al.*, 2013; Acimovic *et al.*, 2014). A clinical trial, ESCORT (ClinicalTrials.gov identifier: NCT02057900; Phase I), relying upon the transplantation of hESC-derived cardiac progenitors for the treatment of severe heart failure, is currently ongoing (Menasche *et al.*, 2015).

Much progress has been made towards the generation of cardiomyocytes (CMs), with a plethora of cell sources and differentiation procedures established. In addition to the potential of PSC-derived CMs for cardiac repair, there are also applications in areas such as drug screening, cardiotoxicity and disease modelling (Chow *et al.*, 2013). From previous work it has become evident that procedures mimicking cardiac embryogenesis, utilising specific stimuli such as combinations of electrical pacing, mechanical strain or hormonal stimulation, enhance the maturity, functionality and yield of differentiated CMs (Acimovic *et al.*, 2014; Savla *et al.*, 2014). The need to efficiently and robustly derive homogeneous populations of cardiomyocytes, capable of functional integration, are all obstacles to be further explored and developed before successful long-term clinical application of *de novo* cardiomyocytes (Acimovic *et al.*, 2014).

1.2 Literature survey

The following review is primarily concerned with experimental investigations on the impact of mechanical cues upon iPSC-CM differentiation yields. The applicability of some of these techniques at a large scale are critically reviewed, before considering the

importance of engineering characterisation, i.e. flow, mixing and suspension dynamics, for stem cell culture applications.

1.2.1 Stem cell therapies

Somatic stem cells are multipotent, capable of differentiating into cell types analogous to their tissue of origin. Somatic stem cells investigated for cardiac repair include bone marrow mesenchymal stem cells (BMSCs), cardiac progenitor cells and adipose-derived stem cells. Pluripotent stem cells are those capable of differentiating into any of the three germ layers within the human body and include embryonic stem cells (ESCs) and induced pluripotent stem cells (iPSCs). ESCs are isolated from the inner cell mass of a blastocyst and are capable of indefinite propagation when cultured under specific conditions. The same is true for iPSCs, artificially derived from somatic cells and made pluripotent through the addition of four transcription factors: OCT-4, SOX2, KLF4 and MYC, various combinations of which can be used (Takahashi and Yamanaka, 2006; Savla *et al.*, 2014). Pluripotent stem cells remain the primary cell source of choice due to their inherent ability to indefinitely propagate and are the most characterised in the area of cardiogenesis. Differentiation potential of ESCs and iPSCs have been reported to be close to identical, however, ethically iPSCs are preferred as they are not derived from human embryos, with the only obstacle to cell availability being the reprogramming efficiency (Lau, 2013). Allogeneic therapies elicit some immune response from expression of minor antigens and possible generation of immunogenic neo-antigens from genomic instability during the reprogramming process (Zhao *et al.*, 2011b). iPSCs also allow for generation of a genetic match and therefore can provide a personalised therapy with next to no risk of immune rejection (Araki *et al.*, 2013).

1.2.1.1 Cardiomyocyte differentiation from stem cells

Kehat *et al.* (2001) first derived early-stage cardiomyocytes from an embryoid body-based culture of human ESCs. Since then, an increasing amount of research into stem cell therapies and the potential to regenerate and repopulate the human heart through implantation of stem cell-derived cardiomyocytes has become an area of great interest. Stem cells can be directed to differentiate into cardiomyocytes through biochemical, chemical and physical stimuli, the end goal of these studies being the reproducible and efficient generation of cells capable of fully integrating and electromechanically coupling with the damaged native myocardium (Ge *et al.*, 2009; Geuss and Suggs, 2013; Acimovic *et al.*, 2014). Caspi *et al.* (2007) proved that transplantation of undifferentiated ESCs

following coronary ligation of a murine heart resulted in teratoma-like structure formation due to limited signalling in the damaged and scarred regions of the myocardium. Application of pre-differentiated ESC-CMs however, resulted in stable engraftment, where the cells survived, proliferated and matured, aligning and forming gap junctions with the recipient myocardium. Similar results have been seen in other studies, seeking to evaluate the feasibility of stem cell-derived cardiomyocyte application in murine models of myocardial infarction (Leor *et al.*, 2007; van Laake *et al.*, 2008).

There is currently no established platform for cardiogenic differentiation culture and many methods exist. Most commonly used methods include three-dimensional embryoid body (EB) or monolayer cultures, often including the application of various growth factors for modulation of signalling cascades of stem cell differentiation towards the cardiac lineage. Current methods are incapable of generating pure and mature populations of cardiomyocytes (Lian *et al.*, 2012; Kreutzer *et al.*, 2014). Originally, the formation of EBs (spherical stem cell aggregates) was the result of suspending cells in media with 20 % Fetal Bovine Serum (FBS). Cells were then cultured on gelatin-coated plates, spontaneously producing all three germ layers, including 5 – 15 % contracting and beating areas. The actual yield of cardiomyocytes however reached less than 1 % (Kehat *et al.*, 2001; Mummery *et al.*, 2003; Burridge *et al.*, 2012). Modifications to improve efficiency and directed differentiation was possible with the identification of growth factors and pathways associated with cardiogenic differentiation (Chen *et al.*, 2014). EB-based techniques may now include serum free suspension under hypoxic conditions (Burridge *et al.*, 2011; Kattman *et al.*, 2011) and forced aggregation protocols to eliminate heterogeneity in EB size (Acimovic *et al.*, 2014). Using BMP4 and FGF2 as mesoderm inducers under hypoxic conditions with a forced aggregation protocol, Burridge *et al.* (2011) achieved 94 % differentiation efficiency of generating beating EBs and observed spontaneous contraction from Day 7 in culture. Both suspension and forced aggregation methods commonly produce 70 – 90 % CMs however, the time constraints and technical complexity led to the development of monolayer based two-dimensional (2-D) methods (Savla *et al.*, 2014). The 2-D differentiation platform consists of cells expanded then differentiated in monolayer cultures via a change of growth to differentiation medium. Mummery *et al.* (2003) first successfully co-cultured ESCs with END-2 (mouse visceral endoderm-like cells), generating 85 % of cells exhibiting ventricular-like action potentials. Further improvements have been obtained through addition of other

cardiogenic growth factors or modulation of the Wnt signalling pathways, without growth factor addition (Laflamme *et al.*, 2007; Lian *et al.*, 2012; Geuss and Suggs, 2013).

1.2.1.2 Scalability

Two-dimensional monolayer differentiation strategies have been shown to produce approximately 2 x 10^8 cardiomyocytes per T225 flask. This translates to roughly 10 flasks needed to yield clinically relevant cell numbers for cardiac repair, manually cultured in parallel and often lacking in online process monitoring and control (Burridge *et al.*, 2012; Mihic *et al.*, 2014). Suspension protocols make use of EB techniques or cell adherence to microcarriers towards high-throughput, scalable and robust three-dimensional (3-D) stirred tank cultures (Ting *et al.*, 2012). Studies by Oh *et al.* (2009) and Phillips *et al.* (2008) proved that microcarrier-expanded stem cells exhibit the capacity to differentiate into cardiomyocytes, however, factors such as coating and microcarrier type, bioreactor design, operating conditions and feeding profile of media all affect this capacity.

A range of microcarrier types are commercially available for cell culture. Typically they are 100 – 300 µm in size, either microporous or macroporous in structure, and are made from a range of materials where cell attachment may be promoted through charged particles or a collagen coating (GE Healthcare Life Sciences, 2013). Fernandes *et al.* (2007) investigated ESC proliferation on Cytodex 3 and Cultispher-S. A 70-fold increase in cell density was achieved on Cultispher-S in serum-free conditions, where the increased macroporosity was believed to protect the shear sensitive cells from undesirable hydrodynamic forces. Rafiq *et al.* (2016) systematically investigated culture of hBMSCs on 13 different commercially available microcarrier types, comparing growth kinetics and metabolite flux. They concluded that the SoloHill Plastic microcarrier was the optimal candidate, yielding the best cell proliferation and proving amenable to xeno-free processing. Lecina *et al.* (2010) also systematically investigated different microcarrier types, DE-53, Cytodex 1, Cytodex 3, FACT, and TOSOH-10 to ascertain the impact of microcarrier concentration, size and shape upon ESC-CM efficiency. Culture utilising the TOSOH-10 microcarriers exhibited a 30 % increase in differentiation yield in comparison to EB culture and between 40 – 80 % increase in differentiation yields in comparison to the other microcarrier types. These studies all highlight the significant physiological influence microcarrier selection has upon a bioprocess and on bioprocess optimisation.

Zandstra *et al.* (2003) first demonstrated the feasibility of large-scale ESC-derived cardiomyocyte production, utilising a EB suspension and stirred spinner flask

differentiation protocol. Advanced function and phenotypic analysis of the resultant cells was not then possible, however considerable yields were achieved. Studies by Bauwens *et al.* (2005) (perfusion-fed bioreactor) and Schroeder *et al.* (2005) (stirred tank bioreactor) continued to provide evidence that 3-D culture methods using EBs were an effective tool for large-scale production of ESC-derived cardiomyocytes. Ma *et al.* (2011) demonstrated clinically relevant numbers of iPSC-derived cardiomyocyte in a 32-day EB suspension protocol. 3-D stirred cultures offer optimisation and control of key bioprocess operating parameters such as temperature, oxygen tension, pH and agitation, thus allowing for process reproducibility and repeatability.

Lam *et al.* (2014) investigated several cardiogenic differentiation protocols including monolayer differentiation techniques, replated ESCs from expansion on microcarriers, ESC-seeded microcarriers (ESC-MC) in static culture and ESC-MC in shaken (N = 110 rpm) and stirred spinner flask cultures (N = 30 rpm). The ESCs seeded onto microcarriers for differentiation in a stirred spinner flask culture, utilising an intermittent agitation profile, was found to yield 2.5-fold more than monolayer cultures and 10-fold higher than the replated, static and shaken suspension cultures. This study was a proof-of-concept comparison over multiple platforms and provided great insight into a scalable protocol, utilising physical cues from the intermittent stirred agitation profile. The two 16-hour intermittent phases were thought to alleviate agitation-induced necrosis due to the stress arising from turbulent eddies, microcarrier collisions and impeller- or vessel-to-microcarrier collisions. Literature has also suggested that intermittent agitation may be used such as to evenly distribute and promote cell attachment to microcarriers in culture. Liu *et al.* (2017), sought to establish a scalable platform for Vaccinia virus production in CV-1 fibroblast cells. To achieve this CV-1 cells were adhered to Cytodex 1 microcarriers utilising intermittent agitation for an initial 2 days in culture. The remainder of the protocol used continuous agitation. Fernandes *et al.* (2009) employed overnight intermittent agitation regimes for adherence of hESCs to Cytodex 3 microcarriers before continuous agitation for the remaining 15 days in culture. Dos Santos *et al.* (2011) and Nienow *et al.* (2016a) also reported improved microcarrier adherence protocols when utilising an intermittent agitation strategy during the first few hours post-inoculation.

1.2.2 Mechanical cues in cardiomyocytes generation

To ascertain effective differentiation strategies, it is apparent that an understanding of how the cardiac lineage is established from an early embryo is fundamental and

cardiomyocyte differentiation should primarily be based on the recapitulation of cardiogenesis *in vivo* (Chen *et al.*, 2014). Physiological cues to direct cardiogenic differentiation would save in chemical costs and provide a scalable source of cardiomyocytes, once optimised (Acimovic *et al.*, 2014). Studies investigating mechanical cues have shown the significant impact upon morphology, maturation, cell density and differentiation of stem cells, depending upon the type of stimulus that is applied, its magnitude and frequency of application (Maul *et al.*, 2011; Geuss and Suggs, 2013). Early research into mechanical cues focused upon vascular cell differentiation from BMSCs using shear stress, two- or three- dimensional structures inducing tension and cyclic stretch, or through the application of pressure (Hamilton *et al.*, 2004; Park *et al.*, 2004; Kreke *et al.*, 2005). A similar approach has been used to produce more efficient differentiation protocols of functional cardiomyocytes (Lau, 2013). Ge *et al.* (2009) cultivated BMSCs in differentiation medium with an extract from infarcted myocardium, applying 4 % cyclic strain at 1 Hz, a mimic of the contractile action of the heart. Individually the biochemical and physical stimuli induced cardiogenic differentiation, but when used in combination the most powerful induction of cardiogenesis was achieved.

Cells within a proximity to vasculature *in vivo* will continuously experience 1 – 2 Hz of cyclic strain, dependent on the lifecycle stage, due to the pulsatile blood flow and the rhythmic contraction of the myocardium with each cardiac cycle (Keung *et al.*, 2010; Zhu *et al.*, 2014). Special devices are made to exert this cyclic strain, such as the Flexercell units, which promote elongation and stretching of the cell membrane on flexible plates. A parametric study by Schmelter *et al.* (2006) investigated cardiomyogenesis of EBs attached to Flexercell plates exposed to varying levels of strain amplitude, between 5 and 20 % of the original plate length, for a fixed duration. It was established that 10 % strain significantly increased the proportion of beating regions. Gwak *et al.* (2008) observed upregulation of cardiac gene markers following differentiation of ESCs seeded onto stretcher platforms with a 10 % strain amplitude at a frequency of 1 Hz. Heo and Lee, (2011) also demonstrated upregulation of cardiogenic markers when Day 6 ESC-EBs were exposed to 10 % cyclic strain at a frequency of 1 Hz for one hour. These studies demonstrate 10 % strain at a frequency of 1 Hz improved the cardiogenic differentiation yields, however without better characterisation of the culture, it cannot be ascertained why these conditions are optimal. Wan *et al.* (2011) exposed ESC-EBs to 10 % cyclic strain at a frequency of 1 Hz for 24 hours on Day 9 of culture and observed a reduction in cardiogenic differentiation yields. This emphasizes why careful characterisation of the

system can inform upon the beneficial cues being imparted to better understand and optimise culture. Kreutzer *et al.* (2014) seeded PSCs onto a stretcher platform and observed that early application of cyclic strain at high frequencies detrimentally impacted upon cell survival and attachment. A variable cyclic strain approach was then adopted which showed no significant difference in cardiogenic gene expression between the static and stretched cultures. These studies demonstrate both the beneficial impact of mechanical cues and the sensitivity to magnitude, time and duration of application.

In addition to the stretch and strain devices mentioned, researchers have also investigated the addition of mechanical cues from hydrodynamic shear stresses to improve upon cardiogenic differentiation yields. Hydrodynamic stresses occur as a frictional force of fluid moving along cell surfaces. Illi *et al.* (2005) first observed the promotion of cardiogenic differentiation from the influence of hydrodynamic shear in monolayer cultures of ESCs, exposed to 10 dyn/cm^2 of laminar fluid shear stress for one hour. More recent studies have investigated hydrodynamic stresses in 3-D suspension cultures. Mogi *et al.* (2013) found that impeller rotational speed affected cardiogenic differentiation. EBs were formed using continuous agitation at a range of speeds and then adhered to plates. Outgrowths from the embryoid bodies began beating after 3 - 4 days, reaching up to 5 – 70 % at N = 30 - 100 rpm. EBs formed at 100 rpm were most uniform in size, increasing the reproducibility of results, and upregulation of cardiogenic genes and mature protein markers were observed. In static conditions no beating outgrowths were observed for two weeks following replating.

Wang *et al.* (2010) observed hydrodynamic shear in suspension cultures to reduce cardiogenic differentiation efficiency but hypothesised that this inhibition could be alleviated through intermittent agitation regimes. Later studies, such as the aforementioned study by Lam *et al.* (2014), have confirmed this and showed intermittent agitation to promote cardiogenic differentiation. Ting *et al.* (2014) investigated single-use wave bags and intermittent agitation for ESC-CM differentiation culture. The minimum rocking rate (30 oscillations/min) for suspension of aggregates was applied with intermittent dwell phases of 66 minutes following 6 minutes of agitation during the first 3 days of differentiation. 9 days of continuous culture followed. Static cultures exhibited ten-fold higher expression of cardiogenic markers over continuous culture, which in turn exhibited 40 % reduction in expression to intermittently agitated cultures.

Correia *et al.* (2014) sought to develop a robust and scalable platform for cardiomyocyte differentiation from iPSCs, utilising a DASGIP bioreactor system to mimic the

physiological microenvironment within the developing heart. A transgenic murine iPSC cell line was used, where the cardiac restricted α-MHC promoter drove expression of puromycin resistance and expression of eGFP. Following monolayer expansion, aggregation to embryoid bodies was performed using orbital shaker platforms before the EBs were transferred to a DASGIP bioreactor system, equipped with a trapezoid-shaped paddle impeller. Three agitation modes were then implemented throughout the hypoxic culture, continuous agitation at N = 90 rpm, yielding 11.3 ± 3.7 CM/seeded iPSC; intermittent agitation where the rotation direction was inverted in intervals of 30 s, producing 6.8 ± 1.1 CM/seeded iPSC, the lowest yield achieved; and intermittent agitation with a stop/start motion in intervals of 30 s (termed 'T_{inv}') with a 'dwell' phase of approximately 0.9 s (termed 'T_{dwell}'), generating 44 ± 2.1 CMs/seeded iPSC. Through assessment of GFP+ cells it was determined that CM/input iPSC yields were most significantly increased for the intermittent agitation mode without a direction change under hypoxic conditions. In comparison to continuous agitation utilising normoxic culture conditions over 1000-fold increase in differentiation yields was obtained. A further 50 % increase in yield was achieved when the differentiation protocol was transferred to a rocking WAVE culture. A pure atrial-like subtype of cardiomyocyte was generated in this study, believed to be influenced through the α-MHC promoter which drove antibiotic resistance, that is mostly active in atrial regions during early foetal development. The selection strategy in this case therefore favoured the production of the immature atrial-like phenotype.

1.2.3 Bioreactor configurations

Different bioreactors have been successfully used in the differentiation procedures outlined above. The DASGIP bioreactor systems, utilised mostly in cell culture applications, are designed for optimal bioprocess performance at a benchtop scale. They are available with two bottom configurations, flat and round, equipped with different impeller designs, commonly a paddle or axial 30° pitch down-pumping impeller. Heathman (2015) utilised this system for the expansion of hBMSCs on polystyrene P102-L microcarriers. The three-blade 30° down pumping impeller was equipped within a flat bottom DASGIP bioreactor and a range of rotational speeds was investigated [N = 80 – 225 rpm]. The minimum speed to suspend the microcarriers was visually determined at 115 rpm, which was then employed during proliferation. Nienow *et al.* (2016b, 2016c) have also reported culture of hBMSCs using the same bioreactor and impeller configuration. Teixeira *et al.* (2017) used a DASGIP bioreactor system for expansion of

hBMSCs cultured on Cytodex 3 microcarriers, magnetically agitated at 52 rpm using a modified four-paddle impeller. DASGIP bioreactors were employed for stem cell differentiation by Correia *et al.* (2014), as mentioned previously, in a flat bottom configuration equipped with a two-blade paddle impeller at N = 90 rpm. Rebelo (2015) used the same bioreactor configuration for the expansion of hBMSCs, agitation increasing incrementally from N = 80 rpm – 110 rpm over the culture period. The flat bottom configuration used by Correia *et al.* (2014) included a small dimple at the centre of the tank, absent in the studies reported by Heathman (2015) and Nienow *et al.* (2016b, 2016c). Venkat *et al.* (1996) suggested the inclusion of a dimple promotes suspension through causing flow convergence below the centre of the impeller.

Olmer *et al.* (2012) designed and tested a range of impeller types within the flat-bottomed DASGIP system, analysing the qualitative suspension and mixing characteristics of each through visualisation of the stained microcarrier distribution following agitation. Axial-flow pitched blade turbine impellers, of varying blade angles and blade diameter were investigated, as well as the two-blade paddle impeller used by Correia *et al.* (2014) and a radial-flow triangular shaped impeller. At lower rotational speeds accumulation of the microcarriers occurred either at the centre of the tank (axial impellers) or towards the reactor walls (radial flow). Increasing the rotational speed increased the distribution homogeneity for the larger diameter pitched blade turbines and the two-blade paddle impeller and so these two impeller types were deemed most suitable for cell culture experiments. The pitched blade turbine design is considered universally more applicable for larger scales, however culture experiments by the iBET group found, in the case of stem cell culture, the paddle impeller performed best (data not published). These studies indicate different configurations using the DASGIP bioreactors, however a systematic comparison of impeller and bioreactor geometry selection for particular applications, such as the investigation reported by Rafiq *et al.* (2016) for microcarrier types, is clearly needed.

1.2.4 Engineering characterisation

Flow, mixing and suspension dynamics can be empirically studied to obtain flow patterns, frequency spectra, quality of suspension and mixing efficiency of differing bioreactor configurations and operating conditions. Collignon *et al.* (2010) investigated agitation conditions based upon the suspension and flow dynamics such as to inform upon impeller selection for optimised cell-microcarrier cultivation, ensuring full suspension at reduced

shear stresses. Teo *et al.* (2012) highlighted that agitation and bioreactor configuration will induce varying degrees of shear that may affect sensitive stem cell differentiation pathways or lead to cell damage. For cardiogenic differentiation processes, shear stresses in excess of 2.5 dyn/cm^2 would cause a reduction in cell expansion and cellular damage, however a mild shear environment was found to promote cell viability and expansion, more so than a negligible shear environment (Lecina *et al.*, 2010; Teo *et al.*, 2012). Ismadi *et al.* (2014) characterised the flow within a cell culture to show minor deviation in shear stresses at various operating conditions significantly impacted upon biological outcomes. Ozturk, (1996) and Langheinrich and Nienow (1999) showed heterogeneity in culture pH due to mixing inefficiencies to result in cell lysis. Flow and mixing dynamics investigations by Ducci and Yianneskis (2007) and Doulgerakis *et al.* (2009) however, characterised the large-scale vortical structures within a bioreactor and showed the potential for mixing enhancement through amending the feed insertion location. From these observations it is evident that rigorous quantitative analysis is crucial to understand any causal relationship between the hydrodynamic environment and biological outcomes.

1.2.4.1 Flow dynamics studies in stirred bioreactors

Different laser-based techniques and computational approaches have been used to characterise the flow field with respect to circulation patterns, vorticity and shear to increase understanding of the interactions between the hydrodynamic environment with process variables (Kresta and Wood, 1993). The flow dynamics within stirred tank bioreactors are typically influenced by the impeller configuration; i.e. axial or radial flow types, impeller clearance, diameter, thickness etc, and the vessel configuration; i.e. flat or round bottomed, baffled or unbaffled (Rutherford *et al.*, 1996). The most commonly used impeller types in cell culture are the radial flow Rushton turbine impeller and axial flow Pitched blade turbine. Distinct circulation patterns are created from each impeller type, characterised by dynamic velocity fields in the axial, radial and tangential directions. Similarly, distinct and highly dynamic vortical structures are generated for each configuration, responsible for enhancing mixing by providing a source of turbulence.

In stirred tank bioreactors the main vortical structures generated are the trailing vortices in the impeller blade's wake, commonly characterised using laser-based techniques such as Particle Image Velocimetry (PIV) or Laser Doppler Anemometry (LDA) (Doulgerakis *et al.*, 2009). Radial Rushton turbine impellers develop a pair of trailing vortices, first characterised by Van't Riet and Smith (1975) using a visualisation technique, behind the upper and lower edges of the leading blade. Both vortices are characterised to move

outward from the blade towards the reactor wall and be slightly inclined, believed to be as a result of the free surface towards the top of the tank whereas the base of the tank is confined (Venkat *et al.*, 1996; Escudié and Liné, 2003). There is some disagreement in the literature regarding how far the trailing vortices extend within the flow, although this will largely depend upon the vortex threshold considered which is not always presented. Ranade *et al.* (2001) characterised the trailing vortices to decay at ≈ 40°, however Chara *et al.* (2016) detected the trailing vortices up to 100° and Sharp *et al.* (2010) found them present until 140°. In these cases, Sharp *et al.* (2010) used an unbaffled cylindrical vessel, whereas Chara *et al.* (2016) and Ranade *et al.* (2001) both used baffled bioreactors, all equipped with a six blade Rushton turbine impeller, D/T = 0.325 - 0.33. Schäfer *et al.* (1998) characterised the mean flow and turbulence structures generated by an axial flow, downward pumping four blade, 45° pitched blade turbine, D/T = 0.33. They describe a single trailing vortex formed behind each turbine blade with minimal radial displacement and a small downward axial divergence until merging into the bulk flow 135° behind the lead impeller, its final axial location lying below the subsequent impeller blade.

Yianneskis *et al.* (1987) showed the dependence of vortex trajectory on impeller configuration. Rushton turbine impellers at various impeller clearances and diameters were investigated. Flow visualisation revealed symmetrical, near horizontal vortical structures above and below the impeller at higher impeller clearances (C/T = 0.5 – 0.25), where increased upward inclination and maximum velocities were achieved as C/T reduced. Lower velocities were generated with decreasing impeller diameter (D/T = 0.5 – 0.25). Both flow velocities and vortical inclination were shown to decrease with rotational speed. Steiros *et al.* (2017) observed the increase of a standard Rushton turbine impeller blade thickness to also slightly increase the axial inclination of the trailing vortex trajectory.

Investigation of the flow field for various impeller and bioreactor configurations is well documented in the literature, of interest in this work is the impact of impeller D/T ratios upon the flow and a comparison between axial and radial impeller types, equipped within baffled and unbaffled configurations. For an axial flow three blade hydrofoil impeller, D/T = 0.33, in a baffled cylindrical vessel, Baldi and Yianneskis (2003) characterised ensemble-averaged axial velocities and velocity magnitudes up to $0.3V_{tip}$ and $0.26V_{tip}$, respectively. The vortical structures were also observed. Originating from the impeller blade, a vortex was shown to develop downward and extend radially towards the bioreactor wall. Story *et al.* (2014) investigated an axial flow six blade Prochem Maxflo

T (PMT) type impeller with *D/T* = 0.35 in a baffled cylindrical vessel and observed ensemble-averaged velocity magnitudes up to $0.5V_{tip}$. The flow field around a Rushton turbine is well documented, works by Yianneskis *et al.* (1987), Costes and Couderc (1988), Stoots and Calabrese (1995) and Deen *et al.* (2002), to name a few, measured radial velocities up to between 0.62 – $0.87V_{tip}$ for a cylindrical baffled vessel equipped with a radial-flow Rushton turbine impeller, *D/T* = 0.33. Similarly, Armstrong and Ruszkowsk (1987), Hockey and Nouri (1996), Schäfer *et al.* (1998) and Gabriele *et al.* (2009) describe peak axial velocities of 0.45 – $0.55V_{tip}$ for a standard baffled mixing vessel equipped with an axial flow 45° or 60° pitched blade turbine with *D/T* = 0.33. A study by Khopkar *et al.* (2004) investigated a six concaved-blade radial flow Scaba impeller, *D/T* = 0.5, in a baffled cylindrical vessel. Ensemble-averaged velocity magnitudes up to $0.25V_{tip}$ were observed with radial velocities reaching ≈ $0.6V_{tip}$. A similar impeller configuration was investigated by Zhao *et al.* (2011a), *D/T* = 0.4, who observed ensemble-averaged radial velocities up to 0.63 – $0.68V_{tip}$ for three variations of concaved blade impeller. The upper and lower trailing vortices, characterised for the concaved design, tended towards each other in the impeller blade wake and did not exhibit the slight axial displacement normally seen with the standard Rushton turbine.

Odeleye *et al.* (2014) showed velocity magnitudes characterised within a bioreactor are also affected by fill volume. Investigations were performed in an unbaffled Mobius 3 L CellReady bioreactor equipped with a three-blade marine impeller, *D/T* = 0.56. Phase-resolved measurements show velocity magnitudes decreasing with fill volume, V_w, up to $0.36V_{tip}$ and $0.29V_{tip}$ for 2.4 and 1 L, respectively. Mean flow characterisation exhibited a radial flow circulation pattern, similar to that of a Rushton turbine. Computational fluid dynamics (CFD) simulations reported by Kaiser *et al.* (2011) also observed radial fluid flow structures from the marine impeller. Ensemble-averaged velocity magnitudes and radial velocities up to $0.25V_{tip}$ and $0.37V_{tip}$ were observed. The trailing vortices were showed to move tangentially away from the impeller blade. Based upon the difference between the ensemble-averaged radial velocities and velocity magnitudes measured by Khopkar *et al.* (2004) and Odeleye *et al.* (2014), although ensemble-averaged velocity magnitudes are not directly observed in the literature for a Rushton turbine, this can be estimated using the ensemble-averaged radial velocities to be $\overline{U_{rz}} \approx 0.3 - 0.5V_{tip}$.

An interesting study by Ramsay *et al.* (2016) characterised the flow field of a "butterfly" impeller for increasing *D/T* = 0.53 – 0.98. It was found that as *D/T* and confinement against the reactor wall increased, ensemble-averaged velocity magnitudes discharged by

the impeller decreased 40 % from ≈ $0.25V_{tip}$ to $0.15V_{tip}$ at D/T = 0.53 and 0.98, respectively. A comparative study by Hall *et al.* (2005) investigated the flow fields created by a baffled, unbaffled and an eccentrically agitated bioreactor. The unbaffled and eccentrically agitated vessels, where the up-pumping six blade 45° pitched blade turbine was placed close to the bioreactor wall, generated a reduction in velocity magnitudes in comparison to the baffled configuration. **Table 1.1** summarises the range of axial and radial impeller types discussed in terms of increasing D/T and the maximum velocity magnitudes obtained through ensemble-averaged measurements.

Tamburini *et al.* (2018) used CFD methods to predict the flow field in both a baffled and unbaffled vessel, equipped with a Rushton turbine impeller. They found that during turbulent flow conditions, the radial and tangential components within the baffled vessel were reduced and converted into axial flow. Radial velocities overall remained dominant. In the unbaffled tank, solid body rotation occurred, and tangential flow dominated with weaker radial flow directed from the impeller region to the bioreactor walls. Larger turbulence was visualised in the baffled tank and axial flow is much stronger. The same effect was also reported by Yoshida *et al.* (2015) and Ciofalo *et al.* (1996). Montante *et al.* (2006) describe the 'vertical flow field', i.e. measurements taken on the *rz*-plane, to maintain approximately the same qualitative structures within both baffled and unbaffled configurations, with a notable reduction in the velocity components. Armenante *et al.* (1997) described a strong dominant axial-flow in a baffled vessel equipped with a pitched blade turbine. In an unbaffled system the axial impeller characteristics were reduced. Two weaker recirculation loops were evident above and below the impeller where a strong radial flow was observed. Hall *et al.* (2004) also described the pitched blade turbine in an unbaffled configuration to show a radial jet, most comparable to that of a Rushton turbine. For both radial- and axial-flow impellers, Hall *et al.* (2004, 2005) and Montante *et al.* (2006) discuss the unbaffled configuration to present significantly diminished radial and axial velocity components as a result of the dominant tangential flow to their baffled counterparts. Nienow *et al.* (2016b, 2016c) highlights that the probes present within the DASGIP configuration produce some baffling in an otherwise unbaffled bioreactor.

Impeller design and flow pattern, combined with bioreactor configuration, all impact upon the flow and vortical structures generated. The studies by Collignon *et al.* (2010) and Ismadi *et al.* (2014) are good examples of flow characterisation to inform upon a cell culture process. Collignon *et al.* (2010) compared several axial impeller configurations within a round bottom bioreactor, operated at the respective determined just suspended

speed, N_{js}. The flow dynamics of each configuration was evaluated to inform upon shear intensity and power consumption. From this investigation, impeller selection for optimal mammalian cell culture conditions was possible, ensuring full suspension whilst minimising the effects of shear. Ismadi *et al.* (2014) investigated the flow dynamics in spinner flasks to assess the impact of agitation upon iPSC proliferation. The maximal local shear rates, τ_{max}, were shown to increase linearly with rotational speed. Optimal cell proliferation was achieved at N = 25 rpm, with shear rates characterised up to 0.984 dyn/cm^2, however microcarrier attachment was no longer maintained at N = 28 rpm, less than 10 % increase in τ_{max} up to 1.08 dyn/cm^2. Such profound opposing effects within a small shear and rotational speed range show how susceptible iPSCs are to their hydrodynamic environment and how invaluable it is to characterise the flow dynamics.

1.2.4.2 Mixing dynamics

Cells cultured within a heterogeneous environment are exposed to spatial gradients in oxygen, pH, nutrients and temperature, especially in larger scale cultures, which can compromise cell viability, proliferation, differentiation pathways, metabolism and overall yields achievable (Lara *et al.*, 2006). Should the characterised mixing times exceed or be of a similar order of magnitude to rate-limiting cellular processes or reactions, then heterogeneities within the flow, either globally or within a localised region, will occur. The impeller and bioreactor configurations may also result in regions of slow mixing or stagnant zones. In both cases, quantifying the mixing time can help predict the presence of heterogeneities and is a good indicator of the mixing performance. Mixing time can also be used as a parameter for comparison or scaling (Doulgerakis *et al.*, 2011). A dimensionless parameter also used for comparison of mixing performance with different bioreactor configurations is the Mixing Number, Nt_m, defined as the number of revolutions required to achieve a specified degree of homogeneity.

$$Nt_m = N \times t_m \quad \textbf{(1.1)}$$

Where N is the rotational speed and t_m is the defined mixing time. With any given bioreactor configuration this value becomes constant in turbulent flow.

Mixing times are characteristically longer for cell culture processes due to the inherent sensitivity of the cells requiring moderate-to-low rotational speeds. Due to slow mixing zones, Ozturk (1996) observed cell lysis from locally elevated pH levels within the region of base addition in a mammalian cell culture. Langheinrich and Nienow (1999) also observed significant differences in pH (up to 1.0 unit) between the bulk and region of

base addition to levels potentially detrimental to cell viability. They concluded that assessment of spatial and temporal mixing dynamics could aid in selection of the location of base addition, or in the selection of operating conditions to circumvent pH excursions. Works published by Ducci and Yianneskis (2007) and Doulgerakis *et al.* (2009) used laser-based techniques to characterise large-scale flow structures (macroinstability and trailing vortices), observing improved feed locations towards mixing enhancement. Utilising a conductivity probe to assess mixing with addition of KCl, Ducci and Yianneskis (2007) showed a 20 – 30 % reduction in measured t_m when insertion is made in the vortex core of the precessional macroinstabilities. Further enhancement was predicted by Doulgerakis *et al.* (2009) in the impeller vicinity with the combined presence of the trailing vortex and macroinstability structures.

These works demonstrate how quantification and assessment of flow and mixing dynamics can be used towards the enhancement of biological outcomes and process optimisation, in this case from the avoidance of culture heterogeneities (Grein *et al.*, 2016). Generally, mixing time, t_m, is the time taken for the bulk flow to reach a specified degree of homogeneity following a perturbation. The techniques for defining t_m are generally categorised into two groups; local and global measurement techniques. Local point-wise measurement methods tend to utilise a probe within the reactor volume that provide the time to homogeneity for a single point within the bulk volume, multiple probes can be included for multiple points of measurement (Kasat and Pandit, 2008). These measurement types are accurate and can be used in large scale industrial tanks, however, they are intrusive and therefore affect the flow patterns and are unable to quantify/identify dead zones. Global volumetric measurement techniques can quantify the degree of mixedness in the entire flow volume. These techniques are non-intrusive to the flow and can identify and quantify unmixed zones. The main drawback of these techniques is the need for a transparent vessel for visual determination which historically was subjective and inaccurate. More recently however, computational image analysis has been employed to circumvent this issue.

Müller (1985) first observed non-subjective global mixing time definition through tracer addition of methylene blue. Black and white images were taken and grey-tone distribution was manually analysed in 60,000 points to obtain t_m. Lee and Yianneskis (1997) proposed a global measurement technique based on the colour-change of a fluid with addition of a small volume of higher temperature fluid. Liquid crystals within the bulk volume changed colour upon contact with the higher temperatures, which was then computationally

analysed to determine mixing. The experiment was considered fully mixed when 95 % of the image pixels reached a uniform hue value. This technique, although proven to be effective with turbulent flows, was restricted to investigating fluids of equal density to the liquid crystal microcapsules such that they were neutrally buoyant.

Melton *et al.* (2002) defined the dual indicator system for mixing time (DISMT). A global measurement technique utilising two indicators, methyl red, which is red under acidic conditions, turning yellow above pH 5.6 and thymol blue, which is blue under basic conditions and turns yellow at pH 8. Both indicators show yellow between pH 5.6 – 8, termed the "mixed within tolerance" range. The dual indictor technique presents 3 distinct colours over the duration of mixing; yellow, representing "mixed within tolerance" at the molecular level; red representing unmixed acidic regions; and blue representing unmixed basic regions. Rapidly mixed yellow regions can be distinguished from slower and unmixed mixed regions though the stepwise changes in colour within the bioreactor. The advantage of the dual indicator is that dynamics of the mixing process can be temporally and spatially assessed. Tan *et al.* (2011) highlighted that this technique indicates colour uniformity when the pH threshold is reached, not pH homogeneity. Comparison with other mixing time techniques should therefore be made conservatively. To demonstrate, Delaplace *et al.* (2004) developed DISMT mixing time measurements, captured on a high-resolution camera with computational frame analysis. Mixing time was defined as the point where the global brightness of the green colour in the RGB images achieved 90 % homogeneity. The mixing number obtained, Nt_m = 108, differs from that previously established for the same bioreactor configuration. Utilising a conductivity probe, Nt_m = 67 was observed (Delaplace *et al.*, 1999, 2004).

Cabaret *et al.* (2007) thoroughly investigated the DISMT technique to optimise both the experimental and post-processing aspects, proving their results to exhibit a high degree of reliability and reproducibility. Measurement accuracy is heavily influenced by the probe size. As mixing kinetics are obtained through image analysis, Cabaret *et al.* (2007) describes pixel size to be the equivalent. Through multiple measurements the minimum sensitivity of 4.48 pixels/cm^2 was determined for reproducible and reliable measurement; equivalent to 7.71m^2 measurement volume for a 720 x 480 pixel camera. Higher resolution cameras are now commonly employed; thus, resolution does not have an impact upon results. Background illumination, including varied light intensities and heterogeneous illumination were also observed to not affect mixing time measurements. In their work, Cabaret *et al.* (2007) presented the distinction between micromixing, when

acid and base are mixed and neutralised at a molecular level, and macromixing, where a tracer is uniformly distributed in the reactor, observed by the mixing time.

Further enhancement of DISMT reproducibility was shown through assessment of t_m using the standard deviation of the green colour component with the utilisation of a syringe pump for base addition, reported by Rodriguez *et al.* (2013) in an orbitally shaken bioreactor system. Through a purposely written code for image post-processing, mixing time of segregated regions were also ascertained, termed 'mixing maps'. As highlighted by Ducci and Yianneskis (2007) and Doulgerakis *et al.* (2009), Rodriguez *et al.* (2014) also observed the mixing time to be highly dependent upon the feed location of base addition. Their studies were undertaken in an orbitally shaken reactor, where insertion close to the edge of the toroidal vortex resulted in more effective mixing, ensuring the avoidance of entrainment of base within the vortex.

Tan *et al.* (2011) investigated the impact of fluid viscosity on t_m in shaken Erlenmeyer flasks, utilising a single indicator colorimetric technique. Both water and polyvinylpyrrolidone solution, eliciting a 38–fold increase in viscosity, were investigated up to V_w = 500 mL. Mixing times up to 2 s in water and 65 s in higher viscosity solutions were observed. Lower fill volumes decreased this difference. Bach *et al.* (2017) also investigated the impact of fluid viscosity on mixing time in a stirred tank reactor equipped with an axial-flow hydrofoil impeller, utilising a conductivity probe to assess homogeneity following addition of NaCl. Mixing time was shown to decrease with increasing N, reaching a plateau as turbulent flow developed. No significant change in t_m was observed between water and two xanthum gum solutions, both of which exhibited shear-thinning properties with increasing shear/rotational speeds. Results were also shown to correlate well with CFD predictions for all conditions investigated.

Kaiser *et al.* (2011) investigated the impact of fill volume on mixing time, using a single indicator colorimetric technique, within a CellReady Mobius bioreactor equipped with a marine impeller. A significant increase in t_m was observed with increasing fill volumes (V_w = 1.5 - 2.5 L) due to increased slow mixing regions at the liquid surface, distant from the impeller region. CFD confirmed the reduction in fluid velocity magnitudes in the upper region of the tank with higher fill volumes. Nt_m = 34 was reported for the marine impeller in turbulent conditions. This was comparable to the performance range for conventional impellers reported by Liepe *et al.* (1998), for which Nt_m = 24 and 30 for Rushton and pitched blade turbine impeller types, respectively. Comparison should however be made conservatively as different mixing time techniques were employed. van

Eikenhorst *et al.* (2014) observed t_m = 15 s for the CellReady Mobius bioreactor in fully turbulent flows utilising a pH probe to determine mixing time. At the same rotational speed and fill volume Kaiser *et al.* (2011) observed t_m = 7 s.

Grein *et al.* (2016) highlight that studies, such as those by Kaiser *et al.* (2011) and van Eikenhorst *et al.* (2014), observe mixing times within a single-phase system and then apply the findings to cell culture practises of a multiple-phase and more complex nature. Mixing time was therefore assessed using a single indicator colorimetric technique in two- and three-phase flows, aerated and non-aerated, in the CellReady Mobius bioreactor at V_w = 1 and 2.4 L. Multiple concentrations of microcarriers (0 – 30 g/L) were also evaluated. In agreement with the findings of Kaiser *et al.* (2011), t_m was shown to increase with fill volume. Higher rotational speeds decreased this difference. Aeration and microcarrier addition showed little impact to mixing time at lower fill volumes, however, when increased to 2.4 L, aeration reduced t_m by approximately 50 % at lower rotational speeds (N = 30 rpm). Interestingly this did not decrease further as N increased (N = 70 rpm), as seen previously, until significantly higher rotational speeds were utilised (N = 110 rpm). Increasing microcarrier concentration significantly increased t_m up to 50-fold at lower rotational speeds (V_w = 2.4 L, N = 30 rpm). As rotational speed increased to N = 70 rpm, the influence of the microcarriers became negligible. In agreement to the results presented by Grein *et al.* (2016), Madhuri *et al.* (2016) also observed increasing aeration to reduce characterised mixing times utilising a dual indictor technique.

The most recently established method to determine mixing combines image analysis with planar laser-induced fluorescence (pLIF). Measurements are non-obtrusively obtained in the laser plane with high spatial resolution. This is limited to smaller volumes due to the laser power required. Preferentially, this method is utilised to observe spatial mixing patterns rather than determine mixing time (Ramsay *et al.*, 2016; Rodriguez *et al.*, 2018).

Another non-invasive global determination method for mixing time is Electrical Resistance Tomography (ERT). One of the advantages of this technique is that transparent vessels and fluid mediums are not required. Mixing is monitored through the placement of small electrodes around the periphery of the vessel which measure electrical conductivity of the two species being mixed. In this manner the whole flow can be accurately and rapidly monitored and assessed, however due to the technical complexity to set these measurements up they are not always suitable to meet a researcher's needs (Cabaret *et al.*, 2007; Carletti *et al.*, 2016; Sardeshpande *et al.*, 2016).

1.2.4.3 Suspension dynamics

Often, cell culture studies focus on biological constraints and parameters without suspension characterisation of a bioreactor. Quality of suspension correlates with other parameters such as mixedness in a suspension culture. Operating at speeds at or above the defined minimum speed required for complete off-bottom suspension, N_{js}, ensures a homogeneous environment for solid phases present within the flow, such as microcarriers (MCs) or embryoid bodies (EBs). This maximises the available surface area for mass transfer processes and minimises unwanted cell-cell agglomeration and cell damage. Cherry and Papoutsakis (1986) defined three mechanisms for potential cell damage within a suspended culture environment; collisions between microcarriers with cells adhered to the surface, collision with the physical bioreactor environment (i.e. probes and impeller), and turbulent eddies. van Wezel (1985) suggested that slow agitation at N_{js} to maintain microcarriers in suspension without unnecessary excessive turbulence would be best for large scale cell cultures, however N_{js} must first be defined. More recent biological investigations, considering the optimisation of CM-differentiation through application of mechanical cues, suggest use of intermittent agitation modes (Correia *et al.*, 2014; Ting *et al.*, 2014) which may result in a degree of EB/MC settling during the intermittent phases. Both the degree of settling and N_{js} depend upon the EB/MC size, morphology and density, properties which are likely to change over the course of differentiation, as well as bioreactor and impeller configuration, the rotational speed and agitation mode employed (Ibrahim and Nienow, 2004; Nienow *et al.*, 2016a). This highlights the need for suspension characterisation to define N_{js} and guarantee full homogeneity and suspension, and to characterise the degree of settling during intermittent agitation modes.

The traditional technique for empirically ascertaining the just suspended speed, N_{js}, was defined by Zwietering as the speed at which solid particles do not remain on the vessel bottom for more than 1-2 seconds. The solid phase is stained to maximise visualisation from the base and the suspension criterion proposed by Zwietering is observed and subjectively assessed (Zwietering, 1958; Nienow, 1997; Ibrahim and Nienow, 2004). Newer, less subjective techniques utilise vertical plane visualisation of the dark stained solid phase, coupled with computational image processing to assess homogeneity of suspension across the reactor volume (Olmos *et al.*, 2015; Pieralisi *et al.*, 2016). Typically, N_{js} must be determined for each reactor configuration due to the large number of contributing factors that affect this parameter. Nienow (1997) stated that operating at lower rotational speeds to N_{js} may result in insufficient transfer rates for efficient cell

growth and optimal differentiation. Application of speeds in excess of N_{js} typically yield little to no improvement in mass transfer rates but may impart excessive shear stresses, impacting upon cell viability and attachment (Nienow *et al.*, 2016a). N_{js} can be calculated from Equation 1.2, originally developed by Zwietering (1958):

$$N_{js} = \frac{S d_p^{0.2} \left(\frac{g\Delta\rho}{\rho_L}\right)^{0.45} \upsilon^{0.1} X^{0.13}}{D^{0.85}} \quad \textbf{(1.2)}$$

Where S is a geometric parameter depending upon the impeller type. This equation was formulated considering particles up to three-times the density of microcarriers, which are considered neutrally buoyant. Ibrahim and Nienow (2004) compared empirically defined N_{js} for microcarriers and found Equation 1.2 to overpredict N_{js} by 50 %, thus visual determination was deemed most appropriate. An article by Ibrahim *et al.* (2012) discusses the need to incorporate porosity with calculations involving particle density. Zwietering's correlation (Equation 1.2) could therefore be modified, using an adjusted density approximation to account for porosity. The effective density, as suggested by Ibrahim *et al.* (2012), can be calculated as follows, where Φ is pore percentage:

$$\rho_{s,eff} = (1 - \Phi)\rho_s + \Phi\rho_L \quad \textbf{(1.3)}$$

Much of the literature emphasizes the sensitivity of cells, especially those grown on microcarriers, to hydrodynamic stresses. A study by Nienow *et al.* (2016c) demonstrates how understanding of the engineering environment can be used to inform upon a cell culture process through establishment of N_{js}, determined visually for a flat-bottom DASGIP bioreactor, equipped with an axial-flow pitched blade turbine impeller, *D/T* = 0.48. Once determined, stem cell cultivation studies at N_{js} = 115.2 rpm ensured minimised shear stresses with a homogenous culture environment.

1.3 Concluding remarks from the literature survey

The growing body of knowledge and studies focusing on cell regeneration and cell therapy, specific to cardiovascular research, show promise towards the reduction of the significant burden in healthcare expenditure and the improvement in patient quality of life. The pluripotency of both embryonic and induced pluripotent stem cells, along with their inherent ability to proliferate indefinitely, means they are the perfect candidate for an unlimited cell source for *in vitro* cardiogenic differentiation and regeneration of the myocardium. Although the field of cardiac regeneration has come a long way, much more work is needed to develop scalable and robust differentiation processes suitable for

clinical applications. Studies by Correia *et al.* (2014), Lam *et al.* (2014) and Ting *et al.* (2014) showed the significant impact of mechanical agitation strategies to optimise differentiation protocols through modulation of the hydrodynamic environment. In the case of Lam *et al.* (2014) and Ting *et al.* (2014), the significantly longer dwell phases and interval times in motion suggest that the observed beneficial impact is not relating to flow cues but rather from the introduction of essentially intermittent monolayer culture conditions. These systems cannot be considered fully three-dimensional with such a large two-dimensional component introduced, however it is evident that mechanical cues will have a key role in the final optimised protocol, alongside other cues. Overall, the impact of intermittent agitation upon CM differentiation has been proven to be beneficial, although no in-depth flow characterisation on the flow dynamics, i.e. fluid velocities, shear and turbulence, currently exists.

The fluid dynamics within traditional glass vessels equipped with conventional impeller types have been rigorously investigated using a plethora of laser-based and visualisation techniques. These studies have not been extensively employed towards characterisation of biological culture conditions for a specific application. The literature review highlighted the need to link engineering characterisation with the biological outcomes to ultimately optimise the process, based on quantifiable characteristics rather than trial-and-error approaches. The DASGIP bioreactor, for example, is mostly utilised in cell culture studies with a flat bottom configuration equipped with either an axial-flow pitched blade turbine (PBT), $D/T = 0.48$, or a radial-flow two-blade paddle impeller, $D/T = 0.97$. Works by Nienow *et al.* (2016b) utilise the flat bottom DASGIP, equipped with the axial PBT impeller, for expansion of hMSCs on microcarriers. Correia *et al.* (2014) utilised the flat bottom DASGIP bioreactor also, equipped with the paddle impeller for iPSC-EB differentiation procedures. Private communications with iBET found the PBT flat bottom configuration of the DASGIP, to detrimentally impact upon iPSC-CM differentiation yields. This suggests the different bioreactor configurations, proven to have a direct impact upon the quality of suspension, mixing dynamics and flow dynamics within the flow, also affected the biological outcomes in each case.

Different laser-based techniques and computational approaches have been used to characterise the flow field with respect to circulation patterns, vorticity and shear. Collignon *et al.* (2010) investigated the flow fields of several axial impeller configurations to establish shear intensity of each impeller type, whilst operating at the empirically determined N_{js}. Through this investigation it was possible to select an

impeller configuration such as to ensure minimal shear intensities, whilst also maintaining full suspension. Two studies investigating proliferation and maintenance of pluripotency in PSCs showed an axial flow PBT, operated at N = 50 – 100 rpm, generated shear forces of 2 – 5.2 dyn/cm^2 (Cormier *et al.*, 2006), whilst culture agitated with a radial paddle impeller at N = 80 – 120 rpm generated shear forces of 4.5 – 7.8 dyn/cm^2 (Kehoe *et al.*, 2010). In both cases pluripotency was maintained, demonstrating the complexity of engineering characteristics on cell behaviour. With greater understanding of the flow regimes and the 3-D environment it may be possible to optimise these processes further.

Vortical structures and characteristic flow velocities for numerous impeller and bioreactor configurations were also explored. For the Rushton turbine, a pair of trailing vortices were shown to form in the impeller blade's wake above and below the blade which deviated radially towards the bioreactor wall and were slightly inclined toward the liquid surface (Van't Riet and Smith, 1975). Schäfer *et al.* (1998) characterised the axial flow PBT to generate a single trailing vortex in the impeller blade wake with minimal radial deviation. For marine impeller, equipped within the CellReady Mobius bioreactor, a single trailing vortex was observed in the impeller blade's wake with little axial or radial deviation, moving tangentially away from the impeller blade (Odeleye *et al.*, 2014). The various studies discussed, investigating a range of impeller and bioreactor configurations, showed axial flow impellers to generally exhibit lower peak velocities to radial flow impellers; that unbaffled bioreactor configurations resulted in a reduction of flow velocity magnitudes in comparison to their baffled counterpart, whilst also favouring tangential flow; and as D/T and confinement of the impeller blade tip to the bioreactor walls increased, the velocity magnitudes decreased; **Table 1.1** summarises these findings.

Suspension and mixing capabilities vary with cell and microcarrier type, bioreactor and impeller configuration and rotational speed employed. Mixing time is a good indicator of mixing performance and can be used as a parameter for comparison or scaling, providing a universal technique for its determination is applied. Generally, mixing time investigations have shown a hyperbolic reduction in t_m with increasing N which plateaus once the turbulent regime is reached. Kaiser *et al.* (2011) showed higher fill volumes within a reactor increased mixing time, which in turn then becomes more influenced by changes in viscosity, aeration and the presence of microcarriers (Tan *et al.*, 2011; Grein *et al.*, 2016). Interestingly, lower fill volumes showed these parameters to have a negligible impact upon t_m. Feed location of the perturbation being measured during mixing time was also shown to affect mixing efficiency (Ducci and Yianneskis, 2007;

Rodriguez *et al.*, 2014). Nienow *et al.* (2016b) demonstrated establishment of N_{js} was beneficial to minimise excessive shear stresses whilst ensuring a homogenous suspension culture environment. Only with the characterisation of N_{js} and t_m can spatial and temporal homogeneity and mixing be realised.

Overall, the benefit to characterising and quantifying biological culture configurations, based upon engineering characteristics, is that the system becomes more understood, offering flexibility in operation, scalability and the prospect of process optimisation. This forms the overall hypothesis of this thesis.

1.4 The present contribution

The study presented by Correia *et al.* (2014) forms the basis of the current work and provides the rationale for exploring the change in the hydrodynamic environment over the three agitation modes reported. To this end, Laser Doppler Anemometry (LDA) measurements were carried out for characteristic flow frequency investigation of the agitations modes described in Correia *et al.* (2014), motivated by the lack of understanding in the hydrodynamic environment, and the desire to correlate this with biological outcomes. Modulation of various identified time components, introduced with intermittent agitation, was performed in parametric studies to correlate the impact these components had upon characteristic flow frequencies imparted. iPSC-CM differentiation cultures were then conducted to demonstrate the importance between the engineering aspects characterised with biological behaviour.

Studies of the flow dynamics, vorticity and shear in two bioreactor configurations were made to improve understanding of the impact reactor bottom geometry and impeller configuration had upon biological culture. Work by Correia *et al.* (private communications) observed the same iPSC-CM differentiation protocol in a round bottom DASGIP configuration, with a larger impeller clearance, to result in a significant reduction in cardiomyocyte differentiation yields. Intermittent agitation was also investigated to supplement understanding of the transient conditions following the 'stop-start' in impeller motion upon the hydrodynamic environment. An attempt was made to characterise the shear, turbulence and velocity profiles during the transient between dwell phases.

Mixing dynamics of both the intermittent and continuous agitation modes were also investigated using a reproducible and reliable technique recently established.

Establishment of t_m was obtained for the first time in a bioreactor configuration often used for cell culture and an attempt was made to investigate the impact of intermittent agitation.

Suspension and settling characterisation were also carried out in two bioreactor configurations to investigate the impact of intermittent agitation modes on the quality of suspension and the extent of settling. Application of various microcarriers in this study served both as a mimic of EBs in culture, before and after differentiation, in addition to a more general comparison of microcarrier types, varying in size, density and porosity.

1.5 Outline of the thesis

The remainder of this thesis comprises five chapters. Chapter 2 outlines the bioreactor and impeller configurations investigated, along with the experimental techniques used to determine the characteristic flow frequencies, suspension and mixing dynamics and the velocity, vorticity, shear and turbulence characteristics within the flow. iPSC differentiation culture and performance analysis are also described.

Chapter 3 presents the results of LDA and cell culture studies using the flat bottom DASGIP bioreactor, equipped with a trapezoidal two-blade paddle impeller. In this chapter investigation of the different agitation modes is reported and parametric studies of three time components, established with the introduction of intermittent agitation, are used to inform upon the experimental conditions investigated in cell culture studies.

The mean flow and hydrodynamic environment generated by the two-blade paddle impeller in both the flat bottom and torispherical round bottom DASGIP configurations was determined using Particle Image Velocimetry (PIV) in Chapter 4 for continuous agitation. Suspension dynamics of both configurations was determined and the influence of intermittent agitation on suspension and settling was then investigated further in the flat bottom configuration.

In Chapter 5 the fluid flow dynamics during intermittent agitation for the flat bottom DASGIP bioreactor, equipped with the paddle impeller, was investigated using PIV. The transient between impeller motion and each dwell phase was studied and the impact upon the overall hydrodynamic environment was evaluated. The DISMT technique was then applied to estimate and compare mixing time for both continuous and intermittent agitation modes in the flat bottom DASGIP system.

Finally, Chapter 6 presents a summary of the main conclusions established with this project, in addition to recommendations for future work.

Impeller Type	Impeller Flow	*D/T*	$\overline{U_{rz}}/V_{tip}$	Reference
Rushton turbine	Radial	0.33	0.3 – 0.5*	* estimated
Hydrofoil	Axial	0.33	0.26	(Baldi and Yianneskis, 2003)
Prochem Maxflo T (PMT)	Axial	0.35	0.5	(Story *et al.*, 2014)
Pitched blade turbine	Axial	0.45	0.55	(Gabriele *et al.*, 2009)
Scaba Impeller	Radial	0.5	0.25	(Khopkar *et al.*, 2004)
Butterfly	Axial	0.53	0.25	(Ramsay *et al.*, 2016)
Marine	Radial	0.56	0.25	(Odeleye *et al.*, 2014)
Butterfly	Axial	0.98	0.15	(Ramsay *et al.*, 2016)

Table 1.1 Literature comparison of ensemble-averaged maximal velocity magnitudes for impeller configurations of increasing *D/T*.

CHAPTER 2 BIOREACTOR CONFIGURATIONS AND EXPERIMENTAL TECHNIQUES

2.1 Introduction

In this chapter the bioreactor and impeller configurations employed in the present work are presented in Section 2.2. Section 2.3 and 2.4 provide an outline of the principles and characteristic parameters of Laser Doppler Anemometry (LDA) and Particle Image Velocimetry (PIV), respectively, utilised for flow frequency and velocity measurements acquired within the bioreactor configurations under investigation. Sections 2.5 and 2.6 outline the techniques employed for measurement of mixing and suspension dynamics, respectively. Rheological measurements are described in Section 2.7. Section 2.8 presents the cell culture protocols for iPSC-CM differentiation and the analytical techniques employed.

2.2 Bioreactor configurations

All measurements were conducted in a flat-bottomed DASGIP Cellferm-pro bioreactor system made of glass (Eppendorf, Germany) with height, H = 0.155 m and diameter, T = 0.062 m, equipped with a non-standard trapezoidal paddle impeller with arms (D = 0.06 m and D/T = 0.97), at an off-bottom clearance, specified in design by the manufacturer, C = 0.01 m (C/H_L = 0.151). The paddle impeller, of blade thickness t_B = 0.002 m, was equipped with a perpendicular magnetic pill, 0.03 m in length and 0.006 m in diameter, as this was inserted for the original magnetically-driven agitation conditions. A working volume of V_w = 200 mL was used for the engineering characterisation and cell culture experiments, corresponding to a liquid height, H_L = 0.0662 m. MilliQ water was used in the engineering characterisation studies to mimic the differentiation media used by Correia *et al.* (2014). A small dimple in the centre of the tank base, with a height of 0.084 m, was present for avoidance of dead-zone formation beneath the impeller. For all experimentation procedures, modifications were made such as to achieve motor-driven agitation from the original magnetically controlled agitation setup used. A mimic of the original magnetic paddle impeller was made from polytetrafluoroethylene. The impeller shaft was extended to connect to either an N-Series Allen Bradley Motor unit, or an MP-Series Low inertia (MPL) Servo motor (Rockwell Automation, Milwaukee, WI, USA), raised above the headplate to achieve the same impeller clearance to the original magnetic

stirrer configuration. This allowed for more precise control of the impeller motion. The original stainless steel headplate was used, with all sampling ports sealed, maintaining the installation of the temperature probe jacket, permanently welded into the headplate. The motor was connected to an Ultra 3000 Servo drive and controlled using the Ultraware software (Rockwell Automation, Milwaukee, WI, USA). A torispherical round-bottomed DASGIP Cellferm-pro bioreactor system (Eppendorf, Germany) with height, H = 0.165 m and internal diameter, T = 0.062 m, equipped with the same impeller configuration at C = 0.017 m (C/H_L = 0.261) was also utilised for the velocity measurements and quality of suspension analysis, described in Sections 2.4 and 2.6, respectively. A schematic representation of both the flat and round-bottom bioreactor geometries are depicted in **Figure 2.1**. The impeller dimensions and geometry are detailed in **Figure 2.2**. For the engineering characterisation studies, the cylindrical DASGIP system was mounted within a large square glass trough filled with 20 L MilliQ water to minimise diffraction due to the curvature of the bioreactor.

Continuous and intermittent agitation modes were investigated. For intermittent agitation, three time-components were defined, namely, the impeller rotational speed N, the interval time, T_{inv} and the dwell/stop time, T_{dwell}. T_{inv} is the time during which the impeller is in motion and T_{dwell} defines how long the impeller is stopped during a dwell phase. In Correia *et al.* (2014) N = 90 rpm for continuous and intermittent agitation modes with and without a direction change were employed at T_{inv} = 30 s and T_{dwell} = 900 ms.

For both the LDA and PIV measurements a cylindrical coordinate reference was employed, as shown in **Figure 2.3**, with the radial, axial and tangential coordinates indicated by r, z and θ, respectively. The origin is positioned in the centre of the bioreactor base and the tangential coordinate, θ = 0° corresponds to a plane located in the centre of the impeller blade, with anti-clockwise rotation being the positive direction when seen from above. It should be noted that in some figures reported, reference is made to negative radial coordinates, r, which, although not consistent with the cylindrical coordinate system employed, is used to discriminate between the left and right bisectors of the reactor volume about the impeller axis. The origin of the phase angular coordinate, φ, is set on the leading blade of the impeller. Phase angle φ = 0° is the vertical plane through the middle of the impeller blade.

The MPL motor unit used can run at a maximum speed of 5000 rpm with a 1.3 kW rated power output and a built-in multi-turn high-resolution encoder, capable of up to two million counts per revolution on position feedback. The N-series motor unit can run at a

maximum speed of 6000 rpm and was equipped with a rotary encoder, capable of up to 4,000 counts per revolution on position feedback.

iPSC culture experiments (described in Section 2.8) were performed using the DASGIP BioBlock, equipped with an online data acquisition and control DASware 4.0 software (Eppendorf, Germany). A support was constructed around the BioBlock to mount the motor for adapted overhead motor-driven agitation. The motor was connected to an Ultra 3000 Servo drive and controlled using the Ultraware software (Rockwell Automation, Milwaukee, WI, USA). The assembled experimental rig is shown in **Figure 2.4**.

2.3 Laser Doppler Anemometry

2.3.1 Principles of operation

Laser Doppler Anemometry (LDA) is an optical-based technique, widely used for non-intrusive, single-point fluid dynamic investigations. This technique is based upon the key principle that scattered light reflected by a moving object exhibits a shifted frequency, proportional to the speed of the moving object. Two laser beams generate a measurement volume in the intersecting region, characterised by an interference pattern comprising light and dark fringes. The spacing between the fringes, λ, depends upon the laser wavelength and angle of intersection between the two beams. Small, neutrally buoyant and reflective seeding particles are inserted into the flow and as each passes through the probe volume, crossing the light and dark fringes, a 'Doppler burst' is generated. The frequency of the Doppler bursts, Doppler frequency, f_D, represents the difference between the incident and resulting scattered light frequencies and is proportional to the velocity component perpendicular to the bisector of the two laser beams, defined in Equation 2.1:

$$u = f_D \times \lambda \quad \textbf{(2.1)}$$

f_D can be measured as the fluctuation of scattered light intensity, detected by a photomultiplier tube, as seeding particles cross the probe volume. The Doppler frequency measured exhibits directional ambiguity, particles moving in opposite directions at the same velocity would equate to the same velocity measured. To resolve this, the Bragg cell, used to split the laser beam, applies a frequency shift, f_S, to one beam such that the measured velocities become proportional to the sum or difference of f_S and f_D, depending on the direction of movement. Velocity, accounting for direction is given in Equation 2.2:

$$u = (f_D \pm f_S) \times \lambda \quad \textbf{(2.2)}$$

2.3.2 Experimental setup

A four-channel Dantec Ltd. LDA system was employed for velocity measurements. One velocity component was measured with the intersecting laser beams entering from the side of the bioreactor using a two-dimensional probe, mounted on a traverse capable of movement in three orthogonal directions: *x*, *y* and *z*, to an accuracy of 0.05 mm. A schematic representation of the working principle of LDA and its arrangement is shown in **Figure 2.5**.

An air-cooled Stellar PRO-L argon ion laser (Laser Physics, Cheshire, UK), providing a maximum output power of 300 mW with a beam diameter of 0.75 mm, was used for the experiments. A transmitter box was positioned and aligned with the incoming beam to maximise the laser light collected. A Bragg cell within the transmitter box splits the laser to two equal intensity beams, one of which is shifted by f_S = 40 MHz. The laser beams are then separated to three different colour channels of three different wavelengths (λ_{green} = 514.5 nm, λ_{blue} = 488 nm and λ_{violet} = 476.5 nm) and are directed into the flow by the probe, working in back-scatter mode. The laser light transmission is received into a single integrated unit and is sent to the photomultiplier. This then converts the light intensity to Doppler bursts, which is then filtered and amplified in a signal processor to determine f_D using Fast Fourier transform frequency analysis.

Upon installation of the laser, the probe was recalibrated and aligned using a pinhole with a diameter of 25 μm, ensuring the pairs of laser beams and receiving optics intersect at the same point with symmetric intensity and size.

PSP-20 Polyamid 20 μm particles (Dantec Dynamics A/S, Skovlunde, Denmark) were used as seeding particles as they were sufficiently small and neutrally buoyant to follow the fluid flow accurately. They were also capable of light scatter to be detected by the photomultiplier unit. The concentration added was minimalised such as to avoid biased signals from multiple particles crossing the probe volume.

LDA velocity data was obtained at two measurement locations, point A (r_A/T = 0.35 and z_A/H_L = 0.28), within a close vicinity to impeller agitation and blade passage; and at measurement point B (r_B/T = 0.35 and z_B/H_L = 0.58), in a plane most likely to represent the bulk flow, + 20 mm in the *z*-direction. **Figure 2.6** (a) is a side view of the experimental rig, showing the two measurement locations A and B. **Figure 2.6** (b) gives a plan view of the bioreactor, schematically showing the orientation of the beams and probe arrangement for measuring the tangential velocity component.

Parametric studies investigating the impact of a change in T_{inv} and T_{dwell} were performed. Three interval times were considered, T_{inv} = 5 s, 15 s and 30 s at constant T_{dwell} = 500 ms and N = 90 rpm. The dwell time was investigated within the range T_{dwell} = 1 ms – 1500 ms at constant T_{inv} = 30 s and N = 90 rpm. In addition, studies were carried out at different rotational speeds where the number of missed revolutions, K^*, defined by Equation 2.3, was kept constant:

$$K^* = N \times T_{dwell} \quad \textbf{(2.3)}$$

At N = 90 rpm, T_{inv} = 30 s and T_{dwell} = 1500 ms, a value of K^* = 2.25 was calculated and maintained constant in subsequent experiments conducted at N = 75, 105 and 120 rpm. This was repeated for T_{dwell} = 500 and 1000 ms at K^* = 0.75 and 1.5, respectively.

A second phase was also introduced such as to validate all single-phase experiments using a mimic of embryoid bodies present in the biological studies. The EB mimics and their properties are discussed in Section 2.6.

2.3.3 Signal processing and data analysis

The photomultipliers amplified the collected Doppler signals, which were then processed by a Burst Spectrum Analyser (BSA) to determine the frequency, f_D, corresponding to the velocity of the particle crossing the probe volume. BSA Flow Software for LDA and PDA was used for acquisition and processing of LDA data (Dantec Dynamics A/S, Skovlunde, Denmark). The velocities measured were validated when f_D was shown to be at least four times higher than the second highest frequency peak in the spectrum of the burst. The signal gain and voltage of the photomultiplier were selected to optimise the data rate of acquisition and the percentage of validated samples. These values were kept constant throughout experimentation such as to minimise any variation of noise or amplitude of signals in latter spectral comparisons. Noise introduced to the signal was also minimised through avoidance of extraneous light sources; all reflective surfaces within the proximity of the experimental rig were covered and no background lighting was applied.

The arrival time for each validated velocity measurement, transition time across the probe volume and, where appropriate during intermittent agitation, the time of each impeller ‘dwell’ were collected. Once 500,000 events or counts of data had been obtained, these were then transferred from the BSA output buffer to the PC.

The N-Series Allen Bradley Motor unit was used for the LDA experiments, integrated with a rotary shaft encoder, it was possible to monitor the rotational speed and correlate

instantaneous velocities with the angle of rotation of the impeller. One marker pulse per revolution was provided from the motor and sent to the BSA to store the corresponding arrival time for subsequent phase-resolved measurements, processed offline. During intermittent agitation a second pulse was provided by the motor encoder upon initiation of each dwell phase such that the arrival time of each dwell could also be stored. Data processing was carried out using a purposely-written MATLAB code (Mathworks, USA).

In the present work time-resolved measurements were performed and analysed using Fast Fourier Transform techniques to convert the tangential velocities to the frequency domain and obtain the energy distribution of the velocity fluctuations in the flow. As measurements performed using LDA are unevenly distributed in time, resampling of the data using the 'nearest neighbour' interpolation with a resampling frequency equal to half the mean measurement data rate was applied. Phase-resolved measurements were executed to analyse the periodic fluctuation of flow motion. Each component of the phase-resolved mean velocity, $\langle U_\varphi \rangle$ is defined using Equation 2.4:

$$\langle U_\varphi \rangle = \frac{1}{M_{i\varphi}} \sum_{i=1}^{M_{i\varphi}} u_{i(\varphi)} \qquad \textbf{(2.4)}$$

Where φ is the phase angle and $M_{i\varphi}$ is the number of samples at that phase angle.

2.3.4 Sources of error and measurement uncertainties

Several sources of error must be considered when carrying out LDA experiments. Laser alignment was carried out by aligning the laser beams to the impeller shaft via visual inspection prior to acquisition. A spirit level was used to ensure the rig was correctly assembled and perfectly horizontal. For phase-resolved measurements, the marker pulse of the encoder was aligned to the midpoint of the impeller paddle blade. The laser beam was positioned in the $\theta = 0°$ plane, in the centre of the bioreactor, and the impeller shaft was slowly rotated until the midpoint of the blade coincided with the laser beam. The marker pulse was then aligned by rotating the shaft sleeving until the marker pulse showed on an oscilloscope at $\theta = 0°$ and at $\varphi = 0°$. Overall this is considered a systematic, not random, source of error with a relatively small impact upon the measured data. The impeller rotational speed was continuously monitored and was noted to vary by no more than ± 3 rpm.

The homogeneous, albeit random, distribution of seeding particles results in a Poisson distribution of particle arrivals. As the acquisition rate of data is not equispaced in time and is dependent upon instantaneous velocities the probability distribution function is

biased towards particles with higher velocities being measured. This velocity bias would result in an overestimation of the mean flow velocities. As such, calculated mean velocities, $\bar{U}$, are weighted using a transition-time weighted average where velocity measurements are weighted according to the transit time, *t*, in the probe volume.

$$\bar{U} = \sum_{i=0}^{N-1} \eta_i \, u_i \quad \textbf{(2.5)}$$

where η_i is the weighting factor of the *i*th particle passing the measurement volume.

$$\eta_i = \frac{t_i}{\sum_{j=0}^{N-1} t_j} \quad \textbf{(2.6)}$$

2.4 Particle Image Velocimetry

2.4.1 Principles of operation

Two-dimensional (2-D) Particle Image Velocimetry (PIV) was used to investigate the flow within the two DASGIP bioreactor configurations. PIV consists of a laser light source used to investigate a working fluid seeded with tracer/seeding particles. The seeding particles used are small in diameter and neutrally buoyant, assumed to faithfully follow and not interact with the flow. The seeding particles are illuminated by a continuous sheet of laser light on the plane of interest which scatter the light. Fluorescently labelled seeding particles are used, together with a wavelength-specific pass filter to remove background light and aid in the distinction between the solid and liquid phases. A high-speed camera records double exposure frames, processed via software to measure the displacement and relative motion of the particles between image frames. The image is divided into 'interrogation areas' and the local displacement vector is computed through a cross-correlation algorithm. The interrogation area size is selected such as to include between 3 – 10 tracer particles, where it is assumed that all particles within that area move in the same direction between frames. A schematic of the working principle of PIV is shown in **Figure 2.7**.

2.4.2 Experimental setup

A green diode laser, with an output power rating of 300 mW and wavelength, λ = 532 nm, was used for the PIV experiments, together with a cylindrical lens, a high resolution (1260 x 1024) NanoSense MKII camera (Dantec Dynamics A/S, Skovlunde, Denmark) and a timing box. A 1 mm vertical laser sheet was produced, intersecting the shaft and illuminating half of the bioreactor mid-section. The camera was placed orthogonal to the

laser sheet. Rhodamine-coated Polymethyl methacrylate spheres, 20 – 50 μm (Dantec Dynamics A/S, Skovlunde, Denmark), were used as seeding particles, coupled with a 570 nm orange light cut-off filter to minimise laser light reflection.

For phase-resolved measurements the PIV system was synchronised with the MPL Servo motor encoder, signalling impeller position $\varphi = 0°$ with a single marker pulse. For each rotational speed employed, a set time delay from the encoder signal at $\varphi = 0°$ was used to perform measurements at each phase angle investigated. For example, at $N = 90$ rpm one revolution (360°) is completed in 0.667 s. For measurement of $\varphi = 90°$ a time delay of 0.167 s is implemented from the encoder signal pulse. The impeller encoder is connected to a timing box such as to synchronise the camera trigger with the desired impeller position. This was done through the Dantec Dynamic Studio software, where a time delay can be selected for instantaneous vector maps at the desired angular position of the leading impeller blade. 12 phase angles were investigated for each continuous agitation condition between $\varphi = 0 – 165°$ in increments of 15°. 500 image pairs were obtained for each measurement condition, with the time delay of acquisition within each pair set to 3.5 – 2 ms for rotational speeds of 75, 90, 105 and 120 rpm, respectively. All experiments were carried out at room-temperature.

The flat-bottomed DASGIP bioreactor was used for the investigation of the intermittent agitation profiles, measurements were obtained separately, either during the intermittent dwell phase or during impeller motion. Intermittent agitation was investigated at $N = 90$ rpm, $T_{inv} = 30$ s and $T_{dwell} = 500$, 900, 1500, 3000, 6000, 9000, 12000, 20000 and 30000 ms. Measurements taken during impeller motion were obtained at a single phase angle of $\varphi = 0°$, for every revolution after the dwell for the total duration of T_{inv}, to investigate the transient between the end of the dwell phase and resuming agitation. 45 image pairs were obtained for each T_{inv} with this measurement repeated over 10 consecutive intervals. Measurements obtained during the impeller dwell phase were obtained in a time-resolved manner at the acquisition frequency rate of 0.02 kHz to maximise capture of the flow over time, balanced with the number of measurements obtained at the longer T_{dwell} durations.

2.4.3 Post-processing and data analysis

A two-pass adaptive correlation analysis was applied to each image with an initial interrogation window of 32 x 32 pixels and a final window size of 16 x 16 pixels. A 50 % interrogation area overlap was used for a final resolution of 8 x 8 pixels. The adaptive correlation analysis estimates velocity vectors in the larger interrogation window and uses

this to inform and improve accuracy for the next correlation step of a smaller window size. The velocity profiles of the radial and axial velocity components, u_r and u_z, respectively, are shown in **Figure 2.8** for four different interrogation windows at varying number of passes. The two-pass option with an initial interrogation window of 32 x 32 pixels was selected and used in this work.

JPIV open source software was used to correlate each image pair. Once the vector maps of the correlated pairs were generated, a normalised median test was performed to detect spurious vectors. Works by Westerweel and Scarano (2005) demonstrated the effectiveness of a single threshold value for erroneous vector detection and an acceptable fluctuation level as a result of PIV cross-correlation. As such, a threshold of 2.0 and a noise level of 0.1 were selected for the median test, based upon the recommendation of the aforementioned study. All flagged erroneous vectors were then replaced with the median value of eight surrounding vectors to that point, a function built-in to the JPIV software. Upon replacement, a 3 x 3 median filter was then applied using JPIV to 3 x 3 vector points. Every vector was replaced by the median of the surrounding vectors, including the original point under investigation. Data processing of the velocity maps was then carried out using a purposely-written MATLAB code (Mathworks, USA).

Similar to the deduction of phase-resolved measurements for LDA, given in Equation 2.4, mean phase-resolved instantaneous velocity fields were calculated using Equation 2.7:

$$\langle U_{(r,z,\varphi)} \rangle = \sum \frac{u(r,z)}{n_\varphi} \qquad \textbf{(2.7)}$$

Where n_φ is the number of velocity fields obtained at phase angle φ on the plane of measurement (r,z). Each phase average was calculated using 500 image pairs or for the 10 repeated measurements during intermittent agitation investigations. Ensemble-averaged data was calculated from 12 phase angles, φ = 0 – 165°, totalling 6,000 image pairs, using Equation 2.8:

$$\overline{U_{(r,z)}} = \sum \frac{u(r,z)}{n} \qquad \textbf{(2.8)}$$

Where n is the number of velocity fields obtained irrespective of the phase angle.

Velocity magnitude considers both the radial and axial velocity components, which is given in Equation 2.9:

$$u_{rz} = \sqrt{(u_r)^2 + (u_z)^2} \qquad \textbf{(2.9)}$$

Where u_{rz} denotes the magnitude, comprised of the radial, *r*, and axial, *z*, components respectively.

Vorticity was calculated from a two-dimensional grid using a central differentiation scheme, given in Equation 2.10:

$$\omega_\theta = {}^{\partial u_z}/_{\partial x_r} - {}^{\partial u_r}/_{\partial x_z} \quad \textbf{(2.10)}$$

Where u_z and u_r represent the velocity measurements taken in the axial and radial directions, respectively.

The standard triple decomposition technique, originally defined by Reynolds and Hussain (1972), was employed to decompose, *u*, the instantaneous velocity measured:

$$u_{(r,z)} = \langle U_{(r,z,\varphi)} \rangle + u'_{(r,z)} \quad \textbf{(2.11)}$$

This decomposition distinguishes between each phase-resolved velocity element, $\langle U \rangle$, related to the periodicity of the flow, i.e. $\langle U_{(r,z,\varphi)} \rangle = \overline{U_{(r,z)}} + \tilde{u}_{(r,z,\varphi)}$, with $\tilde{u}_{(r,z,\varphi)}$ denoting the periodic fluctuation associated to the periodic impeller blade passage and $u'_{(r,z)}$ denoting the random fluctuating turbulent component.

The ensemble-averaged root mean square (r.m.s) for each velocity component is calculated according to Equation 2.12:

$$\overline{U'_{(r,z)}} = \sqrt{\overline{\left(\tilde{u}_{(r,z,\varphi)} + u'_{(r,z)}\right)^2}} \quad \text{or} \quad = \sqrt{\overline{\left(u_{(r,z)} - \overline{U_{(r,z)}}\right)^2}} \quad \textbf{(2.12)}$$

This parameter represents the total velocity fluctuations and can be used as a measure of turbulence and pseudo turbulence for each velocity component.

The mean flow kinetic energy can be calculated using Equation 2.13:

$$\bar{k} = \frac{1}{2}\left(\overline{U_r}^2 + \overline{U_z}^2 + \overline{U_\theta}^2\right) \quad \textbf{(2.13)}$$

Given that a 2-D PIV system was used in this work, no data on the tangential velocity component ($\overline{U_\theta}$) is available. It is possible to estimate $\bar{k}$ using the pseudo-isotropic assumption (Gabriele *et al.*, 2009). Zhao *et al.* (2011) discussed the error of this assumption in comparison to 3-D models and concluded slight error that could be considered negligible. Thus, ensemble-averaged kinetic energy can be calculated:

$$\bar{k} = \frac{3}{4}\left(\overline{U_r}^2 + \overline{U_z}^2\right) \quad \textbf{(2.14)}$$

The kinetic energy of the periodic flow is calculated:

$$\langle k \rangle = \frac{3}{4}(\langle U_r \rangle^2 + \langle U_z \rangle^2) \quad \textbf{(2.15)}$$

The phase-resolved r.m.s distinguishes velocity fluctuations due to random turbulence alone and is calculated:

$$\langle u'_{(r,z)} \rangle = \sqrt{\overline{\left(u'_{(r,z)}\right)^2}} \qquad \text{or} \qquad = \sqrt{\overline{\left(u_{(r,z,\varphi)} - \langle u_{(r,z,\varphi)} \rangle\right)^2}} \quad \textbf{(2.16)}$$

The turbulent kinetic energy (TKE) of the random velocity fluctuations was estimated:

$$\langle k' \rangle = \frac{3}{4}\left(\langle {u'_r}^2 \rangle + \langle {u'_z}^2 \rangle\right) \quad \textbf{(2.17)}$$

The maximum local shear rate, γ_{max}, in the vertical plane was obtained from the principal components of the strain rate tensor, $S_{i,j}$, defined in Equation 2.18:

$$S_{ij} = \begin{pmatrix} 2\frac{\partial u_r}{\partial r} & \left(\frac{\partial u_r}{\partial z} + \frac{\partial u_z}{\partial r}\right) \\ \left(\frac{\partial u_r}{\partial z} + \frac{\partial u_z}{\partial r}\right) & 2\frac{\partial u_z}{\partial z} \end{pmatrix} \quad \textbf{(2.18)}$$

Where S_{zz} and S_{rr} are the local axial and radial strain rates and S_{rz} is the local shear rate. The principle components (eigenvalues) of Equation 2.18, S_1 and S_2 can indicate the highest local rate of stretching, when positive, or rate of compression, when negative (Bouremel *et al.*, 2009; Rodriguez *et al.*, 2016). As measurements were only taken in the vertical plane, the S_3 component of the strain rate tensor in the azimuthal direction must be estimated using the continuity equation whereby (Equation 2.19):

$$S_3 = -S_1 - S_2 \quad \textbf{(2.19)}$$

γ_{max} can then be calculated using Equation 2.20:

$$\gamma_{max} = \frac{(S_i - S_j)_{max}}{2} \quad \textbf{(2.20)}$$

Where selection of any two principal components; S_1 or S_2 is based upon the maximum difference, denoted by the indices *i* and *j* in Equation 2.20.

2.4.4 Sources of error and measurement uncertainties

Several sources of error must be considered when carrying out PIV experiments. Laser alignment is a principle source of error and uncertainty. The laser was initially applied at a reduced intensity and aligned within the bioreactor to the impeller shaft via visual inspection prior to acquisition. A spirit level was used to ensure the rig was correctly

assembled and perfectly horizontal. For phase-resolved measurements, the marker pulse of the encoder was aligned with the midpoint of the impeller paddle blade and the laser sheet was positioned in the $\theta = 0°$ plane, in the centre of the bioreactor. The impeller shaft was rotated until the midpoint of the blade coincided with the laser sheet. The marker pulse was then aligned by rotating the shaft sleeving until the marker pulse showed on an oscilloscope at $\theta = 0°$ and $\varphi = 0°$. Overall this is considered a systematic, not random, source of error with a relatively small impact upon the measured data.

The paddle impeller and shaft were painted with a black matte paint such as to ensure minimal reflection of the laser light. The impeller rotational speed was continuously monitored and was noted to vary by no more than ± 0.5 rpm.

The seeding density of seeding particles used can also be a source of error; too low may bias displacement in the latter auto and cross-correlation analysis; too high may make illumination and data collection difficult. The same concentration, 0.5 μL/mL of seeding particles, was used throughout.

A displacement gradient between interrogation cells is also a source of error. Higher velocity particles in the first interrogation cell may not be present in the second, therefore displacement is biased toward particles with lower velocities which are more likely to be present. Accuracy of measurements were improved through use of the adaptive correlation analysis, the application of the median test, and the 3 x 3 median filter applied.

2.5 Mixing time experiments

Mixing time characterisation was conducted in the flat bottomed DASGIP bioreactor using a global determination method, Dual Indicator System for Mixing Time (DISMT), first described by Melton *et al.* (2002).

As described in Section 1.2.4.2, DISMT is based upon a fast acid-base reaction between NaOH and HCl, monitored with the addition of two pH indicators, Methyl Red and Thymol Blue. Methyl Red is red under acidic conditions, turning yellow once pH 5.6 and above is reached. Thymol Blue is blue under basic conditions, turning yellow at pH 8.0 and below. Both indicators will show yellow in the neutral pH range of 5.6 – 8.0.

2.5.1 DISMT reagent preparation

Thymol Blue indicator was prepared in 70 % EtOH (Ethanol) at a concentration of 1.38 mg/mL. Methyl Red indicator was prepared at a concentration of 1.52 mg/mL in 70 %

EtOH. These stock solutions of the indicators were then added to MilliQ water at a concentration of 4.67 mL/L Thymol Blue and 4.26 mL/L of Methyl Red. The volume of distilled MilliQ water needed was 200 mL per experimental condition investigated, although larger stock solutions were prepared for multiple experiments. The stock solution was then prepared for DISMT through 5μL addition of 0.75 M NaOH, added incrementally until a colour change to bright yellow was visually observed.

2.5.2 Experimental setup

The macromixing time was evaluated in the flat bottomed DASGIP bioreactor configuration. The experimental rig used is depicted in **Figure 2.9**, with a mounted high-speed NET NS4133CU iCube camera with a 1280 x 1024 pixel resolution (NET, Germany), connected to an adjustable arm. To improve system resolution and capture small variations in brightness, the camera was fitted with a macro lens and a white LED back-lit panel was installed to minimise background noise in the images and aid visualisation. Images were acquired at a frame rate of 2 Hz for 5 minutes at each experimental condition to ensure the 'steady state' was achieved. It should be noted that the camera was positioned such as to maximise the field of view to include the entire working volume of the bioreactor.

200 mL of the prepared DISMT stock solution was then added to the DASGIP bioreactor and 15 μL of 0.75 M HCl was inserted and fully mixed until a strong uniform red colour was observed. Impeller agitation was initiated at the rotational speed or agitation mode under investigation and ran for five minutes before initiation of measurement. Image acquisition was initiated before a stoichiometric amount, 15 μL of 0.75 M NaOH, was added through a sample port in the bioreactor headplate. It should be noted that for all experiments conducted the same sample port was used for base addition such as to ensure feed addition location was kept constant.

Mixing time measurements were performed, investigating both continuous and intermittent agitation modes, for which 5 repeats per condition were completed. Continuous agitation modes were investigated at N = 75, 90, 105 and 120 rpm. Intermittent agitation modes were investigated at N = 90 rpm, T_{inv} = 30 s and T_{dwell} = 500, 900, 1500, 3000, 6000, 9000, 12000, 20000 and 30000 ms.

2.6 Suspension characterisation

2.6.1 Solids suspension experimental setup

The suspension of different microcarrier types was evaluated in the two DASGIP bioreactor configurations described in Section 2.2. The same experimental configuration for mixing time experiments was used, shown in **Figure 2.9**. As before, the camera was fitted with a macro lens and a white LED back-lit panel was installed to minimise background noise in the images and aid visualisation. Images were acquired at a frame rate of 2 Hz for 5 minutes to ensure 'steady state' was achieved. The camera was positioned to maximise the field of view to include the entire volume of the bioreactor. The microcarriers were seeded at a concentration of 1 g/L following overnight incubation (approximately 18 hours) in 0.4 % Trypan Blue (Sigma-Aldrich, USA). Once sufficiently wetted and swollen, the microcarriers were filtered using a 40 μm cell strainer with MilliQ water to wash any remaining Trypan Blue not absorbed.

The stained microcarriers were then seeded into the DASGIP bioreactor under investigation and allowed to settle. Continuous impeller agitation was used to investigate the minimum speed required to achieve homogeneity, N_H, for N = 10 – 200 rpm in 10 rpm increments until N = 100 rpm. 20 rpm increments were used thereafter. Each rotational speed was run for a five minute duration to ensure the steady state was achieved. Microcarriers were then allowed to fully settle between each speed investigated. For intermittent agitation modes the degree of settling and quality of suspension over the dwell phases was assessed. Intermittent agitation was investigated at N = 90 rpm, T_{inv} = 30 s and T_{dwell} = 500, 900, 1500, 3000, 6000, 9000, 12000, 20000 and 30000 ms.

The acquired images were then analysed using a purposely-written MATLAB code (Mathworks, USA), which measured the brightness intensity of the greyscale liquid volume. Masking of the area occupied by the impeller shaft and blades and of the image background is performed to ensure accurate analysis of the working volume. The dark Trypan-stained microcarriers exhibited a strong contrast in brightness to the clear, back-lit water within the bioreactor. **Figure 2.10** shows sample images from the suspension characterisation investigation showing (a) fully settled, (b) fully suspended and (c) partially settled conditions, demonstrating the contrast between the solid and liquid phases. The cumulative image brightness, $I_{(N)}$ at the investigated rotational speed, N, was calculated according to Equation 2.21:

$$I_{(N)} = \sum_{n_{tot}} p_{ij} \quad \textbf{(2.21)}$$

Where n_{tot} is the total number of pixels, p, across the area of size i x j, with each pixel having a value between 0 (black) and 1 (white). A suspension or homogeneity index, H_N, could then be determined based upon the image brightness, normalised between the settled and fully suspended states, using Equation 2.22:

$$H_N = 1 - \frac{I_{(N)} - I_\infty}{I_0 - I_\infty} \quad \textbf{(2.22)}$$

Where I_0 represents the initial calculated image brightness when the system is stationary and fully settled in the first frame, and I_∞ denotes when the system is completely suspended and homogeneous, taken as an average from the final few frames of the fastest speed investigated. Data were then fitted into a curve of the form:

$$\frac{1}{1 + e^{-a(x - x_0)}} \quad \textbf{(2.23)}$$

Where the parameters x_0 and a position the curve along the x-coordinate of the curve and control the rate of inclination. Complete system homogeneity and full suspension was determined when H_N = 95 %.

2.6.2 Embryoid body mimics and microcarrier properties

The suspension characterisation was carried out using four microcarrier types, of which three are commercially available; Cytopore 1, Cytodex 3 (both GE Healthcare, USA) and Cultispher-G (Percell Biolytica, Sweden). A fourth type of microcarrier was used, made in a UCL laboratory, named Microcarrier X in this work to ensure anonymity prior to publication. All microcarrier types were investigated in both the flat and round DASGIP bioreactor configurations, with the exception of Microcarrier X, which was investigated in the round bottom tank for continuous agitation only. The remaining microcarrier types were used to investigate both continuous and intermittent agitation modes. Two of the microcarrier types used, Cytodex 3 and Cultispher-G, were also selected to mimic the EB suspension at the start (Day 2) and at the end (Day 9) of iPSC-CM differentiation culture. Selection was made based upon the EB settling characteristics and size reported by Correia *et al.* (2014), where microcarriers of a similar size and settling characteristics reported by the manufacturer were selected.

Table 2.1 summarises the physical characteristics of all the microcarrier types used and the EB characteristics on Day 2 and Day 9 in culture.

2.7 Rheological characterisation

2.7.1 Viscosity measurement

Rheological experiments were carried out using a Malvern Instruments Kinexus Lab + rotational rheometer (Malvern Instruments, Malvern, UK) to measure the viscosity of the cell culture medium used by Correia *et al.* (2014). The media composition can be found in detail in Section 2.8.1 and 2.8.2. Controlled shear deformation was applied to a 1 mL sample between 50 mm parallel plates with a 300 μm gap size. Measurements were performed at room temperature at a specified range of shear rates, applicable to the culture conditions in Correia *et al.* (2014). The range of shear rates were selected based upon Equation 2.24, defined by Metzner and Otto (1957) to define an average shear rate, γ:

$$\gamma = k \times N \quad \textbf{(2.24)}$$

Shear rate is defined as the change in strain over time. k is a non-dimensional constant, dependent upon impeller geometry and N is the rotational speed. For the radial flow paddle impeller used in this work, k was estimated to be similar to the impeller constant determined for a radial flow Rushton turbine, 11.5 (Woziwodzki and Słowiński, 2012).

The maximum shear rate is defined in Equation 2.25 (Robertson and Ulbrecht, 1987):

$$\gamma = 3.3 \times N^{1.5} d_i \left(\frac{\rho}{\mu}\right)^{0.5} \quad \textbf{(2.25)}$$

A range of estimated shear rates, $\gamma \approx 10 - 600$ /s, were then investigated and the viscosity, μ, was calculated using shear stress, τ, and shear rate, γ:

$$\mu = \frac{\tau}{\gamma} = \frac{{}^{F}/_{A}}{\gamma} \quad \textbf{(2.26)}$$

The experimental data later given in Chapters 4 and 5 suggest shear rates reaching up to $\gamma \approx 10$ /s, however as the fluid rheology determined the differentiation media to be a Newtonian fluid, shear rate does not affect the viscosity calculated. Underestimation of the shear rates is likely due to the assumption of the impeller behaving similar to a Rushton Turbine impeller.

2.8 iPSC cell culture and differentiation

The following set of experiments detailed in this section were performed in the IBET labs, Portugal.

2.8.1 iPSC expansion

Cell culture experiments were carried out using both motor-driven and magnetically-driven agitation in the flat bottom DASGIP bioreactor, described in Section 2.2. For cell culture experiments a murine transgenic αPIG-iPS cell line was used, where the puromycin-N-acetyl transferase and the enhanced green fluorescent protein (eGFP) genes were under the control of the cardiac-specific promotor, alpha-myosin heavy chain (α-MHC). iPSCs were expanded in static adherent monolayer cultures on inactivated murine embryonic fibroblasts (iMEFs) in expansion culture medium: Dulbecco's modified Eagle medium, (DMEM + GlutaMAX + 4.5 g/L D-Glucose), supplemented with 15% (*v/v*) fetal bovine serum (FBS), 1 % (*v/v*) non-essential amino acids (NEAA), 2 mM L-glutamine, 50 μM β-mercaptoethanol, 500 μg/mL neomycin sulfate (all from Thermo Fisher Scientific, USA), and 1000 U/mL leukemia inhibitory factor (LIF) (ESGRO, Merck Millipore, Germany), incubated at 37 °C in a humidified atmosphere of 5 % (*v/v*) CO_2. It is worth noting that the neomycin sulfate (Geneticin) was added to the media on alternate passages to select for the iPSCs with the recombinant marker. Monolayer cultures were passaged every two days until passage 6 – 8, depending on cell numbers. Old media was aspired before the culture was washed with phosphate buffered saline (PBS) (Thermo Fisher Scientific, USA), approximately 6 mL/T25 flask was used. 2 mL of 0.05 % Trypsin-EDTA (Thermo Fisher Scientific, USA) was then added to the monolayer cultures and incubated at 37°C for three minutes. Detachment of cells was visually confirmed under an inverted microscope before Trypsin inactivation with 4 mL of expansion media. The cells and media were then pipetted to a small falcon tube and centrifuged for 5 minutes at 160 g. The supernatant was removed and resuspended in 3 mL of fresh media. This was homogeneously mixed before 1 mL aliquots to three fresh T25 flasks. Total volume was then made up to 7 mL with expansion media, before incubation at 37°C. Cell samples following centrifugation could be counted to monitor cell proliferation. Cells were incubated in 0.1 % (*v/v*) Trypan Blue and PBS (all reagents from Thermo Fisher Scientific, USA) in a 1:9 ratio before being added to a Fuchs-Rosenthal haemocytometer cell counting chamber. Ruptured or compromised cells take up the stain and viable cells are shown white under an inverted microscope to be counted.

2.8.2 Cardiomyocyte differentiation

To initiate cardiogenic differentiation, iPSCs were aggregated to form embryoid bodies (EBs) in orbitally shaken vented cap Erlenmeyer flasks agitated at N = 80 rpm (Day 0).

Cells were inoculated at 0.7 x 10^5 cells/mL in V_w = 100 mL of differentiation medium prepared using a vacuum filter, comprising; Iscove's modified Dulbecco's medium (IMDM + GlutaMAX) supplemented with 20% (*v/v*) FBS, 1 × NEAA, 1% (*v/v*) Pen/Strep, 50 μM β-mercaptoethanol (all from Thermo Fisher Scientific, USA) and 100 μM ascorbic acid (Wako, Germany), incubated at 37°C in a humidified atmosphere of 5 % (*v/v*) CO_2. On Day 1, shaking frequency was increased to N = 90 rpm.

Following completion of bioreactor silanization and sterilisation, pH and dissolved oxygen (DO) probe calibration, suspension culture could be initialised. On Day 2 aggregates were transferred to the DASGIP bioreactor at a concentration of 150 aggregates/mL, in a total volume, V_w = 200 mL of differentiation media. Cultures were run until Day 9 under controlled dissolved oxygen (DO) and temperature (T) conditions [CO_2: 5 %; DO: 4 % O_2 Tension; Aeration: 0.1 VVM; T: 37°C], whilst pH was monitored. This was performed using the DASGIP BioBlock (Eppendorf, Germany), shown in **Figure 2.4**, all ancillary tubing and the control station are removed for clarity. For each experimental run, one magnetically-driven and one motor-driven agitation culture were performed in parallel. The magnetically-driven control was operated at N = 90 rpm, T_{inv} = 30 s and T_{dwell} = 900 ms, according to the most favourable differentiation condition, previously reported by Correia *et al.* (2014). Motor-driven agitation was performed at N = 90 rpm, T_{inv} = 30 s for two experimental conditions at T_{dwell} = 500 ms and 1500 ms. Cell samples were taken at Day 0, 2, 4, 6, 7 and 9 for subsequent analysis.

2.8.3 Aggregate size, morphology and concentration

Aggregate concentration, size and morphology were assessed, using an inverted microscope (DMI6000, Leica), from 1 mL samples distributed into a well of a 24-well plate. Image analysis using ImageJ open source software (National Institutes of Health, USA) captured aggregate diameter, measured as the mean value of the Feret diameters, aggregate roundness, calculation for which is given below in Equation 2.27, and elongation, given below in Equation 2.28. Cell aggregates were analysed based on the contrast between the cells and background. Aggregates on the edge of the images were excluded to ensure only whole aggregates were analysed. 20 images per sample were recorded to ensure a representative portion of the aggregate population was analysed. An aggregate count was made from analysed images and aggregate concentration was calculated. Aggregates were also manually counted using a light microscope in a 1 mL sample, 100 μL of which was aliquoted into 10 wells of a 96 microwell plate. An average

of the two counts was then used. **Figure 2.11** shows a microscope image of aggregates taken on Day 6, along with the ImageJ selection of aggregates to be measured.

Using ImageJ, roundness was calculated according to Equation 2.27:

$$Roundness, \emptyset = 4\pi \times \frac{Area}{a^2} \quad \textbf{(2.27)}$$

where the major axis, 'a', is the longest diameter of the particle's fitted ellipse. 1.0 represents a perfect circle with increasing elongation resulting in a value closer to 0.0.

Elongation in ImageJ was calculated using the aspect ratio of the major and minor axis of the fitted ellipse. The minor axis, denoted 'b', is the shortest diameter:

$$Elongation, AR = \frac{a}{b} \quad \textbf{(2.28)}$$

2.8.4 Cell concentration, viability and metabolic activity

For the assessment of cell concentration and cell viability, aggregates were first dissociated. Aggregated samples were centrifuged for five minutes at 300 g and washed with PBS before incubation with 0.25 % Trypsin-EDTA at 37°C on a thermomixer, run for five minutes at 900 rpm. The Trypsin was then inactivated through addition of differentiation media and again centrifuged and resuspended in fresh culture medium. Viable cell counts were performed using a Fuchs-Rosenthal haemocytometer, as described in 2.8.1. Aggregate viability and membrane integrity were also evaluated through incubation with 0.05 µL/mL of the DNA-dye propidium iodide (PI) and 0.1 µL/mL of the enzyme substrate fluorescein diacetate (FDA) (Sigma-Aldrich, Germany). **Figure 2.11** shows the aggregates at Day 6 exhibiting FDA positive live cells, shown green, and dead or ruptured cells, shown in red from acquisition of PI.

The metabolic activity of the cells was quantified through measurement of glucose uptake and lactate release in sample supernatants, centrifuged for five minutes at 300 g. Measurements were performed in triplicate using the YSI 7100 MBS system (YSI Life Sciences, USA). The specific metabolic rates, *q*, were calculated using Equation 2.29:

$$q = \frac{\Delta C/\Delta t}{\overline{[X]}} \quad \textbf{(2.29)}$$

Where $\Delta C/\Delta t$ represents the change in metabolite concentration over time and $\overline{[X]}$ is the average cell concentration within the same time frame. The apparent Lactate, *LAC*, from Glucose, *GLU*, yield, $Y_{LAC/GLU}$ was calculated using Equation 2.30:

$$Y_{LAC/GLU} = {}^{q_{LAC}}/_{q_{GLU}} \quad \textbf{(2.30)}$$

2.8.5 Cell phenotype analysis

Phenotypic analysis of cell samples taken at Day 0 and Day 9, corresponding to the start and end of differentiation, was performed using a CyFlow® space instrument (Sysmex Partec GmbH, Germany). On Day 0, pluripotency assessment was undertaken using OCT-4 and SSEA-1 markers and early differentiation marker SSEA-4. On Day 9, expression of the cardiac specific marker, cardiac troponin T (cTnT) and GFP were quantified and assessed. Dissociation of aggregates on Day 9 was necessary before the cell samples were centrifuged at 300 g for five minutes and the supernatant removed. 'Washing buffer', consisting of 95 % PBS and 5 % FBS, was then used to resuspend the cells. This wash was repeated several times whilst the antibodies were prepared according to the compositions shown in **Table 2.2**. For detection of extracellular cell-surface epitopes, i.e. SSEA-1 and SSEA-4, 100 µL of the primary antibody stock or its respective isotype control, IgM and IgG3, respectively, was used to resuspend the cell pellet, which was then incubated for 1 h at 4°C. Cells were then washed and resuspended in Washing buffer multiple times. For detection of the intracellular epitopes, OCT-4 and cTnT, cells were fixed and permeabilised using BD Cytofix/Cytoperm (BD, USA) according to the manufacturer's protocol. In short, a 50:50 solution of washing buffer and 'Inside Fix' was used to resuspend the cell pellet, which was then incubated for 20 minutes at ambient temperature. Cells were then centrifuged at 300 g for five minutes and resuspended in 'Inside Stain. This was then centrifuged and resuspended in 'Inside Perm'. Following another centrifugation step, the supernatant was removed and cells were incubated with 100 µL of the OCT-4 and cTnT primary antibody stock or isotype control IgG1 and goat IgG, respectively, for ten minutes at ambient room temperature, covered. 'Inside Perm' was then added before a final centrifugation step and resuspension in 'Inside Stain'. Cells were analysed using CyFlow space (Sysmex Partec GmbH, Germany), where 10,000 events were measured per sample. A control for both the extracellular and intracellular samples was also used, consisting of cells without the addition of an antibody, for comparison to each isotype control during measurement. The final determined percentage of antibody expression was the measured value for each primary isotope, minus the isotype control reading, demonstrated in Equation 2.31:

$$OCT\text{-}4_{final}(\%) = OCT\text{-}4_{measured}(\%) - IgG1_{measured}\ (\%) \quad \textbf{(2.31)}$$

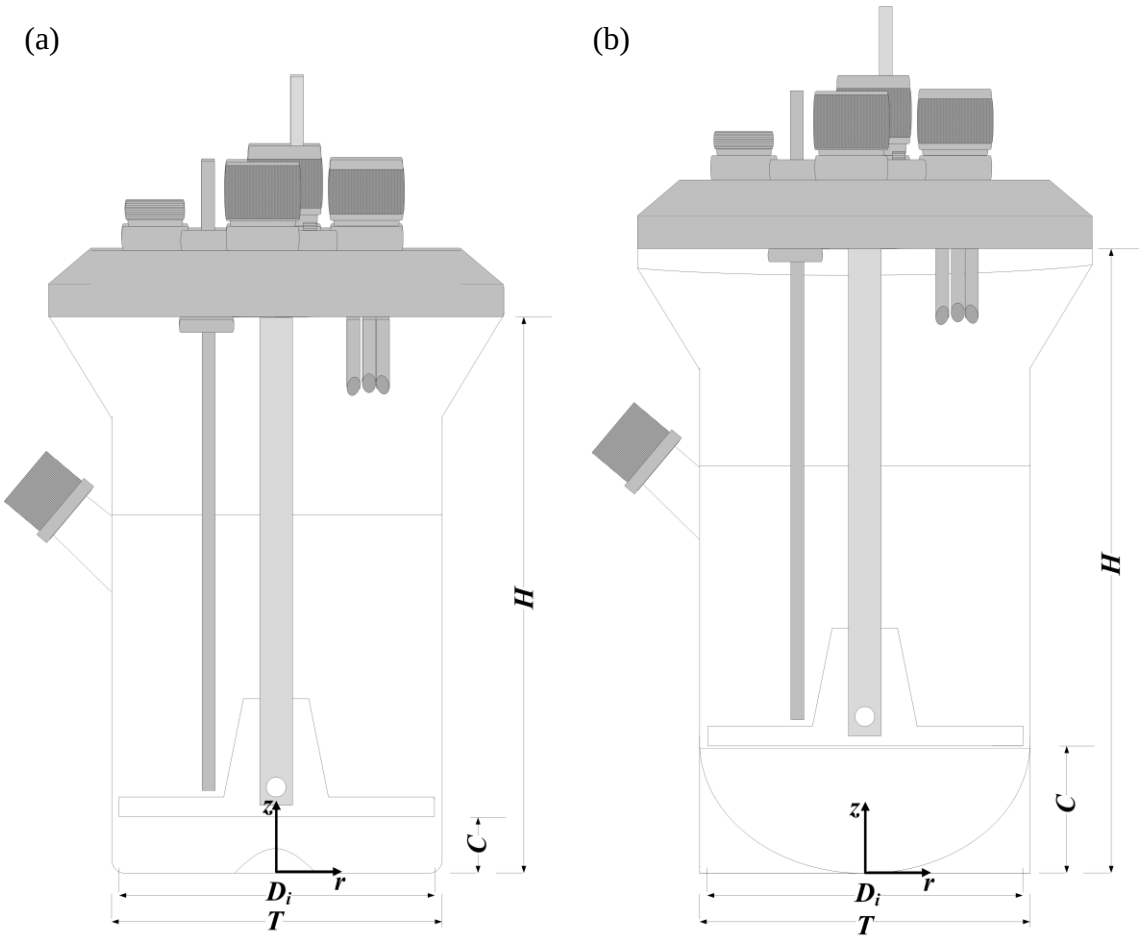

Figure 2.1 Schematic diagram of the flat (a) and round (b) bottom DASGIP bioreactor configurations.

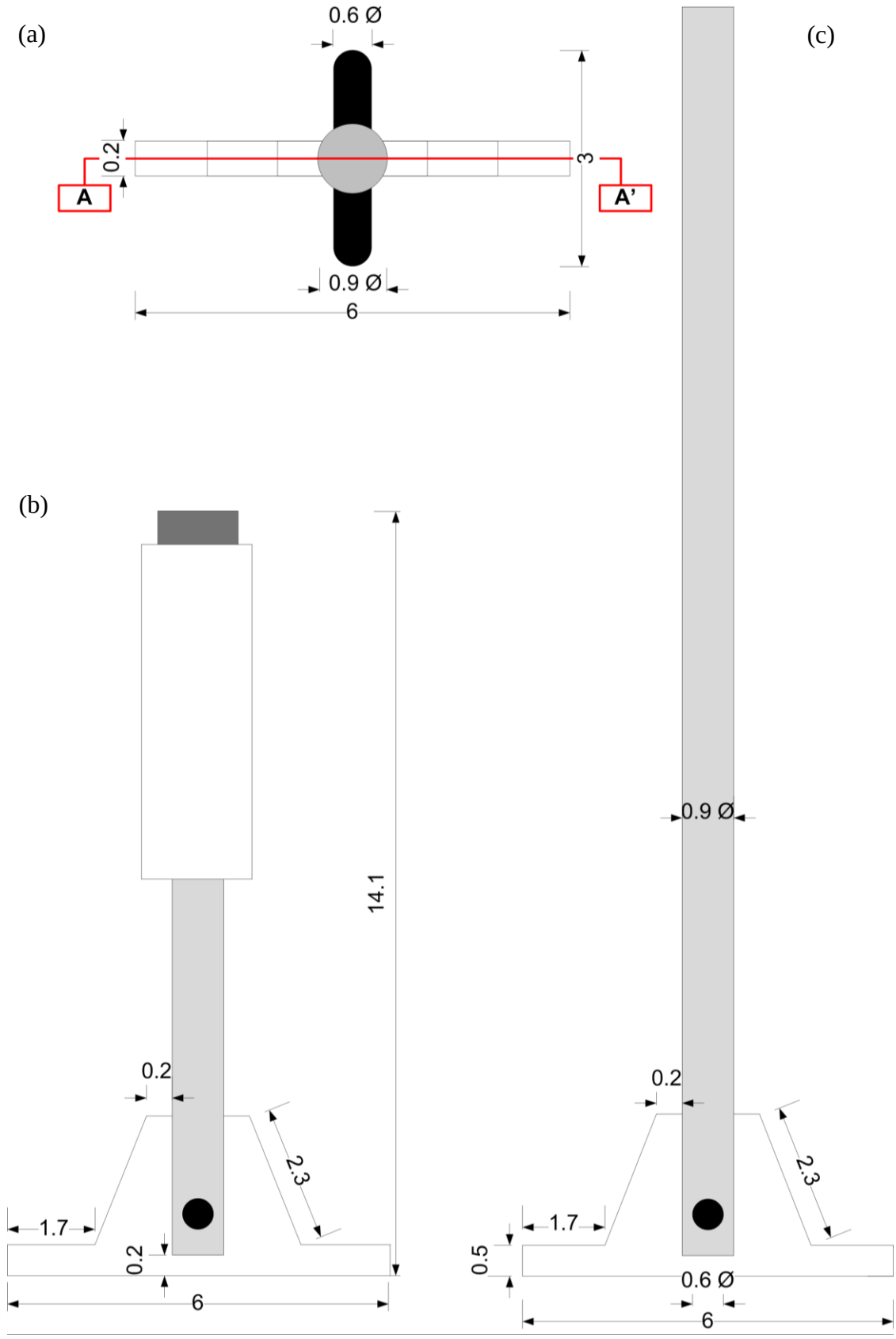

Figure 2.2 Impeller dimensions and geometry: (a) top view; (b) side view of the original magnetic paddle impeller (through A – A'); (c) side view of the impeller used for motor-driven agitation (through A – A'). Units in cm.

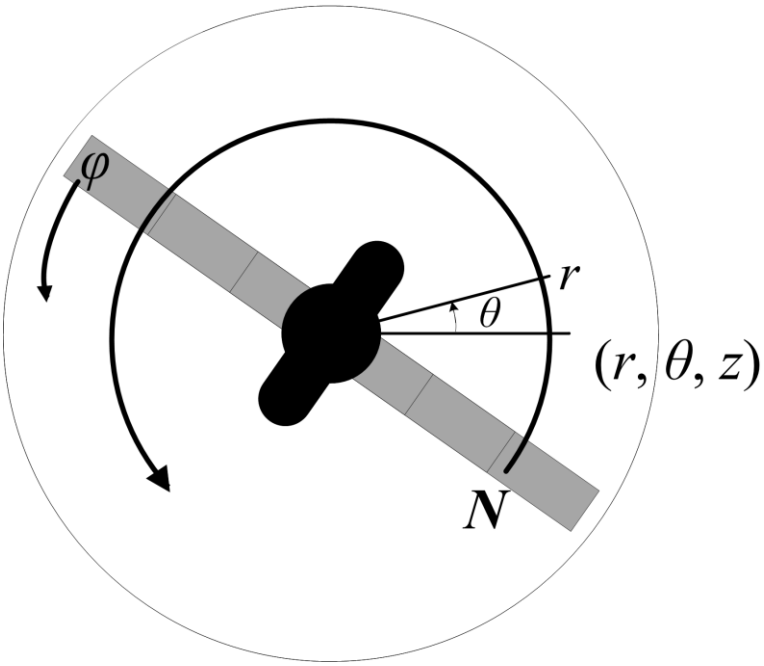

Figure 2.3 Bioreactor horizonal cross-section with cylindrical coordinate reference system.

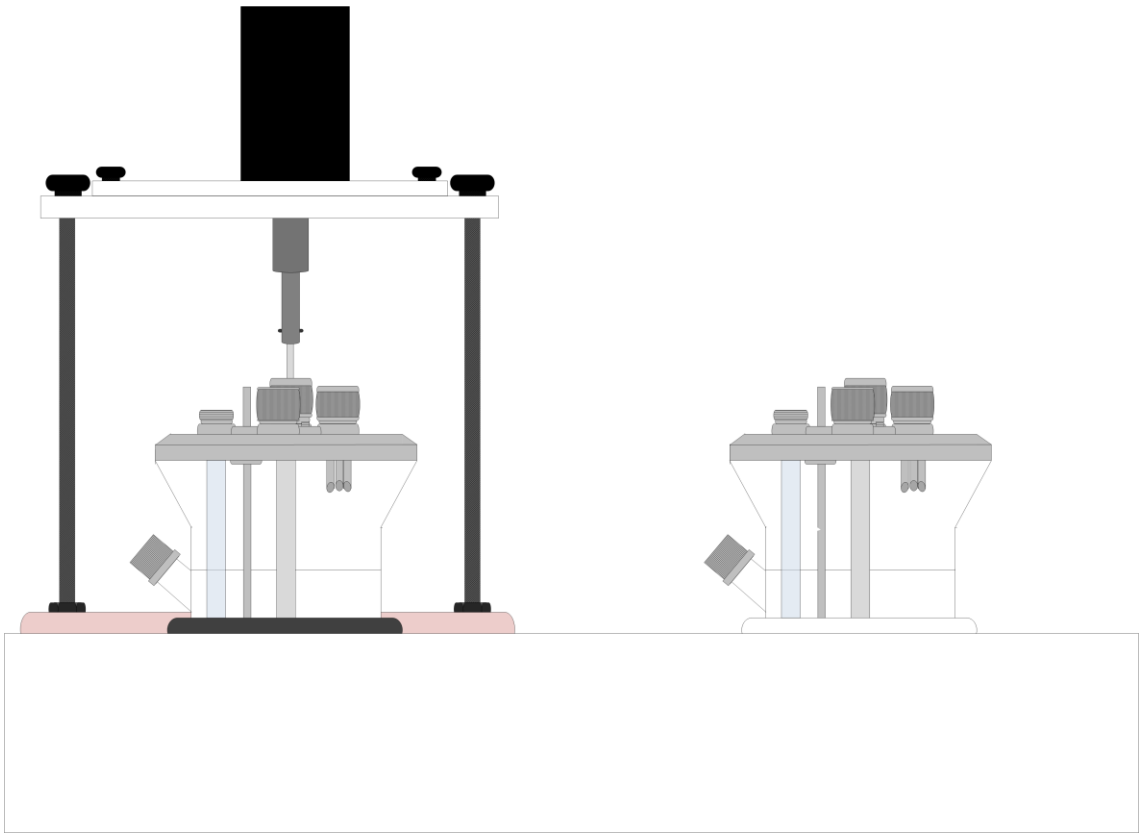

Figure 2.4 BioBlock experimental rig showing one magnetically agitated DASGIP bioreactor (right) and one modified motor-driven bioreactor (left).

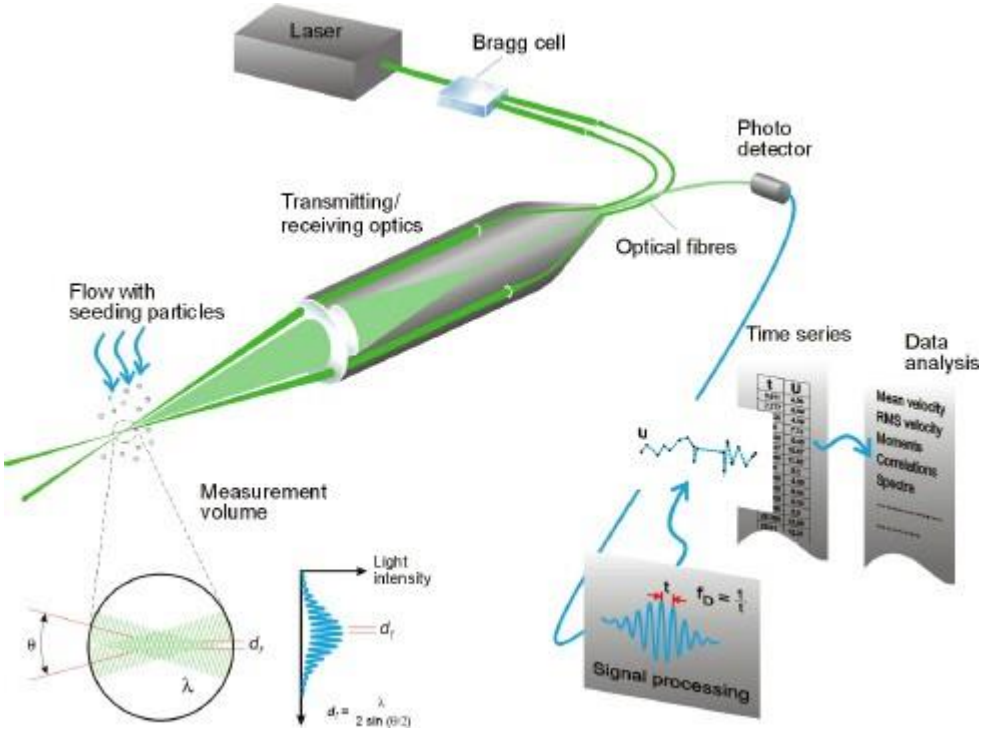

Figure 2.5 Schematic of the working principle of LDA. Image taken from www.dantecdynamics.com.

(a)

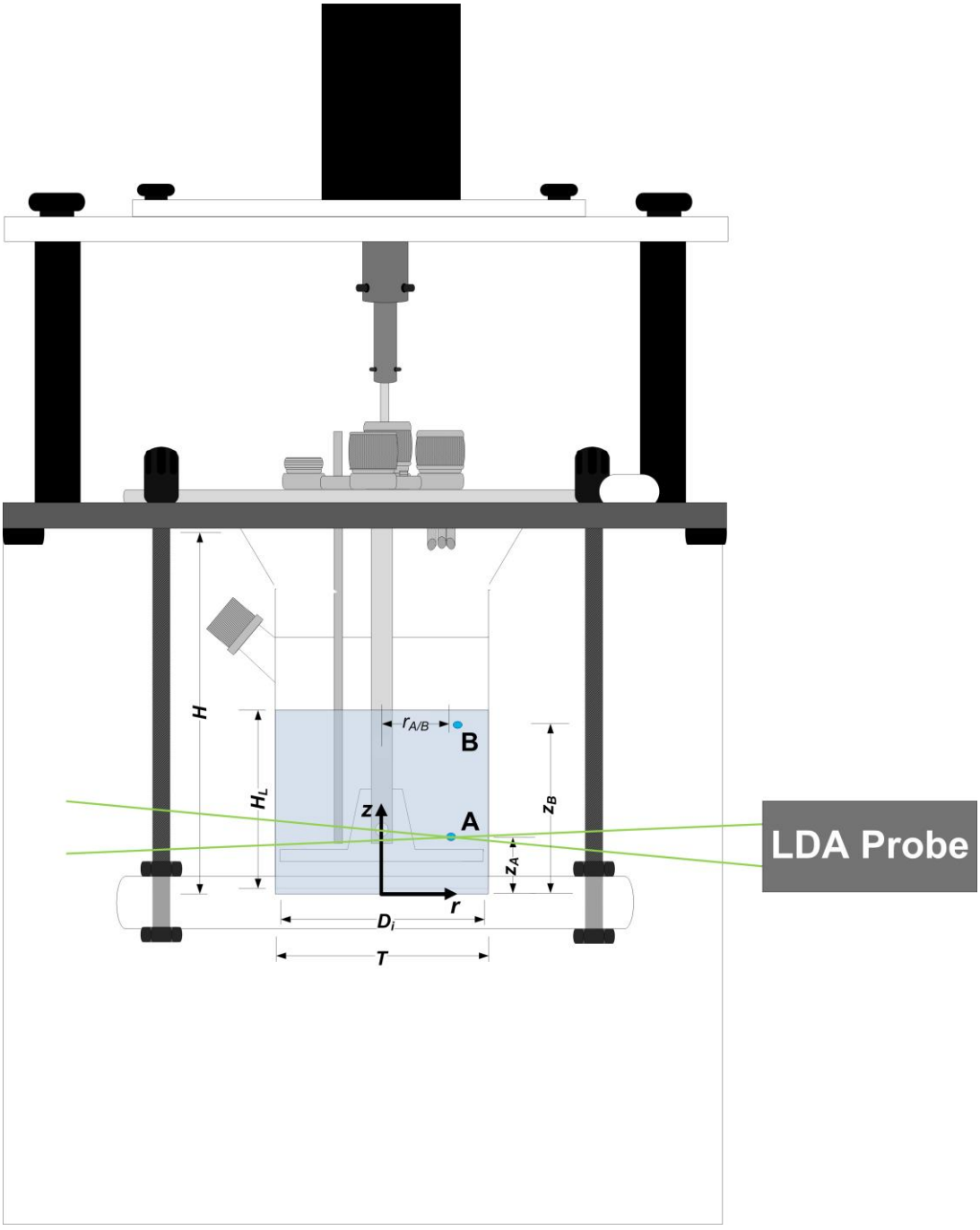

(b)

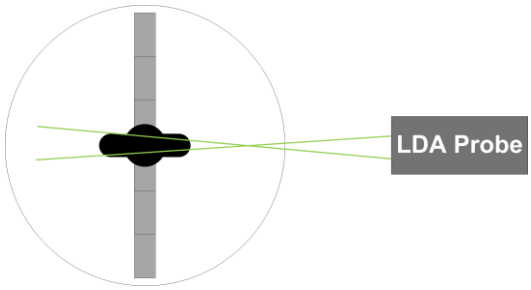

Figure 2.6 Experimental setup and probe arrangement used for LDA: (a) measurement locations A and B; (b) tangential velocity component.

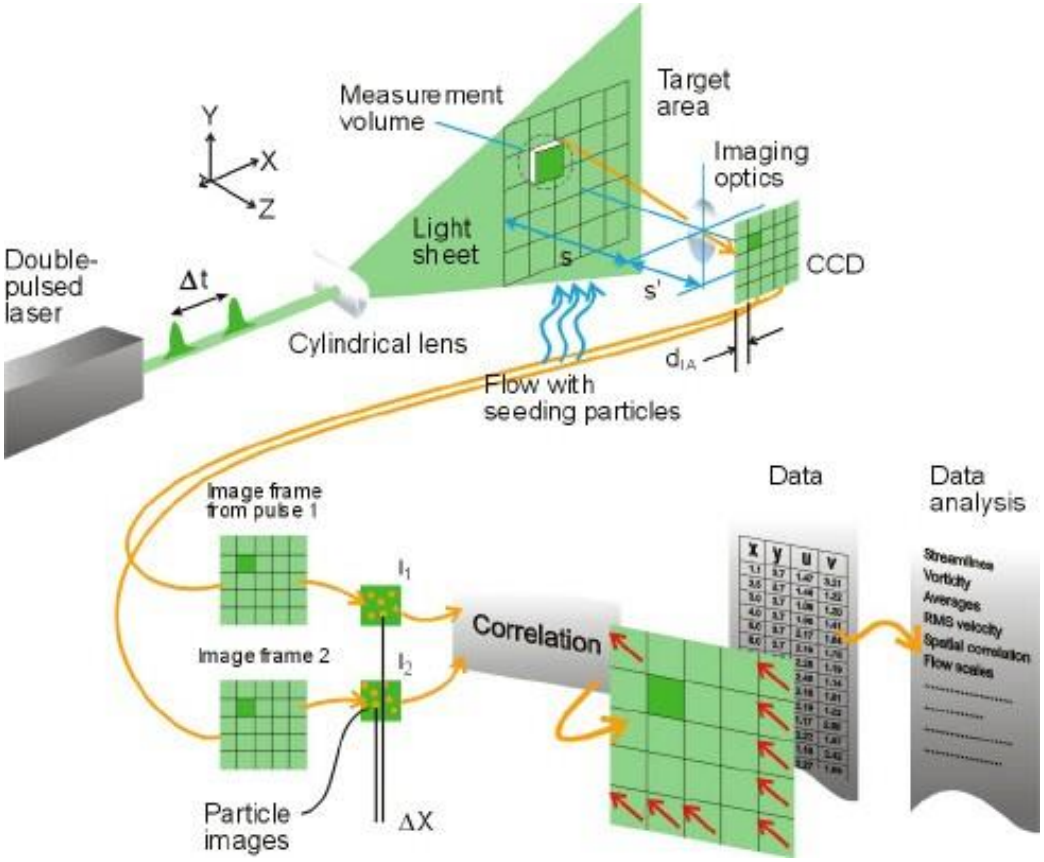

Figure 2.7 Schematic of the working principle of PIV. Image taken from www.dantecdynamics.com.

(a)

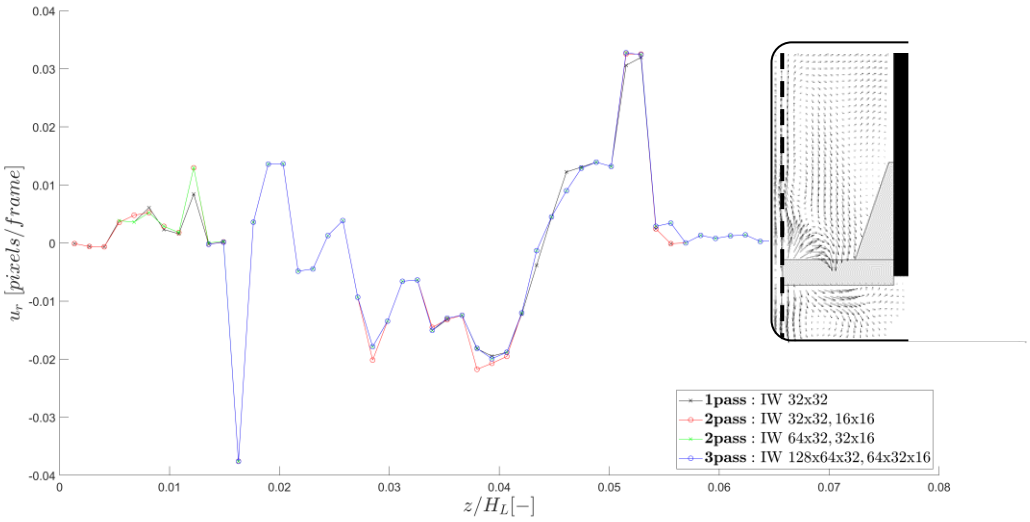

(b)

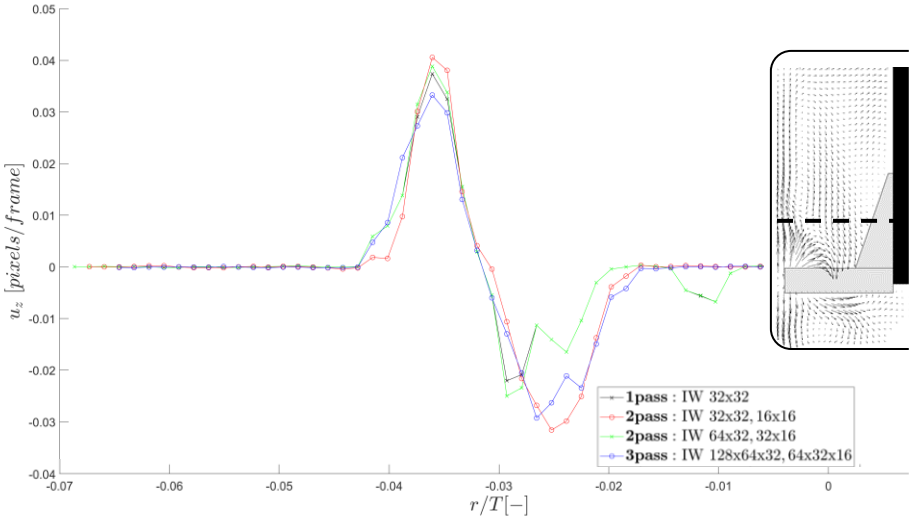

Figure 2.8 Velocity profiles obtained for four different interrogation window parameters: (a) u_r at r/T = 0.45; (b) u_z at z/H_L = 0.5

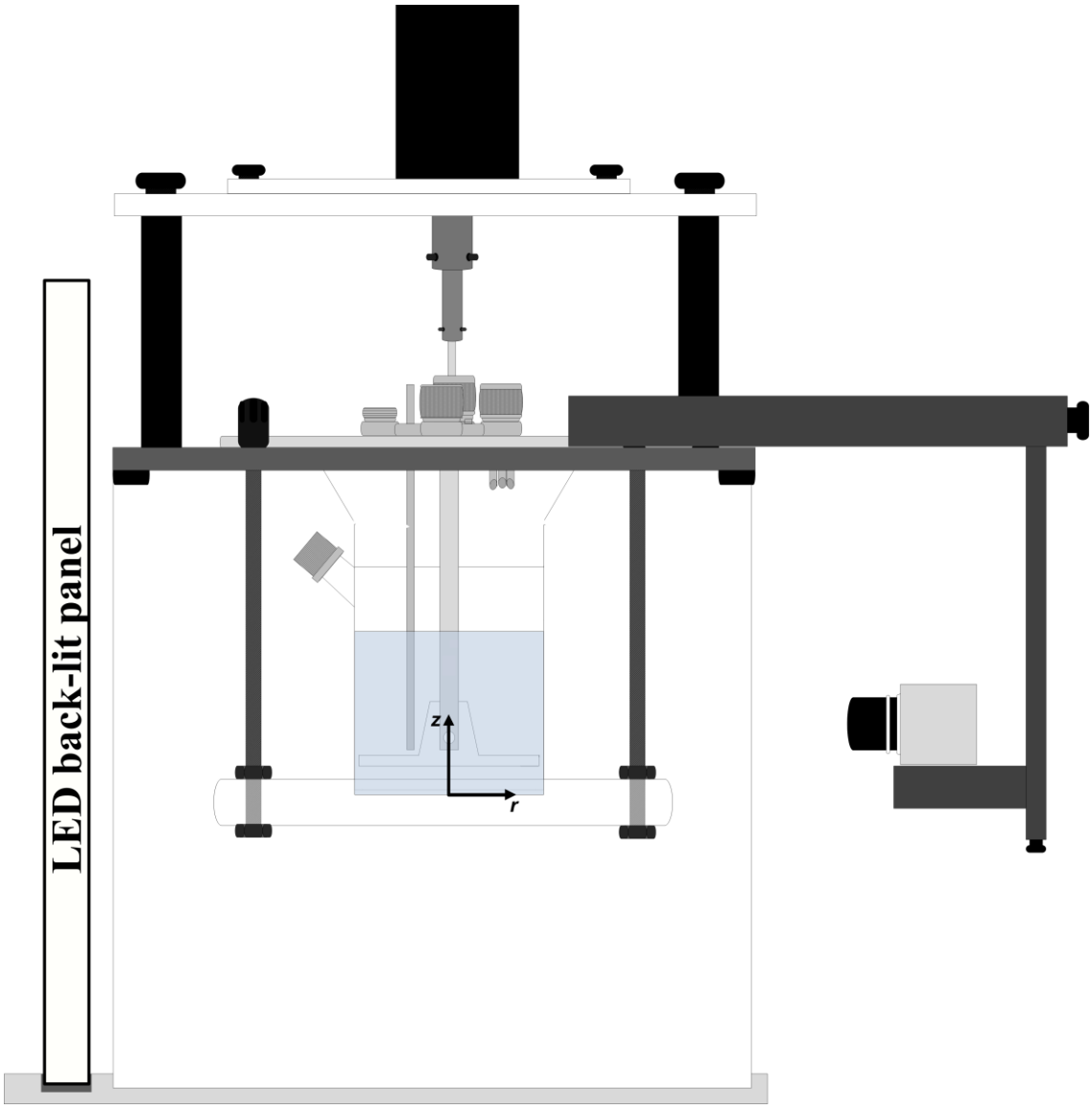

Figure 2.9 Experimental setup used for the suspension characterisation experiments.

(a)

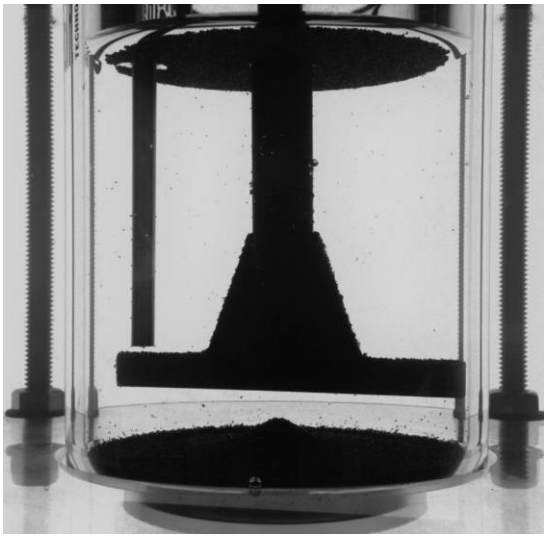

(b)

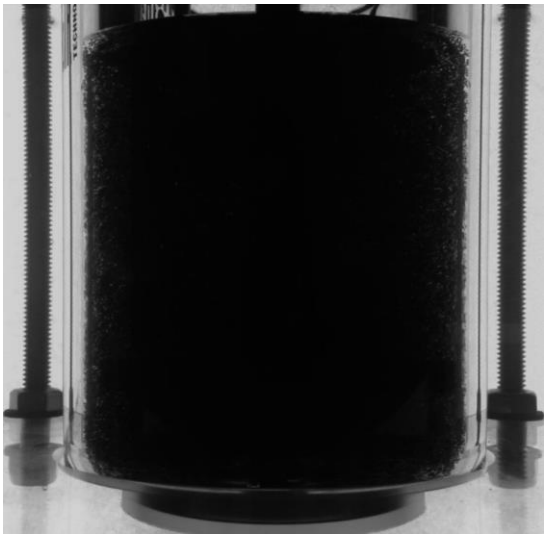

(c)

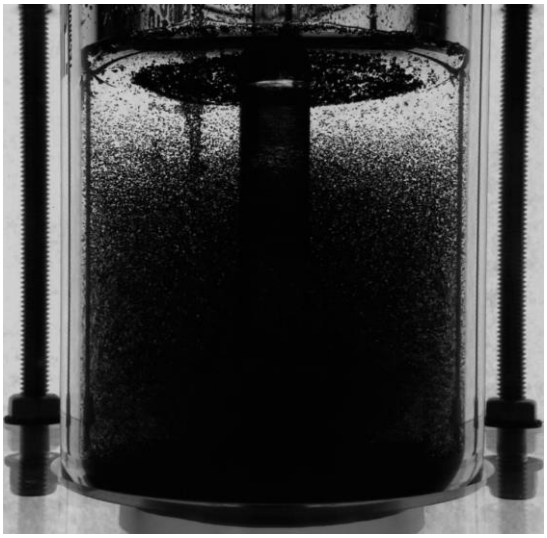

Figure 2.10 Sample images acquired during suspension characterisation; (a) fully settled; (b) fully suspended; (c) partially settled.

(a)

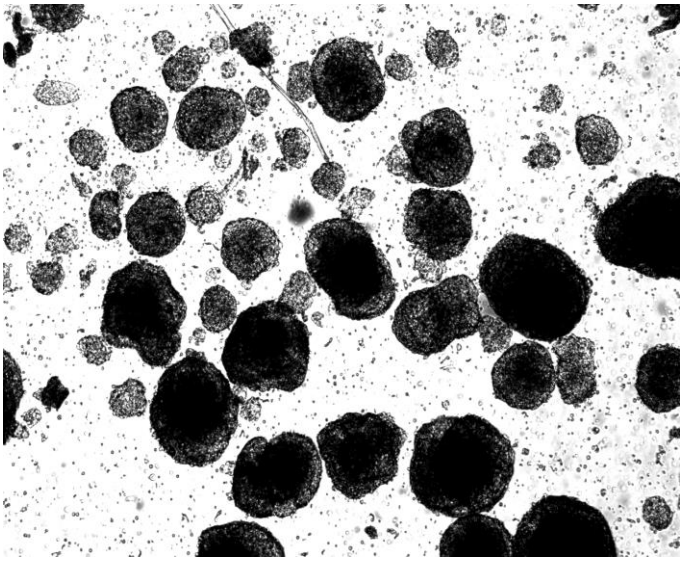

(b)

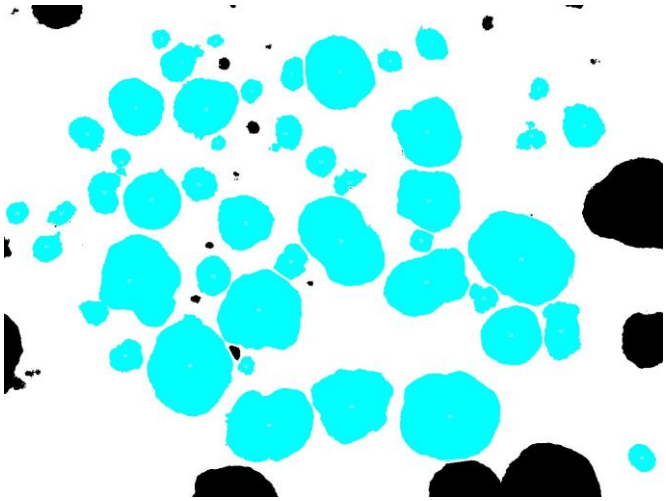

(c)

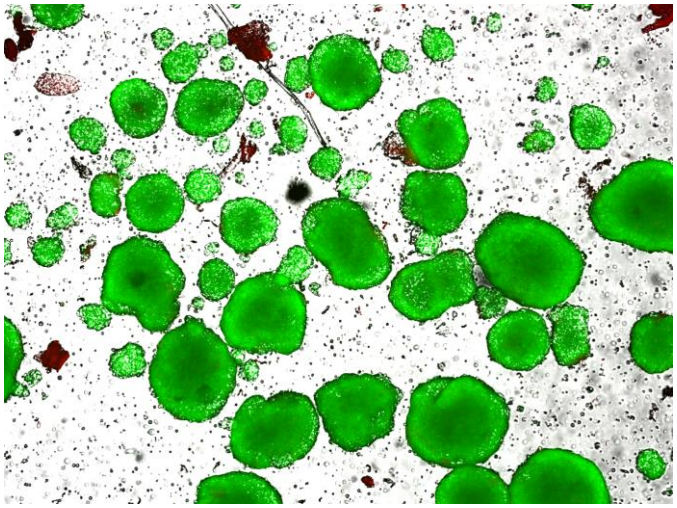

Figure 2.11 Cell images of Day 6 aggregates used for calculation of aggregate size, morphology, concentration and viability: (a) original image; (b) ImageJ selected aggregates for measurement; (c) FDA and PI stained aggregates.

	Density, ρ (g/mL)	**Diameter, D_{50} (µm)**	**Porosity, Φ (-)**	
Embryoid bodies (Day 2)	1.002	155	*	(Correia *et al.*, 2014)
Cytodex 3	1.04	175	Non/micro-porous	(GE Healthcare, USA)
Embryoid bodies (Day 9)	1.0024	384	*	(Correia *et al.*, 2014)
Cultispher-G	1.04	255	50 %, pore size 10 – 30 µm	(Percell Biolytica, Sweden)
Cytopore 1	1.03	235	> 90 %, pore size 30 µm	(GE Healthcare, USA)
Microcarrier X	1.39	354	94 – 38 %, size dependent	-

* *not measured*

Table 2.1 Microcarrier and embryoid body density, size and porosity.

Extracellular	Antibody (Ab)	Ab (µL)	Washing Buffer (µL)	Inside Perm (µL)	
	SSEA-4	20	80	-	(BD, USA) Cat: 560126, Lot: 4092971
	IgG3	2.5	97.5	-	(BD, USA) Cat: 555578, Lot: 4021633
	SSEA-1	6.0	94	-	(BD, USA) Cat: 560127, Lot: 4304638
	IgM	0.5	199.5	-	(BD, USA) Cat: 553474, Lot: 4114580
Intracellular	OCT-4	20	-	80	(BD, USA) Cat: 560253, Lot: 5195617
	IgG1	83.4	-	16.6	(BD, USA) Cat: 557721, Lot: 6032520
	Nanog	10	-	90	(R & D Systems, USA) Cat: ICI1997P, Lot: ABCL0214041
	Goat IgG	10	-	90	(Santa Cruz Biotechnology, USA) Cat: SC-3887, Lot: #G0214
	cTnT	1	-	199	(Thermo Fisher Scientific, USA) Cat: MA5-12960
	Goat IgG	1		199	(Thermo Fisher Scientific, USA) Cat: REFA11001, Lot: 1787787

Table 2.2 Antibody stock solutions made for flow cytometry.

CHAPTER 3 FLOW FREQUENCY ANALYSIS AND BIOLOGICAL INVESTIGATION OF AN iPSC-DERIVED CARDIOMYOCYTE DIFFERENTIATION PROCESS [*]

3.1 Introduction

Myocardial infarction is one of the most prevalent manifestations of cardiovascular disease, causing cellular death through necrosis and/or apoptosis in the myocardium, ultimately leading to heart failure (Burridge *et al.*, 2012). Patients survive a myocardial infarction in cases where no more than 35 % of the left ventricle is compromised, however, the matured myocardium has an inherent regenerative capacity limited to 1 % *per annum* (Zandstra *et al.*, 2003). Currently, treatment for cardiovascular diseases is primarily symptomatic, comprising of pharmaceuticals and implantable devices with heart transplantation being the last resort (Chen *et al.*, 2014; Tonsho *et al.*, 2014). These treatments may not be suitable for all patients, with heart transplantation facing immunological incompatibility, rejection and demand outweighs supply. *De novo* cardiomyocytes (CMs) offer a plausible and safer alternative for patient-specific cell replacement therapy (Acimovic *et al.*, 2014). Kehat *et al.* (2001) first derived foetal CMs from a three-dimensional (3-D) suspension culture of human embryonic stem cells (hESCs). From this initial work, an increasing amount of research investigating regeneration of the adult myocardium using stem-cell derived CMs has been undertaken.

---

[*] Most of the results presented in this chapter are included in:

Samaras, J. J., Abecasis, B., Serra, M., Ducci, A., Micheletti M. (2018), "Impact of hydrodynamics on iPSC-derived cardiomyocyte differentiation processes", *Journal of Biotechnology*, Accepted.

Samaras, J. J., Abecasis, B., Serra, M., Ducci, A., Micheletti M. (2017), "Measuring and manipulating the hydrodynamic environment of an iPSC-derived cardiomyocyte differentiation process", *25th European Society for Animal Cell Technology Meeting: Cell Technologies for Innovative Therapies*, Lausanne, Switzerland.

Samaras, J. J., Serra, M., Ducci, A., Micheletti M. (2018), "Characterisation and correlation of flow dynamics relating to an iPSC-derived cardiomyocyte differentiation process", *16th European Conference on Mixing*, Toulouse, France.

Many differentiation strategies have been investigated such as to improve cardiogenic yields in a cost-effective and reproducible manner, as discussed in Chapter 1. Cardiomyocyte differentiation should be primarily based upon recapitulation of early embryo cardiogenesis *in vivo*. Indeed, the most promising differentiation strategies seek to emulate the biochemical and physiological cues within the developing heart for more consistent and efficient differentiation. One such physiological cue is the cyclic mechanical strain induced from the rhythmic beating of the myocardium, initiated from as early as the third week post-coitum.

A study by Ge *et al.* (2009) showed cardiogenic differentiation of bone marrow-mesenchymal stem cells through monolayer co-culture with an extract of infarcted myocardium and the addition of 4 % biaxial cyclic strain from a custom-made device at 1 Hz. Individually, this study showed monolayer co-culture with the myocardium extract, a biochemical stimulus, and the monolayer culture with the addition of 4 % cyclic strain at 1 Hz, a mechanical stimulus, to both induce differentiation. When the two stimuli were used in combination, the most powerful induction of cardiogenesis was achieved.

Increasing research has since explored the beneficial impact of mechanical cues as an inducer of cardiogenic differentiation, without the addition of expensive growth factors. These mechanical cues may be applied through mechanical stretch/strain devices on monolayer cultures, such as that used by Ge *et al.* (2009), or through hydrodynamic forces induced from impeller agitation in 3-D suspension culture. Lam *et al.* (2014) systematically compared different modes of ESC culture for cardiogenic differentiation and reported a 10-fold increase in differentiation yields using intermittently stirred bioreactor protocols in comparison to static and shaken suspension cultures. Ting *et al.* (2014) reported a 40 % improvement in cardiomyogenesis with application of intermittent agitation for the first three days of ESC-microcarrier culture in comparison to static culture protocols. Correia *et al.* (2014) investigated different agitation modes under hypoxic culture conditions for an induced pluripotent stem cell (iPSC)-derived cardiomyocyte differentiation process. This included continuous and intermittent agitation, with and without a change in impeller direction. **Table 3.1** summarises each agitation condition and the corresponding yields achieved. Overall, it was found that differentiation yields were highest using intermittent agitation without a direction change, whilst introducing the direction change proved detrimental to cardiogenic differentiation.

Research investigating the optimisation of cardiogenic differentiation protocols seldom considers the engineering aspects such as the impact of the induced characteristic flow

frequencies upon differentiation. Several studies investigating the addition of mechanical stimuli have explored the application of frequencies in the range of 0.033 – 1 Hz, induced from stretch/strain devices or from hydrodynamic shear, all resulting in varying degrees of success in improving cardiomyogenesis. Laser-based techniques are often used to investigate flow dynamics within 3-D systems. Laser Doppler Anemometry (LDA) is a non-intrusive single-point technique, used to investigate instantaneous flow velocities. Once the flow dynamics have been characterised, they can then be correlated with biological outcomes and optimised flow conditions can more easily be transferred and developed in both the same and different types of bioreactor.

The present chapter provides an in-depth investigation of flow frequencies under different agitation modes and aims to correlate them with existing iPSC-CM differentiation yields.

3.2 Results

This section of the chapter is divided into three parts; rheological assessment of the culture medium used by Correia *et al.* (2014) is given in Section 3.2.1, flow frequency analysis using LDA is presented in Section 3.2.2 and biological studies pertaining to an iPSC-CM differentiation process are presented in the subsequent Section 3.2.3. The rheological assessment was made such as to determine the suitability of a non-reactive fluid mimic, such as water, for the engineering characterisation studies. The flow frequency analysis investigated three agitation modes, first described in Correia *et al.* (2014), using the bioreactor configuration described in Section 2.2, before parametric studies sequentially investigating three individual time components identified in subsections 3.2.2.1 – 3.2.2.3. Based upon the parametric studies, biological studies in Section 3.2.3 were designed to assess the impact of engineering characteristics on cardiogenic differentiation yields.

3.2.1 Rheological analysis

The engineering characterisation studies in this work were performed such as to assess the culture conditions and the impact of varying agitation mode on an iPSC-CM differentiation process. For the engineering characterisation studies, described in this chapter and in Chapters 4 and 5, to represent the culture conditions under investigation, the differentiation culture medium, made according to the protocol given in Section 2.8.2, was investigated. Rheological assessment of the culture viscosity was performed as described in Section 2.7.1. **Figure 3.1** shows the differentiation medium shear stress

response (a) and viscosity (b) measured for increasing shear rates. Shear stress was shown to linearly increase with increasing shear rate and the viscosity remains constant at $\mu \approx$ 0.001 Pa.s. These rheological properties show a Newtonian fluid, with viscosity comparable to water. For simplicity and optimal visualisation, the characterisation studies were performed using clear MilliQ water.

3.2.2 Flow frequency analysis

Initially, investigation sought to characterise the energy spectrum of the tangential velocity component for the three agitation modes first introduced in Correia *et al.* (2014). This was performed to assess if a correlation existed between the characteristic flow frequencies and the achieved differentiation yields. Instantaneous velocity data were obtained using the LDA system, previously described in Section 2.3, and were transformed into the frequency domain using a Fast Fourier Transform (FFT) analysis in a purposely written MATLAB code. The tangential velocity component, u_θ, was investigated as this is directly impacted from impeller motion. **Figure 3.2** depicts the instantaneous tangential velocity time-series plot for N = 90 rpm and its resultant energy spectrum. Measurements were obtained at point A (**Figure 2.6** a), r_A/T = 0.35 and z_A/H_L = 0.28, close to the impeller region.

The three agitation modes investigated by Correia *et al.* (2014) and the corresponding differentiations yield are given in **Table 3.1**. Three characteristic time components were identified in this work: the rotational speed, N, the time interval in which the impeller is in motion, T_{inv}, and the duration of the dwell phase, T_{dwell}. **Figure 3.3** shows the energy spectra, kinetic energy per unit of frequency, $E_\theta(f)$, obtained for the three agitation modes. **Figure 3.3** (a) shows the energy spectrum obtained for continuous agitation, N = 90 rpm. As expected, two significant frequency peaks at f = 1.5 and 3.0 Hz are observed from the periodic rotation of the two paddle blades, each revolving at 1.5 rps. The lower intensity peaks at f = 4.5, 6.0, 7.5 and 9.0 Hz are harmonics. The energy spectrum obtained for the intermittent agitation profile, without a direction change, N = 90 rpm, T_{inv} = 30 s and T_{dwell} = 900 ms, is shown in **Figure 3.3** (b). Two similar frequency peaks at f = 1.5 and 3.0 Hz are presented, in addition to a lower range of frequency peaks. These are harmonics of the interval time frequency, occurring at $f = 1/T_{inv}$ = 0.033 Hz. The characteristic energy associated to these low frequency peaks reaches a maximum value of approximately 6 % (at f = 0.033 Hz) the maximum peak at f = 3.0 Hz, corresponding to impeller rotation, considered as a cumulative influence however, the low frequency peaks represent a

quantitative addition to the overall energy of the spectrum. **Figure 3.3** (c) gives the energy spectrum for the intermittent with a direction change agitation profile, N = 90 rpm and T_{inv} = 30 s. The lower range of frequency peaks, seen previously, are present at harmonics of $1/T_{inv}$, however the energy associated with these frequencies is shown to have been amplified approximately 700-fold. The integral of the energy intensities associated with the low frequency peaks for each agitation mode is given in **Figure 3.3** (d). Correlating the energy spectra in **Figure 3.3** with the differentiation yields achieved by Correia *et al.* (2014) in **Table 3.1**, it can be inferred that the lower range of frequency peaks, obtained through application of intermittent agitation, may have had a beneficial impact upon cardiogenesis, providing a conservative amplification of such frequencies. **Figure 3.3** (b) gives the energy spectrum for the highest differentiation yield, showing the addition of the lower range of frequencies. **Figure 3.3** (c) suggests an upper limit to the energy density associated with the lower range of frequencies, at which intermittent agitation becomes detrimental to differentiation yields.

Phase-resolved analysis was obtained using Equation 2.4 over one revolution, where the term $u_\theta - \overline{u_\theta}$ represents the periodic oscillatory component, $\tilde{u}_\theta$, and the turbulent fluctuating component, u'_θ, according to Reynolds and Hussain's (1972) triple decomposition. **Figure 3.4** (a) and (b) shows the average periodic tangential velocity component, $\tilde{u}_\theta$, and the corresponding fluctuating component, u'_θ, respectively, over one revolution for the continuous agitation mode, N = 90 rpm. The sinusoidal wave shape of the tangential velocity component, shown in **Figure 3.4** (a), reflects the pulsatile cyclic motion, characteristic of impeller rotation as the paddle blades pass near the measurement volume. The two sinusoids are not identical, indicating asymmetry in the motion of the two paddle impeller blades within the bioreactor. This is common and can be visually observed during cell culture as the impeller is self-assembled. Standard deviation of the tangential velocity component shows with increasing impeller blade proximity to the measurement volume, the random fluctuating component also increases (**Figure 3.4** b) within the range u'_θ = 0.016 – 0.028 m/s. The time-series plot (a), periodic tangential velocity (b) and fluctuating tangential velocity (c), over one revolution is given for the intermittent flow without direction change, shown in **Figure 3.5**. The dwell is clearly recognisable by the drop in velocity (**Figure 3.5** a). There is little change in the periodic tangential component in comparison to continuous agitation (**Figure 3.5** b), but a slight increase in fluctuation during the intermittent impeller agitation mode is evident (**Figure 3.5** c).

The intermittent motion with direction change showed significant amplification of the lower range of frequency peaks, so it is interesting to observe the phase-resolved periodic flow. **Figure 3.6** overlays for comparison the velocity time-series plot (a) the periodic velocity fluctuation, $\tilde{u}_\theta$ (b) and the random component fluctuation, u'_θ (c) for the continuous and the intermittent with a direction change agitation modes. The inversion in velocity with the impeller direction change is clearly evident in **Figure 3.6** (a). The periodic velocity component in **Figure 3.6** (b) shows the inversion in impeller direction to slightly reduce the range in velocity over an impeller rotation. 45 revolutions are completed within each interval (T_{inv} = 30 s), therefore the phase-resolved data is an average of 45 revolutions with a positive velocity followed by the direction change and 45 revolutions with a negative velocity. This totals one minute of data recording, where measurements were acquired for a total of 20 – 60 minutes, depending upon the rotational speed. The sinusoidal periodic wave is less smooth, again indicating variation over the average impeller revolution. **Figure 3.6** (c) therefore shows the random fluctuating component to have increased approximately four-fold with the direction change condition in comparison to continuous agitation.

A secondary measurement position was investigated to assess the flow frequencies in the bulk flow. Measurements were obtained at point B (**Figure 2.6** a), r_B/T = 0.35 and z_B/H_L = 0.58, + 20 mm in the *z*-direction. **Figure 3.7** and **Figure 3.8** give the resultant energy spectra for continuous agitation and intermittent without a direction change agitation at point A (a) and point B (b). It is interesting to observe that the peak intensities associated to the impeller blade passage were significantly diminished (> 90 %) at location B, but the energy intensity of the low frequency peaks was less affected. **Figure 3.8** (c) gives the summation of the first six significant low frequency peaks measured at location A and B for the intermittent agitation condition. An approximate 10 % decrease in the cumulative low frequency peak intensity is observed with the measurement location change. This suggests that the low frequency flow structures introduced with intermittent agitation are present at a reactor scale, with a 10 % difference in intensity between the impeller region and bulk flow, whereas the periodic passage of the impeller blades is shown to impact the impeller region, decreasing more than 90 % in the bulk flow. For continuous agitation, the velocity time-series plot (**Figure 3.9** a) shows a diminished range in velocities at measurement location B in comparison to **Figure 3.2** (a), the periodic tangential velocities (**Figure 3.9** b) show no sinusoidal wave-shape associated to the passage of the impeller blades, which is also reflected in the fluctuating turbulent

component (**Figure 3.9** c). The same conclusions are observed for intermittent agitation. All remaining measurements were performed within the impeller region at measurement position A.

Continuous and intermittent agitation modes were also investigated using the addition of a second phase to confirm the results obtained are representative of the biological studies. As described in Section 2.6.2, two types of microcarriers were selected as embryoid body (EB) mimics, Cytodex 3 for the start of differentiation and Cultispher-G to represent the EBs at the end of differentiation. **Figure 3.10**, **Figure 3.11** and **Figure 3.12** compare the resultant energy spectra from a single phase (a), a two-phase system with Cytodex 3 (b) and a two-phase system with Cultispher-G (c) for continuous agitation, N = 90 rpm (**Figure 3.10**), intermittent agitation without a direction change, N = 90 rpm, T_{inv} = 30 s and T_{dwell} = 500ms (**Figure 3.11**) and intermittent agitation with a longer dwell phase, T_{dwell} = 1000 ms (**Figure 3.12**). Measurements of the single phase system and the two-phase system seeded with Cytodex 3 show very little difference in the resultant energy spectra for all 3 conditions investigated. When Cultispher-G was seeded into the flow volume, amplification of the energy intensities was observed. An approximate 45 % increase in the frequency associated to the impeller blade passage (f = 3.0 Hz) was generated during continuous agitation (**Figure 3.10** a and c), with an apparent reduction in the energy intensity of all harmonics. Interestingly, no significant change is observed with the addition of Cultispher-G for intermittent agitation with a shorter dwell time, T_{dwell} = 500 ms (**Figure 3.11** a and c), however increasing the dwell to T_{dwell} = 1000 ms (**Figure 3.12** a and c) increases amplification of the low frequency peaks between a single- and two-phase system by approximately two-fold, with little apparent change in the frequency peaks associated to impeller rotation. **Figure 3.13** shows a comparison of the intermittent energy spectra by plotting the summation of the energy associated to the low frequency peaks for the single and two-phase flows. As discussed, no significant difference is obtained at T_{dwell} = 500 ms (**Figure 3.13** a), however increasing the dwell duration resulted in the energy intensity associated to the lower range of frequencies to double with the addition of Cultispher-G. This suggests that the intermittent agitation mode has a more pronounced impact upon the flow towards the end of differentiation.

The subsequent sections explore how variation of each of the three time components identified would impact upon the characteristic flow frequencies present. As intermittent agitation without a direction change was associated with the best differentiation

performance in Correia *et al.* (2014), variations of the time components associated to this mode of operation were explored in more detail.

3.2.2.1 Impact of time component, T_{inv}

Investigation of the impact of T_{inv} upon the resultant energy spectra were carried out using T_{inv} = 30, 15 and 5 s at constant N = 90 rpm and T_{dwell} = 500 ms. **Figure 3.14** shows the velocity-time series indicating T_{inv} and T_{dwell} in a 30 s time period for three conditions of T_{inv}. From the time-domain data it is not immediately evident that there are significant frequency changes with a change in T_{inv}. **Figure 3.15** shows the corresponding energy spectra for decreasing interval times of T_{inv} = 30 (a), 15 (b) and 5 s (c). As previously observed, the spectra all show the low frequency peaks in addition to the standard peaks associated to the periodic impeller blade passage. As the interval time is decreased, the low frequency peaks, plotted in the insets, become spread over a larger range and increase in their respective energy intensities. As previously noted, these low frequency peaks occurred at $1/T_{inv} = f_{inv}$ = 0.033 Hz with harmonics for T_{inv} = 30 s (a), f_{inv} = 0.06 Hz with harmonics for T_{inv} = 15 s, (b) and f_{inv} = 0.2 Hz with harmonics for T_{inv} = 5 s (c). The increase in energy intensity can be attributed to the increase in stopping frequency from the shortened interval time. Considering a 30 s measurement window, T_{inv} = 30 s introduces one dwell phase, T_{inv} = 15 s introduces two dwell phases and T_{inv} = 5 s introduces 6 dwell phases. The shorter interval time therefore induces a more pronounced effect upon the flow. The two main peaks associated to impeller blade passage are seen to reduce in intensity with the reduction in interval time. This is due to an equal and unchanging amount of overall energy available to the system at N = 90 rpm, which is partially transferred to the low frequency peaks during intermittent impeller agitation. **Figure 3.16** shows the integral of the energy associated with the first six significant low frequency peaks for each of the T_{inv} conditions investigated. The inverse relationship between interval time and the energy associated to the characteristic low frequency peaks is clearly observed.

Phase-resolved analysis over one revolution of the impeller shows little variation in the periodic velocity values, $\tilde{u}_\theta$ (a) and fluctuating velocity values, u'_θ (b), with decreasing interval time, as shown in **Figure 3.17**. This suggests that the change in T_{inv} has little impact upon the average velocities in one revolution measured. Phase-resolved analysis was therefore considered between two dwell phases instead of over one revolution. **Figure 3.18** shows the average velocities taken between each dwell phase, $\tilde{u}_\theta$, for the three interval times investigated, T_{inv} = 30 s (a), T_{inv} = 15 s (b) and T_{inv} = 5 s (c). As before,

impeller rotation between dwell phases is denoted by the sinusoidal waves. The number of completed revolutions decreases as T_{inv} decreases, shown by approximately 90 sinusoids at T_{inv} = 30 s and 15 sinusoids at T_{inv} = 5 s. Although the same dwell duration is used, a larger drop in velocity after the dwell can be observed, before a steady state is achieved. The drop becomes more pronounced as T_{inv} decreases. This suggests that the velocity gains less momentum when the shorter intervals are used, thus impacting upon the velocity drop observed.

3.2.2.2 Impact of time component, T_{dwell}

Investigation of the impact of T_{dwell} upon the resultant energy spectra was carried out and the results are shown in **Figure 3.19** at T_{dwell} = 1 (a), 500 (b), 900 (c) and 1500 ms (d) at constant N = 90 rpm and T_{inv} = 30 s. **Figure 3.19** (a) shows a spectrum comparable to the one obtained at continuous agitation, given in **Figure 3.3** (a). Due to the very short dwell time (T_{dwell} = 1 ms), the inertia of the flow is such that no profound effect on fluid flow is noted within the vessel. Observing the energy spectra for increasing dwell times (**Figure 3.19** b – d), the range in low frequency peaks remained unaffected, however the associated energy intensity is shown to increase with T_{dwell}. **Figure 3.20** (a – d) display the velocity time-series plots for T_{dwell} = 1, 500, 900 and 1500 ms, respectively, at N = 90 rpm and T_{inv} = 30 s. As expected, the shortest dwell time shows no drop in fluid velocities. Increasing the dwell phase resulted in a longer drop in the velocity, thus increasing the loss in fluid inertia. This results in the amplification of the energy intensity of the low frequency peaks. **Figure 3.21** shows the integral of the energy associated with the first six significant low frequency peaks for continuous agitation (N = 90 rpm and T_{dwell} = 0 ms) and intermittent agitation for T_{dwell} = 1 – 1500 ms at N = 90 rpm and T_{inv} = 30 s. The cumulative energy is shown to increase significantly with the increase in dwell and the corresponding number of missed revolutions during the dwell, i.e. K^*.

Observing the periodic velocity values, $\tilde{u}_\theta$ (a), and turbulent component, u'_θ (b), between two dwell phases is shown in **Figure 3.22** for T_{dwell} = 1 (a), 500 (b), 900 (c) and 1500 ms (d). An increasing drop in velocity can be observed in the transient directly after the dwell with increasing dwell duration. This also suggests an increasing loss in flow inertia with the longer dwell phase, thus impacting upon the velocity drop, as expected and the time needed to reach steady state.

3.2.2.3 Impact of time component, *N*

Once the impact of the time components T_{dwell} and T_{inv} had been investigated in a parametric study, an attempt was made to determine a scale-invariant parameter at which the low frequency peaks would be the same for different rotational speeds, *N*. It would then be possible to recreate the low frequency peaks, originally implemented by Correia *et al.* (2014), with an alternative selection of operating conditions (*N*, T_{inv} and T_{dwell}), to potentially establish a more robust procedure for cell differentiation. To assess preservation of the low frequency peaks at various rotational speeds, the number of missed revolutions, K^*, defined in Equation 2.3, was selected as a scale-invariant parameter to be kept constant.

Experiments were investigated at *N* = 75, 90, 105 and 120 rpm, with four constant values of K^* = 0.75, 1.05, 1.5 and 2.25. The selected rotational speeds represent the typical range applicable for PSC-cardiogenic differentiation protocols. The values of K^* were selected based upon *N* = 90 rpm, T_{inv} = 30 s and T_{dwell} = 500, 700, 1000 and 1500 ms. **Figure 3.23** (a – d) give the energy spectra at K^* = 0.75 for *N* = 75 – 120 rpm, respectively. As it can be observed from the insets, all experiments exhibited similar low frequency peaks when K^* was kept constant. The main frequency peaks associated with the impeller blade passage reflect the changes in rotational speed, with the apparent increase in overall power available to the system at increasing speeds. Observing the velocity time-series plots in **Figure 3.24** (a – d) at K^* = 0.75 for *N* = 75 – 120 rpm, respectively, it is again evident that an increasing amount of overall energy is available to the system with the increase in the velocity range with rotational speed.

To quantitatively assess the suitability of the number of missed revolutions to preserve the low frequency peaks, the integral of the energy associated with the first six significant low frequency peaks at K^* = 0.75, 1.05, 1.50 and 2.25 with increasing *N* is given in **Figure 3.25**. The cumulative energy measured for K^* is approximately constant with *N*, thus confirming that the number of missed revolutions can be used as a decisional parameter to consistently recreate the low frequency spectrum across the selected range of time scales.

The periodic tangential velocity component between dwell phases normalised against the corresponding tip speed, $\tilde{u}_\theta / V_{tip}$, is plotted in **Figure 3.26** for K^* = 2.25 at *N* = 75 (a), 90 (b), 105 (c) and 120 rpm (d). Observing the maximum drop in velocity between *N* = 75 and 120 rpm, less than 20 % difference in the two values is observed. The time needed to

resume the steady state between N = 75 – 120 rpm is also shown to vary up to approximately 10 %. This suggests a similar drop in velocity and time to achieve steady state whilst maintaining the number of missed revolutions.

To summarise, **Figure 3.27** shows the integral of the energy intensities associated to the low frequency peaks for each rotational speed investigated at the different K^* conditions. A cluster for each K^* condition can be observed, proving that the number of missed revolutions for a range of speeds and dwell durations does recreate the low frequency peaks detected. This may introduce the possibility to operate the differentiation process at lower rotational speeds, thus reducing the characteristic frequencies associated to the impeller rotation. The user may also be able to operate at faster rotational speeds to maximise mixing efficiency and mass transfer within the flow. The complexity of a cell culture system however, as highlighted in Chapter 1, suggests that a myriad of contributing factors, such as mixing, suspension and shear, are all likely to impact upon the obtained differentiation yields and thus must also be characterised before further optimisation and better understanding of the system is possible.

The results obtained in Section 3.2.2 established two main flow parameters affected by the variation of the three time components; the spectrum peak intensities and their associated frequencies. The results from Section 3.2.2.2 suggest that T_{dwell} impacts directly upon the energy intensities associated to the low frequency peaks. Changing the interval time, T_{inv}, in Section 3.2.2.1, was shown to not only impact upon energy intensity, but also upon the peak frequencies generated. To investigate the impact of the low frequency peaks upon biological outcomes, both time components T_{inv} and T_{dwell} would need to be simultaneously amended to preserve a constant associated peak intensity at a different range of low frequencies. In addition, the CM-differentiation yields published by Correia *et al.* (2014) showed the best and worst agitation modes were associated to the lowest (intermittent agitation without a direction change) and the highest (intermittent agitation with a direction change) low frequency peak associated intensities. The biological studies were designed, given the complexity of the biological system, to investigate the impact of adjusting a single time component, T_{dwell}, associated to the single parameter change of peak intensity, upon cardiogenic differentiation.

3.2.3 iPSC-cardiomyocyte differentiation studies

The next stage of this investigation sought to ascertain the performance of an iPSC-CM differentiation culture in response to a change in hydrodynamic cues. Specifically,

modulation of the energy intensities associated with the low frequency peaks was investigated through modulation of T_{dwell}. Two cell culture experiments were conducted from monolayer iPSC expansion to differentiation in a three-dimensional bioreactor culture. The original differentiation protocol, reported by Correia *et al.* (2014), was initiated at Day 2 until Day 9 in culture, with the selection process occurring from Day 9 until Day 16. As differentiation yield was the performance parameter under investigation, culture was run until Day 9 only. Two dwell conditions were investigated, T_{dwell} = 500 and 1500 ms, representing a decrease/increase in the dwell duration from the control condition at T_{dwell} = 900 ms [all at N = 90 rpm and T_{inv} = 30 s]. T_{dwell} = 500 ms represents an approximate 44 % reduction in the cumulative energy associated to the low frequency peaks in comparison to the control condition, whilst T_{dwell} = 1500 ms represents an increase of approximately 67 %. For each experimental run, performance was assessed by expression of the cardiac specific marker, cardiac troponin T (cTnT).

To ascertain meaningful biological outcomes, consistency in aggregate seeding and cell pluripotency between the experimental condition and the respective control condition at the start of cell culture were assessed. Prior to aggregation of iPSCs, phenotypic analysis was performed on Day 0. **Figure 3.28** shows a largely undifferentiated pluripotent cell population, indicated by high expression of pluripotency markers, OCT-4 (87.35 ± 3.7 %) and SSEA-1 (86.11 ± 1.7 %) for both experimental runs. For murinal iPSCs SSEA-4 is a marker for the early stages of differentiation. **Figure 3.28** gives a slightly larger range between the two experimental runs (52.64 ± 7.07 %), however this is within the measurement error, discussed in detail at the end of this section, and generally both runs exhibit a high level of pluripotency. Aggregates were inoculated at 159 ± 4 aggregates/mL for all bioreactors on Day 2 and showed relative uniformity in size, D_{50} = 157.44 ± 12.48 μm.

Measurement of aggregate number, size and cell number from Day 2 – Day 9 are given in **Figure 3.29**, (a), (b) and (c), respectively. Generally, an increase in cell and aggregate number and in aggregate size can be observed. The error bars represent the inherent biological variability, in addition to the systematic error associated with the cell/aggregate counting procedures. Over the course of differentiation, an increase in aggregate size and elongation is expected. Keung *et al.* (2014) describe mature cardiomyocytes to typically exhibit $D_{50} \geq 100$ μm with a rod-shaped morphology. PSC-derived CMs often display an immature/foetal-like phenotype, maintaining the round morphology of PSCs, and are typically much smaller in size, around 10 – 20 μm in diameter (Keung *et al.*, 2014).

Correia *et al.* (2014) comment on the differentiation protocol favouring the production of immature foetal-like cells. In this work the same protocol is used, thus no significant increase in aggregate size is observed (**Figure 3.29** b). **Figure 3.30** (a and b) show the aggregate roundness and elongation over the differentiation process. In accordance with the previous observation, no significant decrease in aggregate roundness or increase in aggregate elongation is evident.

It is possible to approximate the average number of cells/aggregate based on the measured concentrations. It is then possible to approximate the average cell size based upon the measured aggregate sizes.

$$D_{50,cells} = \frac{D_{50,agg}}{\sqrt[3]{cells/_{agg}}} \quad \textbf{(3.1)}$$

The number of cells/aggregate and approximate cell size are given in **Figure 3.31** (a) and (b), respectively. Error propagation was calculated arithmetically. An increase in cell number from Day 2 – Day 9 can be observed as cells continue to proliferate during the differentiation protocol. Approximate cell size in **Figure 3.31** (b), D_{50} = 15 and 12 μm for experimental run 1 (T_{dwell}500 and control 1) and experimental run 2 (T_{dwell}1500 and control 2), respectively, shows no significant change over time, although standard deviation is shown to increase on average by 32 % from Day 2 to Day 9. Generally, stem cells are smaller than differentiated cells. Li *et al.* (2016) discuss the typical sizes of single stem cells to be 3 – 10 μm, depending upon the cell type and cell source. Considering immature differentiated CMs are typically 10 – 20 μm in size (Keung *et al.*, 2014), a significant increase in cell size may not be observed. It is also worth noting that the work of Correia *et al.* (2014), with numerous biological repeats, showed almost identical calculated cell sizes (data not published) to the results obtained in this work.

Figure 3.32 presents the measured glucose (a) and lactate (b) concentrations over the differentiation process to assess metabolic activity. The increasing consumption of glucose and production of lactate suggests cell metabolic activity and proliferation. Using Equation 2.29 it was possible to calculate the rates of consumption and production of glucose and lactate, respectively, given in **Figure 3.32** (c). On Day 2 the rates of consumption, q_{GLU}, and production, q_{LAC}, are highest, representing a metabolically active cell population. As the culture time increases, q_{GLU} and q_{LAC} decrease, showing the depletion in glucose availability and reduction in cell metabolism. It is worth noting that although high concentrations of lactate are generally considered detrimental to iPSC

proliferation (Chen *et al.*, 2010; Abecasis *et al.*, 2017), the lactate concentration did not reach toxic levels in this work, generally considered at 50mM and above (Schroeder *et al.*, 2005; Niebruegge *et al.*, 2008). Observing q_{LAC} and q_{GLU}, the rate of production of lactate is approximately double the rate of consumption of glucose. When the yield of lactate on glucose, $Y_{qLAC/qGLU} \approx 2$, this suggests that almost all glucose is consumed and converted into lactate via glycolysis. **Figure 3.32** (d) gives the average yield of lactate on glucose for each bioreactor condition. For all experimental conditions, $Y_{qLAC/qGLU} \approx 2$, with the exception of T_{dwell} = 1500 ms, which gives a lower yield. The value of $Y_{qLAC/Qglu} < 2$ for T_{dwell} = 1500 ms indicates a higher energetic metabolism from the reduction in lactate production, suggesting that once lactic acid is produced within the cells, this was then partially catabolised through the TCA cycle, producing a higher amount of energy within the cell in comparison to glycolysis alone. This is reflected by the slightly larger increase in cell and aggregate concentrations over the culture period.

Cells remained largely viable over the course of differentiation in all conditions investigated. Fluorescein diacetate (FDA) is taken up by viable cells and is converted into the fluorescent green metabolite fluorescin. Propidium iodide (PI) is a nucleus red dye which stains the nucleus of dead cells with a compromised cell membrane. Live stains using addition of FDA and PI in both experimental run 1, comparing T_{dwell} = 500 ms with the control (**Figure 3.33**) and experimental run 2, comparing T_{dwell} = 1500 ms with the control (**Figure 3.34**) are shown. Strong uptake of FDA in all conditions is apparent, representing good cell viability throughout the culture.

This work and the original study by Correia *et al.* (2014) use a transgenic iPSC cell line, expressing green fluorescent protein (GFP) with cardiogenic differentiation. The original study by Correia *et al.* (2014) measured cardiomyocyte differentiation yields through GFP expression using flow cytometry. As can be seen from **Figure 3.35** for Day 9 aggregates in experimental run 1 (a) and 2 (b), GFP expression within the cells is very limited and sporadic. Phenotypic analysis on Day 9 measured both GFP expression of the cells and cardiac specific, cardiac troponin T (cTnT) expression. This is shown in **Figure 3.36**, where a significant reduction in GFP expression, between 75.5 – 94 %, in comparison to cTnT expression, is observed. This suggests the cell population lost their propensity to express GFP, likely as a result of the instability of inheritance and expression of the transgene. Consequently, cardiogenic differentiation yields in this work were calculated based upon cTnT expression.

Table 3.2 summarises these results and aims to compare cardiomyocyte purity, number and yield per input iPSC, normalised against the control condition for each experimental run. Overall, it is shown that as T_{dwell} was increased from 500 ms – 1500 ms the cardiogenic differentiation efficiency increased up to 66 % when compared to the control condition (T_{dwell} = 900 ms, using magnetically-driven agitation). Concordantly, the differentiation yield was shown to decrease at the shorter dwell time in comparison to the control condition. It can be seen from **Table 3.2** that no significant change in CM purity is attained. Purity was not compromised during the different biological cultures run as the percentage differences, + 10.7 % and - 4.6 %, were within the experimental error of 22.4 and 20.7 %, respectively. The error values were calculated based upon propagation of the error determined in Correia *et al.* (2014); 15 % for cardiomyocyte purity, 2.5 % for cardiomyocyte number and 5 % for cardiomyocyte yield. Differences observed between CM number and CM yield (**Table 3.2**) are due to variability of the iPSC inoculum density. Following the same protocols in Correia *et al.* (2014), aggregate concentration for inoculation was maintained constant between runs, this varied by up to 3 %. Both values are presented to show that adjustment of the frequency peak intensities, from changing T_{dwell}, impact upon CM differentiation efficiency most prolifically through CM number and yield (**Table 3.2**).

3.3 Concluding remarks

The objectives of the work presented in this chapter were to investigate the characteristic flow frequencies of different agitation modes within a DASGIP bioreactor configuration and to correlate this to biological outcomes of a iPSC-CM differentiation process. Specifically, the influence of three time components, defined during continuous and intermittent agitation modes, upon the main flow parameters, i.e. the spectrum peak intensities and their associated frequencies, were investigated in detail. Biological investigation of a single flow parameter, in this case the spectrum peak intensities, was then performed, showing the impact of flow cues upon a biological process. This work shows a relationship between the hydrodynamic environment and cell differentiation yields associated with the engineering characteristics. It is evident that an optimal range of the low frequencies and their amplification exists, and that a combination of both engineering and biological investigation is essential to establish causal relationships and exploit flow cues to optimise a differentiation process.

In recreating the three agitation modes first investigated by Correia *et al.* (2014), it was possible to investigate the characteristic flow frequencies with each agitation mode explored. It was found that introduction of low frequency peaks during intermittent agitation, related to the time components T_{inv} and T_{dwell}, proved beneficial to cardiogenic yields. Two-phase studies revealed an increase in the energy intensities associated to the low frequency peaks with addition of Cultispher-G, representing the physical properties of the EBs at the end of differentiation where cardiogenic yields were highest. This suggests moderate amplification of the low frequency peaks earlier in the differentiation process may continue to increase differentiation yields. The initial proof-of-concept biological study undertaken in this chapter showed a conservative 67 % increase in the cumulative low frequencies, from T_{dwell} = 900 ms to 1500 ms, is beneficial for cardiogenic differentiation through improved cardiogenic yields up to 66 %. Engineering characterisation for the intermittent agitation mode with a direction change showed the detrimental impact of significant (700-fold) amplification of the low frequency region on cardiomyocyte generation. A threshold to amplification of energy intensities associated with the low frequency peaks is apparent. This demonstrates the importance of careful selection of operating parameters when considering a cell culture process.

Enhancement of cardiogenic yields increases the cost-effectiveness of the number of CMs produced/L. This in turn would contribute to the development of mass, clinically relevant numbers of CMs, through modulation of flow cues alone. This would reduce the overall need for additional chemicals or growth factors and longer differentiation protocols. The work in this chapter provides a proof-of-concept biological study, directly linking engineering parameters to the differentiation process outcomes. A well-established differentiation platform, i.e. a murine iPSC cell line utilising a spontaneous differentiation protocol, previously reported in the literature (Correia *et al.*, 2014), was used. Future work can further validate the outcomes discussed within this chapter and can transfer the knowledge attained to an optimised directed differentiation protocol, using more clinically relevant human PSC lines.

(a)

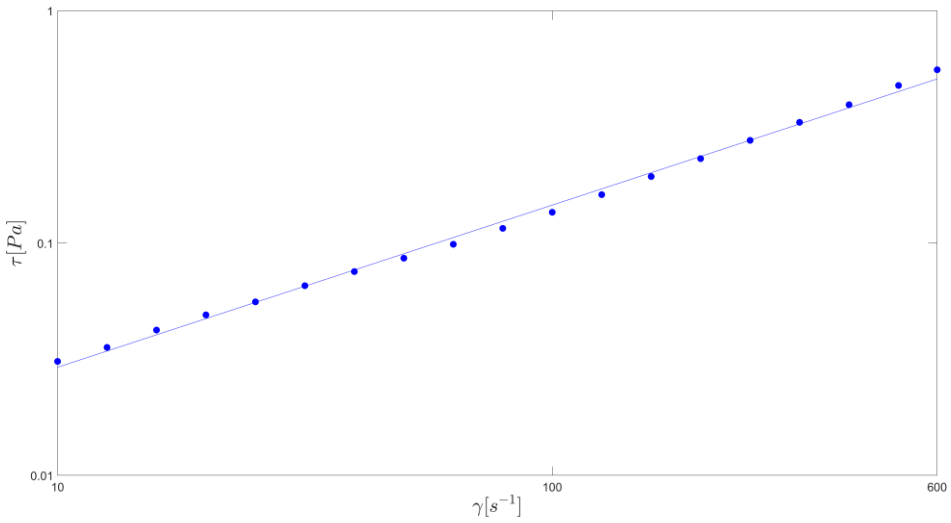

(b)

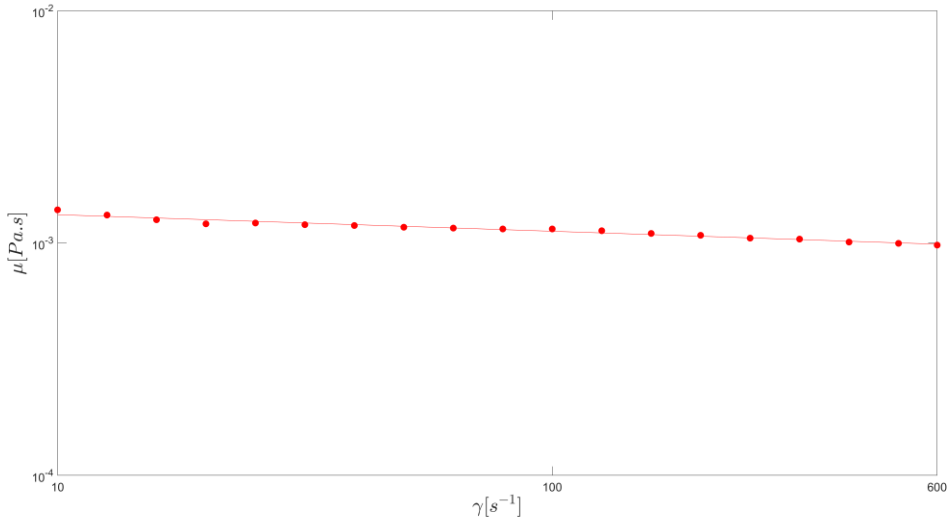

Figure 3.1 Rheological characterisation of iPSC differentiation medium for γ = 10 – 600 s^{-1}: (a) log-log plot of shear stress; (b) log-log plot of viscosity.

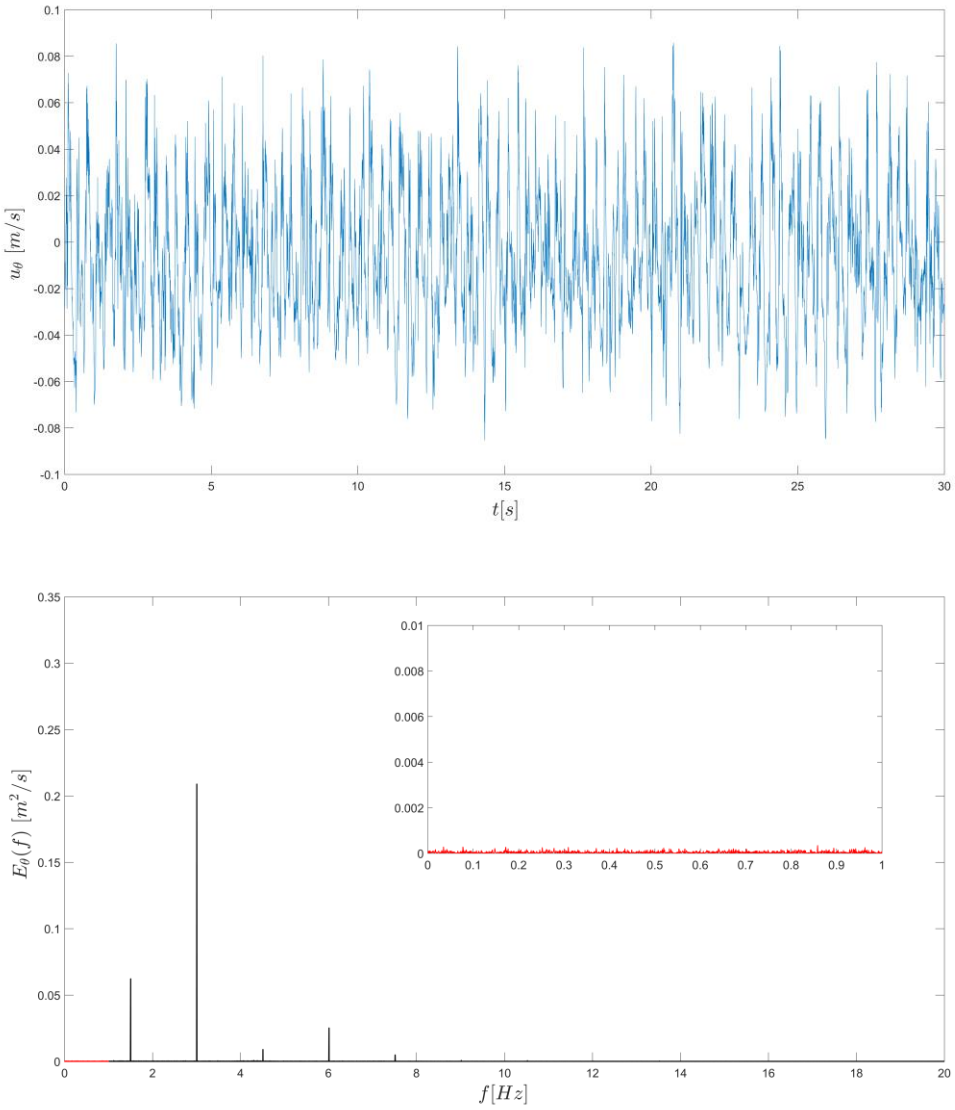

Figure 3.2 Instantaneous velocity time series and resultant energy spectrum from FFT analysis, N = 90 rpm.

(a)

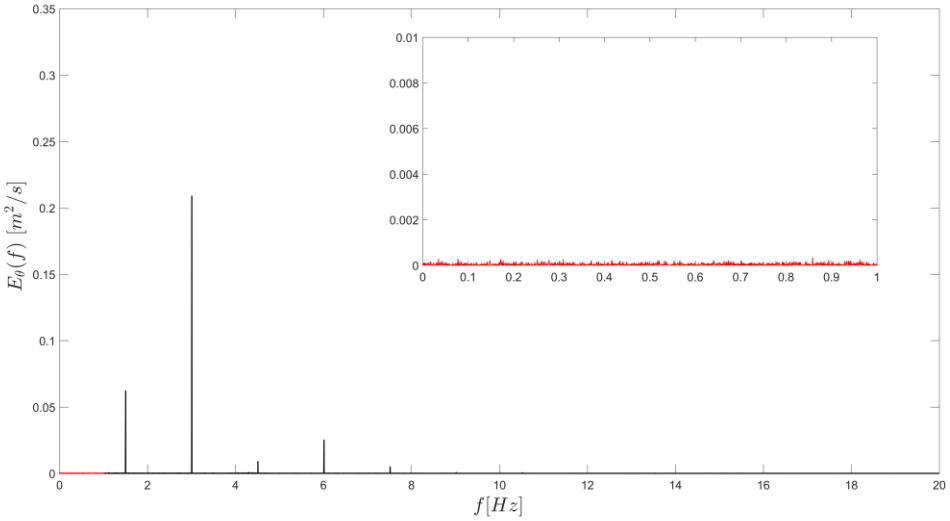

(b)

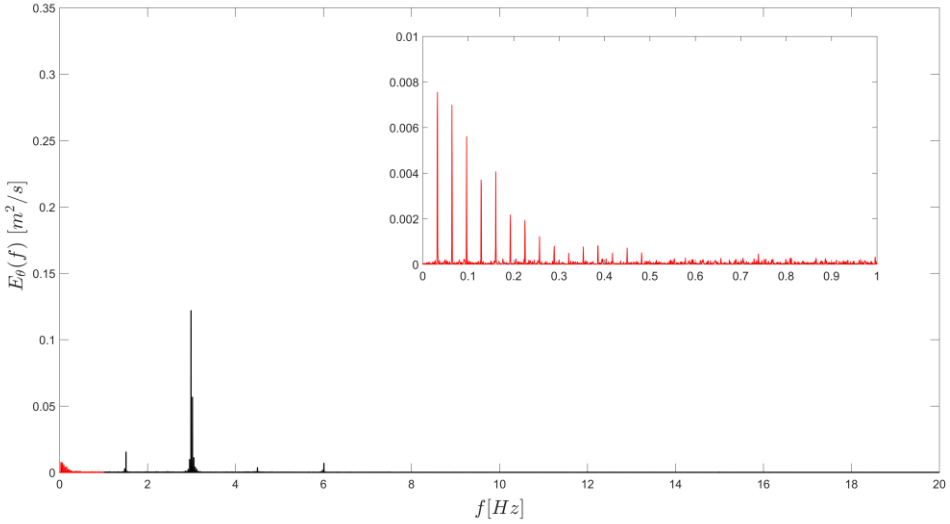

(c)

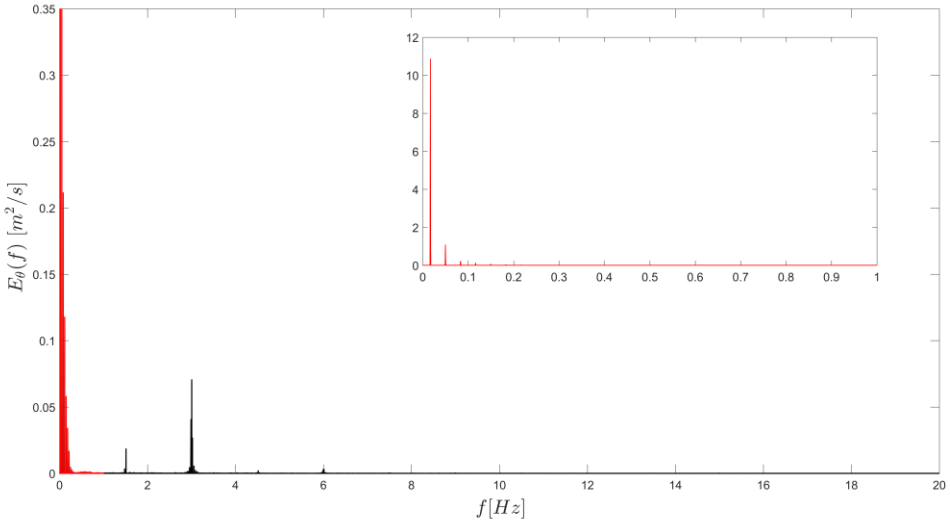

(d)

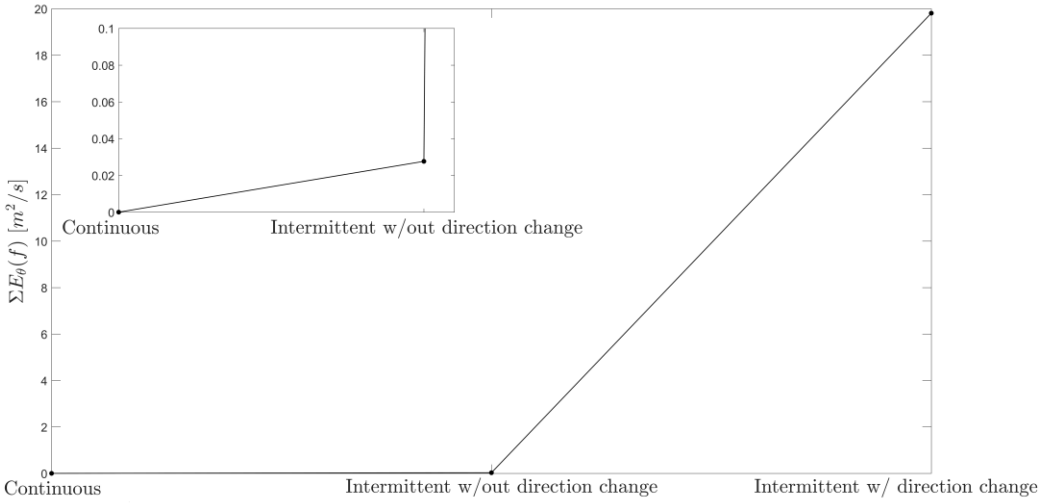

Figure 3.3 Energy spectra of the instantaneous tangential velocity: (a) continuous agitation, N = 90 rpm; (b) intermittent agitation without direction change, N = 90 rpm, T_{inv} = 30 s, T_{dwell} = 900 ms; (c) intermittent agitation with direction change, N = 90 rpm, T_{inv} = 30 s; (d) low frequency energy summation for the three agitation modes.

(a)

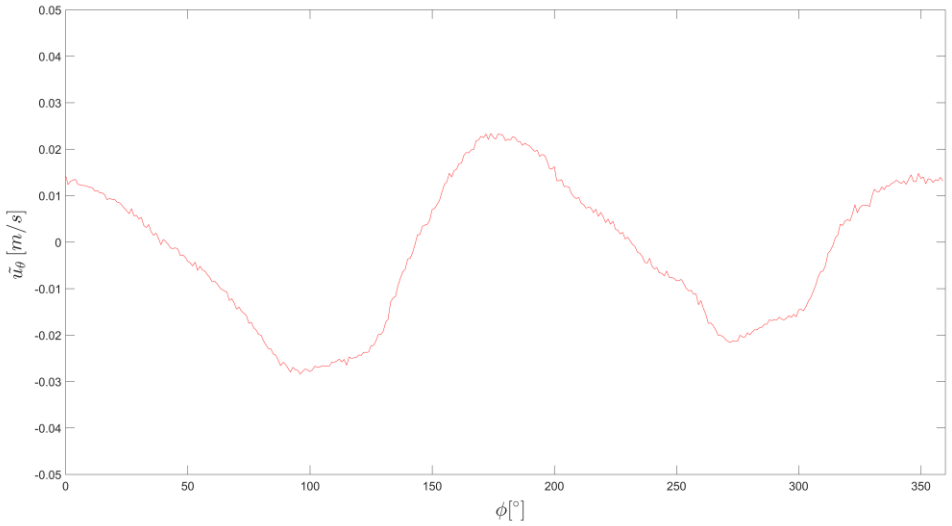

(b)

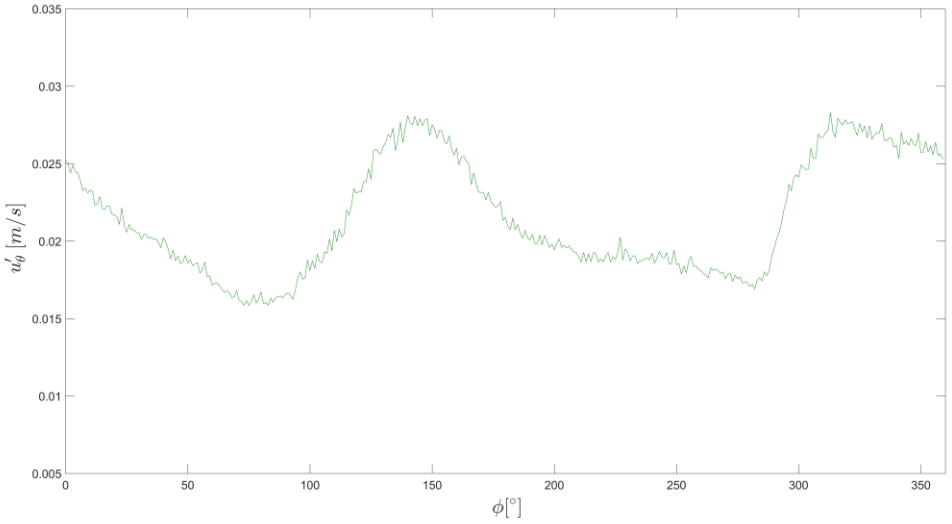

Figure 3.4 Phase-resolved analysis of continuous agitation, N = 90 rpm, for phase angles, φ = 0 – 360°: (a) periodic tangential velocity component, $\tilde{u}_\theta$; (b) tangential fluctuating component, u'_θ.

(a)

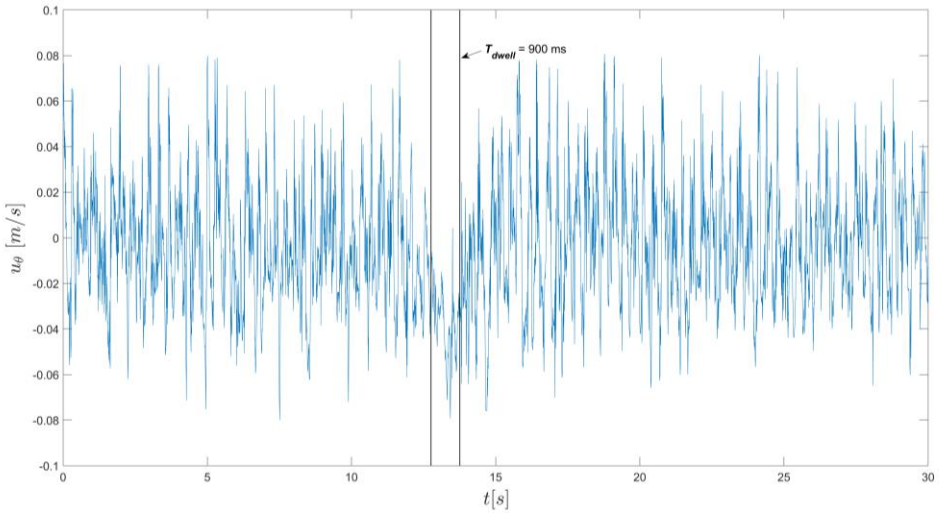

(b)

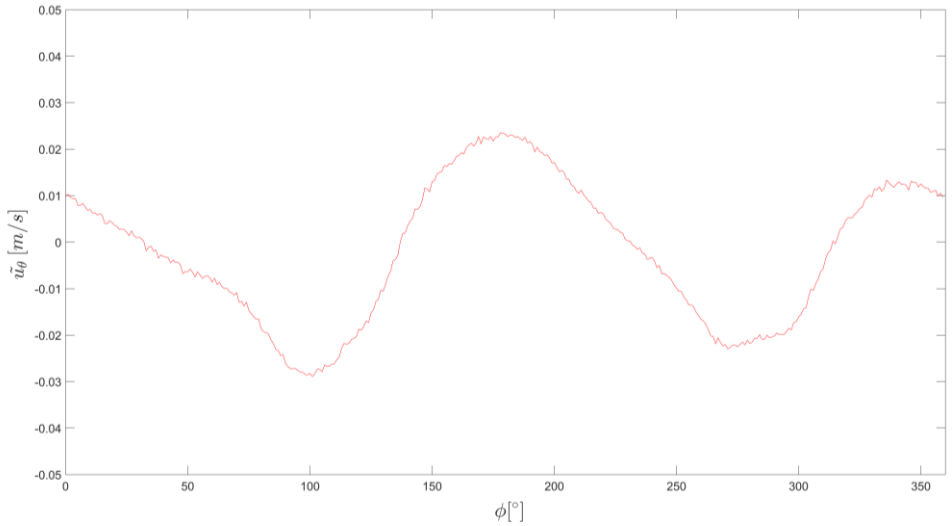

(c)

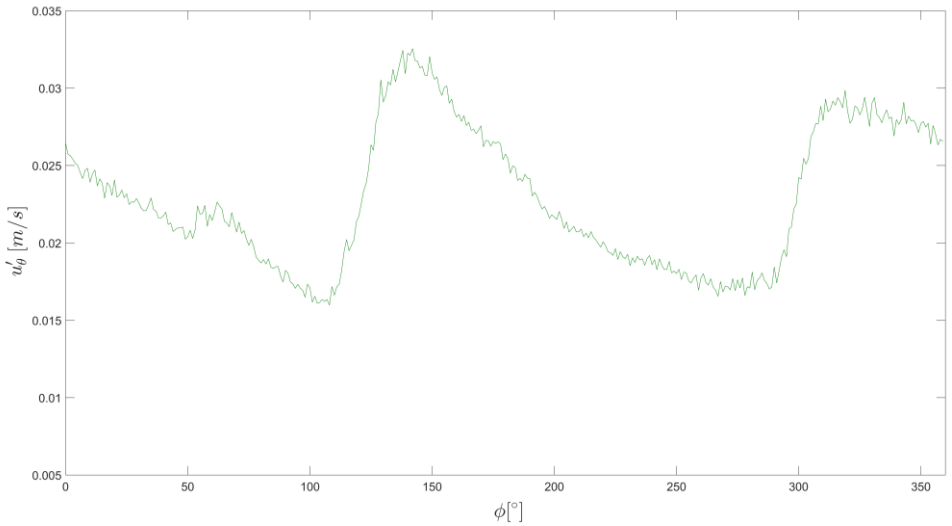

Figure 3.5 Intermittent agitation without a direction change, N = 90 rpm, T_{inv} = 30 s, T_{dwell} = 900 ms: (a) velocity time-series plot; (b) periodic tangential velocity component, $\tilde{u}_\theta$; (c) tangential fluctuating component, u'_θ.

(a)

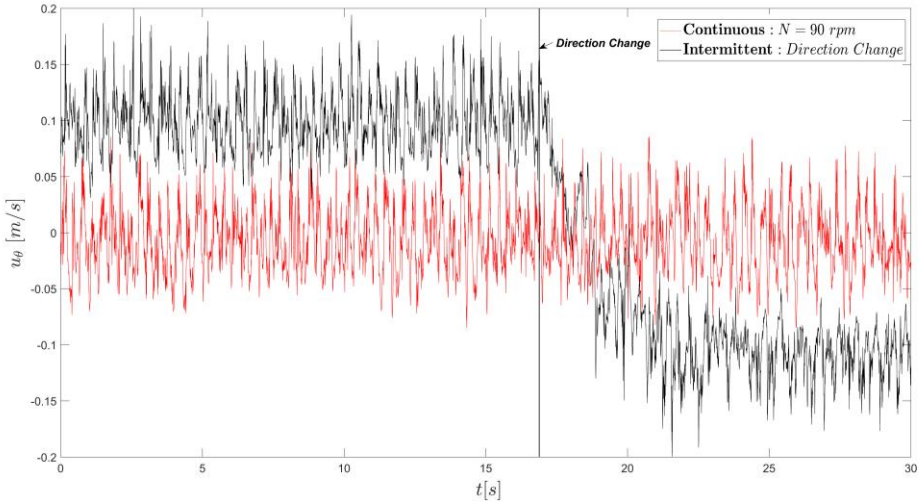

(b)

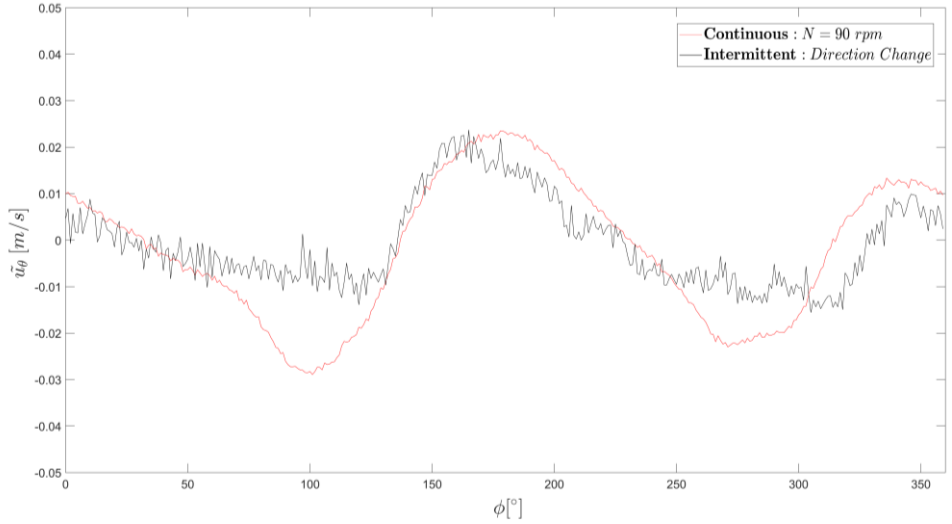

(c)

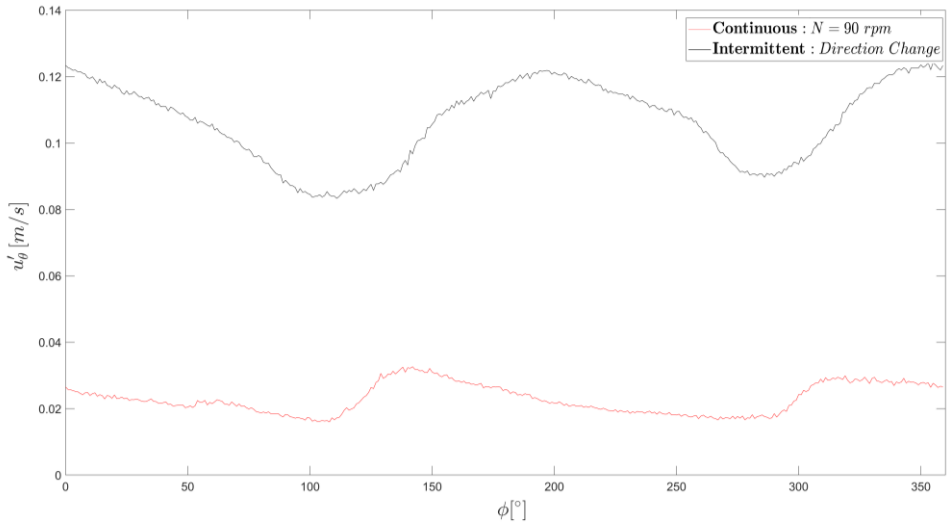

Figure 3.6 Intermittent agitation with a direction change (black), N = 90 rpm, T_{inv} = 30 s, overlaid with continuous agitation (red), N = 90 rpm: (a) velocity time-series plot; (b) periodic tangential velocity component, $\tilde{u}_\theta$; (c) tangential fluctuating component, u'_θ.

(a)

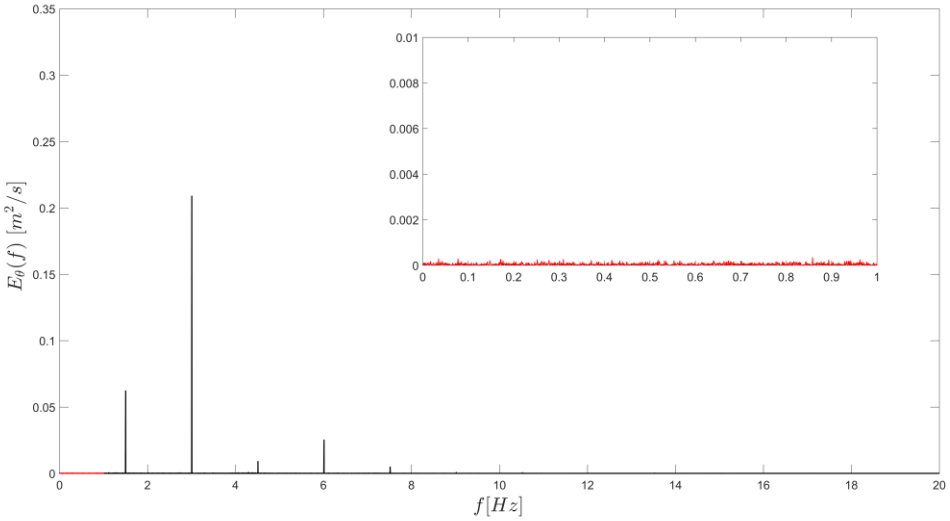

(b)

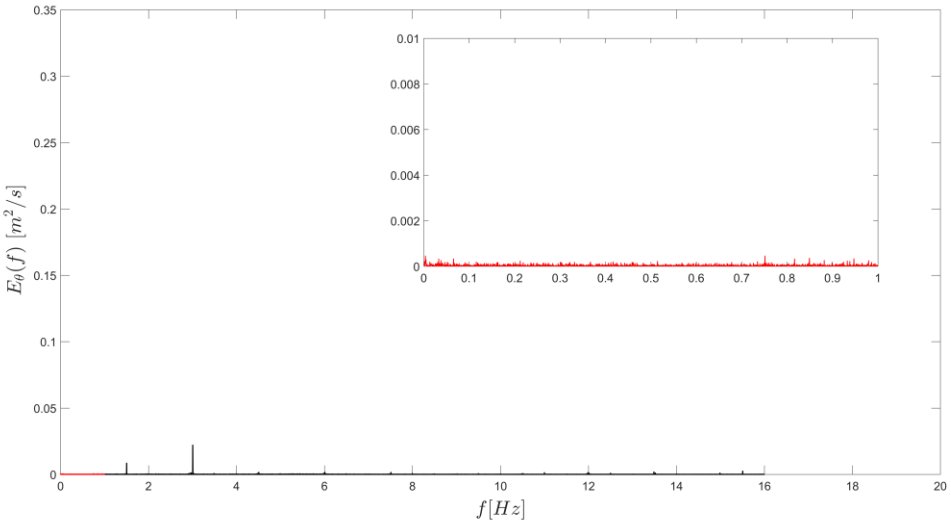

Figure 3.7 Energy spectra of the instantaneous tangential velocity for continuous agitation, N = 90 rpm: (a) measurement position A [r_A/T = 0.35 and z_B/H_L = 0.28]; (b) measurement position B, + 20 mm z-direction [r_B/T = 0.35 and z_B/H_L = 0.58].

(a)

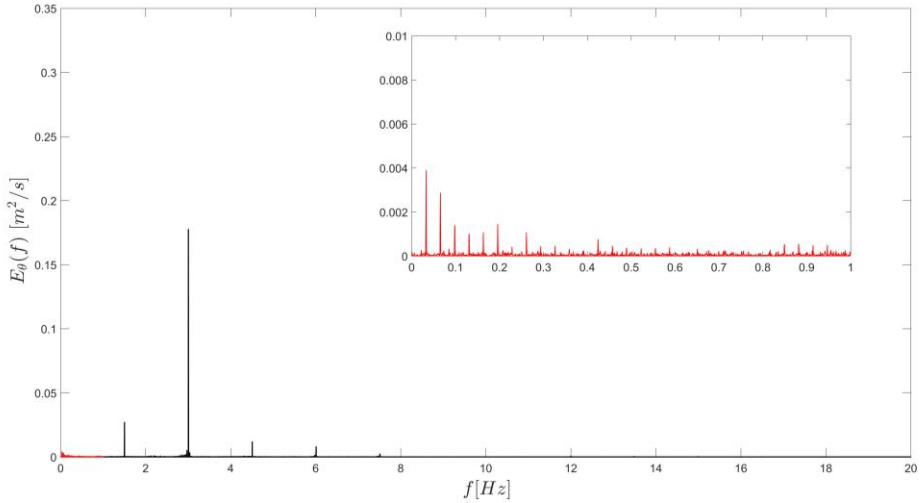

(b)

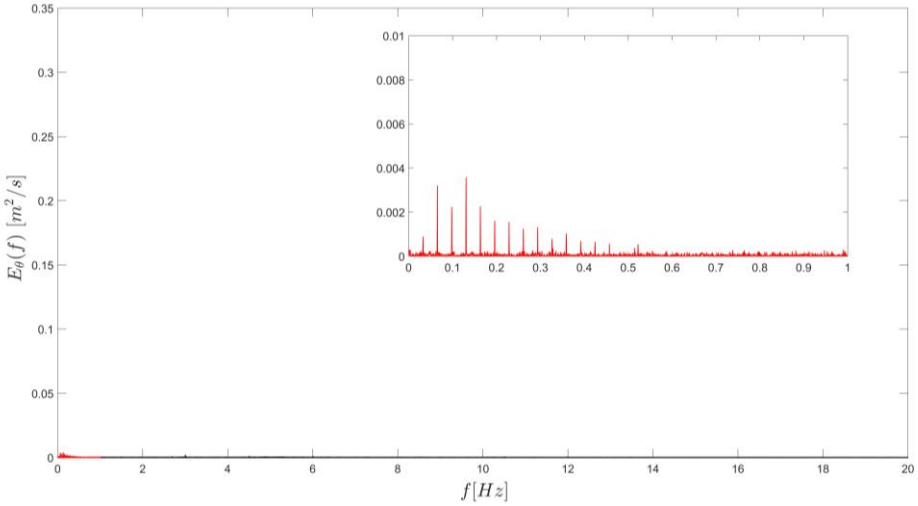

(c)

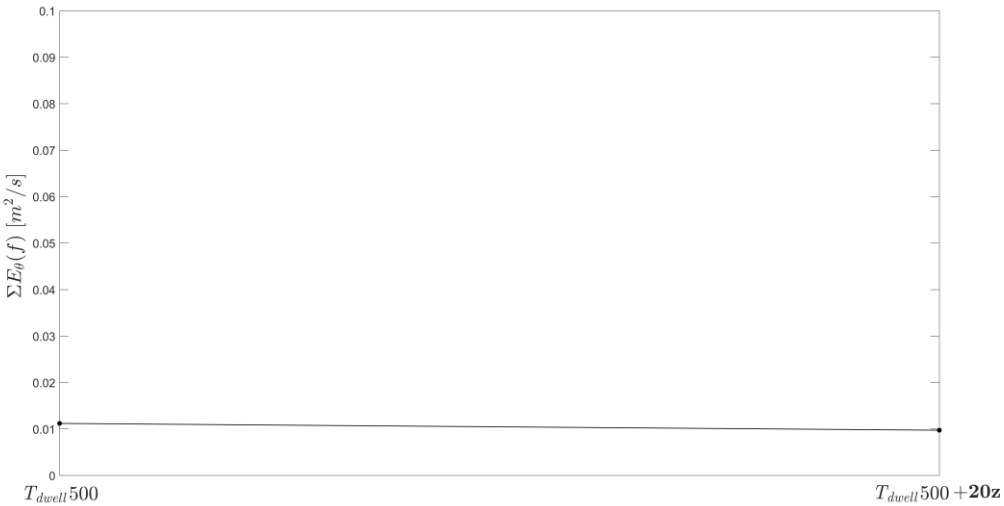

Figure 3.8 Energy spectra of the instantaneous tangential velocity for intermittent impeller agitation, N = 90 rpm, T_{inv} = 30 s, T_{dwell} = 500 ms: (a) measurement position A; (b) measurement position B, + 20 mm z-direction; (c) energy intensity summation of low frequency peaks.

(a)

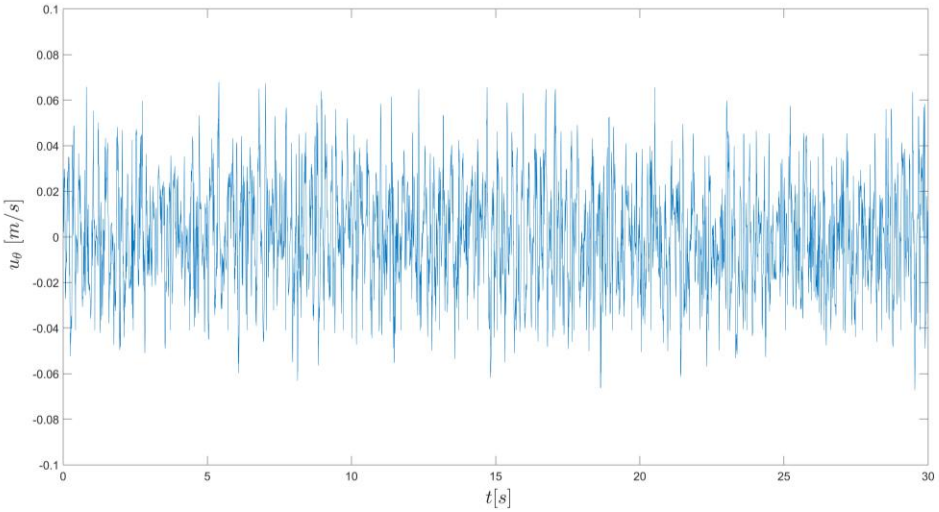

(b)

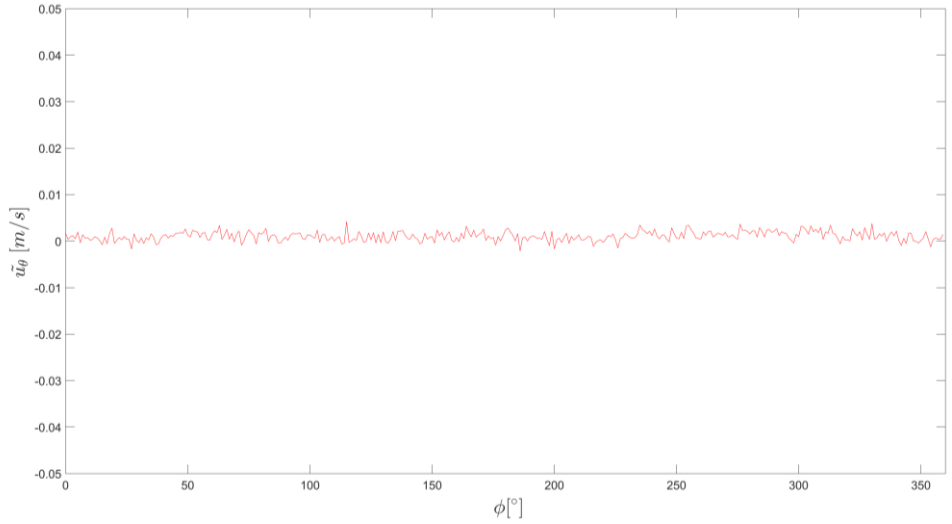

(c)

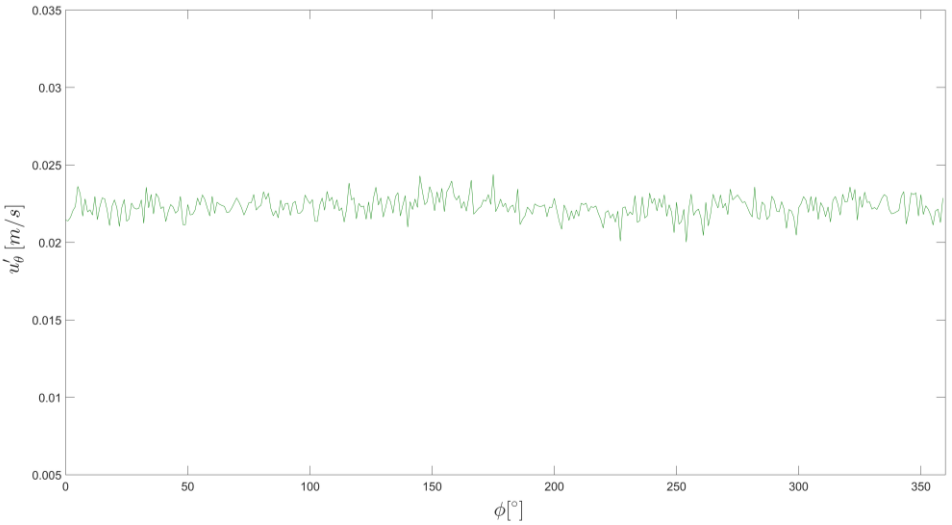

Figure 3.9 Continuous agitation measured at position B [r_B/T = 0.35 and z_B/H_L = 0.58], N = 90 rpm: (a) velocity time-series plot; (b) periodic tangential velocity component, $\tilde{u}_\theta$; (c) tangential fluctuating component, u'_θ.

(a)

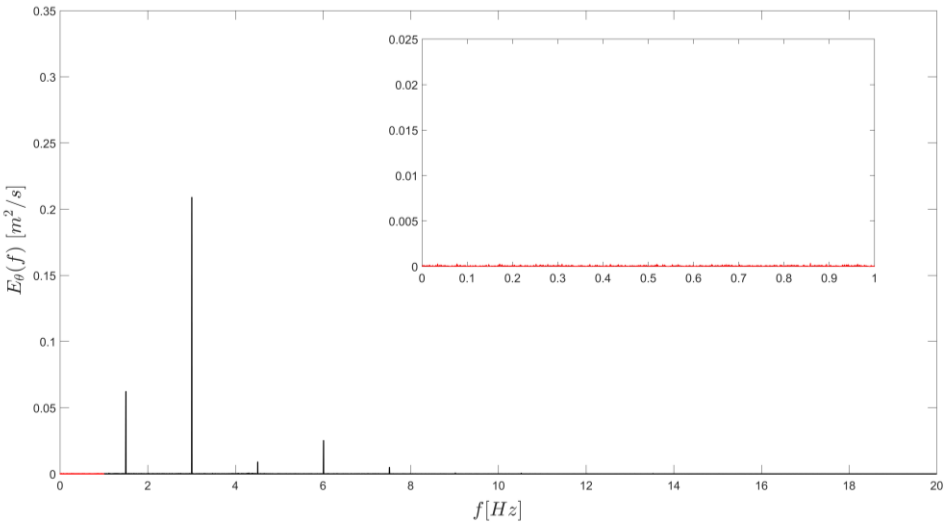

(b)

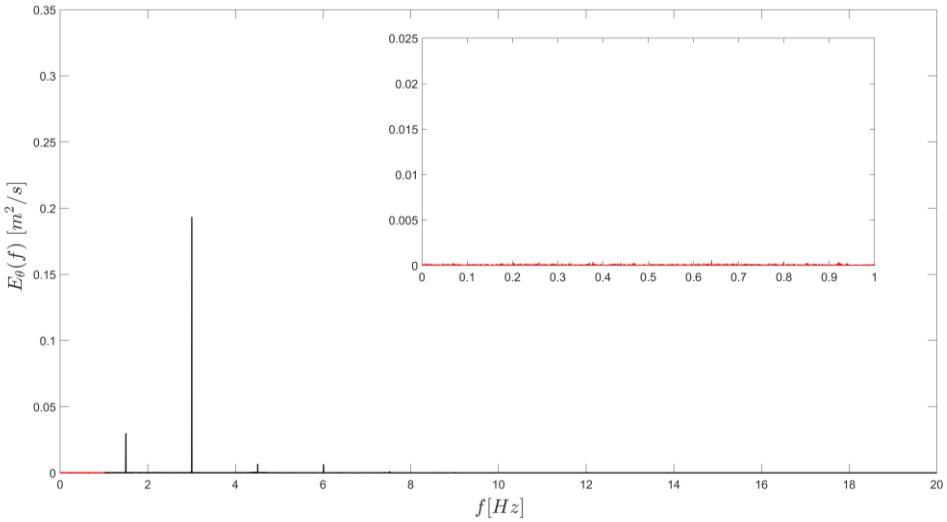

(c)

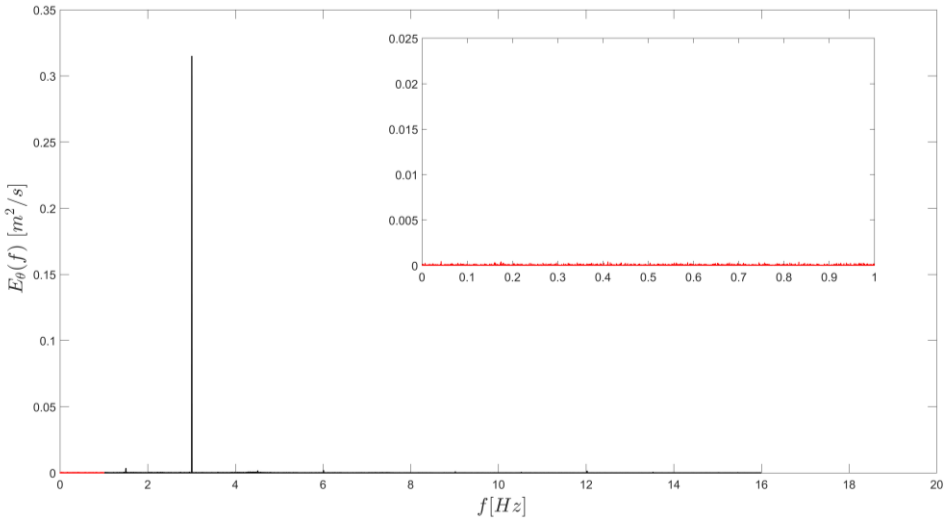

Figure 3.10 Energy spectra of the instantaneous tangential velocity for continuous agitation, N = 90 rpm: (a) single phase measurement; (b) two phase measurement with Cytodex 3; (c) two phase measurement with Cultispher-G.

(a)

(b)

(c)

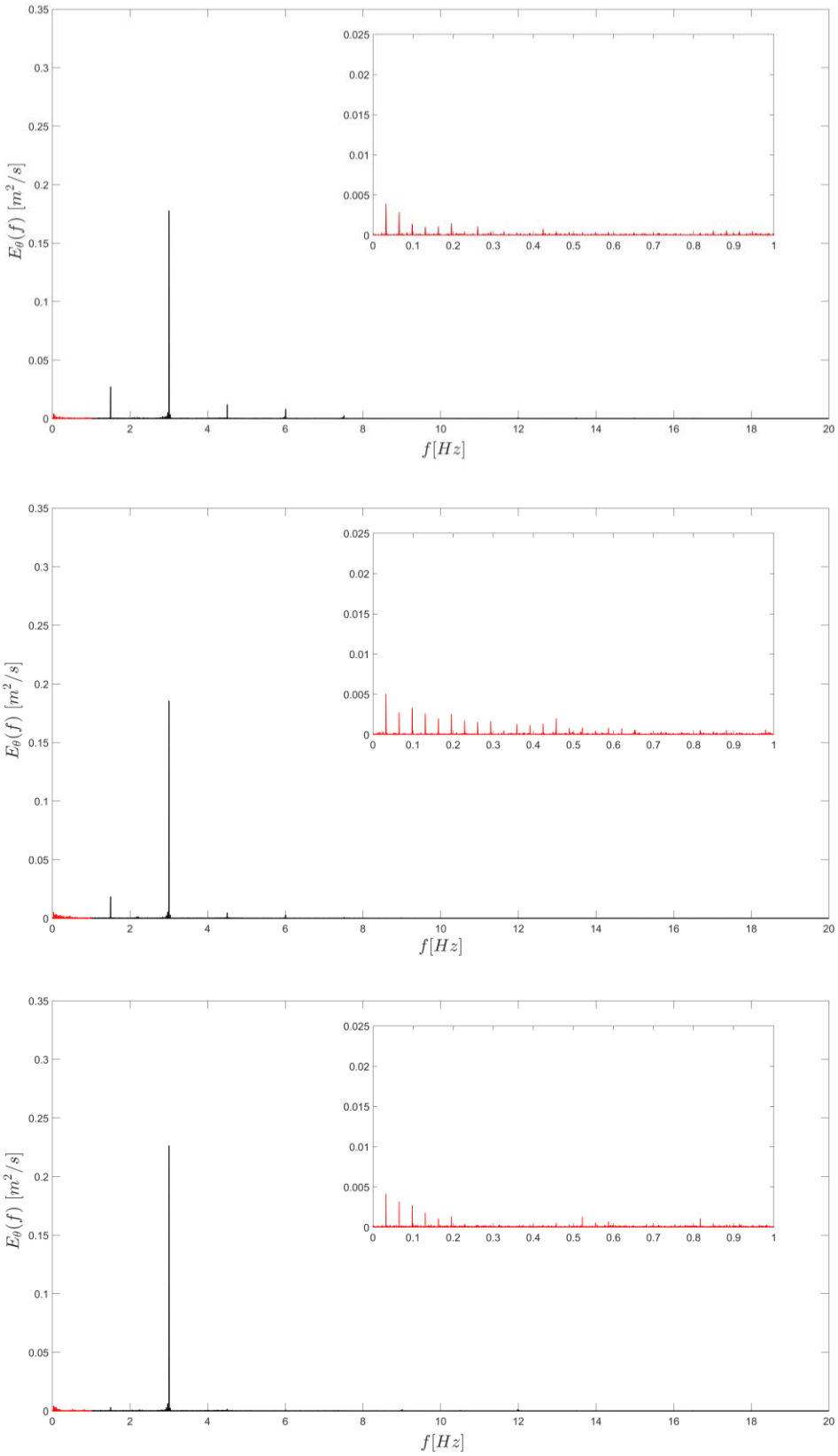

Figure 3.11 Energy spectra of the instantaneous tangential velocity for intermittent agitation, N = 90 rpm, T_{inv} = 30 s, T_{dwell} = 500 ms: (a) single phase measurement; (b) two phase measurement with Cytodex 3; (c) two phase measurement with Cultispher-G.

(a)

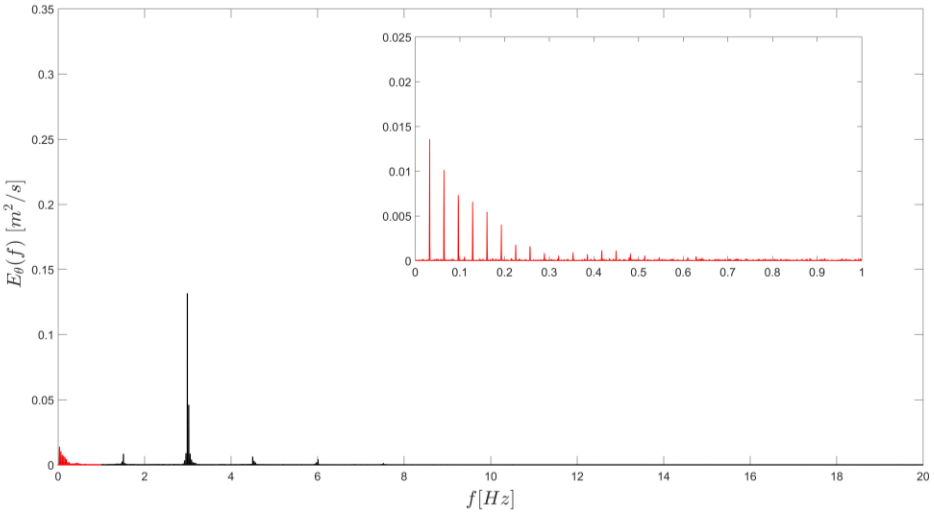

(b)

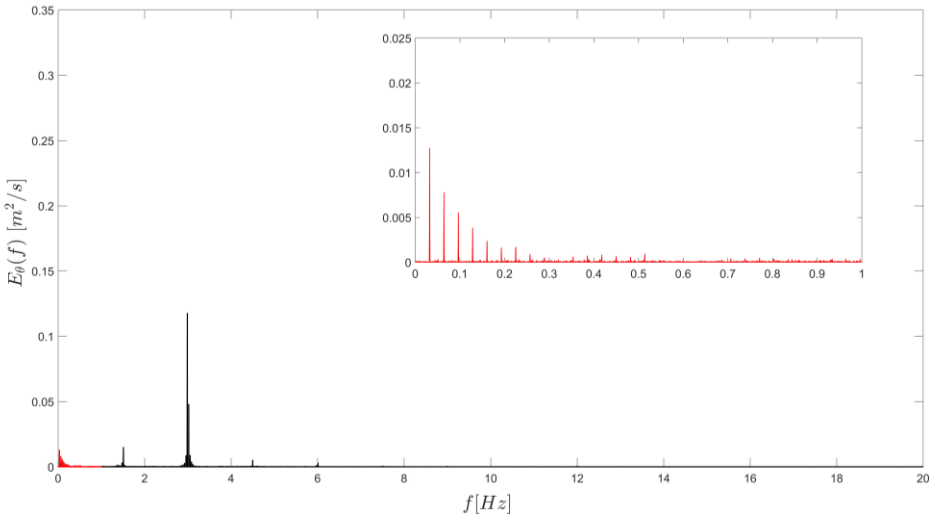

(c)

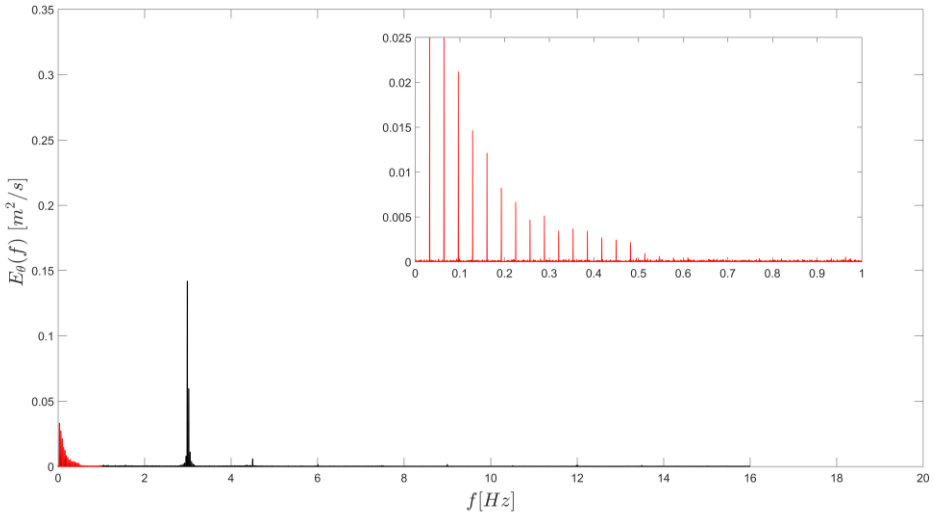

Figure 3.12 Energy spectra of the instantaneous tangential velocity for intermittent agitation, N = 90 rpm, T_{inv} = 30 s, T_{dwell} = 1000 ms: (a) single phase measurement; (b) two phase measurement with Cytodex 3; (c) two phase measurement with Cultispher-G.

(a)

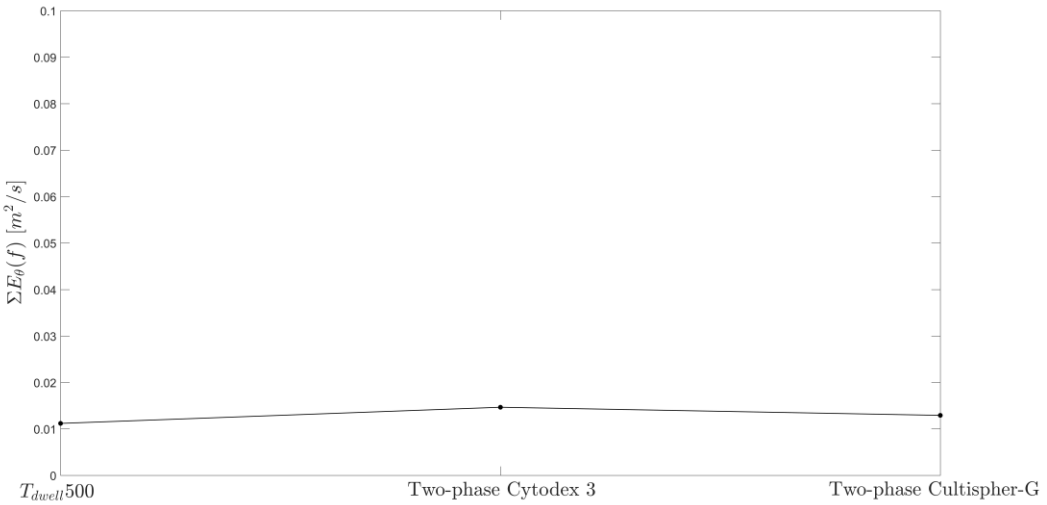

(b)

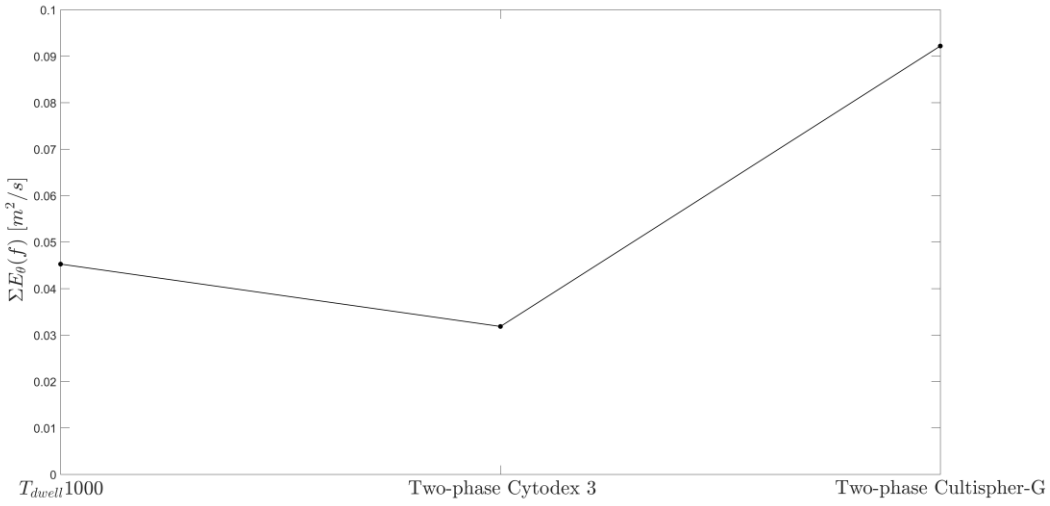

Figure 3.13 Energy intensity summation for low frequency peaks: (a) N = 90 rpm, T_{inv} = 30 s, T_{dwell} = 500 ms; (b) N = 90 rpm, T_{inv} = 30 s, T_{dwell} = 1000 ms.

(a)

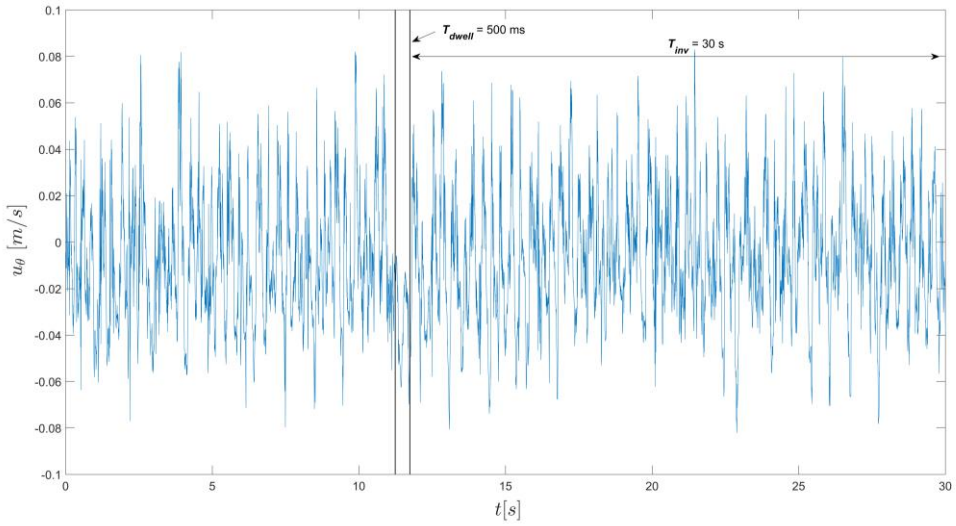

(b)

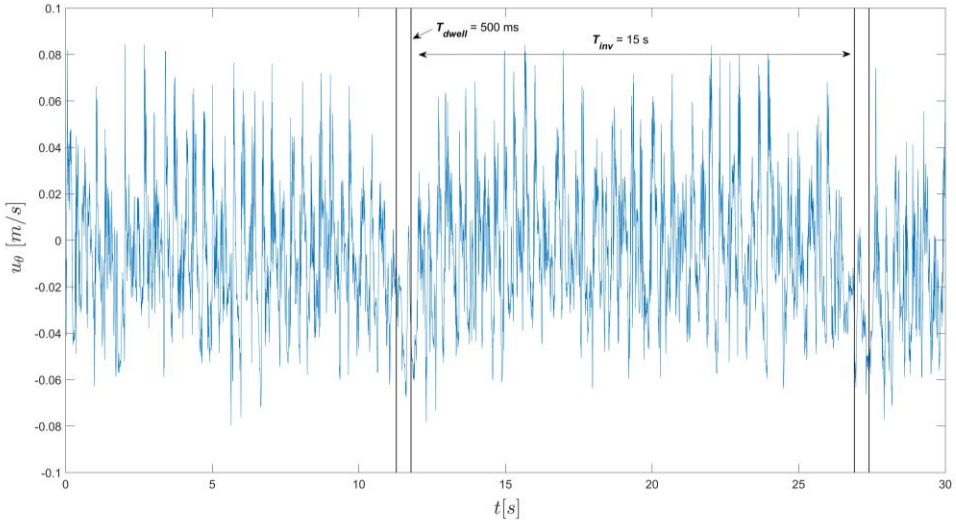

(c)

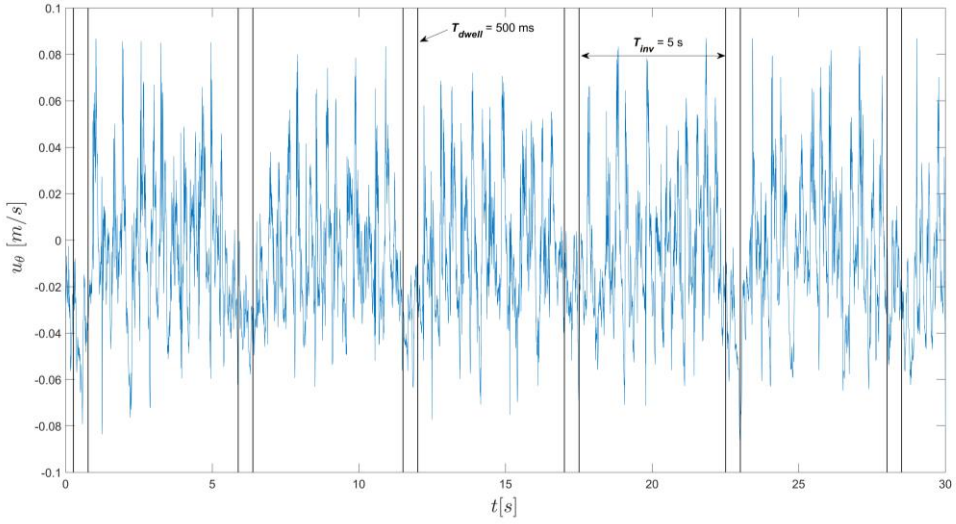

Figure 3.14 Velocity time-series plots indicating T_{inv} and T_{dwell} in a 30 s time frame, N = 90 rpm and T_{dwell} = 500 ms: (a) T_{inv} = 30 s; (b) T_{inv} = 15 s; (c) T_{inv} = 5 s.

(a)

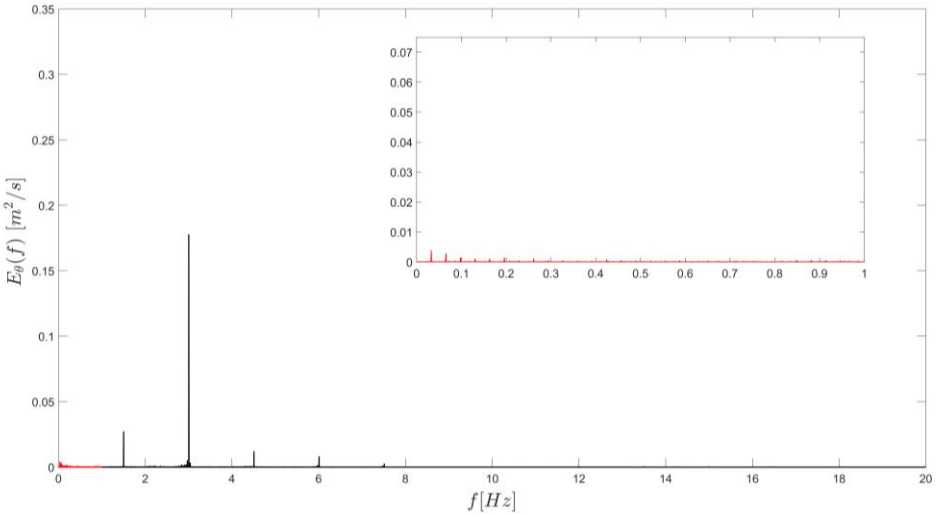

(b)

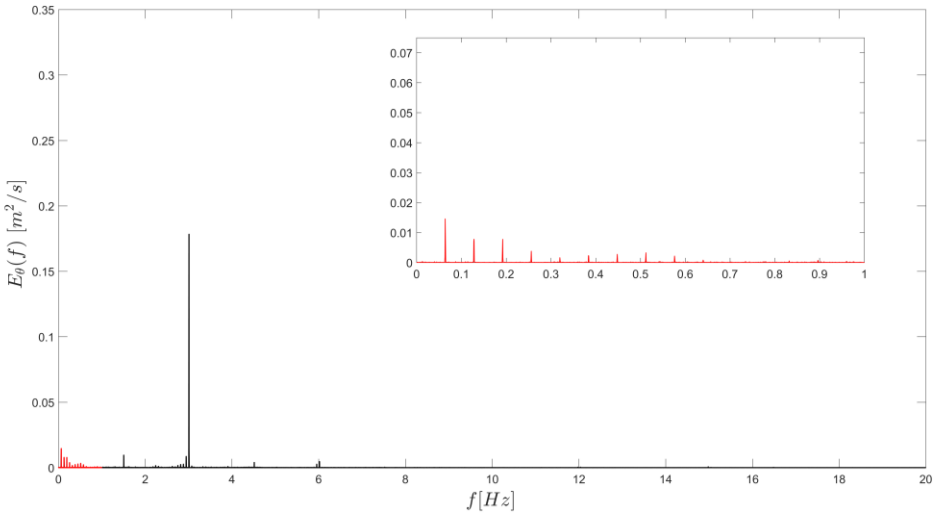

(c)

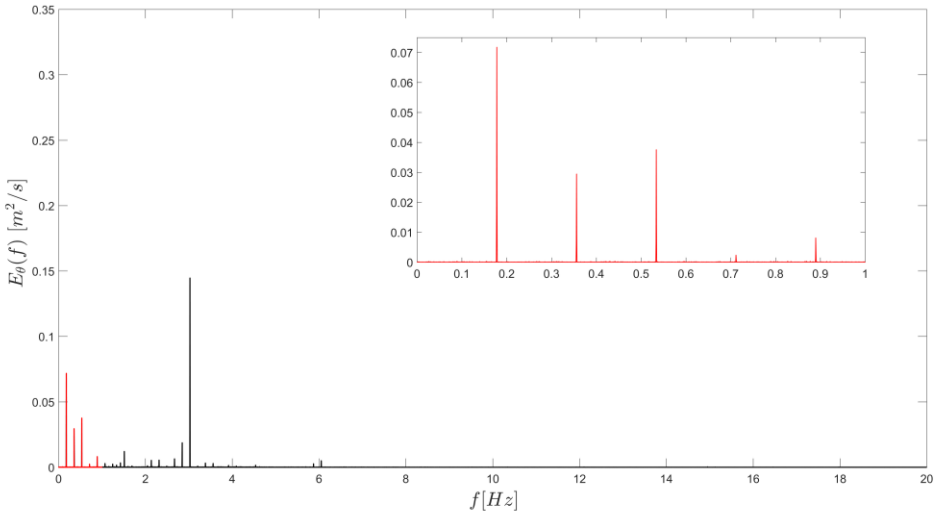

Figure 3.15 Energy spectra of the instantaneous tangential velocity data at intermittent agitation motion, N = 90 rpm and T_{dwell} = 500 ms: (a) T_{inv} = 30 s; (b) T_{inv} = 15; (c) T_{inv} = 5 s.

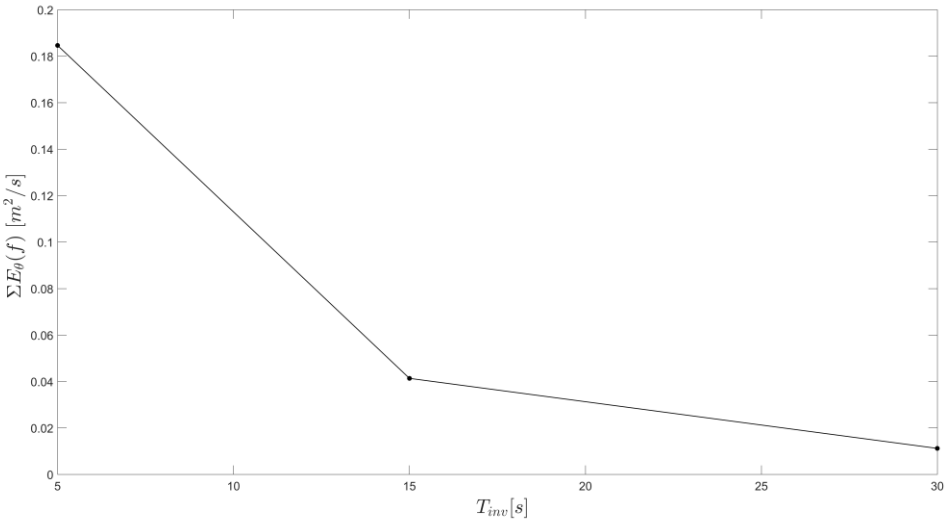

Figure 3.16 Energy intensity summation for low frequency peaks, N = 90 rpm, T_{dwell} = 500 ms and T_{inv} = 5 - 30 s.

(a)

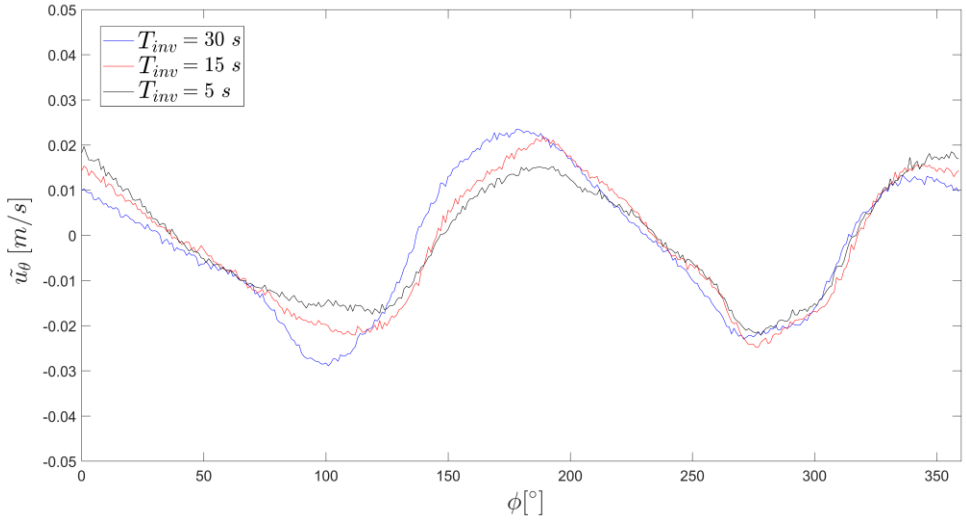

(b)

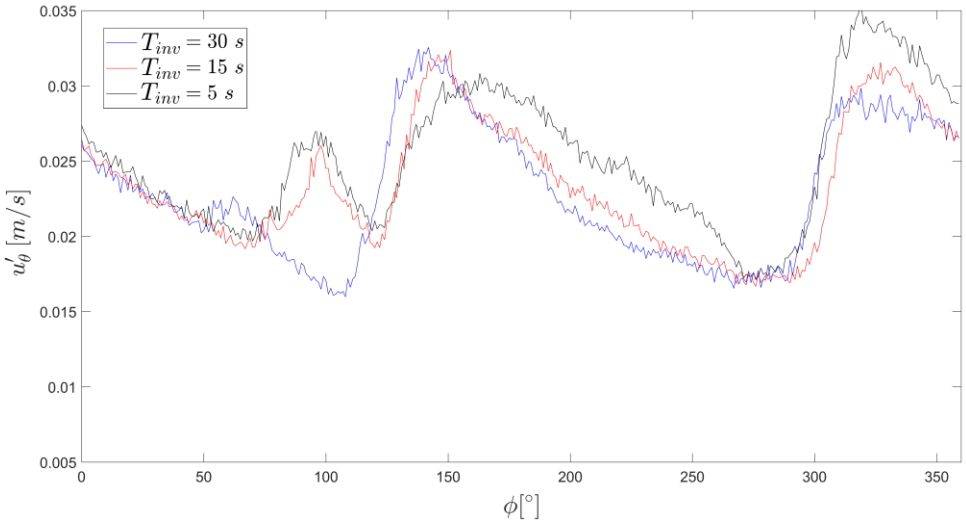

Figure 3.17 Phase-resolved analysis taken between each revolution for T_{inv} = 30 s (blue), T_{inv} = 15 s (red) and T_{inv} = 5 s (black) at N = 90 rpm and T_{dwell} = 500 ms: (a) periodic tangential velocity component, $\tilde{u}_\theta$; (b) tangential fluctuating component, u'_θ.

(a)

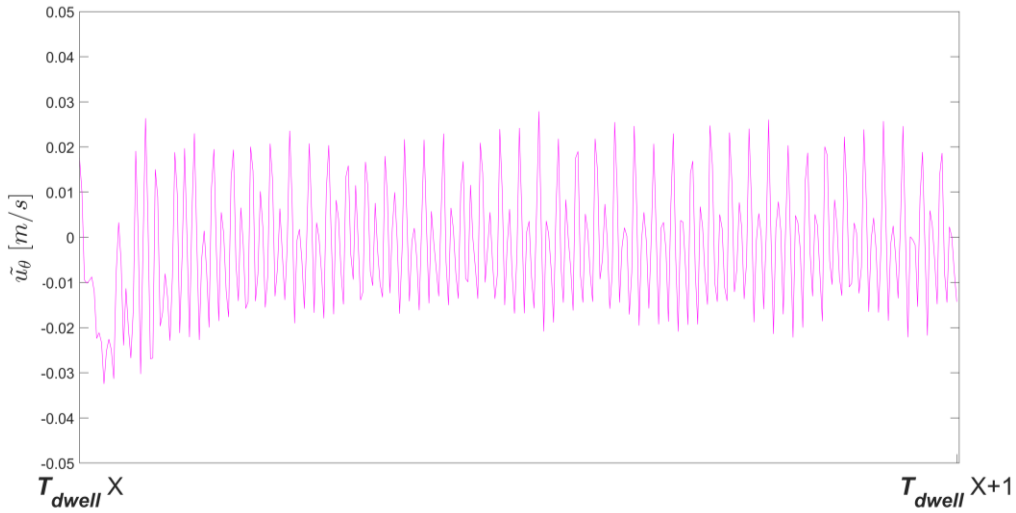

(b)

(c)

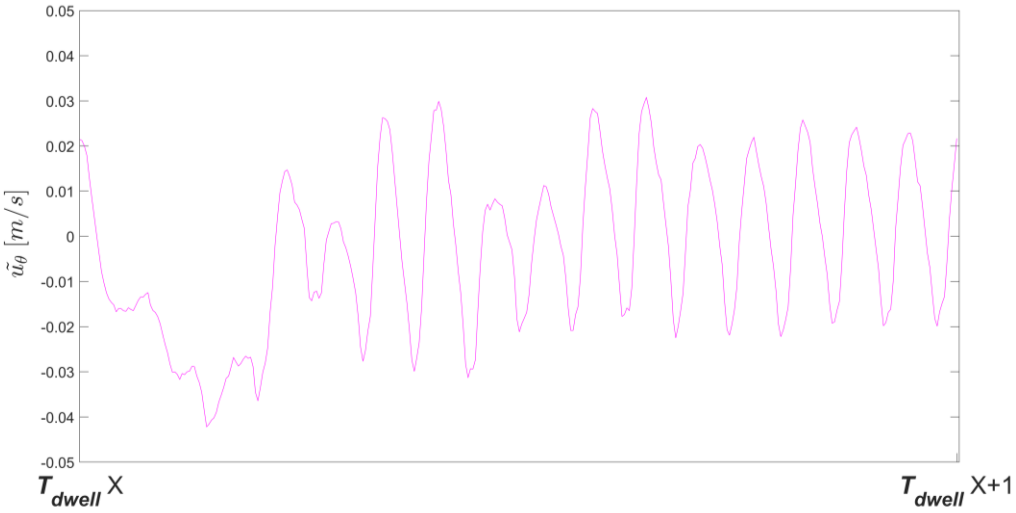

Figure 3.18 Periodic tangential velocities, $\tilde{u}_\theta$, averaged between each dwell phase, N = 90 rpm and T_{dwell} = 500 ms: (a) T_{inv} = 30 s; (b) T_{inv} = 15 s; (c) T_{inv} = 5 s.

(a)

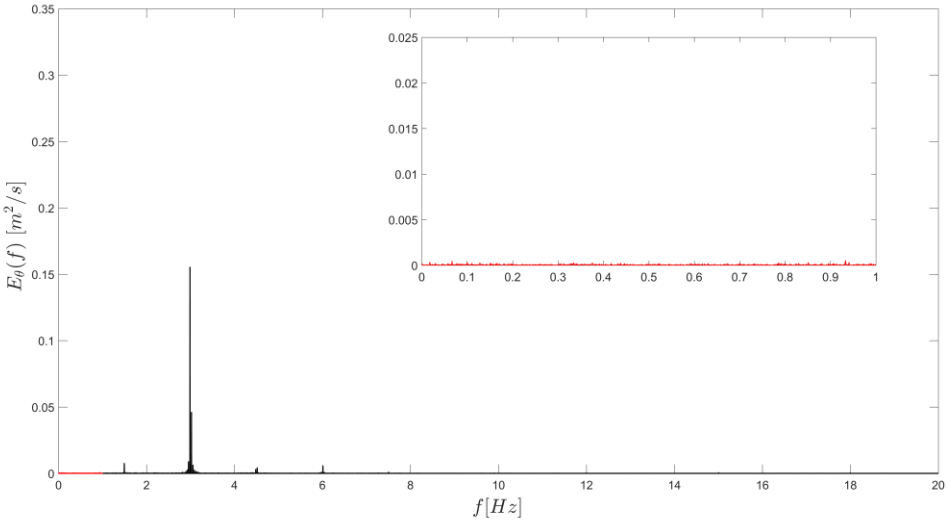

(b)

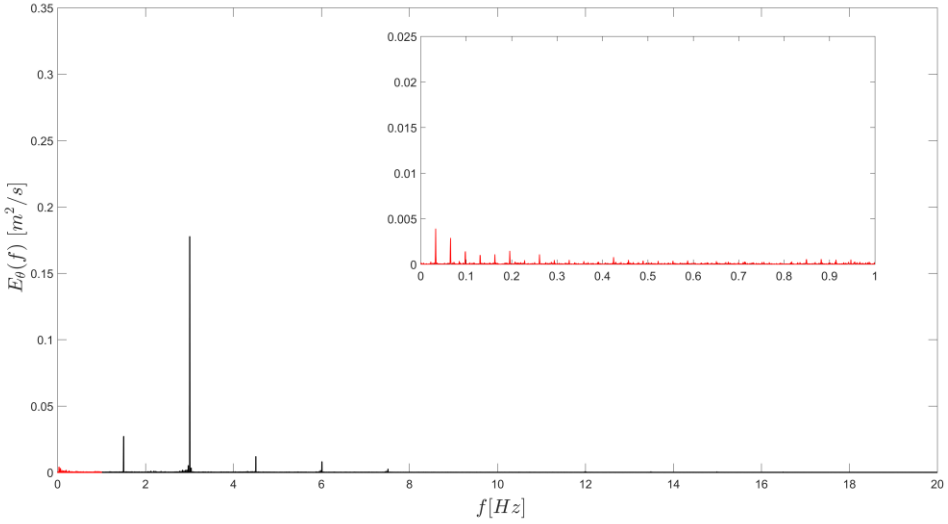

(c)

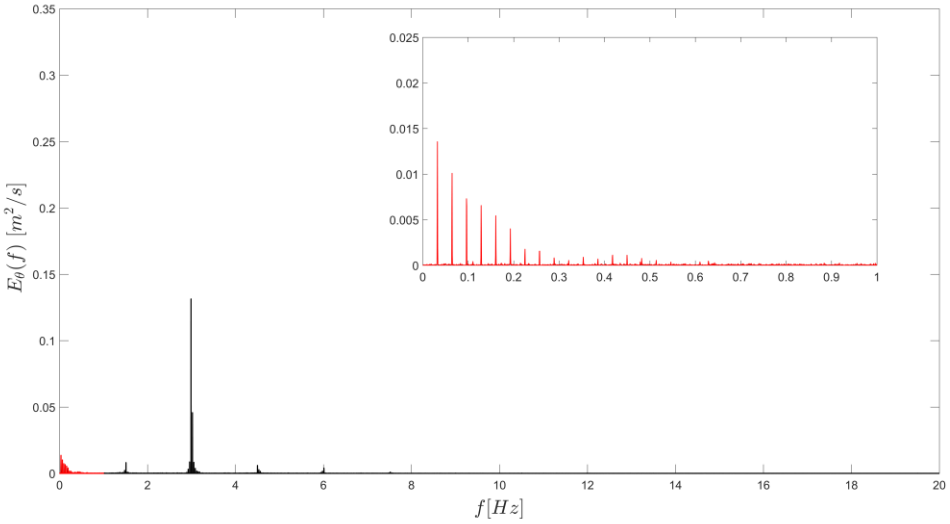

(d)

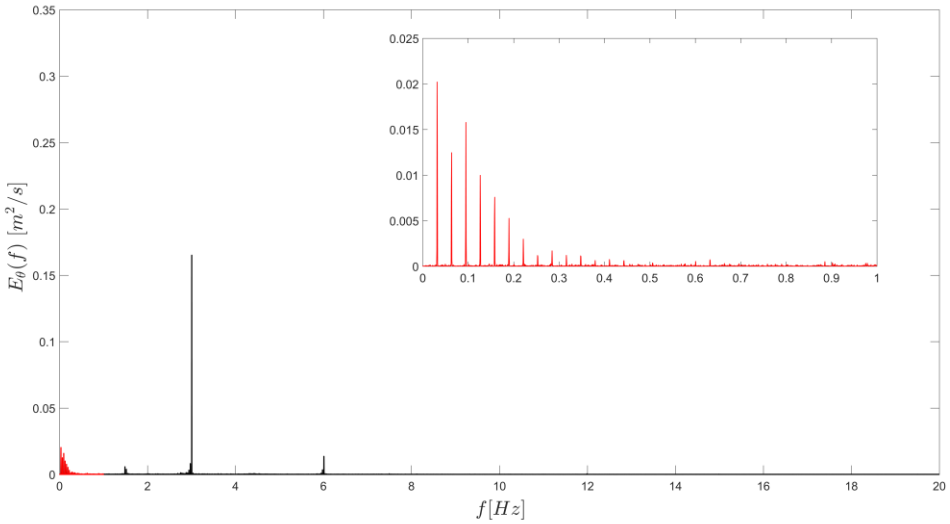

Figure 3.19 Energy spectra of the instantaneous tangential velocity data at intermittent agitation motion, N = 90 rpm and T_{inv} = 30 s: (a) T_{dwell} = 1 ms; (b) T_{dwell} = 500 ms; (c) T_{dwell} = 900 ms; (d) T_{dwell} = 1500 ms.

(a)

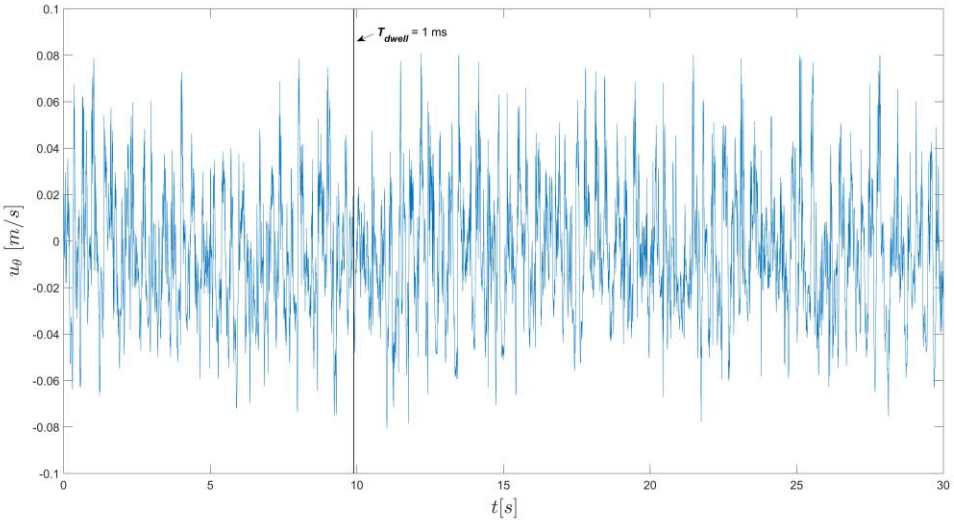

(b)

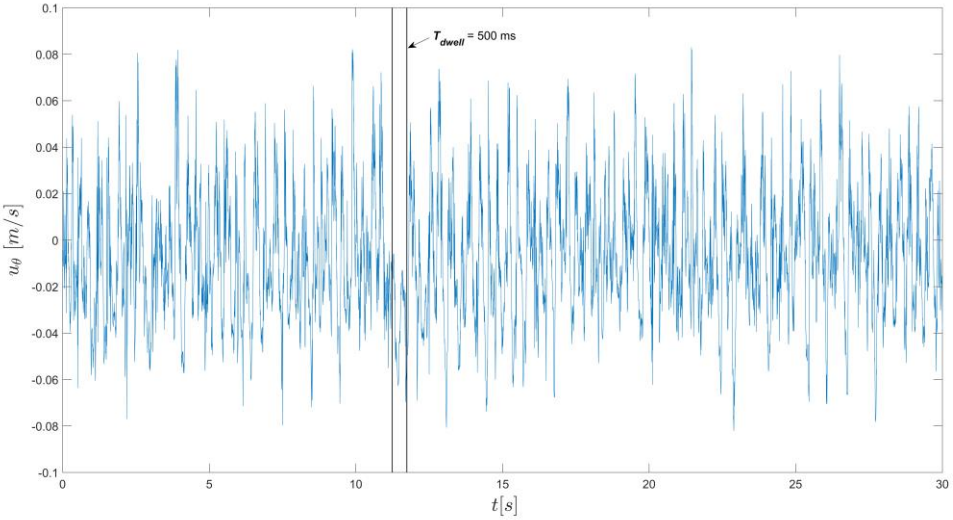

(c)

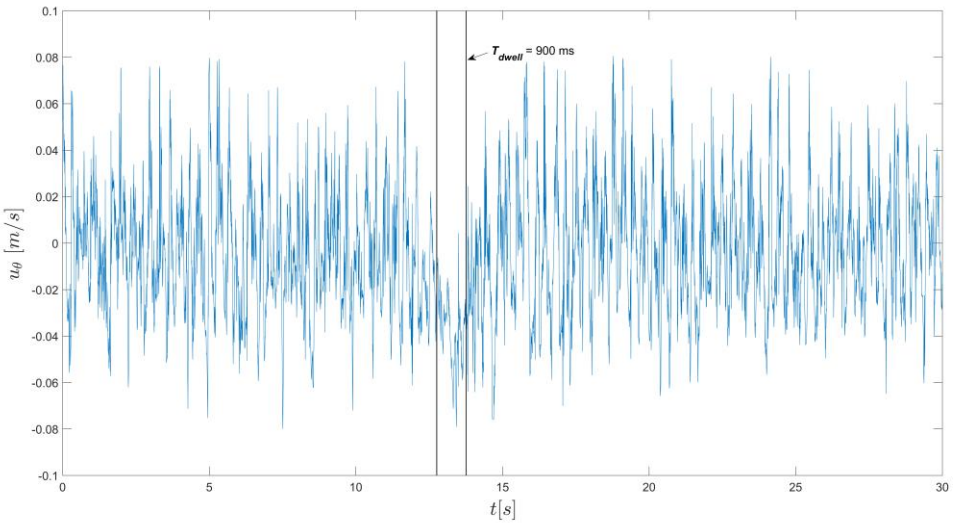

(d)

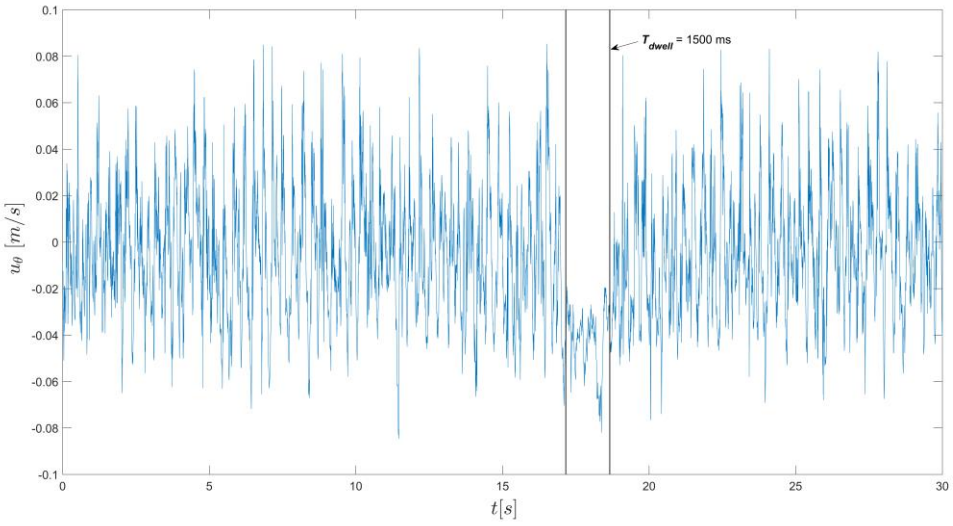

Figure 3.20 Velocity time-series plots indicating T_{dwell} in a 30 s time frame, N = 90 rpm and T_{inv} = 30 s: (a) T_{dwell} = 1 ms; (b) T_{dwell} = 500 ms; (c) T_{dwell} = 900 ms; (d) T_{dwell} = 1500 ms.

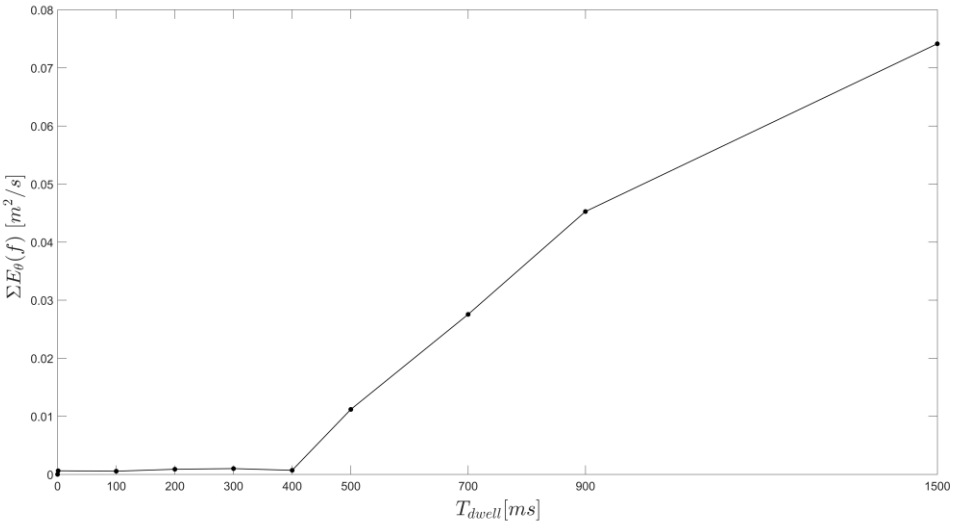

Figure 3.21 Energy intensity summation for low frequency peaks, N = 90 rpm, T_{inv} = 30 s and T_{dwell} = 1 – 1500 ms.

(a)

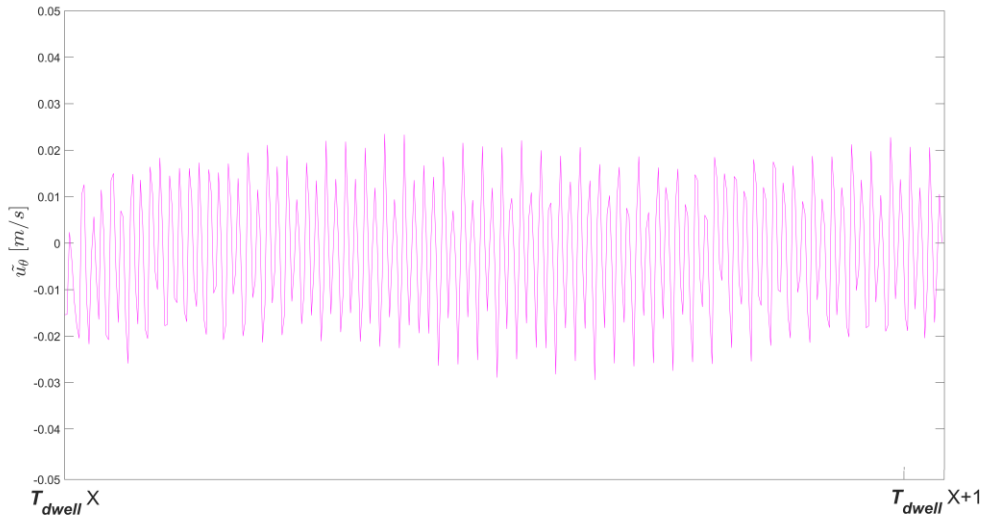
0.05
0.04
0.03
0.02
0.01
0
-0.01
-0.02
-0.03
-0.04
-0.05
$\tilde{u}_\theta\ [m/s]$
T_{dwell} X
T_{dwell} X+1

(b)

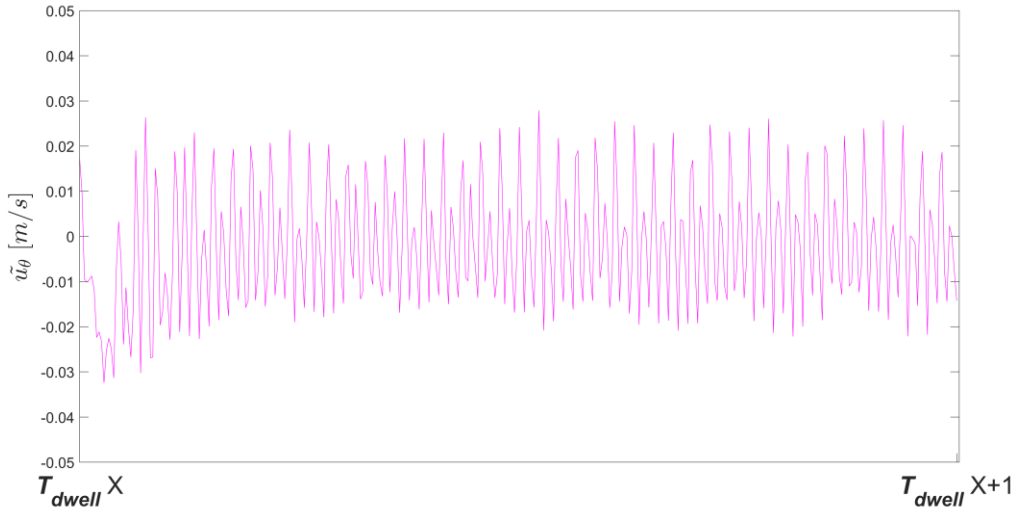
0.05
0.04
0.03
0.02
0.01
0
-0.01
-0.02
-0.03
-0.04
-0.05
$\tilde{u}_\theta\ [m/s]$
T_{dwell} X
T_{dwell} X+1

(c)

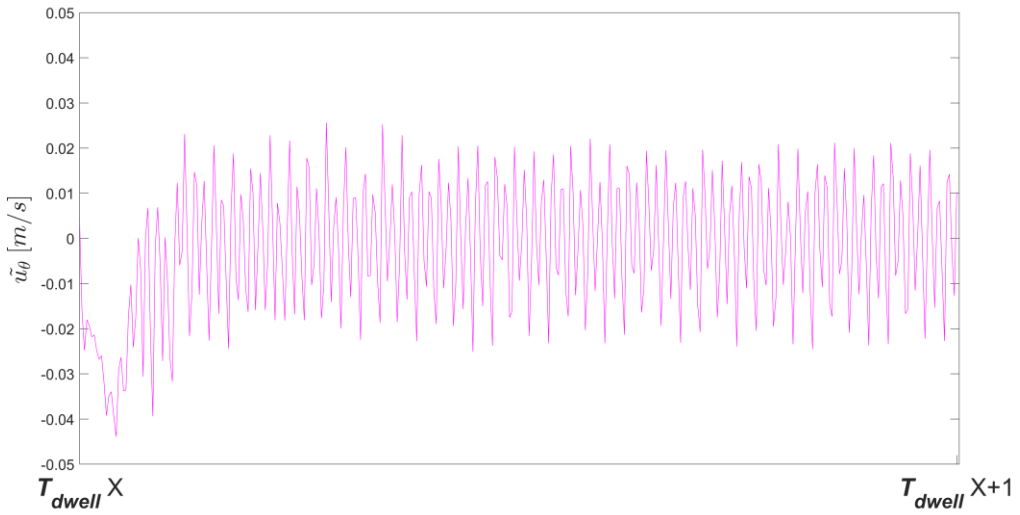

(d)

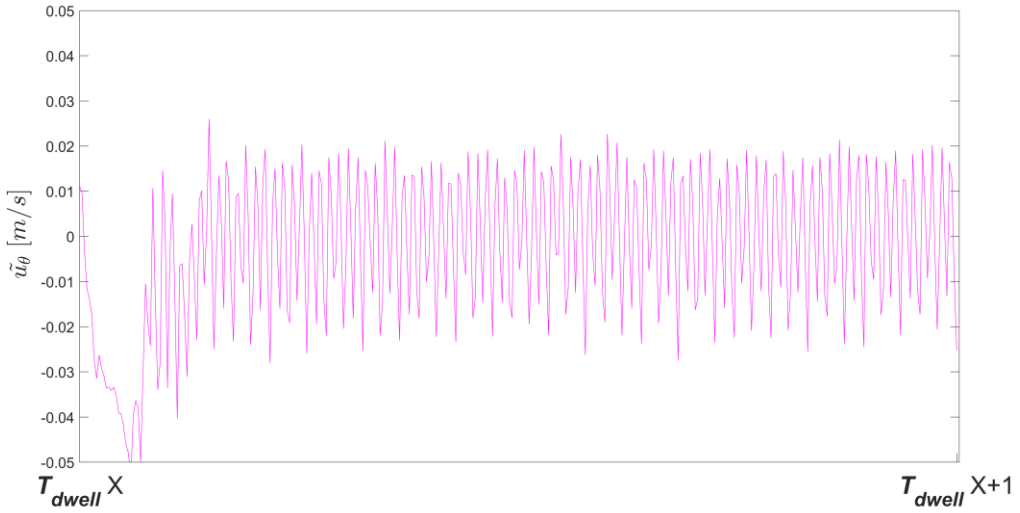

Figure 3.22 Periodic tangential velocities, $\tilde{u}_\theta$, averaged between each dwell phase, N = 90 rpm and T_{inv} = 30 s: (a) T_{dwell} = 1 ms; (b) T_{dwell} = 500 ms; (c) T_{dwell} = 900 ms; (d) T_{dwell} = 1500 ms.

(a)

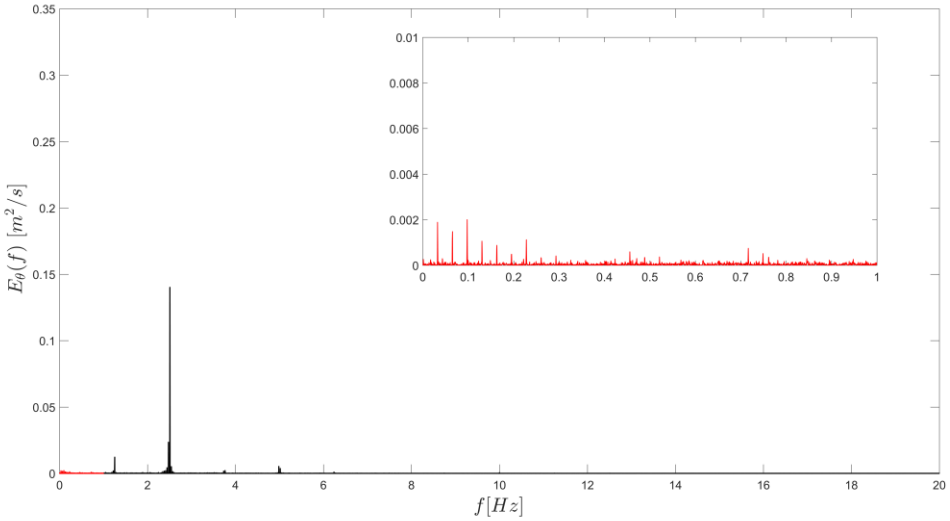

(b)

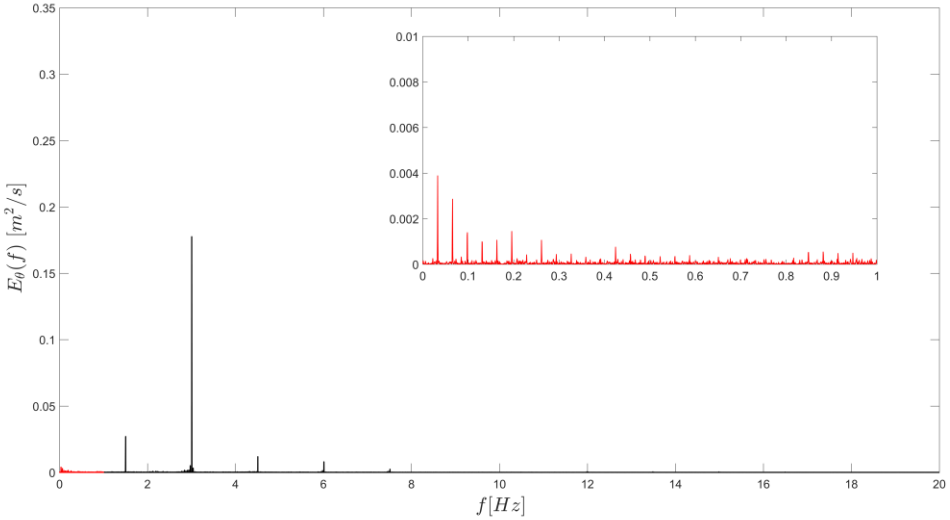

(c)

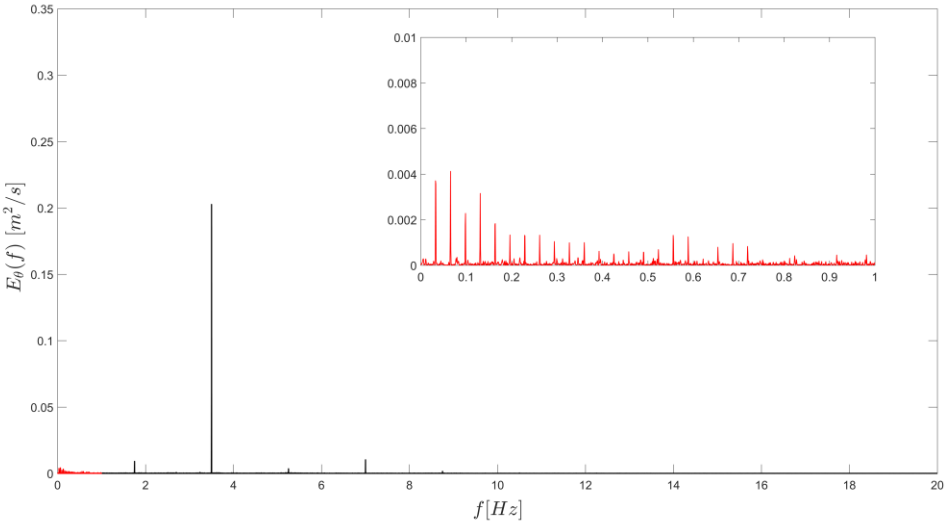

(d)

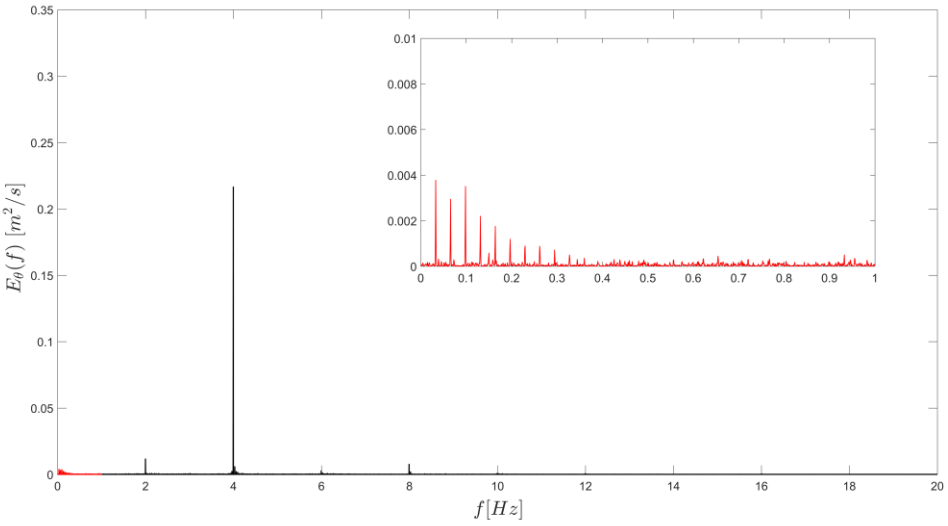

Figure 3.23 Energy spectra of the instantaneous tangential velocity data at intermittent agitation motion, K^* = 0.75: (a) N = 75 rpm, T_{inv} = 30 s and T_{dwell} = 600 ms; (b) N = 90 rpm, T_{inv} = 30 s and T_{dwell} = 500 ms; (c) N = 105 rpm, T_{inv} = 30 s and T_{dwell} = 430 ms; (d) N = 120 rpm, T_{inv} = 30 s and T_{dwell} = 375 ms.

(a)

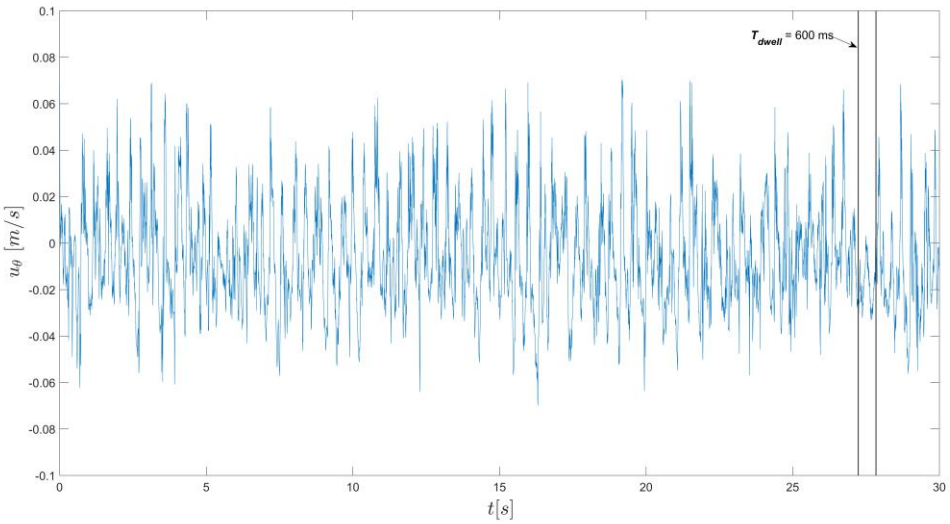

(b)

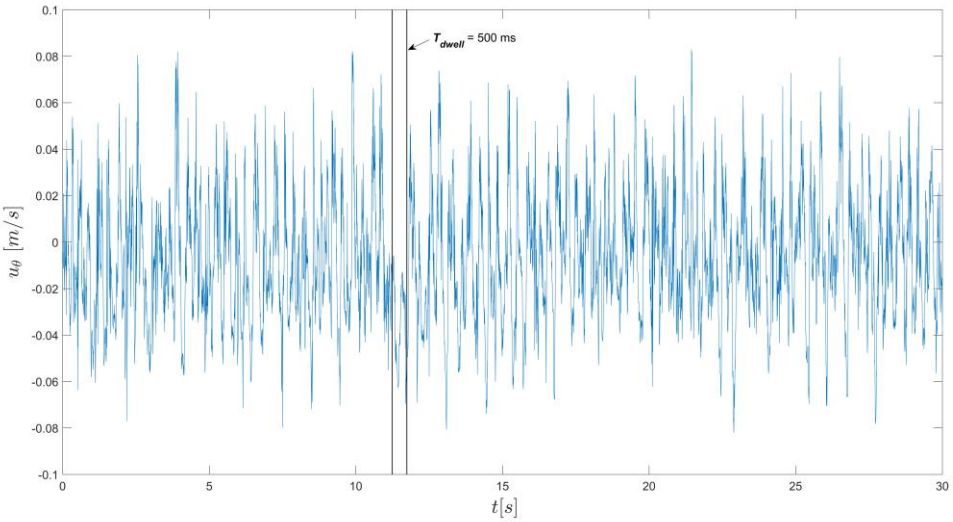

(c)

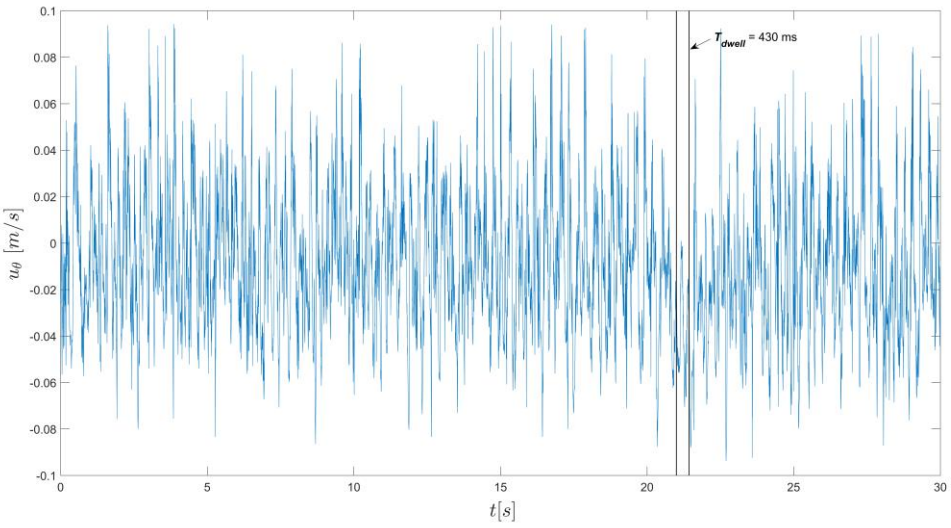

(d)

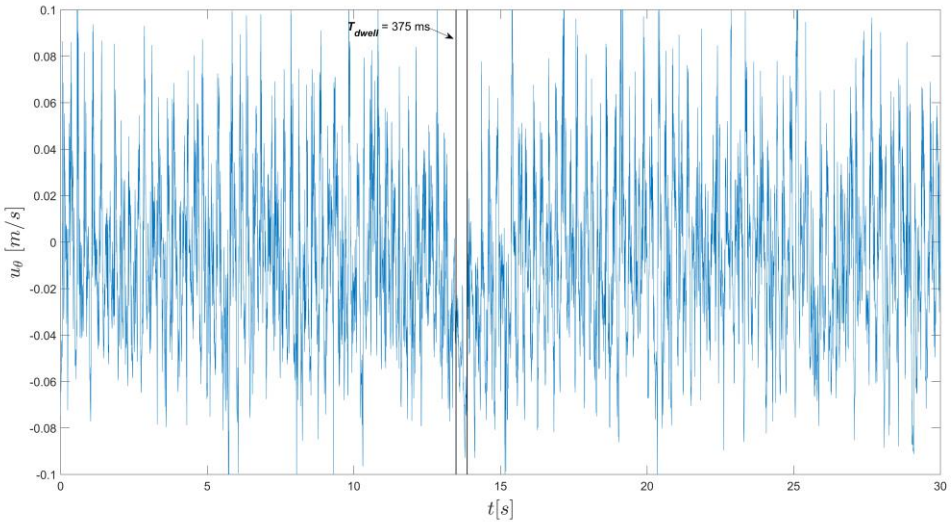

Figure 3.24 Velocity time-series plots indicating T_{dwell} in a 30 s time frame, K^* = 0.75: (a) N = 75 rpm, T_{inv} = 30 s and T_{dwell} = 600 ms; (b) N = 90 rpm, T_{inv} = 30 s and T_{dwell} = 500 ms; (c) N = 105 rpm, T_{inv} = 30 s and T_{dwell} = 430 ms; (d) N = 120 rpm, T_{inv} = 30 s and T_{dwell} = 375 ms.

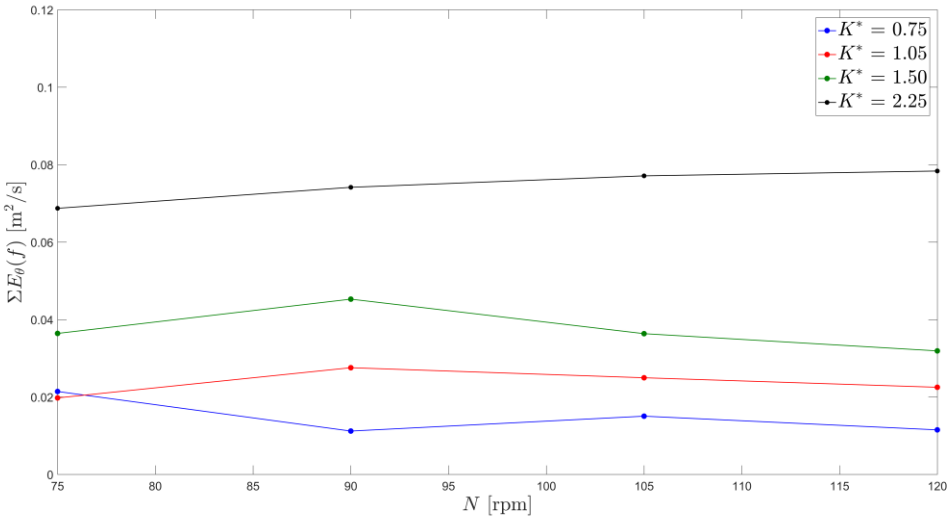

Figure 3.25 Energy intensity summation for low frequency peaks, K^* = 0.75 (blue), 1.05 (red), 1.50 (green) and 2.25 (black) at N = 75 - 120 rpm, T_{inv} = 30 s and T_{dwell} = 500 – 1500 ms (T_{dwell} at reference speed N = 90 rpm).

(a)

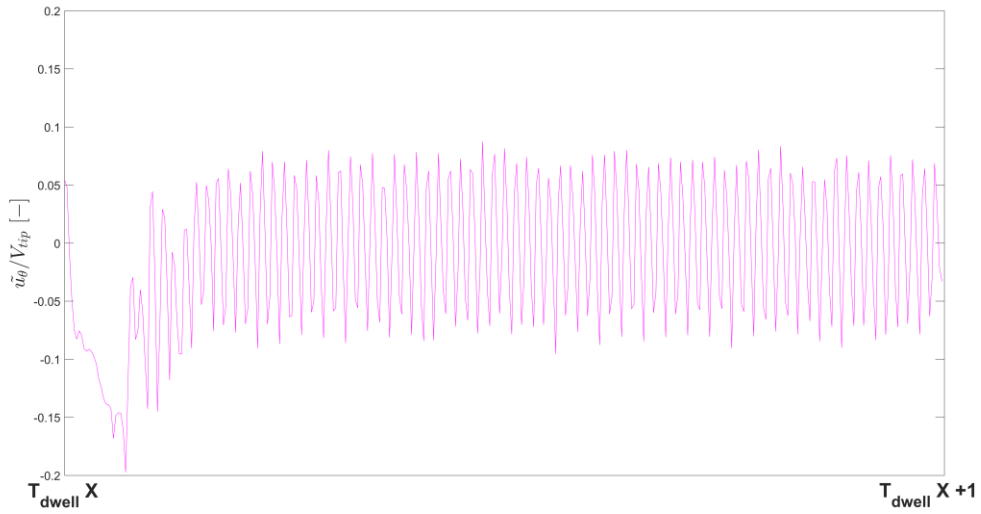
0.2
0.15
0.1
0.05
0
-0.05
-0.1
-0.15
-0.2
$\tilde{u}_\theta/V_{tip}$ [−]
T dwell X
T dwell X +1

(b)

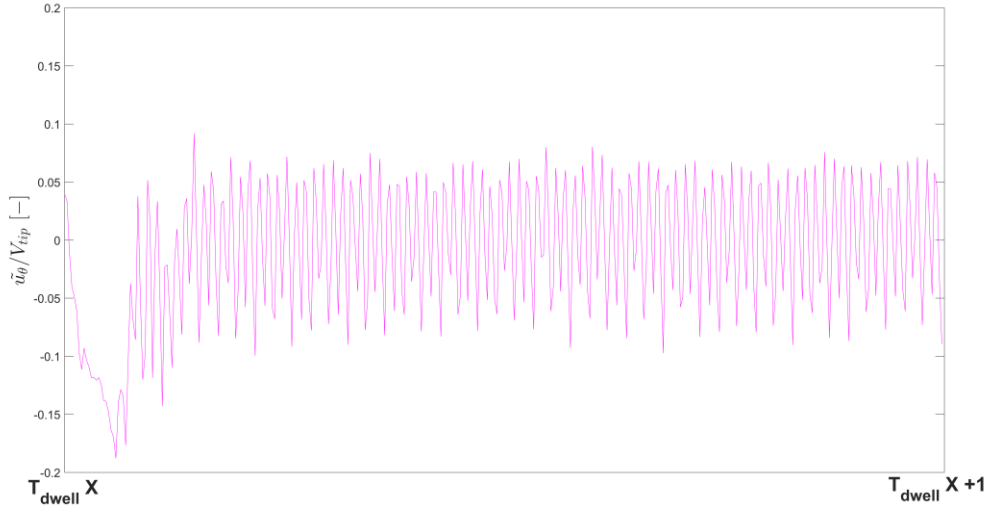
0.2
0.15
0.1
0.05
0
-0.05
-0.1
-0.15
-0.2
$\tilde{u}_\theta/V_{tip}$ [−]
T dwell X
T dwell X +1

(c)

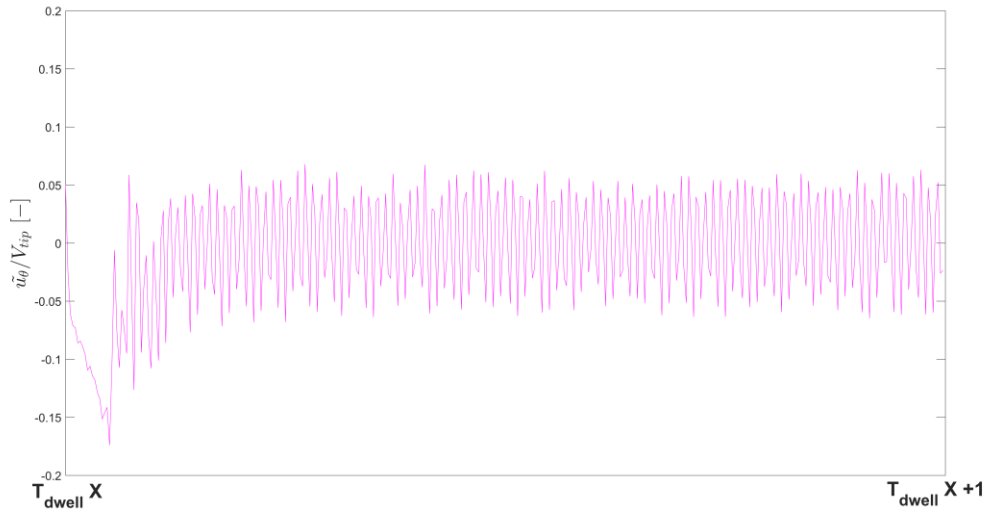

(d)

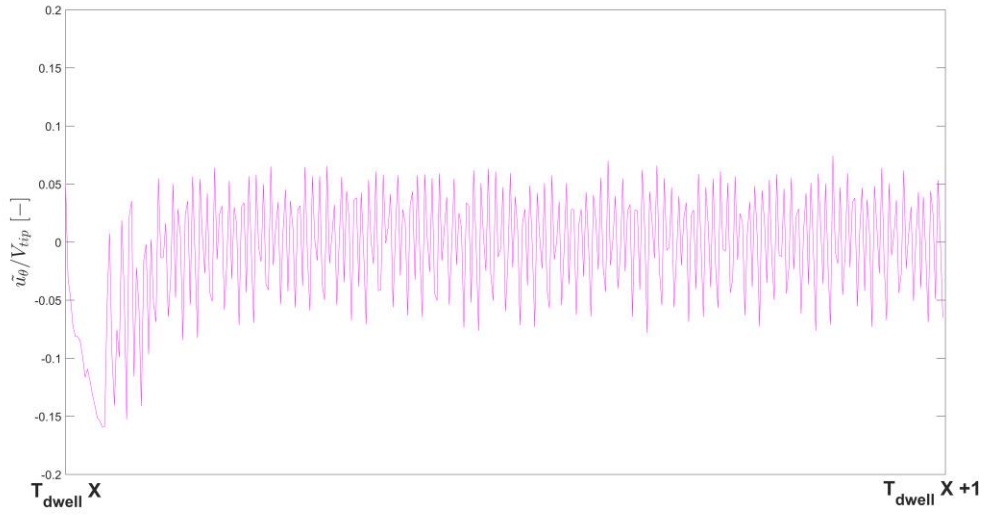

Figure 3.26 Periodic mean tangential velocities, $\tilde{u}_\theta/V_{tip}$, averaged between each dwell phase, K^* = 2.25: (a) N = 75 rpm, T_{inv} = 30 s and T_{dwell} = 1800 ms; (b) N = 90 rpm, T_{inv} = 30 s and T_{dwell} = 1500 ms; (c) N = 105 rpm, T_{inv} = 30 s and T_{dwell} = 1290 ms; (d) N = 120 rpm, T_{inv} = 30 s and T_{dwell} = 1125 ms.

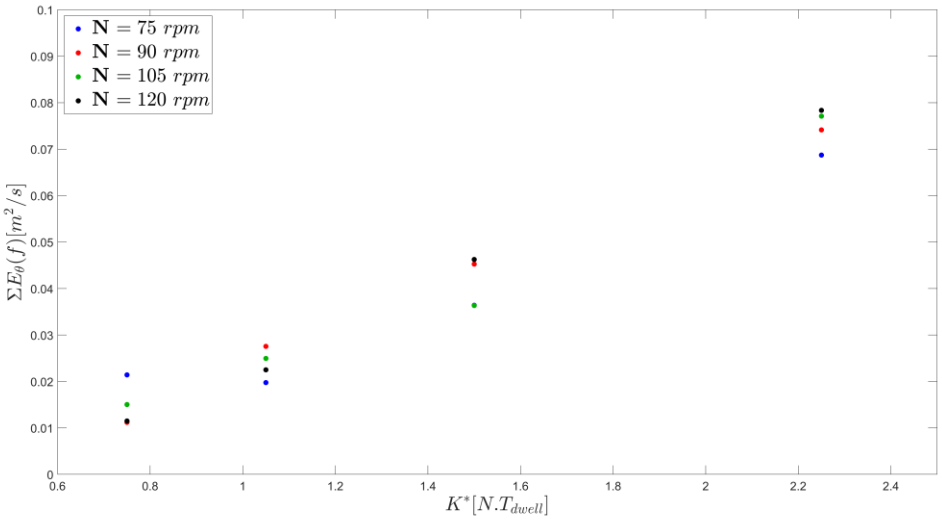

Figure 3.27 Low frequency energy summation for increasing K^* at all rotational speeds investigated.

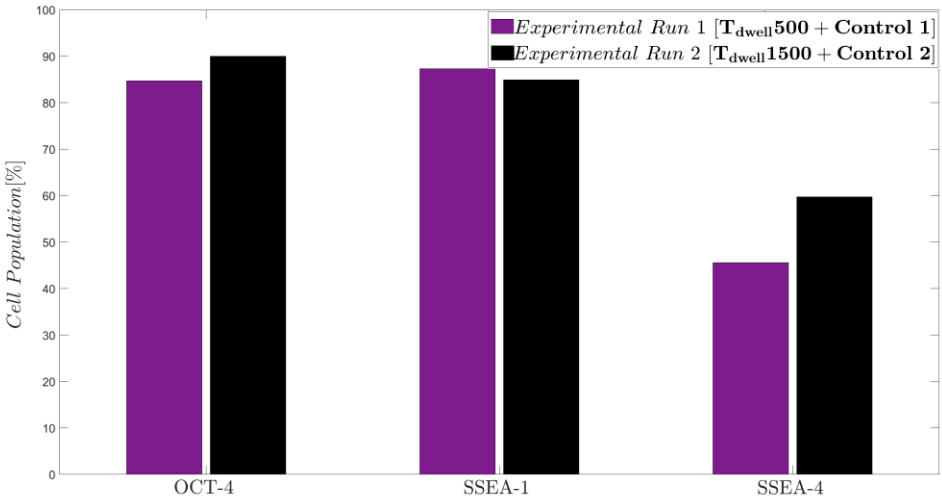

Figure 3.28 Phenotypic analysis on Day 0 assessing for cell pluripotency markers, OCT-4 and SSEA-1, and early differentiation marker, SSEA-4, in both experimental runs.

(a)

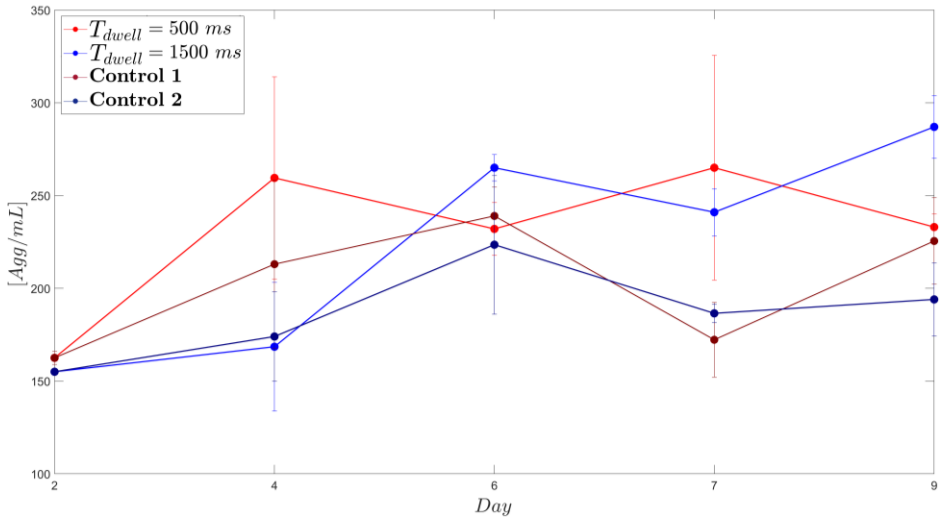

(b)

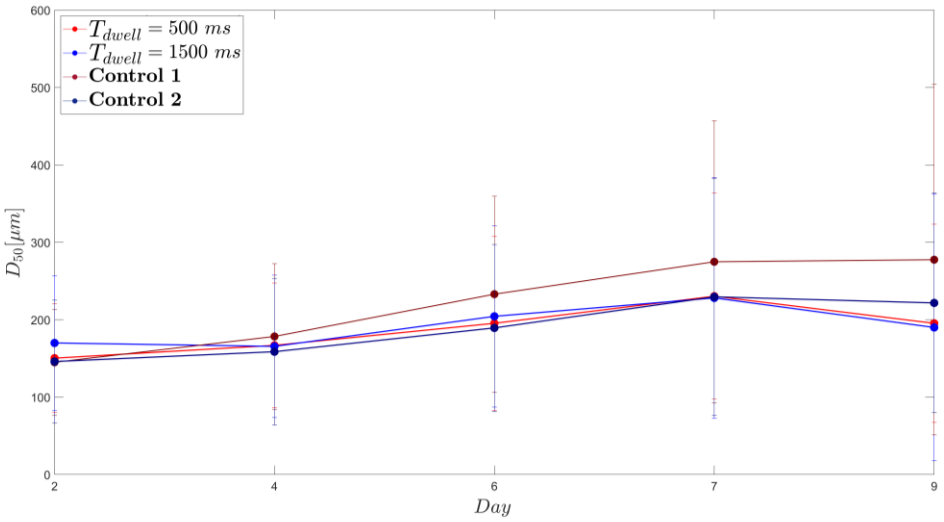

(c)

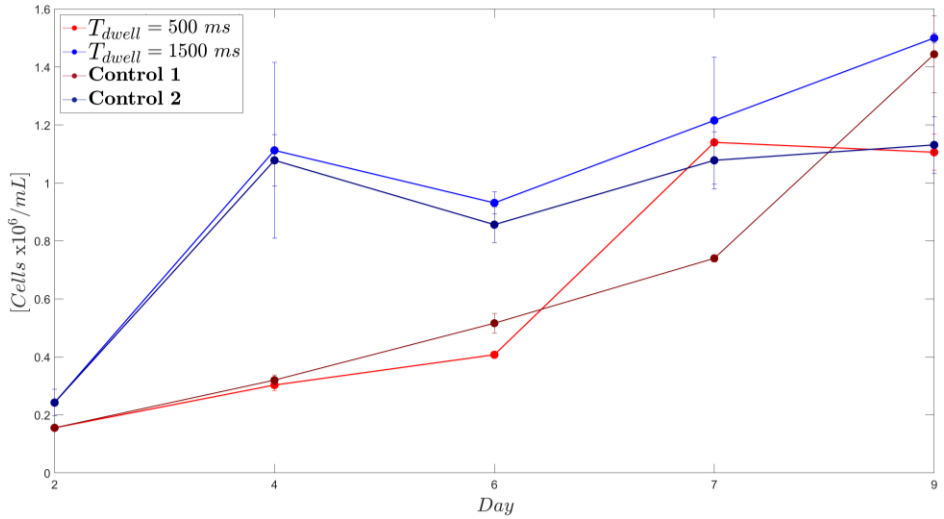

Figure 3.29 Bioreactor sampling at Day 2, 4, 6, 7 and 9: (a) aggregate concentration; (b) aggregate size; (c) cell concentration.

(a)

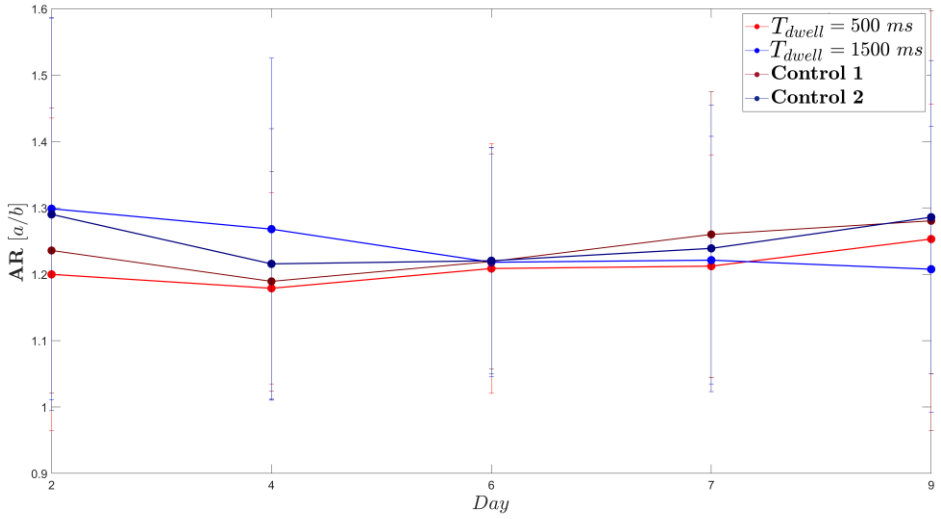

(b)

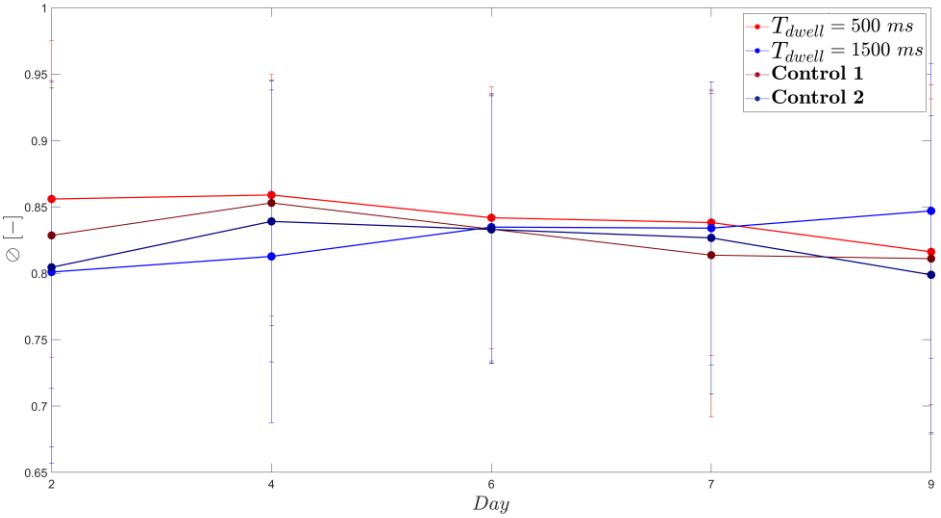

Figure 3.30 Bioreactor sampling at Day 2, 4, 6, 7 and 9: (a) aggregate elongation; (b) aggregate roundness.

(a)

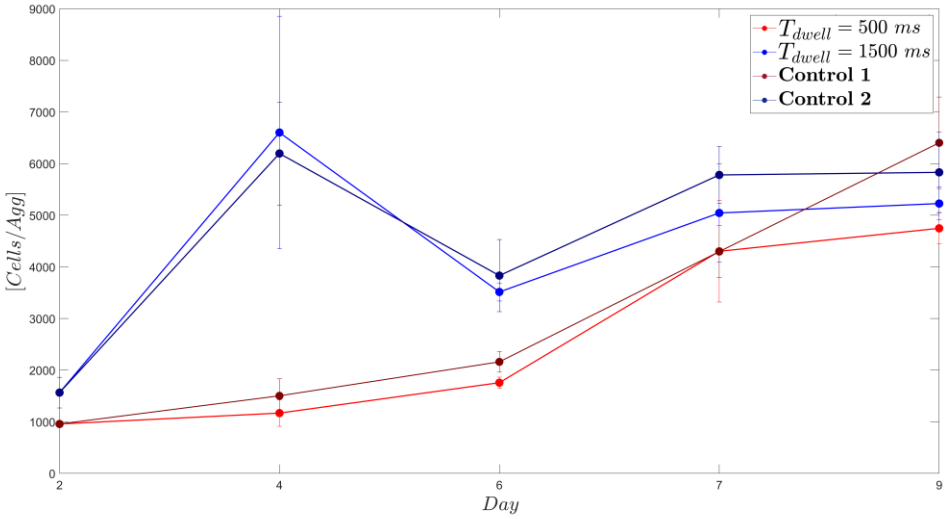

(b)

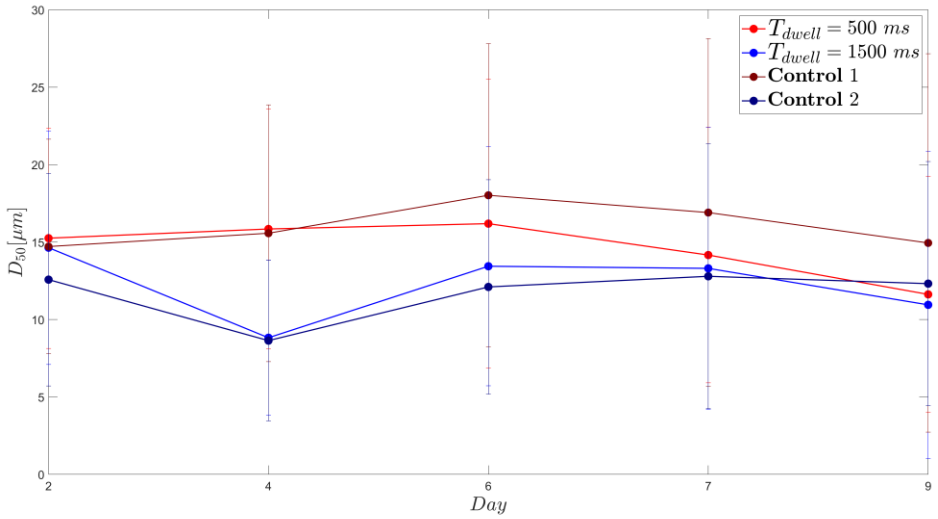

Figure 3.31 Bioreactor sampling at Day 2, 4, 6, 7 and 9: (a) approximate number of cells per aggregate; (b) approximate cell size, D_{50}.

(a)

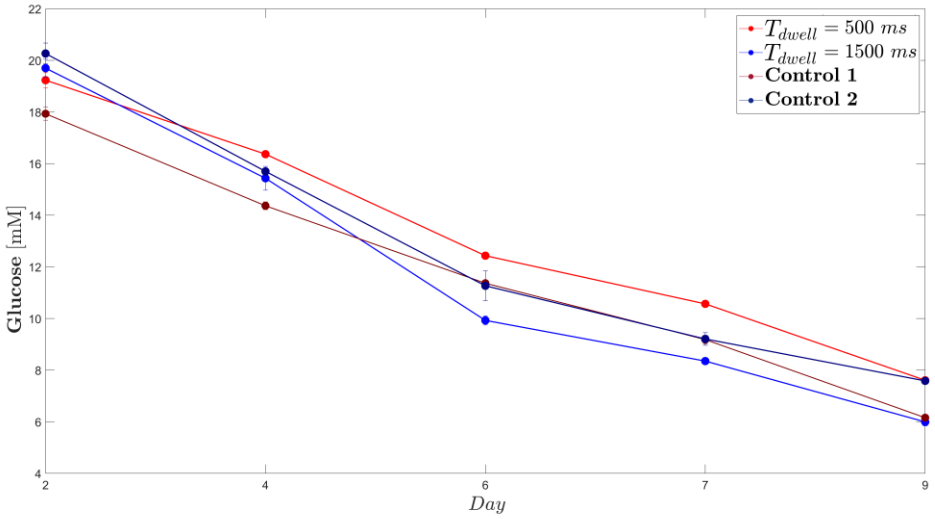
$T_{dwell} = 500\ ms$
$T_{dwell} = 1500\ ms$
Control 1
Control 2
Glucose [mM]
Day

(b)

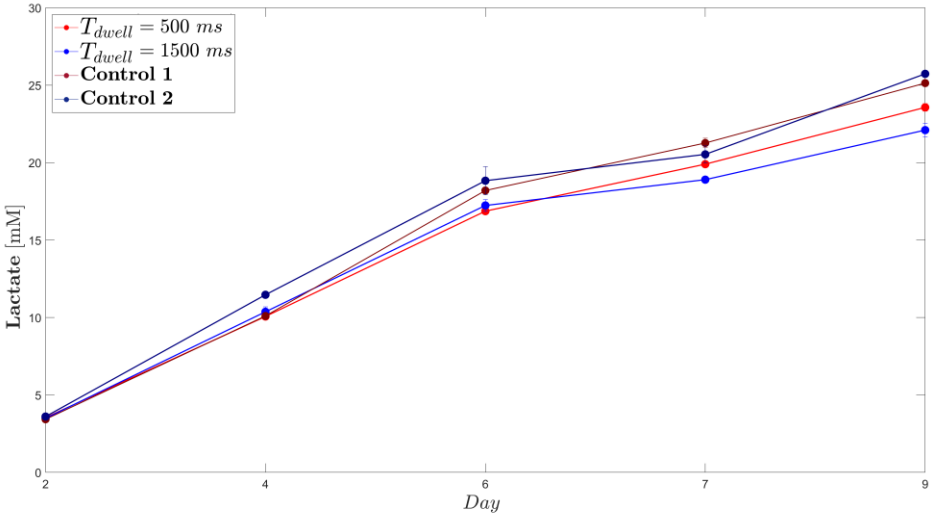
$T_{dwell} = 500\ ms$
$T_{dwell} = 1500\ ms$
Control 1
Control 2
Lactate [mM]
Day

(c)

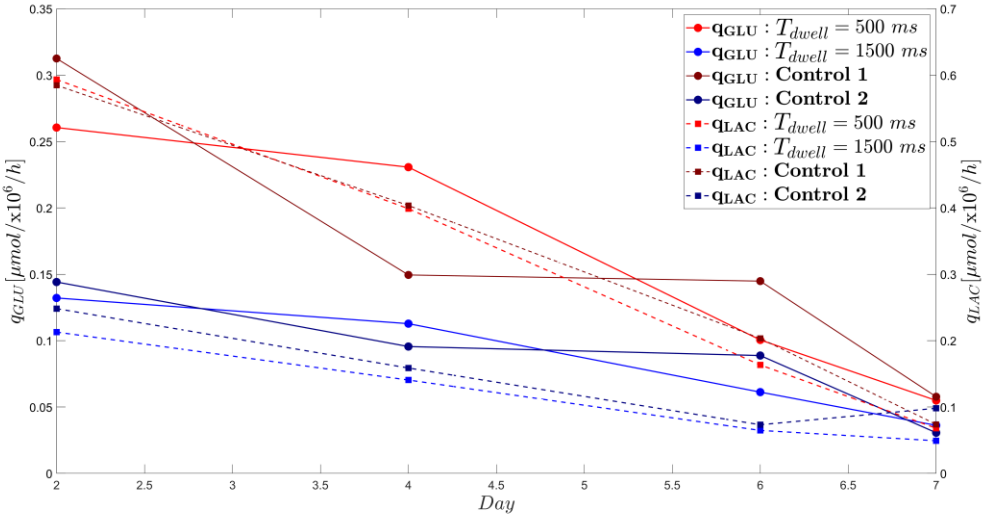

(d)

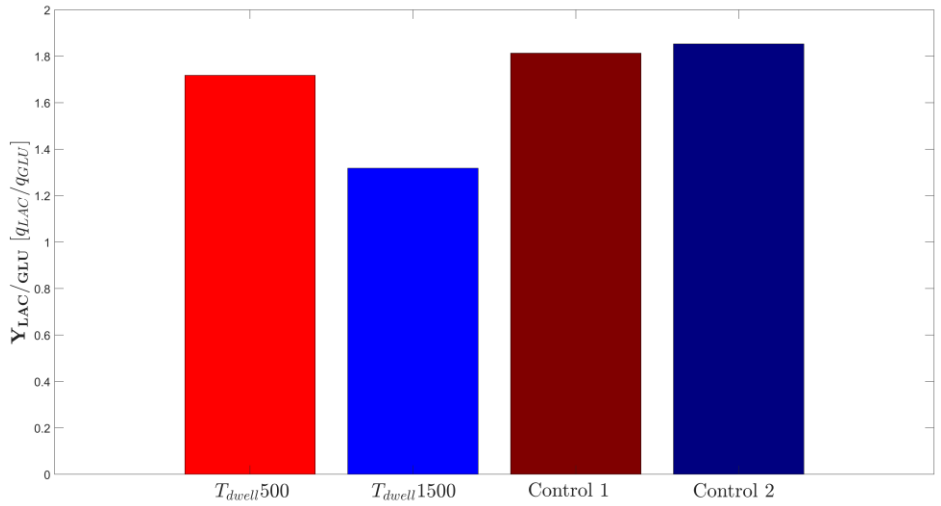

Figure 3.32 Bioreactor sampling at Day 2, 4, 6, 7 and 9: (a) glucose concentration; (b) lactate concentration; (c) rate of consumption (left) and production (right) of glucose and lactate, respectively; (d) average yield of lactate on glucose.

T_{dwell} = 500 ms	Control Condition [1]
Day 2	
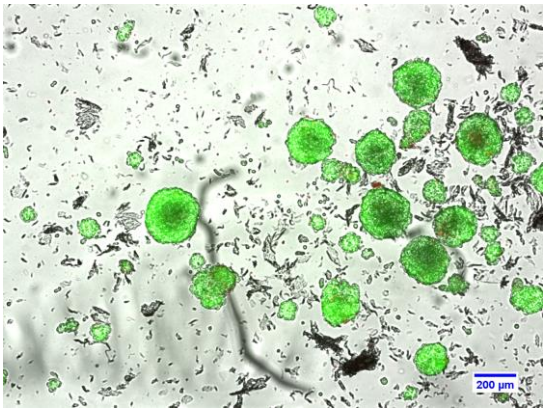	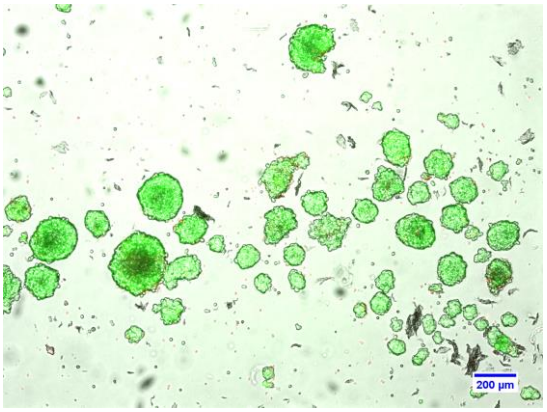
Day 4	
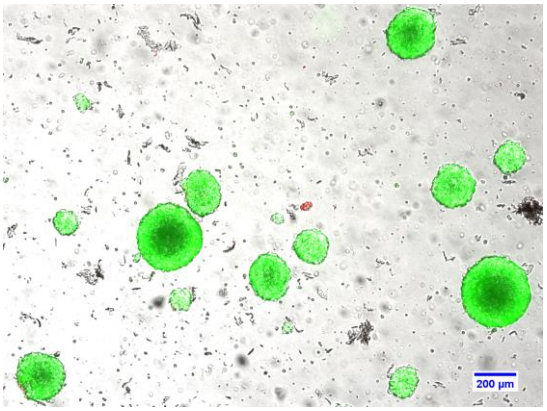	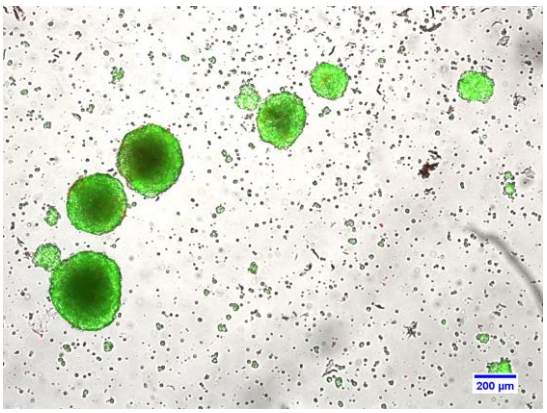
Day 6	
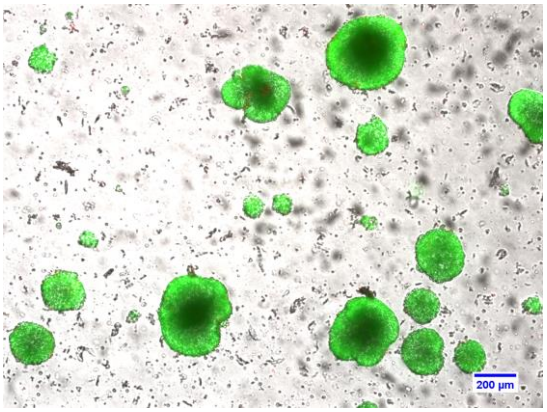	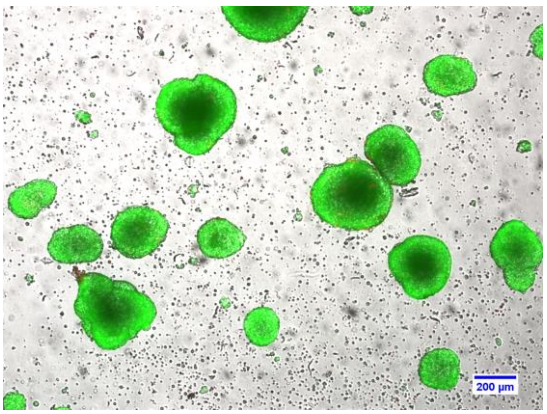

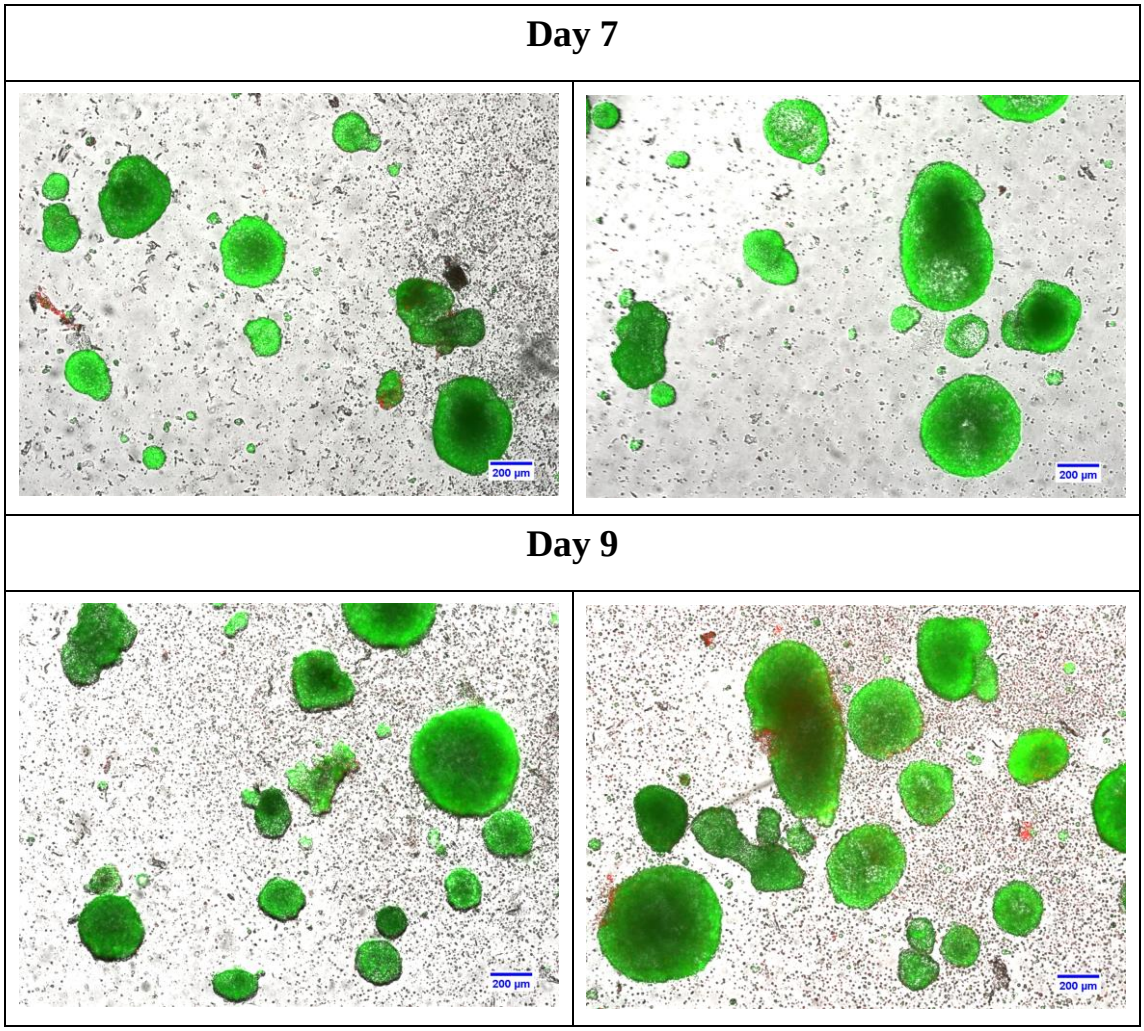

Figure 3.33 Live/dead cell stain of iPSC and cardiosphere aggregates from merged phase contrast and fluorescence images at Day 2 - 9 of iPSC-CM differentiation culture run 1. Motor-driven agitation, T_{dwell} = 500 ms condition (left) and magnetically-driven agitation, control condition (right). Scale bars represent 200 µm.

T_{dwell} = 1500 ms	Control Condition [2]
Day 2	
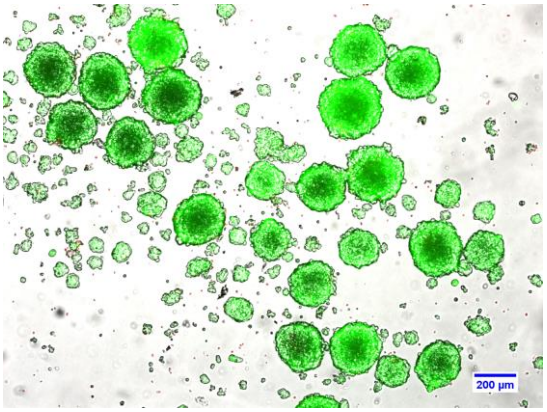	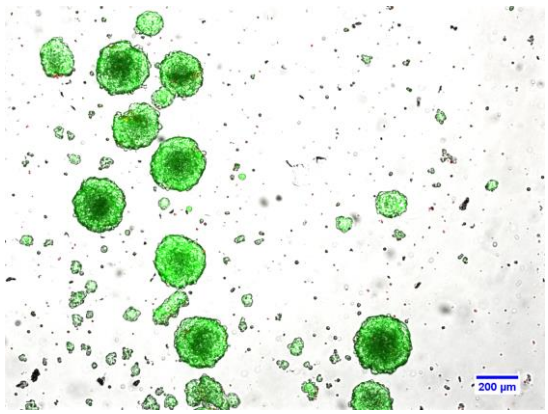
Day 4	
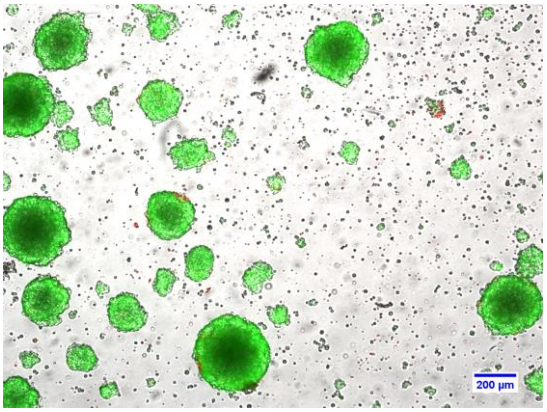	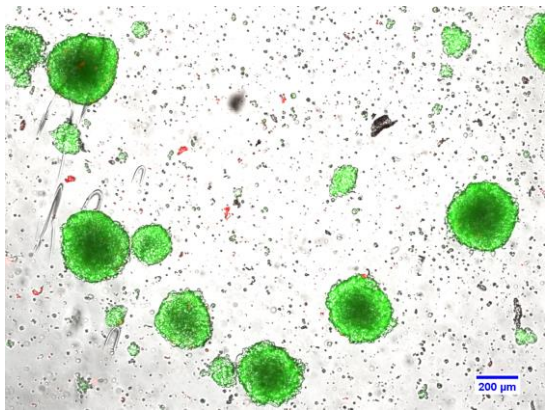
Day 6	
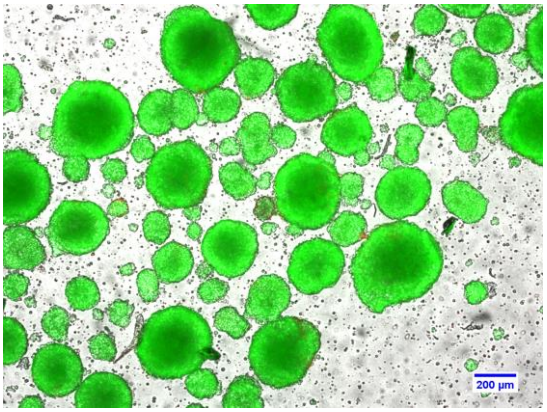	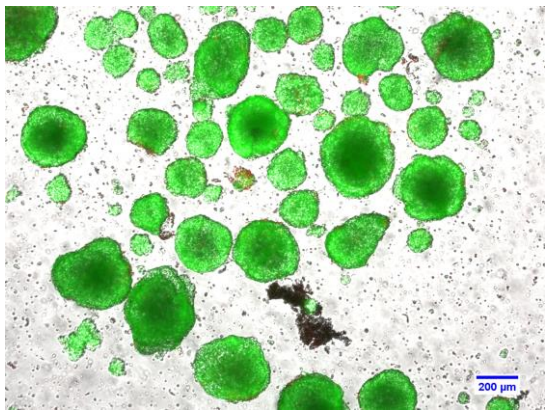

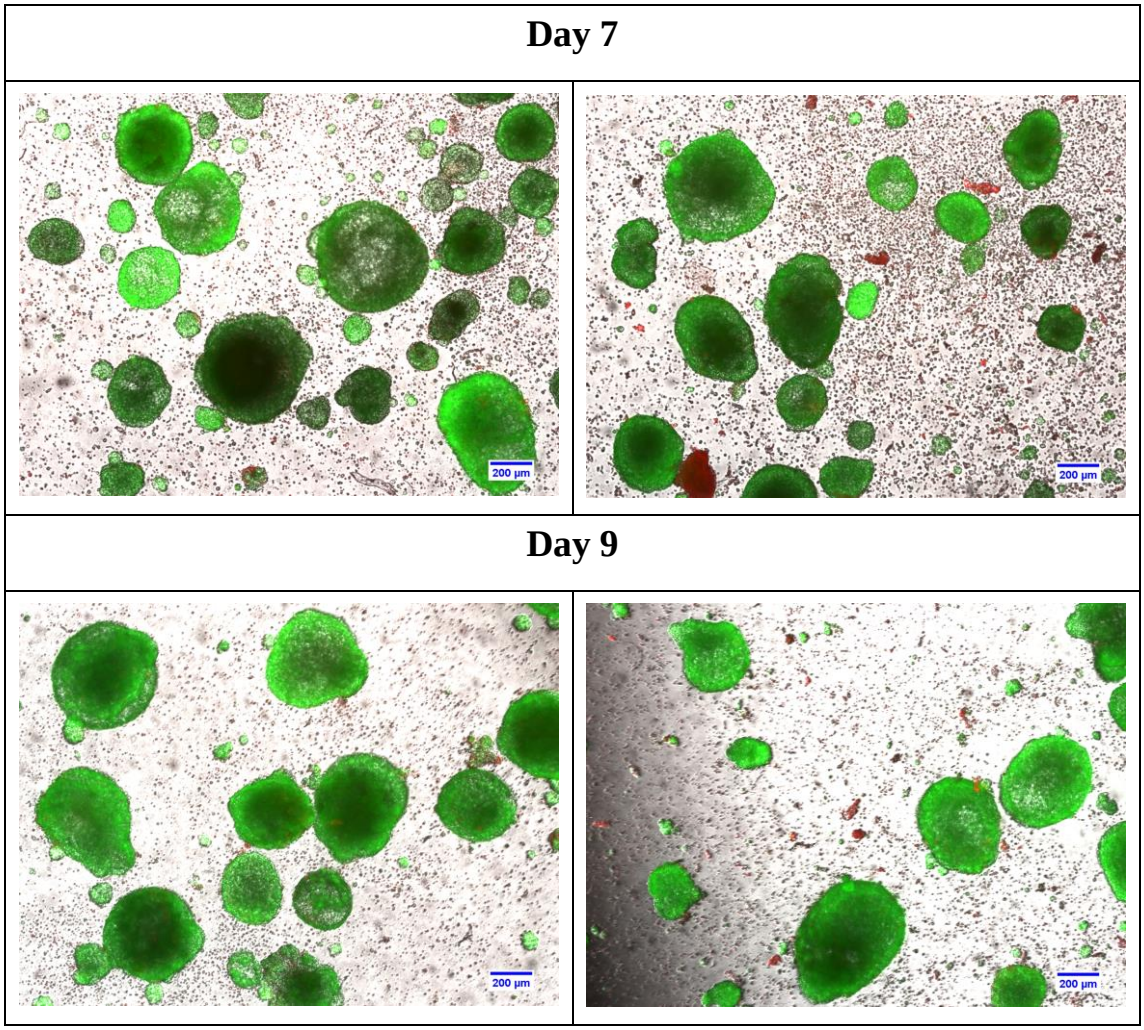

Figure 3.34 Live/dead cell stain of iPSC and cardiosphere aggregates from merged phase contrast and fluorescence images at Day 2 - 9 of iPSC-CM differentiation culture run 2. Motor-driven agitation, T_{dwell} = 1500 ms condition (left) and magnetically-driven agitation, control condition (right). Scale bars represent 200 µm.

(a)

T_{dwell} = 500 ms	Control Condition [1]
Day 9 GFP expression	
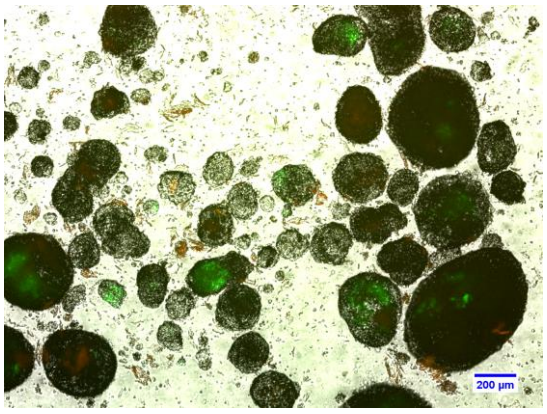	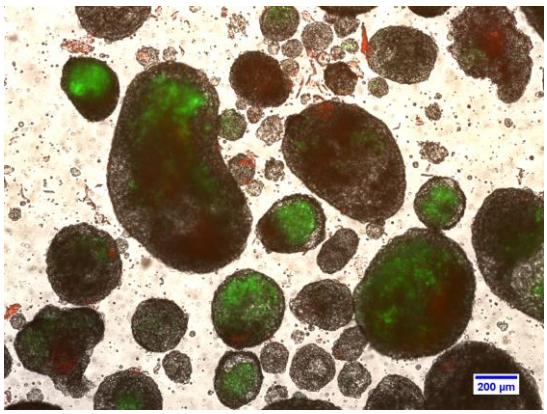
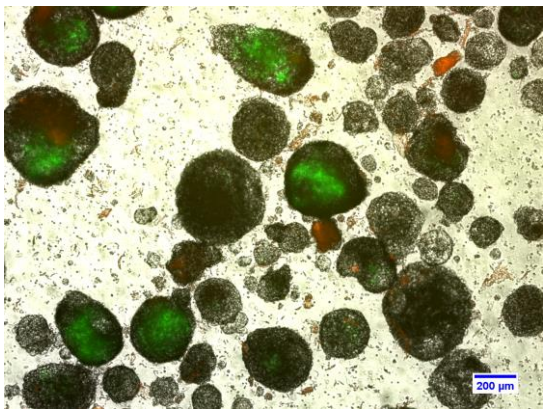	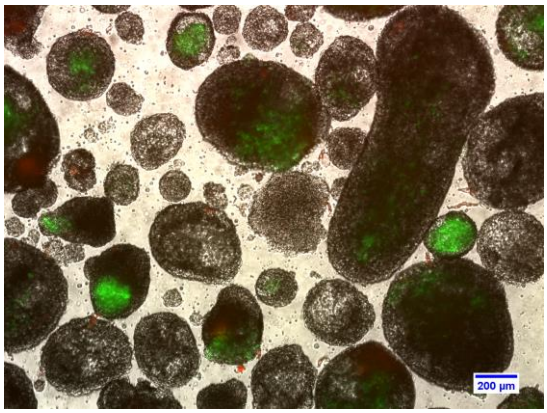

(b)

T_{dwell} = 1500 ms	Control Condition [2]
Day 9 GFP expression	
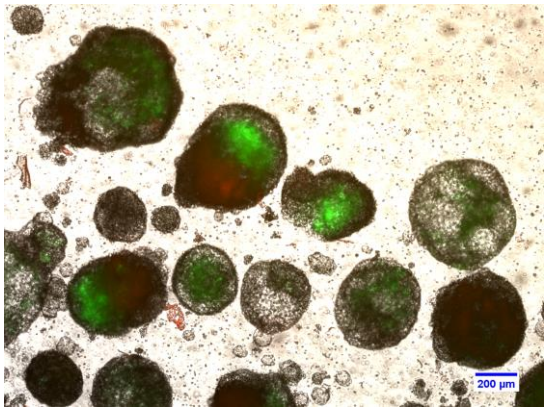	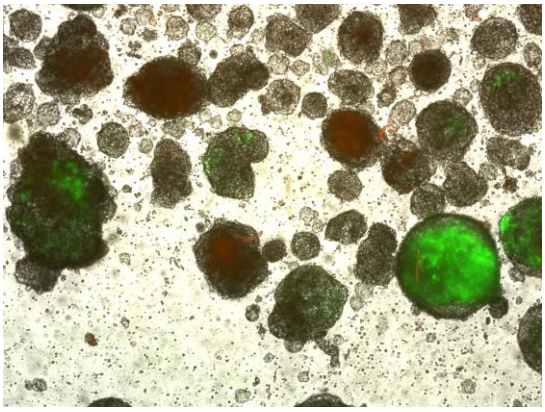
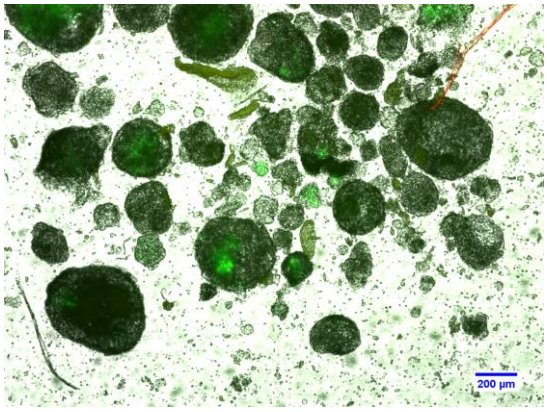	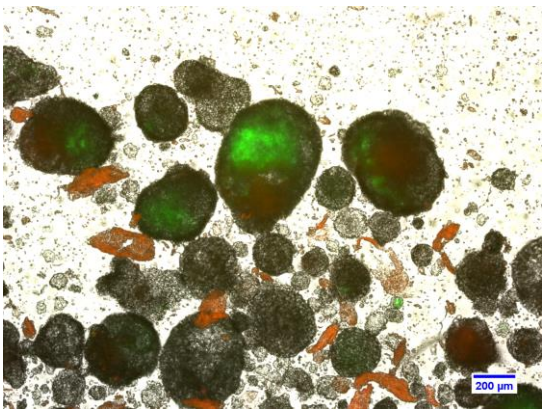

Figure 3.35 GFP expression of cardiosphere aggregates from merged phase contrast and fluorescence images at Day 9. Scale bars represent 200 µm; (a) experimental run 1, T_{dwell} = 500 ms (left) and control condition (right); (b) experimental run 2, T_{dwell} = 1500 ms (left) and control condition (right).

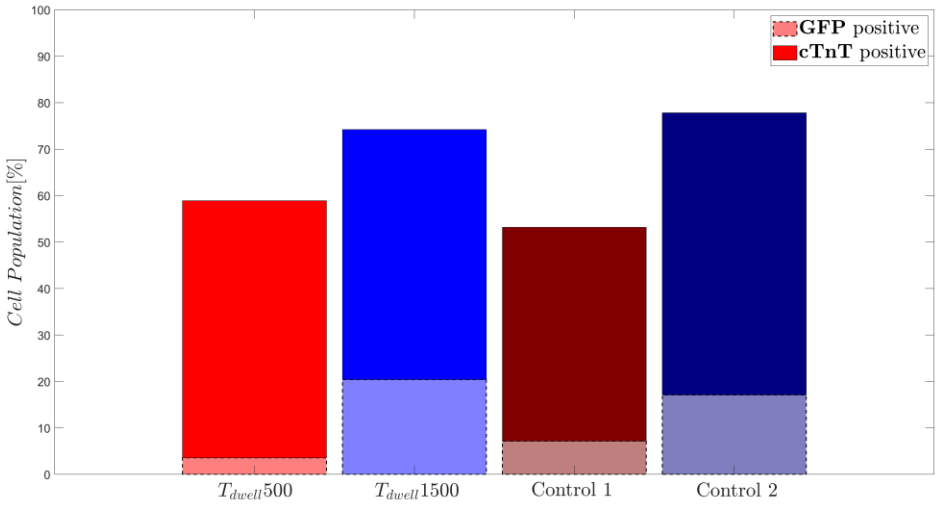

Figure 3.36 Phenotypic analysis on Day 9, assessing for cardiogenic differentiation markers, GFP and cTnT for all experimental runs.

Hypoxic conditions	**Continuous Agitation** [N = 90 rpm]	**Intermittent Agitation w/out direction change** [N = 90 rpm, T_{inv} = 30 s, T_{dwell} = 900 ms]	**Intermittent Agitation w/ direction change** [N = 90 rpm, T_{inv} = 30 s]
Yield (CMs/input iPSC)	11.3 ± 3.7	44.0 ± 2.1	6.8 ± 1.1
		Highest yield	***Lowest yield***

Table 3.1 Differentiation yields for three agitation modes, obtained in Correia *et al.* (2014)

	T_{dwell} **500**	T_{dwell} **1500**
Cardiomyocyte Purity [% cTnT positive*]	+ 10.7 ± 22.4 %	- 4.6 ± 20.7 %
Cardiomyocyte Number [-]	- 15.2 ± 3.3 %	+ 26.5 ± 4.1 %
Cardiomyocyte Yield [#CMs/input iPSC]	- 20.0 ± 6.5 %	+ 65.6 ± 10.2 %

Table 3.2 Cardiomyocyte number, yield and purity at Day 9 of differentiation in stirred culture, operated under intermittent agitation (T_{dwell} = 500 or 1500 ms), normalised against the magnetic agitation control condition (T_{dwell} = 900 ms) run in parallel.

CHAPTER 4 FLOW DYNAMICS AND SUSPENSION CHARACTERISATION IN DASGIP BIOREACTORS [*]

4.1 Introduction

The flow frequency analysis and biological study presented in the previous chapter were carried out using a flat bottom DASGIP bioreactor system, equipped with a non-conventional two blade paddle impeller. The purpose was to investigate the impact of mechanical flow cues, imparted from various agitation modes, upon biological outcomes. The impact of the bioreactor configuration was not considered, although it was mentioned that cell culture yields from biological studies utilising a round bottom DASGIP were detrimentally affected. The changes in embryoid body (EB) suspension during the intermittent agitation modes must also be studied to ascertain the extent EB settling to occur during the different T_{dwell} conditions considered. A fundamental understanding of the fluid dynamics occurring in each bioreactor configuration would also be useful to provide a basis for justification of the cell culture findings and help elucidate which and why a particular configuration is favourable.

The DASGIP bioreactor systems, utilised mostly in cell culture applications, are designed for optimal bioprocess performance at a benchtop scale and are available in different reactor and impeller configurations. Heathman (2015) and Nienow *et al.* (2016) used a flat bottom DASGIP bioreactor for the expansion of human mesenchymal stem cells,

---

[*] Some of the results presented in this chapter are included in:

Samaras, J. J., Abecasis, B., Serra, M., Ducci, A., Micheletti M. (2018), "Impact of hydrodynamics on iPSC-derived cardiomyocyte differentiation processes", *Journal of Biotechnology*, Accepted.

Samaras, J. J., Abecasis, B., Serra, M., Ducci, A., Micheletti M. (2017), "Measuring and manipulating the hydrodynamic environment of an iPSC-derived cardiomyocyte differentiation process", *25th European Society for Animal Cell Technology Meeting: Cell Technologies for Innovative Therapies*, Lausanne, Switzerland.

Samaras, J. J., Serra, M., Ducci, A., Micheletti M. (2018), "Characterisation and correlation of flow dynamics relating to an iPSC-derived cardiomyocyte differentiation process", *16th European Conference on Mixing*, Toulouse, France.

derived from bone marrow (hBMSCs), on polystyrene P102-L microcarriers. A three-blade 30° pitched blade turbine impeller was equipped. Rebelo (2015) used a flat bottom DASGIP bioreactor configuration, equipped with a two-blade paddle impeller, for the expansion of hBMSCs. Correia *et al.* (2014), used the same bioreactor-impeller configuration for the differentiation protocol of induced pluripotent stem cells (iPSCs). A small dimple at the centre of the tank was present in the flat bottom configuration used, which was absent in the studies reported by Heathman (2015) and Nienow *et al.* (2016). Venkat *et al.* (1996) suggested that the inclusion of a dimple causes flow convergence below the centre of the impeller, promoting suspension. The DASGIP bioreactor is also available with a torispherical round bottom configuration, although to the author's knowledge no biological studies can be found in the literature with this configuration.

The aforementioned studies indicate different configurations of the DASGIP bioreactor used in cell culture, however little consideration is given to which is optimally suited for each application. Work by Correia *et al.* (private communications) found the round bottom configuration of the DASGIP, as well as the flat bottom configuration equipped with a pitched blade turbine, to be detrimental upon iPSC-CM differentiation yields. Ibrahim and Nienow (1996) suggested the use of a round bottom bioreactor, coupled with an axial flow impeller type, to prevent dead zone formation for optimal suspension. This highlights that suspension characterisation alone is not sufficient for successful cell culture, although it clearly represents a factor that must be considered.

A range of microcarrier types are commercially available for cell culture. Typically, they vary in shape, size, density, material, surface charge or coating and may be microporous or macroporous in structure (GE Healthcare Life Sciences, 2013). Seldom studies are undertaken investigating culture on a range of different microcarrier types. Rafiq *et al.* (2016) systematically investigated culture of hBMSCs on 13 microcarrier types, observing Plastic SoloHill microcarriers as the optimal candidate in terms of growth kinetics, amenability to xeno-free processing and ease of cell harvest from the microcarrier surface. This study highlighted the influence microcarrier selection may have upon biological outcomes and bioprocess yields.

Suspension within a reactor is often characterised by the minimum rotational speed required to achieve off-bottom suspension, N_{js}, or 'just suspended speed', defined by Zwietering (1958) as the speed at which particles are suspended off the reactor bottom for 2 s or more. N_{js} is calculated from Equation 1.2 for specific impeller and bioreactor configurations, originally considering particles up to almost three-times the density of

microcarriers. When compared to empirical suspension characterisation, Ibrahim and Nienow (2004) found that Equation 1.2 overpredicted N_{js} for microcarriers by 50 %. Ibrahim *et al.* (2012) suggested that porosity, towards the determination of an 'effective density' (Equation 1.3), should also be considered in theoretical derivations of N_{js}.

Nienow *et al.* (2016) investigated suspension dynamics, determined visually, for a flat-bottom DASGIP bioreactor equipped with a pitched blade turbine, seeded with plastic SoloHill microcarriers; ρ = 1.022 – 1.046 g/cm^3, $D_{50} \approx$ 150 µm. N_{js} was determined as 115.2 rpm and hBMSC proliferation culture was performed at this speed to guarantee full suspension and minimise hydrodynamic stresses. Collignon *et al.* (2010) systematically investigated various axial impeller configurations to evaluate shear stress levels at N_{js}. They observed shear stress could be minimised through impeller selection, whilst ensuring full suspension within the bioreactor was achieved. Both studies highlight the advantage of correlating the suspension and flow dynamics to biological outcomes.

Investigation of the flow dynamics can increase understanding of the interaction between the hydrodynamic environment with process variables, such as operating conditions and bioreactor configuration (Kresta and Wood, 1993). **Table 1.1** in Chapter 1 summarises flow field investigations in terms of impeller *D/T* and velocity magnitudes and shows that a reduced distance of the impeller blade tip to the bioreactor wall results in a confinement of the impeller jet and induces a reduction of the local velocity magnitudes. In addition, Hall *et al.* (2004, 2005) and Montante *et al.* (2006) observed unbaffled configurations to significantly diminish fluid circulation patterns and radial and axial velocities, as a result of solid body rotation and the dominant tangential flow, to the baffled counterparts.

The present work was undertaken to provide an in-depth investigation of the fluid and suspension dynamics occurring in two unbaffled DASIP bioreactor configurations to then correlate with the cell culture findings of Correia *et al.* (private communications) to establish why a particular configuration is favourable. Suspension dynamics were also assessed for intermittent agitation modes to demonstrate the impact of flow characteristics on EB sedimentation at the start and end of the differentiation process.

4.2 Results

This chapter is divided into two main parts: flow field characterisation of two DASGIP bioreactor configurations (flat and round) is presented in Section 4.2.1, and suspension characterisation studies are given in Section 4.2.2. A range of microcarrier types were used to also assess the impact of microcarrier properties on the quality of suspension.

The standard triple decomposition technique of the instantaneous velocity, u, of Equation 2.11 was employed to distinguish between the mean flow, $\overline{U}$, periodic fluctuations due to the blade passage,$\tilde{u}$, and the turbulent component, u', as described in Section 2.4.

All velocities have been normalised by $V_{tip} = \pi ND$, while vorticity component and shear rate are normalised by πN.

4.2.1 Mean flow characteristics

4.2.1.1 Velocity magnitude and decomposition to radial and axial velocity components

Two-dimensional (2-D) contour maps of the ensemble-averaged velocity magnitude obtained from the radial and axial components, $\overline{U_{rz}}/V_{tip}$, superimposed with the corresponding velocity vector fields, are given in **Figure 4.1** (a – d) for N = 75 – 120 rpm (Re_i = 4500 – 7200), respectively. The impeller Reynolds number (Re_i) is calculated according to Equation 4.1:

$$Re_i = \frac{\rho N D^2}{\mu} \qquad \textbf{(4.1)}$$

Where the fluid viscosity and density is that of water and the impeller diameter is 6 cm. Usually this calculated range of Re_i represents a transitional flow regime with poor flow scaling, however the results presented in this Chapter and Chapter 5 suggest operation closer to a turbulent flow regime with good scaling against the impeller tip speed evident. This will be discussed throughout. Each figure shows the flat bottom bioreactor configuration on the left-half of the plot, shifted such as to present the impeller at the same level in comparison to the round bottom and has counter-clockwise impeller rotation. The round bottom configuration is shown on the right-half, where all measurements are inverted to coincide with clockwise impeller rotation. The non-dimensional contour maps indicate that the velocity fields scale relatively well with V_{tip} for all the impeller rotational speeds considered, both in terms of magnitude ($\overline{U_{rz}}$ = 0 – 0.1 V_{tip}) as well as flow direction. The highest attained non-dimensional velocity magnitudes above the impeller were observed to decrease by 8.5 % ($\overline{U_{rz}}$ = 0.094 – 0.086 V_{tip}) in the flat bottom configuration with increasing rotational speed. Similarly, the upper impeller discharge zone for the round bottom configuration exhibited a 5 % reduction with increasing rotational speed ($\overline{U_{rz}}$ = 0.121 – 0.115 V_{tip}). This behaviour is related to the reduced clearance between the impeller tip and the bioreactor wall preventing radial

flow acceleration, becoming more pronounced at greater rotational speeds. Consequently, the impeller discharge zone shows reduced radial flow due to the large *D/T*, with the bioreactor wall splitting and redirecting the impeller jet into two axial streams. This is more evident in the flat bottom reactor (left-half), where the radial jet instantly impinges on the bioreactor wall at a vertical position of $z/H_L \approx 0.26$, which leads to the formation of two counter-rotating circulation zones of equal intensity, above and below the impeller region. This is less pronounced in the round bottom reactor (right-half), where there is a clear imbalance between the two circulation loops, with the upper loop being denoted by velocity intensities nearly two times greater than the lower loop. Comparison of the upper circulation region across the two bioreactor configurations shows the round bottom reactor is characterised by velocities greater than the corresponding circulation zone of the flat bottom (approximately 24 % increase in velocity magnitude). This suggests the round configuration is more effective to draw in cells, aggregates or microcarriers floating on the free surface and in the bulk flow towards the impeller region. The top circulation loops in both configurations reach a height of approximately $z/H_L \approx 0.9$. Conversely, the circulation loop present below the impeller in the flat bottom reactor, characterised by velocity magnitudes 20 % higher, suggests more efficient lift of cell aggregates and microcarriers, which would result in a lower defined just suspended speed.

The distributions of the ensemble-averaged radial and axial velocity components are given in **Figure 4.2** and **Figure 4.3**, respectively, for rotational speeds $N = 75 – 120$ rpm (a – d). The radial velocity component (**Figure 4.2**) is very weak ($0 – 0.03V_{tip}$) throughout the vessel and is approximately three times lower than the axial velocity component (**Figure 4.3**) ($0 – 0.1V_{tip}$). Considering the splitting and redirection of the radial impeller jet into two axial streams, this is expected and flow patterns analogous to an axial flow impeller are evident.

A quantitative comparison of the axial circulation loops, emanating from and returning to the impeller region, can be obtained from **Figure 4.4**. Radial profiles of the ensemble-averaged axial velocity component are shown at three elevations, indicated in the inset diagram. In accordance with the contour maps shown previously in **Figure 4.1**, **Figure 4.2** and **Figure 4.3**, it is evident the velocities scale well with the impeller tip velocity for both bioreactor configurations. The axial velocity profile for the bulk flow was taken at $z/H_L = 0.775$ and shows positive axial velocities closest to the bioreactor wall, indicating upward flow, which then decrease closer towards the middle of the tank $r/T \approx 0.3$, showing the downward flow of the upper circulation loop. This then plateaus to $\overline{U_z} \approx 0V_{tip}$

towards the impeller axis. Comparison between the two bioreactor configurations shows similar axial velocity profiles, although the negative velocity region, associated to the returning stream of the upper loop, is limited to a lower range of radial distances, r/T = 0.2 – 0.4 in the flat bottom and r/T = 0.15 – 0.38 in the round. This suggests a more pronounced loop in the flat and a wider recirculation loop in the round bottom. The second elevation considered was above the impeller at z/H_L = 0.388. The profiles for the two bioreactor configurations are similar, but as previously mentioned, the round bottom bioreactor exhibits a wider recirculation loop, in addition to greater positive and negative axial velocities. This indicates a stronger upper recirculation loop in comparison to the flat bottom bioreactor. The lowest elevation profile was obtained below the impeller at z/H_L = 0.182 (**Figure 4.4**). Two distinct axial profiles are now observed between the bioreactor configurations, the round bottom system showing weak downward flow and the apparent absence of a prominent lower circulation loop. Negative axial velocities are observed closest to the bioreactor wall in the flat bottom configuration, which then increase to positive values at $r/T \approx 0.4$ as radial coordinates closer to the impeller axis are considered. This indicates the presence of a lower circulation loop. It is interesting to note that at $r/T \approx 0 – 0.25$, in proximity of the dimple at the base, the axial velocity changes sign again, suggesting a second smaller circulation loop.

The 2-D ensemble-averaged velocity fields and contour maps of the root mean square (r.m.s) of both the radial and axial velocity components for the two DASGIP configurations are given in **Figure 4.5** and **Figure 4.6**, respectively. The ensemble-averaged r.m.s for each velocity component is calculated according to Equation 2.12, and therefore accounts for both the pseudo-turbulence, periodic fluctuations induced by the blade passage, and the random fluctuations due to the local presence of turbulence. The contour maps in both **Figure 4.5** and **Figure 4.6** (a - d) are again shown to scale well for increasing impeller tip velocity, exhibiting minimal variation in the circulation loops with increasing speed. This suggests that the mean flow is fully developed and exhibits a fully turbulent regime at the rotational speeds investigated. Values reported in the literature observed r.m.s velocity components for an axial flow hydrofoil impeller of $\overline{U'_z}$ and $\overline{U'_r}$ = $0.1V_{tip}$ (Baldi and Yianneskis, 2003), $\overline{U'_z}$ = $0.15V_{tip}$ and $\overline{U'_r}$ = $0.11V_{tip}$ for an axial flow marine impeller (Odeleye *et al.*, 2014), $\overline{U'_z}$ = $0.12 – 0.14V_{tip}$ and $\overline{U'_r}$ = $0.15V_{tip}$ for an axial flow downward pumping pitched blade turbine (Schäfer *et al.*, 1998; Aubin *et al.*, 2004) and $\overline{U'_z}$ = $0.32 – 0.35V_{tip}$ and $\overline{U'_r}$ = $0.32 – 0.33V_{tip}$ for a radial flow Rushton turbine impeller (Wu and Patterson, 1989; Escudié and Liné, 2003). Ensemble-averaged r.m.s

values obtained for axial flow impellers are shown to be most comparable to the velocity fluctuations measured in this work (0 – 0.1V_{tip}). The regions associated to the top of the vessel exhibit axial and radial r.m.s values up to 0.043V_{tip} for both bioreactor configurations, suggesting a limited degree of mixing in this region, investigated in the next chapter. A maximum difference up to 98.3 % and 99.7 % between the impeller zone and the bulk fluid r.m.s. velocity levels can be observed for the flat and round bottom configurations, respectively. The axial and radial r.m.s velocities in the impeller region reach up to 0.098 V_{tip} for the flat configuration and 0.110 V_{tip} for the round. This would suggest a slightly increased level of turbulence in the round configuration. It is also worth noting that r.m.s values in the impeller region are equivalent to the ensemble-averaged axial velocities and are in fact three times larger than the measured radial velocities, indicating large velocity fluctuations (random and periodic).

Upon examination of the radial direction fluctuations, $\overline{U'_r}/V_{tip}$ obtained in both configurations and shown in **Figure 4.5**, it can be seen that most fluctuation occurs within the impeller region. Interestingly, the flat and round bottom configurations exhibit almost equal radial fluctuation below the impeller, however, within the bulk flow up to $z/H_L \approx$ 0.9 a larger region of fluctuation for the round bottom can be observed. Observing a comparison of the phase-resolved decompositions at φ = 0, 15, 30 and 45° for both pseudo-turbulence from periodic impeller motion (a), $\langle k \rangle$, and the turbulence resulting from random velocity fluctuations (b), $\langle k' \rangle$, it can be seen in **Figure 4.7** that both periodic turbulence and random velocity fluctuations exist within a slightly larger region at a higher intensity within the round bottom bioreactor above the impeller blade. Pseudo-turbulence from impeller blade rotation is not significantly different below the impeller and any differences observed can be considered to be within the experimental error.

The fluctuation of the ensemble-averaged axial velocity component, $\overline{U'_z}/V_{tip}$, is given in **Figure 4.6**. As expected, the most significant velocity fluctuations occur within the impeller region, where the two trailing vortices are formed. Larger fluctuation of the axial velocity component occurs below the impeller in the flat bottom configuration, again shown by the higher level of turbulence in **Figure 4.7** (b) and larger fluctuation of $\overline{U'_z}/V_{tip}$ is apparent above the impeller in the round configuration.

Due to the distortions in the bioreactor glass at the base, it was not possible to directly measure the tangential component using PIV, however an idea of the intensity of this component can be obtained from the LDA measurements already described in Chapter 3.

The ensemble-averaged tangential velocities, $\overline{U_\theta}$ and velocity fluctuation, $\overline{U'_\theta}$, measured at point A (r/T = 0.35 and z/H_L = 0.28) were 0.106 m/s and 0.022 m/s, respectively. For comparison, the PIV measurements in the same point gave $\overline{U_z}$ = 0.014 m/s, $\overline{U'_z}$ = 0.025 m/s, $\overline{U_r}$ = 0.002 m/s and $\overline{U'_r}$ = 0.021 m/s. The greater intensity of the tangential mean flow (at least one order of magnitude greater than the axial and radial components) is expected due to the unbaffled configuration of the DASGIP bioreactor, a large proportion of the energy within the fluid is directed into the dominant tangential direction where the flow is subject to solid body rotation. Despite this difference, the velocity fluctuations of the three components are more comparable, implying that the trailing vortex generated by the paddle impeller induces velocity variation of similar magnitude in every direction.

Given the unbaffled bioreactor geometry and the large impeller size (D/T = 0.98), the ensemble-averaged velocity and r.m.s intensities (up to $0.1V_{tip}$) show relatively good agreement with axial flow impellers reported in literature. As mentioned in Chapter 1, it is known that a reduced gap between the impeller blade tip and the bioreactor wall results in the suppression of the impeller jet. **Table 1.1** summarises a range of axial and radial impeller types and shows a moderate-to-strong negative correlation between increasing D/T and velocity magnitude (correlation coefficient of -0.62). Different bioreactor configurations, fill volumes, impeller geometries etc. will all affect the velocity profiles observed, however a general pattern is perceived. The apparent suppression of the impeller jet with increasing D/T is also documented in the work of Ramsay *et al.* (2016) for a butterfly impeller, who showed that maximal ensemble-averaged velocity magnitudes decreased by 40 % ($0.25V_{tip}$ – $0.15V_{tip}$) when the non-dimensional impeller diameter is increased D/T = 0.53 – 0.98. This is also shown in the work of Hall *et al.* (2005), who investigated eccentrically agitated vessels equipped with a pitched blade turbine and reported velocity magnitudes up to $0.12V_{tip}$ from the impinging impeller jet. Comparison to the baffled centrally agitated configuration, this gave an approximate 56 % reduction in velocity magnitude with the change in bioreactor configuration from baffled to unbaffled and from eccentrically agitated to central agitation.

Tamburini *et al.* (2018) used computational flow dynamics to predict the flow field in a baffled and unbaffled vessel, equipped with a Rushton turbine impeller. They found the radial and tangential components within the baffled vessel were reduced and converted into axial flow, where the radial component within the flow remained dominant. In the unbaffled tank, solid body rotation occurred, and tangential flow dominated. The same effect was also reported by Yoshida *et al.* (2015) and Ciofalo *et al.* (1996). Montante *et*

al. (2006) observed a Rushton turbine impeller equipped within baffled and unbaffled configurations to maintain the same qualitative structures when measured on the *rz*-plane, with a notable reduction in the velocity components for an unbaffled bioreactor. Armenante *et al.* (1997) described a strong dominant axial-flow circulation loop in a baffled vessel equipped with a pitched blade turbine. In an unbaffled system the axial impeller characteristics were reduced. Two weaker circulation loops were evident above and below the impeller, where a strong radial flow was observed. Hall *et al.* (2004) also described the pitched blade turbine in an unbaffled configuration to generate a radial jet, most comparable to that of a Rushton turbine.

The literature presents peak mean flow velocities with a clear distinction between axial and radial flow impellers. Works by Yianneskis *et al.* (1987), Costes and Couderc (1988) and Stoots and Calabrese (1995), to name a few, measured peak radial velocities between $0.62 – 0.87V_{tip}$ for a standard baffled mixing vessel equipped with a radial-flow Rushton turbine impeller, $D/T = 0.33$. Armstrong and Ruszkowsk (1987), Hockey and Nouri (1996) and Schäfer *et al.* (1998) describe peak axial velocities of $0.45 – 0.55V_{tip}$ for a standard baffled mixing vessel equipped with an axial flow 45° or 60° pitched blade turbine with $D/T = 0.33$. Generally, these results suggest that radial velocities generated by a radial-flow impeller are, at their peak, larger than their axial-flow counterpart

Three non-conventional characteristics of the impeller and bioreactor configuration used in this work are the large impeller *D/T*, the axial nature of the radial flow impeller, and the unbaffled nature of the DASGIP, although some baffling is anticipated from the insertion of the probes (Nienow *et al.*, 2016b). As discussed above, unbaffled configurations diminish radial and axial velocity components, increasing confinement between the impeller blade and bioreactor wall and axial flow impellers in comparison to radial flow impellers, all result in reduced velocity components and lower peak velocities.

4.2.1.2 Vorticity and trailing vortices characterisation

Ensemble-averaged vorticity, $\overline{\omega_\theta}$, was obtained for the two bioreactor configurations. The contour maps of the ensemble-averaged vorticity are shown in **Figure 4.8** (a – d) at rotational speeds, $N = 75 – 120$ rpm, respectively. Please note the inversion of impeller rotation between the flat and round bottom configurations for the purposes of visual comparison. The flow is shown to scale well with almost identical vortical structures depicted at all speeds. As seen previously, there is a small reduction in vorticity with increasing *N*. Both configurations confirm the presence of two counter-rotating

circulation loops, above and below the impeller blades. The top vortex shows a clockwise structure from $z/H_L \approx 0.26$ to 0.9, suggesting the vortex is moving up the tank until a high level within the bulk flow. The lower vortex is much less intense in the round bottom tank, although a small vortical cell is apparent. For the flat bottom configuration, the two counter-rotating vortical structures with opposite vorticity show equal absolute vorticity magnitude, $|\overline{\omega_\theta}/\pi N|$ in the range of 0 – 2.5.

To better visualise the vortices generated in the impeller wake, 2-D phase-resolved contour maps of the vorticity were vertically stacked for 24 phase angles, φ = 0 – 345°. This is shown in **Figure 4.9** (a - d) for the flat-bottomed configuration at increasing rotational speeds and in **Figure 4.10** (a - d) for the round configuration. A very high inclination of the upper vortex is observed in both cases, moving upwards from $z/H_L \approx 0.3$ until $z/H_L \approx 0.7$ in the flat and until $z/H_L \approx 0.8$ in the round. The upper vortex intensity is highest at φ = 30° and decays as it moves up the tank. Space-averaged vorticity values, $\omega_\theta{}^*$, within the upper vortex show a 52 % decay in the average vorticity ($\langle\omega_\theta{}^*\rangle/\pi N$ = -4.1 – -1.95) between φ = 30 - 165° in the flat bottom configuration and a 44 % decrease ($\langle\omega_\theta{}^*\rangle/\pi N$ = -3.44 – -1.92) in the round bottom. Over a full impeller rotation, the upper vortex is 10 % more intense in the flat bottom configuration although similar values are expected. The lower vortex is identifiable in the flat bottom reactor for almost the full impeller rotation, decaying by approximately 44 % at φ = 120° ($\langle\omega_\theta{}^*\rangle/\pi N$ = 2.83 – 1.58). Conversely, up to 78 % decay in the lower vortex intensity is measured in the round bottom reactor ($\langle\omega_\theta{}^*\rangle/\pi N$ = 3.37 – 0.76), showing a transient vortex with much more rapid decay behind the leading blade. On average, the lower vortex is 19 % more intense in the flat bottom configuration over a full impeller rotation.

A 3-D visualisation of the trailing vortices generated behind the blade over a full rotation is shown in **Figure 4.11** (a – d) for increasing rotational speeds, where the trailing vortices were identified from iso-vorticity surfaces ($|\langle\omega_\theta\rangle/\pi N|$ = 1.5). As suggested by the ensemble-averaged vorticity in **Figure 4.8** and in accordance with the phase-resolved stacked contour maps in **Figure 4.9** and **Figure 4.10**, the two vortices are separated above and below the impeller blade. The upper vortices are shown to curve upward, extending axially behind the blades. The lower vortex within the flat bottom tank is nearly horizontal and maintains a relatively significant swirling intensity throughout all phase angles considered. In contrast, the round bottom configuration shows a weaker intensity lower vortex. Overall, there is no radial displacement of the trailing vortices, as typically seen

for a radial flow impeller. This behaviour is expected given the proximity of the bioreactor wall to the impeller blade tips and the axial nature of the flow.

To gain a better understanding of the axial evolution of the two trailing vortices, the axial coordinate of the centre of each trailing vortex was calculated using the weighted average given by Equation 4.2:

$$Z_g = \frac{\sum \omega_i \times z_i}{\sum \omega_i} \quad \textbf{(4.2)}$$

where ω_i and z_i are the vorticity and axial coordinates of any point within the stated iso-vorticity boundaries. **Figure 4.12** shows the locus of the trailing vortices axes over an azimuthal distance of 0 – 150° behind the leading blade. Estimates are provided for both bioreactor configurations at each rotational speed investigated (i.e. N = 75 – 120 rpm). The vortex axis is visualised with a line fitted through the axial coordinate of the vortex centre obtained for each phase angle. It is evident that the trailing vortices axes are independent of the rotational speed. The inclination of the upper vortex is higher (29.1°) for the round bottom bioreactor than for the flat bottom (22.9°), however, for the flat bottom configuration the vortex intensity continues over a larger range of phase angles following the lead blade. The upper vortex is seen to decay below the defined vorticity threshold at 85 – 110° for the flat bottom tank, whilst for the round bottom this occurs at 85 - 95°. Interestingly, as N increases for both bioreactor configurations, the upper vortex intensity decays faster into the bulk flow. As discussed for the same observation in velocity magnitudes, this behaviour is related to the large impeller D/T preventing radial flow acceleration, becoming more pronounced at greater rotational speeds.

As previously mentioned, the trailing vortices were visualised using a threshold of $|\langle\omega_\theta\rangle/\pi N| = 0.09$. Schaffer *et al.* (2000) applied a similar method, employing a threshold of dimensionless vorticity, defined below, to identify the contour of trailing vortices;

$$\xi = \omega \frac{T}{V_{tip}} \quad \textbf{(4.3)}$$

Schaffer *et al.* (2000) proposed values of ξ = 13 and 7 for Rushton and pitched blade turbine impellers, respectively, as a good means for definition and comparison across the literature. Escudié *et al.* (2004) found this technique of trailing vortex identification to overestimate the trailing vortices in their own experiments, finding threshold values of $\xi \approx 60$ better suited to their Rushton turbine configuration. A second technique explored by Escudié *et al.* (2004) was originally suggested by Jeong and Hussain (1995) and was

shown to successfully identify the trailing vortices. This method was however more computationally intense and complex, requiring measurement of all three velocity components. As discussed previously, the bioreactor configuration used in this work resulted in a reduction of the axial and radial velocity components measured to those observed in the literature. As a result, the intensity of vorticity measured is also reduced. The threshold values proposed by Schaffer *et al.* (2000) give $\xi {}^{D}/_{T} = \frac{\omega_\theta}{\pi N} = 4.29$ and 2.31 for the radial Rushton and axial pitched blade turbine impellers, respectively, both at *D/T* = 0.33. Relatively good agreement with axial flow impellers has been shown in this work thus far, however, applying the same vorticity threshold as a pitched blade turbine impeller was found to underestimate the trailing vortices. Thus, a slightly lower threshold was applied for clarity and clearer illustration of the trailing vortices, however comparison with characterised trailing vortices for other impeller types must be made with due care considering the different thresholds and/or different methods for identification used.

Trailing vortices characterised in the literature showed that for a Rushton turbine, the most commonly used radial flow impeller, two counter-rotating trailing vortices are produced, above and below the impeller. As discussed in Chapter 1, these vortices extend behind the leading impeller blade and exhibit small upward axial displacement, extending radially towards the vessel wall (Escudié *et al.*, 2004). The lower vortex angle of inclination is shown to be ≈ -4.4° and -6.5° for the flat and round bottom reactors, respectively. This confirms, as seen previously, that the lower vortex for both bioreactor configurations exhibits very little change in the axial direction, most similar to the trailing vortices typically generated from Rushton turbine impellers. Trailing vortices generated by pitched blade turbines exhibit similar characteristics to the upper vortex generated by the paddle impeller of the DASGIP bioreactor. Schäfer *et al.* (1998) determined the vortex axis to extend down in the axial direction to a height of z/H_L = 0.222 from the impeller (z/H_L = 0.335), whilst the radial coordinate remains constant (r/T = 0.16).

4.2.1.3 Shear and turbulence

As the DASGIP bioreactors are primarily used in cell culture applications, rigorous characterisation of the fluid shear stresses generated is paramount. The ensemble-averaged contour maps of the maximum local shear rates, $\overline{\gamma_{max}}/\pi N$, experienced throughout both bioreactor configurations were obtained and are shown in **Figure 4.13** (a – d). Equation 2.20 shows γ_{max} to be calculated from principal components S_i and S_j. These components are the eigenvalues of the matrix given in Equation 2.18, calculated

based upon the rates of change of the radial and axial components in the axial and radial directions. This is detailed in Section 2.4.3. Shear rates up to $\overline{\gamma_{max}}/\pi N$ = 1.4 – 1.26 for N = 75 - 120 rpm in the flat bottom configuration are created at the impeller tip, where the flow impinges on the reactor wall, and at the interface between the top and bottom circulation loops. In the round configuration, shear rates are approximately 11 % lower, up to values of $\overline{\gamma_{max}}/\pi N$ = 1.22 – 1.09 for N = 75 - 120 rpm. This is likely due to the confinement at the impeller tip with the curved surface of the round bottom. The areas of highest characterised shear are observed at the impeller blade's edge, at the interface between the upper and lower vortices, at the bottom edge of the upper vortex, closest to the impeller blade, and up the bioreactor wall from the impinging radial jet. The flat bottom configuration also shows higher areas of shear down the bioreactor wall below the impeller blade.

The highest shear rate obtained corresponds to a dimensional shear stress of $\bar{\tau} \approx 0.0657$ dyn/cm^2, calculated using Equation 2.26. Previous works by Ismadi *et al.* (2014) observed iPSC proliferation to be detrimentally affected by shear stresses greater than 1 dyn/cm^2, whilst mammalian cell damage was shown to occur at values in excess of 1.5 dyn/cm^2, both of which are well above those reported in this work (Elias *et al.*, 1995; Ismadi *et al.*, 2014). For continuous agitation modes the DASGIP bioreactors are considered low shear when equipped with the paddle impeller configuration, used in this work. It is worth noting however that the results presented are ensemble-averaged data, phase-resolved analysis, discussed in detail in the next chapter, observed dimensional shear stresses up to 0.1238 dyn/cm^2, 88 % higher than the highest ensemble-averaged shear stresses measured, however still roughly 9-fold smaller than the values in literature estimated to diminish stem cell proliferation.

A quantitative comparison of the shear rates across the bioreactor volume at a range of rotational speeds, can be observed in **Figure 4.14**. Radial profiles of the ensemble-averaged maximum shear rates are shown at three selected elevations, indicated in the inset diagram. Overall, it is evident that the shear intensity scales well with the impeller tip velocity for both bioreactor configurations, although as observed previously for the vorticity and velocity components, a slight reduction in shear (up to 10 %) can be observed as N increases. As before, this behaviour is related to the large impeller D/T preventing radial flow acceleration, becoming more pronounced at greater rotational speeds. The shear profile for the bulk flow was obtained at z/H_L = 0.775 and shows highest values of shear closest to the bioreactor wall as a result of the impinging radial jet, which

then drops ($r/T \approx 0.45$) and increases once more with the upper vortex recirculation loop ($r/T \approx 0.4$). Previous sections showed lower vorticity but a wider recirculation loop for the round bottom configuration. The shear rates are shown to be slightly lower at these locations in the bulk flow and towards the impeller axis shear rates diminish significantly. The second elevation considered was above the impeller at $z/H_L = 0.388$. As before, the highest shear rates can be observed at the bioreactor walls ($r/T \approx 0.48$) before a drop ($r/T \approx 0.45$) and rise in shear with the incidence of the upper vortical cell at $r/T \approx 0.35 – 0.4$. The highest shear rates are attained in this region, associated with the impinging jet travelling upward at the bioreactor wall. The larger upper circulation loop and higher velocity magnitudes for the round bottom configuration result in a wider area of increased shear above the impeller. This is evident in the shear profile by the higher peak in shear with a diminished drop in shear towards the impeller axis ($r/T \approx 0.2 – 0.4$). The lowest elevation profile was observed below the impeller at $z/H_L = 0.182$ (**Figure 4.14**). The flat bottom configuration exhibits the same spike in shear intensity at the bioreactor wall ($r/T \approx 0.48$) from the downward flow of the impinging radial jet, which again drops at the interface between the impinging jet and lower circulation loop ($r/T \approx 0.45$). This is absent for the round bottom configuration due to the curvature of the vessel and measurements are not obtained until $r/T \approx 0.41$. Shear rate is observed to marginally increase with the lower circulation loop ($r/T \approx 0.4 – 0.43$ for the flat bottom, $r/T \approx 0.37 – 0.4$ for the round), decrease within the loop ($r/T \approx 037$ and $r/T \approx 0.34$ for the flat and round bottom, respectively) and increase with the strong recirculation upwards towards the impeller. The vortices provide the main source of turbulence in stirred tank bioreactors. The shear profiles demonstrate elevated intensities of shear with the incidence of each vortical cell, identified in **Figure 4.8**.

Observing the standard deviation to the maximum measured shear rate, $\overline{\gamma'_{max}}/\pi N$, across all measurements gave an indication of the overall fluctuation in shear over an impeller revolution for each speed, shown in **Figure 4.15**. As with the r.m.s velocity plots shown in **Figure 4.5** and **Figure 4.6**, it can be seen that the regions of highest fluctuation are closest to the impeller tip region. This is apparent both above and below the impeller for the flat bottom configuration, coinciding with the two equal-intensity vortical cells formed, whilst the round bottom configuration shows the strongest fluctuation of shear above the impeller. This is where **Figure 4.8** showed a more prominent upper vortex is formed in comparison to below the impeller. This substantiates the prominence of the vortical cells as a source of turbulence and the incidence of shear.

Turbulence is an instability generated by fluid shear and, as mentioned previously, it is expected that the regions of greatest shear will also translate to the regions of greatest turbulence. The overall ensemble-averaged mean flow kinetic energy, $\bar{k}/{V_{tip}}^2$, for each bioreactor configuration can be quantified using Equation 2.14. The ensemble-averaged contour maps of $\bar{k}/{V_{tip}}^2$ are given in **Figure 4.16** (a – d) for increasing rotational speeds. As previously observed, kinetic energy also scales well with increasing rotational speed. There is a significant difference (up to 99.99 %) between the flow kinetic energy in the bulk and impeller region reaching values up to 0.0056 V_{tip}^2 and 0.0075 V_{tip}^2 above the impeller in the flat and round bottom configurations, respectively. Axial and radial flow impellers have been characterised in the literature with ensemble-averaged mean flow kinetic energy from ≈ 0.015 and 0.1, respectively (Wu *et al.*, 1989; Aubin *et al.*, 2001; Zhao *et al.*, 2011a; Odeleye *et al.*, 2014). As discussed previously, the bioreactor configuration used in this work generates a reduction of measured flow dynamics due to the large impeller diameter, the unbaffled configuration and the axial flow-like properties of the impeller. As such, a reduction in observed turbulence measured is expected. More commonly, the phase-resolved kinetic energy associated to the periodic flow fluctuations, $\langle k \rangle/{V_{tip}}^2$, or the turbulent kinetic energy, $\langle k' \rangle/{V_{tip}}^2$ are discussed in the literature, however the mean flow kinetic energy represented by ensemble-averaged data gives a good definition of overall fluctuations spatially. The two phase-resolved components of turbulence will be explored in-depth in the next chapter.

The highest region of kinetic energy in **Figure 4.16** is observed up the bioreactor wall, extending from z/H_L ≈ 0.34 – 0.7 in the flat configuration and z/H_L ≈ 0.34 – 0.75 in the round. This is also directed downward in the flat bottom configuration, reflecting the equal splitting and redirection of the radial impeller jet into two axial streams, discussed previously. This is almost negligible for the round configuration. Both configurations show a second region of increased kinetic energy associated to the upper recirculation loop, drawn down towards the impeller. This recirculation loop was observed in Section 4.2.1.1 to be more intense and wider for the round bottom configuration, thus higher kinetic energy is observed. The space-averaged flow kinetic energy above the impeller (z/H_L = 0.3 - 0.7) confirms a 36 % increase within the round bottom configuration. Below z/H_L = 0.3, a 24 % increase in the kinetic energy is obtained within the flat bottom configuration, characterised by values up to $\bar{k}/{V_{tip}}^2$ = 0.0054 and 0.0026 for the round. Note the similarity in maximum kinetic energy above and below the impeller for the flat bottom configuration, $\bar{k}/{V_{tip}}^2$ = 0.056 and 0.054, respectively. Conversely, the round

bottom configuration exhibited up to 70.3 % difference in measured kinetic energy values above and below the impeller. This reiterates the identified symmetry within the flat bottom configuration above and below the impeller. Kinetic energy was also shown to scale well with up to 11.6 % difference observed across all rotational speeds investigated.

The flat and round bottom configurations are shown to exhibit similar flow characteristics above the impeller region. Velocity magnitudes and mean flow kinetic energy are shown to deviate up to 24 % and 36 % in the round bottom configuration, respectively, however both bioreactor configurations are shown to generate an upper vortex with a high inclination at similar intensities (< 10 % difference). Both bioreactors exhibit low levels of shear, favourable for cell culture, and both scale well across various rotational speeds. Irrespective of the similarities outlined, the main difference between the two bioreactor configurations is the lower vortex observed within the flat bottom configuration. Conception of this lower vortex can be attributed to the lower impeller clearance and the geometry of the flat bottom with the inclusion of the dimple. This lower vortex is observed to create a region of increased flow turbulence, shear and circulation, anticipated to better lift cells and particles at the base of the tank, preventing settling and stagnation. An in-depth quality of suspension investigation is undertaken in the next section to investigate this hypothesis and to help postulate why a particular bioreactor configuration is favourable with regards to cell culture.

4.2.2 Suspension characterisation

Cell culture studies in the literature often lack rigorous suspension characterisation within the bioreactor configurations used. The suspension dynamics were considered using four microcarrier types, of which three (Cytopore 1, Cytodex 3 and Cultispher-G) were used to investigate both continuous and intermittent agitation modes in the two bioreactor configurations. The fourth type of microcarrier (Microcarrier X) was used to investigate suspension characteristics within the round bottom configuration, utilising a continuous agitation mode. Two of the microcarrier types used, Cytodex 3 and Cultispher-G, were selected to represent a mimic of the embryoid body (EB) suspension at the start (Day 2) and the end (Day 9) of iPSC-CM differentiation culture. **Table 2.1** summarises the physical characteristics of the microcarrier types used and the EBs on Day 2 and Day 9.

Figure 4.17 shows a suspension characterisation experiment using Cytodex 3 microcarriers in the flat bottom configuration. **Figure 4.17** (a) shows the fully settled system with the Trypan Blue stained microcarriers at the base of the bioreactor,

corresponding to a homogeneity index, H = 0 %. As the rotational speed is increased the microcarriers begin to lift from the base, **Figure 4.17** (b) depicts a partially suspended system ($H \approx 75$ %). A fully homogeneous system is shown in **Figure 4.17** (c) and corresponds to $H \geq 95$ %. For visualisation purposes, **Figure 4.18** (a - c) depicts each of the commercially available microcarrier types investigated following hydration in PBS. The differences in both size and porosity are evident. **Figure 4.18** (a) shows variation in the size of Cultispher-G microcarriers, where porosity is evident by the undefined edges and apparent texture of the relatively spherical beads. In contrast, **Figure 4.18** (b) shows Cytodex 3 to exhibit good uniformity in size with the microporous/non-porous nature, shown by smooth spherical beads. Cytopore 1 are the most porous and are uniformly slightly larger in size than Cultispher-G. The porosity is evident in **Figure 4.18** (c) by the mesh-like structures. Cytopore 1 are also observed to be relatively spherical in shape.

The homogeneity index, H, determined using Equation 2.22 for increasing rotational speeds is given in **Figure 4.19**. Comparison is made for each microcarrier type in the flat bottom configuration (a) and then in the round (b), separated for clarity. A comparison between the two bioreactor configurations is then observed (c). H does not increase whilst the system is fully settled, showed up to ≈ 10 rpm for Cytopore 1, ≈ 20 rpm for Cultispher-G and Cytodex 3 and up to ≈ 40 rpm for Microcarrier X. As the rotational speed is increased the degree of homogeneity increases, representing 'lift' of the microcarriers. **Figure 4.19** (a) in the flat bottom configuration shows Cytopore 1 is first to reach system homogeneity, considered at $H \geq 95$ %, with the minimum speed required to reach complete suspension and system homogeneity, N_H, determined as N_H = 25.2 rpm. Cytodex 3, which exhibit a decrease in both size and porosity, lift at N_H = 37.6 rpm. Cultispher-G, the largest in size with a reduction in porosity to Cytopore 1, are the least efficient to lift, N_H = 53.6 rpm. Overall, this suggests that smaller microcarriers more efficiently suspend at lower rotational speeds, unless the microcarrier exhibits a highly porous structure. In agreement with the observations made for the flat bottom configuration, the round bottom configuration (**Figure 4.19** b), shows the highly porous Cytopore 1 to lift most efficiently at N_H = 32.2 rpm. The smallest microcarriers, Cytodex 3 are second to suspend at N_H = 44.8 rpm, followed by Cutlispher-G at N_H = 67.0 rpm. Microcarrier X, the largest in size and highest in density, with highly variable porosity, is the least efficient to lift, shown by the significantly reduced curve gradient and N_H = 163.8 rpm.

Calculation of the correlation coefficient between the change in size, density and porosity with the achieved minimum speed to suspend in the round configuration shows the strongest correlation between increasing density and suspension (0.98 correlation coefficient). Strong correlation is also observed with increasing microcarrier diameter and the speed required to lift (0.91 correlation coefficient), however due to the highly variable porosity with Microcarrier X, the impact of porosity upon suspension cannot so easily be correlated. Excluding Microcarrier X, weak negative correlation is observed for increasing porosity and decreasing the speed required to suspend (-0.3). Similar correlation coefficients were calculated for the flat bottom configuration. Due to the multiple factors shown to impact upon N_H, this assessment can be used to predict qualitative changes to the suspension characteristics with change in microcarrier type.

Figure 4.19 (c) compares the suspension dynamics of the two bioreactor configurations. System homogeneity is unanimously reached at lower rotational speeds within the flat bottom configuration, considering the same microcarrier type. An approximate 16 - 22 % increase in N_H was observed for Cytopore 1, Cytodex 3 and Cultispher-G in the round bottom configuration. This was predicted from Section 4.2.1, where a stronger lower vortex is present within the flat bottom configuration. **Table 4.1** summarises the observed values of N_H. Based on the poor performance of Microcarrier X and its inability to suspend at rotational speeds relevant to stem cell cultures, this microcarrier type was no longer considered in further analysis.

It is interesting to note the characterised just suspended speed for plastic SoloHill microcarriers (ρ = 1.022 – 1.046 g/cm^3, $D_{50} \approx$ 150 μm) by Nienow *et al.* (2016) within a flat bottom DASGIP bioreactor, notably without the presence of the dimple, equipped with an axial-flow three-blade pitched turbine impeller. These microcarriers exhibit similar physical characteristics to Cytodex 3 (ρ = 1.04 g/cm^3, $D_{50} \approx$ 175 μm), however were observed to reach full suspension at N_{js} = 115.2 rpm, significantly higher than N_H = 37.6 rpm found in this work. This significant difference is most likely attributed to the method of suspension characterisation; N_{js} is subjectively characterised from beneath the bioreactor by Zwietering's (1958) 1 – 2 s criterion, whereas the measurements in this work considered system homogeneity and N_H from the vertical plane using computational image processing techniques. The difference may also be attributed to the inclusion of the dimple in the DASGIP configuration used in this work, suggested by Venkat *et al.* (1996) to promote suspension capabilities, and also from the change in impeller configuration from an axial flow pitched blade turbine to the paddle impeller with large *D/T*.

Figure 4.20 presents the dimensionless time needed to fully suspend and reach 95 % homogeneity, Nt_H, which also can be interpreted as the number of revolutions at speed N to achieve system homogeneity. **Figure 4.20** (a) provides a comparison across the number of revolutions required to reach 95 % homogeneity for increasing rotational speeds. In accordance with **Figure 4.19**, **Figure 4.20** (a) demonstrates Cytopore 1 to lift quickest at the lowest rotational speeds in both bioreactor configurations. Interestingly, Cytodex 3 can be seen to take the longest time to lift at N_H. Comparison at N = 70 rpm, the first speed to exhibit full suspension for all bioreactor and microcarrier configurations, it can be seen that Cultispher-G in the round bottom reactor takes the longest to suspend (Nt_H = 38.5), followed by Cytodex 3 in the round bottom (Nt_H = 29.4). There is then a moderate decrease in Nt_H, where Cultispher-G is then suspended in the flat bottom reactor (Nt_H = 12.3), followed closely by Cytodex 3 (Nt_H = 10.1). The quickest to suspend for the round bottom configuration, followed by the flat bottom at N = 70 rpm was Cytopore 1 (Nt_H = 7.2 and 4.8, respectively). It is interesting to observe that although Cytodex 3 in the round bottom configuration was characterised to suspend at lower rotational speeds, Cultispher-G in the flat bottom configuration was observed to suspend faster. From N = 80 – 200 rpm Cultispher-G is observed to consistently suspend faster than Cytodex 3 for both bottom configurations, suggesting that although higher rotational speeds are required to achieve initial suspension, once suspended Cultispher-G is more efficiently lifted. This can possibly be attributed to the increase in microcarrier porosity with Cultispher-G. According to Equation 1.3, porosity results in a reduction of the effective density of a particle. Applying Equation 1.3, the effective density for Cultispher-G is ≈ 1.02 g/cm^3 and Cytodex 3 has a density of 1.04 g/cm^3. Although not significantly different, this may partially be attributable to the changes in suspension observed. Overall, **Figure 4.20** (a) and **Figure 4.19** show the flat bottom bioreactor configuration to suspend the microcarrier types investigated at lower rotational speeds, whilst also requiring a lesser number of revolutions to achieve full suspension.

Figure 4.20 (b) depicts Nt_H for increasing rotational speeds, normalised against N_H. For N/N_H = 1, Cultispher-G in the flat bottom configuration is observed to suspend fastest, although **Figure 4.20** (a) shows the rotational speed is over double the rotational speed for Cytopore 1, N_H = 53.6 rpm and N_H = 25.5 rpm, respectively. As discussed previously, Cytodex 3 is shown for both configurations to require the highest number of revolutions to suspend. This plot also shows Nt_H to plateau as the rotational speed is increased. This observed plateau is termed the homogeneity-time constant, H_t, and represents the

minimum number of revolutions to achieve system homogeneity, **Table 4.2** summarises. A grouping is apparent for the flat bottom bioreactor configuration, exhibiting relatively low H_t values. Cultispher-G and Cytodex 3 also show similarity in the defined H_t values within the round bottom bioreactor. Although not perfect, this introduces the idea that a correlation may exist between the microcarrier and bioreactor combination with a characteristic dimensionless H_t value. As the plateau generally seems to occur from $N/N_H \approx 2$, H_t can be used to estimate the minimum number of revolutions required to achieve full suspension and homogeneity when $N/N_H > 2$.

As Section 4.2.1 illustrated, both the flat and round bottom configurations exhibit very similar flow characteristics above the impeller region. **Figure 4.21** (a – c) demonstrates the similarities between the sedimentation characteristics of the flat and round bottom bioreactors for Cytopore 1, the significance of these plots will be discussed further on. Due to the similarities demonstrated within the bulk flow however, settling characterisation of the three microcarrier types was therefore performed in the flat bottom bioreactor configuration. In addition, results by Correia *et al.* (private communications), as discussed previously, found the round bottom configuration unfavourable for stem cell culture, thus no further analysis was performed using this configuration.

System suspension and homogeneity during intermittent agitation conditions was investigated such as to determine the time to resuspend and the extent of settling during the dwell. **Figure 4.22** shows the degree of homogeneity in the flat bottom DASGIP bioreactor over time for all three microcarrier types at N = 90 rpm, T_{inv} = 30 s and T_{dwell} = 30,000 ms. The plot is shown for a much longer dwell time, T_{dwell}, than those considered in the previous chapter to better demonstrate the extent of settling between each microcarrier type. Homogeneity is observed to drop up to 10 % during the dwell time for Cytopore 1, up to 20 % for Cytodex 3 and up to 65 % for Cultispher-G. As Cultispher-G is also considered a mimic of the larger EBs in the cell culture experiments at the end of differentiation, this suggests the extent of settling to increase at the end of the differentiation protocol. As discussed in the Section 3.2.2, the main frequency peaks corresponding to impeller blade passage exhibit higher intensities within the impeller region. In **Figure 4.22**, the EBs at the end of differentiation (Cultispher-G) occupy the bottom 35 % of the tank, within the impeller region, at the end of the dwell. Upon resuspension they will be exposed to the higher shear and turbulence levels, characterised within the impeller region in Section 4.2.1.3. Should significantly longer dwell durations be applied during cell culture, T_{dwell} could be adjusted towards the end of differentiation

such as to maintain the same extent of settling from the Day 2 EBs (Cytodex 3) to Day 9 (Cultispher-G). This would avoid inhomogeneous accumulation within the impeller region.

Figure 4.23 (a – c) shows the first dwell phase during intermittent agitation at N = 90 rpm from a fully settled system at t = 0 s. The dwell phase is initiated at t = 30 s and varies in duration from T_{dwell} = 500 – 30,000 ms. The average drop in homogeneity is overlaid for the dwell times indicated in the figure legend by *. It can be observed that as T_{dwell} increased, the extent of sedimentation increases. In accordance to the suspension characteristics observed previously in **Figure 4.19**, Cytopore 1 settles the least during the dwell (H = 89.6 %), Cytodex 3 settles to H = 79.5 % and Cultispher-G, the largest microcarrier type, drops further to H = 34.6 %. To better ascertain the extent of settling during the dwell, **Figure 4.23** (d) shows the highest drop in homogeneity, averaged from 10 consecutive dwell phases, at increasing dwell durations. Interestingly, the three dwell conditions investigated in the biological studies in Section 3.2.3, T_{dwell} = 500, 900 and 1500 ms, show a drop in suspension of less than 3 %. This suggests that for the biological data obtained, the observed changes in differentiation efficiency were not attributed to the extent of settling with the increase in dwell. As before, Cultispher-G, representing the EB mimic at the end of differentiation, exhibits a greater extent of settling, which overall is shown to increase with dwell duration.

A constant rate of settling is apparent in **Figure 4.23** (a – c) for each microcarrier type with increasing dwell. The gradient of settling for each microcarrier type was approximated for each dwell duration and plotted in **Figure 4.24**. The settling gradient remained predominantly linear for increasing T_{dwell}, although clearly for Cultispher-G a faster rate of settling is apparent at longer dwell durations (T_{dwell} = 9000 – 30,000 ms).

As mentioned previously, **Figure 4.21** (a – c), observed the similarities in settling characteristics between the flat and round bottom DASGIP configurations for Cytopore 1. Up to 4.5 % difference in settling was observed for Cytopore 1 (**Figure 4.21** a and b) and the approximate settling gradients in both configurations (**Figure 4.21** c) are shown to be very similar, again with the most deviation occurring at longer dwell durations. This suggests similar settling characteristics between the two configurations investigated.

Based on the settling gradients in **Figure 4.24**, it was possible to calculate an empirical settling rate for each microcarrier type, shown in **Figure 4.25**. Two lines were fitted and extrapolated from T_{dwell} = 10,000 ms (▬) and 20,000 ms (▬ ▬) to T_{dwell} = 30,000 ms,

and an average rate of settling was determined. **Table 4.3** summarises the rates of settling determined and compares settling velocities from published manufacturer values, the calculated theoretical values using Stokes's law of settling, and the empirical settling velocities using the average settling rate (both shown in blue). The calculated settling velocities are given in a range due to the range of microcarrier sizes specified by the manufacturer. The settling velocities, empirically approximated from **Figure 4.25**, represent one third of the manufacturer published velocities, which in turn are one third of the calculated settling velocities. It should be noted however that the method for determining settling velocity by the manufacturer are not published. As proven by the comparison in determining the 'just suspended speed' by Nienow *et al.* (2016) with the results discussed above, the method for characterising the suspension dynamics greatly impacts upon the values obtained. The calculated settling velocities based upon Stokes's law are significantly higher than the empirical and manufacturer published values. One justification for this incongruity could be that Stokes's law assumes a solid spherical particle, **Figure 4.19** and **Figure 4.20** showed the significance porosity may have on suspension. As discussed previously, Ibrahim *et al.* (2012) suggested Equation 1.3 to calculate the effective density, accounting for porosity. This can be used to adapt Stokes's law, demonstrated in Equation 4.4:

$$u_{s,eff} = \sqrt{\frac{2 \times (((1-\Phi)\rho_s + \Phi\rho_L) - \rho_L) \times g \times V}{C_D \times A \times \rho_L}} \quad \textbf{(4.4)}$$

Cytodex 3 remains unchanged as it is considered microporous/non-porous. Cultispher-G, with 50 % porosity, gives an improved calculated settling velocity, u_s = 0.43 - 0.73 cm/s. This is approximately 30 % lower than the original calculated values, however remains significantly higher than the settling velocities observed in this work (approximate four-fold increase). Cytopore 1, with porosity more than 90 %, significantly reduces the estimated range using Stokes's Law by ≈ 70 % to u_s = 0.2 – 0.24 cm/s. This is now within the manufacturer's given range but remains three-fold higher than the empirically-determined values. Other assumed components within Equation 4.4, such as the drag coefficient, C_D, which was estimated for a smooth sphere in turbulent flow, are also factors that would cause a discrepancy in settling velocities calculated and is another parameter which must be optimised further. Overall**,** it is evident that Cultispher-G settles the fastest, whilst Cytopore 1 and Cytodex 3 have similar settling characteristics, with Cytopore 1 settling slowest. Evidently, calculations using Stokes's Law must be optimised in future works to better reflect settling characteristics observed empirically.

As shown and discussed in **Figure 4.13** and **Figure 4.16** in Section 4.2.1.3, the impeller region within the DASGIP bioreactors exhibits the highest levels of turbulence and shear. During a sensitive process such as a stem cell culture, prolonged and excessive exposure to the harsher local environment in the impeller region may impact upon yield, cell displacement from microcarriers and cell differentiation pathways. Utilising the settling rates empirically defined from **Figure 4.25**, given in **Table 4.3**, it is possible to define a maximum T_{dwell} to ensure the extent of microcarrier settling does not coincide with the impeller region. **Table 4.4** demonstrates the calculated maximum dwell durations, $T_{dwell\ (max)}$, to preserve suspension above the impeller region, represented by the area highlighted on the tank (considered at $H \approx 30$ %). This represents an operational consideration when designing biological cultures with intermittent agitation modes.

The final important consideration relating to intermittent agitation modes during cell culture is the time for the system to fully resuspend following a dwell phase. This is given in **Figure 4.26** for all microcarrier types investigated within the flat bottom bioreactor at increasing dwell durations. With the restart in impeller motion it can be observed that full resuspension occurs rapidly (t_r = 2 – 4 s). As expected, Cytopore 1 is the quickest to resuspend given it requires the least number of revolutions to lift (**Figure 4.20**) and is shown to settle the least (**Figure 4.23** d). Cultispher-G is the next quickest to resuspend, in accordance with previous trends observed in **Figure 4.20**, where suspension was observed to occur quickly in comparison to the non-porous microcarrier Cytodex 3.

4.3 Concluding remarks

The objectives of the work presented in this chapter were to investigate the flow dynamics of two DASGIP bioreactor configurations and to correlate this with the biological outcomes found by Correia *et al.* (private communications). In addition to mean flow characterisation, suspension within both bioreactor configurations was also characterised such as to inform upon the efficiency of each bioreactor configuration to 'lift' particles within the flow. Intermittent agitation modes were then employed during the suspension characterisation studies such as to determine settling characteristics for three different commercially available microcarriers, two of which served as a mimic for the embryoid bodies generated on Day 2 and Day 9 of cell culture. This work showed the bioreactor configuration can have a significant impact upon the flow dynamics, which in turn impact upon the particle suspension. It is evident from the characterisation studies and the biological outcomes described by Correia *et al.* (2014) that an optimal configuration for

cell culture uses the flat bottom bioreactor configuration. The rigorous characterisation of both bioreactor types is novel to the field and can be used to inform upon future studies utilising each of the two bioreactor configurations investigated.

The flow characterisation studies found that a reduction in impeller clearance, combined with a flat bottom geometry, created two equal counter rotating vortices above and below the impeller region. This resulted in more efficient suspension of microcarriers at lower rotational speeds. The two-blade paddle impeller configuration had a very high *D/T* which resulted in a reduction of the axial and radial velocity components, however this also created extremely low shear stresses in the regions of highest anticipated shear. Both bioreactor configurations proved to scale well across a range of rotational speeds and it was interesting to note the top vortex which extended axially up the bioreactor wall over a full rotation. Although both bioreactor configurations proved very similar, the two key defining differences were the areas of increased velocity magnitudes and turbulence in the upper impeller region for the round bottom configuration, and the addition of an equal intensity counter-rotating lower vortex in the flat bottom configuration. This lower vortex is anticipated to generate a region of improved mixing, characterised in the next chapter, with the apparent increase of flow turbulence below the impeller to better 'lift' cells and particles at the base of the reactor.

Having investigated the flow dynamics, three commercially available microcarrier types were then investigated, all of which are commonly used in cell culture. In accordance with the flow characterisation studies, it was found that the flat bottom configuration of the DASGIP bioreactor resulted in more favourable suspension characteristics. A comparison was also made between the microcarrier types and it was found that density and size had the greatest influence upon suspension and settling characteristics, although porosity also was observed to play an important role. Smaller sized microcarriers proved to require lower rotational speeds to lift, however took a longer time to achieve full homogeneity, due to their non-porous nature. A dimensionless homogeneity-time constant, H_t, representing the number of revolutions required to reach homogeneity, was defined. This was determined with the microcarrier and bioreactor combination and can be used to estimate the shortest time or least number of revolutions required to fully suspend at $\approx 2 \times N_H$. Settling characterisation studies illuminated the need for the inclusion of porosity in theoretical settling velocity calculations. The larger sized microcarriers, used as a mimic of EBs at the end of differentiation, were shown to settle

fastest. This suggested the intermittent agitation modes, applied during cell culture, to result in variable degrees of settling as EB characteristics evolved over time.

The previous chapter investigated three dwell durations during the biological studies, T_{dwell} = 500, 900 and 1500 ms. Observing the homogeneity between the two microcarriers considered as mimics of the EBs at Day 2 and Day 9, the start and end of differentiation, respectively, it was shown that up to 3 % reduction in homogeneity occurs between T_{dwell} = 500 and 1500 ms. With the biological data available, it can be concluded that the observations in differentiation efficiency were not impacted from the change in cell suspension, although future studies investigating a longer dwell duration may benefit from the rigorous characterisation performed in this chapter.

(a)

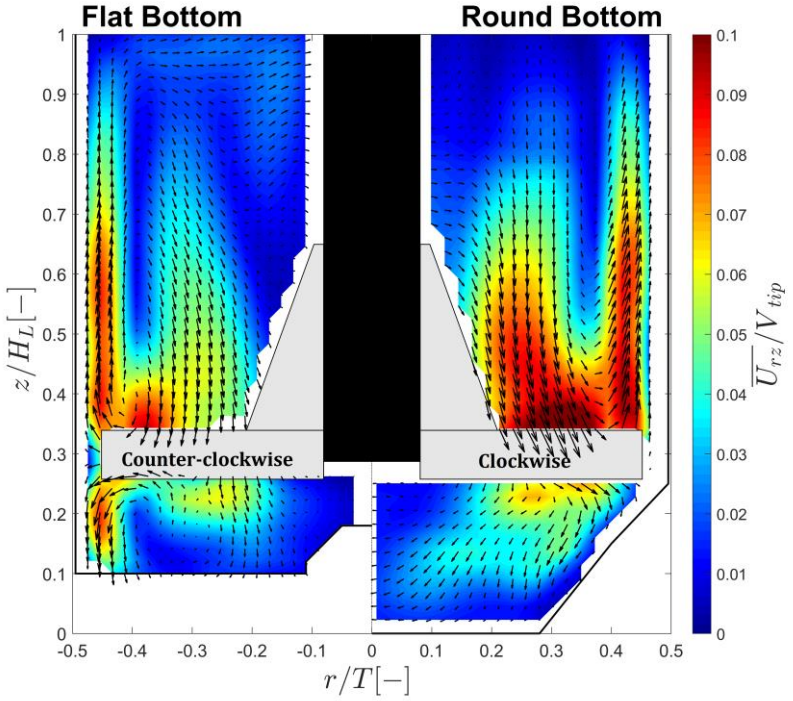
Flat Bottom
Round Bottom
Counter-clockwise
Clockwise
$z/H_L[-]$
$r/T[-]$
$\overline{U_{rz}}/V_{tip}$

(b)

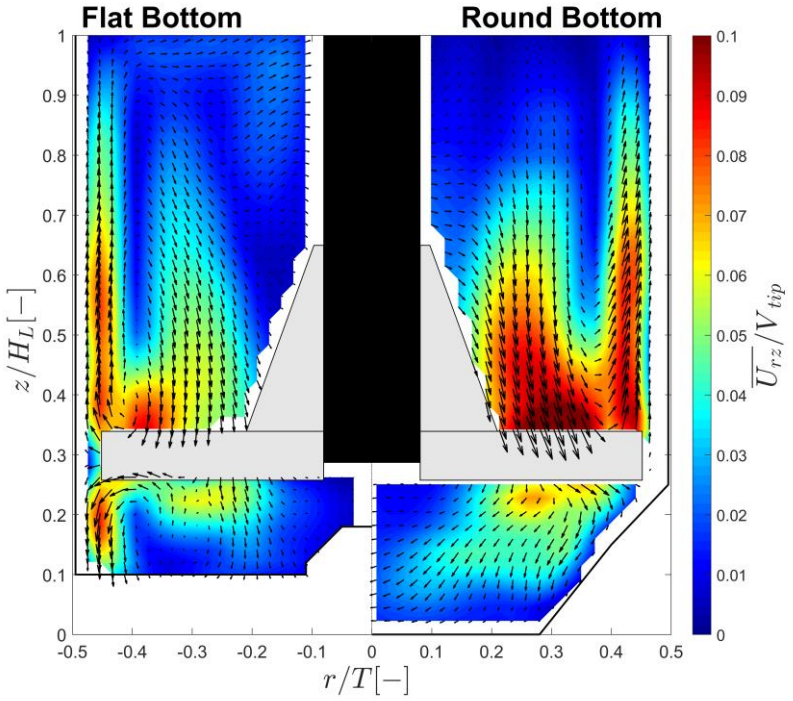
Flat Bottom
Round Bottom
$z/H_L[-]$
$r/T[-]$
$\overline{U_{rz}}/V_{tip}$

(c)

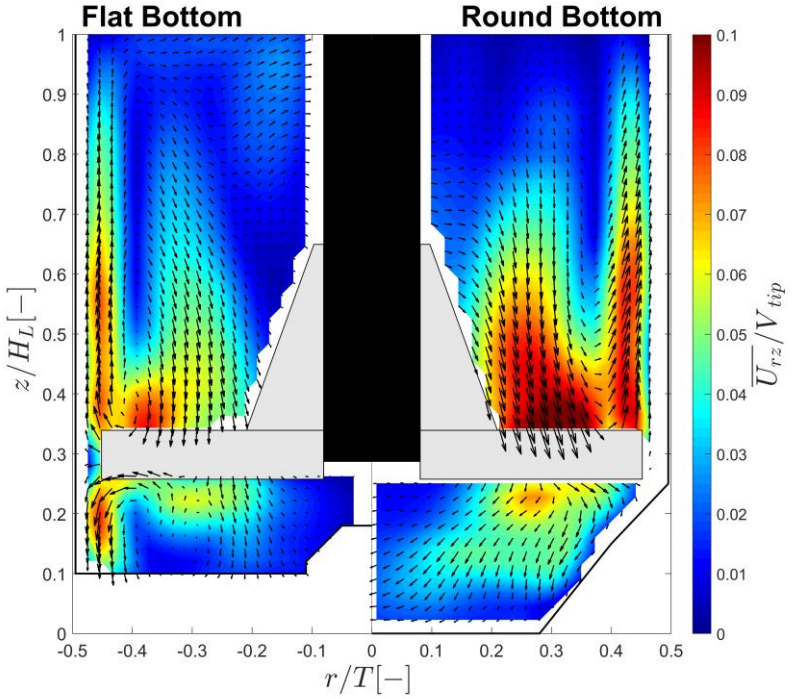

(d)

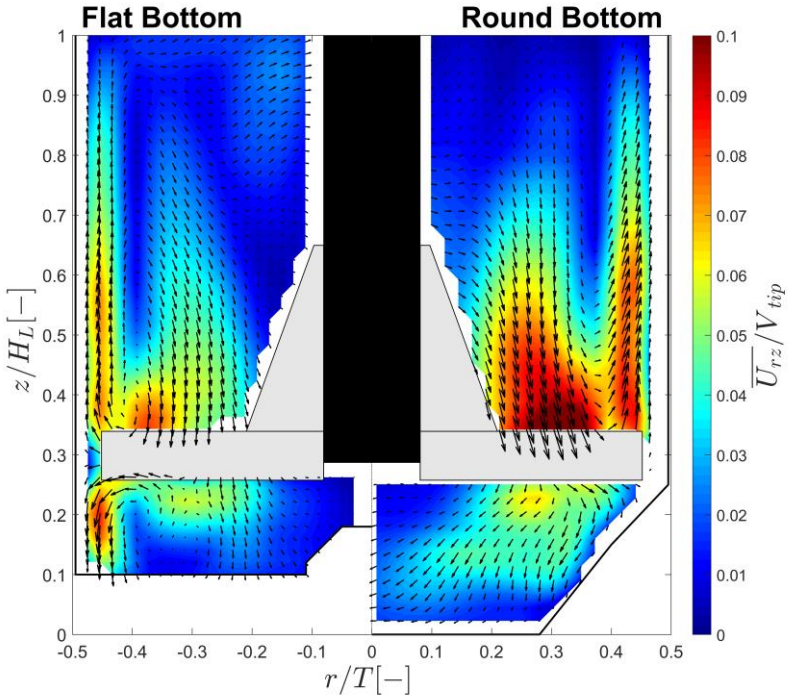

Figure 4.1 Contour maps of ensemble-averaged velocity magnitudes, $\overline{U_{rz}}/V_{tip}$: (a) N = 75 rpm; (b) N = 90 rpm; (c) N = 105 rpm; (d) N = 120 rpm.

(a)

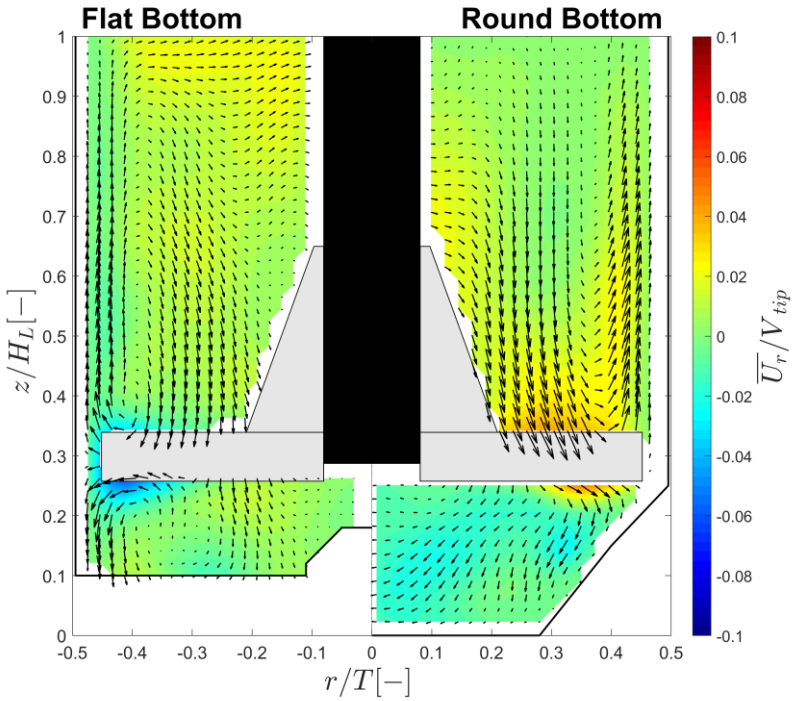
Flat Bottom
Round Bottom
$z/H_L[-]$
$r/T[-]$
$\overline{U_r}/V_{tip}$

(b)

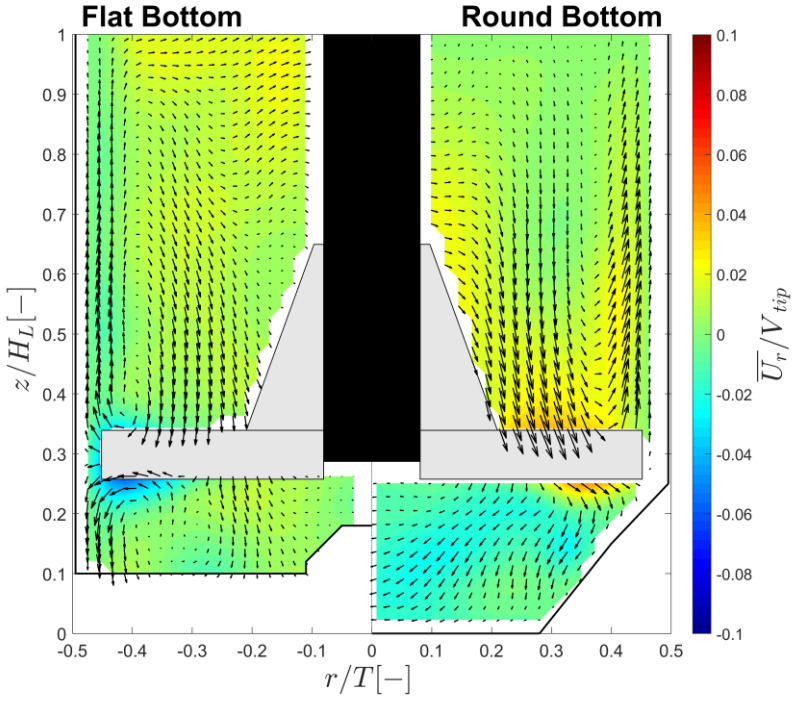
Flat Bottom
Round Bottom
$z/H_L[-]$
$r/T[-]$
$\overline{U_r}/V_{tip}$

(c)

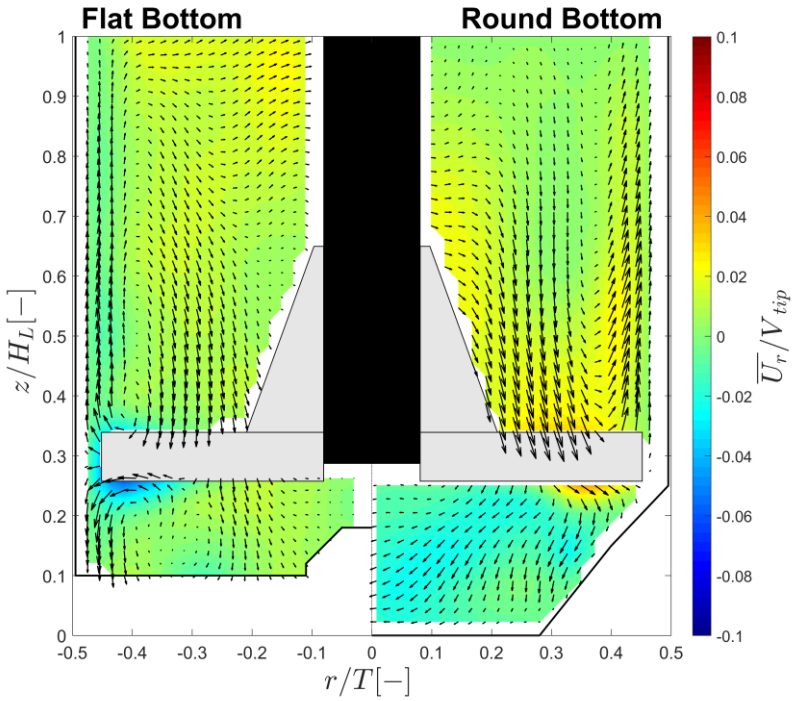

(d)

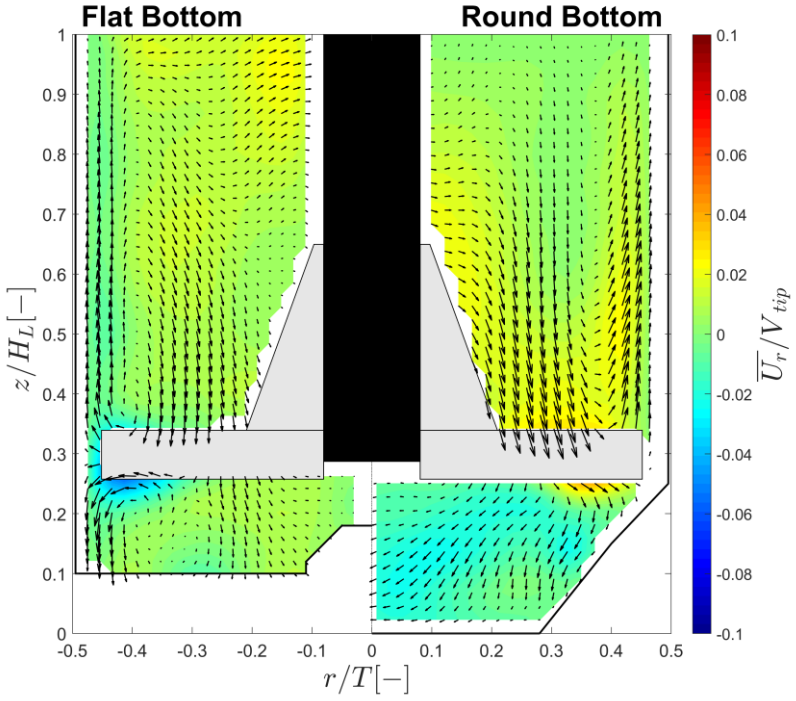

Figure 4.2 Contour maps of the ensemble-averaged radial velocity component, $\overline{U_r}/V_{tip}$: (a) N = 75 rpm; (b) N = 90 rpm; (c) N = 105 rpm; (d) N = 120 rpm.

(a)

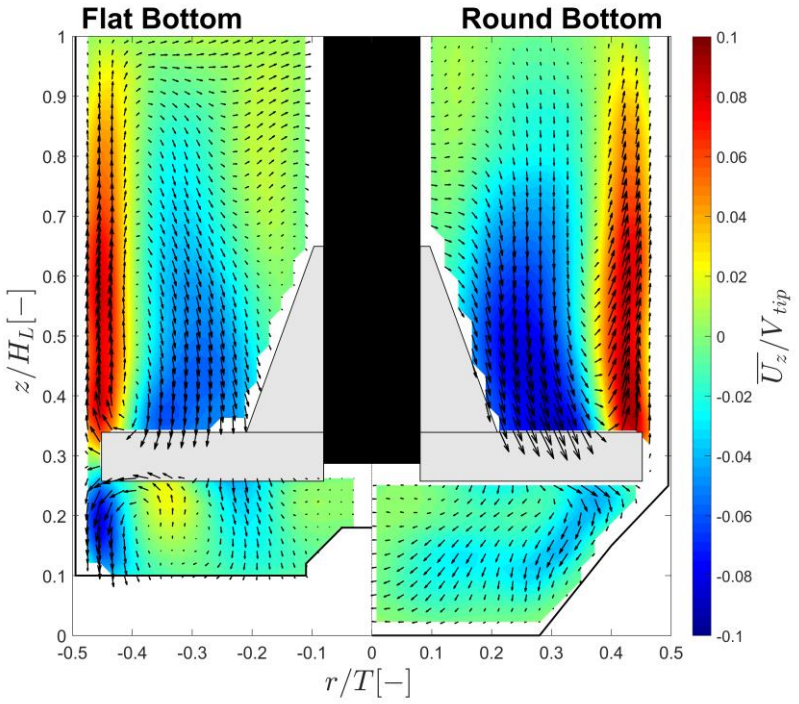
Flat Bottom
Round Bottom
$z/H_L[-]$
$r/T[-]$
$\overline{U_z}/V_{tip}$

(b)

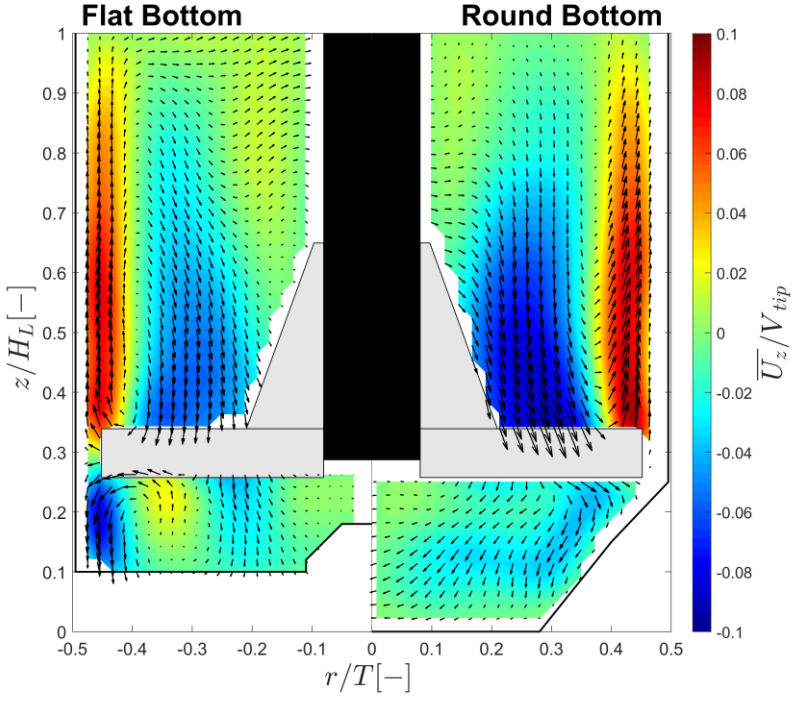
Flat Bottom
Round Bottom
$z/H_L[-]$
$r/T[-]$
$\overline{U_z}/V_{tip}$

(c)

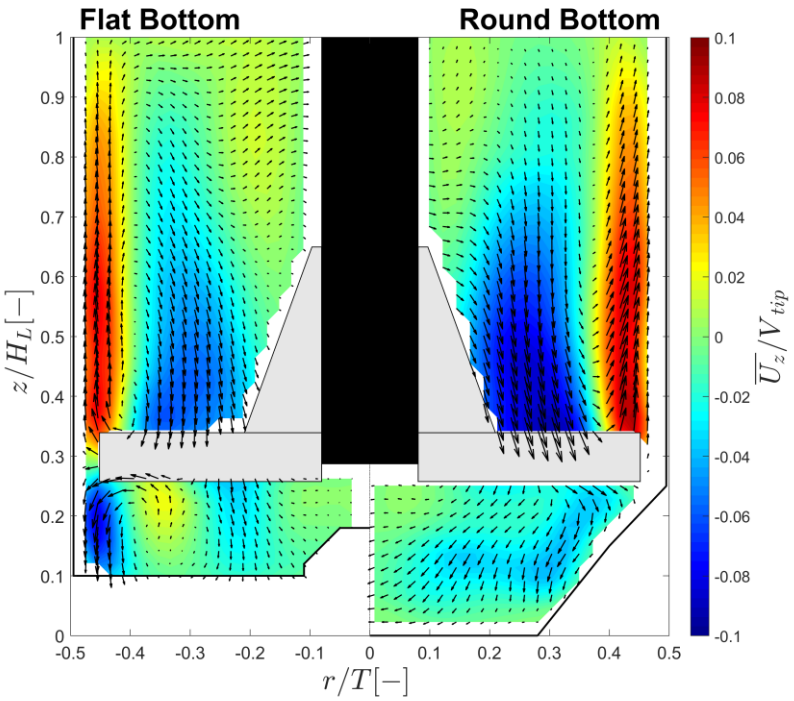

(d)

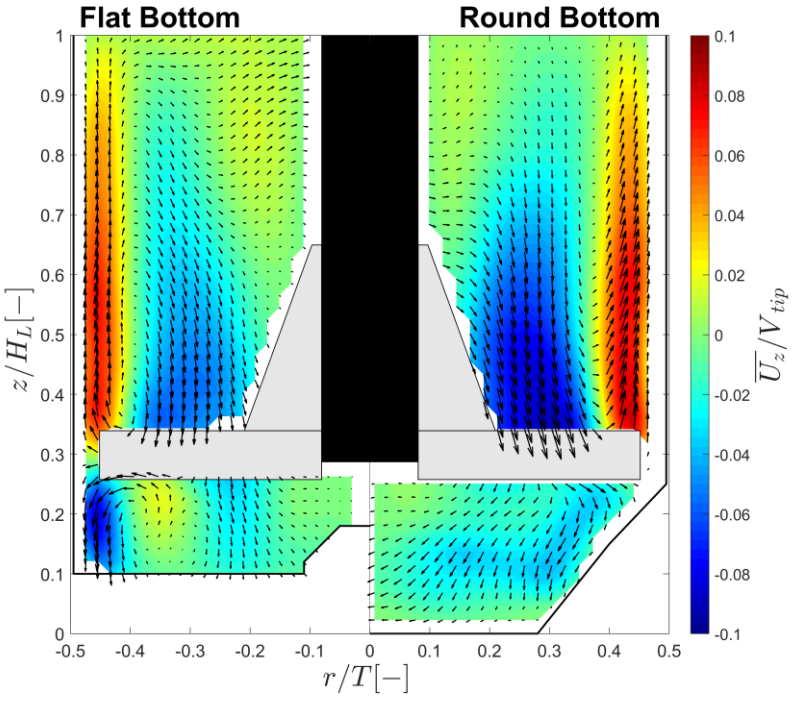

Figure 4.3 Contour maps of the ensemble-averaged axial velocity component, $\overline{U_z}/V_{tip}$: (a) N = 75 rpm; (b) N = 90 rpm; (c) N = 105 rpm; (d) N = 120 rpm.

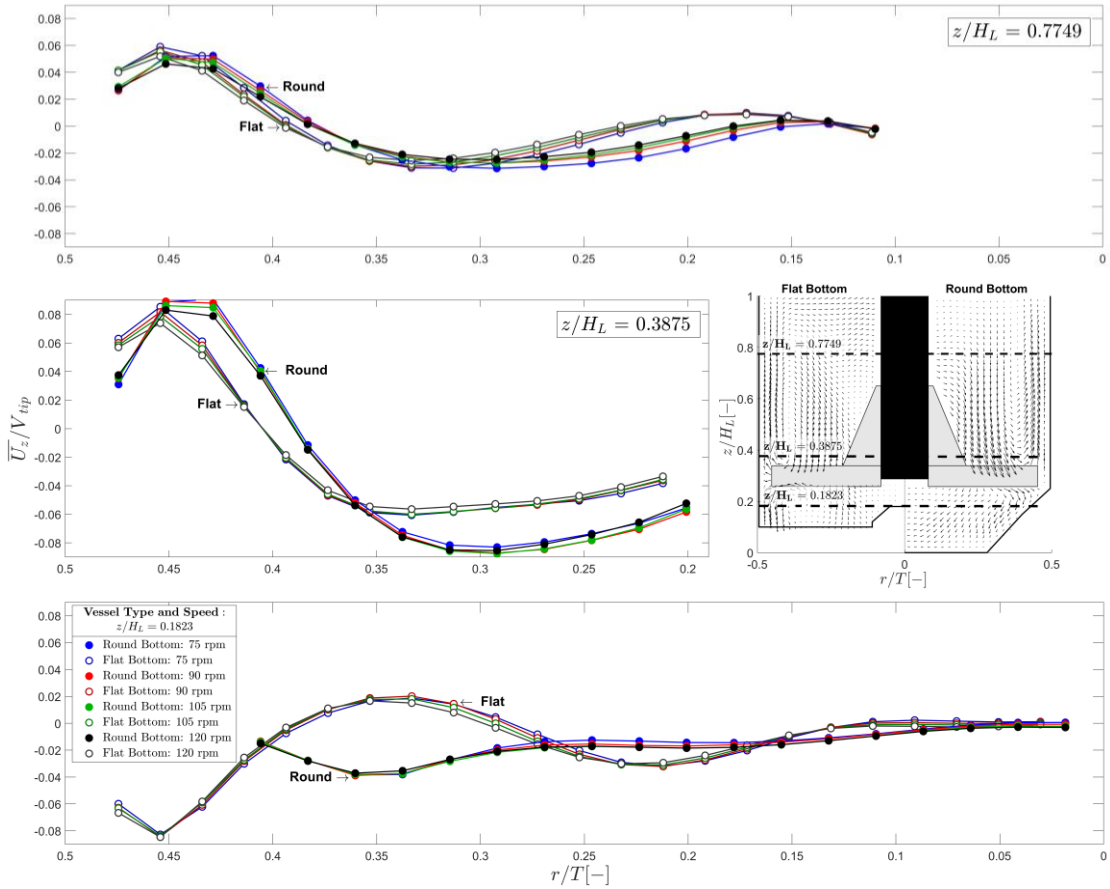

Figure 4.4 Comparison of ensemble-averaged axial velocity profiles, $\overline{U_z}/V_{tip}$, for the flat and round bottom bioreactors at three elevations, z/H_L = 0.7749, 0.3875 and 0.1823, with increasing rotational speeds N = 75 – 120 rpm.

(a)

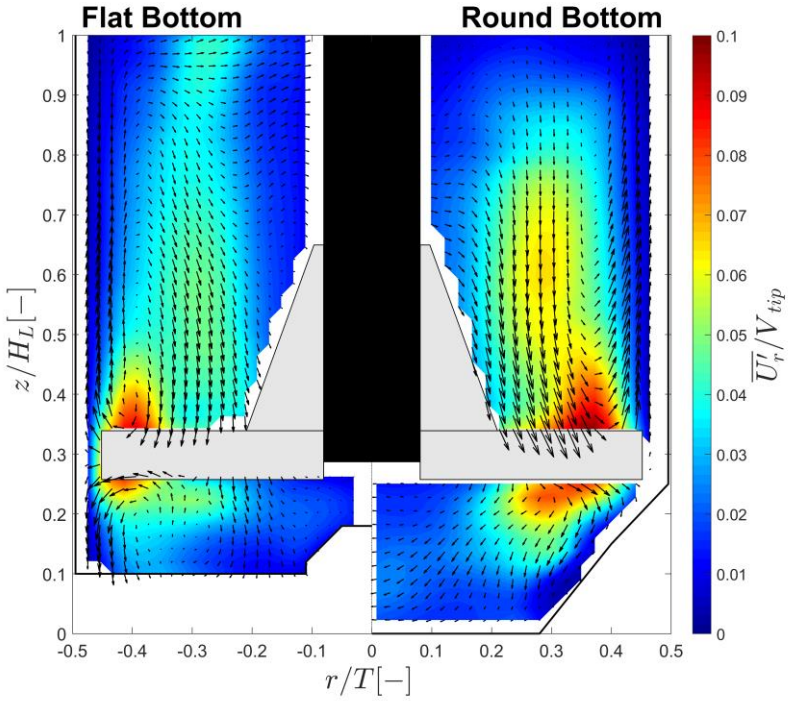
Flat Bottom
Round Bottom
$z/H_L[-]$
$r/T[-]$
$\overline{U_r'}/V_{tip}$

(b)

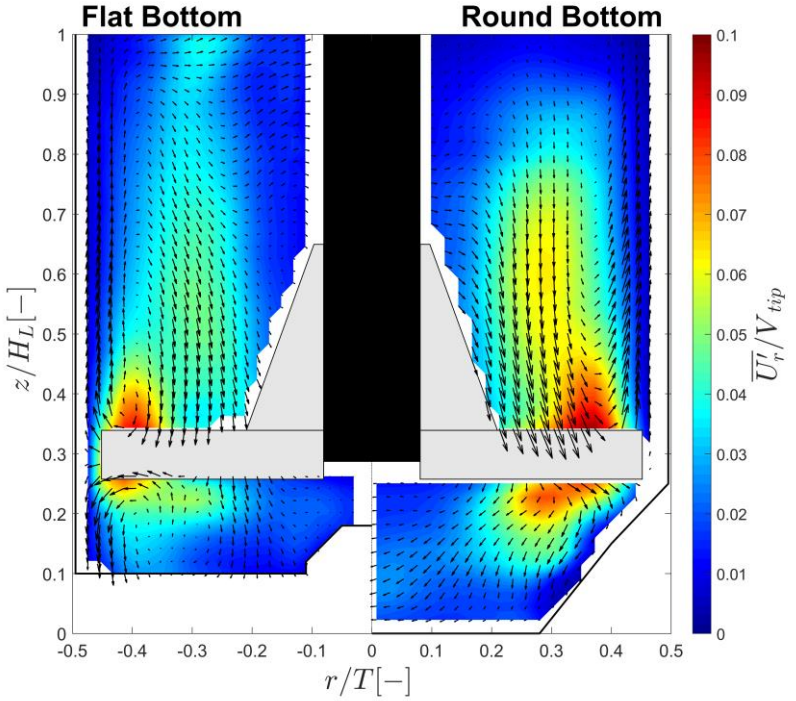
Flat Bottom
Round Bottom
$z/H_L[-]$
$r/T[-]$
$\overline{U_r'}/V_{tip}$

(c)

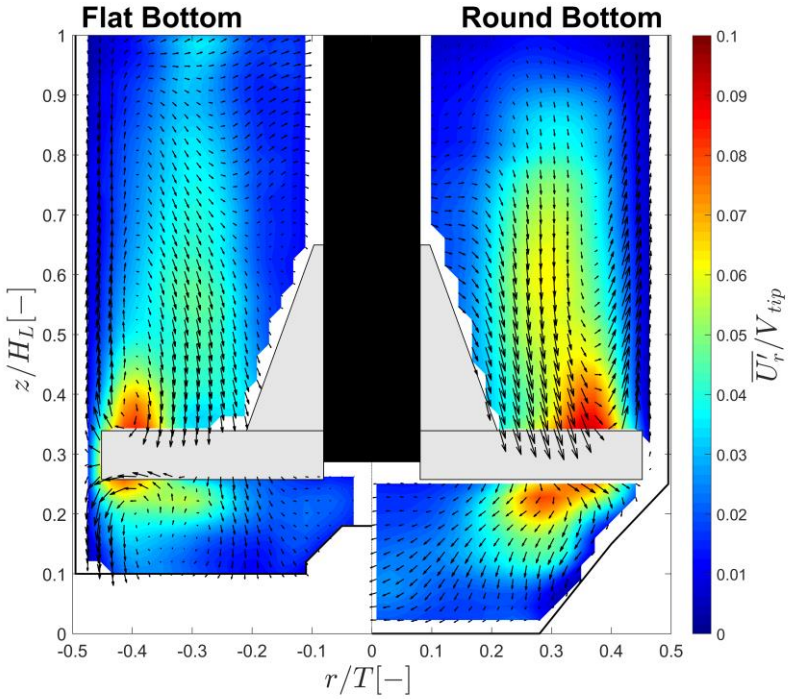

(d)

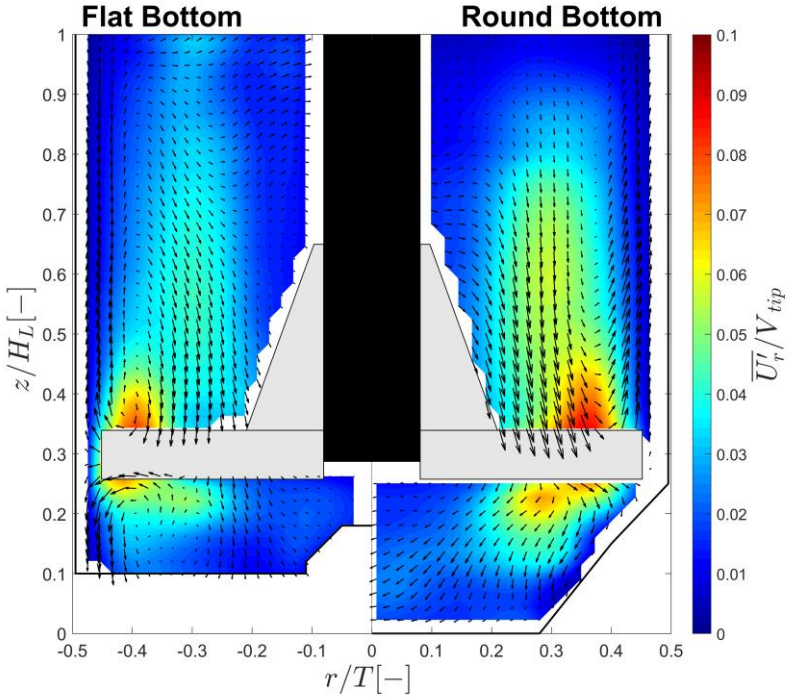

Figure 4.5 Contour maps of ensemble-averaged r.m.s radial velocity component, $\overline{U'_r}/V_{tip}$: (a) *N* = 75 rpm; (b) *N* = 90 rpm; (c) *N* = 105 rpm; (d) *N* = 120 rpm.

(a)

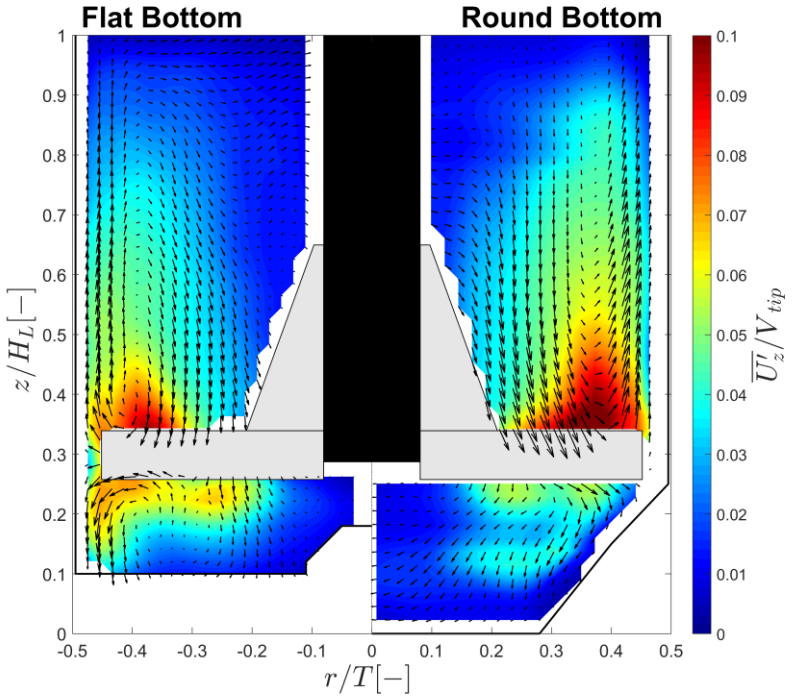
Flat Bottom
Round Bottom
$z/H_L[-]$
$r/T[-]$
$\overline{U_z'}/V_{tip}$

(b)

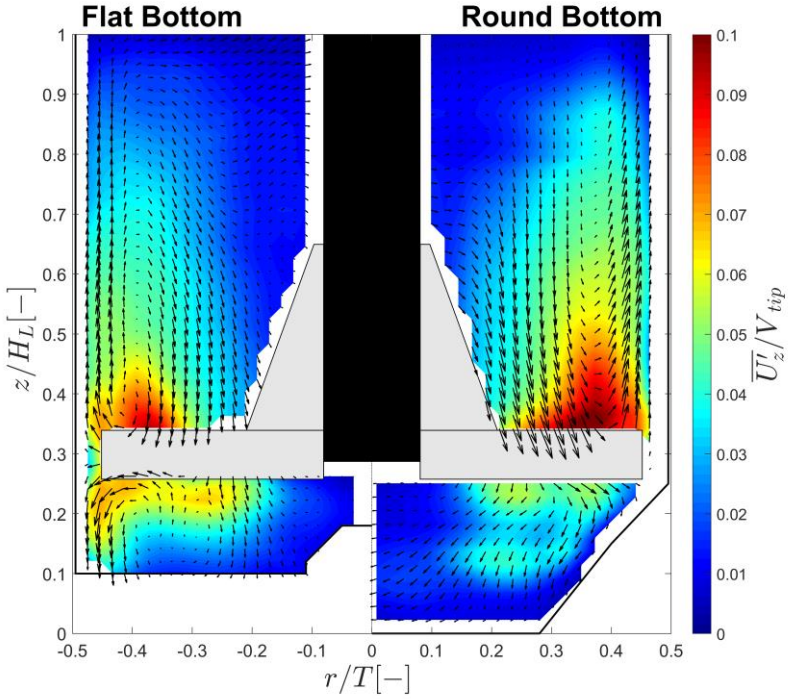
Flat Bottom
Round Bottom
$z/H_L[-]$
$r/T[-]$
$\overline{U_z'}/V_{tip}$

(c)

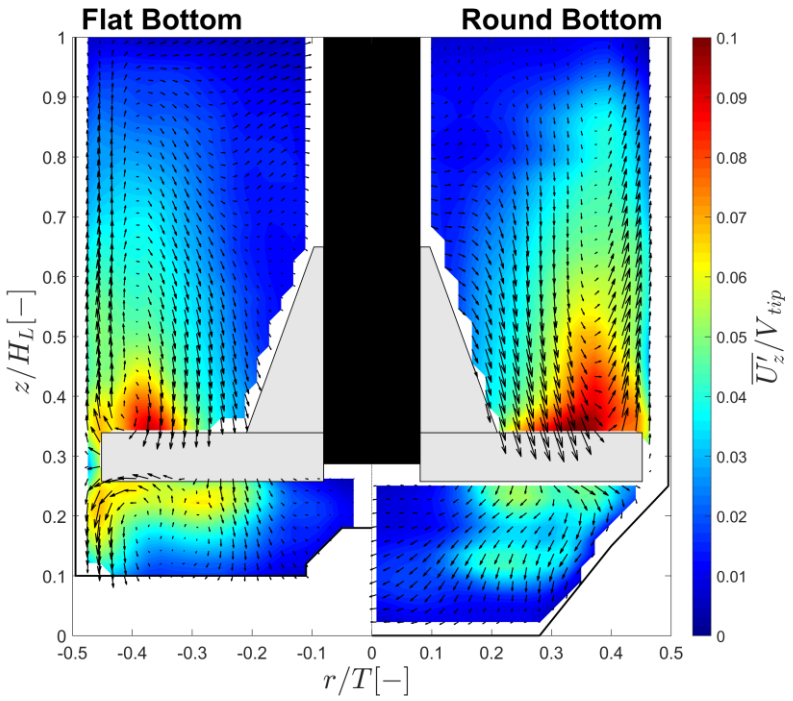

(d)

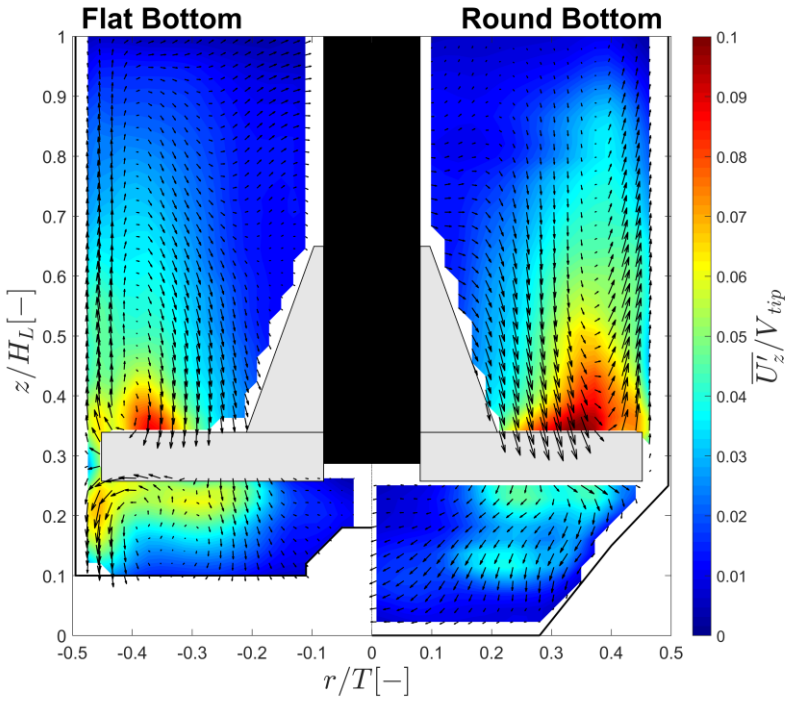

Figure 4.6 Contour maps of ensemble-averaged r.m.s axial velocity component, $\overline{U'_z}/V_{tip}$: (a) N = 75 rpm; (b) N = 90 rpm; (c) N = 105 rpm; (d) N = 120 rpm.

(a)

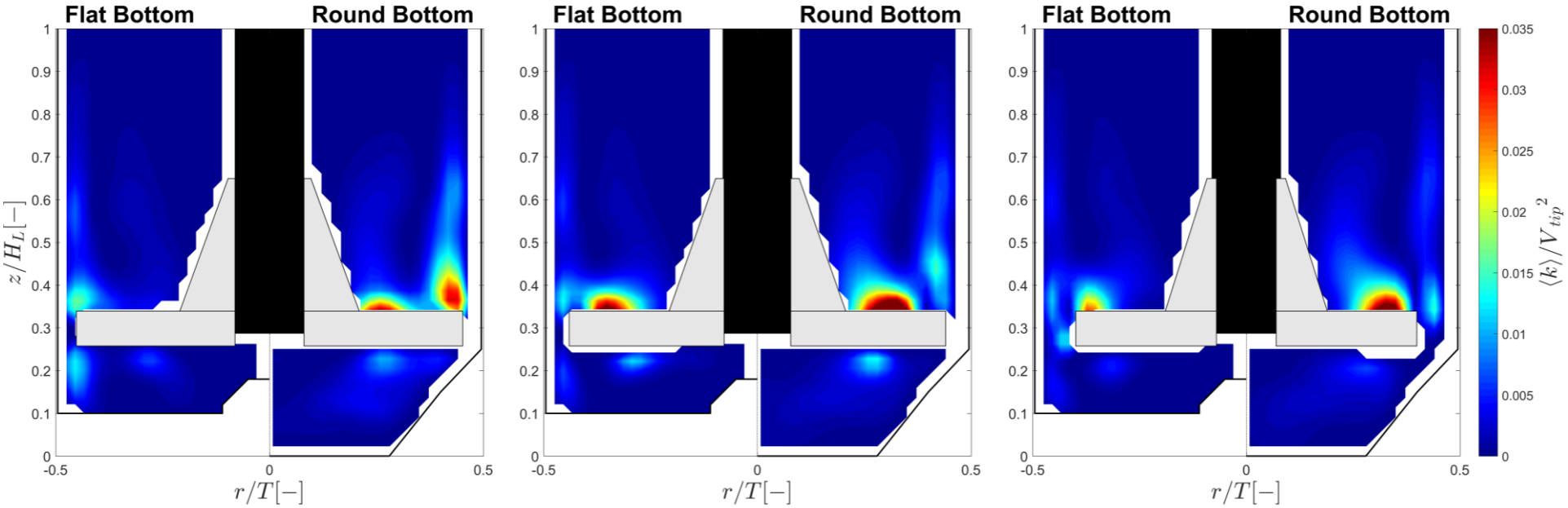

φ = 0° **φ = 15°** **φ = 30°**

[186]

(b)

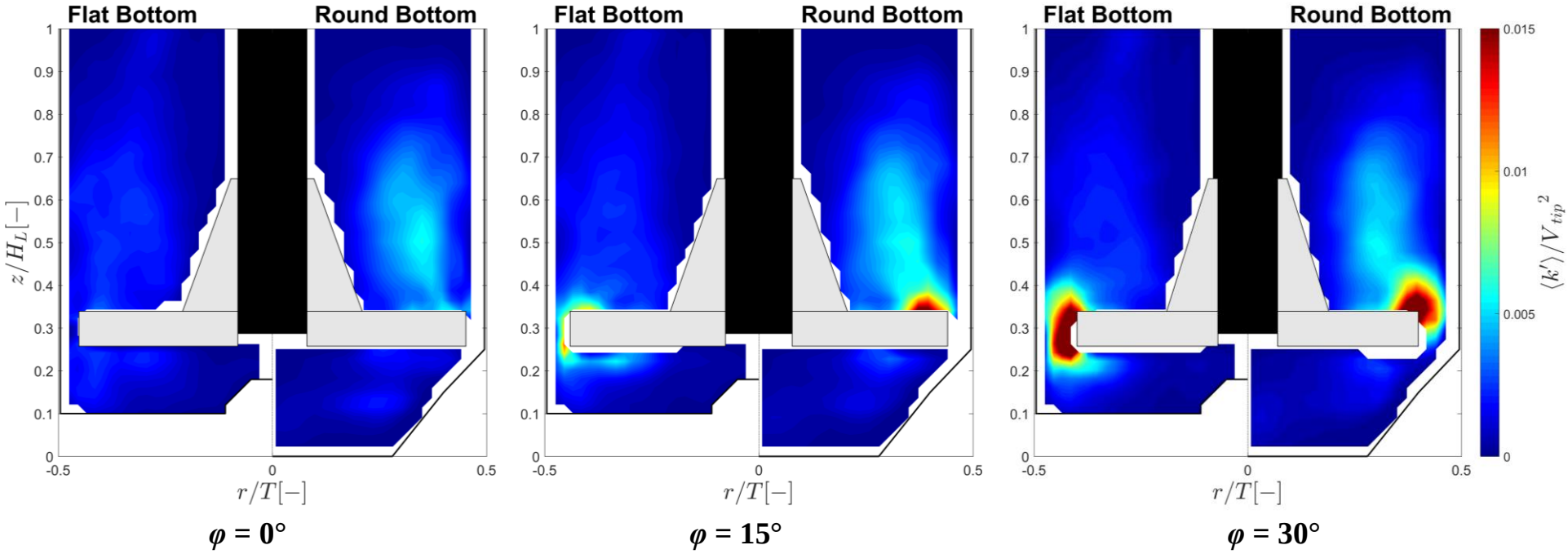

Figure 4.7 Contour maps of phase-resolved kinetic energy at φ = 0, 15 and 30°, N = 90 rpm: (a) periodic kinetic energy, $\langle k \rangle$; (b) turbulent kinetic energy, $\langle k' \rangle$.

[187]

(a)

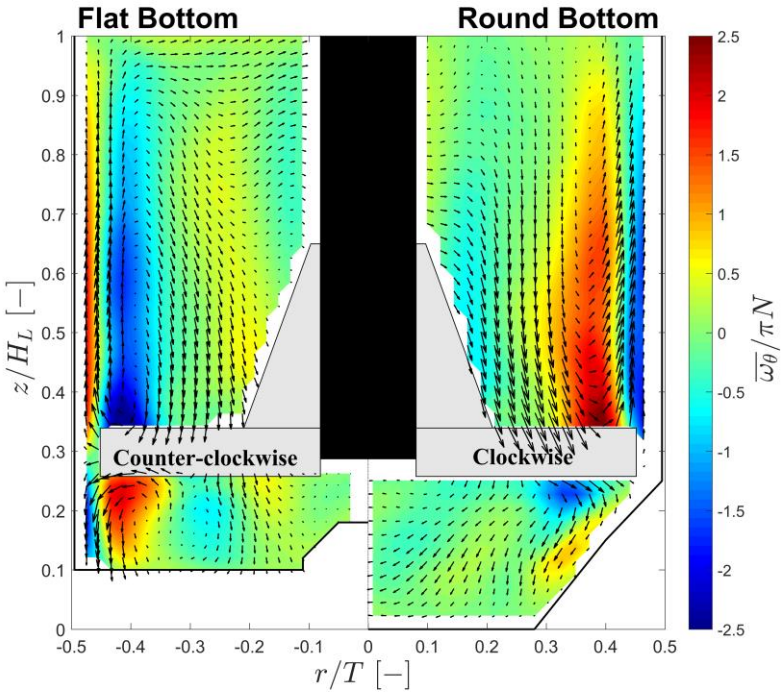
Flat Bottom
Round Bottom
Counter-clockwise
Clockwise
z/H_L [−]
r/T [−]
$\overline{\omega_\theta}/\pi N$

(b)

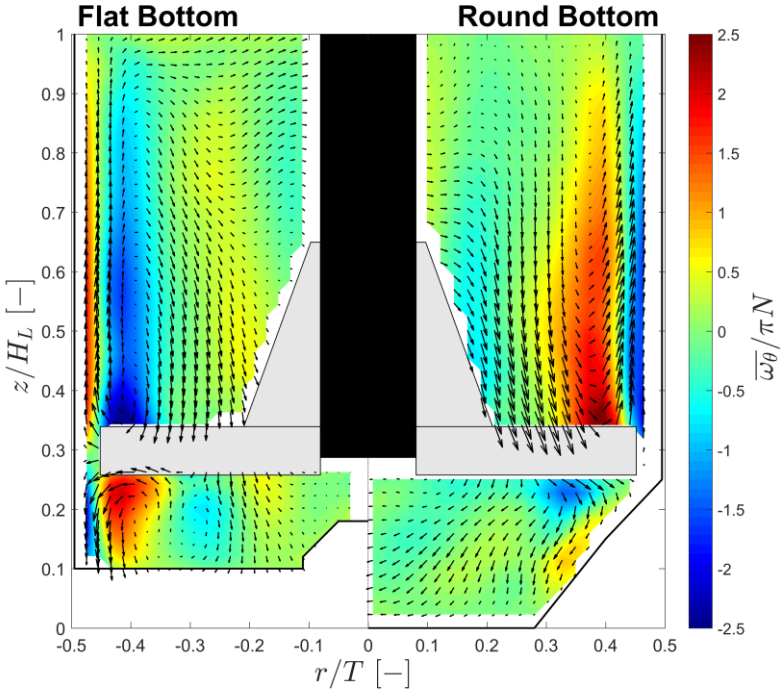
Flat Bottom
Round Bottom
z/H_L [−]
r/T [−]
$\overline{\omega_\theta}/\pi N$

(c)

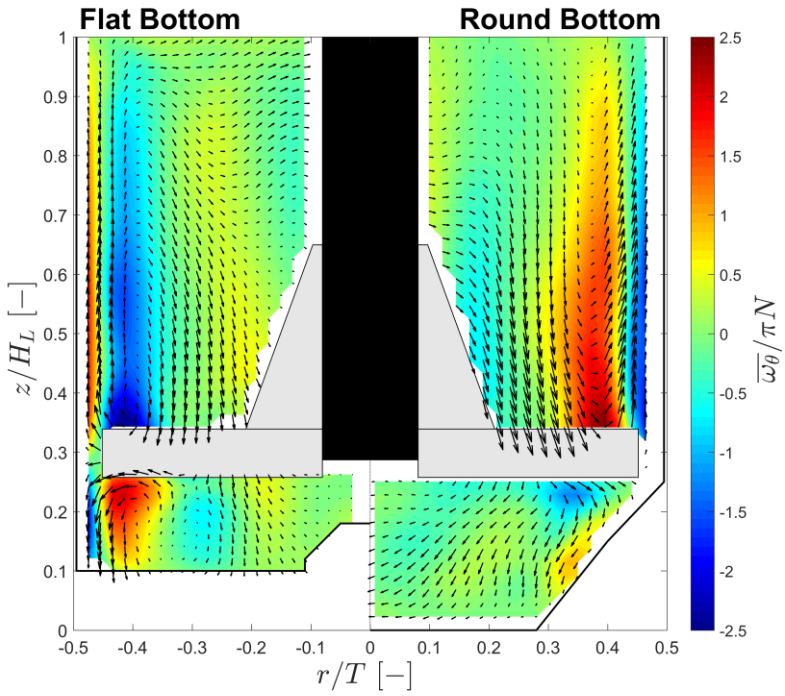

(d)

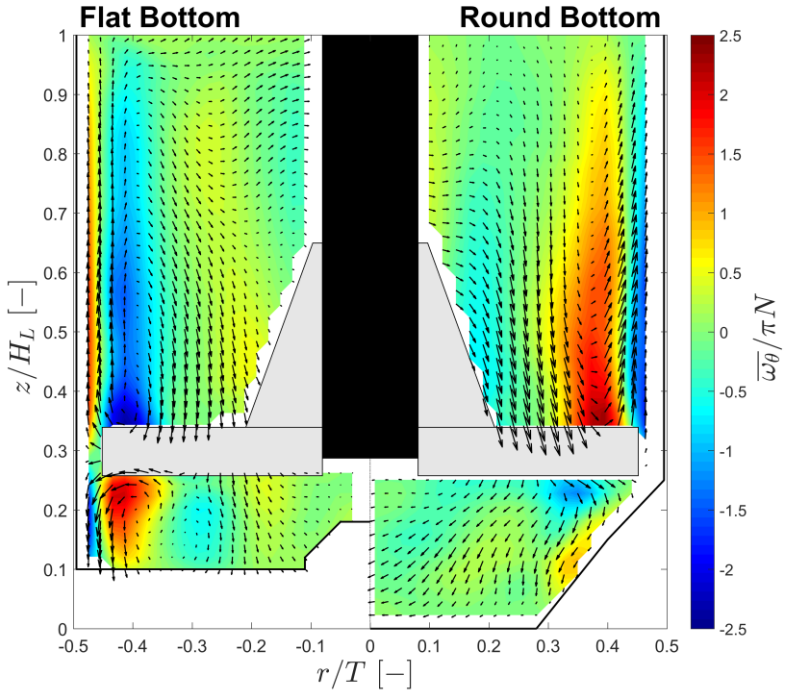

Figure 4.8 Contour maps of ensemble-averaged flow vorticity, $\overline{\omega_\theta}/\pi N$: (a) N = 75 rpm; (b) N = 90 rpm; (c) N = 105 rpm; (d) N = 120 rpm.

(a)

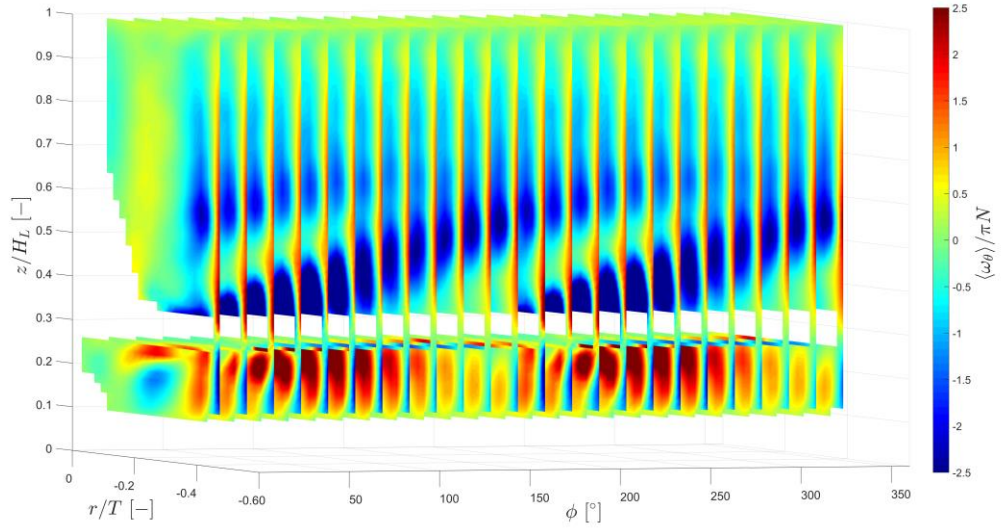
z/H_L [−]
r/T [−]
ϕ [°]
$\langle\omega_\theta\rangle/\pi N$

(b)

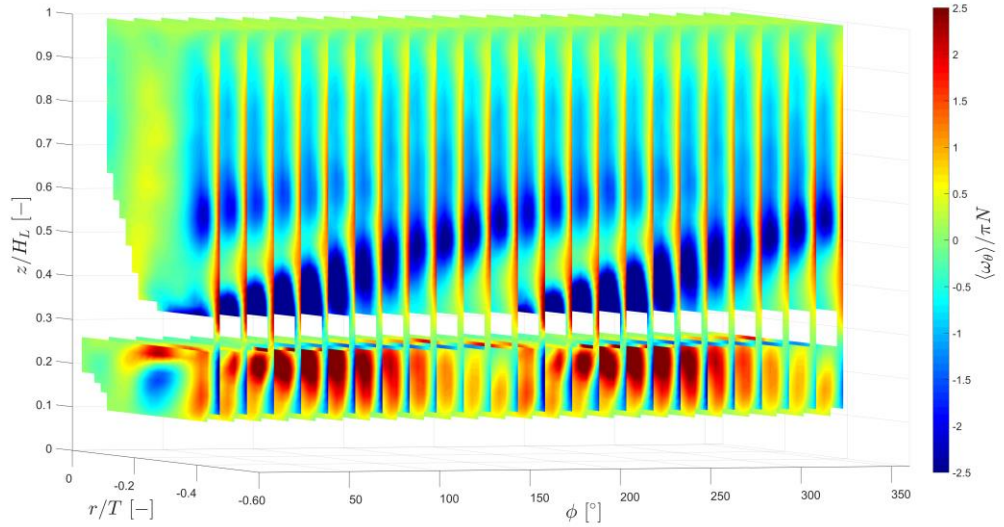
z/H_L [−]
r/T [−]
ϕ [°]
$\langle\omega_\theta\rangle/\pi N$

(c)

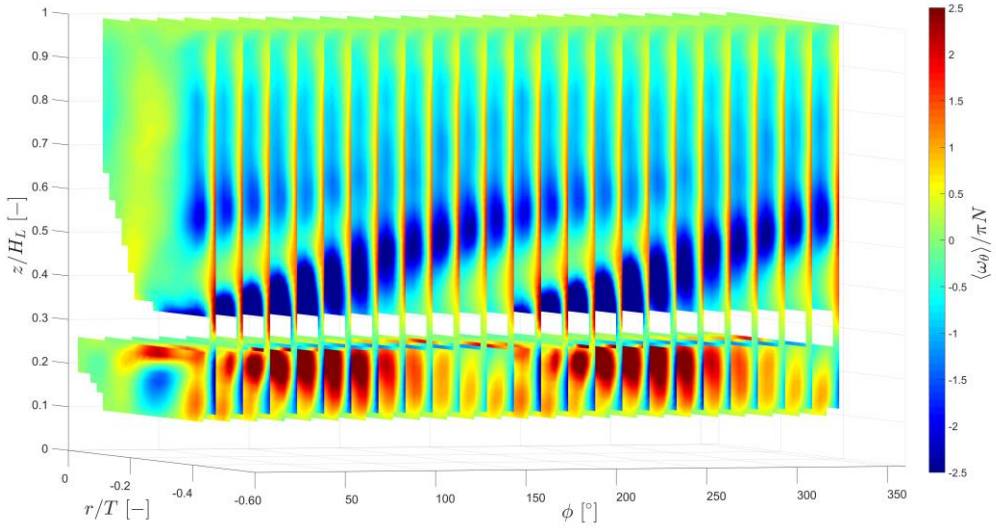

(d)

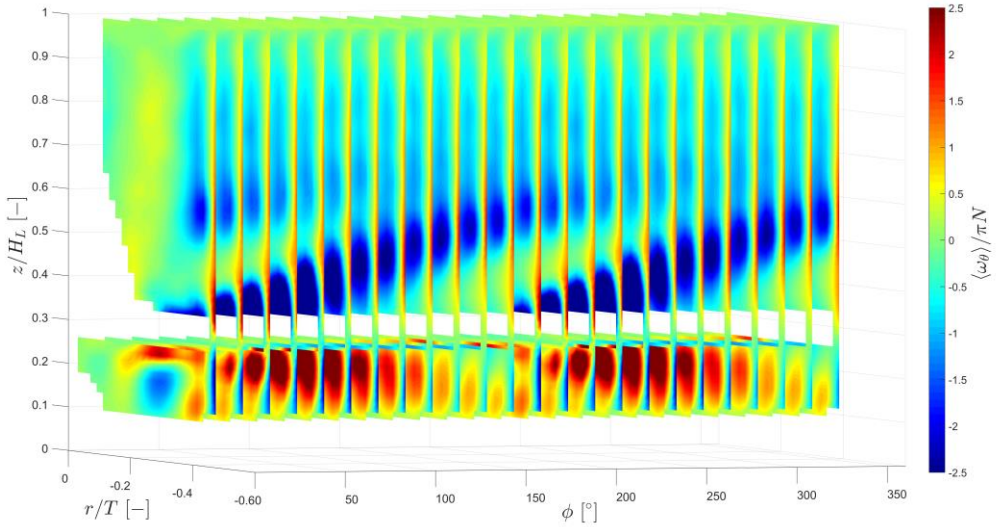

Figure 4.9 Staggered contour maps of the phase-resolved vorticity, $\langle\omega_\theta\rangle/\pi N$, for increasing φ = 0 – 345° in the flat bottom configuration: (a) N = 75 rpm; (b) N = 90 rpm; (c) N = 105 rpm; (d) N = 120 rpm.

(a)

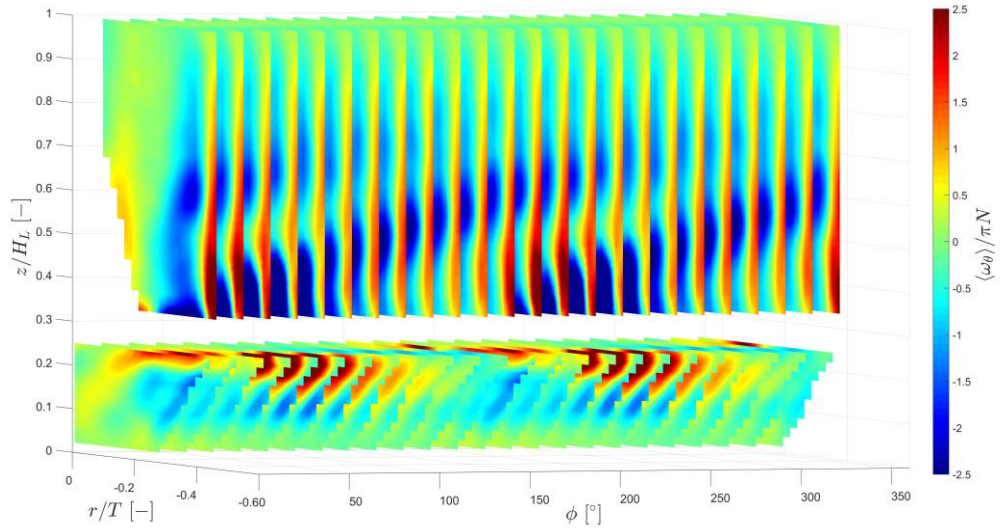
z/H_L [−]
r/T [−]
ϕ [°]
$\langle\omega_\theta\rangle/\pi N$

(b)

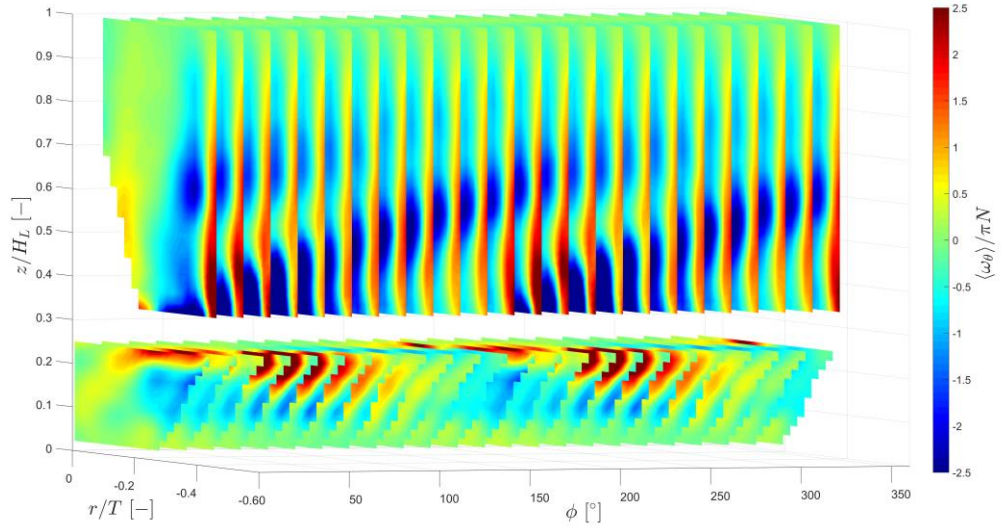
z/H_L [−]
r/T [−]
ϕ [°]
$\langle\omega_\theta\rangle/\pi N$

(c)

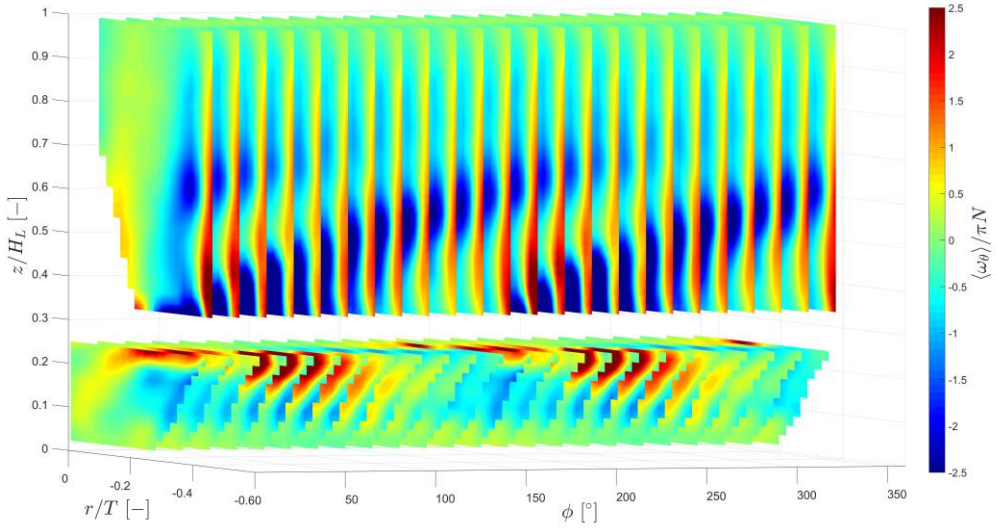

(d)

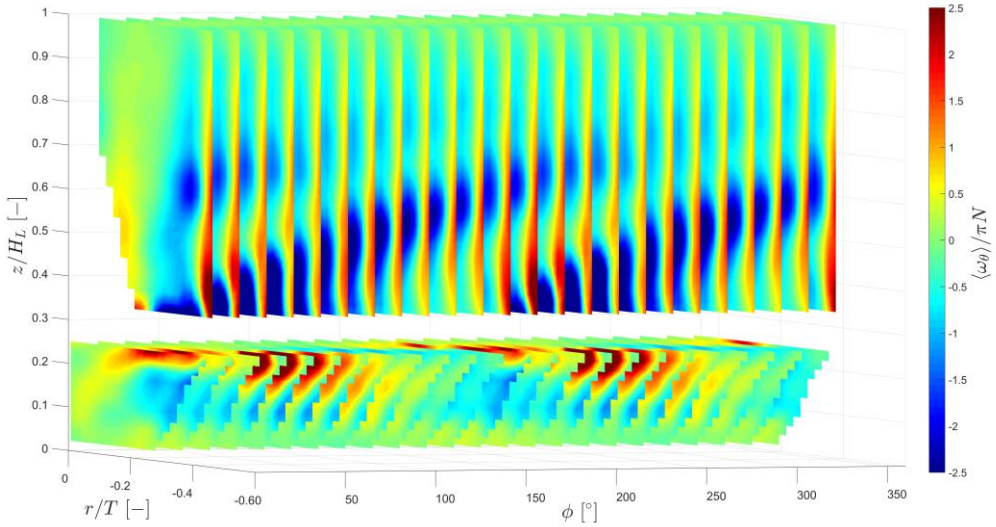

Figure 4.10 Staggered contour maps of the phase-resolved vorticity, $\langle\omega_\theta\rangle/\pi N$, for increasing φ = 0 – 345° in the round bottom configuration: (a) N = 75 rpm; (b) N = 90 rpm; (c) N = 105 rpm; (d) N = 120 rpm.

(a)

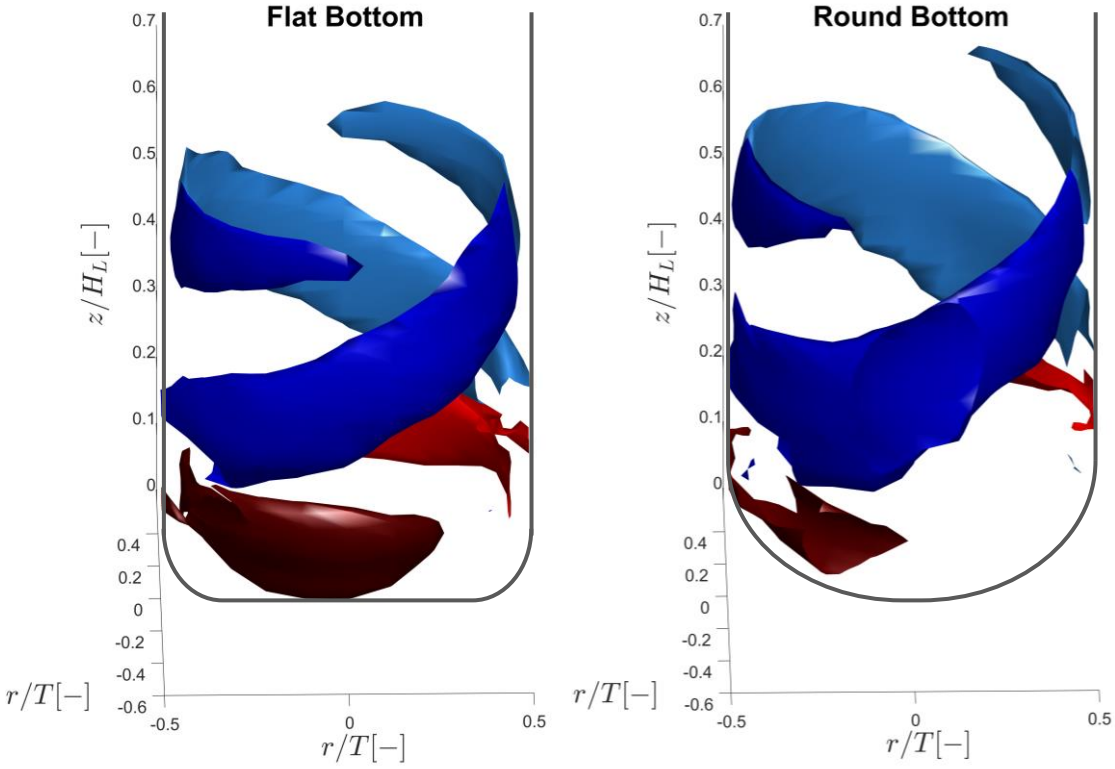
Flat Bottom
Round Bottom
$z/H_L[-]$
$r/T[-]$
$r/T[-]$

(b)

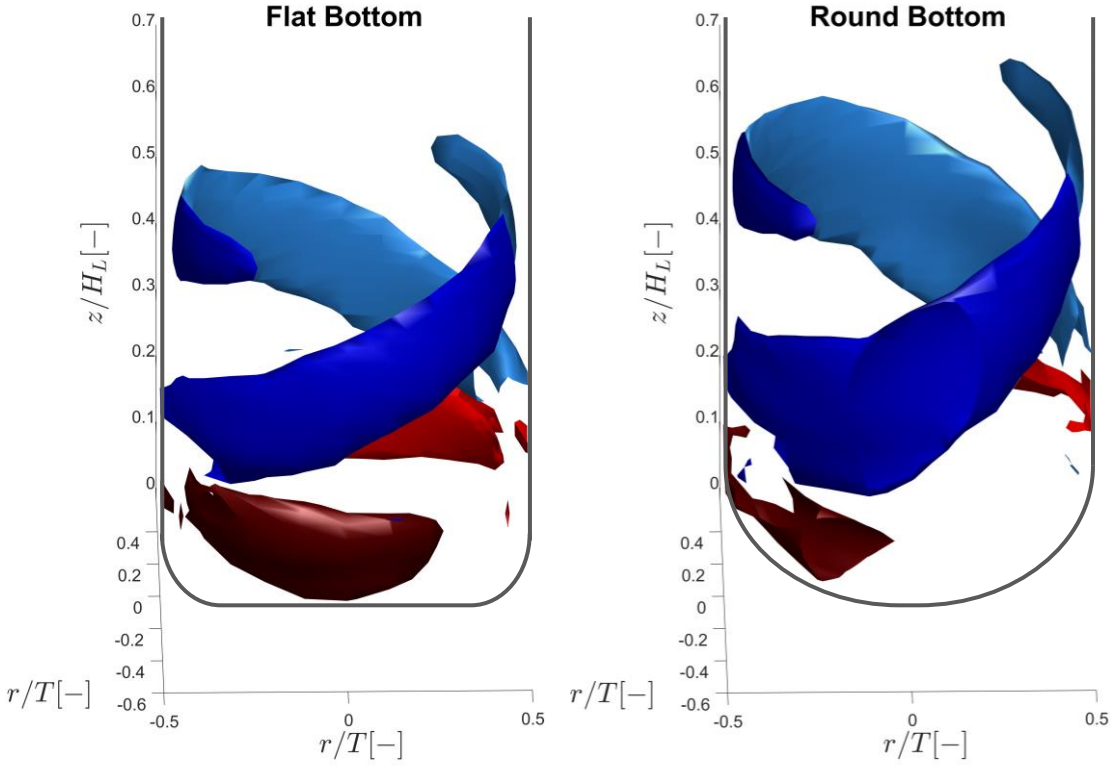
Flat Bottom
Round Bottom
$z/H_L[-]$
$r/T[-]$
$r/T[-]$

(c)

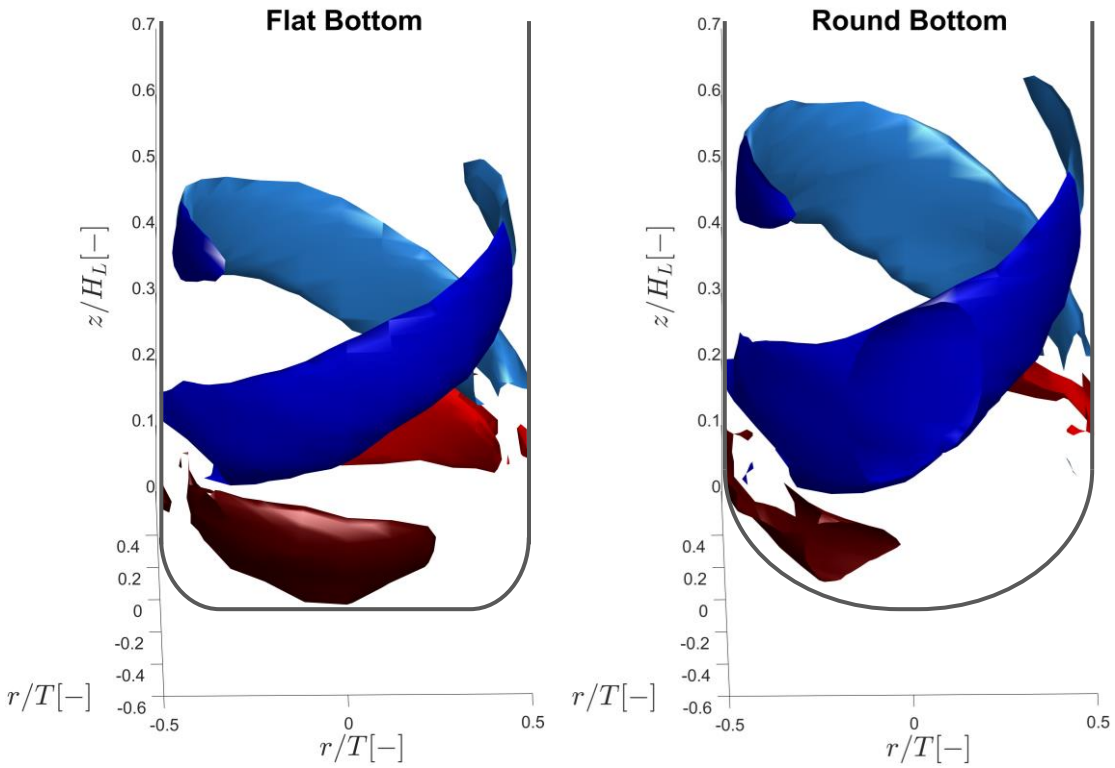

(d)

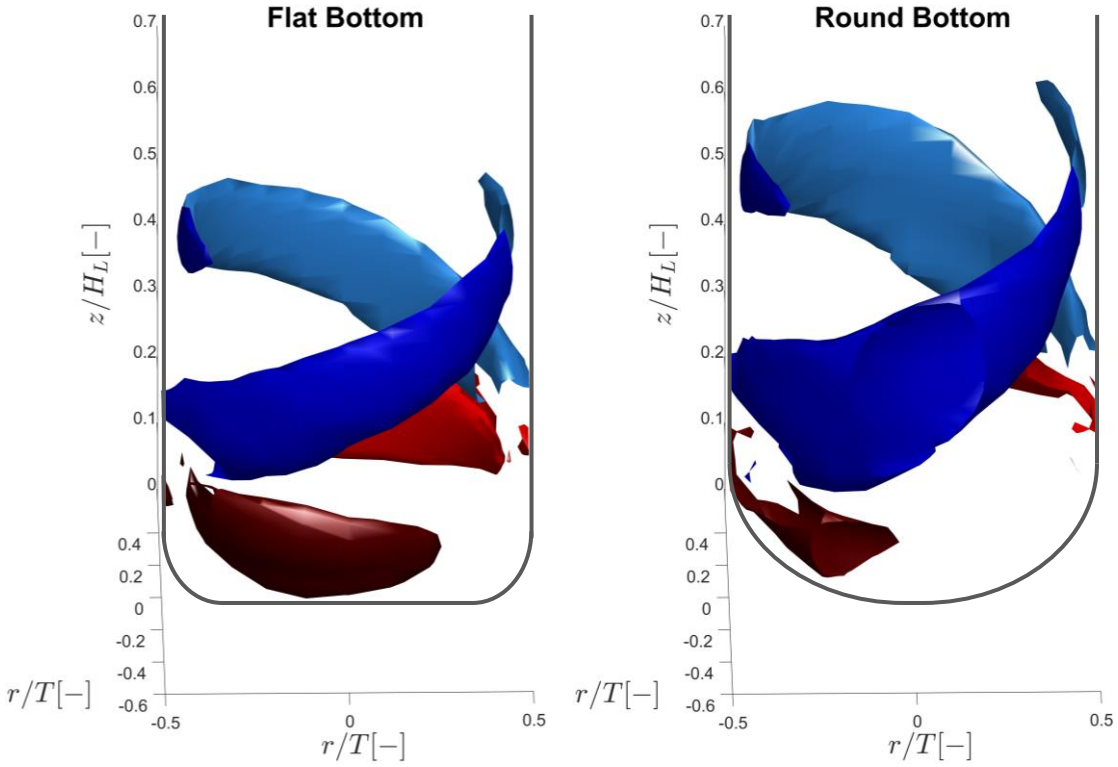

Figure 4.11 3-D visualisation of the trailing vortices for the flat (left) and round (right) bottom bioreactors, indicating two vortices associated to $\langle\omega_\theta\rangle/\pi N$ = -1.5 (blue) and $\langle\omega_\theta\rangle/\pi N$ = 1.5 (red): (a) N = 75 rpm; (b) N = 90 rpm; (c) N = 105 rpm; (d) N = 120 rpm.

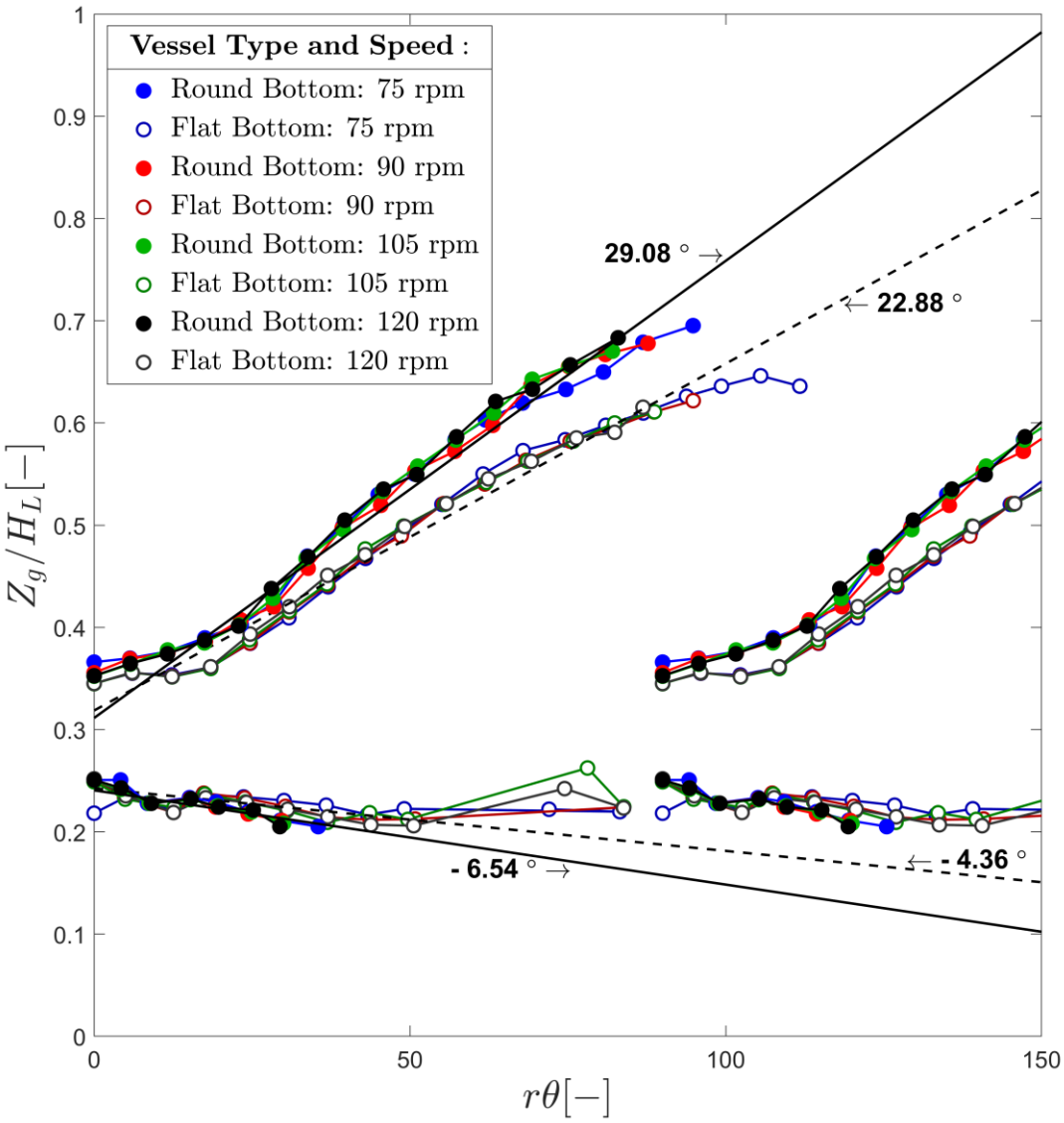

Figure 4.12 Variation of the axial coordinate of the vortex centre with increasing phase angle.

(a)

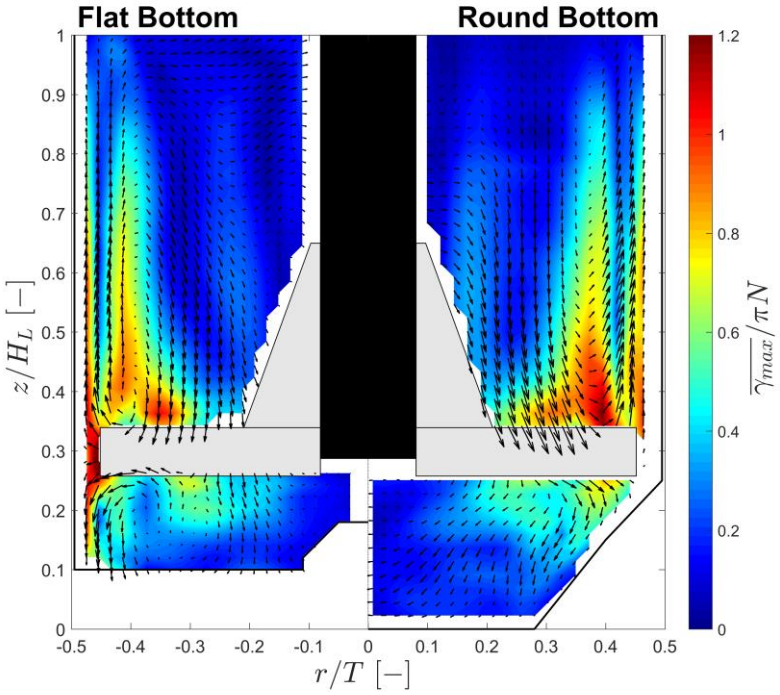
Flat Bottom
Round Bottom
z/H_L [−]
r/T [−]
$\overline{\gamma_{max}}/\pi N$

(b)

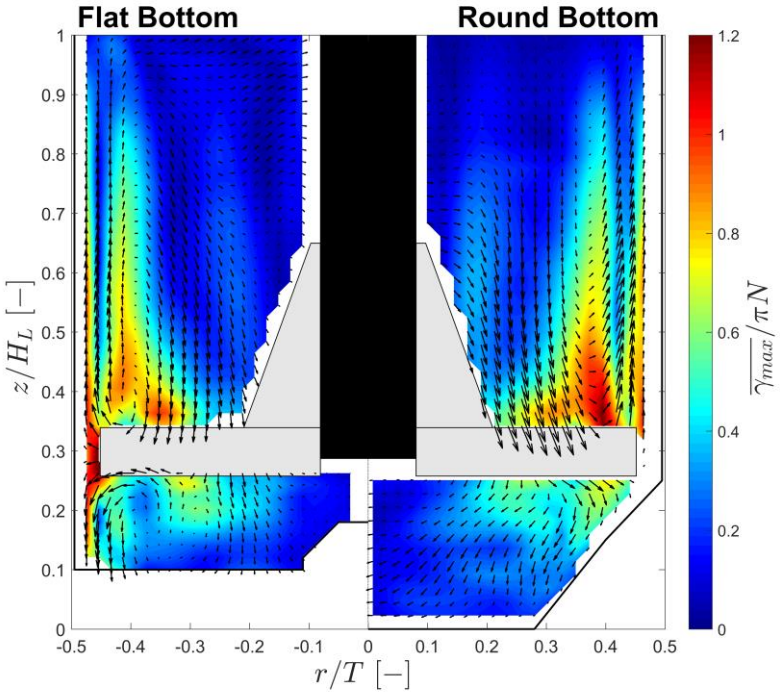
Flat Bottom
Round Bottom
z/H_L [−]
r/T [−]
$\overline{\gamma_{max}}/\pi N$

(c)

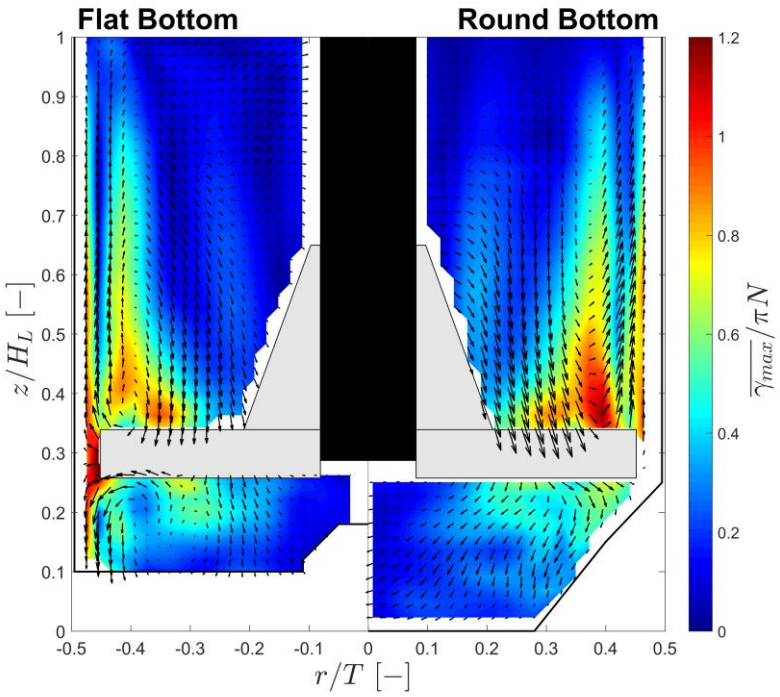

(d)

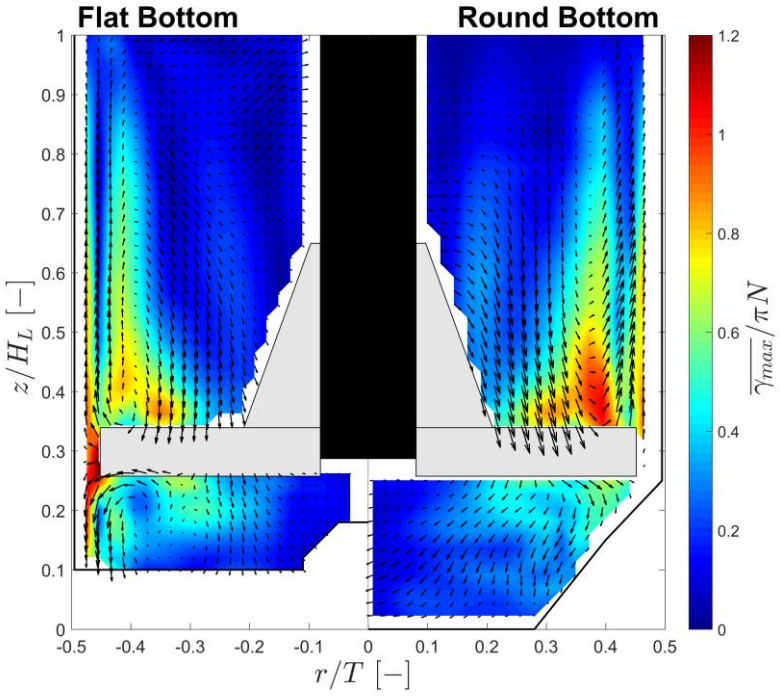

Figure 4.13 Contour maps of ensemble-averaged maximum local shear rate, $\overline{\gamma_{max}}/\pi N$: (a) N = 75 rpm; (b) N = 90 rpm; (c) N = 105 rpm; (d) N = 120 rpm.

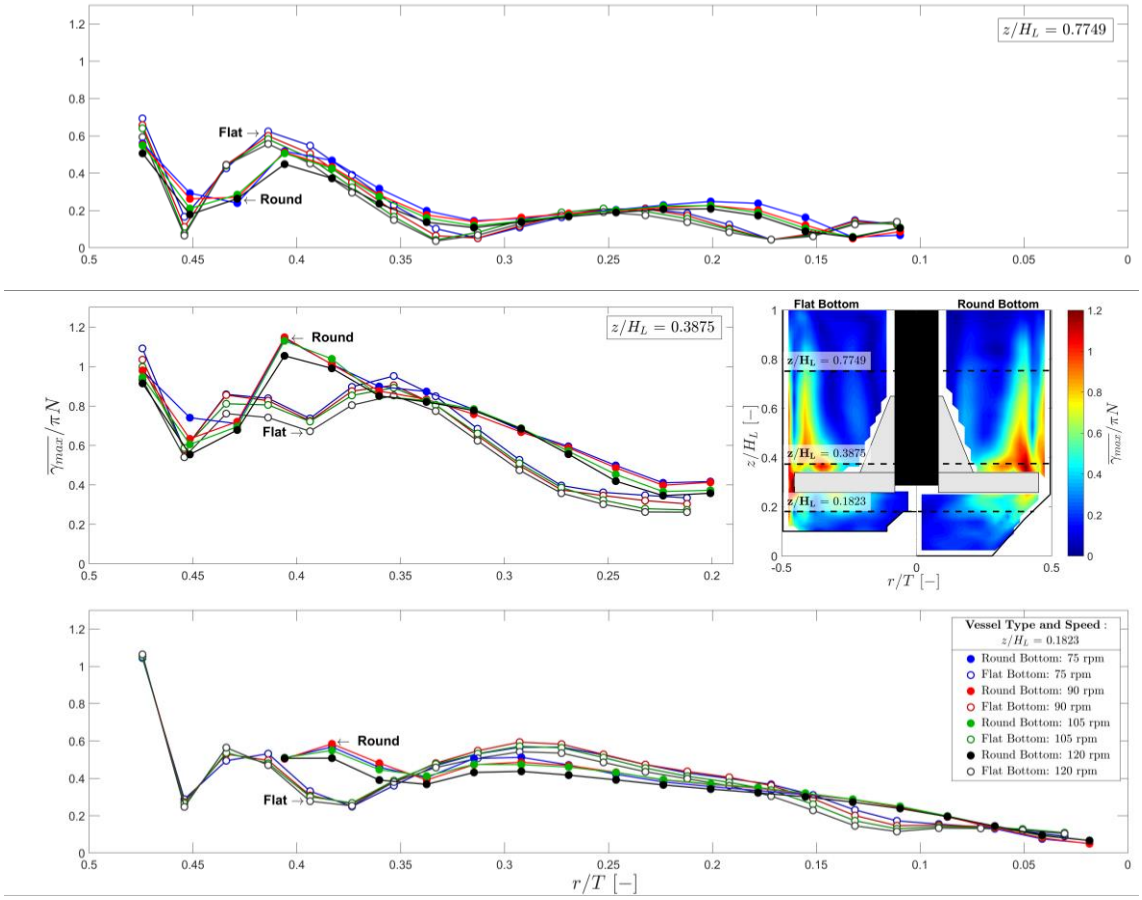

Figure 4.14 Comparison of ensemble-averaged maximum local shear rate profiles, $\overline{\gamma_{max}}/\pi N$, for the flat and round bottom bioreactors at three elevations, z/H_L = 0.7749, 0.3875 and 0.1823, with increasing rotational speeds N = 75 – 120 rpm.

(a)

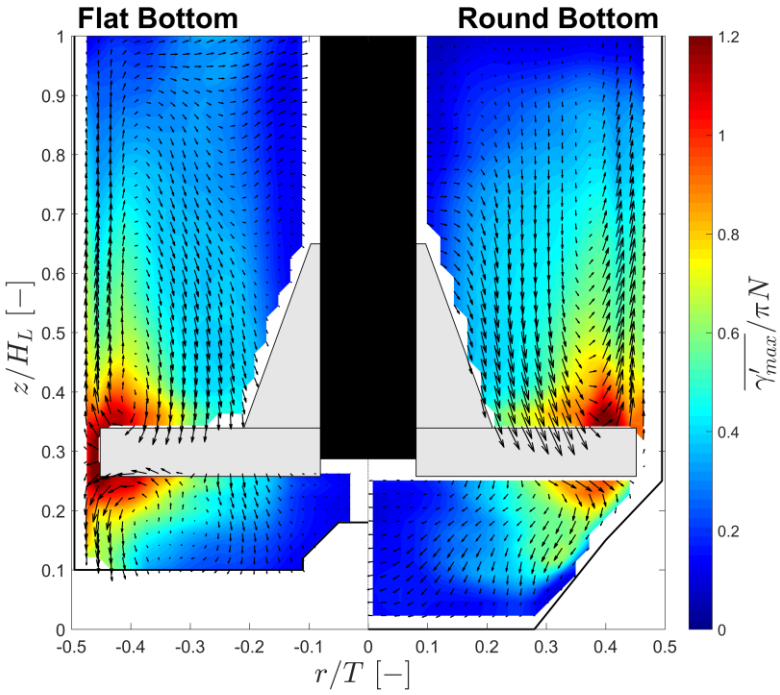
Flat Bottom
Round Bottom
z/H_L [−]
r/T [−]
$\overline{\gamma'_{max}}/\pi N$

(b)

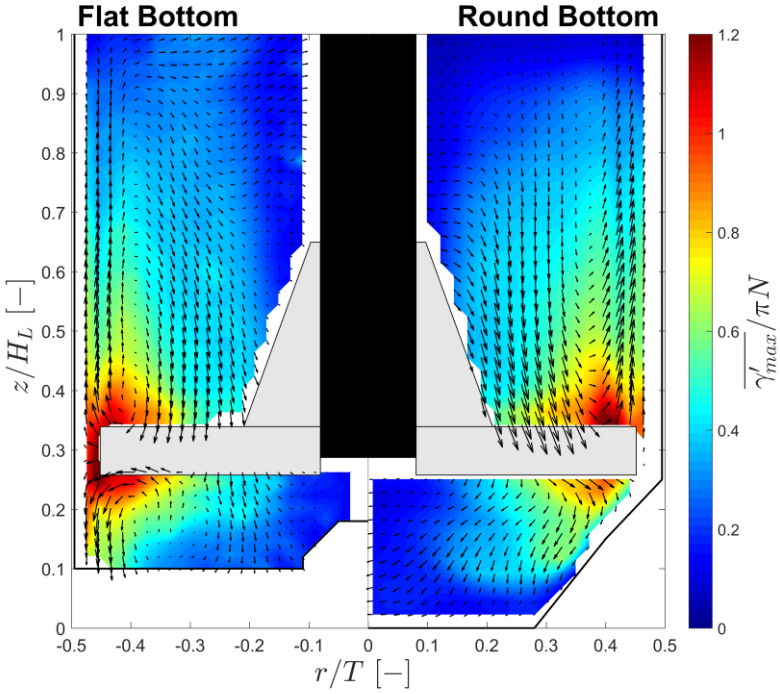
Flat Bottom
Round Bottom
z/H_L [−]
r/T [−]
$\overline{\gamma'_{max}}/\pi N$

(c)

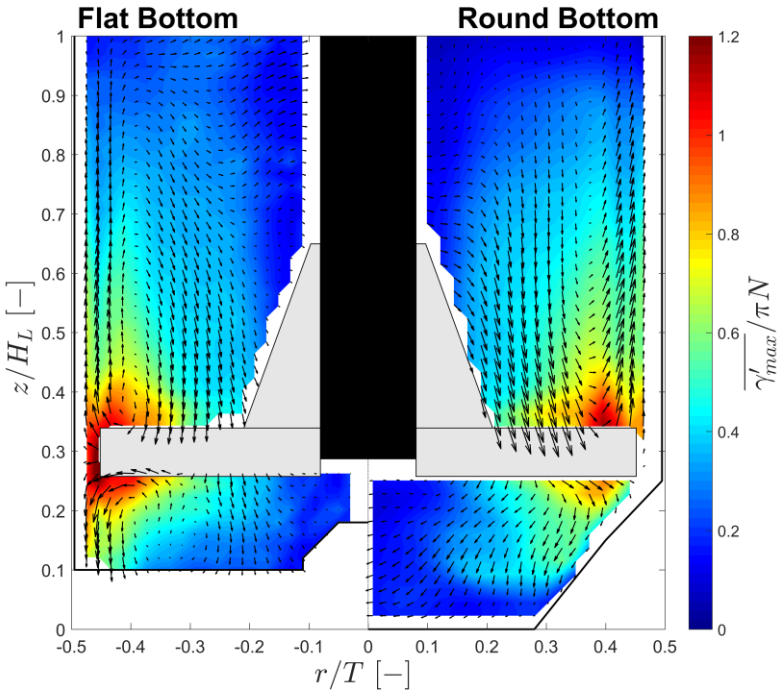

(d)

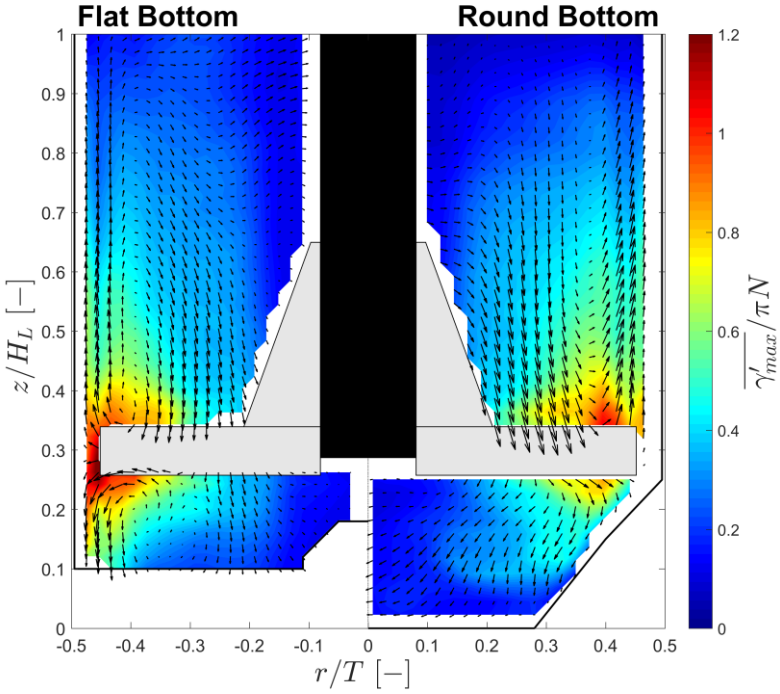

Figure 4.15 Contour maps of ensemble-averaged standard deviation of the maximum local shear rate, $\overline{\gamma'_{max}}/\pi N$: (a) N = 75 rpm; (b) N = 90 rpm; (c) N = 105 rpm; (d) N = 120 rpm.

(a)

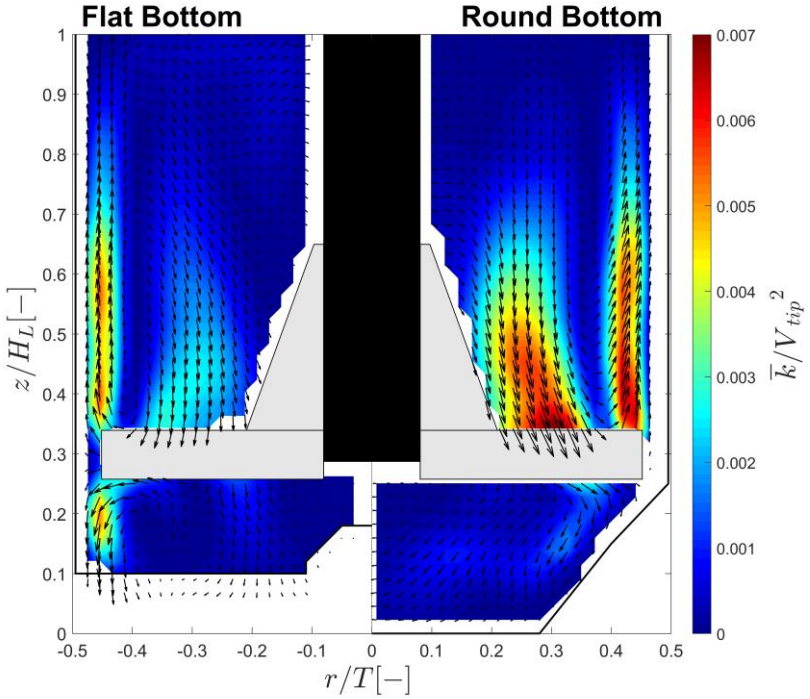
Flat Bottom
Round Bottom
$z/H_L[-]$
$r/T[-]$
$\overline{k}/V_{tip}^2$

(b)

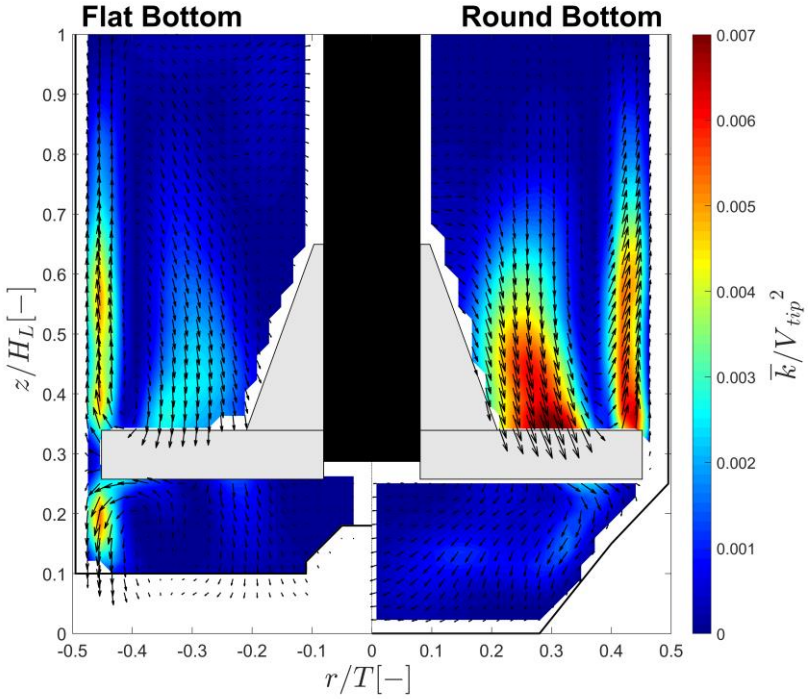
Flat Bottom
Round Bottom
$z/H_L[-]$
$r/T[-]$
$\overline{k}/V_{tip}^2$

(c)

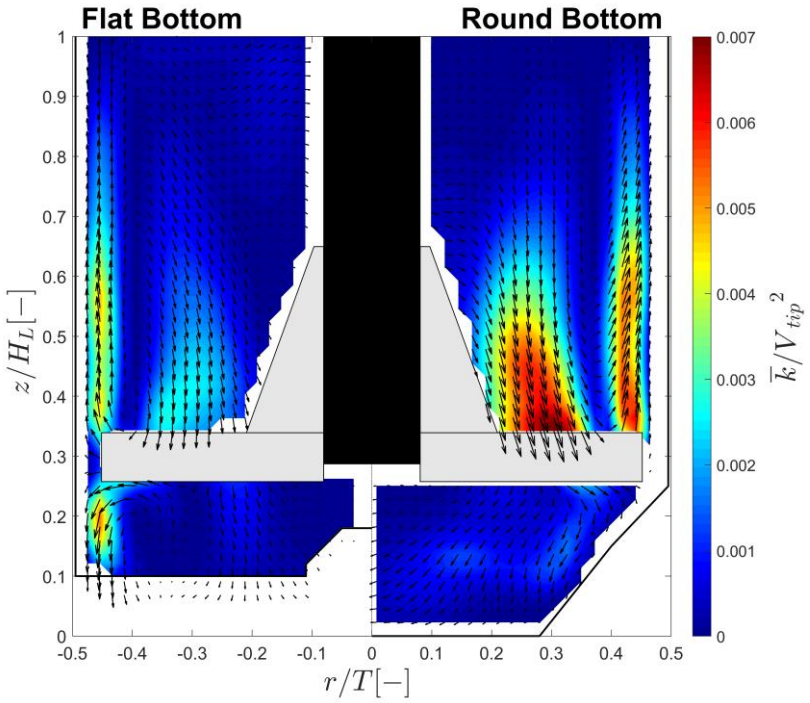

(d)

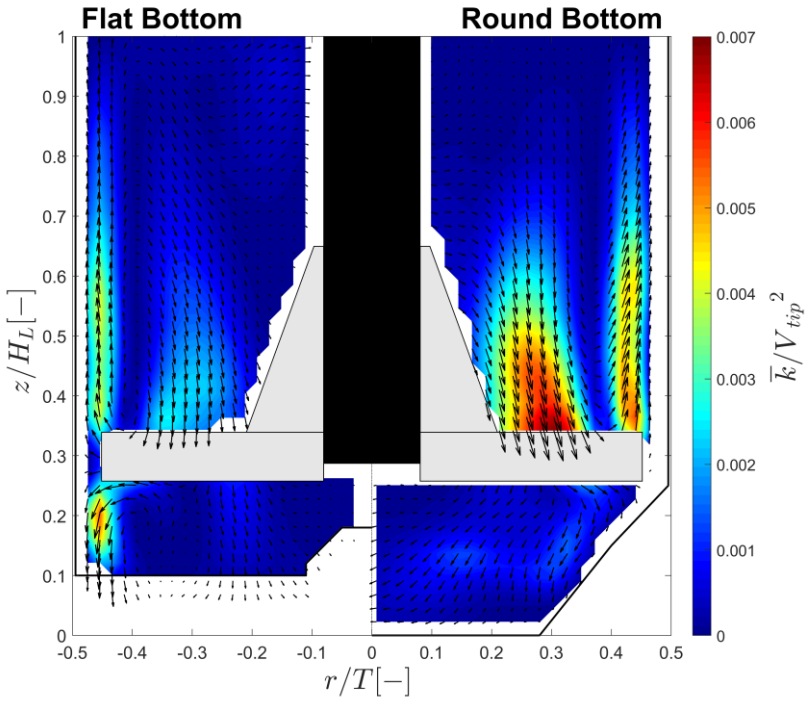

Figure 4.16 Contour maps of ensemble-averaged mean flow kinetic energy, $\overline{k}/{V_{tip}}^2$: (a) N = 75 rpm; (b) N = 90 rpm; (c) N = 105 rpm; (d) N = 120 rpm.

(a)

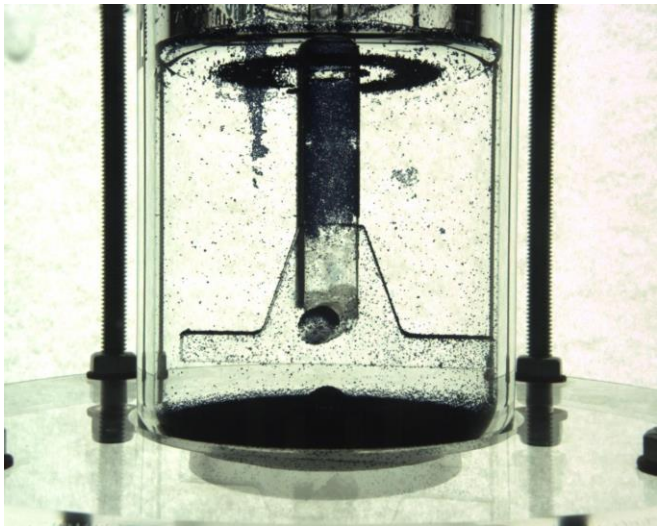

(b)

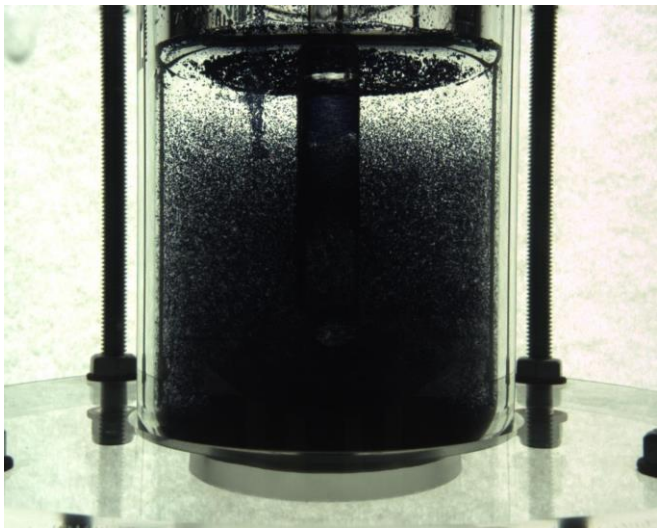

(c)

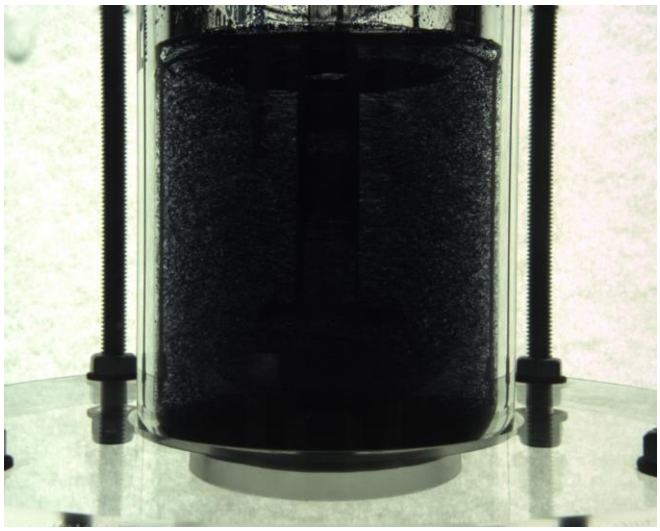

Figure 4.17 Visualisation of the suspension technique used for the flat bottom configuration seeded with Cytodex 3: (a) fully settled system; (b) partially suspended system; (c) fully suspended and homogeneous system.

(a)

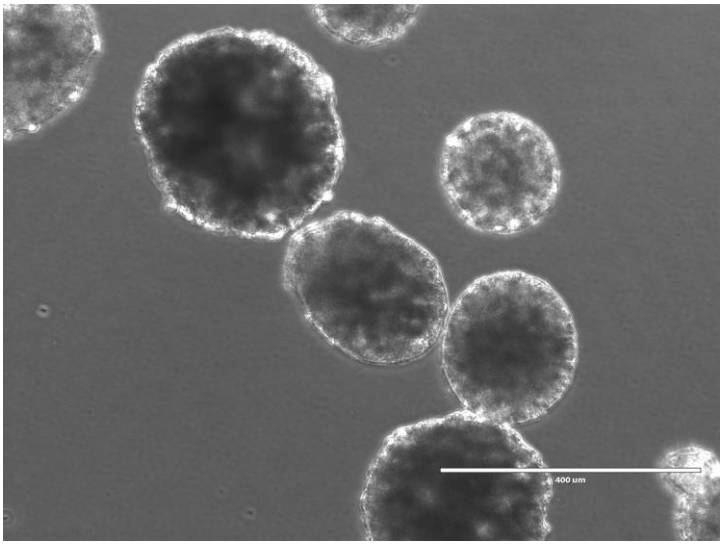

(b)

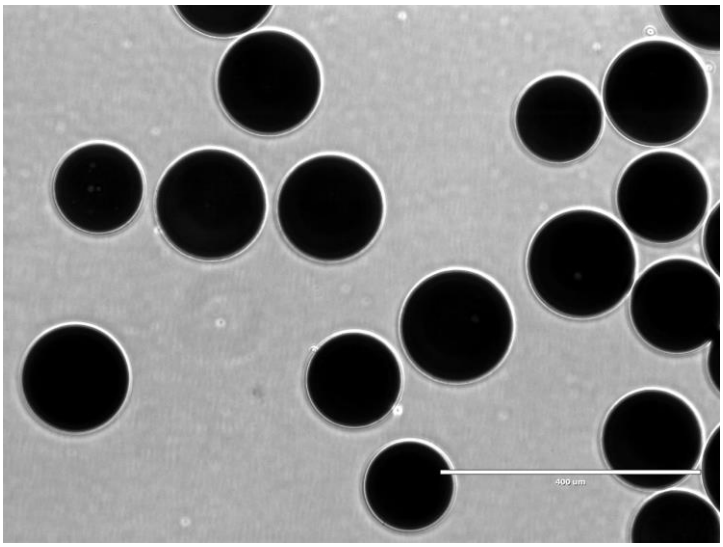

(c)

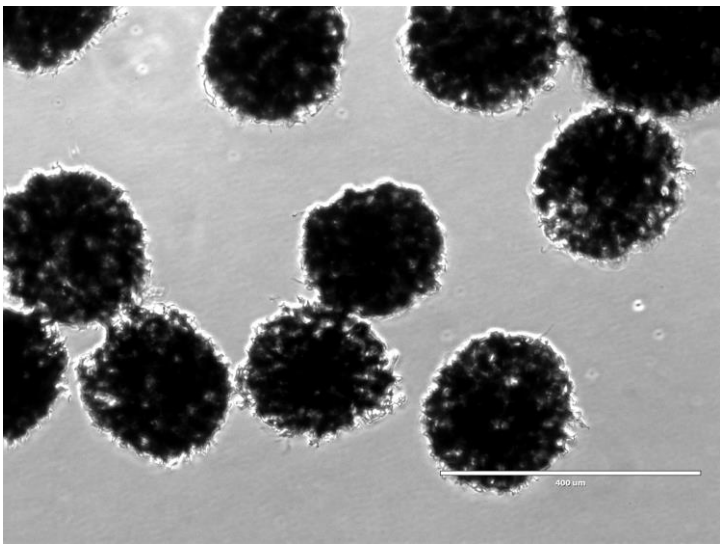

Figure 4.18 Microscope images of swollen microcarriers. Scale bar represents 400 μm: (a) Cultispher-G; (b) Cytodex 3; (c) Cytopore 1.

(a)

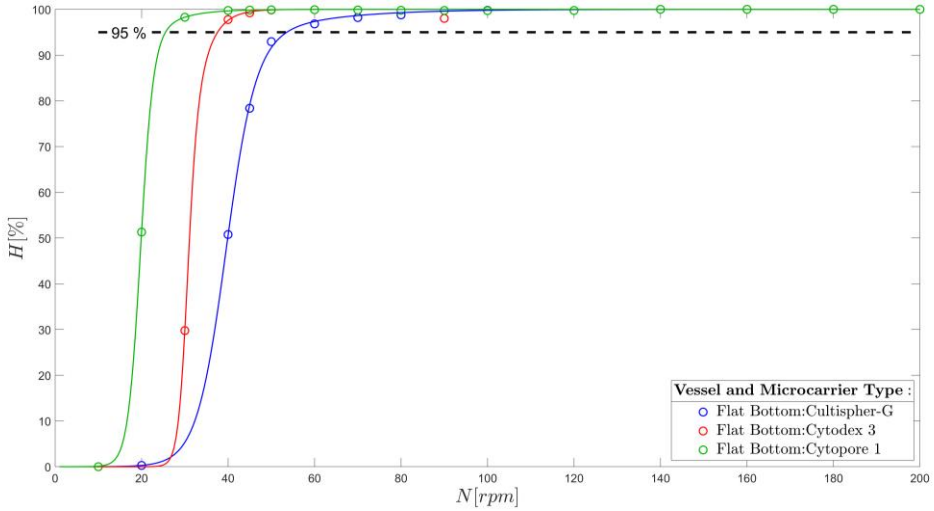

(b)

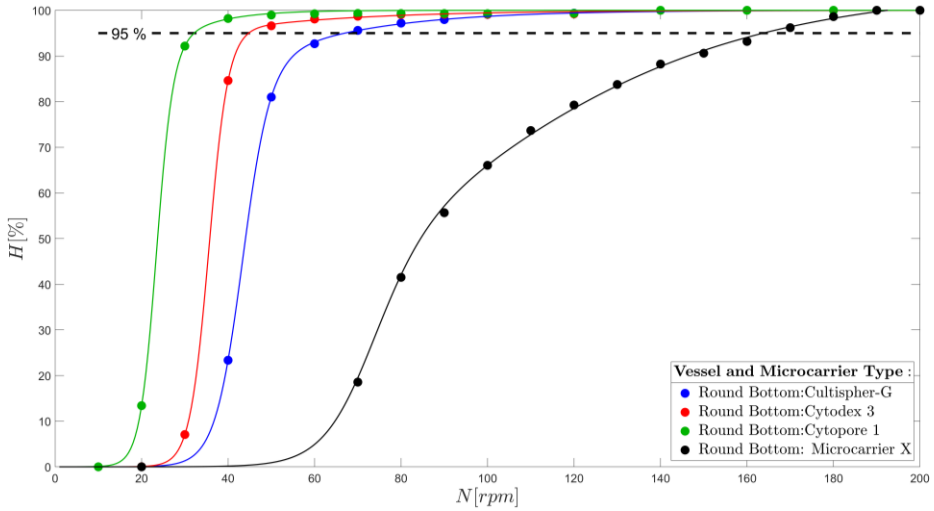

(c)

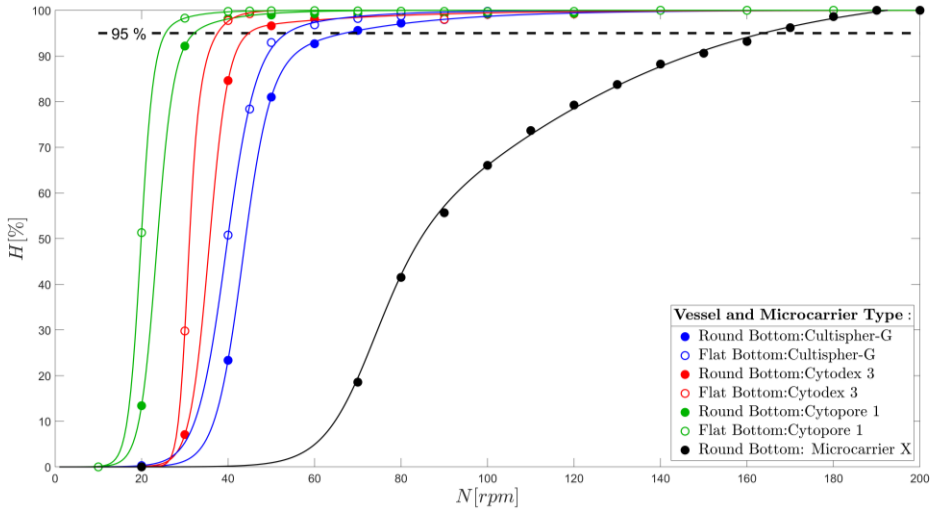

Figure 4.19 Variation of the homogeneity index, *H*, with increasing rotational speeds for different microcarrier and bioreactor combinations: (a) flat bottom configuration; (b) round bottom configuration; (c) both bioreactor configurations.

(a)

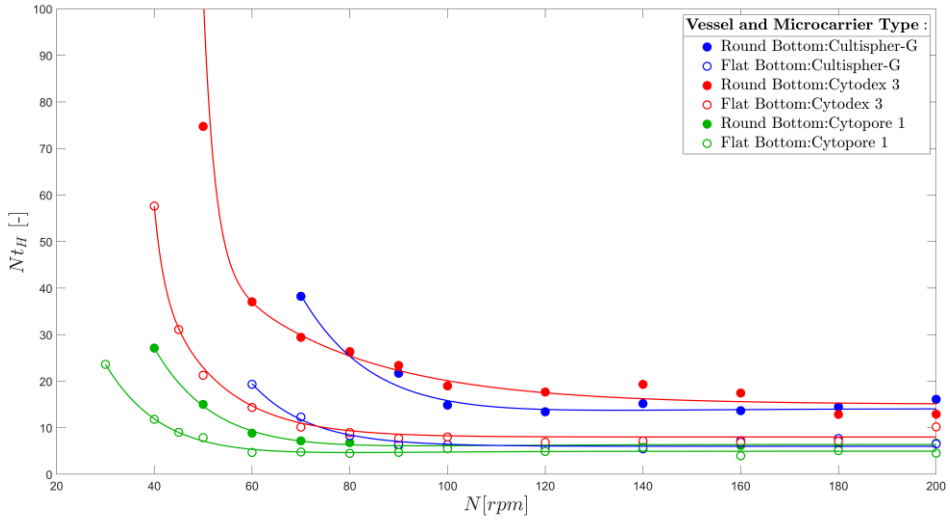

(b)

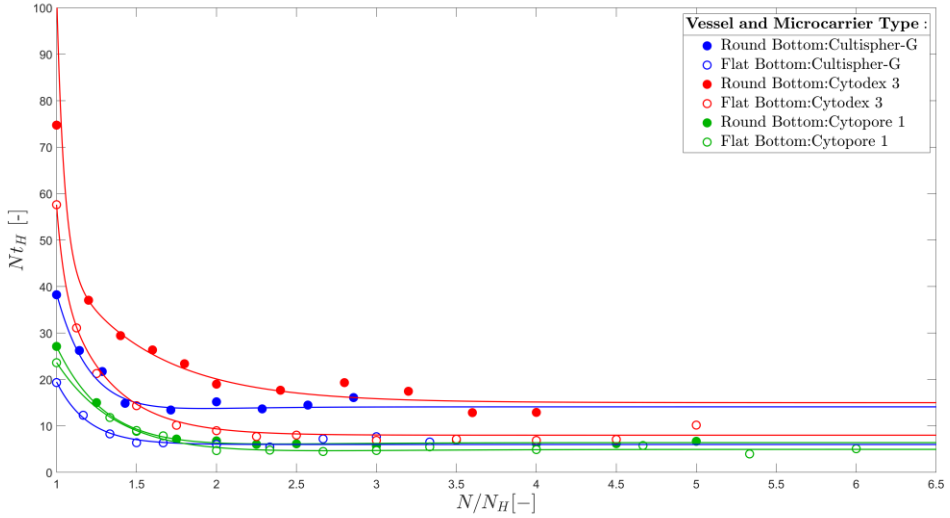

Figure 4.20 Variation of the time to reach 95 % homogeneity, Nt_H, for different microcarrier and bioreactor combinations: (a) increasing rotational speed, N; (b) normalised to N/N_H.

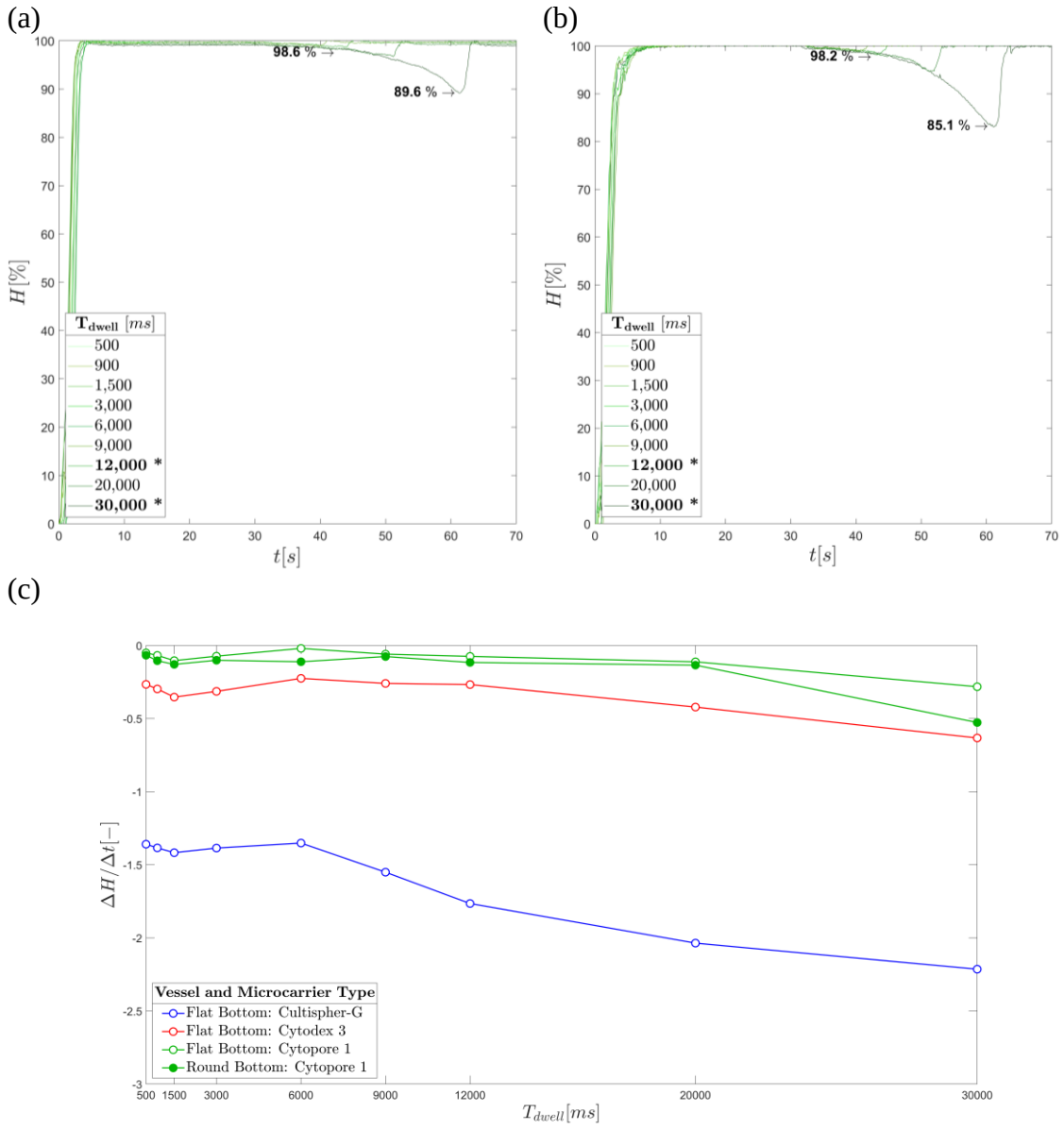

Figure 4.21 Suspension and settling comparison between the flat and round bottom DASGIP configurations using Cytopore 1: (a) round bottom configuration homogeneity over time; (b) flat bottom configuration homogeneity over time; (c) settling gradients.

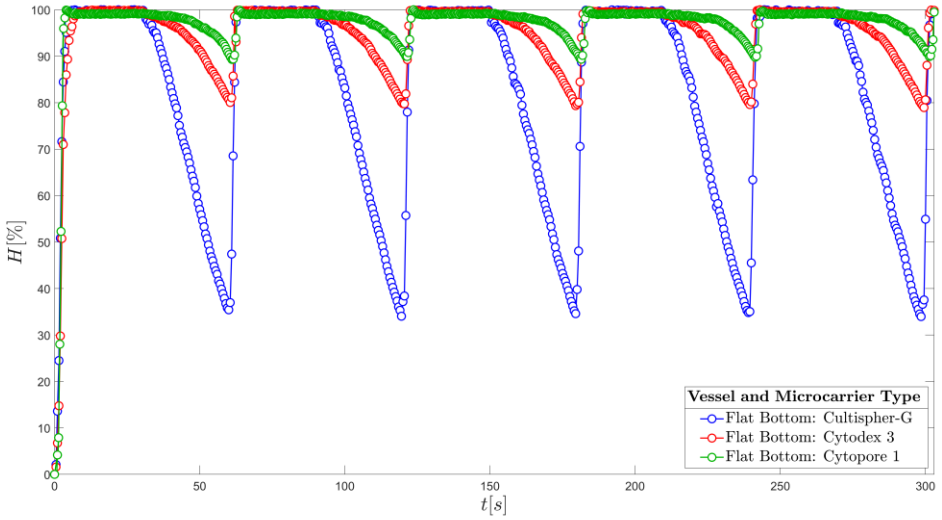

Figure 4.22 Suspension characterisation of intermittent agitation over time [N = 90 rpm, T_{inv} = 30 s and T_{dwell} = 30 s] for all microcarrier types in the flat bottom configuration.

(a)

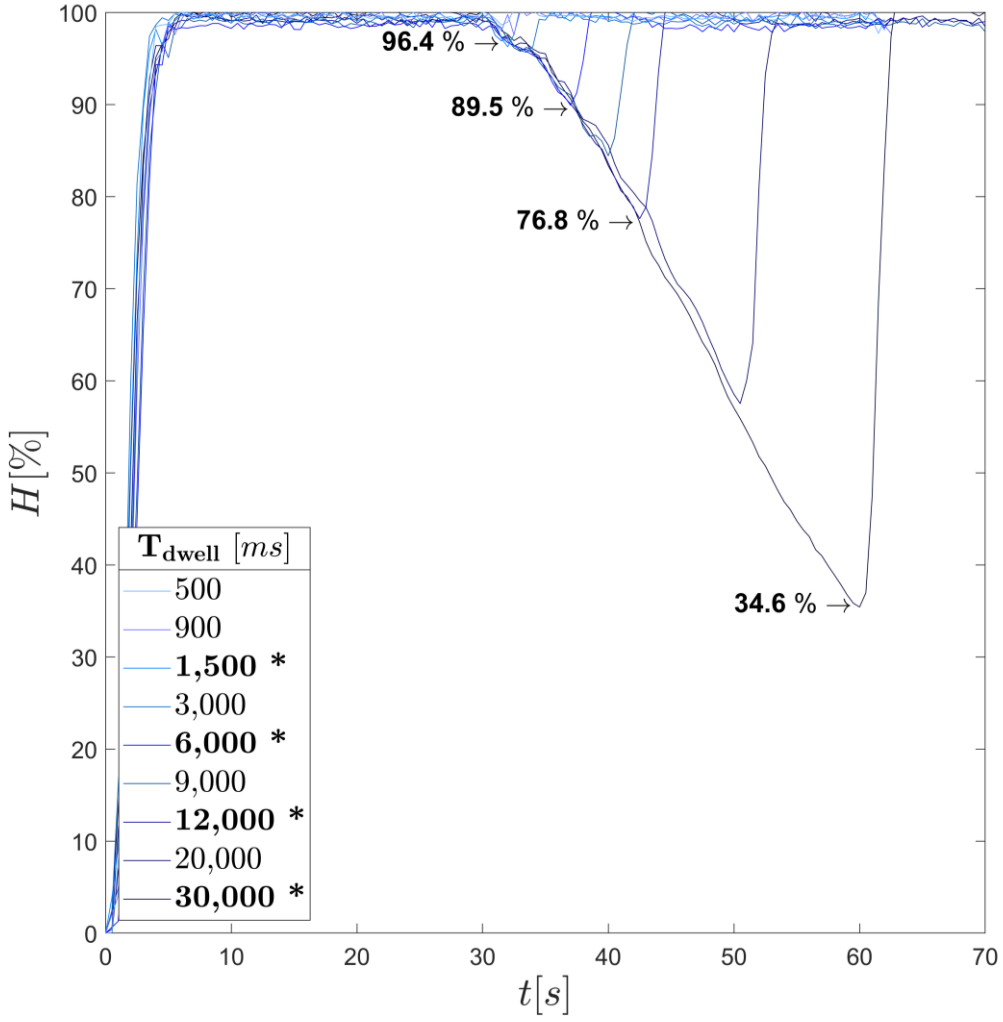
96.4 % →
89.5 % →
76.8 % →
34.6 % →
$\mathbf{T_{dwell}}$ $[ms]$
500
900
1,500 *
3,000
6,000 *
9,000
12,000 *
20,000
30,000 *
$H[\%]$
$t[s]$
0
10
20
30
40
50
60
70
80
90
100

(b)

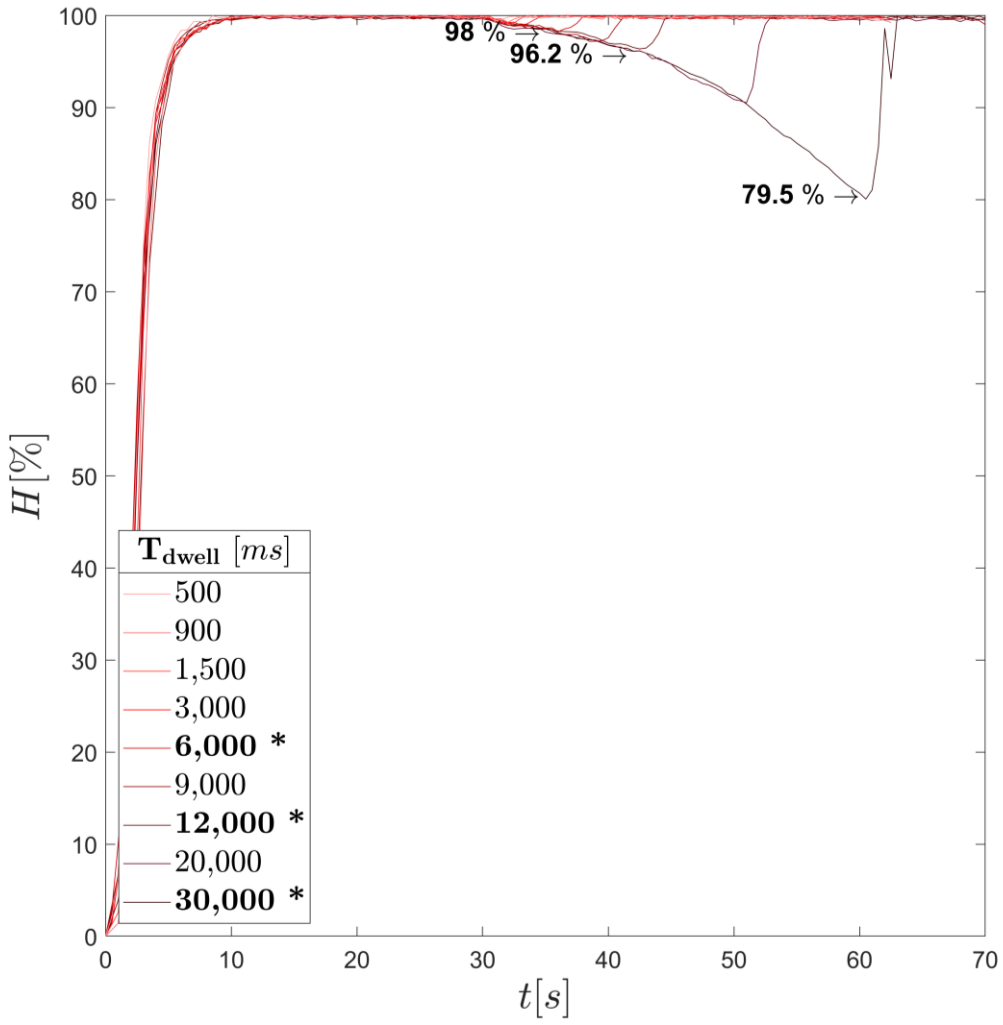
98 %
96.2 %
79.5 %
$\mathbf{T_{dwell}}$ $[ms]$
500
900
1,500
3,000
6,000 *
9,000
12,000 *
20,000
30,000 *
$H[\%]$
$t[s]$
0
10
20
30
40
50
60
70
80
90
100

(c)

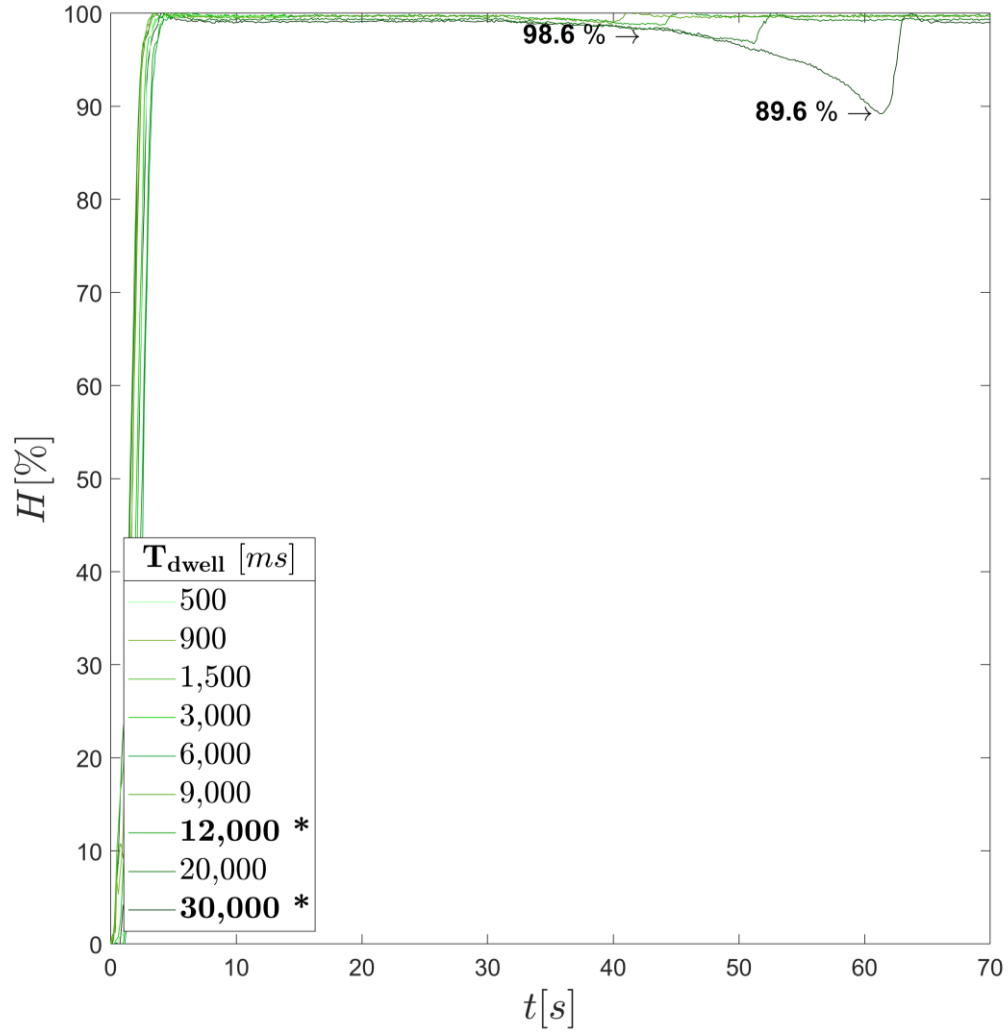

(d)

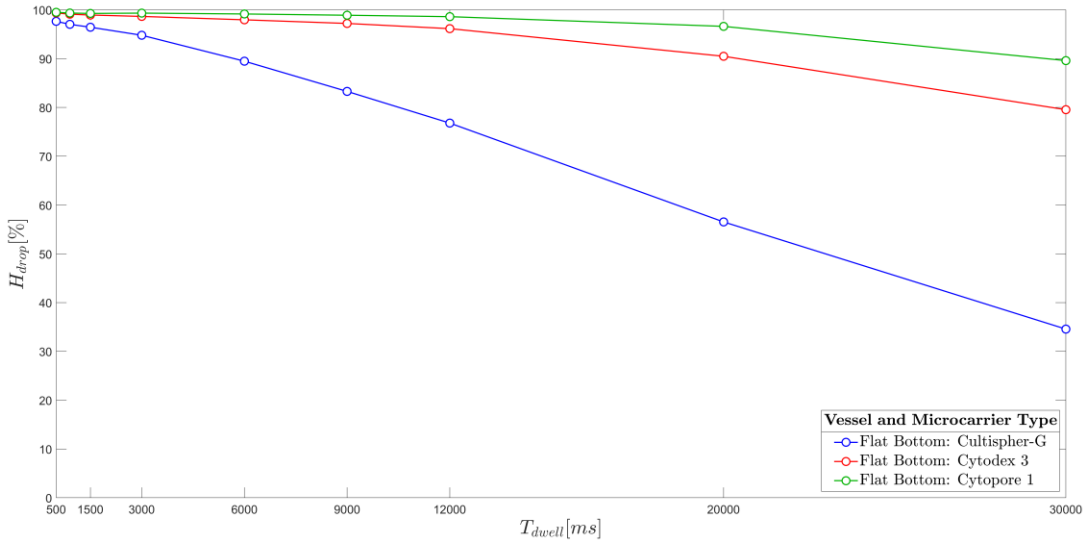

Figure 4.23 Variation of the degree of homogeneity for increasing dwell time, T_{dwell}, with intermittent agitation: (a) Cultispher-G; (b) Cytodex 3; (c) Cytopore 1; (d) average drop in homogeneity.

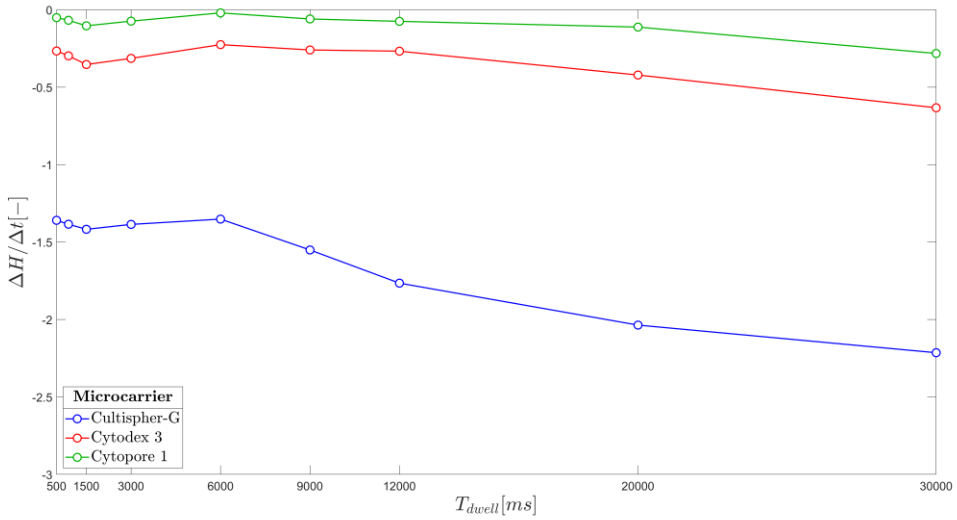

Figure 4.24 Settling gradient $\Delta H/\Delta t$ for each microcarrier type at increasing T_{dwell}.

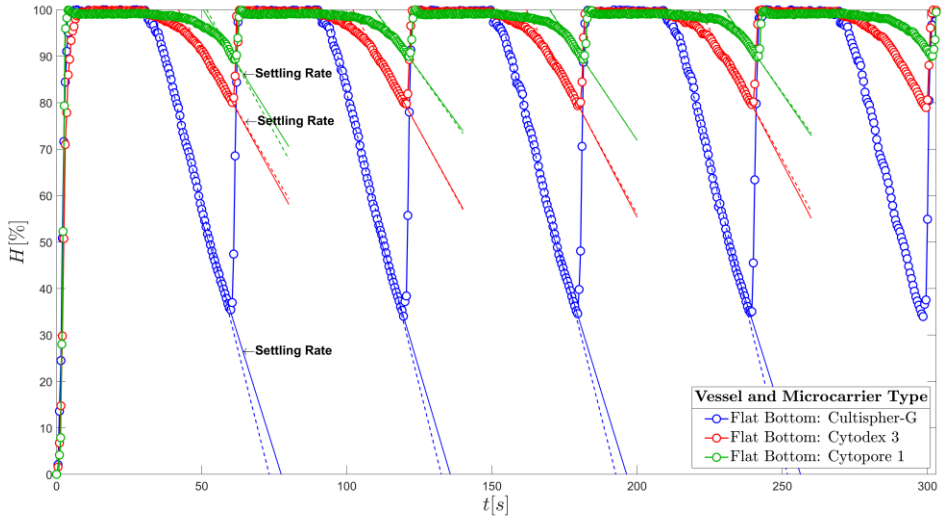

Figure 4.25 Variation in the degree of homogeneity for the three microcarrier types during intermittent agitation. Rate of settling extrapolated from drop in homogeneity for 10 s (___) and 20 s before resuspension (_ _).

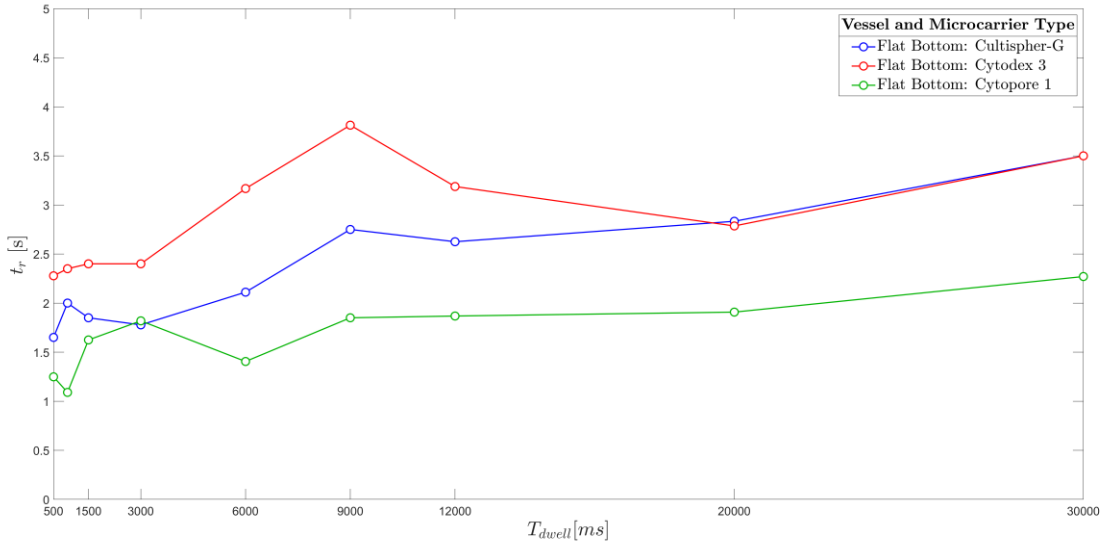

Figure 4.26 Time to fully resuspend, t_r, following a dwell phase during intermittent agitation for three microcarrier types.

Bioreactor: Microcarrier Type	D_{50} [μm]	ρ [g/cm^3]	Φ [%]	N_H [rpm]
Flat Bottom: Cytopore 1	235	1.03	Macroporous > 90 %, (pore size 30 μm)	25.5
Round Bottom: Cytopore 1				32.2
Flat Bottom: Cytodex 3	175	1.04	Non-porous/microporous	37.6
Round Bottom: Cytodex 3				44.8
Flat Bottom: Cultispher-G	255	1.04	Macroporous ≈ 50 %, (pore size 10 - 30 μm)	53.6
Round Bottom: Cultispher-G				67.0
Round Bottom: Microcarrier X	354	1.39	Macroporous ≈ 94 – 38 %	163.8

Table 4.1 Diameter, density, porosity and minimum rotational speed to reach 95 % of homogeneity, N_H, for different microcarrier and bioreactor combinations.

Reactor: Microcarrier Type	H_t [-]
Round Bottom: Cultispher-G	14.1
Flat Bottom: **Cultispher-G**	6
Round Bottom: Cytodex 3	15
Flat Bottom: **Cytodex 3**	8
Round Bottom: Cytopore 1	6.4
Flat Bottom: **Cytopore 1**	4.95

Table 4.2 Homogeneity-time constant, H_t, for different microcarrier and bioreactor combinations.

	Manufacturer u_s [cm/s]	Stokes's Equation u_s [cm/s]	Average rate of settling [%/s]	Calculated u_s [cm/s]
Cultispher-G	-	0.6 – 1.03	2.27	0.155
Cytodex 3	0.2 – 0.267*	0.6 – 0.78	1.14	0.075
Cytopore 1	0.216 – 0.317*	0.65 – 0.75	0.94	0.073

Table 4.3 Comparison of settling velocity, u_s, obtained from manufacturer manuals*, Stokes's equation and experimental data (blue).

*obtained from (GE Healthcare Life Sciences, 2013).

	Impeller centre line	≈ $T_{dwell\ (max)}$ [ms]
Cultispher-G	30 %	30,837
Cytodex 3	30 %	61,404
Cytopore 1	30 %	74,468

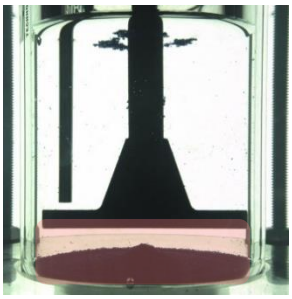

Table 4.4 Comparison between the maximum dwell time, $T_{dwell\ (max)}$ required to preserve a level of suspension above the impeller centre line (shaded in red) for different microcarrier types.

CHAPTER 5 FLOW AND MIXING DYNAMICS IN DASGIP BIOREACTORS [*]

5.1 Introduction

The flow frequency analysis and biological study presented in Chapter 3 were carried out using a flat bottomed DASGIP bioreactor system, equipped with a non-conventional two blade paddle impeller. The purpose was to investigate the impact of mechanical flow cues imparted from various agitation modes upon biological outcomes. The previous chapter introduced the use of Particle Image Velocimetry (PIV) to investigate the mean flow such as to determine the impact of bioreactor configuration on flow and suspension dynamics, however, the impact of the intermittent agitation modes on the mixing and flow dynamics, i.e. velocity, shear rate and turbulence levels, were not investigated.

As discussed in the previous chapters, flow regime is very important for embryoid body or microcarrier-cell culture with regards to cell attachment, viability, growth and differentiation yield. A balance is sought such as to achieve full suspension and efficient mixing, ensuring spatial and temporal homogeneity, with optimal shear stresses and turbulence levels imparted upon the flow to avoid loss of cell viability, cell detachment or undesirable differentiation pathways. The work in the present chapter was undertaken to characterise the mixing dynamics and flow dynamics for a flat bottom DASGIP bioreactor, focusing upon shear stresses and turbulence imparted. This was performed such as to determine and quantify the changes in flow and mixing dynamics with the different agitation modes in an attempt to correlate this with the biological outcomes observed in Chapter 3 and help clarify why intermittent agitation is favourable.

5.2 Results

This section of the chapter is divided into two main parts: 1) the temporal characterisation within the flow of the flat bottom DASGIP bioreactor for both continuous and intermittent

---

[*] Some of the results presented in this chapter are included in:

Samaras, J. J., Serra, M., Ducci, A., Micheletti M. (2018), "Characterisation and correlation of flow dynamics relating to an iPSC-derived cardiomyocyte differentiation process", *16th European Conference on Mixing*, Toulouse, France.

agitation modes is presented in Section 5.2.1 and 5.2.2, respectively; 2) the assessment of mixing dynamics for both agitation modes is described in the subsequent Section 5.2.3. The main conclusions of this work are then summarised in Section 5.3.

As was previously seen in Section 4.2.1 and described in Section 2.4.2, a PIV system was used to obtain both phase-resolved and ensemble-averaged velocity data such as to characterise the flow field of two DASGIP bioreactor configurations. It was found that the flat-bottomed configuration induced better and more efficient 'lift' at the base of the bioreactor due to a strong lower trailing vortex, present during continuous motion. As this work focuses upon the recreation of an iPSC-cardiomyocyte cell culture process undertaken within the flat bottom configuration, this chapter seeks to determine the impact of agitation mode upon the fluid flow and mixing dynamics in the same configuration. Phase-resolved measurements investigating continuous agitation demonstrate the evolution of measured velocities over an impeller revolution and the periodic fluctuation of measured parameters such as shear and turbulence. Mixing performance was also characterised. Intermittent modes of agitation were then investigated and the impact of T_{dwell} upon the flow and mixing dynamics was assessed before, during and directly after the dwell phase.

5.2.1 Continuous agitation flow dynamics

Two-dimensional (2-D) phase-resolved contour maps of velocity magnitude, $\langle U_{rz} \rangle / V_{tip}$, superimposed with velocity vector fields, are given in **Figure 5.1** for φ = 0 – 60° at N = 90 rpm. In **Figure 5.1** data are only shown for φ = 0 – 60° because the velocity field displays greatest variation in this range of phase angles. The contour maps shown are all for a reference speed of N = 90 rpm, given the scalability of the velocity field with V_{tip}, shown in the previous chapter (See **Figure 4.1 – 4.6**). As the impeller rotates, the velocity magnitudes are shown to increase in intensity, corresponding to the trailing vortex formation behind the blade. The most intense velocity magnitudes are confined to the impeller region, associated to the upper and lower trailing vortices and up the bioreactor wall from the impinging radial jet. With impeller blade rotation from φ = 0 – 45°, there is a general increase in the velocity magnitude intensity and the top vortex appears to dominate. As the impeller continues to rotate further, the velocity magnitudes are shown to decrease with increasing measurement plane distance from the impeller blade and the two vortices are shown to display similar intensities. It is interesting to note the highest

reached velocity magnitude of $\langle U_{rz} \rangle / V_{tip}$ = 0.22 – 0.23 at φ = 45° is approximately 145 % higher than the ensemble-averaged results discussed in Chapter 4 (See **Figure 4.1**).

Decomposition of the velocity magnitude yields both the axial and radial velocity components. **Figure 5.2** (a – b) show the phase-resolved analysis of the dominant axial component within the flow. **Figure 5.2** (a) shows 2-D contour maps of the axial velocity component for increasing phase angle, φ = 0 – 60°. The regions of largest axial motion are at the bioreactor wall, extending up from the formation of the upper circulation loop, and below the impeller where the lower recirculation loop is drawn in towards the impeller. **Figure 5.2** (a) shows the largest intensities of axial motion when the impeller is aligned to the bioreactor wall (φ = 0°) and the impinging radial jet is redirected axially into two streams. In the impeller blade's wake this axial component is shown to diminish. **Figure 5.2** (b), shows the variation of the axial velocity component with phase angle, φ = 0 – 345°, for increasing rotational speeds at r/T = 0.45 and z/H_L = 0.35, a point close to the impeller blades. The reduction in axial motion in the range of phase angles considered, φ = 0 – 155° is clearly shown. As the trailing impeller blade approaches the plane of measurement, φ = 155 – 180°, the axial velocity component increases with proximity to the impeller tip. The phase-resolved axial velocity component shows very good scalability among all the rotational speeds investigated.

2-D contour maps of the normalised radial velocity component at phase angles, φ = 0 – 60° are given in **Figure 5.3** (a), while the phase-resolved radial velocities for a full impeller rotation at a point close to the impelled blade tip are plotted in **Figure 5.3** (b). As seen with the ensemble-averaged data presented in the previous chapter, **Figure 5.3** (a) shows the radial component to be less intense in comparison to the axial component (up to 73 % reduction), due to the large impeller D/T. The radial component is highest within the core of the two trailing vortices, above and below the impeller blade. **Figure 5.3** (b) plots the radial component for increasing rotational speeds at r/T = 0.45 and z/H_L = 0.35. As the impeller blade moves further from the plane of measurement the direction/sign of the radial component is inverted. A weak positive radial displacement towards the bioreactor walls is detected when the blade is in the measurement region, while a prevalent radial suction occurs after the blade passage, shown by negative radial velocities at φ = 45 – 165°. This demonstrates the fluctuation of radial velocity directionality over an impeller revolution.

A direct comparison of phase-resolved quantities of the three velocity components can be obtained by combining the PIV (axial and radial component) and LDA results (tangential component). The variation of the phase-resolved periodic velocity component, $\tilde{u} = (\langle U \rangle - \overline{U})$, at point A ($r/T$ = 0.35 and z/H_L = 0.28), are given in **Figure 5.4** (a), showing tangential velocities (blue) ranging from $\tilde{u}_\theta$ = - 0.034 – 0.029, axial velocities (black), $\tilde{u}_z$ = - 0.033 – 0.026 and radial velocities (red) of $\tilde{u}_r$= - 0.020 – 0.033. **Figure 5.4** (b) shows the variation of the velocity fluctuations, $u' = (u - \langle U \rangle)$ for the tangential direction (blue), u'_θ = 0.016 – 0.032, the axial direction (black), u'_z = 0.011 – 0.016 and the radial direction (red), u'_r = 0.007 – 0.019. The trailing vortex generated by passage of the impeller blade induces periodic variation of the three velocity components of similar magnitude, however turbulence levels in the axial and radial directions are reduced to almost half that in the tangential direction. This implies a degree of turbulence anisotropy, which was measured according to the method of Lee and Yianneskis (1998), using the absolute difference between turbulence levels in the axial, radial and tangential directions, normalised with the tip speed. According to Kresta and Wood (1993), r.m.s components shown to differ by 25 – 50 % could still be regarded as isotropic, with highly anisotropic flows expected to vary much more significantly, up to 200 %. For the data presented in **Figure 5.4** (b), $|u'_z - u'_r|/V_{tip}$ = 0.01 and $|u'_\theta - u'_r|/V_{tip}$ = 0.05. According to Kresta and Wood (1993) the results obtained can be considered isotropic. Considering the whole flow, anisotropy is evident observing the PIV data on the *rz* plane, given in **Figure 5.5**. Differences between the radial and axial r.m.s components are observed (up to 0.2 V_{tip}), corresponding to approximately 197 % variation under identical conditions. This is indicative of strong axial anisotropy, visualised most intensely where the radial jet impinges with the bioreactor wall. It is interesting to observe anisotropy is not restricted to the impeller region, however this is likely attributed to the axial displacement of the trailing vortices, as determined in the previous chapter. Interestingly, Brunazzi *et al.* (2005) observed larger regions of anisotropic turbulence in unbaffled vessels equipped with a Rushton turbine in comparison to baffled vessels.

To put the results of this work into perspective, investigation within baffled vessels, equipped with both axial-flow pitched blade turbine impellers (Hockey and Nouri, 1996; Schäfer *et al.*, 1998) and radial-flow Rushton turbine impellers (Lee and Yianneskis, 1998) describe a similar degree of anisotropy within the impeller stream. Differences up to 0.15 V_{tip} were measured, with radial r.m.s values greater than tangential and both

greater than the axial component. These differences in r.m.s values were found to tend towards zero within the bulk flow, as distance from the impeller region increased.

It should be noted that given the degree of anisotropy identified, the values of kinetic energy, in Sections 5.2.2.3 and 5.2.2.4, obtained from the radial and axial components according to Equations 2.15 and 2.17, may be underestimated in the proximity of the impeller and bioreactor wall, where the degree of anisotropy is most significant.

In the previous chapter it was shown that the ensemble-averaged maximum shear rates generated shear stresses up to 0.0657 dyn/cm^2, far below the quoted shear stresses of 1 dyn/cm^2 found in the literature to affect stem cell proliferation and viability (Ismadi *et al.*, 2014). However, shear stress fluctuations generated by blade passage and/or turbulence levels should be considered. In this perspective, the phase-resolved maximum local shear rates are shown in **Figure 5.6** (a – b) for phase angles φ = 0 - 60°. To provide a visualisation of the maximum shear regions with respect to the trailing vortices position within the reactor, the shear rates are overlaid with the phase-resolved vector fields in **Figure 5.6** (a), while in **Figure 5.6** (b) trailing vortices boundaries are visualised by a continuous line obtained for $|\langle\omega_\theta\rangle|/\pi N$ = 1.0. It is interesting to observe the evolution of shear as the impeller rotates. At φ = 0°, the highest shear rates are located close to the wall and the impinging jet, which is split and deflected vertically. As the impeller rotates, a high shear region at the upper border of the upper trailing vortex develops. At φ = 30° and 45° higher shear rates are observed between the two trailing vortices, either towards the blade tip or the bioreactor wall. This high shear region in between the trailing vortices continues to persist at greater phase angles when the blade moves away from the measurement plane (φ = 60°). When the shear rate is observed at the edge of the upper vortex (r/T = 0.35 and z/H_L = 0.35) (see **Figure 5.6** c), its values show a sudden increase at low phase angle, followed by a subsequent gradual decrease for φ > 60°. The decrease in shear in the impeller blade's wake, corresponds to the decay in intensity of the two trailing vortices. As described in the previous Chapter, it was then possible to calculate the shear stress from the determined shear rate using Equation 2.26. The above analysis shows that dimensional shear stresses can reach a maximum of ≈ 0.1238 dyn/cm^2, corresponding to an approximate 88 % increase in comparison to the ensemble-averaged result. However, this value remains 9-fold below the values reported in literature to impair iPSC cell proliferation (Ismadi *et al.*, 2014).

Kinetic energy can be subdivided into the energy associated to the periodicity of the flow induced by the blade passage, $\langle k \rangle / {V_{tip}}^2$, and the kinetic energy associated to the random fluctuations due to turbulence, $\langle k' \rangle / {V_{tip}}^2$. 2-D contour maps of the periodic kinetic energy are shown in **Figure 5.7** (a) and (b) for φ = 0 – 60°, either with the vector fields overlaid or the trailing vortices outlined, respectively. All contour maps show that the regions of greatest $\langle k \rangle / {V_{tip}}^2$ are directly associated to the formation of the trailing vortices in the impeller blade's wake, and the intensity decays as the distance from the impeller tip increases. The highest intensities (**Figure 5.7** b) occur at the interfaces between the trailing vortices. This is in agreement with the result of Zhao *et al.* (2011), who observed that the maximum kinetic energy occurred at the interface between the upper and lower trailing vortices generated by a radial flow turbine impeller, reaching up to $\langle k \rangle / {V_{tip}}^2$ = 0.14. Similarly, Escudié and Liné (2003) reported periodic kinetic energy values up to 0.13 V_{tip}^2 for a Rushton turbine. Values of $\langle k \rangle$ were observed in this work to reach a maximum of 0.039 V_{tip}^2, an approximate 7-fold increase to the observed ensemble-averaged, $\bar{k}$ = 0.0056 V_{tip}^2, discussed in the previous chapter. Although the DASGIP configuration is equipped with a radial flow paddle impeller, the previous chapter observed significant similarity to the flow generated from an axial flow impeller. This is due to the large *D/T* diverging the radial jet from impeller motion into two axial streams. For an axial flow marine impeller, Odeleye *et al.* (2014) presented phase-resolved $\langle k \rangle / {V_{tip}}^2$ values of 0.03. Aubin *et al.* (2001) obtained non-dimensional kinetic energy values in the range of 0.024 – 0.14 V_{tip}^2 for various axial flow impellers operating in upward and downward pumping modes, while Schäfer *et al.* (1998) showed $\langle k \rangle$ to reach up to 0.058 V_{tip}^2 for a pitched blade turbine. Clearly there is some variation owing to factors such as change in impeller clearance, diameter, pumping mode, blade width, etc., however the measured value of $\langle k \rangle / {V_{tip}}^2$ in this work is within the range of values reported in the literature for an axial flow impeller.

Similar to the shear profile observed previously in **Figure 5.6** (c), **Figure 5.7** (c) demonstrates consideration of $\langle k \rangle / {V_{tip}}^2$ at the edge of the upper vortex (*r/T* = 0.35 and z/H_L = 0.35), plotted over one impeller revolution. Kinetic energy is shown to increase at low phase angle (φ = 15°) and to rapidly decrease in the impeller blade's wake (φ > 30°), corresponding to the decay of the trailing vortex intensity. The non-dimensional kinetic energy is shown to scale well with V_{tip}^2 for all the impeller rotational speeds considered.

Turbulence occurring from random fluctuations within the tank, $\langle k' \rangle / {V_{tip}}^2$, was calculated according to Equation 2.17. 2-D turbulent kinetic energy contour maps are shown in **Figure 5.8** (a) and (b) for φ = 0 – 60° with the vector fields overlaid and trailing vortices boundaries, respectively. Similar to the periodic kinetic energy, **Figure 5.8** (a and b) demonstrate that the regions of greatest turbulence occur at the interfaces and at the core of the trailing vortices. This is in agreement with the literature, where phase-resolved measurements of turbulence levels reached maximum values in the core of the trailing vortices (Lee and Yianneskis, 1998; Derksen *et al.*, 1999; Ranade *et al.*, 2001). It can be observed that the maximum achieved turbulence levels are approximately half of the periodic motion ($\langle k' \rangle / \langle k \rangle$ = 0.024/0.039 ${V_{tip}}^2$). Tamburini *et al.* (2018) predicted the flow field of baffled and unbaffled mixing vessels, equipped with a Rushton turbine impeller, using computational fluid dynamics. They observed larger turbulence intensities in the baffled configuration, whilst the unbaffled configuration showed the flow to be dominated by the tangential component and solid body rotation. Hall *et al.* (2004) also observed unbaffled vessels equipped with a pitched blade turbine to be dominated by tangential solid body rotation, which contained the majority of the kinetic energy of the flow. Thus, periodic kinetic energy is expected to dominate.

As before, **Figure 5.8** (c) demonstrates consideration of the turbulent kinetic energy at the edge of the upper vortex (r/T = 0.35 and z/H_L = 0.35), plotted over one impeller revolution. **Figure 5.8** (c) shows the regions of highest turbulence occur in the impeller blade's wake. As with the other components, a decay is observed with distance from the impeller tip and the plane of measurement. This indicates intense turbulence generated in the trailing vortices, in a relatively small region of the bioreactor, which dissipates rapidly. Unexpectedly, turbulent kinetic energy is demonstrated to scale poorly with ${V_{tip}}^2$, showing up to approximately 44 % deviation between the investigated rotational speeds. The results presented in the previous chapter showed faster decay in the upper trailing vortex intensity with increasing rotational speed (Section 4.2.1.2). The same observation was made for ensemble-averaged and phase-resolved velocity magnitudes, r.m.s components of velocity, shear rates, and mean flow kinetic energy and periodic kinetic energy, although notably a reduction of up to approximately 10 % with increasing rotational speed was observed. This behaviour was attributed to the large impeller D/T preventing radial flow acceleration, becoming more pronounced at greater rotational speeds. This may be the cause for the unexpected poor turbulent kinetic energy scalability.

5.2.2 Intermittent agitation flow dynamics

To gain a better understanding of the beneficial introduction of intermittent agitation on cardiomyocyte differentiation yields, concluded in Section 3.2.3, PIV was also used to assess the change in velocity magnitudes, shear and turbulence for intermittent agitation at a reactor scale. The core focus is on the transient between each dwell phase with the restart in motion and the impact upon the flow during the dwell. As with the suspension studies, undertaken in Section 4.2.2, longer durations of T_{dwell} were investigated than those first encountered in Chapter 3 such as to inform upon the future design of studies investigating a longer duration of dwell on biological outcomes.

5.2.2.1 Velocity magnitudes

The evolution of the flow during the dwell was investigated to characterise the drop in fluid motion and the time to reach a static system. PIV measurement was also separately acquired directly after the dwell phase, with the restart in impeller motion, to characterise the flow during the transient. To assess the impact of intermittent agitation and be able to apply a phase-resolved analysis, PIV measurements were acquired with the impeller in the position φ = 0°. This allowed a direct comparison with the phase-resolved data obtained for continuous agitation. During the time interval when the impeller is moving (T_{inv} = 30 s), phase-resolved analysis was carried out based on measurements taken at a frame rate of 0.0015 kHz, corresponding to one measurement for every revolution, i.e. 45 image pairs. During the dwell phase, T_{dwell}, a phase-resolved analysis was carried out based on measurements acquired at an increased frame rate of 0.02 kHz to maximise capture resolution. For both sets of experiments measurement was taken over 10 consecutive intermittent intervals and the average was made. It should be noted that in the following section the phase-resolved notation for intermittent flow is unchanged with respect to the notation used before for continuous flow.

To gain insight into the spatial decomposition of the flow with dwell duration, profiles of the phase-resolved axial velocity component were obtained at three elevations. This is given in **Figure 5.9** for increasing dwell durations. As a reference, the phase-resolved axial profile measured at φ = 0° for continuous agitation is shown in blue with a filled marker. The axial velocity component was selected for comparison as it gives a measure of directionality within the flow and it is the dominant velocity component in the *rz* plane. The data shown in **Figure 5.9** corresponds to the end of the dwell, i.e. $t = T_{dwell}$, and therefore provides an assessment of whether the flow has maintained any inertia before

the impeller is restarted. The axial profile for the bulk flow was taken at z/H_L = 0.725. It can be observed that similar profiles of the axial component exist closest to the bioreactor wall, with intensity decreasing with dwell duration. For $T_{dwell} \geq$ 6000 ms the axial flow does not exhibit any motion by the end of the dwell. It is interesting to note that the axial profiles at lower dwell durations, T_{dwell} = 100 – 1500 ms, do not follow the same profile for continuous agitation, showing a deviation in flow direction closer to the bioreactor axis, where inertia is slower due to the lower radius of rotation. For example, at $r/T \approx 0.35$ the continuous mode shows an axial velocity $\langle U_z \rangle / V_{tip} \approx 0.003$, representing an almost static flow, while in the intermittent case at T_{dwell} = 250 ms $\langle U_z \rangle / V_{tip}$ = -0.067, showing a downward direction in flow (**Figure 5.9**). Similarly, at $r/T \approx 0.13$, the continuous axial profile shows no motion, $\langle U_z \rangle / V_{tip} \approx 0.002$, while the intermittent agitation mode, T_{dwell} = 250 – 1500 ms, exhibit a perpetual upward axial flow between $\langle U_z \rangle / V_{tip} \approx 0.03 – 0.17$. This suggests continued motion within the flow once the impeller rotation is stopped.

The second elevation in **Figure 5.9** was observed above the impeller at z/H_L = 0.354. The continuous reference line shows both strongly positive and negative axial values, indicating strong upward flow towards the bioreactor wall ($r/T \approx 0.38 – 0.47$) and downward flow towards the bioreactor axis ($r/T \approx 0.35$), associated to the upper circulation loop. A similar profile, with a reduction in intensity, is generated at T_{dwell} = 100 ms until $r/T \approx 0.3$, where the flow direction inverts and is observed to no longer be drawn towards the stationary impeller region. With the stop in impeller motion the flow is pushed away from the impeller region, indicated by positive axial velocities, until $T_{dwell} \approx$ 9000 ms. For $T_{dwell} \geq$ 9000 ms the flow does not exhibit axial motion.

The final elevation considered was observed below the impeller at z/H_L = 0.167 (**Figure 5.9**). Here the continuous reference line represents the lower circulation loop, showing negative axial velocity values closest to the bioreactor wall and weak positive axial velocities representing the recirculation towards the impeller ($r/T \leq 0.38$). Once impeller rotation is stopped, the flow below the impeller is observed to predominantly be pushed downwards, away from the impeller region. For $T_{dwell} \geq$ 12,000 ms the flow is estimated to become fully static. Based upon the observations, it can also be estimated that the drop in velocity occurs fastest within the bulk flow and most slowly within the impeller region.

To observe the impact of the transient between dwell phases, space-averaged results are presented, calculated according to Equation 5.1:

$$X^* = \frac{1}{A}\int_A X \, dA \qquad \textbf{(5.1)}$$

Where A is the measurement area and X^* represents one of the following parameters: velocity magnitude, shear rate and kinetic energy.

Figure 5.10 shows the space-averaged velocity magnitude, $\langle U_{rz}^* \rangle / V_{tip}$, considered over the entire bioreactor volume. **Figure 5.10** (a) shows $\langle U_{rz}^* \rangle / V_{tip}$ for one dwell time condition (T_{dwell} = 20,000 ms), where three separate regions can be distinguished: an interval of impeller rotation (T_{inv} = 30 s), starting at Nt = 0 (Region 1); a dwell phase occurring at Nt = 45 for a duration of T_{dwell} = 20,000 ms (Region 2); followed by a successive interval of impeller rotation starting at Nt = 75 (Region 3). This represents a composition of two different sets of experiments. Regions 1 and 3 were measured during impeller rotation at a frame rate of 0.0015 kHz (φ = 0°). Region 2 was measured in a second set of experiments during the dwell at a frame rate of 0.02kHz. For Regions 1 and 3, an initial spike can be observed following the dwell phase, which after approximately 4 revolutions is shown to reach a consistent level of fluctuation, between Nt = 5 and 45. An average was taken at Nt = 5 - 45, shown by the red continuous line, and is considered hereafter as the 'steady state'. Region 2 shows a second, less intense spike when impeller motion is stopped, remaining elevated for approximately one revolution, before the velocity magnitude is observed to decay. The restart in impeller motion in Region 3 is characterised by the same initial spike observed in Region 1.

Figure 5.10 (b) shows the space-averaged velocity magnitudes considering a range of dwell durations, T_{dwell} = 500 – 30,000 ms. For comparison, $\langle U_{rz}^* \rangle / V_{tip}$ for continuous agitation (measurements taken at φ = 0°) is shown as a constant blue line at $\langle U_{rz}^* \rangle / V_{tip}$ = 0.0271. Region 1, representing impeller rotation during the defined 'steady state' for all measurements is the same, thus the results are shown to overlap. The initiation of the dwell is shown at Nt = 45 (Region 2) before the restart in impeller rotation (Region 3), which is staggered and shown to no longer superimpose due to the different lengths of T_{dwell}. A fully static flow is observed from approximately $T_{dwell} \geq$ 9000 ms. The amplitude of the spike in velocity magnitude following the dwell is shown to linearly increase with T_{dwell} duration (35 – 138 %). The increasing spike is observed to plateau when a fully static system is reached, between T_{dwell} = 12,000 – 30,000 ms, showing 6 % variation. It is apparent that the shorter dwell conditions maintain some degree of inertia in the flow, generating smaller spikes in magnitude. There is less acceleration as the flow is already moving, therefore the highest amplification of the spike is observed when lower velocities or a static flow occur directly before the restart in impeller rotation. Focusing upon the second less intense spike at the start of the dwell phase (Nt = 45), an approximate increase

of 7 % from the determined 'steady state' is achieved. An unexpected increase in $\langle U_{rz}^{*} \rangle / V_{tip}$ during the steady state is obtained between continuous and intermittent agitation. This may be attributed to the interval time of T_{inv} = 30 s not being sufficient for the flow to fully develop and reach the same average steady state for continuous agitation. This might have a beneficial effect upon the process overall, but the main difference is related to the spikes observed.

It can be seen in **Figure 5.10** (b) that all the plots superimpose in Region 1 and at the beginning of the dwell phase, this is because all experiments were taken at a fixed impeller speed, N = 90 rpm, and interval time, T_{inv} = 30 s. To best visualise what occurs with the stop in impeller motion, an average of the different dwell experiments was taken (**Figure 5.10** c). The space-averaged velocity magnitude during continuous agitation is plotted for all phase angles (blue, see inset), showing that across the bioreactor volume velocity magnitudes increase with impeller passage, decrease as distance from the measurement plane and the impeller blade tip increases, before increasing as the impeller nears the measurement plane once more. A similar profile can be identified following approximately 1 missed revolutions during the dwell phase (red, see inset), showing the continued inertia of the flow. The increased intensity observed during intermittent agitation is attributed to the spike, discussed previously. Overall, **Figure 5.10** (c) clearly shows the decay in flow velocity magnitude as the number of missed revolutions increases, indicating after approximately one missed revolution flow deceleration rapidly occurs. It is difficult to estimate the exact point when velocity magnitudes within the tank reach 0 as PIV measurement relies upon movement within the flow, however it can be estimated that the most significant drop in velocities to reach static flow occur at approximately $Nt \approx 10 – 20$ missed revolutions.

The contour maps in **Figure 5.11** (a – d) show velocity magnitudes at N = 90 rpm and T_{inv} = 30 s, measured following a dwell duration of T_{dwell} = 1, 100, 500, 900 and 1500 ms at $t = T_{dwell}$ (a) and for the first five revolutions after the restart of the impeller rotation for T_{dwell} = 900 ms (b), T_{dwell} = 9000 ms (c) and T_{dwell} = 30,000 ms (d). In **Figure 5.11** (a), the reduction in magnitude can be clearly identified following the stop in impeller motion. At T_{dwell} = 1 ms the trailing vortices are evident, although below the impeller closer to the axis the flow is much less intensely drawn up and mainly diverted downwards due to the blade blockage. Increasing the dwell duration to T_{dwell} = 100 ms, less flow is drawn toward the impeller region, although some degree of circulation is still apparent. Magnitudes overall have not significantly decreased. Increasing the duration of the dwell to 500 ms,

the upper recirculation is almost indistinguishable, with a strong upward motion of the flow deflected away by the impeller blade. Similarly, the lower recirculation is also very weak, with a strong downward direction of the flow. Longer dwell durations at T_{dwell} = 900 – 1500 ms, show the overall velocity magnitude intensity within the flow has significantly diminished, with the apparent formation of a very weak upper circulation loop towards the free surface faintly visible. This corresponds to the instant previously identified in **Figure 5.10** (c), where flow continues motion for one revolution, approximately corresponding to 667 ms, before starting to decay.

Figure 5.11 (b – d) depict the contour maps of velocity magnitude after the restart of the impeller for T_{dwell} = 900, 9000 and 30,000 ms. This represents when the flow can be considered minimally decelerated at T_{dwell} = 900 ms (b), when the flow is almost fully static, T_{dwell} = 9000 ms (c) and a fully static system at T_{dwell} = 30,000 ms (d). **Figure 5.11** (b) demonstrates the slow initial increase of velocity magnitudes for T_{dwell} = 900 ms, with the increasing number of revolutions. Increasing to T_{dwell} = 9000 ms, shown in **Figure 5.11** (c), the strong acceleration with impeller motion is clearly seen. The strongest amplification is observed within the impeller region. The lower recirculation can be seen to form strongly initially, dominating the flow almost instantaneously from the restart in impeller motion. The upper recirculation is most strongly formed after three revolutions. As impeller rotation continues, this initial burst in velocity magnitudes is seen to diminish and the two circulation loops appear to equalise in intensity. This corresponds to the spike observed with the restart in impeller motion observed for approximately 4 revolutions before the steady state (**Figure 5.10** a). Further increasing to T_{dwell} = 30,000 ms, shown in **Figure 5.11** (d), a very similar profile to **Figure 5.11** (c) is presented, with a slightly smaller region of intense velocity magnitudes at t = 0 s from the impeller restart in motion.

5.2.2.2 Local shear rate

Of great interest, as highlighted previously, is the shear forces imparted within the bioreactor during intermittent agitation. To observe the impact of the transient between dwell phases, space-averaged results are presented for shear rate, $\langle\gamma^*_{max}\rangle/\pi N$, in **Figure 5.12**, calculated according to Equation 5.1. For reference, the value of the space-averaged $\langle\gamma^*_{max}\rangle/\pi N$ at φ = 0° for the continuous agitation mode is shown as a constant blue line at $\langle\gamma^*_{max}\rangle/\pi N$ = 0.295. As before, **Figure 5.12** (a) shows a spike in shear during the transient with the restart in impeller motion. This spike is shown to linearly increase with longer durations of dwell from +20 – 82 % the respective steady state value. For $T_{dwell} \geq$ 12,000 ms, when the flow is considered fully static, the maximum spike is nearly constant,

showing 8 % variation. During intermittent agitation, the average shear rate during the steady state in impeller rotation, is unexpectedly shown to be higher than the continuous reference. This may again be attributed to the interval time of T_{inv} = 30 s not being sufficient for the flow to fully develop and reach the same average steady state for continuous agitation. **Figure 5.12** (b) focuses upon the region at the start of the dwell phase. The black dashed line at Nt = 45 indicates the stop in impeller motion, the coloured dashed lines thereafter represent the restart in impeller motion for the corresponding colour dwell time. A second spike, as observed previously in **Figure 5.10** (b), is apparent at the start of the dwell phase, generating an average transient 5 % increase from the observed steady state before shear rate begins to decay.

The highest achieved local shear rate, $\langle\gamma_{max}\rangle/\pi N$ = 4.67, measured following the dwell phase from phase-resolved data (not space-averaged) is equivalent to dimensional shear stresses of τ = 0.220 dyn/cm^2. This is an approximate 235 % increase to maximum ensemble-averaged shear stresses and 78 % higher than phase-resolved shear stresses attained at φ = 45°, both from continuous agitation. This value, however, remains almost 5-fold lower than the values reported in literature to impair stem cell culture proliferation, although due to the sensitive nature of stem cells, the level of shear within the flow is most likely also a contributing factor to the differentiation pathway.

The contour maps in **Figure 5.13** (a – d) show the local shear rate at N = 90 rpm and T_{inv} = 30 s, measured at the end of the dwell for T_{dwell} = 1, 100, 500, 900 and 1500 ms (a) and for the first five revolutions with the restart in impeller rotation after the dwell for T_{dwell} = 900 ms (b), T_{dwell} = 9000 ms (c) and T_{dwell} = 30,000 ms (d). The shear maps at the end of the dwell for T_{dwell} = 1 – 100 ms (**Figure 5.13** a) show the higher regions of shear at the upper and lower edges of the impeller tip and the bioreactor wall. Longer dwell durations diminish the circulation loops, with a strong downward flow at r/T = 0.25, evident after 500 ms. As before, shear intensity is observed to most significantly decay after the first revolution for T_{dwell} = 900 and 1500 ms.

Figure 5.13 (b) demonstrates the restart in impeller motion following T_{dwell} = 900 ms to exhibit little acceleration and thus very little amplification in shear intensity. As the number of impeller revolutions during impeller rotation (Nt) increases, the shear rates can be seen to increase and reformation of the two circulation loops is evident. Increasing the dwell duration to T_{dwell} = 9000 ms, shown in **Figure 5.13** (c), the strong amplification of shear at t = 0 s is evident. The regions of strongest shear are confined to the impeller region and are shown to diminish with increasing Nt until an apparent steady state

between the fourth and fifth revolutions. T_{dwell} = 30,000 ms, shown in **Figure 5.13** (d), shows a very similar profile to **Figure 5.13** (c) with a slight reduction in shear at Nt = 1.

5.2.2.3 Periodic kinetic energy

Space-averaged periodic kinetic energy, $\langle k^* \rangle / {V_{tip}}^2$, are presented in **Figure 5.14** (a and b), calculated according to Equation 5.1. For reference, the value of the space-averaged $\langle k^* \rangle / {V_{tip}}^2$ at φ = 0° for continuous agitation mode is shown in blue at $\langle k^* \rangle / {V_{tip}}^2$ = 0.001. As previously observed in **Figure 5.10** and **Figure 5.12**, the spike occurring during the transient with the restart in impeller motion is shown to increase linearly, between 65 – 379 %, until $T_{dwell} \geq$ 12,000 ms, where reduced variation in the spike intensity is observed (19 %). As before, an unexpected increase in $\langle k^* \rangle / {V_{tip}}^2$ during the steady state can be observed between continuous and intermittent agitation. This may again be attributed to the interval time (T_{inv} = 30 s) not being sufficient for the flow to fully develop and reach the same average steady state for continuous agitation. **Figure 5.14** (b) again focuses upon the region at the start of the dwell phase, where an approximate 6.5 % reduction in the periodic kinetic energy from the steady state is now apparent. The second spike previously observed for shear rate and velocity magnitude with the stop in impeller motion is now absent.

The contour maps in **Figure 5.15** (a – d) show the periodic kinetic energy at N = 90 rpm and T_{inv} = 30 s, measured at the end of the dwell for T_{dwell} = 1, 100, 500, 900 and 1500 ms (a) and for the first five revolutions with the restart in impeller rotation after the dwell for T_{dwell} = 900 ms (b), T_{dwell} = 9000 ms (c) and T_{dwell} = 30,000 ms (d). The rapid decay of the kinetic energy is clearly shown (**Figure 5.15** a).

Figure 5.15 (b) demonstrates very little kinetic energy directly following the restart in impeller motion for T_{dwell} = 900 ms. Increasing Nt, the kinetic energy is shown to increase at the interface between the two reforming circulation loops and the impeller blade. Increasing the dwell duration to T_{dwell} = 9000 ms (**Figure 5.15** c), a significant initial increase in the kinetic energy content within the flow is apparent with the spike observed in **Figure 5.14** (a). The intensity of kinetic energy is shown to diminish with continued impeller rotation, with an apparent steady state reached at Nt = 4 – 5. Further extending the dwell duration to T_{dwell} = 30,000 ms, (**Figure 5.15** d), a very similar profile is observed to T_{dwell} = 9000 ms, with a reduced region of kinetic energy at Nt = 1, which then increases more significantly for approximately 3 revolutions until an apparent steady state.

5.2.2.4 Turbulent kinetic energy

The final parameter observed is the random fluctuating turbulent kinetic energy, $\langle k' \rangle / {V_{tip}}^2$. Observation of the space-averaged turbulent kinetic energy, $\langle k^{*\prime} \rangle / {V_{tip}}^2$, is shown in **Figure 5.16** (a – b). For reference, the continuous space-averaged value of $\langle k^{*\prime} \rangle / {V_{tip}}^2$ at φ = 0° is shown in blue at $\langle k^{*\prime} \rangle / {V_{tip}}^2$ = 0.00093. A significant spike with the restart in impeller motion is again observed to linearly increase with dwell duration (47 – 168 %) from the steady state until $T_{dwell} \geq$ 6,000 ms. For the longer dwell durations (T_{dwell} = 6,000 – 30,000 ms) less significant amplification of the spike (29.7 %) is observed. **Figure 5.16** (b) shows the turbulence level when impeller motion is stopped (Nt = 45) and a second spike is again apparent. This generates a 15 % transient increase from the observed steady state, approximately lasting 200 ms before rapidly decaying.

The contour maps in **Figure 5.17** (a – d) show the turbulent kinetic energy at N = 90 rpm and T_{inv} = 30 s, measured at the end of the dwell for $t = T_{dwell}$ = 1, 100, 500, 900 and 1500 ms (a) and for the first five revolutions with the restart in impeller rotation after the dwell for T_{dwell} = 900 ms (b), T_{dwell} = 9000 ms (c) and T_{dwell} = 30,000 ms (d). Turbulence is observed to rapidly decay after T_{dwell} = 100 ms and can be considered negligible as the dwell duration is increased. This corresponds to the transient 200 ms spike in turbulence observed previously.

Figure 5.17 (b) demonstrates almost negligible levels of turbulence levels with the restart in impeller motion following T_{dwell} = 900 ms. This is similar to what is observed for continuous agitation at the same phase angle (**Figure 5.8**), φ = 0°. Increasing to T_{dwell} = 9000 ms (**Figure 5.17** c), a significant increase in turbulence intensity is observed within the impeller region. The level of turbulence is shown to diminish with increasing Nt and an apparent steady state is observed for Nt = 4 – 5. Further extending the dwell until T_{dwell} = 30,000 ms, (**Figure 5.17** d), shows similar levels of turbulence to **Figure 5.17** (c), with a slight initial reduction in intensity, as previously observed for velocity magnitude, shear rate and periodic kinetic energy.

The main focus of this work was the determination of the impact intermittent agitation has upon the flow dynamics. Overall, the application of intermittent agitation has shown to generate a spike in velocity magnitude, shear rate, periodic kinetic energy and turbulence during the transient both at the start and end of the impeller dwell phase. The more intense impulse generated with the restart in impeller motion was shown to intensify with dwell duration until a static flow was achieved at $T_{dwell} \approx$ 12,000 ms, where the spike

intensity was observed to plateau. The following section seeks to characterise the mixing time within the DASGIP bioreactor and assess the impact intermittent agitation modes have upon the mixing dynamics.

5.2.3 Mixing dynamics

The next section of this chapter seeks to spatially and temporally characterise the mixing dynamics for continuous and intermittent agitation modes within the flat-bottom DASGIP configuration. Mixing time experiments using the DISMT methodology, previously discussed in Chapter 1 and detailed in Section 2.5, were undertaken for continuous rotational speeds of N = 75 – 120 rpm, and for intermittent conditions, T_{dwell} = 500 – 30,000 ms. Mixing was assessed within a single-phase as Grein *et al.* (2016) showed no change in determined mixing characteristics when measurement was performed with microcarriers at rotational speeds in excess of 70 rpm.

To illustrate measurement, **Figure 5.18** presents five snapshots taken at increasing time instants from the moment of feed insertion until a 'fully mixed' state is reached. The images shown in **Figure 5.18** (a - e) were not taken at specific time-intervals but selected so as to visualise the significant spatial evolution during the mixing process. At the initial stages of the experiment the drop of sodium hydroxide inserted into the flow, shown as dark blue, can be seen to break up and disperse within the bulk flow (**Figure 5.18** a - b). Insertion was made from the same port hole within the bioreactor headplate, thus this varied by a maximum radial distance of ≈ 10 mm, corresponding to the diameter of the port. As previously seen in Section 5.2.1, the regions of greatest shear and turbulence are locally concentrated within the impeller region and up the bioreactor walls. As the alkaline fluid (blue) is dispersed and reaches the bioreactor walls, neutralisation (yellow) can be seen to locally occur within the initial predominantly acidic solution (red) (**Figure 5.18** b - c). As the number of revolutions increases, the neutralised region at the bioreactor walls can be seen to expand towards the bulk of the bioreactor. The central region is shown to remain as a largely alkaline fluid (dark blue) and below the impeller remains acidic (**Figure 5.18** c - d). As mixing continues the reactor volume is eventually shown to be globally neutralised (yellow), finally achieving a 'well mixed' state (**Figure 5.18** e). The entrainment observed around the impeller shaft can be attributed to a swirling motion present in this region. Direct characterisation of this tangential swirling motion was not possible as PIV measurement was restricted to the *rz*-plane due to the impossibility to visually access the flow from the base of the bioreactor.

Similar to the method used in Rodriguez *et al.* (2013, 2014), the standard deviation of the green channel, σG, across the measurement volume in time was used to determine the mixing time, where a fully mixed steady state is considered when the maximum standard deviation of the readings was 5 %, i.e. $\sigma G = 0.05$. **Figure 5.19** (a – d) shows the variation of σG with the number of bioreactor revolutions, Nt, for continuous rotational speeds of N = 75, 90, 105 and 120 rpm, respectively. One of the five experimental repeats for each rotational speed is shown. At the beginning of each experiment the standard deviation of the green channel is zero (the system is homogeneous), which then rapidly increases with the base tracer addition until a peak standard deviation is reached. This peak represents the dispersion time, t_D, of the tracer and the initiation of the mixing process. Standard deviation then reduces and is shown to tend towards zero, plateauing at $\sigma G \approx 0.0121$. For the estimation of the mixing time, t_m, an exponential decay curve was fitted from the peak value in standard deviation, as indicated in **Figure 5.19**. This was performed such as to minimise the scatter of mixing time data due to signal noise. Overall it can be seen that the determined mixing number, Nt_m, and dispersion number, Nt_D, decreases with increasing rotational speed, indicating an increasingly quick transition to a well-mixed state from the increase in flow turbulence. Well mixed volumes are, in theory, achieved when the standard deviation reaches zero. The discrepancy ($\sigma G = 0 – 0.0121$) therefore represents the inherent error from the technique, which was found to vary by 10.5 % overall, showing good consistency for all experiments and repeats undertaken. This systematic error of the system is due to pixel inhomogeneity in the camera sensitivity.

Figure 5.20 shows the dispersion time, t_D (a) and dispersion number, Nt_D (b), for increasing rotational speeds, N = 75 – 120 rpm. Large variability is evident, expected to decrease with rotational speed as turbulence develops. Generally, the dispersion time and dispersion number are both shown to decrease with rotational speed, suggesting less completed revolutions are required for the tracer to become fully dispersed. **Figure 5.21** (a and b) show the average mixing time, t_m, and mixing number, Nt_m, respectively, for the four rotational speeds investigated. **Figure 5.21** (a) shows a linear decrease from t_m = 32 s for N = 75 rpm to t_m = 16 s for N = 120 rpm. Although a relatively large standard deviation is evident, ranging from 7 – 55 % of the mean, a general decrease with rotational speed can be observed. The number of revolutions required to achieve a well-mixed state, i.e. the mixing number, is shown in **Figure 5.21** (b). Mixing number can be used as an indicator of flow turbulence. For increasing Re a turbulent flow regime is considered when the mixing number is shown to plateau. **Figure 5.21** (b) shows an overall 20 %

decrease in Nt_m from N = 75 – 120 rpm. The level of variation reduces to 3.5 % from $Nt_{m(105)}$ = 33.14 to $Nt_{m(120)}$ = 31.97.

Kaiser *et al.* (2011) and van Eikenhorst *et al.* (2014) both determined mixing number for an axial flow marine impeller, Nt_m = 34 – 36.7 at N = 50 – 250 rpm and for V_w = 1.5 – 2.5 L. Liepe *et al.* (1998) defined mixing numbers of Nt_m = 30 and 24 for an axial flow pitched blade turbine and a radial flow Rushton turbine impeller. Works by Lee and Yianneskis (1997), Micheletti *et al.* (2003) and Ducci and Yianneskis (2007) determined mixing numbers in the range Nt_m = 17 - 47 for a radial flow Rushton turbine impeller, employing a range of rotational speeds and working volumes (V_w = 1 – 120 L and N = 50 – 2165 rpm). In addition to the impeller and tank configuration selected, the determined mixing number is also affected by the technique employed and the definition of considering a 'fully mixed' state. It must be noted in this work that lower working volumes and rotational speeds were used than those observed in the literature. Kaiser *et al.* (2011) and Grein *et al.* (2016) both observed a reduction in mixing number with lower fill volumes, although higher rotational speeds will decrease mixing number further until a fully turbulent flow is reached. As such, the determined mixing numbers in this work ($Nt_m \approx$ 32) are most closely within the ranges observed for an axial flow impeller (Nt_m = 30 - 37).

To spatially observe the mixing dynamics, the local mixing number map, reconstructed from the average of five experimental repeats, is shown in **Figure 5.22** (a – d), for rotational speeds N = 75 – 120 rpm. Generally, the maps show a region of slower mixing, qualitatively identified in **Figure 5.18**. The swirling motion induced by the rotation of the impeller causes entrapment of the acidic fluid close to the shaft, implying limited pH exchange. The non-dimensional mixing times in this region are ≈ 4 – 7-fold longer than those closest to the bioreactor wall and within the impeller region. The PIV measurements in **Figure 5.6** (b) and **Figure 5.8** (b) showed the regions of increased shear and turbulence occur at the interfaces between the trailing vortices and at the bioreactor walls. This creates a more 'active' mixing region, distinguishable from the slow mixing region. The mixing maps in **Figure 5.22** (a – d) show that increasing rotational speed markedly decreases the locally defined Nt_m in the bulk volume, however the slower mixing region appears to be less affected, becoming more distinguished with increasing speed.

To spatially observe the variation occurring between the five experimental repeats, the local standard deviation from the average mixing number, σNt_m, was used to construct the maps observed in **Figure 5.23** (a – d) for increasing rotational speeds, N = 75 – 120 rpm, respectively. Overall it can be seen that for the 5 experimental repeats performed at each

speed, the region of highest standard deviation occurs within the region closest to the impeller shaft, previously identified as the slow mixing region. Generally, as N is increased the region of standard deviation is confined. The space-averaged standard deviation is shown to reduce by approximately 73 % for N = 90 – 120 rpm.

Using a threshold value of Nt_m = 18, it was possible to distinguish between the fast and slow mixing regions and evaluate each independently. **Figure 5.24** (a – h) demonstrates this segregation: (a – d) represent mixing maps of the fast mixing region for N = 75 – 120 rpm; (e – h) represent the slow mixing region. Overall, there is an increase in the size of the fast mixing region, from 78 % to 96 % the total volume, with the increase in rotational speed (**Figure 5.24** a – d). Conversely, the slow mixing region in **Figure 5.24** (e – h), shows an 81 % decrease in size with increasing N. Although relatively low Reynolds are considered in these experiments (Re_i = 4500 - 7200), the significant decrease in the region of slow mixing with N, suggests that the flow is approaching turbulence.

Figure 5.25 (a and b) compares the standard deviation profiles of the green channel in the segregated fast mixing (blue) and slow mixing (red) regions, with the average result (green) for N = 75 and 120 rpm, respectively. It can be seen that for the lower rotational speed, N = 75 rpm (**Figure 5.25** a), the slow mixing region takes a longer time to fully disperse the tracer and shows a higher peak in standard deviation. This suggests that more colours are observed in this region, representing higher variation. The mixing number is also shown to increase. Increasing the rotational speed to N = 120 rpm (**Figure 5.25** b), the three mixing profiles superimpose initially, showing a similar dispersion number, with a slight increase observed once more for the mixing number in the slow mixing region.

As previously discussed in Chapter 1, cells cultured within a heterogeneous environment are exposed to spatial gradients in oxygen, pH, nutrients and temperature, which can compromise cell viability, proliferation, differentiation pathways, metabolism and overall yields achievable (Lara *et al.*, 2006). Ozturk (1996) observed cell lysis from locally elevated pH levels within the region of base addition due to the presence of slow mixing zones. Assessment of the mixing dynamics could aid in the selection of feed insertion or the operating conditions required to circumvent pH excursions. The biological studies undertaken by Correia *et al.* (2014) utilised a continuous rotational speed of N = 90 rpm. At this speed, approximately 14 % of the bioreactor volume can be considered a region of ‘slow mixing’, with a space-averaged mixing number of approximately Nt_m = 22 for the slow region and Nt_m = 13 for the fast mixing region. This suggests that feed addition within the flow will take approximately 13 revolutions to become fully mixed within the

bulk volume, and a further 9 revolutions to reach homogeneity in the remaining 14 % of the bioreactor volume. Considering the iPSC-differentiation protocol described by Correia *et al.* (2014) lasts for a total duration of 16 days, 9 days for differentiation and a further 7 days for purification, a concentration gradient persisting for up to ≈ 22 revolutions is not likely to be detrimental to the overall process. The application of intermittent agitation, shown in Chapter 3 to be beneficial towards iPSC-CM differentiation yields, may also further improve upon the characterised mixing dynamics.

For the estimation of the mixing time in the DASGIP bioreactor operating under intermittent modes of agitation, mixing was again defined at σG = 0.05. In this case however an exponential curve could not be fitted, as with the continuous process, due to the stop in impeller motion during measurement. **Figure 5.26** (a) plots the standard deviation of the green channel for continuous agitation (green), N = 90 rpm, and intermittent agitation (pink), T_{dwell} = 9000 ms, where the dwell occurs in the middle of the mixing process. The two curves show distinct changes in the mixing profile with intermittent agitation. Observing the standard deviation profile for intermittent agitation (pink), it is interesting to monitor the mixing process during the dwell phase, indicated between the black (start, t = 4.3 s) and blue (end, t = 13.3 s) vertical lines. The initial gradient, indicating mixing, is increased for the intermittent agitation mode, suggesting improved mixing as a result of the continued flow inertia and the observed spike in shear and turbulence at the start of the dwell, previously determined in Section 5.2.2 (images 2, 3, 4 and 5, shown). A noticeable deceleration in mixing can then be observed, coinciding with the decay of fluid motion (images 5 and 6). Approximately eight seconds from the impeller stop in motion, the mixing within the bioreactor begins to substantially slow (images 6 and 7), coinciding with the estimation of 9 – 12 s for the flow to become fully static. At this point, mixing is predicted to occur via diffusion. The restart in impeller motion at the end of the dwell phase shows the second significant spike in shear rate and turbulence (previously observed in Section 5.2.2), associated with a rapid decline in the mixing profile (images 7 and 8). Overall, mixing time is shown to decrease with intermittent agitation.

Figure 5.26 (b) shows four mixing profiles for increasing dwell durations, where the mixing time experiment begun from the same point in time. The plots shown indicate dispersion and mixing directly after the restart in impeller motion, thus exploiting the impact of the second, more intense spike in shear rate and turbulence. A rough approximation of the gradient for each curve until the peak (t = 0 – t_D) is; T_{dwell} = 1500

ms, gradient 0.02; T_{dwell} = 6000 ms, gradient 0.027; T_{dwell} = 20,000 ms, gradient 0.032; and T_{dwell} = 30,000 ms, gradient 0.0324. From the increasing gradients of each profile, it can be remarked that the rate of dispersion linearly increases with the magnitude of the spike in shear and turbulence, with similar dispersion occurring when the flow is fully static before impeller motion (T_{dwell} = 20,000 and 30,000 ms). Repeats were not made with the same feed insertion timed with the dwell, therefore an average could not be made and variation in mixing performance is expected. Nevertheless, the results presented are representative of the impact of intermittent motion and the timing between feed insertion and the dwell phase.

The moment of insertion with respect to the timing of the dwell phase should be carefully considered to improve the mixing time. **Figure 5.26** (a) shows a general case, where the dwell is occurring in the middle of the mixing process and a small increase in mixing was apparent in comparison to continuous agitation. **Figure 5.26** (b) shows when base insertion is made at the end of the dwell phase, making use of the larger spike in shear rate and turbulence, previously observed at this point in Section 5.2.2. Mixing is shown to be maximised with faster mixing times occurring with the larger spike intensity. The best insertion time from these plots can be estimated to be at the end of the dwell phase such as to fully exploit the second more intense spike observed in shear rate and turbulence, whilst avoiding any decay in flow velocities during the dwell.

The overall mixing times and mixing numbers, determined following five experimental sets with base insertion at various timepoints with respect to the dwell, is presented in **Figure 5.27** (a and b), respectively, for increasing dwell durations. According to the results obtained in Section 5.2.2, there is continued inertia within the flow for approximately one revolution before motion is shown to decay. This suggests that for T_{dwell} = 500 ms there is little deceleration in fluid motion, however the mixing time (a) and mixing number (b) are shown to significantly reduce by approximately 71 %. This can be attributed to the spikes introduced for shear rate and turbulence, with no loss in flow inertia. As T_{dwell} increases, flow inertia and thus mixing efficiency decays, however the amplification of the spike in shear and turbulence following the dwell phase also increases. The changes observed in measured mixing time and mixing number (**Figure 5.27** a and b) reflect this trade-off between flow deceleration, where mixing continues to occur but at a slower rate, and the increasing spike of shear and turbulence after the dwell, thus boosting mixing. Overall, mixing is improved in comparison to continuous agitation, although this is highly dependent on when the dwell occurs with respect to feed insertion.

Once the flow becomes fully static, from T_{dwell} = 12,000 - 30,000 ms, the observed spike in shear rate and turbulence plateaus and unless feed insertion is made at the end of the dwell phase, as previously observed, the mixing process occurring during the dwell will rely upon diffusion, thus t_m is observed to generally increase.

A final comparison of the average (a) and standard deviation (b) mixing maps for both continuous (left) and intermittent (right) agitation is made in **Figure 5.28**. Comparison is made using T_{dwell} = 500 ms as the shortest dwell condition investigated. **Figure 5.28** (a) shows the local mixing number for continuous agitation (left, N = 90 rpm) and intermittent agitation (right, N = 90 rpm, T_{inv} = 30s and T_{dwell} = 500 ms). The significant drop in mixing number, as previously shown in **Figure 5.27** (b), is immediately evident. **Figure 5.28** (b) shows the standard deviation within the five experimental repeats measured for both agitation conditions. Overall, the level of standard deviation is significantly reduced with intermittent agitation. Most noticeable is the apparent absence of the region of 'slow mixing', identified previously. This suggests that the introduction of intermittent agitation, from as low as T_{dwell} = 500 ms, breaks up the region of entrainment and entrapment around the impeller. This accounts for the significantly reduced level of standard deviation between measurements and the faster global mixing times observed.

5.3 Concluding remarks

When considering the beneficial impact of implementing intermittent agitation during cell culture, the main flow parameters of interest are the changes in shear rate, turbulence and mixing following a dwell phase of varying durations. This chapter sought to characterise the flow and mixing dynamics within the DASGIP bioreactor flat-bottom configuration, a system which has not previously been rigorously characterised, and to determine of impact intermittent agitation.

The flow characterisation studies showed the greatest regions of shear rate and turbulence during continuous agitation to occur within the trailing vortices formed, where the radial jet impinges upon the bioreactor wall and at the interface between the upper and lower trailing vortices. The application of intermittent agitation showed significant changes to the flow profiles characterised. Close observation of the flow at the beginning of the dwell phase showed a small transient spike in velocity magnitudes, shear rate and kinetic energy before the flow parameters were observed to decay. Measurement of fluid velocities during the dwell suggested that the flow has an inertia of one revolution. Increasing the dwell duration showed a static flow was reached at approximately $T_{dwell} \geq$ 12,000 ms.

With the restart in impeller motion after the dwell phase, a second more intense spike was observed, remaining elevated for approximately 4 – 5 revolutions. This was shown to linearly increase with dwell duration (T_{dwell} = 500 – 12,000 ms) until a static flow was achieved before the dwell ($T_{dwell} \geq$ 12,000 ms) and the observed spike intensity was shown to plateau.

The main focus of this work was the determination of the impact intermittent agitation has upon the flow dynamics and the subsequent biological outcomes. When considering the cell culture protocol described in Chapter 3, a dwell duration of 1500 ms was the longest explored. The flow characterisation of intermittent agitation observed an average 5 % spike in shear rate at the start of the dwell phase and a 20 - 43 % spike in shear with the restart in impeller motion following T_{dwell} = 500 - 1500 ms. Considering turbulence, an average 15 % spike in the level of turbulence is achieved at the start of the dwell phase and a 47 – 65 % spike is observed with the restart in impeller motion for T_{dwell} = 500 - 1500 ms, respectively. Further increasing the dwell duration significantly intensifies the second spike observed, however the impact that this may have upon differentiation efficiency cannot be assessed without further biological studies to correlate.

The mixing time measurements characterised the mixing dynamics within the DASGIP bioreactor, operating under continuous agitation mode at four rotational speeds. Mixing times, t_m = 32.11 – 15.98 s and mixing number, Nt_m = 40.14 – 31.97, were determined for the increasing rotational speeds. The final two measurements of mixing number, $Nt_{m(105)}$ = 33.14 and $Nt_{m(120)}$ = 31.97, showed 3.5 % variation between them, thus it can be considered that the flow is approaching a fully turbulent regime. Spatial assessment of the mixing number showed a region of slower mixing around the rotating impeller shaft. Observing the spatial variation in standard deviation between the five experimental repeats, the region of entrainment and slowest mixing caused the highest level of fluctuation between measurements, generally decreasing in size and the level of variation with the increase in rotational speed. This again suggests the flow is approaching turbulence with the apparent decrease in standard deviation with speed.

The introduction of intermittent agitation overall showed a beneficial impact upon the mixing processes within the bioreactor. The two observed spikes for the shear rate and turbulence were demonstrated to have a perceptible positive impact upon the mixing profile, however the timing of feed insertion with respect to the dwell phase affects the extent of mixing enhancement this may have. As dwell duration increased, two conflicting elements were apparent: the decline in mixing efficiency with the deceleration

of flow, until a static flow where mixing will occur via diffusion; and the increasing spike intensity in shear rate and turbulence, at the end of the dwell phase. When feed insertion is timed with the end of the dwell phase, fully exploiting the second, more intense spike in shear rate and turbulence, mixing was shown to be improved. This impact can be maximised with the larger spike intensities associated to longer dwell durations. In this manner, it was also possible to avoid the detrimental impact of longer dwell durations decelerating fluid motion should mixing occur before the next dwell phase. Furthermore, the introduction of intermittent agitation was shown to disrupt the swirling slow mixing region around the rotating impeller shaft, resulting in a significant reduction in standard deviation between experimental repeats, and also enhancing the mixing time.

[244]

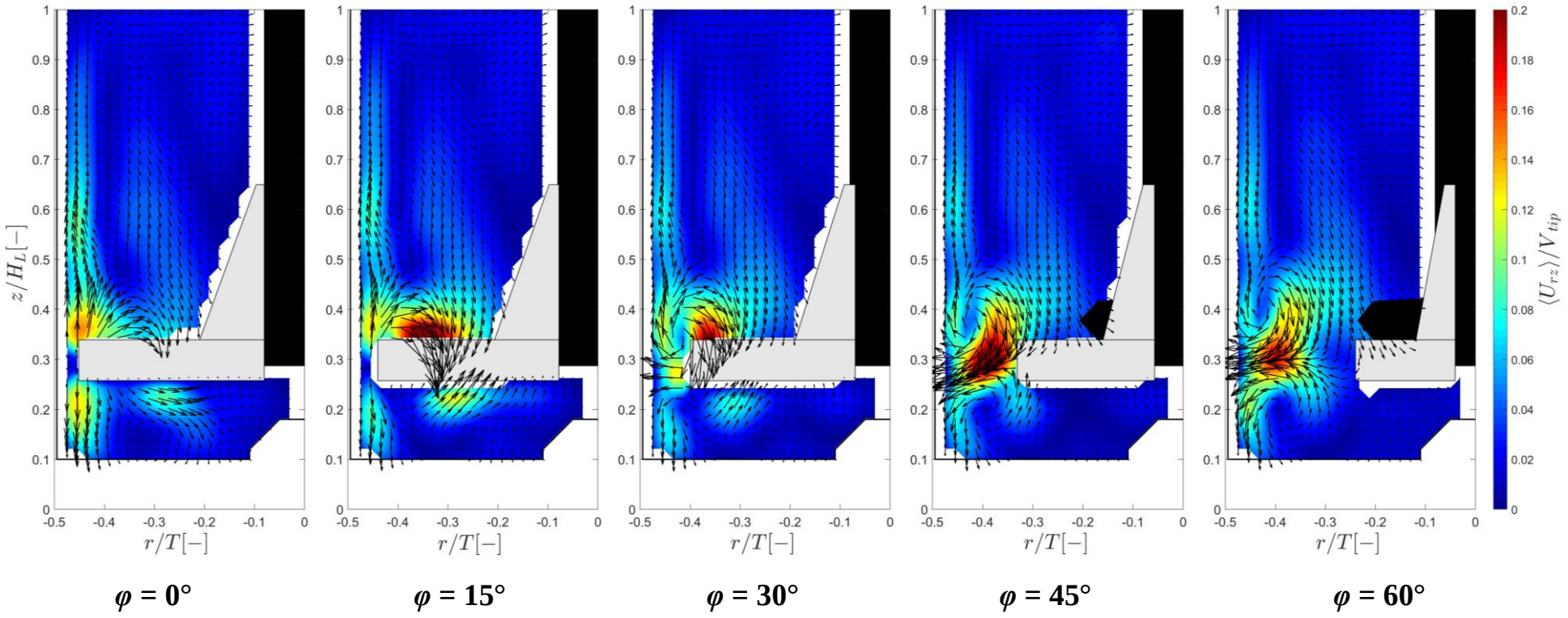

Figure 5.1 Contour maps of phase-resolved velocity magnitudes for continuous agitation, $\langle U_{rz}\rangle/V_{tip}$, N = 90 rpm, φ = 0 - 60°.

(a)

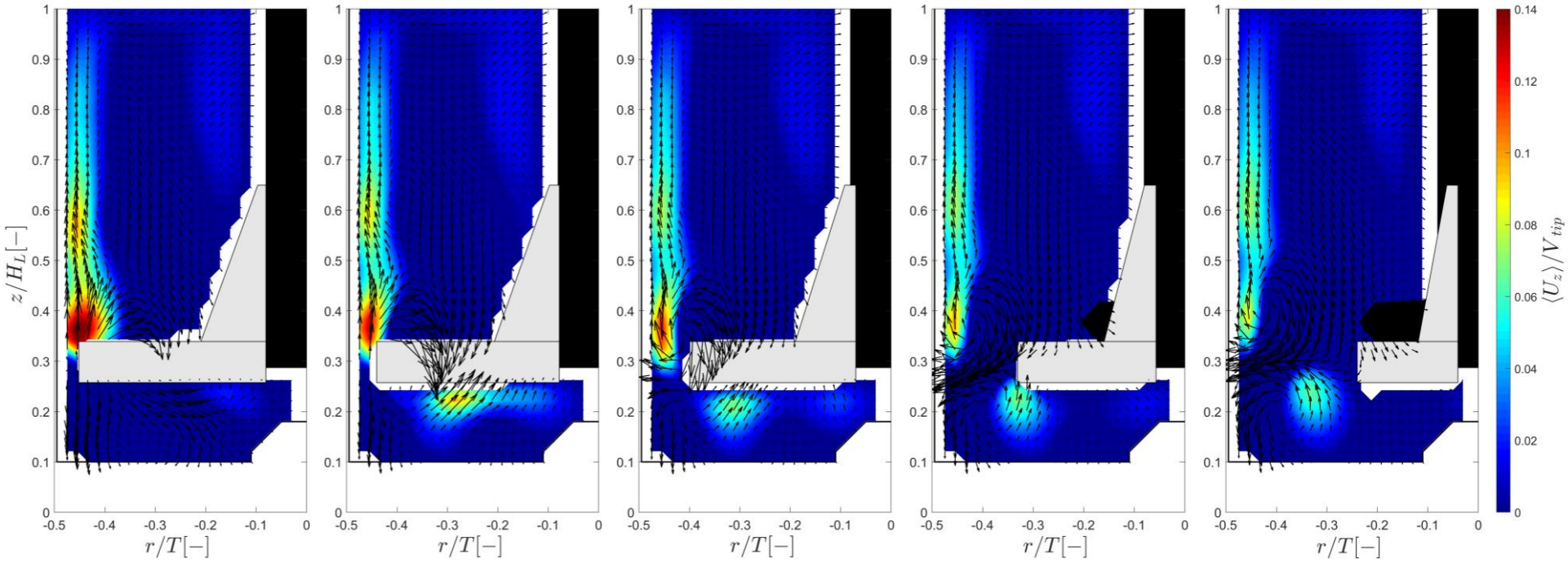

φ = 0° **φ = 15°** **φ = 30°** **φ = 45°** **φ = 60°**

[245]

(b)

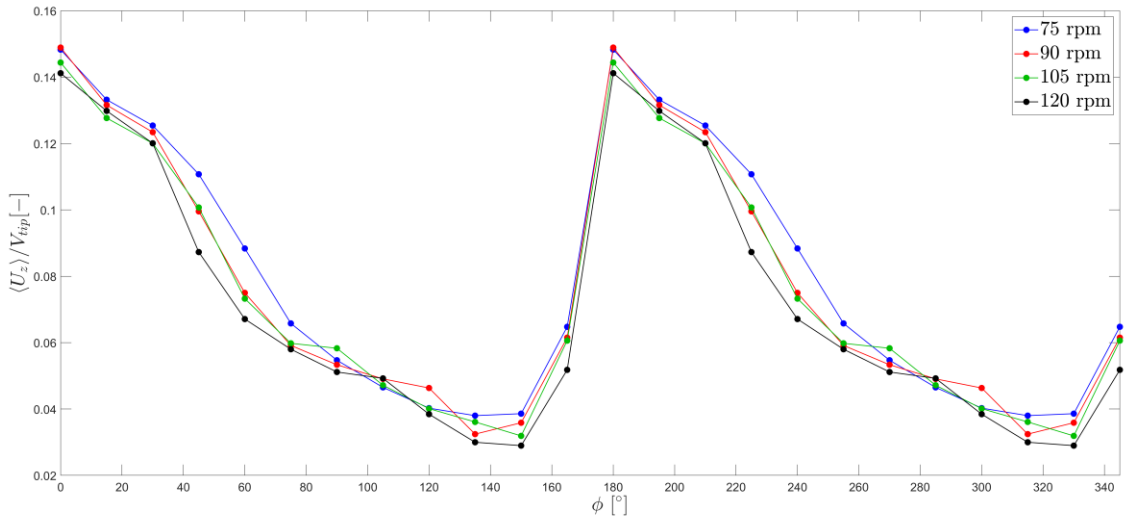

Figure 5.2 Phase-resolved non-dimensional axial velocity component, $\langle U_z \rangle / V_{tip}$: (a) contour maps of the axial velocity for continuous agitation modes, N = 90 rpm, φ = 0 - 60°; (b) axial velocities for a single point above impeller blade tip (r/T = 0.45, z/H_L = 0.35) for N = 75 – 120 rpm, φ = 0 – 345°.

(a)

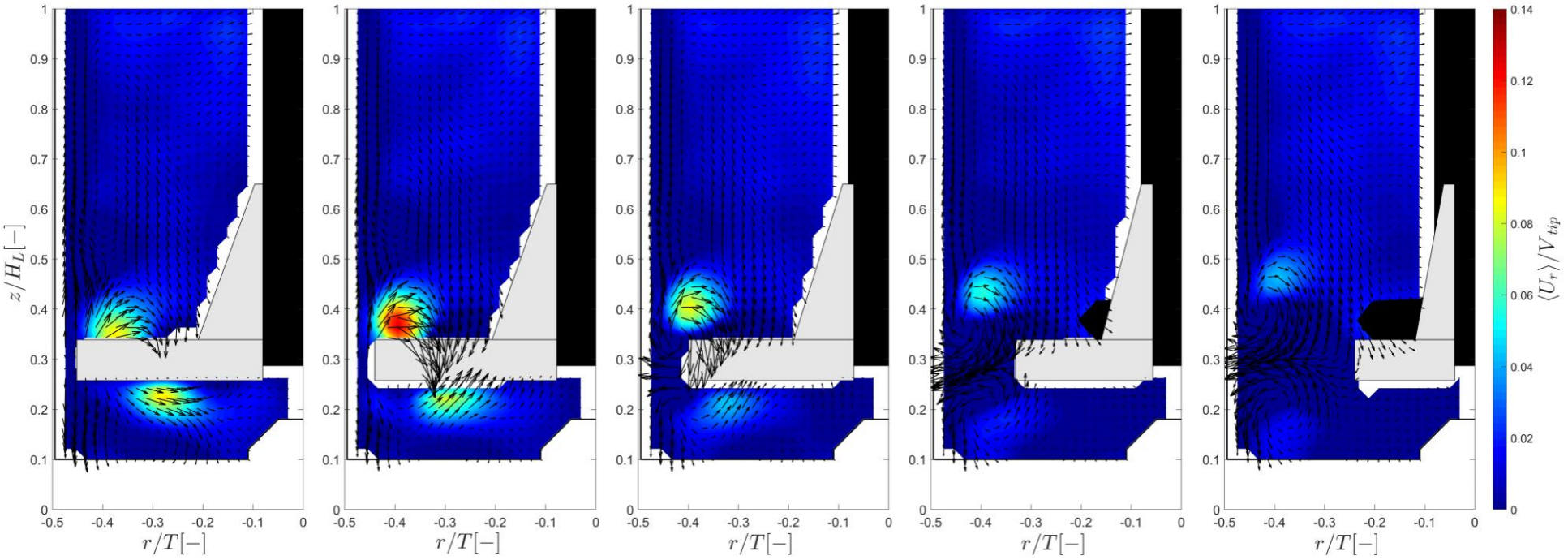

φ = 0° **φ = 15°** **φ = 30°** **φ = 45°** **φ = 60°**

[247]

(b)

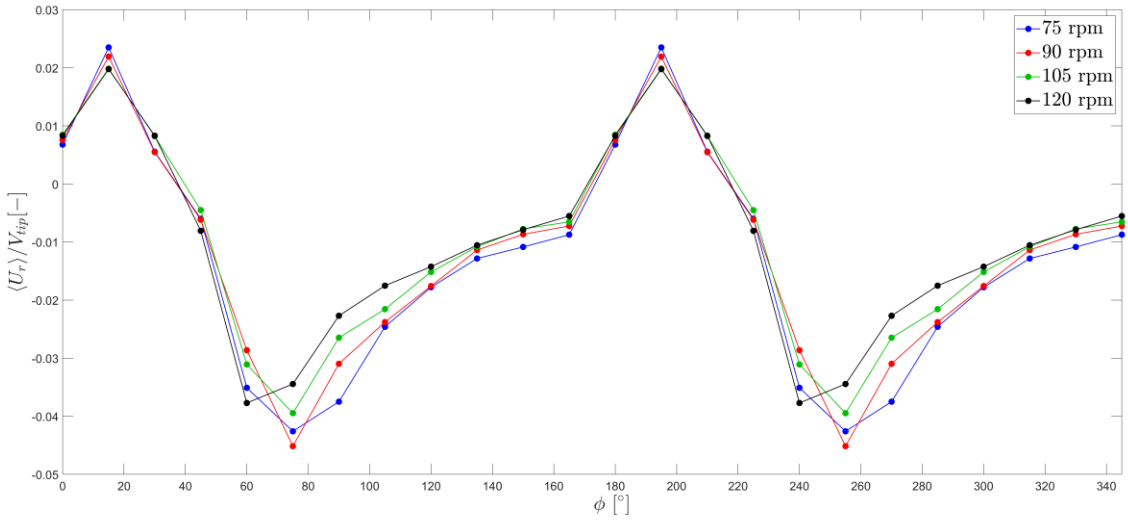

Figure 5.3 Phase-resolved non-dimensional radial velocity component, $\langle U_r \rangle / V_{tip}$: (a) contour maps of the radial velocity for continuous agitation modes, N = 90 rpm, φ = 0 - 60°; (b) radial velocities for a single point above impeller blade tip (r/T = 0.45, z/H_L = 0.35) for N = 75 – 120 rpm, φ = 0 – 345°.

(a)

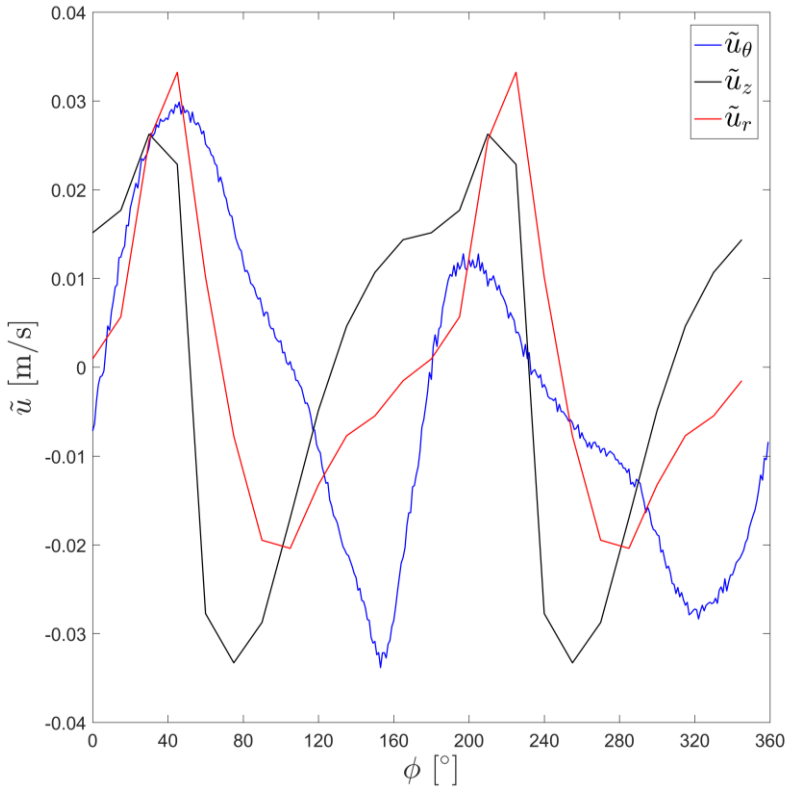

(b)

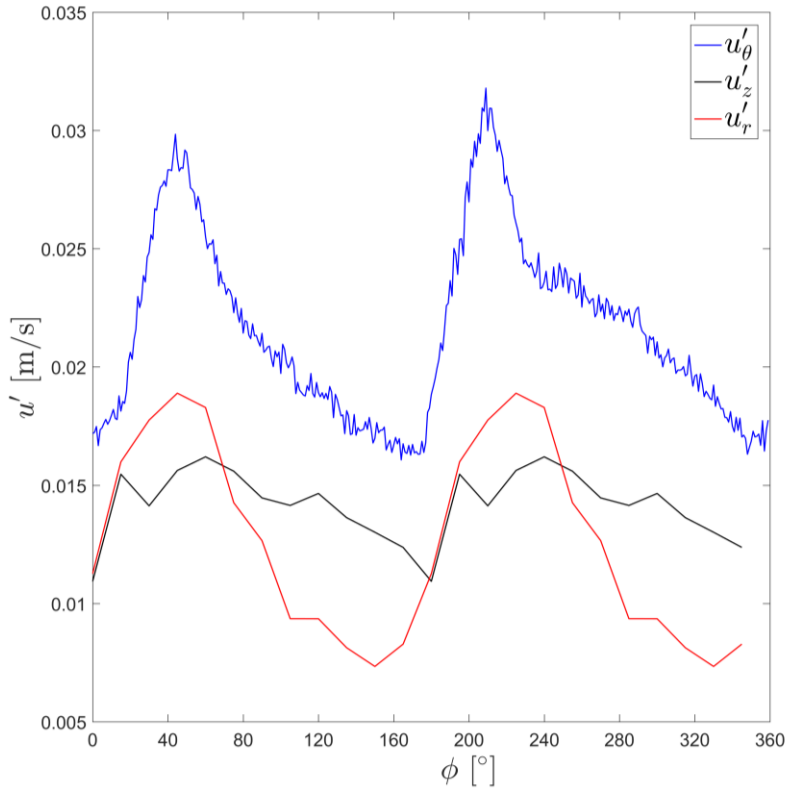

Figure 5.4 Phase-resolved analysis of the dimensional tangential (blue), axial (black) and radial (red) velocity components at point A (r/T = 0.35 and z/H_L = 0.28) , N = 90 rpm: (a) periodic velocity fluctuations, $\tilde{u}$; (b) turbulent velocity fluctuations, u'.

[250]

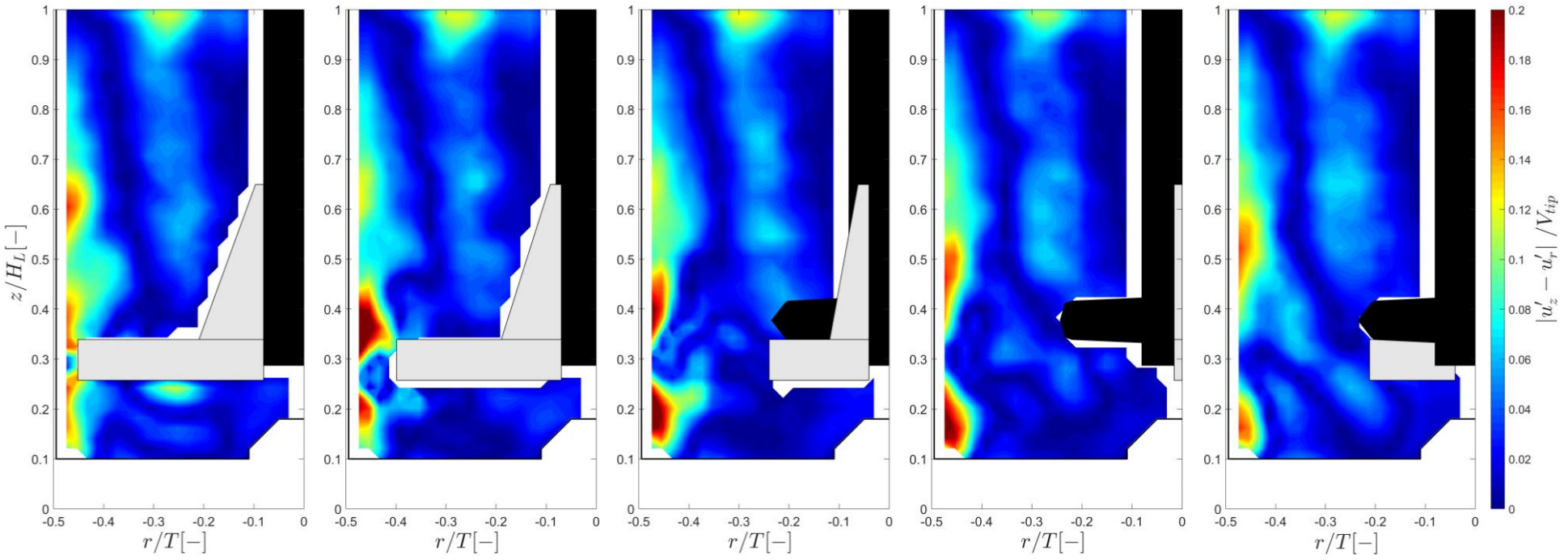

Figure 5.5 Contour maps of the absolute difference between the axial and radial turbulence levels, $|(u'_z - u'_r)|/V_{tip}$, at φ = 0 - 120° and N = 90 rpm.

(a)

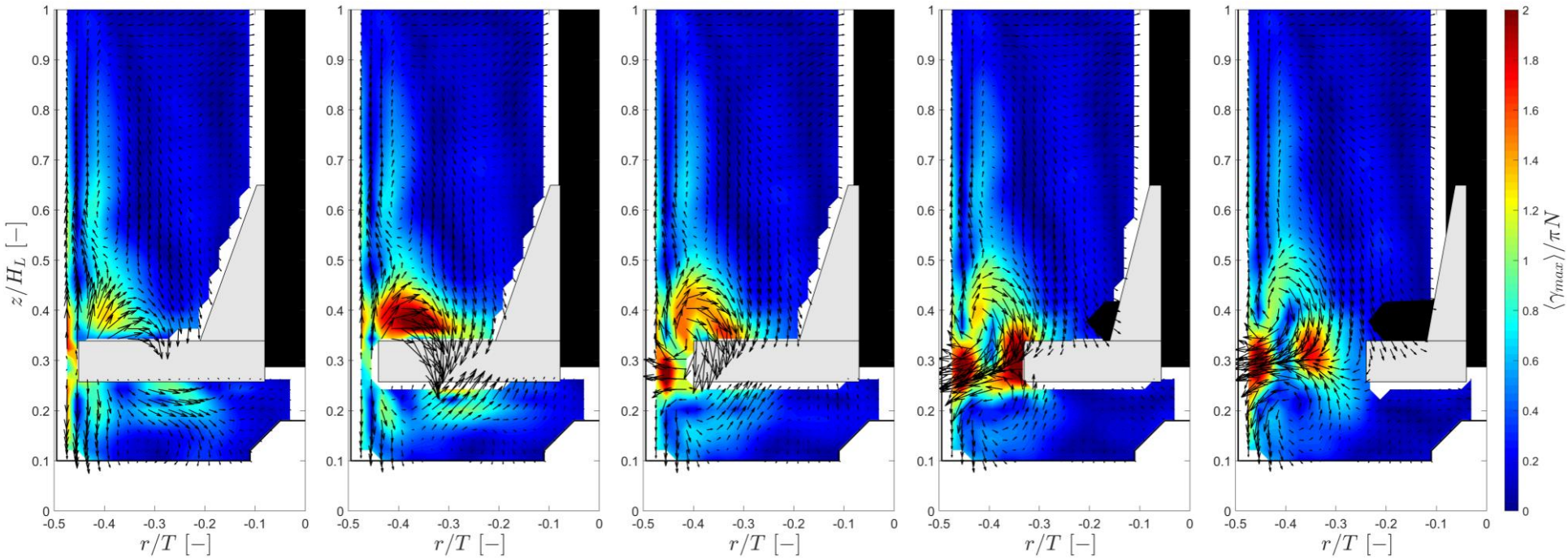

φ = 0° **φ = 15°** **φ = 30°** **φ = 45°** **φ = 60°**

[251]

(b)

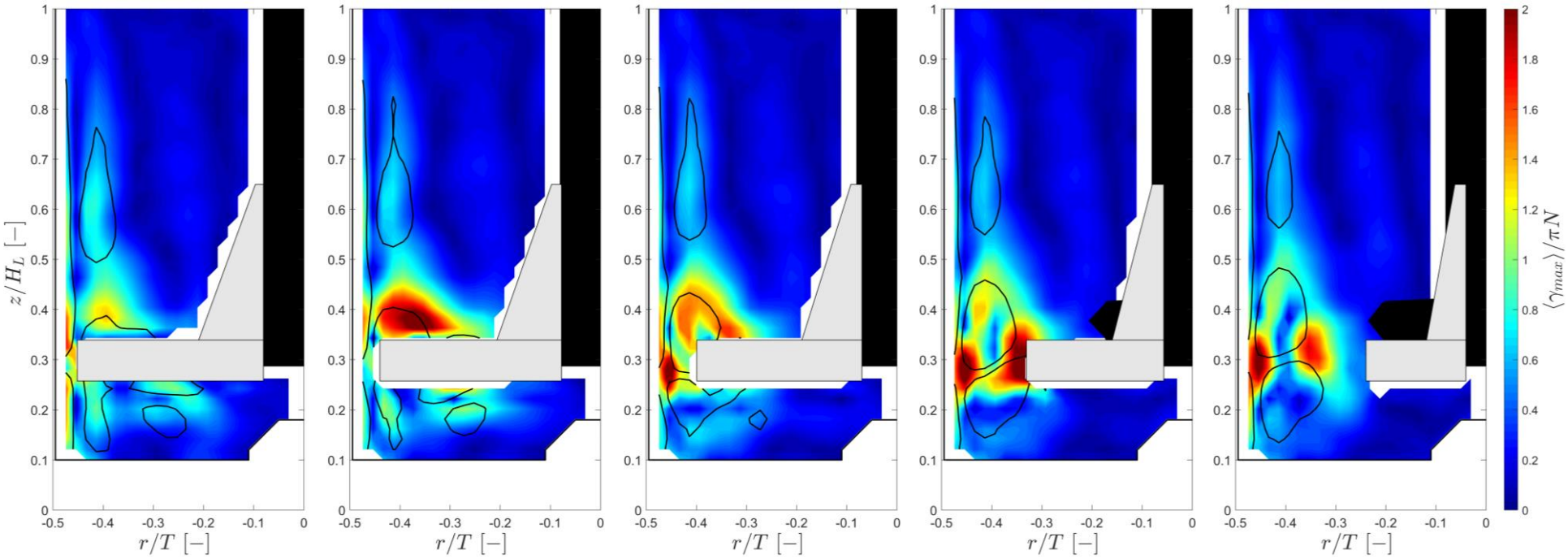

φ = 0° **φ = 15°** **φ = 30°** **φ = 45°** **φ = 60°**

[252]

(c)

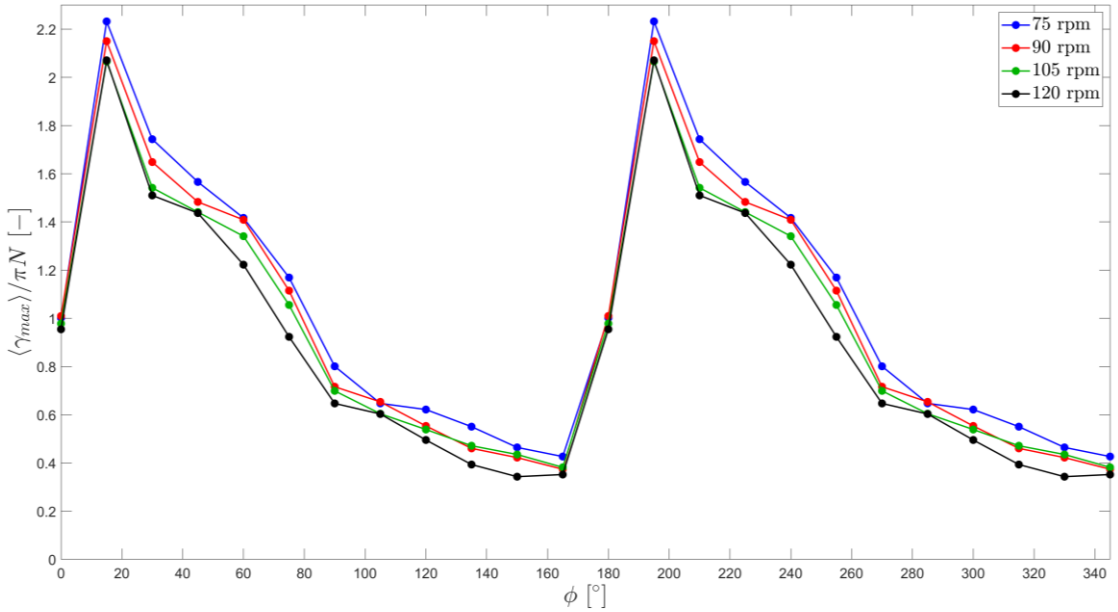

Figure 5.6 Phase-resolved non-dimensional local shear rate, $\langle\gamma_{max}\rangle/\pi N$: (a) contour maps of shear rate with vector fields, N = 90 rpm, φ = 0 - 60°; (b) contour maps of shear rate with delineated trailing vortices, N = 90 rpm, φ = 0 - 60°; (c) local shear rate for a single point at the edge of the top vortex (r/T = 0.35, z/H_L = 0.35) for N = 75 – 120 rpm, φ = 0 – 345°.

(a)

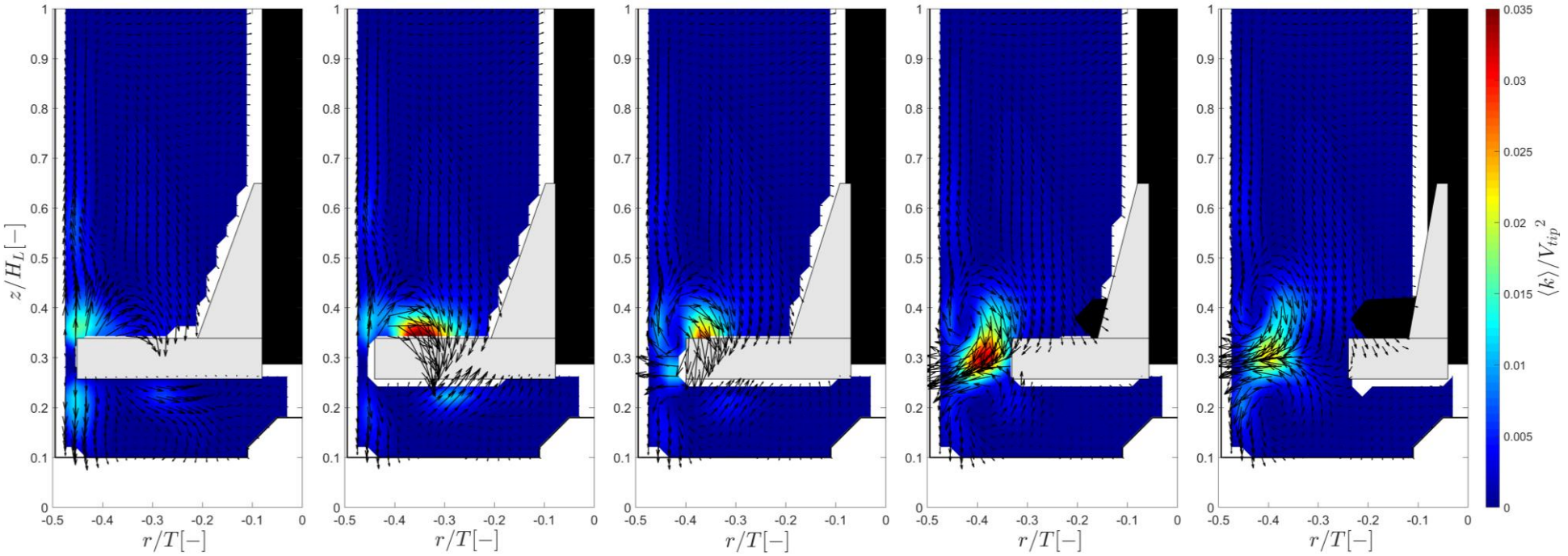

φ = 0° **φ = 15°** **φ = 30°** **φ = 45°** **φ = 60°**

[254]

(b)

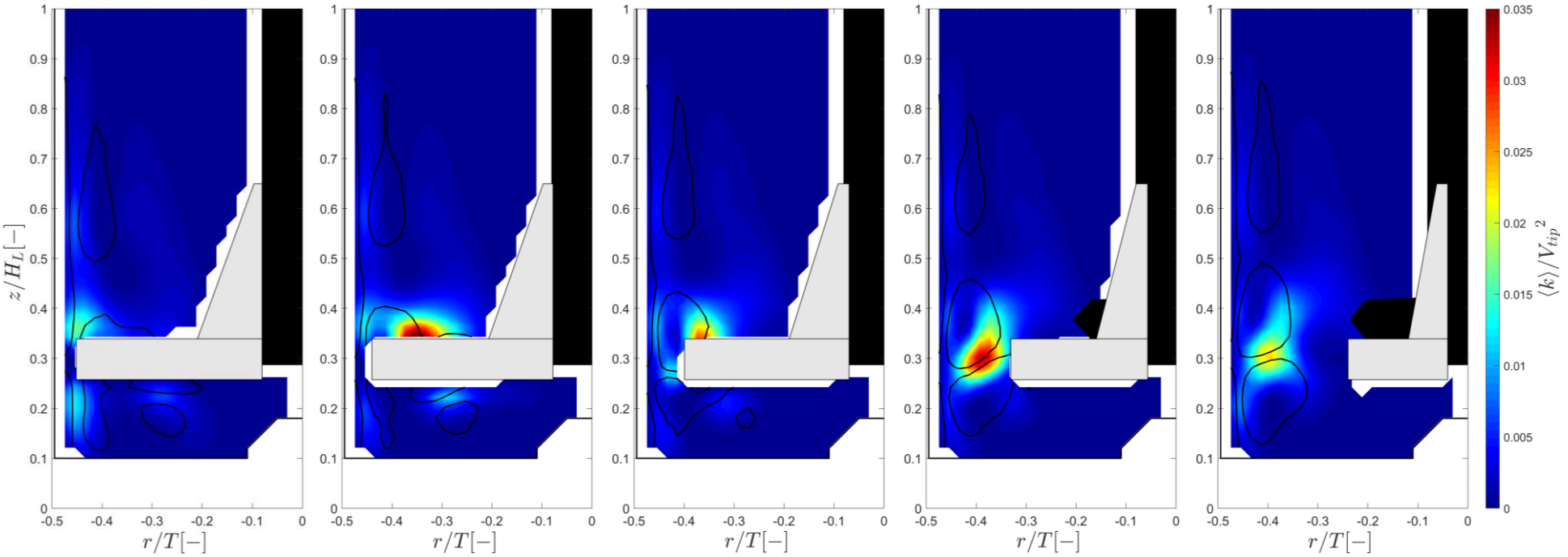

φ = 0° **φ = 15°** **φ = 30°** **φ = 45°** **φ = 60°**

[255]

(c)

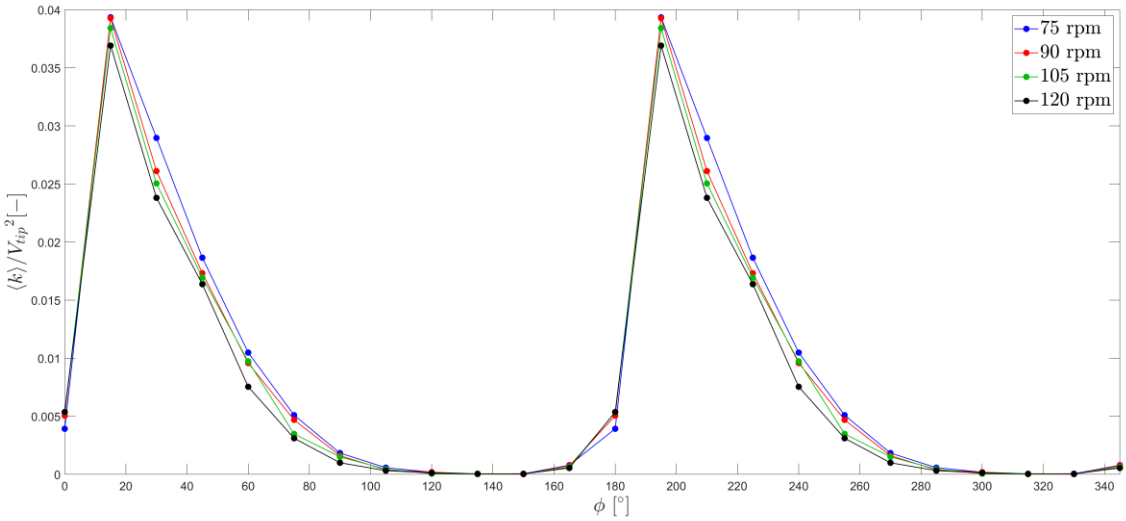

Figure 5.7 Phase-resolved non-dimensional periodic kinetic energy, $\langle k \rangle / V_{tip}{}^2$: (a) contour maps of kinetic energy with vector fields, N = 90 rpm, φ = 0 - 60°; (b) contour maps of kinetic energy with delineated trailing vortices, N = 90 rpm, φ = 0 - 60°; (c) periodic kinetic energy for a single point at the edge of the top vortex (r/T = 0.35, z/H_L = 0.35) for N = 75 – 120 rpm, φ = 0 – 345°.

(a)

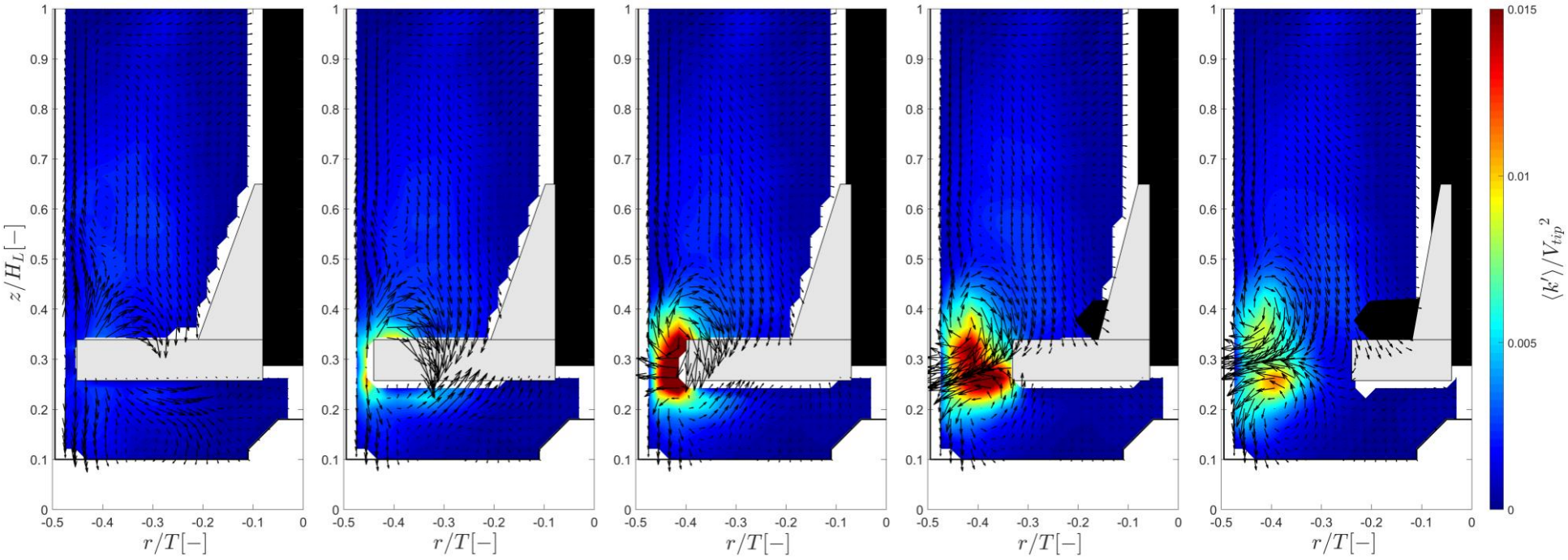

φ = 0° **φ = 15°** **φ = 30°** **φ = 45°** **φ = 60°**

[257]

(b)

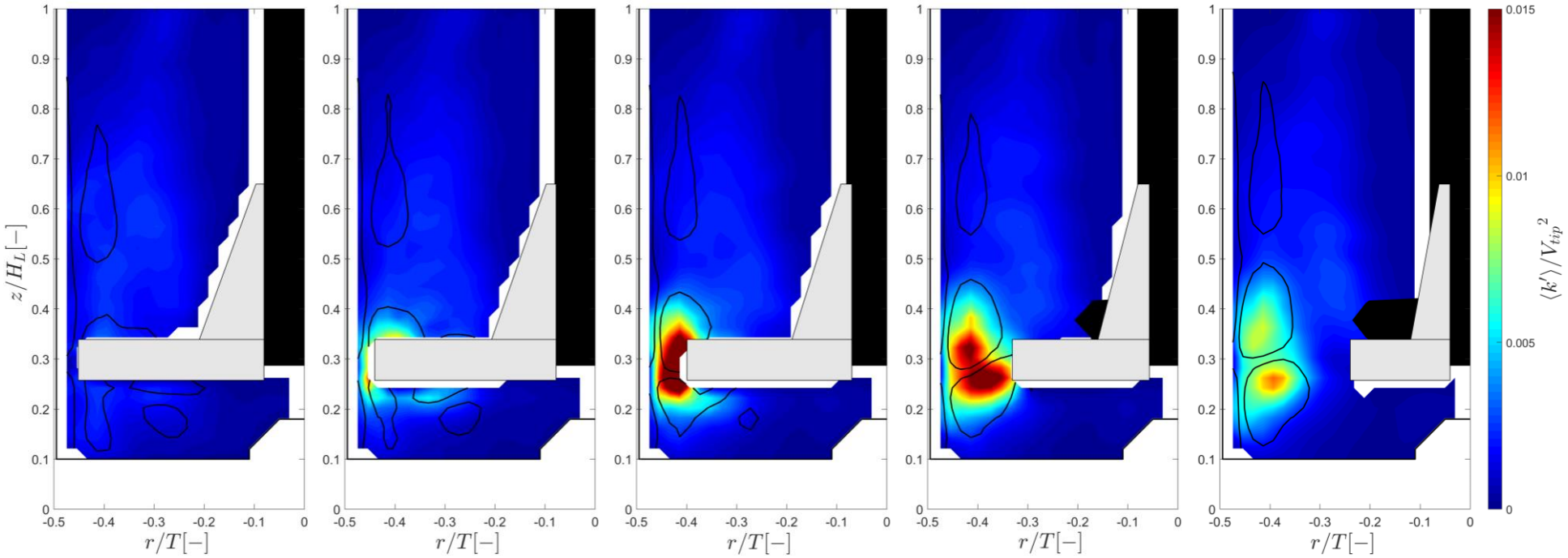

φ = 0° **φ = 15°** **φ = 30°** **φ = 45°** **φ = 60°**

[258]

(c)

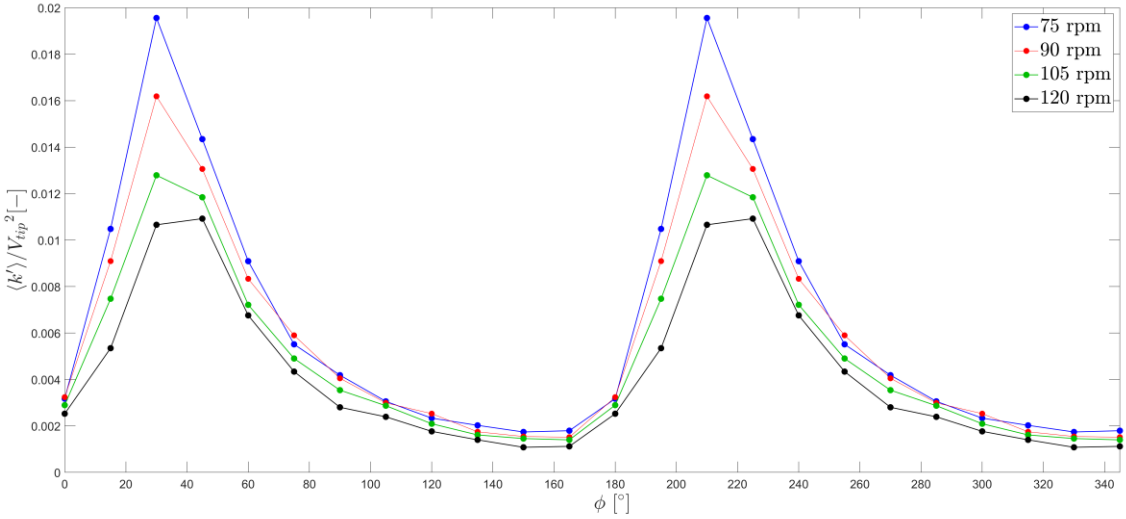

Figure 5.8 Phase-resolved non-dimensional turbulent kinetic energy, $\langle k' \rangle / V_{tip}{}^2$: (a) contour maps of turbulent kinetic energy with vector fields, N = 90 rpm, φ = 0 - 60°; (b) contour maps of turbulent kinetic energy with delineated trailing vortices, N = 90 rpm, φ = 0 - 60°; (c) turbulence for a single point within the top vortex (r/T = 0.425, z/H_L = 0.35) for N = 75 – 120 rpm, φ = 0 – 345°.

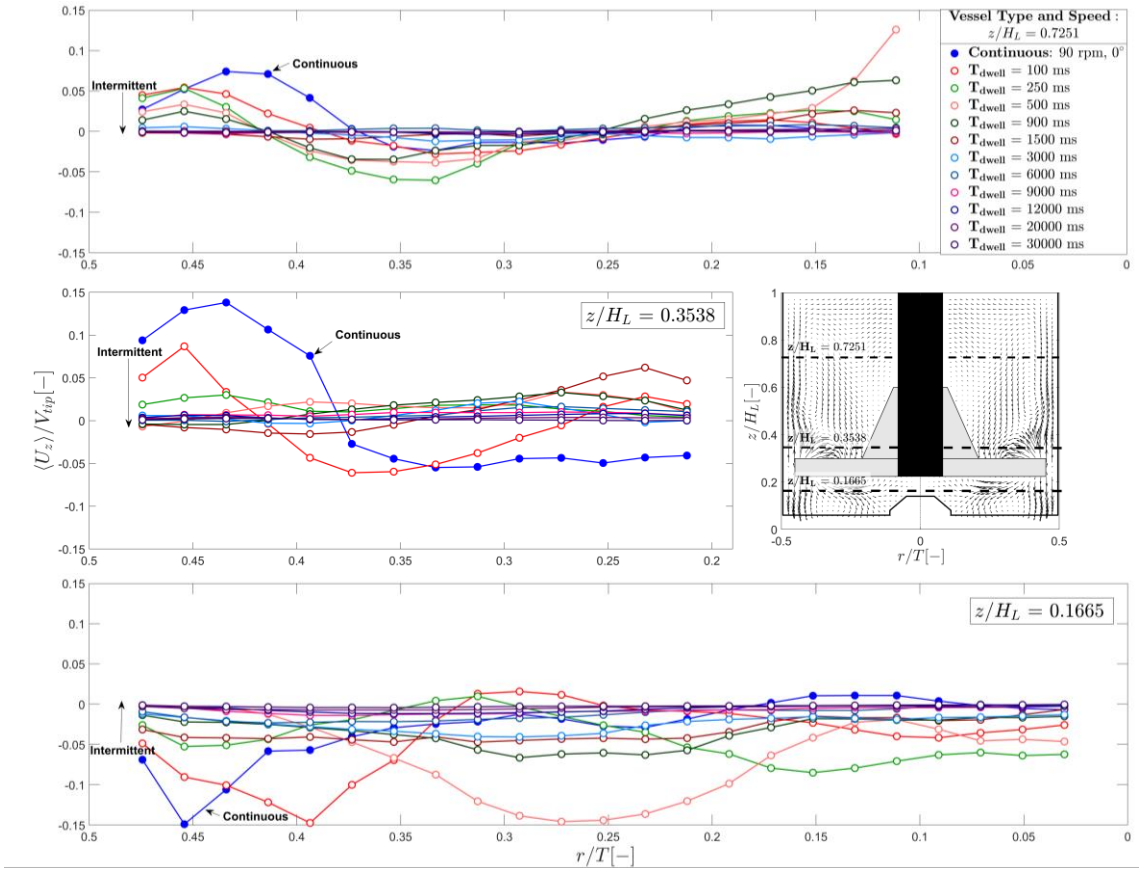

Figure 5.9 Comparison of phase-resolved non-dimensional axial velocity profiles, $\langle U_z \rangle / V_{tip}$, for continuous and intermittent agitation modes at three elevations, z/H_L = 0.7251, 0.3538 and 0.1665.

(a)

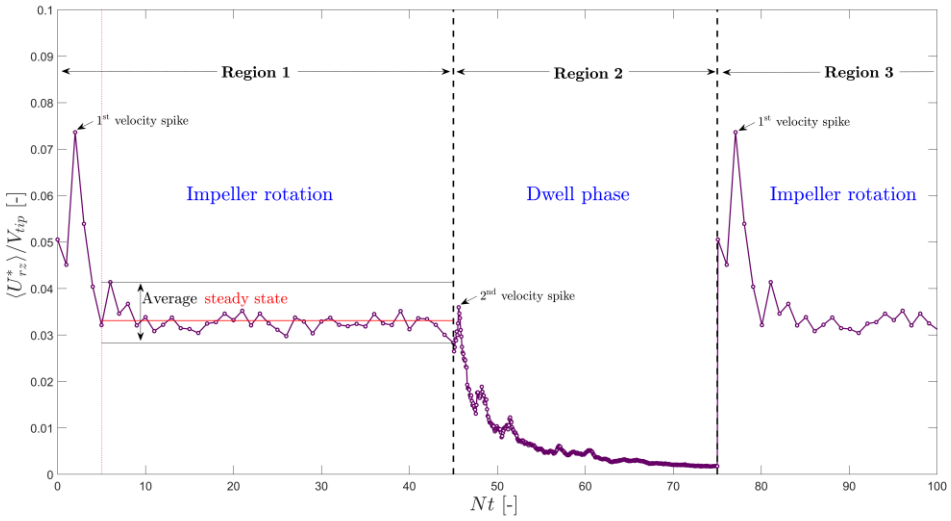
Region 1
Region 2
Region 3
1st velocity spike
Impeller rotation
Dwell phase
Impeller rotation
Average steady state
2nd velocity spike
1st velocity spike
$\langle U^*_{rz} \rangle / V_{tip}$ [-]
Nt [-]

(b)

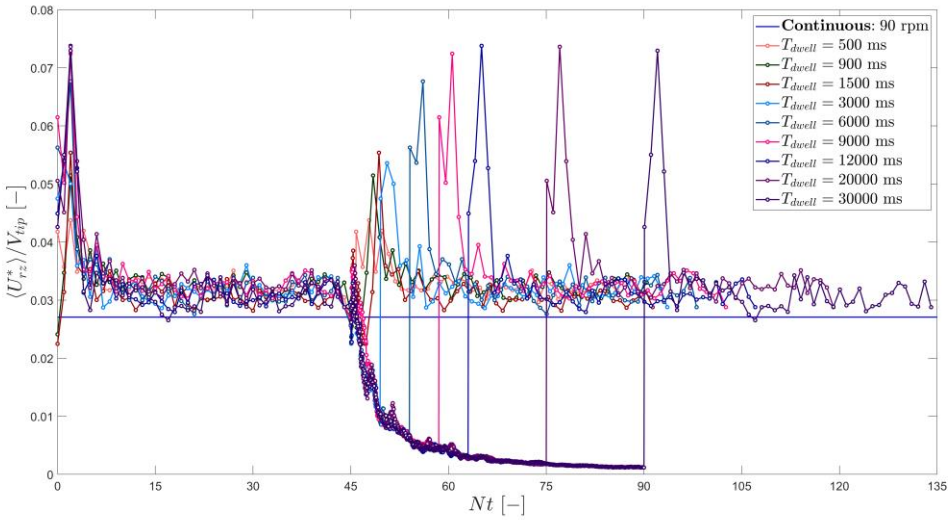
Continuous: 90 rpm
T_{dwell} = 500 ms
T_{dwell} = 900 ms
T_{dwell} = 1500 ms
T_{dwell} = 3000 ms
T_{dwell} = 6000 ms
T_{dwell} = 9000 ms
T_{dwell} = 12000 ms
T_{dwell} = 20000 ms
T_{dwell} = 30000 ms
$\langle U^*_{rz} \rangle / V_{tip}$ [−]
Nt [−]

(c)

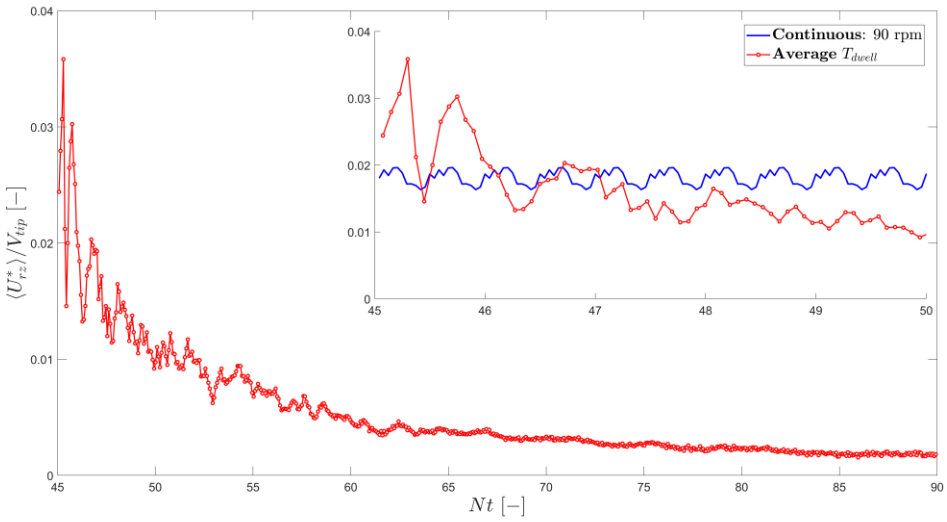

Figure 5.10 Space-averaged phase-resolved velocity magnitudes, $\langle U^*_{rz} \rangle / V_{tip}$ for continuous and intermittent agitation: (a) intermittent agitation, T_{dwell} = 20,000 ms; (b) overall space-averaged velocity magnitude for intermittent and continuous agitation; (c) space-averaged velocity magnitude during the dwell, averaged for all dwell conditions (red) and continuous agitation (blue, see inset).

(a)

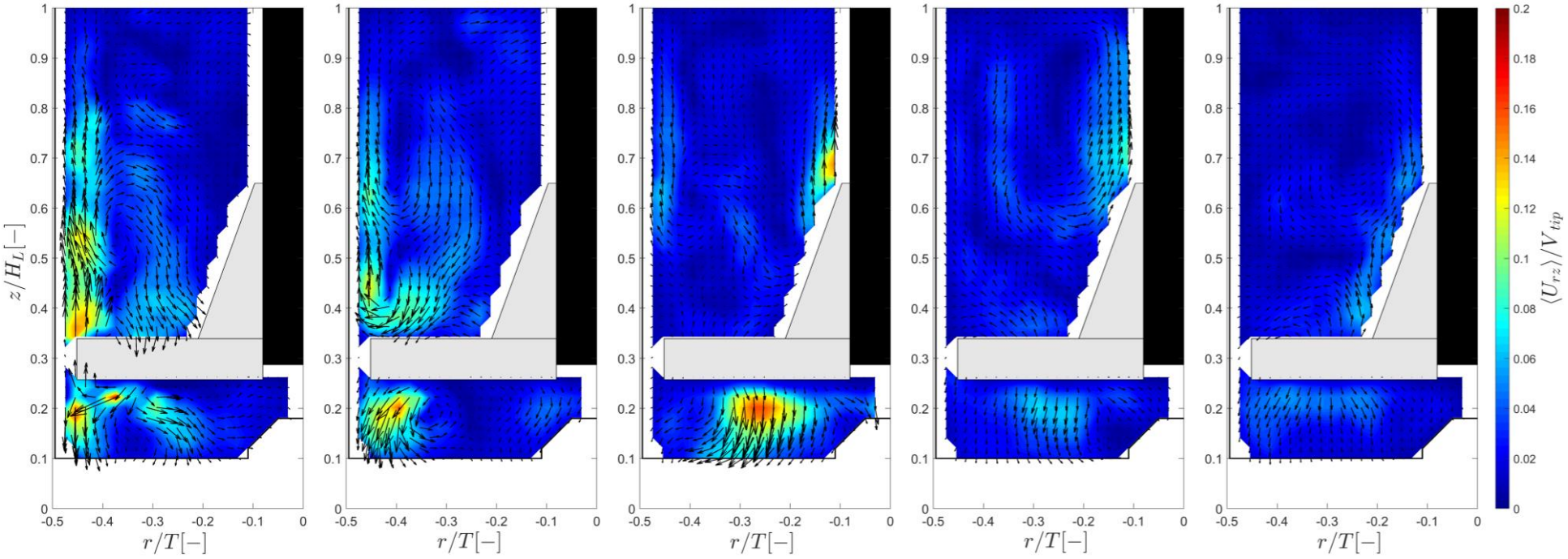

T_{dwell} = 1 ms **T_{dwell} = 100 ms** **T_{dwell} = 500 ms** **T_{dwell} = 900 ms** **T_{dwell} = 1500 ms**

[263]

(b)

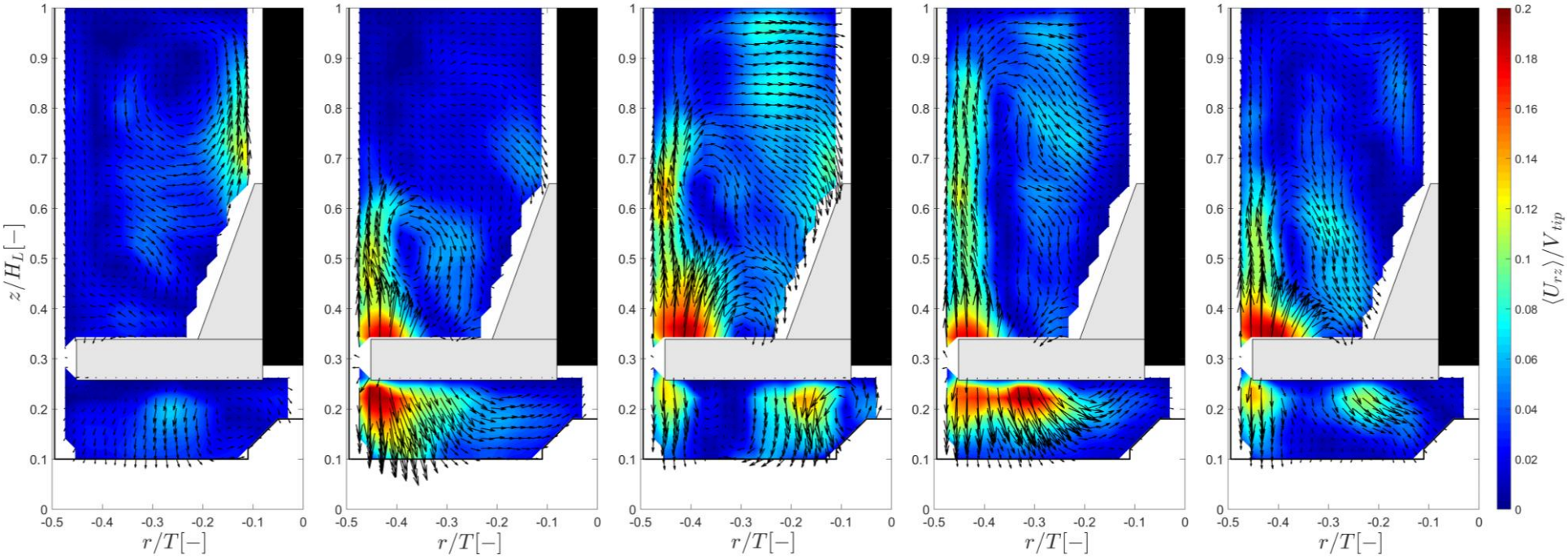

***Nt* = 1** ***Nt* = 2** ***Nt* = 3** ***Nt* = 4** ***Nt* = 5**

[264]

(c)

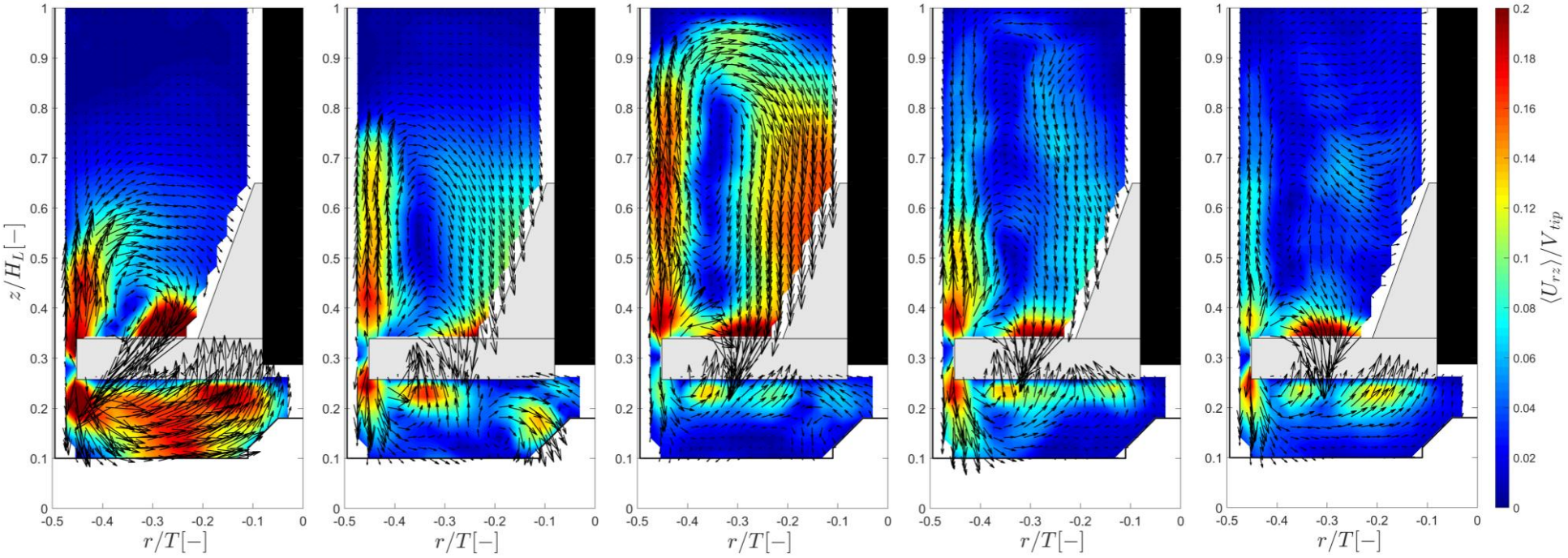

***Nt* = 1** ***Nt* = 2** ***Nt* = 3** ***Nt* = 4** ***Nt* = 5**

[265]

(d)

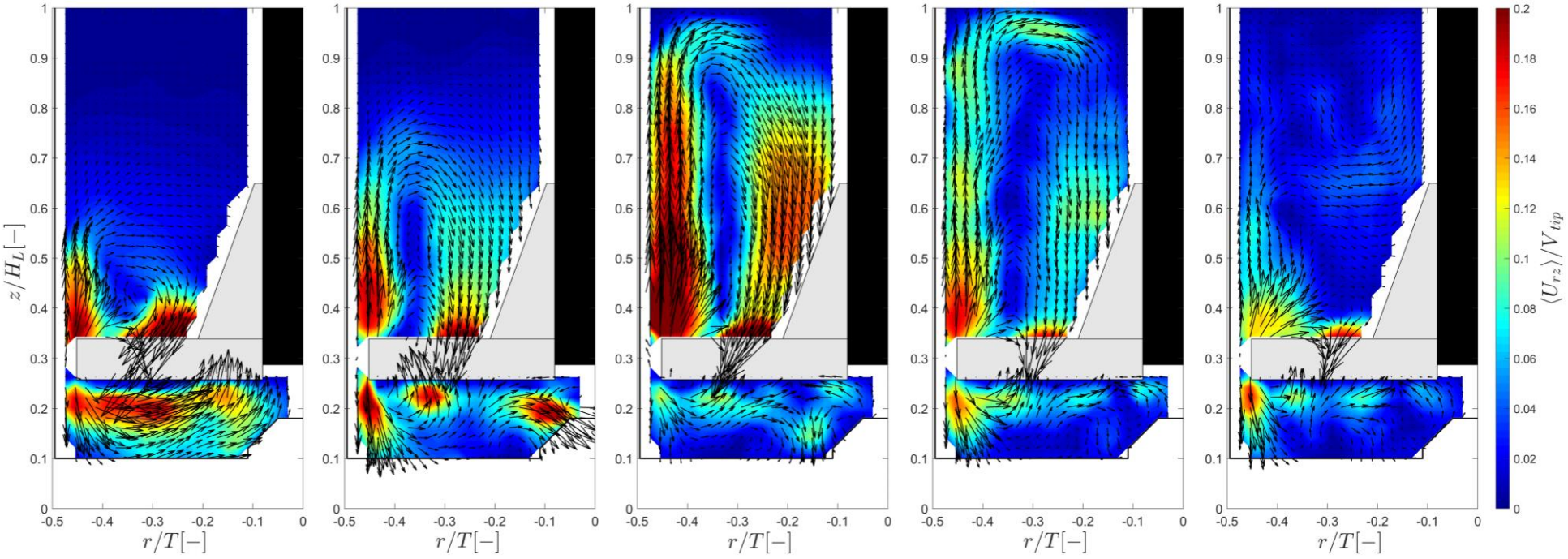

Figure 5.11 Contour maps of velocity magnitude with vector fields, N = 90 rpm: (a) during the dwell, T_{dwell} = 1 – 1500 ms; (b - d) Nt = 1 – 5 revolutions after the dwell, T_{dwell} = 900 ms (b); T_{dwell} = 9000 ms (c); T_{dwell} = 30,000 ms (d).

(a)

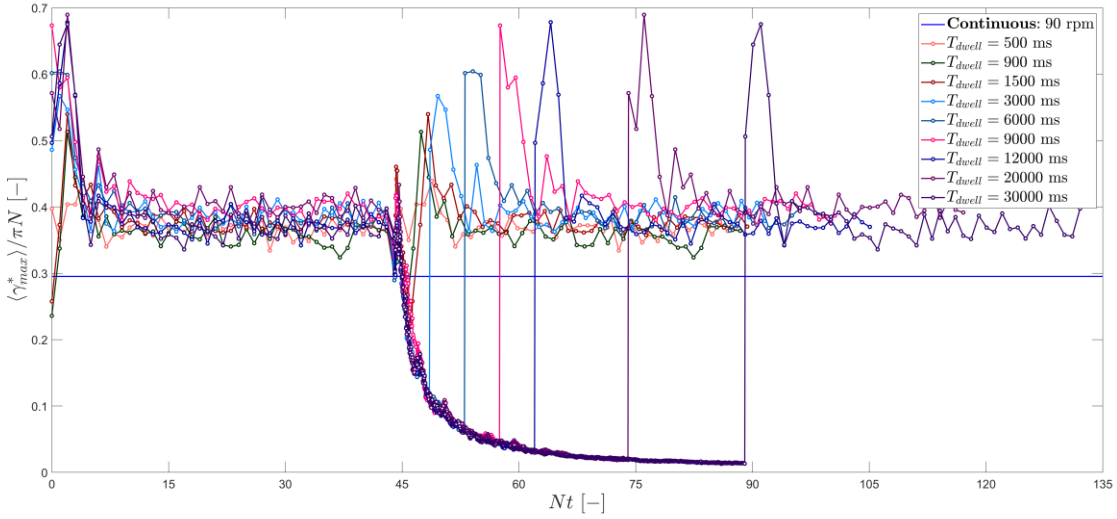

(b)

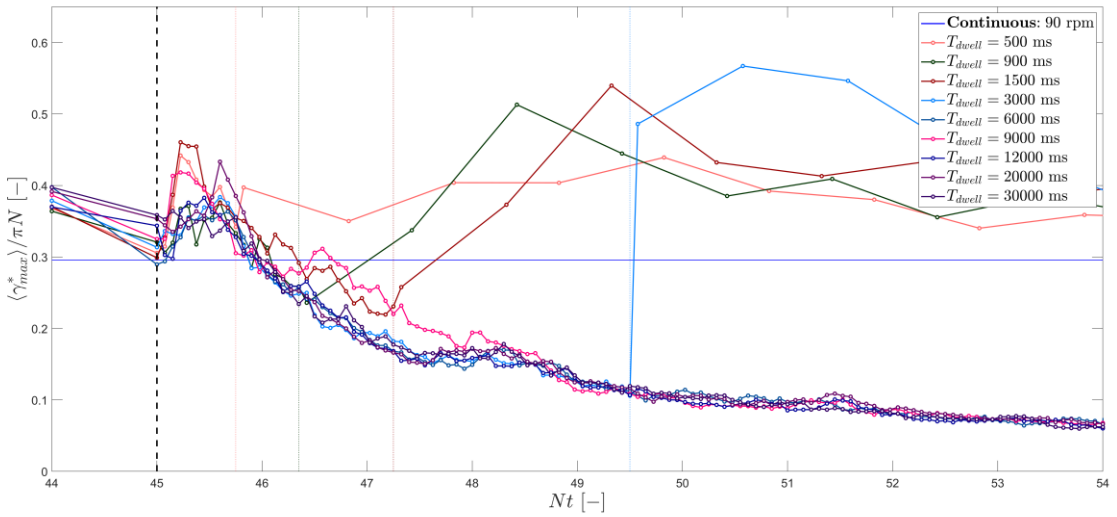

Figure 5.12 Space-averaged phase-resolved local shear rate, $\langle \gamma^*_{max} \rangle / \pi N$, for continuous and intermittent agitation: (a) overall space-averaged shear rate for intermittent and continuous agitation; (b) space-averaged shear rate at the start of the intermittent dwell phase, Nt = 45.

(a)

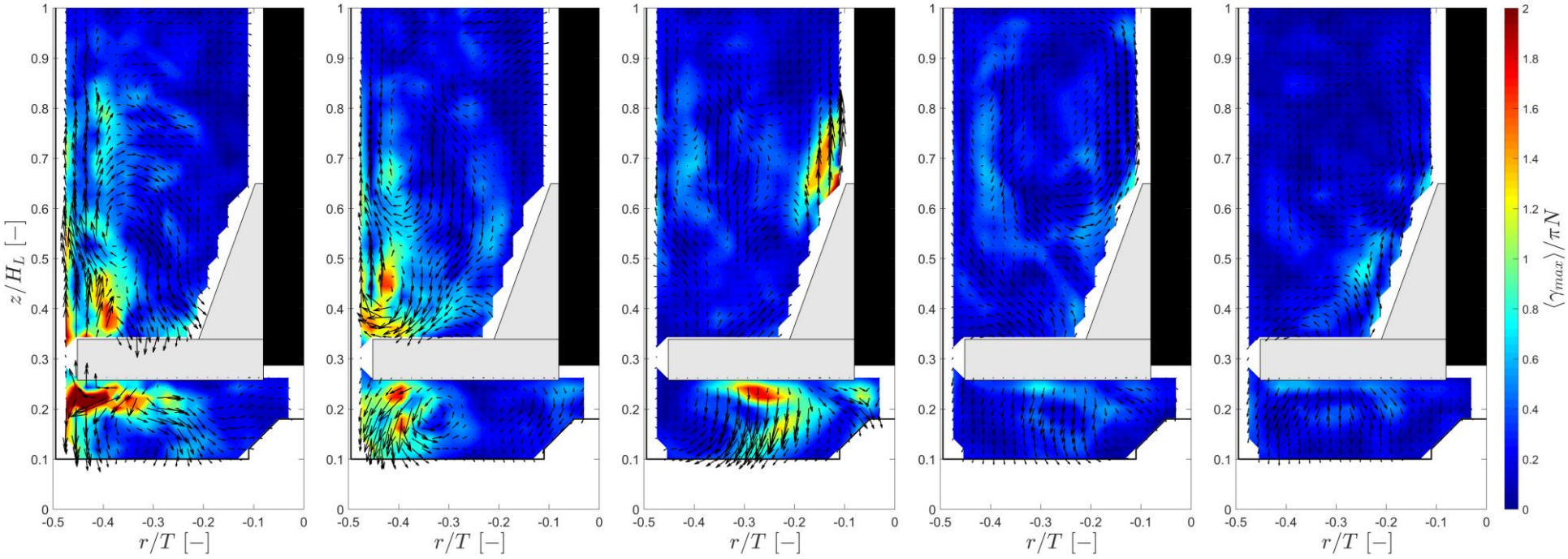

***T*_{dwell} = 1 ms** | ***T*_{dwell} = 100 ms** | ***T*_{dwell} = 500 ms** | ***T*_{dwell} = 900 ms** | ***T*_{dwell} = 1500 ms**

[268]

(b)

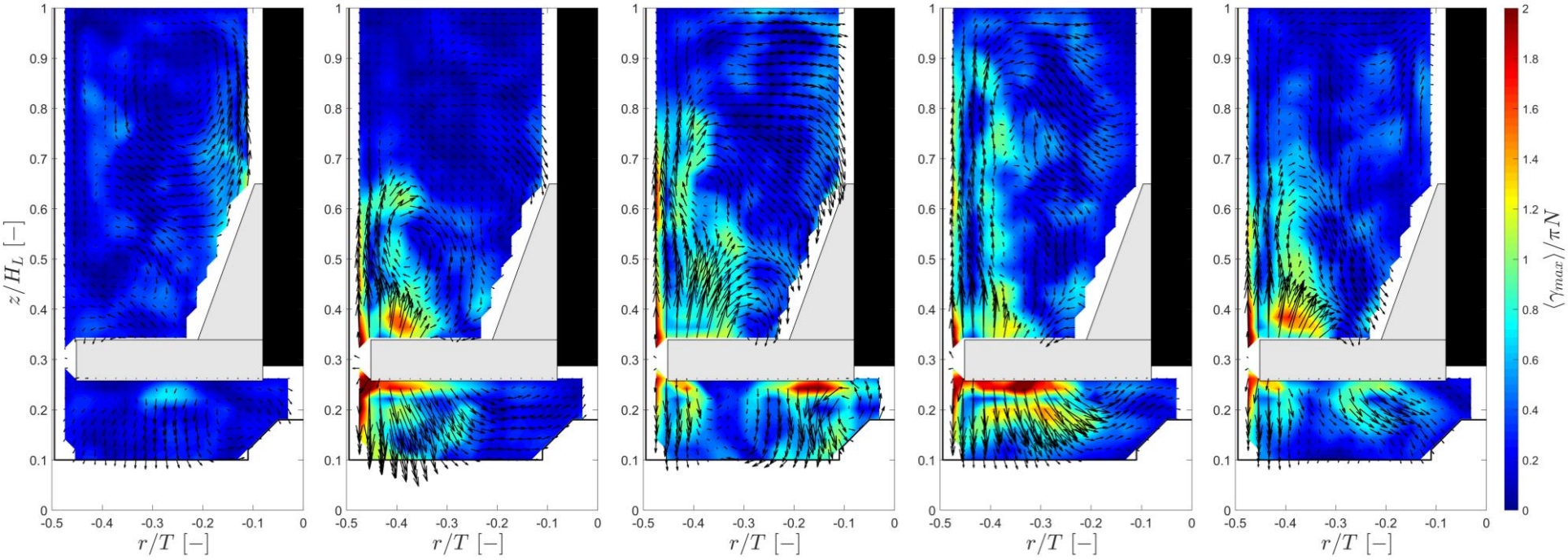

***Nt* = 1** ***Nt* = 2** ***Nt* = 3** ***Nt* = 4** ***Nt* = 5**

[269]

(c)

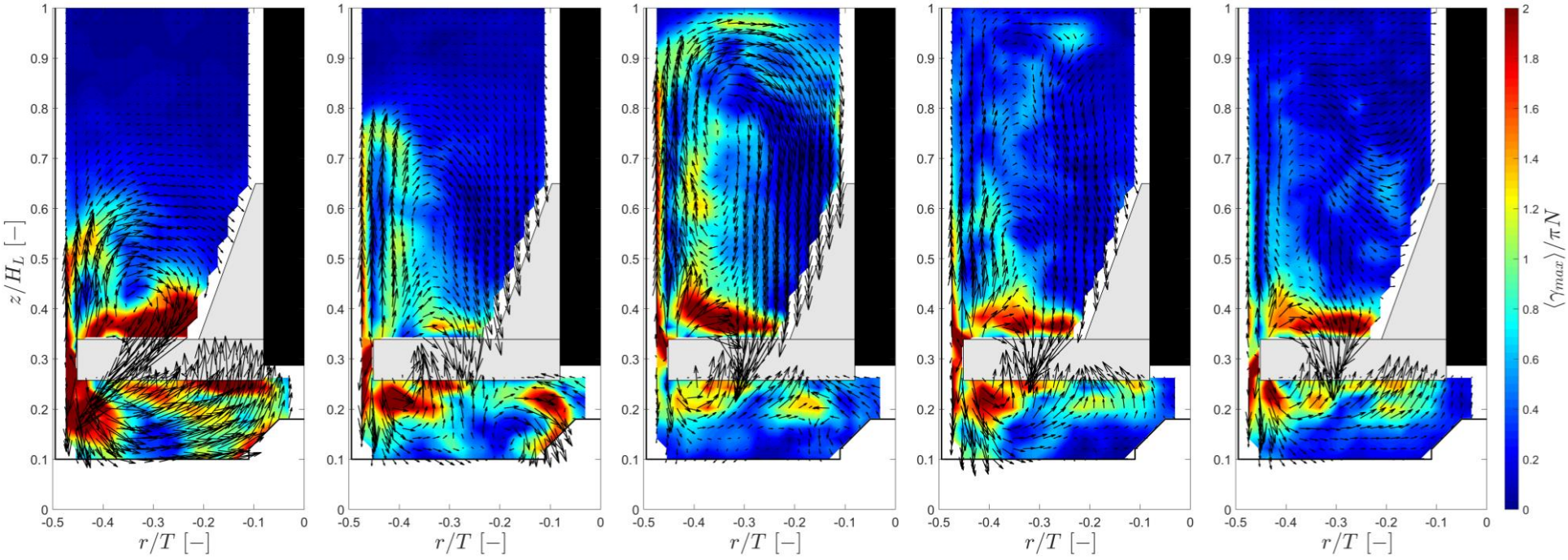

***Nt* = 1** ***Nt* = 2** ***Nt* = 3** ***Nt* = 4** ***Nt* = 5**

[270]

(d)

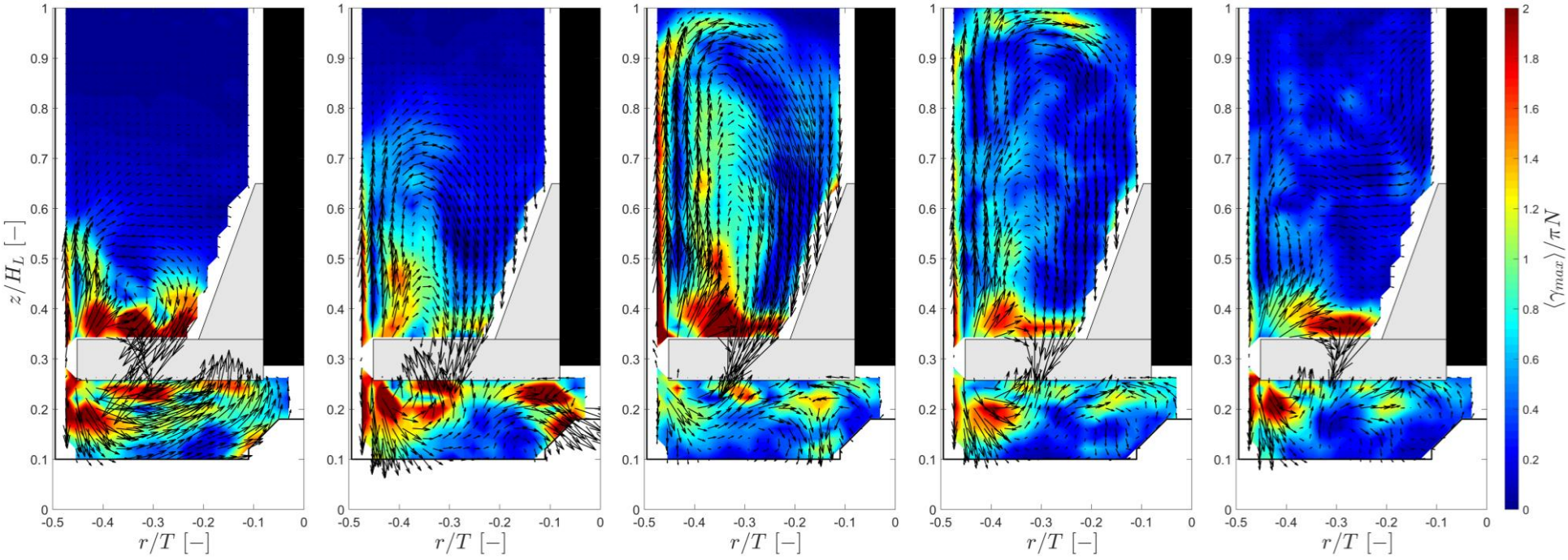

Figure 5.13 Contour maps of local shear rate, $\langle\gamma_{max}\rangle/\pi N$, with vector fields, N = 90 rpm: (a) during the dwell, T_{dwell} = 1 – 1500 ms; (b - d) Nt = 1 – 5 revolutions after the dwell, T_{dwell} = 900 ms (b); T_{dwell} = 9000 ms (c); T_{dwell} = 30,000 ms (d).

(a)

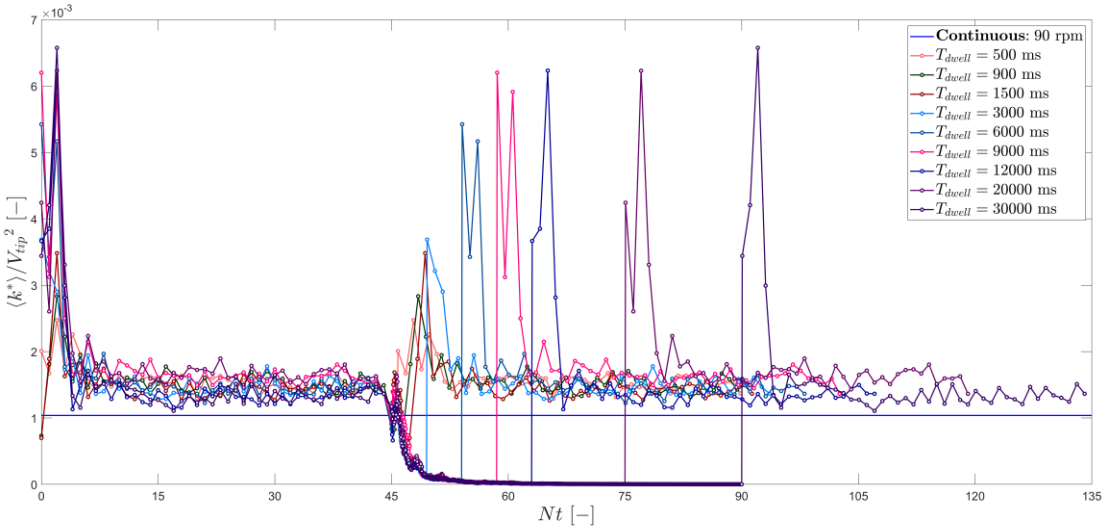

(b)

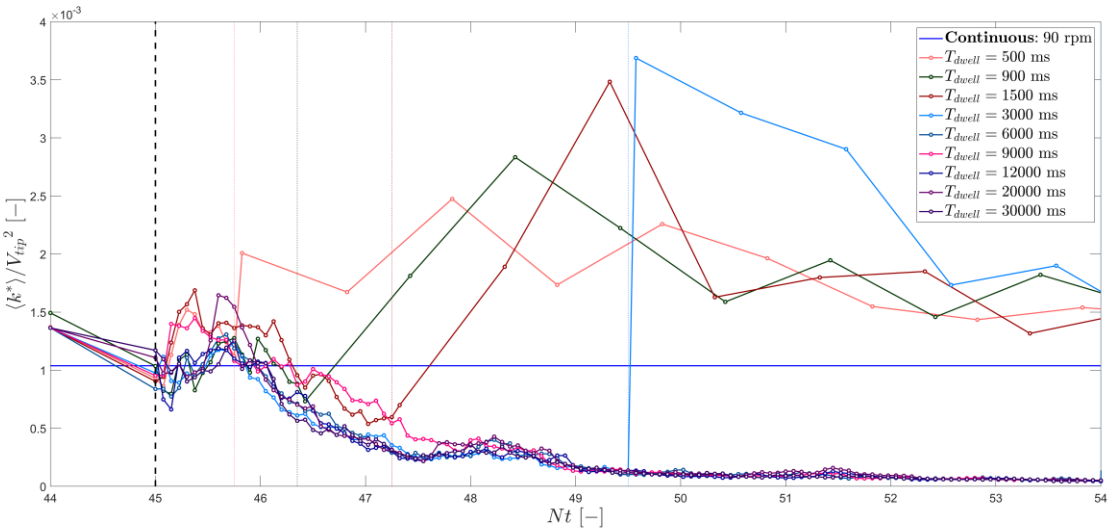

Figure 5.14 Space-averaged phase-resolved periodic kinetic energy content, $\langle k^* \rangle / V_{tip}{}^2$, for continuous and intermittent agitation: (a) overall space-averaged kinetic energy for intermittent and continuous agitation; (b) space-averaged periodic kinetic energy at the start of the intermittent dwell phase, Nt = 45.

(a)

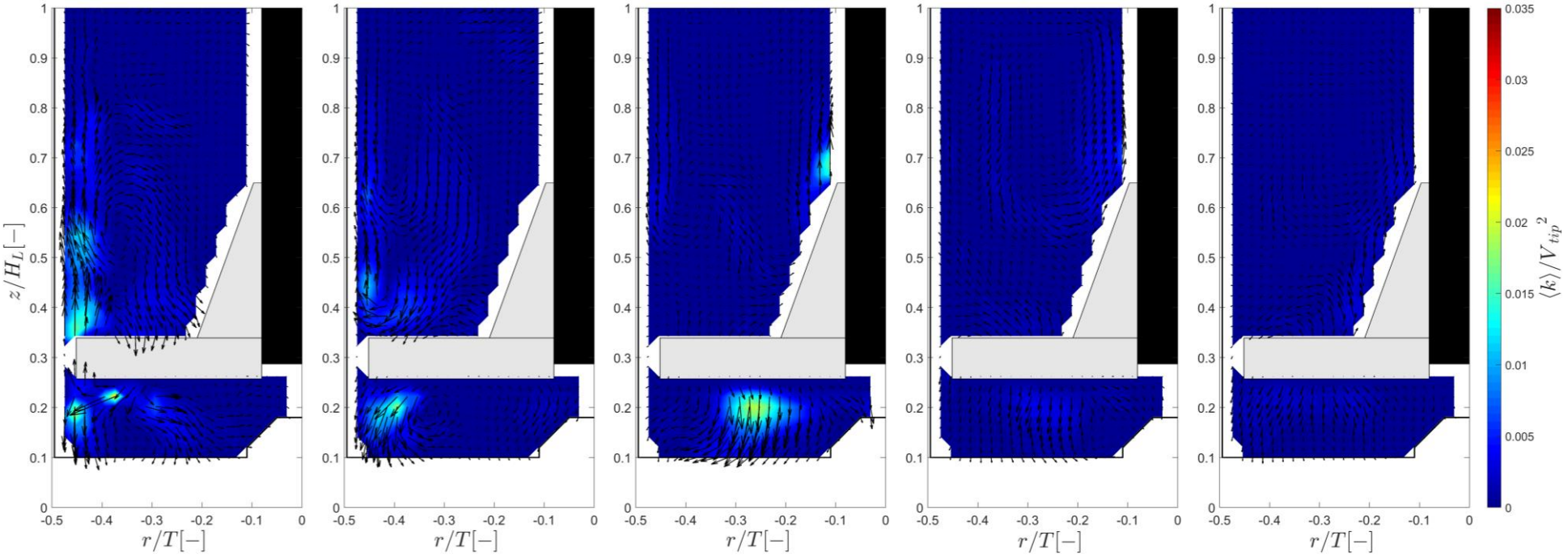

T_{dwell} = 1 ms **T_{dwell} = 100 ms** **T_{dwell} = 500 ms** **T_{dwell} = 900 ms** **T_{dwell} = 1500 ms**

[273]

(b)

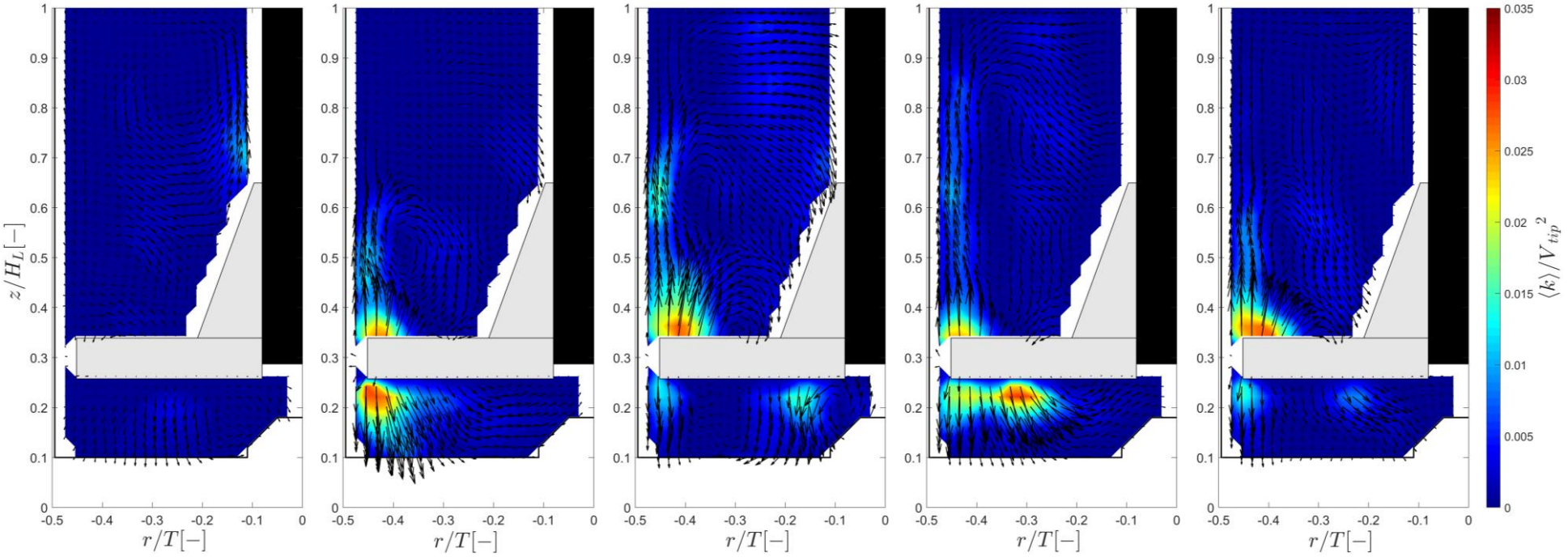

***Nt* = 1** ***Nt* = 2** ***Nt* = 3** ***Nt* = 4** ***Nt* = 5**

[274]

(c)

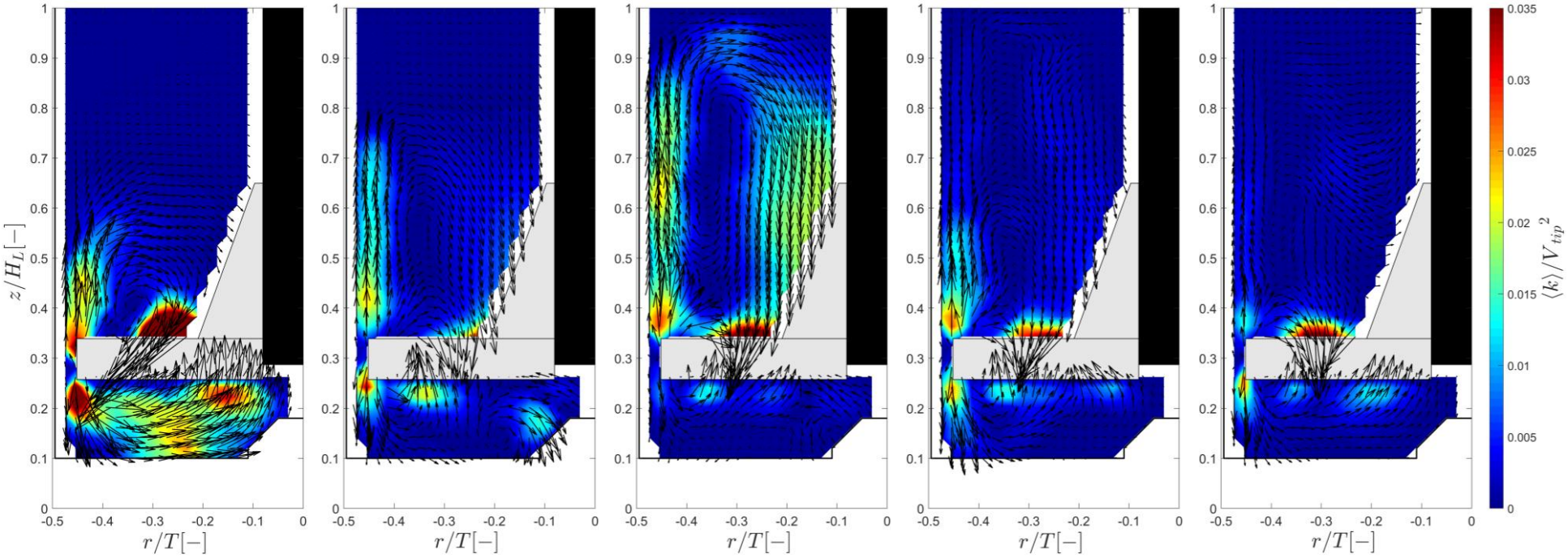

***Nt* = 1** ***Nt* = 2** ***Nt* = 3** ***Nt* = 4** ***Nt* = 5**

[275]

(d)

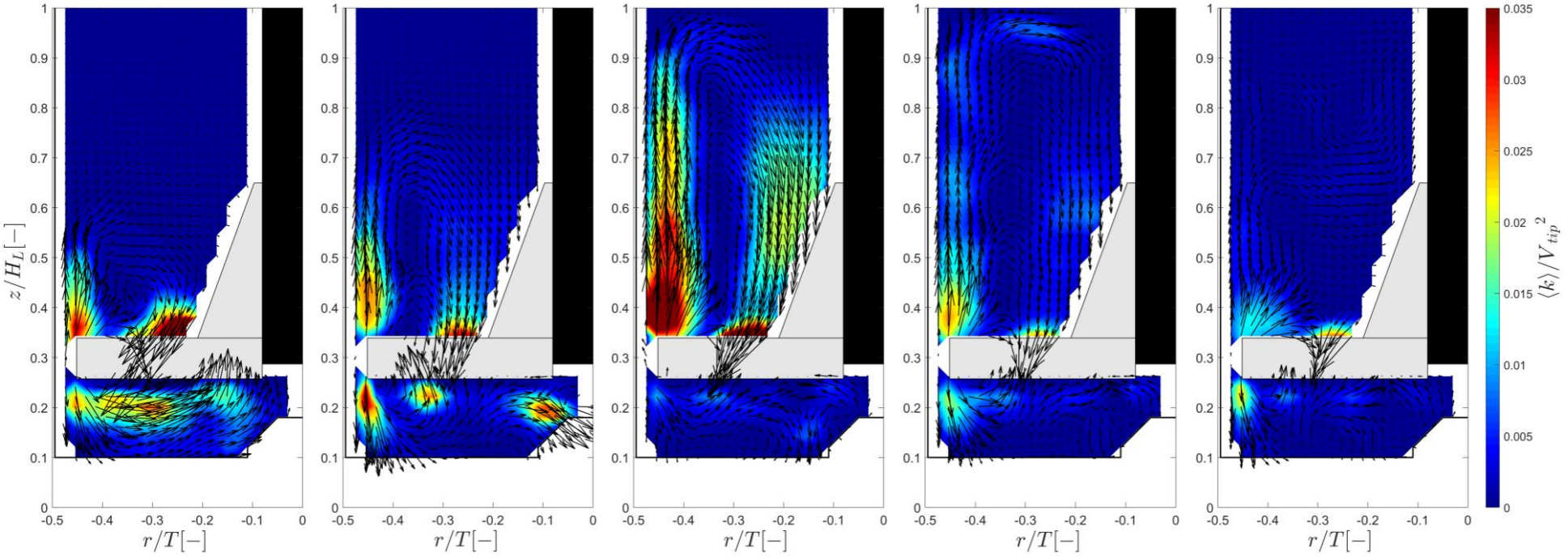

Figure 5.15 Contour maps of periodic kinetic energy, $\langle k \rangle / V_{tip}{}^2$, with vector fields, N = 90 rpm: (a) during the dwell, T_{dwell} = 1 – 1500 ms; (b - d) Nt = 1 – 5 revolutions after the dwell, T_{dwell} = 900 ms (b); T_{dwell} = 9000 ms (c); T_{dwell} = 30,000 ms (d).

[276]

(a)

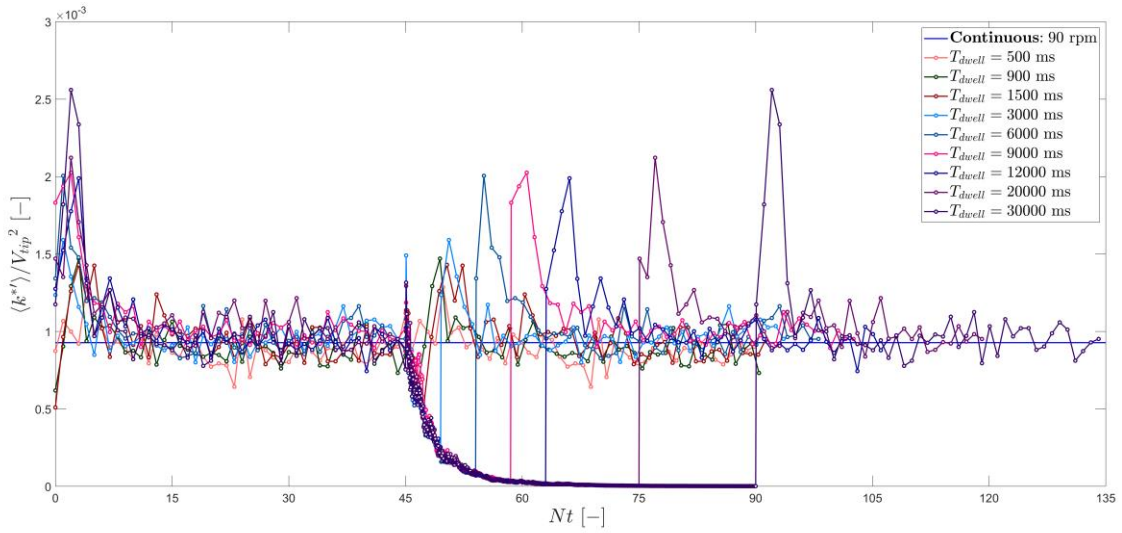

(b)

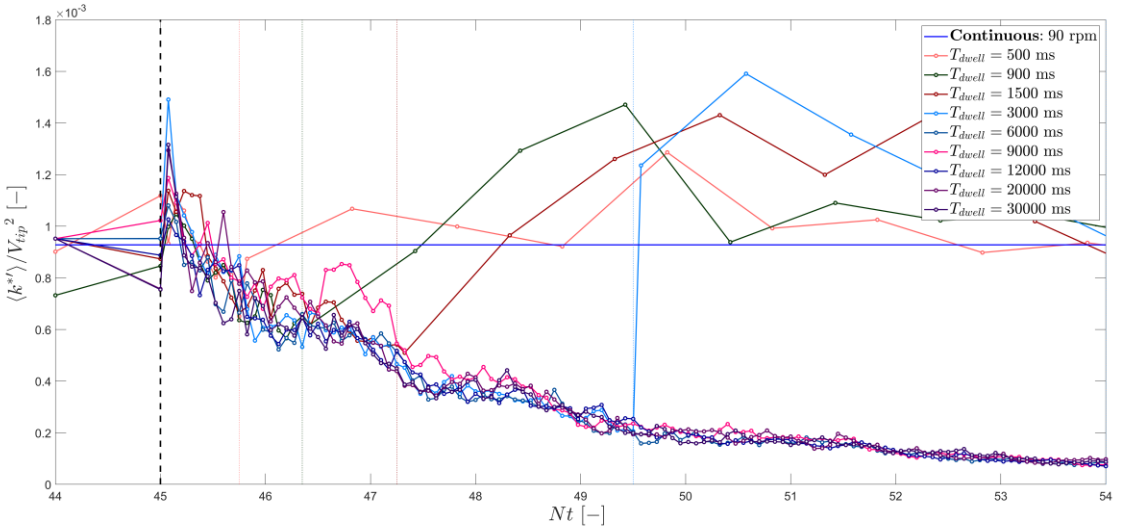

Figure 5.16 Space-averaged phase-resolved turbulent kinetic energy content, $\langle k^{*\prime} \rangle / V_{tip}{}^2$, for continuous and intermittent agitation: (a) overall space-averaged turbulent kinetic energy for intermittent and continuous agitation; (b) space-averaged turbulent kinetic energy at the start of the intermittent dwell phase, Nt = 45.

(a)

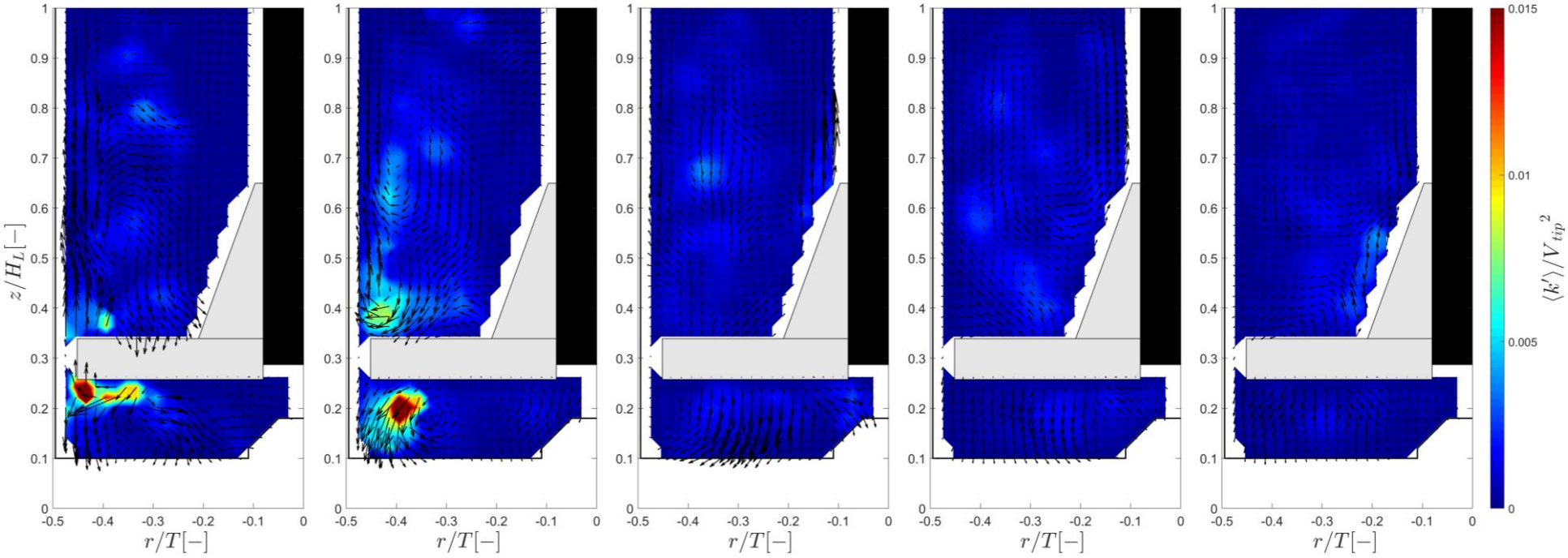

T_{dwell} = 1 ms **T_{dwell} = 100 ms** **T_{dwell} = 500 ms** **T_{dwell} = 900 ms** **T_{dwell} = 1500 ms**

[278]

(b)

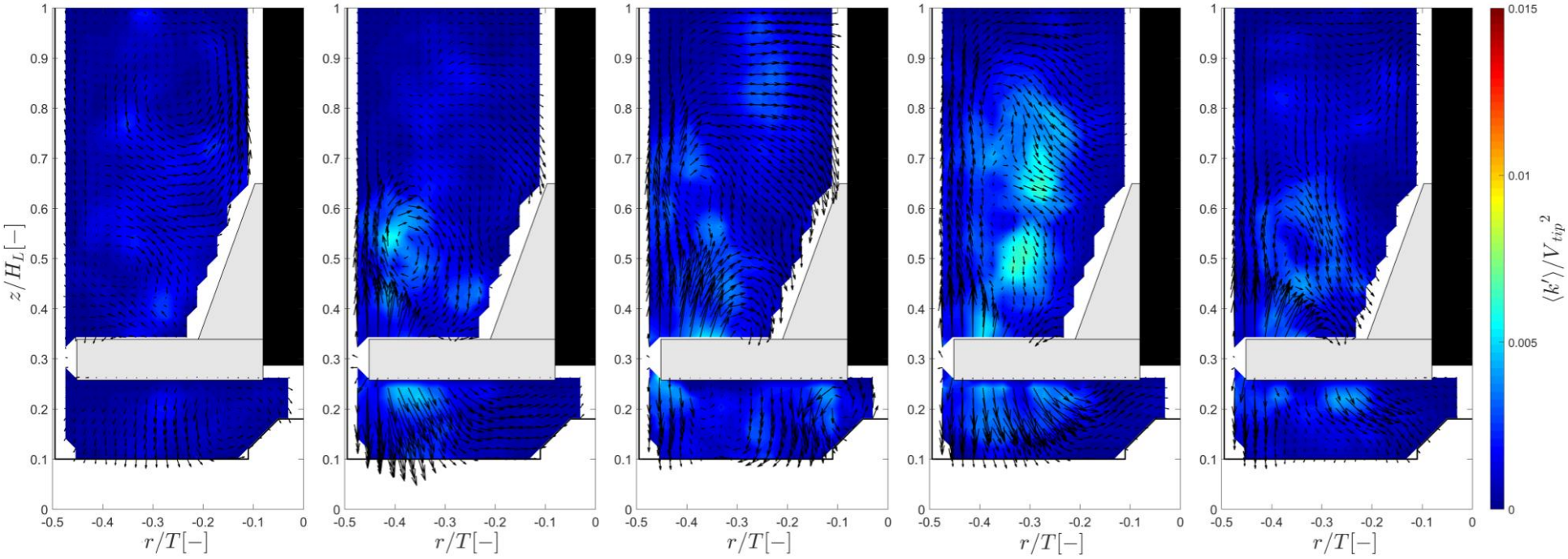

***Nt* = 1** ***Nt* = 2** ***Nt* = 3** ***Nt* = 4** ***Nt* = 5**

[279]

(c)

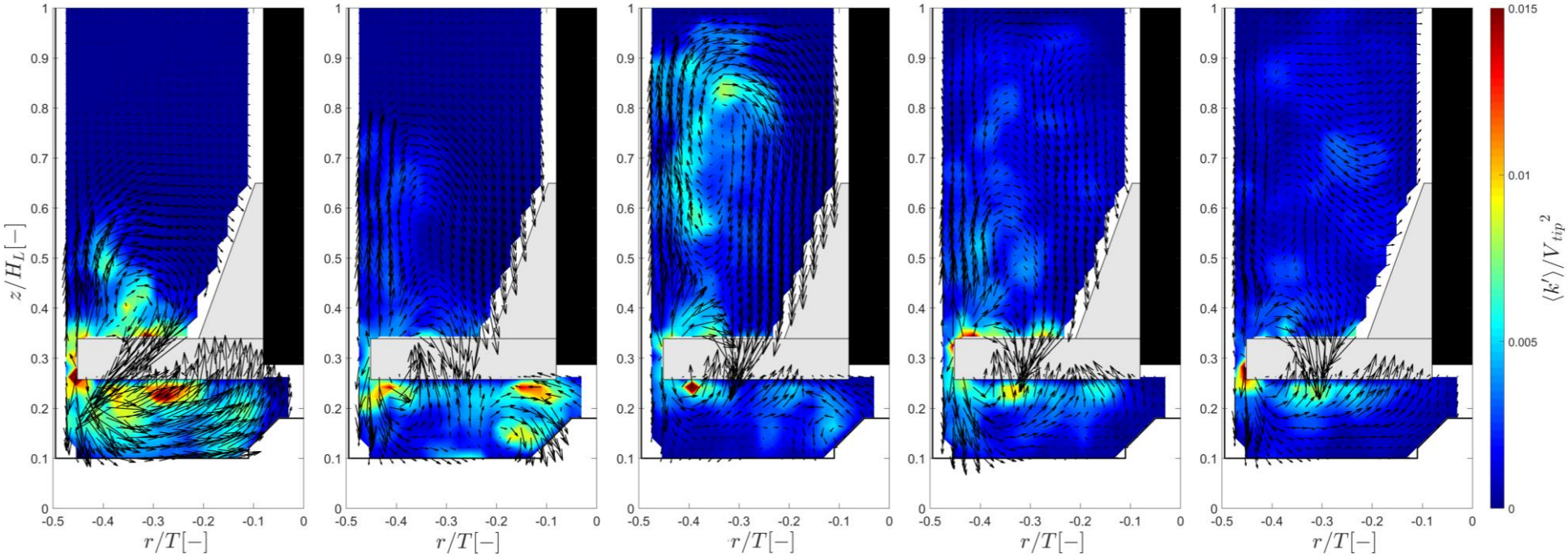

***Nt* = 1** ***Nt* = 2** ***Nt* = 3** ***Nt* = 4** ***Nt* = 5**

[280]

(d)

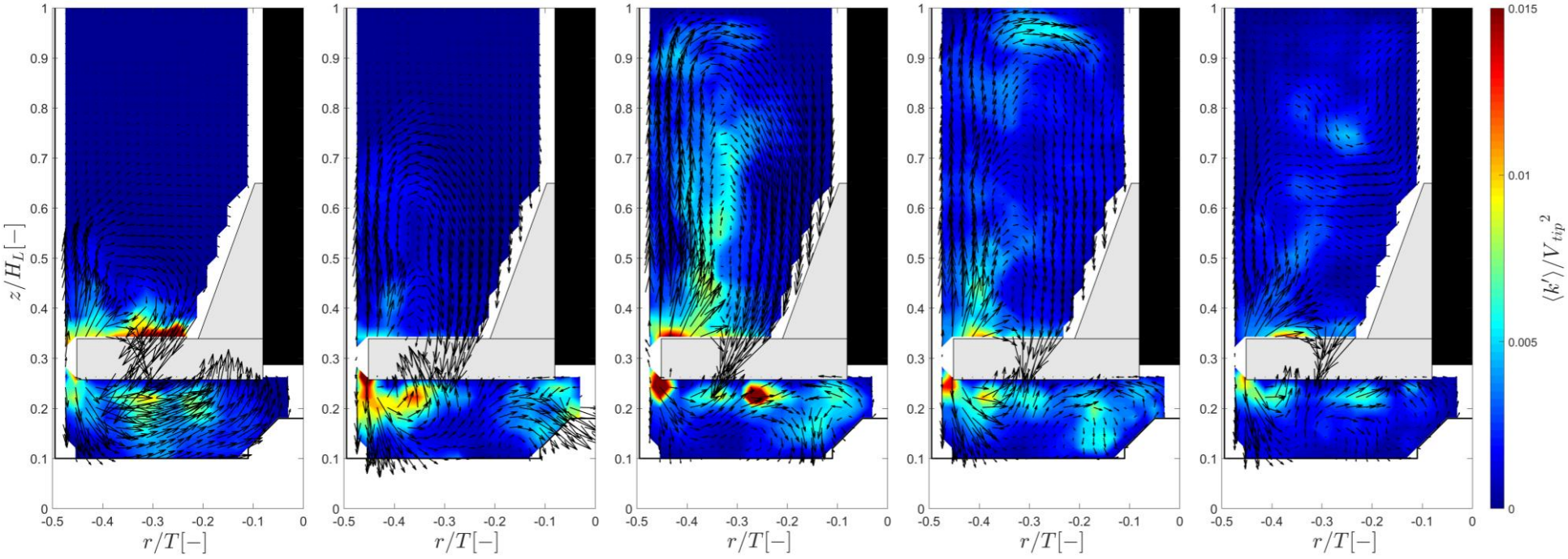

Figure 5.17 Contour maps of turbulent kinetic energy, $\langle k' \rangle / V_{tip}{}^2$, with vector fields, N = 90 rpm: (a) during the dwell, T_{dwell} = 1 – 1500 ms; (b - d) Nt = 1 – 5 revolutions after the dwell, T_{dwell} = 900 ms (b); T_{dwell} = 9000 ms (c); T_{dwell} = 30,000 ms (d).

[281]

[282]

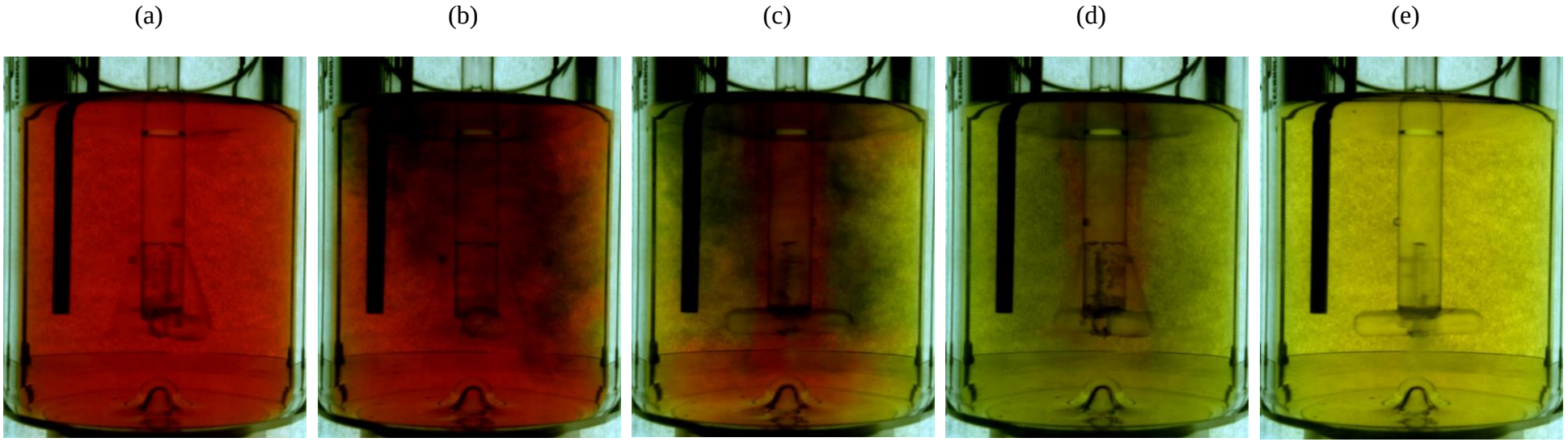

Figure 5.18 Spatial evolution of the mixing dynamics inside the flat-bottom DASGIP bioreactor at N = 90 rpm.

(a)

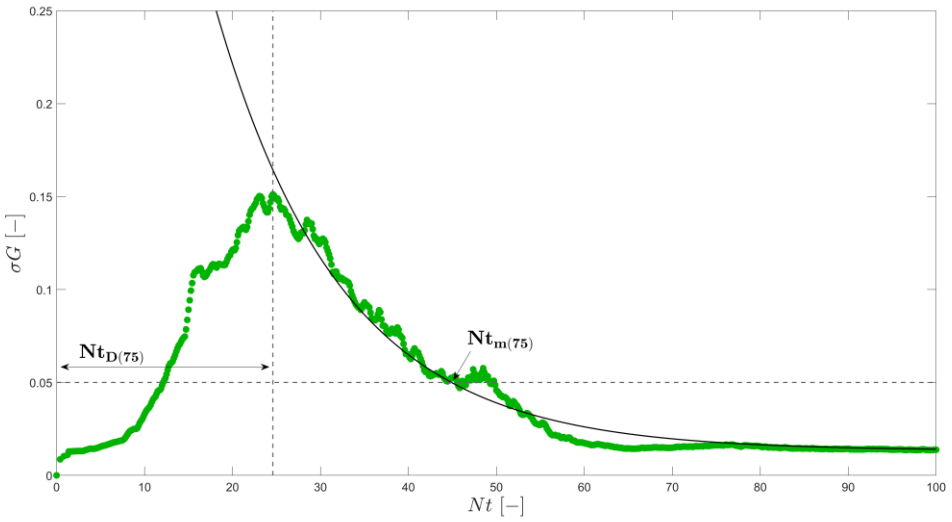
0.25
0.2
0.15
0.1
0.05
0
σG [–]
$\mathbf{Nt_{D(75)}}$
$\mathbf{Nt_{m(75)}}$
0
10
20
30
40
50
60
70
80
90
100
Nt [–]

(b)

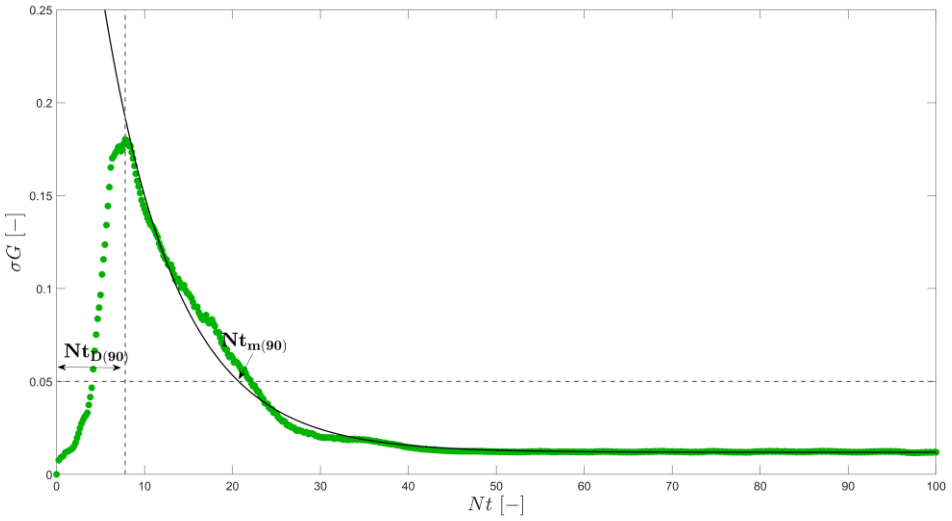
0.25
0.2
0.15
0.1
0.05
0
σG [–]
$\mathbf{Nt_{D(90)}}$
$\mathbf{Nt_{m(90)}}$
0
10
20
30
40
50
60
70
80
90
100
Nt [–]

(c)

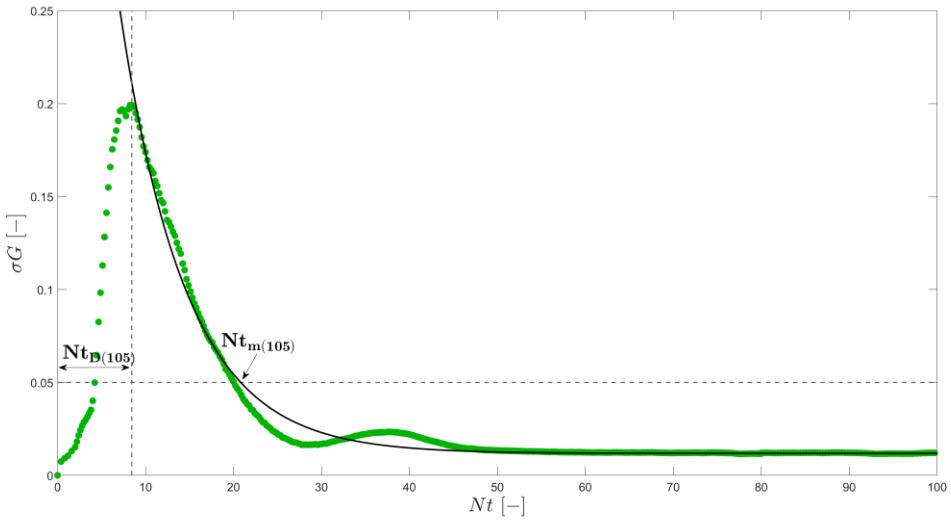

(d)

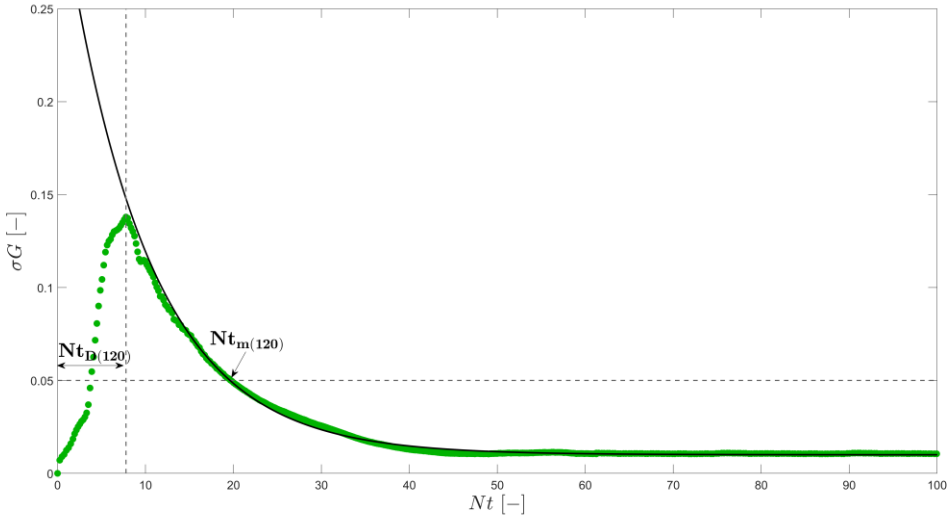

Figure 5.19 Variation of the standard deviation of the normalised green channel output, σG, dispersion number, Nt_D and mixing number, Nt_m, both indicated: (a) N = 75 rpm; (b) N = 90 rpm; (c) N = 105 rpm; (d) N = 120 rpm.

(a)

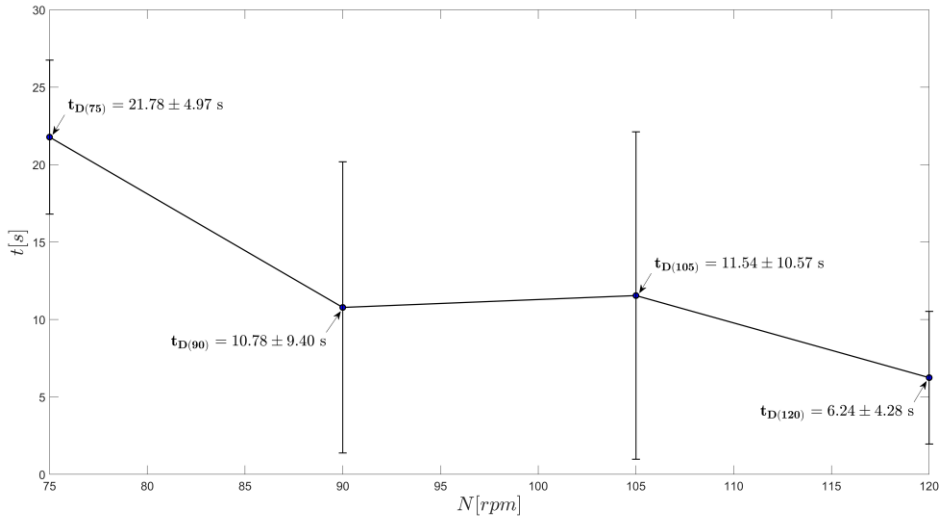

(b)

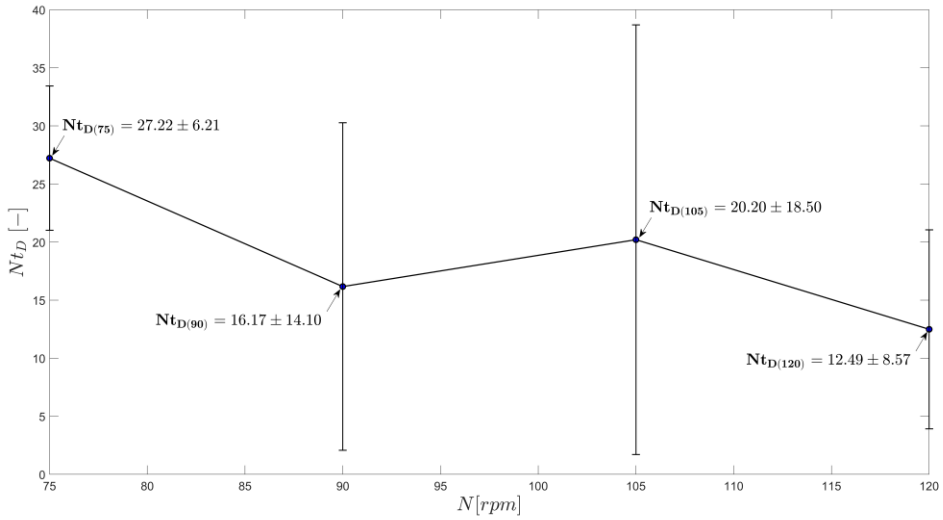

Figure 5.20 Average measured dispersion time of the tracer for all continuous rotational speeds investigated, N = 75 – 120 rpm: (a) dispersion time, t_D; (b) dispersion number, Nt_D.

(a)

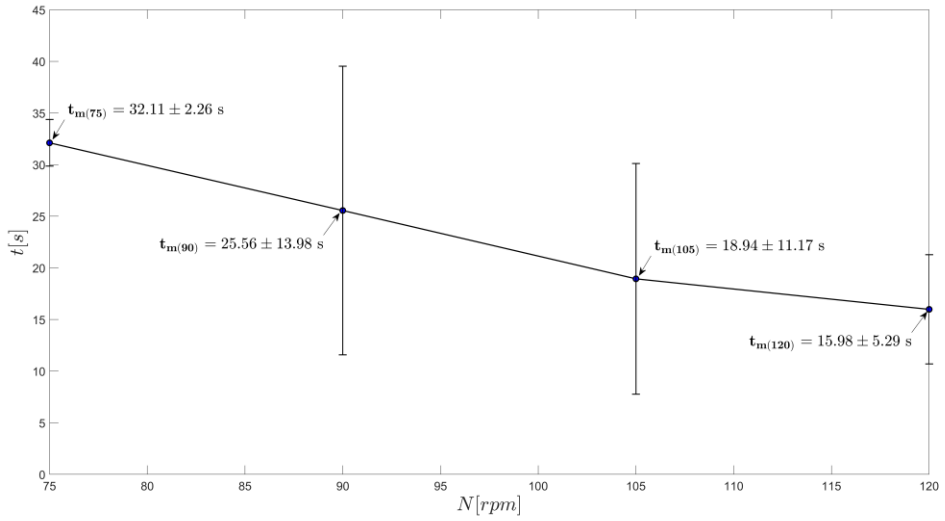

(b)

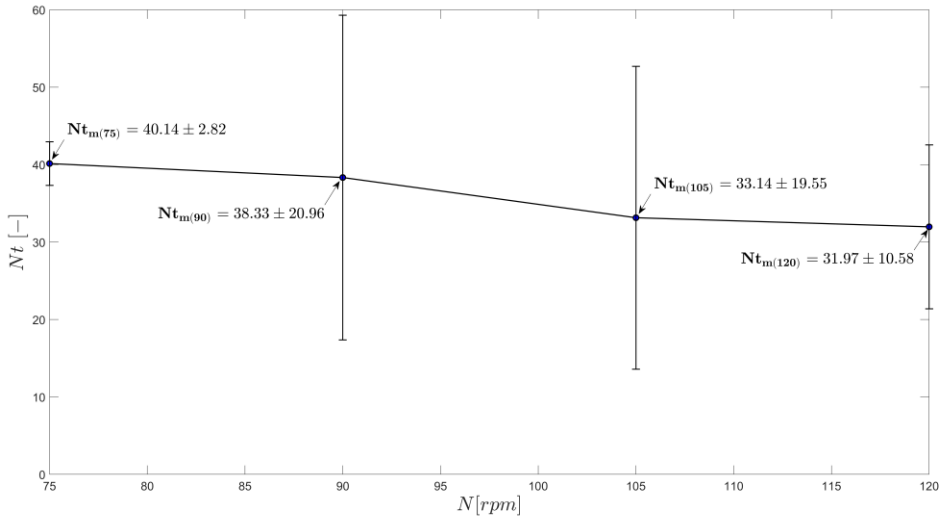

Figure 5.21 Average mixing time of the tracer for all continuous rotational speeds investigated, N = 75 – 120 rpm: (a) mixing time, t_m; (b) mixing number, Nt_m.

(a)

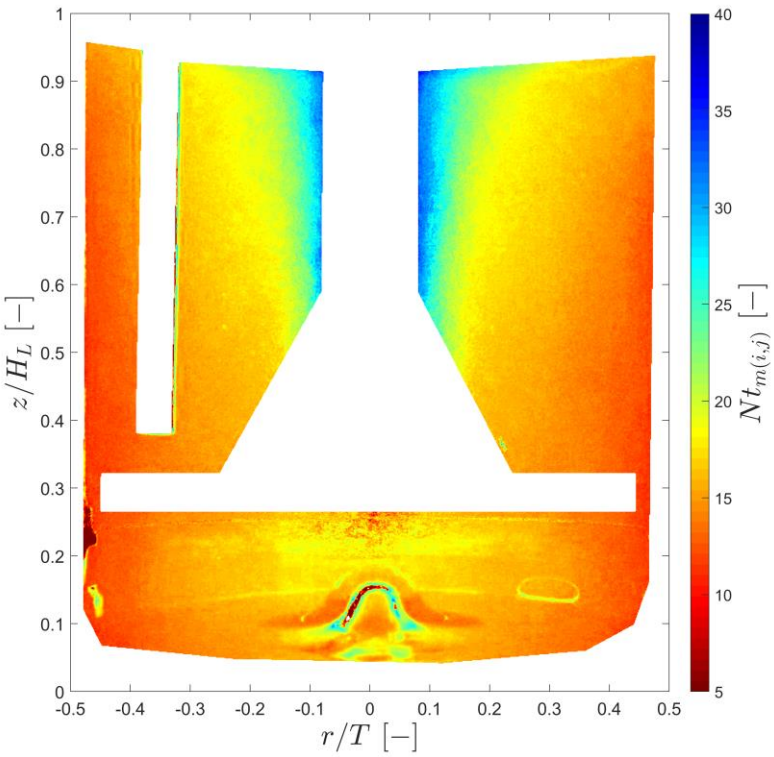

(b)

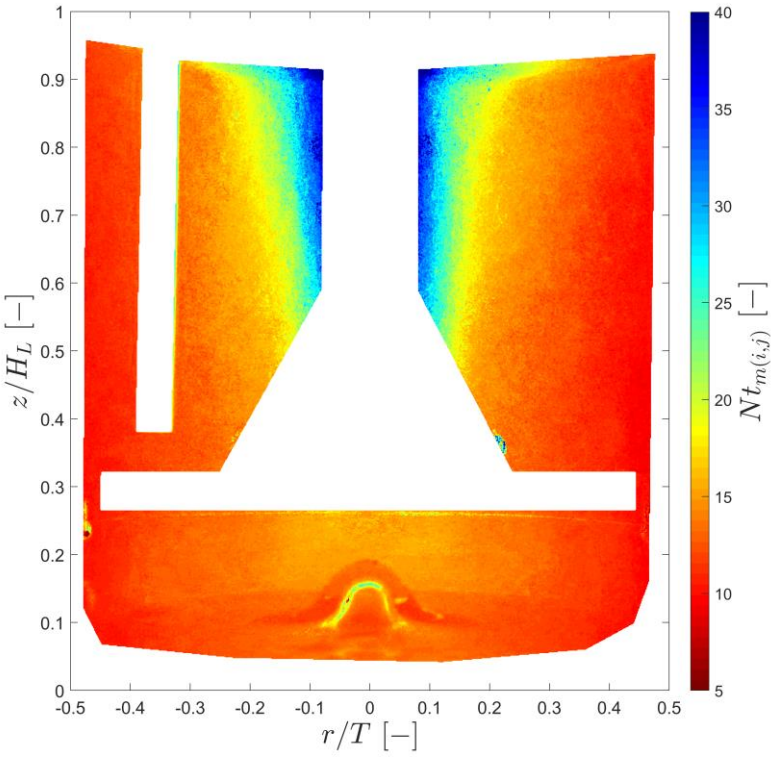

(c)

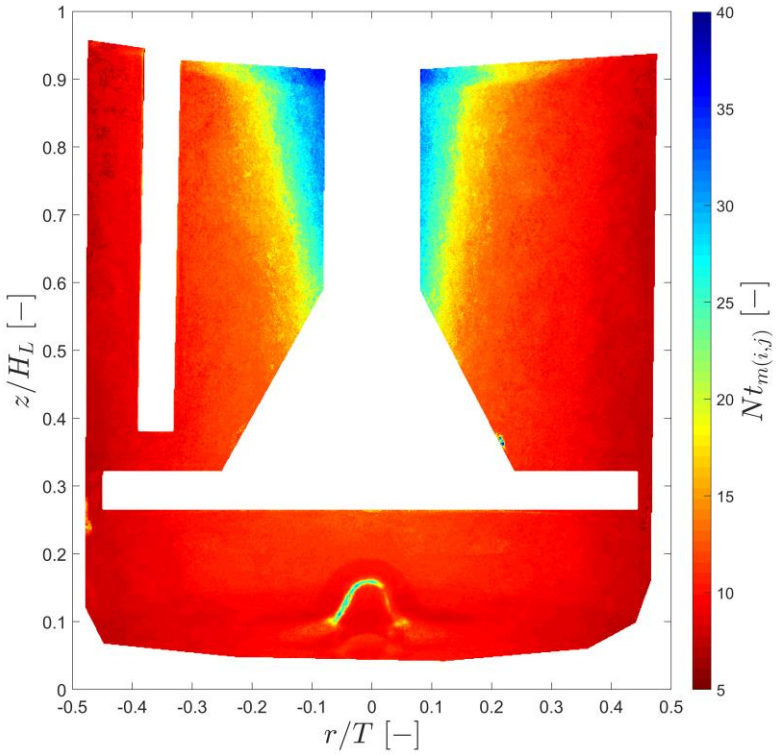

(d)

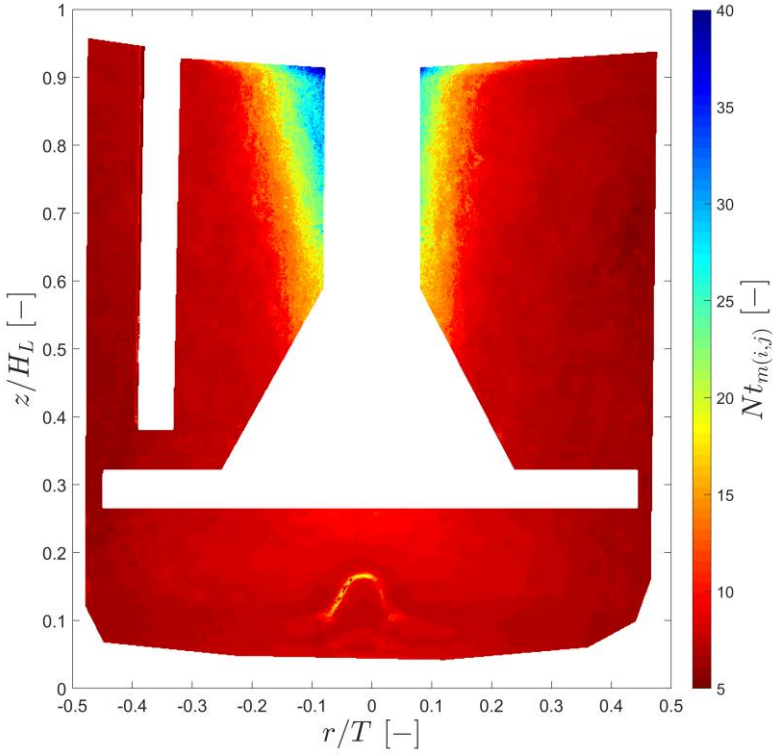

Figure 5.22 Average mixing number map for increasing rotational speeds: (a) N = 75 rpm; (b) N = 90 rpm; (c) N = 105 rpm; (d) N = 120 rpm.

(a)

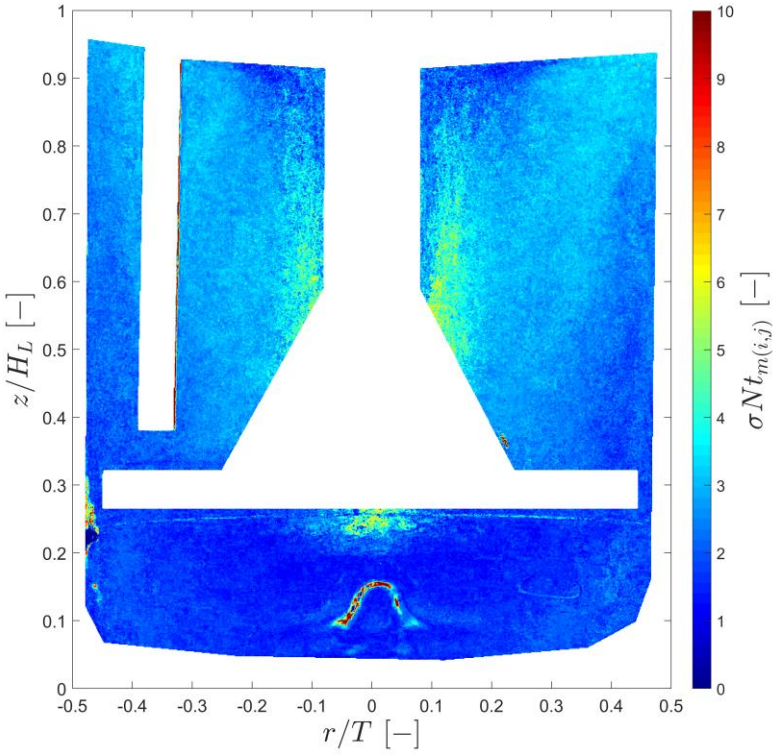

(b)

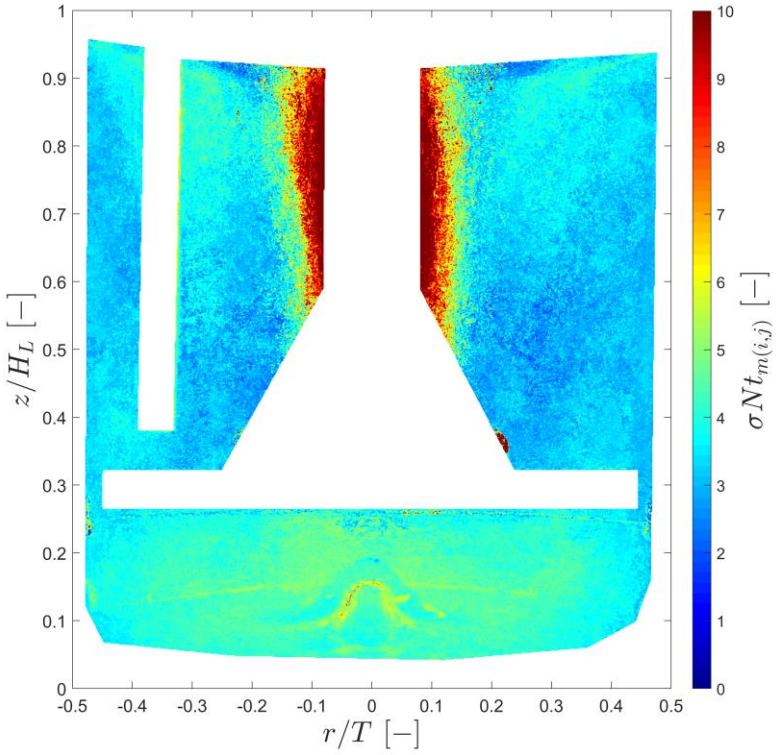

(c)

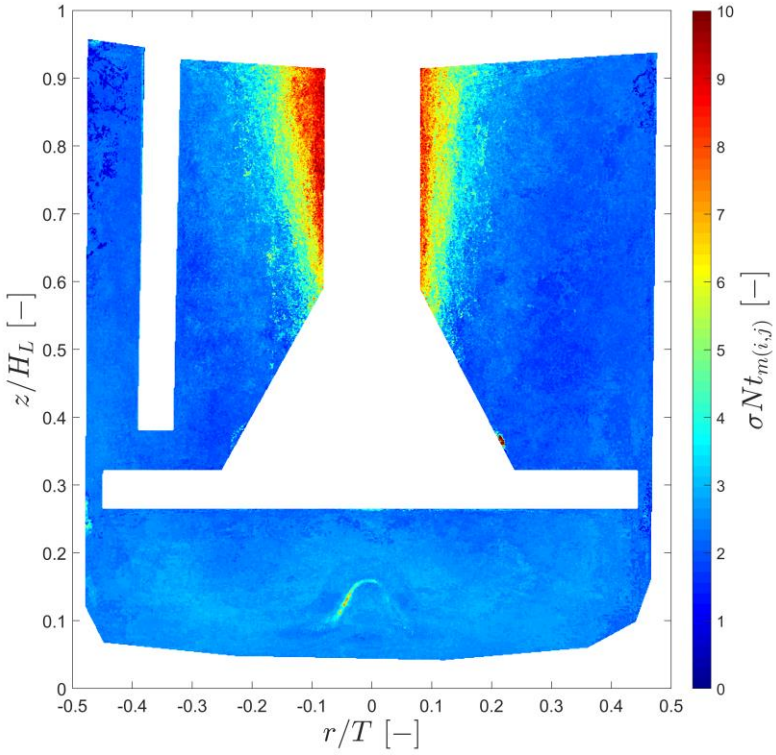

(d)

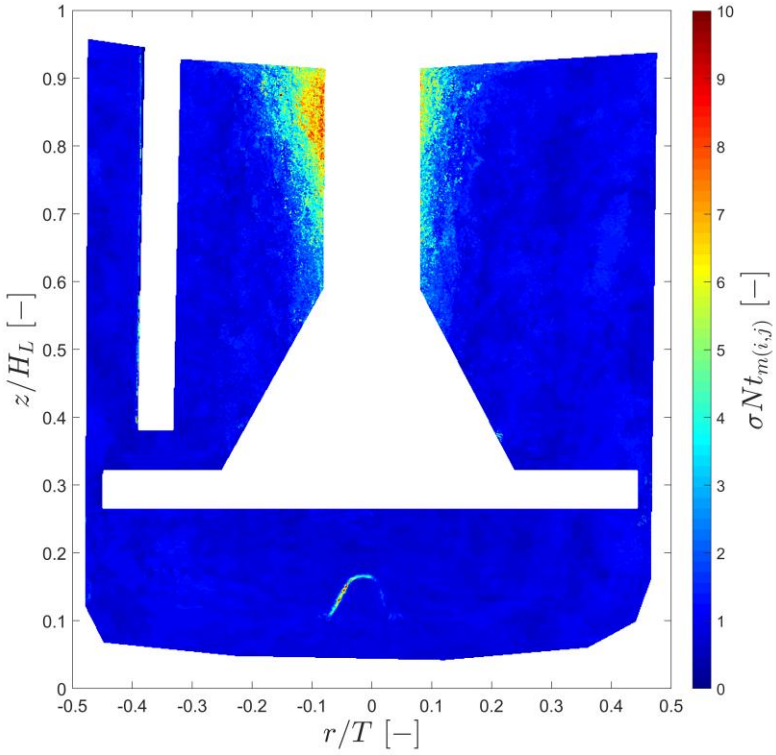

Figure 5.23 Standard deviation of the average mixing number maps for increasing rotational speeds: (a) N = 75 rpm; (b) N = 90 rpm; (c) N = 105 rpm; (d) N = 120 rpm.

[291]

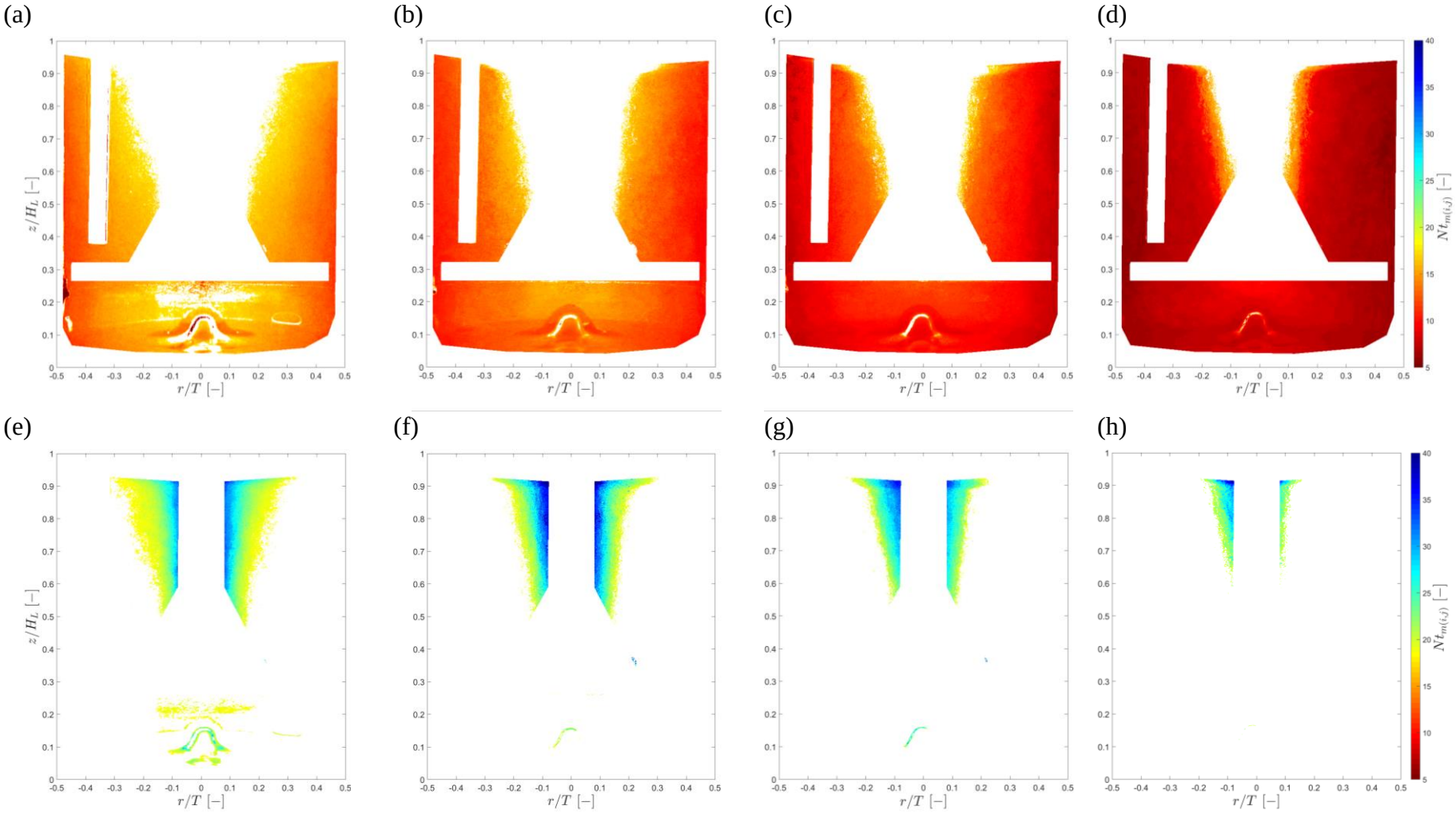

Figure 5.24 Segregation of fast and slow mixing regions using the threshold Nt_m = 18 from average mixing maps: (a – d) fast mixing regions at N = 75 rpm (a); 90 rpm (b); 105 rpm (c); 120 rpm (d); (e – h) slow mixing regions at N = 75 rpm (e); 90 rpm (f); 105 rpm (g); 120 rpm (h).

(a)

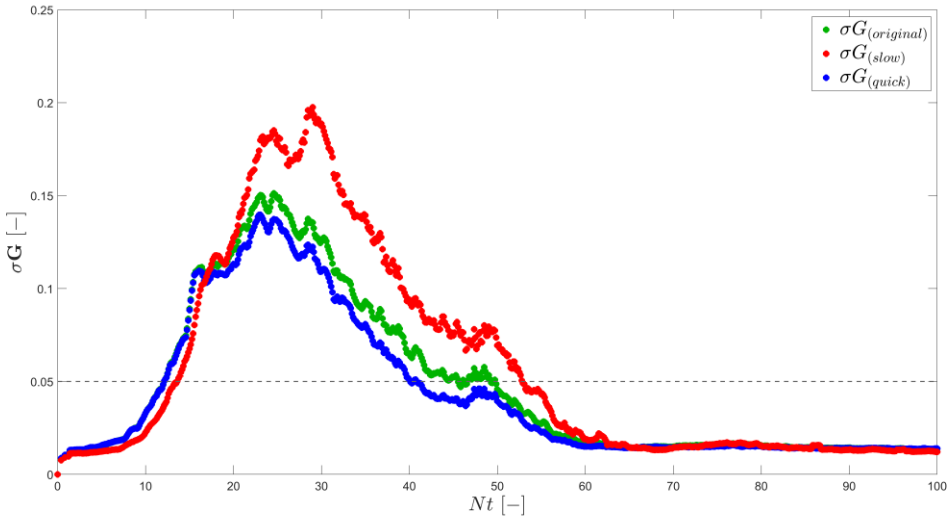

(b)

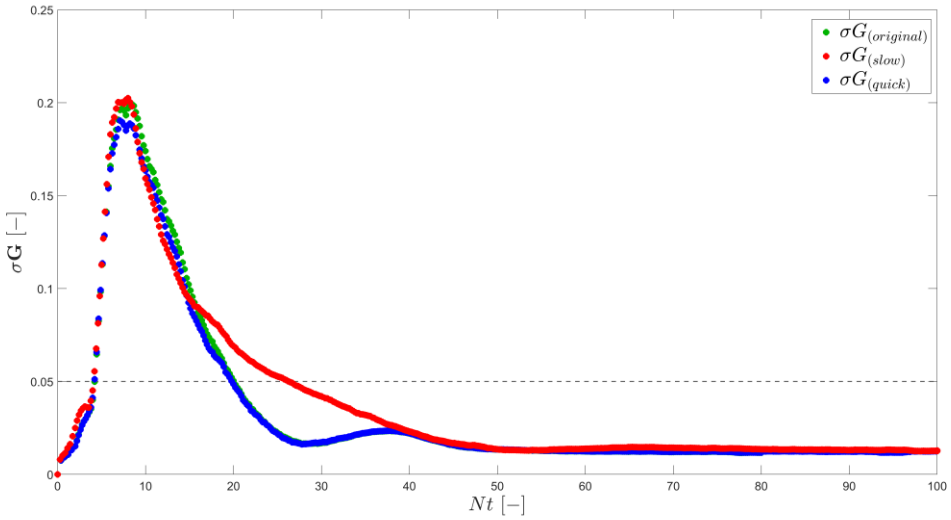

Figure 5.25 Standard deviation profiles of the normalised green channel in the segregated fast mixing (blue) and slow mixing (red) regions with the overall result (green): (a) N = 75 rpm; (b) N = 120 rpm.

(a)

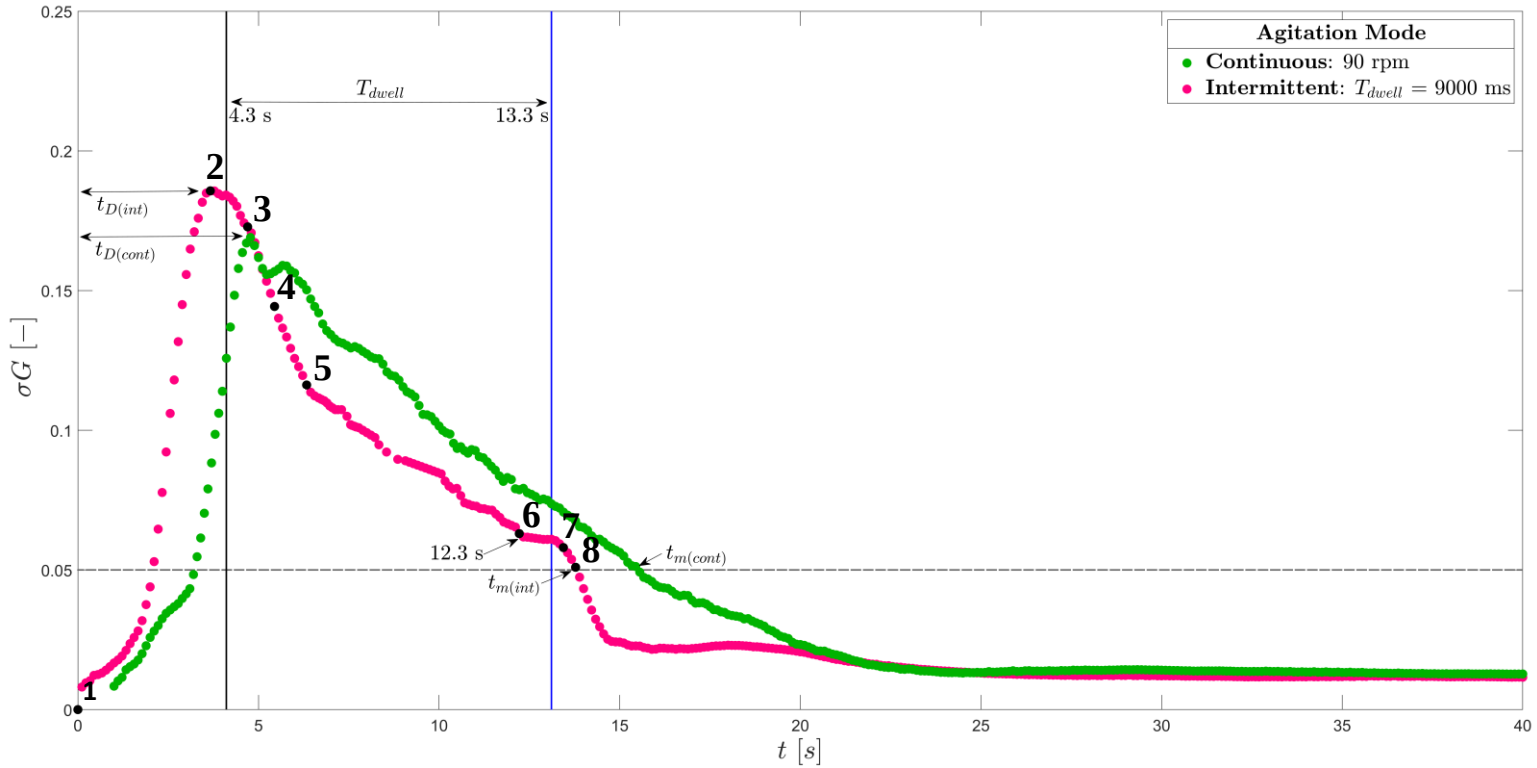
Agitation Mode
Continuous: 90 rpm
Intermittent: T_{dwell} = 9000 ms
T_{dwell}
4.3 s
13.3 s
$t_{D(int)}$
$t_{D(cont)}$
12.3 s
$t_{m(cont)}$
$t_{m(int)}$
σG [–]
t [s]
1
2
3
4
5
6
7
8

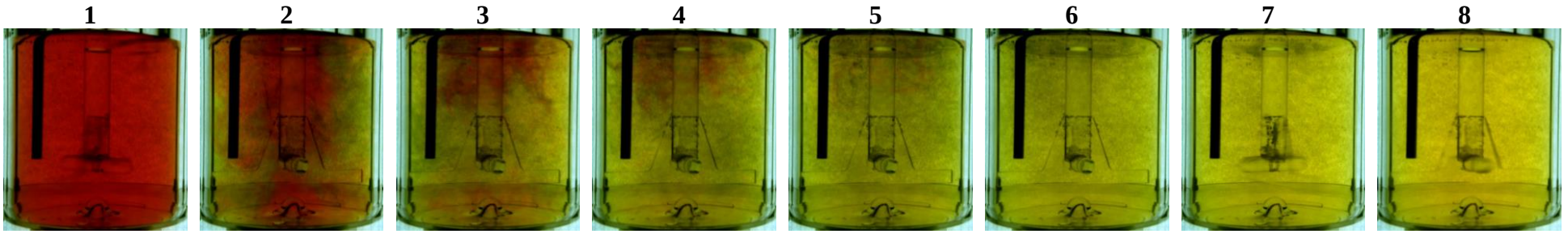
1
2
3
4
5
6
7
8

[293]

(b)

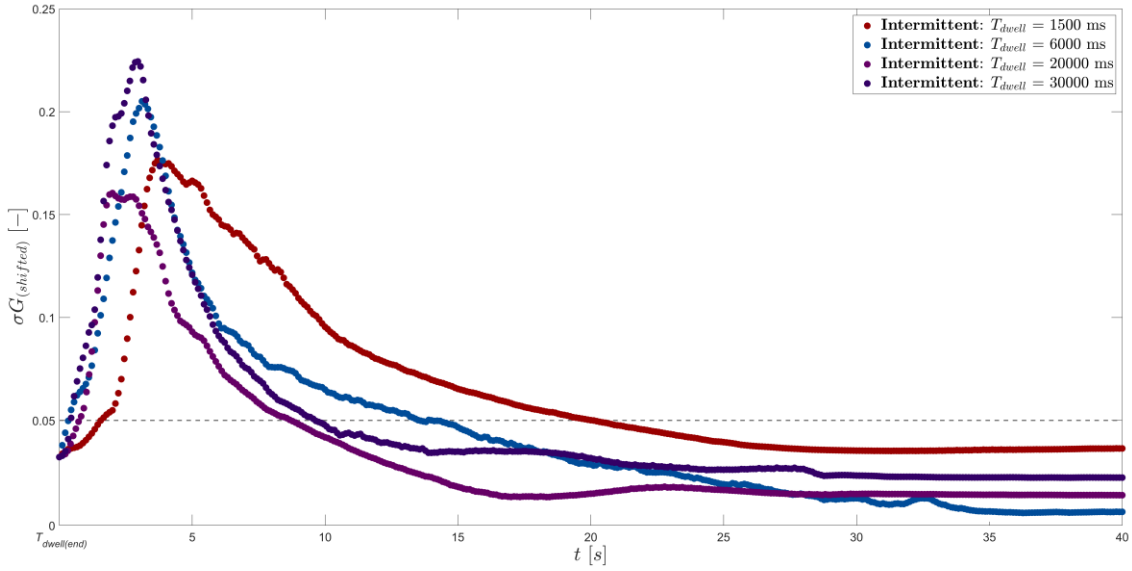

Figure 5.26 Intermittent agitation mixing profiles: (a) continuous (green, N = 90 rpm) and intermittent (pink, N = 90 rpm, T_{inv} = 30 s and T_{dwell} = 9000 ms) agitation, indicating various timepoints throughout mixing (1 – 8) visualised beneath; (b) intermittent agitation, T_{dwell} = 1500 – 30,000 ms when tracer is added during the dwell.

(a)

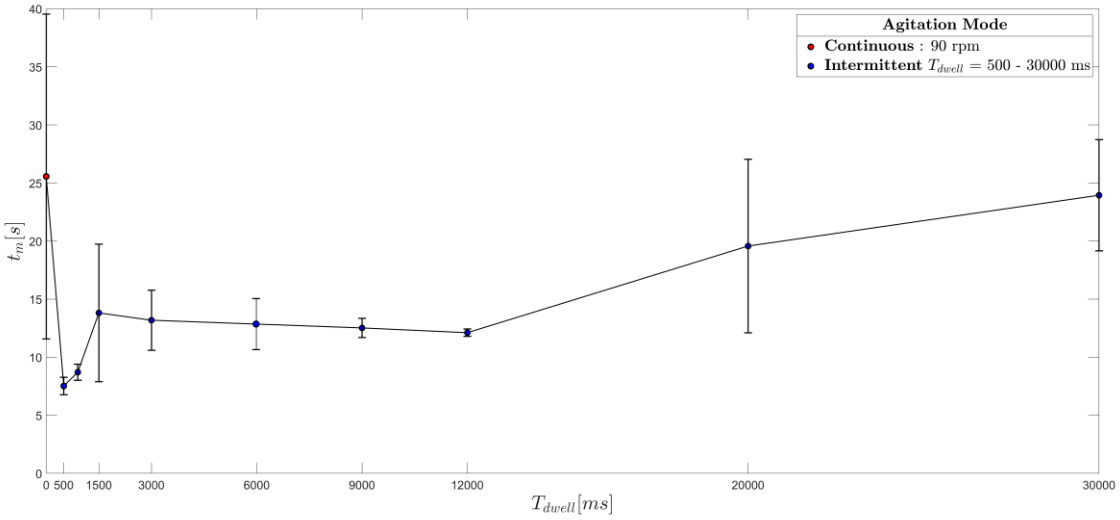

(b)

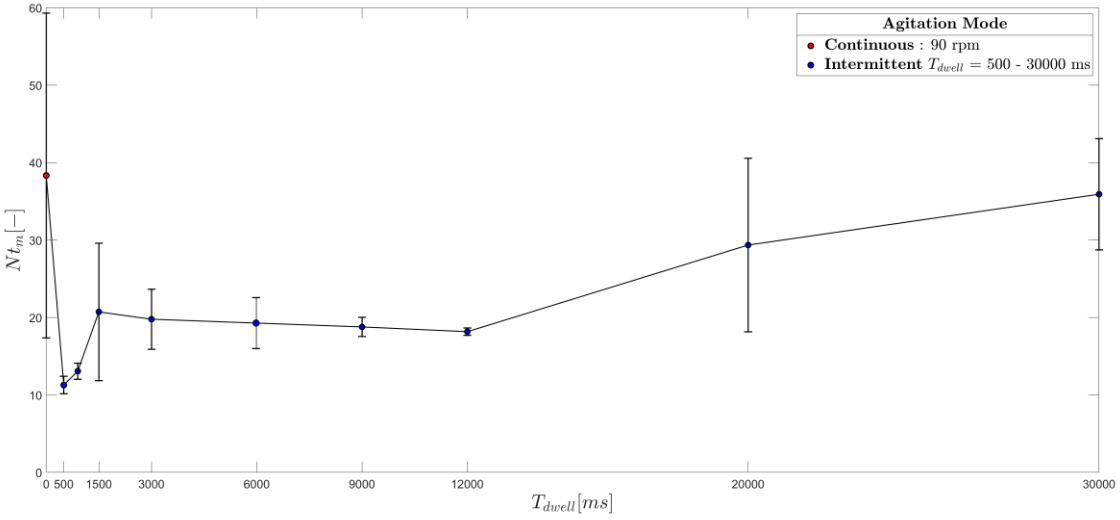

Figure 5.27 Average measured mixing time of the tracer for both continuous and interrmitent agition conditions investigated, N = 90 rpm, T_{inv} = 30 s and T_{dwell} = 0 – 30,000 ms: (a) mixing time, t_m; (b) mixing number, Nt_m.

(a)

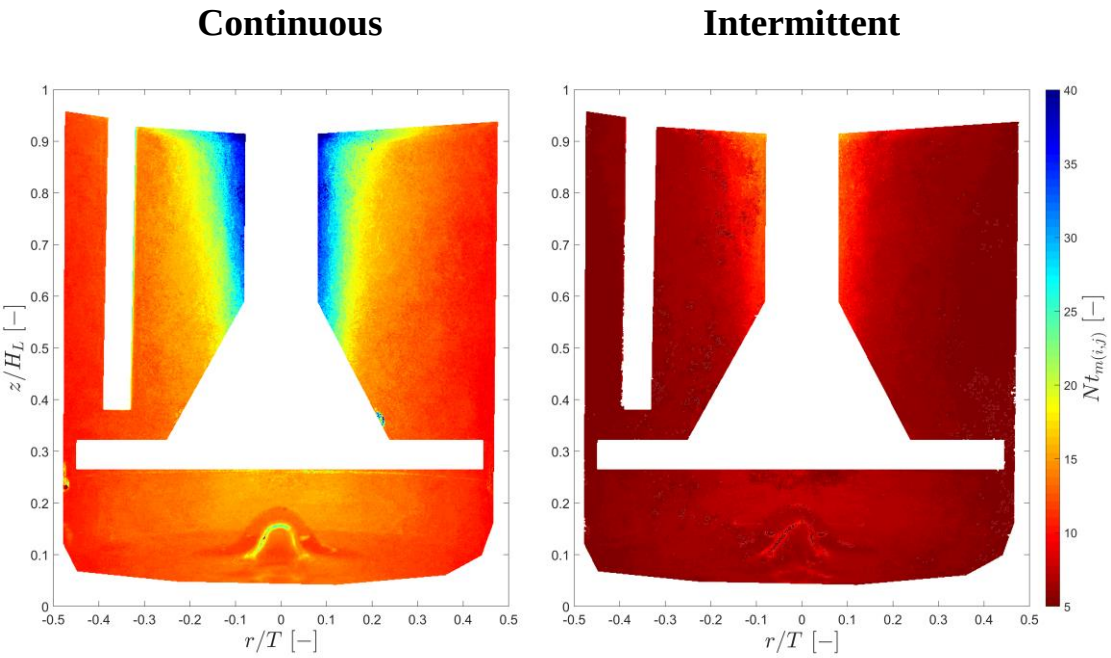

(b)

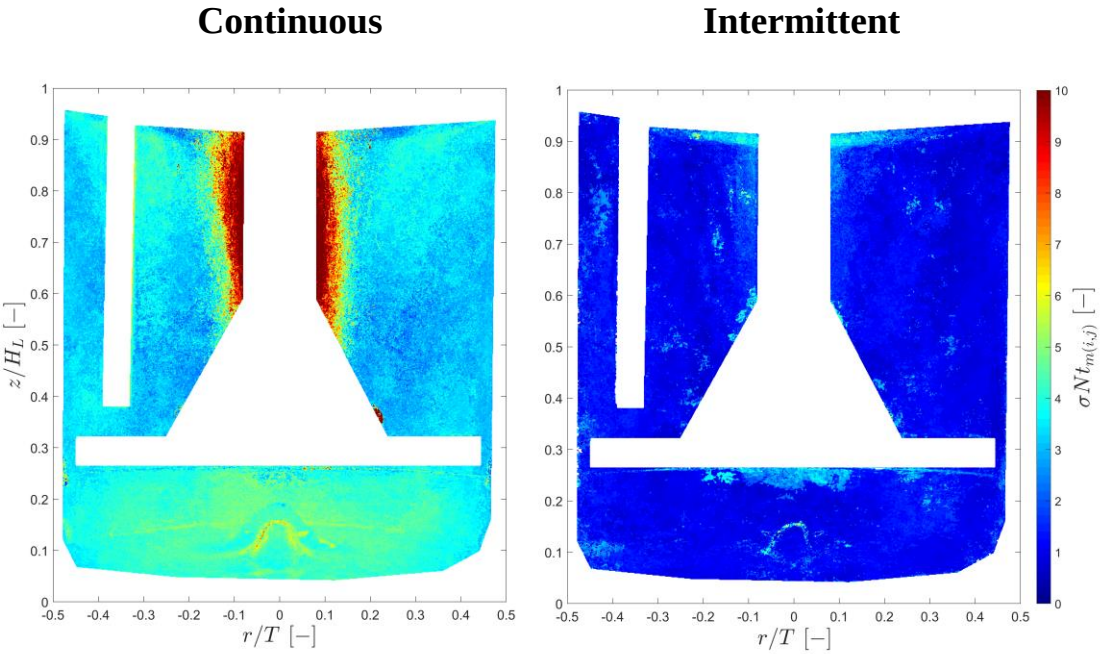

Figure 5.28 Mixing maps comparing both continuous (left, N = 90 rpm) and intermittent (right, N = 90 rpm, T_{inv} = 30 s and T_{dwell} = 500 ms) agitation modes: (a) average local mixing number maps; (b) standard deviation of mixing number maps.

CHAPTER 6 CONCLUSIONS

6.1 The present contribution

The objective of this research work was to investigate the flow, mixing and suspension dynamics of a DASGIP bioreactor operating under continuous and intermittent agitation modes to correlate with the biological outcomes of an iPSC-CM differentiation process.

Investigation into the characteristic flow frequencies of both continuous and intermittent agitation modes were measured using Laser Doppler Anemometry (LDA) for a flat-bottomed DASGIP bioreactor. Modulation of three identified time components, introduced with the different agitation modes, was investigated in an attempt to determine their impact upon the flow frequencies. In addition, iPSC-CM differentiation studies were conducted with the desire to demonstrate the importance between the engineering aspects characterised with biological outcomes of a cell differentiation process.

The mean flow characteristics were measured for two DASGIP bioreactor configurations; a flat-and round-bottomed vessel, using whole field Particle Image Velocimetry (PIV). The impact of the bottom geometry and impeller clearance on flow, vorticity, shear and turbulence were investigated at a range of impeller rotational speeds and each individual system was characterised. Subsequently, suspension dynamics for each bioreactor configuration were investigated and combined with the flow characterisation results, in an attempt to characterise the significant reduction in cardiomyocyte differentiation yields obtained by Correia *et al.* (private communication) for the round bottom geometry.

A more in-depth analysis of the suspension and settling characteristics for the flat bottom DASGIP bioreactor configuration were performed, measuring the impact of the intermittent agitation mode on suspension quality. Multiple microcarrier types were utilised to derive the impact of physical properties, such as porosity, size and density, on the suspension dynamics.

In view of the significant impact intermittent agitation had upon the characteristic flow frequencies and differentiation yields, the transient conditions within the whole flow field were investigated using Particle Image Velocimetry. Velocity profiles, shear and turbulence were assessed for the transient following the stop-start in impeller motion, during the dwell phase and during continuous agitation. This was performed to enhance

understanding of the impact of intermittent agitation upon the hydrodynamic environment.

Finally, the mixing dynamics for the flat bottom DASGIP configuration were investigated for continuous and intermittent agitation modes. This was performed using the DISMT technique and both rotational speed and dwell duration were characterised.

6.2 Main findings of the investigation

Characteristic flow frequencies for both continuous and intermittent agitation modes were first obtained at the three experimental conditions first described by Correia *et al.* (2014); continuous agitation at N = 90 rpm, intermittent agitation with a direction change every 30 s and intermittent agitation with a stop-start in impeller motion every 30 s (T_{inv}) for a dwell duration of approximately 0.9 s (T_{dwell}). As expected, continuous agitation generated frequencies corresponding to impeller blade rotation, N = 1.5 rps / 90 rpm, at f = 1.5 and 3.0 Hz, with harmonics. Introduction of intermittent agitation generated a range of lower intensity low frequency peaks at $f = 1/T_{inv}$ = 0.033 Hz, with harmonics, in addition to slightly reduced intensity frequency peaks corresponding to the impeller periodic rotation. Intermittent agitation with a direction change also generated the low frequency peaks at $f = 1/T_{inv}$ = 0.033 Hz, with harmonics, however the intensity of these peaks was significantly amplified by approximately 700-fold. Consideration of these initial findings with the differentiation yields published in Correia *et al.* (2014) suggested the introduction of the low frequency peaks with intermittent agitation resulted in an approximate 290 % increase in cardiogenic differentiation yield from the continuous agitation equivalent. Intermittent agitation with a direction change, which generated a 700-fold amplification in the low frequency peaks intensity, resulted in an approximate 40 % decrease in cardiogenic differentiation yield from the continuous agitation equivalent. This indicated the beneficial effect of intermittent agitation and the introduction of the low frequency peaks on cardiogenic differentiation. Above a certain threshold this beneficial influence was observed to be reversed.

Parametric studies observing the impact of modulation of the three defined time components, N, T_{inv} and T_{dwell}, showed rotational speed to affect the characteristic frequencies associated to impeller blade passage, T_{inv} to affect both the low frequency range and associated intensity and T_{dwell} to affect the low frequency peak intensities. Preservation of the low frequency peak intensities was achieved across various rotational speeds using the number of missed revolutions during the dwell phase, K^*, as a constant.

The initial engineering characterisation studies suggested a drastic change in the low frequency peak intensities to generate both the highest and lowest differentiation yields. The impact of more conservative changes to the low frequency peak intensities was therefore assessed through modulation of T_{dwell} in subsequent biological studies. A dwell duration of T_{dwell} = 500 ms, representing an approximate 44 % reduction in the cumulative low frequency peak intensities from T_{dwell} = 900 ms, the original intermittent condition investigated in Correia *et al.* (2014), was found to reduce cardiogenic differentiation yields by 20 %. A second dwell duration of T_{dwell} = 1500 ms, which increased the cumulative low frequency peak intensities by approximately 67 %, was found to boost differentiation yields by 66 %. This provides further insight into the strong correlation between the low frequency peak intensities and cardiogenic differentiation yields.

Mean flow measurements for flat and round bottom DASGIP bioreactor systems with a change in impeller clearance, were made to assess differences in flow pattern, shear, turbulence and vorticity. The PIV measurements obtained in both bioreactor configurations showed the paddle impeller equipped to generate two trailing vortices; the upper vortex is shown to have a high inclination, travelling up the bioreactor wall in the impeller blades' wake, whilst the lower vortex is shown to change in intensity with the bottom geometry and impeller clearance. The flat bottom configuration showed two equal counter-rotating trailing vortices, while the round configuration exhibited a weaker trailing vortex below the impeller. Based upon vorticity, velocity magnitudes and the highest achieved levels of shear and turbulence, it was observed that the paddle impeller configuration exhibited flow characteristics most comparable to an axial flow impeller.

Dimensional shear stresses of $\bar{\tau} \approx 0.0657$ dyn/cm^2 were measured, these being approximately 15-fold below the maximum shear stress reported by Ismadi *et al.* (2014) to be detrimental towards iPSC proliferation. Due to the highly sensitive nature of iPSCs, although no impact on cell viability is predicted, the level of shear within the flow is most likely also a contributing factor to the differentiation pathway.

The variation in quality of suspension was then investigated for each bioreactor configuration. It was observed that the lower trailing vortex below the impeller, generated with the flat bottom geometry, corresponded to an improvement in the suspension dynamics. Three commercially available microcarriers investigated in both the flat and round geometries showed a 16 – 21 % reduction in the minimum speed required to suspend when using the flat bottom configuration. Measurement of the number of impeller revolutions required to achieved homogeneity, Nt_H, also showed the flat bottom

configuration to exhibit more efficient lift of the microcarriers. For all conditions investigated, a plateau in Nt_H was observed, this was termed the homogeneity-time constant, H_t, representing the minimum number of revolutions required to suspend and was determined to be specific for the microcarrier and bioreactor combination used. H_t was established at speeds in excess of 2 x N_H (the minimum speed needed to achieve homogeneity). Observing the suspension dynamics of the microcarrier types used, it was found that density, size and porosity all influence upon suspension. Smaller sized microcarriers generally required lower rotational speeds to lift, however, were shown to take a longer time to achieve full homogeneity due to their non-porous nature. Increasing microcarrier density was observed to significantly increase the speed and time needed to achieve system homogeneity. Mimics of the embryoid bodies (EBs) in iPSC-CM culture at the start (Day 2) and end (Day 9) of differentiation were characterised to suspend at N_H = 38 and 54 rpm, respectively, requiring approximately 8 revolutions to lift.

Suspension dynamics of the flat bottom DASGIP configuration operating under intermittent agitation modes was investigated, focusing upon the time required to resuspend following a dwell phase, and the extent of settling to occur during the dwell. Resuspension of the microcarriers, irrespective of the dwell phase duration, was shown to occur rapidly. The extent of settling was found to increase with dwell duration and was also affected by microcarrier properties, in a similar fashion to suspension characteristics. Porous microcarriers were shown to settle the least during the dwell phase, whilst the larger microcarriers were shown to settle much faster. This suggested the intermittent agitation modes applied during cell culture would result in variable degrees of settling as EB characteristics evolved over time.

Flow frequency analysis observed the mimic of EBs at the end of differentiation, which were larger in size, to increase the energy associated to the characteristic low frequency peaks by approximately two-fold. This was in comparison to single-phase and two-phase systems using the mimic of the EBs at the start of differentiation, which were smaller in size. It was observed that this amplification would occur for longer dwell durations. Considering the above observation, it can be hypothesised that the greater and faster extent of settling exhibited by the larger EBs, was the contributing factor to the amplification of the low frequency peaks. A longer dwell duration results in a greater extent of settling. An increase in EB size, at the same dwell duration, also results in a greater extent of settling. Both dwell duration and EB size are therefore shown to increase amplification of the low frequency peaks.

Phase-resolved assessment of velocity fields, shear and turbulence were obtained for the flat bottom DASGIP configuration, operating under both continuous and intermittent agitation modes. The PIV measurements showed the greatest regions of both shear and turbulence to coincide with the interfaces between trailing vortices, the impeller tip and the bioreactor wall. During intermittent agitation the flow exhibited a continued inertia of one revolution at the start of the dwell phase before velocities begun to decay until approximately T_{dwell} = 12 s, when the flow was estimated to become fully stationary.

Based upon space-averaged results considering the entire flow volume, a small transient impulse (+5 % and +15 % the considered steady state) in shear rate and turbulence at the incidence of the dwell phase was observed. A second, more intense spike was observed with the restart in impeller motion, the magnitude of which was shown to linearly increase with the dwell duration, until longer dwell times where a static flow was reached at the end of the dwell ($T_{dwell} \geq$ 12,000 ms), and the observed spike was shown to plateau. The maximum amplification in the transient after the dwell reached up to 82 % and 168 %, respectively for shear and turbulence, although strong axial anisotropy was observed where the radial jet collides with the bioreactor wall, suggesting underestimation of the turbulent and periodic kinetic energy characterised in this region. The investigation of suspension dynamics concluded the time required to resuspend particulates following a dwell phase was rapid, irrespective of dwell duration. This can be attributed to the amplification of the spike in shear rate and turbulence following the dwell increasing with dwell duration. It should also be noted that the highest shear stresses, determined at T_{dwell} = 30,000 ms, remained 5-fold lower than those in literature deemed detrimental to iPSC cell proliferation (Ismadi *et al.*, 2014).

The biological investigation observed an increase in the energy intensity associated to the characterised low frequency peaks to increase the cardiogenic differentiation yield. This occurred as a result of a conservative increase in the dwell duration. Excessive amplification proved detrimental to biological outcomes. The increase in the second impulse of shear and turbulence with dwell duration can likewise be correlated with the increase in differentiation efficiency, although the same limitation to the level of amplification before becoming detrimental to differentiation yields will likely apply.

Mixing dynamics were assessed in the flat bottom DASGIP bioreactor configuration, operating under both continuous and intermittent agitation modes, using DISMT. Two distinct segregated regions of mixing were observed during continuous agitation; a fast mixing region in the bulk flow, which accounts for 78 – 96 % the total flow volume,

depending upon the rotational speed applied, and a slow mixing region around the impeller shaft. Mixing number was measured to be up to 7-fold higher in the slow mixing region, where swirling circumferential flow around the impeller caused a region of entrapment and limited pH change was visualised to occur. This region caused the most significant variability between experimental repeats. As rotational speed increased this region of slow mixing decreased in size and standard deviation. The overall mixing number for the flat bottom DASGIP bioreactor configuration, equipped with the two-blade paddle impeller, was found to be $Nt_m = 40.14 – 31.97$ for $N = 75 – 120$ rpm, reaching a plateau at $N = 105 – 120$ rpm. $Nt_m = 31.97$ is within the performance range of conventionally used impellers ($Nt_m = 17 – 47$), such as the Rushton turbine, marine impeller and the pitched blade turbine impeller (Lee and Yianneskis, 1997; Liepe *et al.*, 1998; Micheletti *et al.*, 2003; Ducci and Yianneskis, 2007; van Eikenhorst *et al.*, 2014), although much variation in mixing performance is reported in the literature, depending upon the mixing time definition and the measurement technique utilised.

The mixing dynamics were shown to significantly improve with intermittent agitation. The two observed spikes for the shear rate and turbulence were demonstrated to have a significant positive impact upon the mixing profile, however the timing of feed insertion with respect to the dwell phase was shown to also strongly influence the extent of mixing enhancement this may have. As the dwell duration was increased, a trade-off between two conflicting elements was apparent: the deterioration of mixing efficiency with the decay of fluid motion, until a static flow was reached, where mixing via diffusion dominated; and the increasing intensity of the spike in shear rate and turbulence, at the end of the dwell phase. It was suggested that timing feed insertion with the end of the dwell phase could fully exploit the second, more intense spike observed for shear rate and turbulence, improving the mixing efficiency. As longer dwell durations were observed to increase the spike intensity, the beneficial impact of feed insertion at the end of the dwell can be maximised for longer dwell durations. In addition, ensuring the maximum time interval of impeller rotation following the dwell would result in a fully mixed system before the subsequent dwell phase (t_m was shorter than T_{inv}), avoiding the detrimental impact upon mixing due to flow deceleration during the dwell. The stop-start motion of the impeller also aided in the break-up of the swirling slow mixing region, significantly reducing the variability between experimental repeats and enhancing the mixing time.

As highlighted, the impeller region represents the area of highest shear and turbulence, both of which have been shown to spike during the transient between dwell phases,

depending upon the dwell duration. Excessive levels of shear and turbulence could prove detrimental to cell proliferation or differentiation pathways. The extent of EB settling and the amplification of the energy associated to the low frequency peaks are both determined by dwell duration, which has been shown to have more significant influence at the end of differentiation with the increase in EB size. In addition, accumulation of the settled aggregates within the impeller region may occur, exposing cells to harsher levels of shear and turbulence than in the bulk flow, especially during the transient between a dwell phase and impeller motion with the observed impulse in shear and turbulence. Thus, careful consideration of dwell duration should be made, considering the influence both at the start and end of differentiation.

6.3 Recommendations for future work

The Laser Doppler Anemometry results presented in Chapter 3 provided an extensive characterisation of the three determined time components, N, T_{inv} and T_{dwell}, and their individual impact upon the characteristic flow frequencies. Measurements were taken in two discrete points within the bioreactor, one above the impeller blade between the bioreactor wall and impeller shaft, the other higher in the bulk region of the flow. Measurement below the impeller region and closer to the impeller blade tip would be beneficial for further comparison of the tangential velocity component with PIV data, and for a better understanding of flow frequencies in the regions of highest shear and turbulence.

To gain further insight into the impact of the three time components upon biological outcomes, the following suggestions explore the main conditions of interest; biological studies and flow frequency analysis investigating extended ranges in low frequency intensity (through larger adjustment of T_{dwell}); biological studies and further engineering characterisation of varying ranges in the low frequency peaks, maintaining energy intensity (through adjustment of T_{dwell} and T_{inv}); biological studies investigating a range of rotational speeds, maintaining constant the number of missed revolutions during the dwell phase (through adjustment of N and T_{dwell}); biological studies to apply the knowledge obtained in this thesis towards optimisation of the differentiation protocol of human stem cell lines. The in-depth characterisation of extended dwell durations in Chapters 4 and 5 would benefit from additional biological data to correlate with the more drastic changes in flow suspension and flow dynamics in relation to biological outcomes.

The results obtained in Chapters 4 and 5 sought to characterise two DASGIP bioreactor configurations from an engineering perspective. Works in the literature have also described the DASGIP system equipped with an axial flow pitched blade turbine-type impeller for cell culture studies (Nienow *et al.*, 2016b). Thus, characterisation and comparison should also be made to this configuration. A mimic of the DASGIP bioreactor configurations investigated could also be made such as to ensure full, unencumbered optical access to the base of the tank for $r\theta$-plane measurements. Due to the unbaffled nature of the DASGIP the tangential component within the flow is dominant, however flow field quantification of this velocity component was not possible in this work. In addition, the inclusion of all probes utilised during a typical cell culture process should also be applied to future measurements. The use of either clear or blacked out probe mimics must be first investigated however, to maximise the field of view without compromising measurement accuracy.

The comparison with mixing number determined in the literature for a range of impeller types highlighted the large variability in mixing dynamics reported, due to inconsistencies in mixing time definition and measurement technique. Assessment of mixing dynamics either utilising a second technique, or with various impeller-bioreactor configurations utilising the DISMT technique, described in this thesis, would be beneficial for improved comparison of mixing performance for other impeller types.

The mixing dynamics investigation in Chapter 5 suggested the enhancement of mixing from the introduction of intermittent agitation with feed insertion made at the end of the dwell phase. Additional studies carried out using a timing box and syringe pump for feed insertion can increase the robustness and reproducibility of the results obtained and provide additional data for more quantitative comparisons.

As discussed in Chapters 3 and 4, the addition of a second phase during engineering characterisation provided insight into how the intensity of the low frequency peaks and extent of settling both increased at the end of differentiation, with the larger sized embryoid bodies. Addition of a second phase, for the investigations conducted in Chapter 5, may also show similar impact upon the impulse intensity observed during intermittent agitation or may significantly impact upon the mixing efficiencies measured. More data is therefore needed on the flow and mixing dynamics in the presence of a second phase, mimicking the embryoid bodies both at the start and end of differentiation, to provide a better representation of the cell culture conditions being characterised.

REFERENCES

Abecasis, B., Aguiar, T., Arnault, É., Costa, R., Gomes-Alves, P., Aspegren, A., Serra, M. and Alves, P. M. (2017) 'Expansion of 3D human induced pluripotent stem cell aggregates in bioreactors: Bioprocess intensification and scaling-up approaches', *Journal of Biotechnology*, 246, pp. 81–93. doi: 10.1016/j.jbiotec.2017.01.004.

Acimovic, I., Vilotic, A., Pesl, M., Lacampagne, A., Dvorak, P., Rotrekl, V. and Meli, A. C. (2014) 'Human pluripotent stem cell-derived cardiomyocytes as research and therapeutic tools.', *BioMed research international*, 2014, pp. 1–15. doi: 10.1155/2014/512831.

Araki, R., Uda, M., Hoki, Y., Sunayama, M., Nakamura, M., Ando, S., Sugiura, M., Ideno, H., Shimada, A., Nifuji, A. and Abe, M. (2013) 'Negligible immunogenicity of terminally differentiated cells derived from induced pluripotent or embryonic stem cells.', *Nature*, 494, pp. 100–4. doi: 10.1038/nature11807.

Armenante, P. M., Luo, C. and Chou, C. (1997) 'Velocity profiles in a closed, unbaffled vessel: comparison between experimental LDV data and numerical CFD predictions', *Chemical Engineering Science*, 52(20), pp. 3483–3492.

Armstrong, S. G. and Ruszkowsk, S. (1987) 'Measurement and comparison of flows generated by different types of impeller in a stirred tank', in *Proc. Colloq. on Mechanical Agitation*. Toulouse, p. 1.9-1.16.

Aubin, J., Mavros, P., Fletcher, D. F., Bertrand, J. and Xuereb, C. (2001) 'Effect of axial agitator configuration (up-pumping, down-pumping, reverse rotation) on flow patterns generated in stirred vessels', *Chemical Engineering Research and Design*, 79(8), pp. 845–856. doi: 10.1205/02638760152721046.

Aubin, J., Le Sauze, N., Bertrand, J., Fletcher, D. F. and Xuereb, C. (2004) 'PIV measurements of flow in an aerated tank stirred by a down- and an up-pumping axial flow impeller', *Experimental Thermal and Fluid Science*, 28(5), pp. 447–456. doi: 10.1016/j.expthermflusci.2001.12.001.

Bach, C., Yang, J., Larsson, H., Stocks, S. M., Gernaey, K. V., Albaek, M. O. and Krühne, U. (2017) 'Evaluation of mixing and mass transfer in a stirred pilot scale bioreactor utilizing CFD', *Chemical Engineering Science*, 171, pp. 19–26. doi:

10.1016/j.ces.2017.05.001.

Baldi, S. and Yianneskis, M. (2003) ‘On the direct measurement of turbulence energy dissipation in stirred vessels with PIV’, *Industrial and Engineering Chemistry Research*, 42(26), pp. 7006–7016. doi: 10.1021/ie0208265.

Barad, L., Schick, R., Zeevi-Levin, N., Itskovitz-Eldor, J. and Binah, O. (2014) ‘Human embryonic stem cells vs human induced pluripotent stem cells for cardiac repair’, *Canadian Journal of Cardiology*, 30(11), pp. 1279–1287. doi: 10.1016/j.cjca.2014.06.023.

Bauwens, C., Yin, T., Dang, S., Peerani, R. and Zandstra, P. W. (2005) ‘Development of a perfusion fed bioreactor for embryonic stem cell-derived cardiomyocyte generation: oxygen-mediated enhancement of cardiomyocyte output.’, *Biotechnology and bioengineering*, 90(4), pp. 452–61. doi: 10.1002/bit.20445.

Bouremel, Y., Yianneskis, M. and Ducci, A. (2009) ‘On the utilisation of vorticity and strain dynamics for improved analysis of stirred processes’, *Chemical Engineering Research and Design*, 87(4), pp. 377–385. doi: 10.1016/j.cherd.2008.11.016.

Brunazzi, E., Galletti, C., Paglianti, A. and Pintus, S. (2005) ‘Screening tool to evaluate the levels of local anisotropy of turbulence in stirred vessels’, *Industrial and Engineering Chemistry Research*, 44(15), pp. 5836–5844. doi: 10.1021/ie0489103.

Burridge, P. W., Keller, G., Gold, J. D. and Wu, J. C. (2012) ‘Production of de novo cardiomyocytes: human pluripotent stem cell differentiation and direct reprogramming’, *Cell Stem Cell*, 10(1), pp. 16–28. doi: 10.1016/j.stem.2011.12.013.Production.

Burridge, P. W., Thompson, S., Millrod, M. A., Weinberg, S., Yuan, X., Peters, A., Mahairaki, V., Koliatsos, V. E., Tung, L. and Zambidis, E. T. (2011) ‘A universal system for highly efficient cardiac differentiation of human induced pluripotent stem cells that eliminates interline variability’, *PLoS ONE*, 6. doi: 10.1371/journal.pone.0018293.

Cabaret, F., Bonnot, S., Fradette, L. and Tanguy, P. A. (2007) ‘Mixing time analysis using colorimetric methods and image processing’, *Ind. Eng. Chem. Res.*, 46(14), pp. 5032–5042.

Carletti, C., Montante, G., De Blasio, C. and Paglianti, A. (2016) ‘Liquid mixing dynamics in slurry stirred tanks based on electrical resistance tomography’, *Chemical*

Engineering Science., 152, pp. 478–487. doi: 10.1016/j.ces.2016.06.044.

Caspi, O., Huber, I., Kehat, I., Habib, M., Arbel, G., Gepstein, A., Yankelson, L., Aronson, D., Beyar, R. and Gepstein, L. (2007) 'Transplantation of human embryonic stem cell-derived cardiomyocytes improves myocardial performance in infarcted rat hearts', *Journal of the American College of Cardiology*, 50, pp. 1884–1893. doi: 10.1016/j.jacc.2007.07.054.

Chara, Z., Kysela, B., Konfrst, J. and Fort, I. (2016) 'Study of fluid flow in baffled vessels stirred by a Rushton standard impeller', *Applied Mathematics and Computation*, 272, pp. 614–628. doi: 10.1016/j.amc.2015.06.044.

Chen, A., Ting, S., Seow, J., Reuveny, S. and Oh, S. (2014) 'Considerations in designing systems for large scale production of human cardiomyocytes from pluripotent stem cells.', *Stem cell research & therapy*, 5(12), pp. 1–13. doi: 10.1186/scrt401.

Chen, X., Chen, A., Woo, T. L., Choo, A. B. H., Reuveny, S. and Oh, S. K. W. (2010) 'Investigations into the metabolism of two-dimensional colony and suspended microcarrier cultures of human embryonic stem cells in serum-free media', *Stem Cells and Development*, 19(11), pp. 1781–1792. doi: 10.1089/scd.2010.0077.

Cherry, R. S. and Papoutsakis, E. T. (1986) 'Hydrodynamic effects on cells in agitated tissue culture reactors', *Bioprocess Engineering*, 1(1), pp. 29–41. doi: 10.1007/BF00369462.

Chow, M., Boheler, K. R. and Li, R. a (2013) 'Human pluripotent stem cell-derived cardiomyocytes for heart regeneration, drug discovery and disease modeling: from the genetic, epigenetic, and tissue modeling perspectives.', *Stem cell research & therapy*, 4(97), pp. 1–13. doi: 10.1186/scrt308.

Ciofalo, M., Brucato, A., Grisafi, F. and Torraca, N. (1996) 'Turbulent flow in closed and free-surface unbaffled tanks stirred by radial impellers', *Chemical Engineering Science*, 51(14), pp. 3557–3573.

Collignon, M. L., Delafosse, A., Crine, M. and Toye, D. (2010) 'Axial impeller selection for anchorage dependent animal cell culture in stirred bioreactors: Methodology based on the impeller comparison at just-suspended speed of rotation', *Chemical Engineering Science*, 65(22), pp. 5929–5941. doi: 10.1016/j.ces.2010.08.027.

Cormier, J. T., zur Nieden, N. I., Rancourt, D. E. and Kallos, M. S. (2006) 'Expansion

of undifferentiated murine embryonic stem cells as aggregates in suspension culture bioreactors.', *Tissue engineering*, 12, pp. 3233–3245. doi: 10.1089/ten.2006.12.ft-254.

Correia, C., Serra, M., Espinha, N., Sousa, M., Brito, C., Burkert, K., Zheng, Y., Hescheler, J., Carrondo, M. J. T., Sarić, T. and Alves, P. M. (2014) 'Combining hypoxia and bioreactor hydrodynamics boosts induced pluripotent stem cell differentiation towards cardiomyocytes.', *Stem cell reviews*, 10(6), pp. 786–801. doi: 10.1007/s12015-014-9533-0.

Costes, J. and Couderc, J. P. (1988) 'Study by Laser Doppler Anemometry of the turbulent flow induced by a Rushton turbine in a stirred tank: Influence of the size of the units—II. Spectral analysis and scales of turbulence', *Chemical Engineering Science*, 43(10), pp. 2765–2772. doi: 10.1016/0009-2509(88)80019-8.

Deen, N. G., Solberg, T. and Hjertager, B. H. (2002) 'Flow generated by an aerated Rushton impeller: two-phase PIV experiments and numerical simulations', *The Canadian Journal of Chemical Engineering*, 80, pp. 1–15. doi: 10.1002/cjce.5450800406.

Delaplace, G., Bouvier, L., Moreau, A., Guérin, R. and Leuliet, J. C. (2004) 'Determination of mixing time by colourimetric diagnosis - Application to a new mixing system', *Experiments in Fluids*, 36(3), pp. 437–443. doi: 10.1007/s00348-003-0741-7.

Delaplace, G., Dieulot, J., Brienne, J. and Leuliet, J. (1999) 'Détermination expérimentale et prédiction des temps de circulation et de mélange pour un système d'agitation hélicoïdal', *The Canadian Journal of Chemical Engineering*, 77, pp. 447–457. doi: 10.1002/cjce.5450770303.

Derksen, J. J., Doelman, M. S. and Van Den Akker, H. E. A. (1999) 'Three-dimensional LDA measurements in the impeller region of a turbulently stirred tank', *Experiments in Fluids*. Lisbon, 27, pp. 522–532. doi: 50202.

Doppler, S. a, Deutsch, M.-A., Lange, R. and Krane, M. (2013) 'Cardiac regeneration: current therapies-future concepts.', *Journal of thoracic disease*, 5(5), pp. 683–97. doi: 10.3978/j.issn.2072-1439.2013.08.71.

Doulgerakis, Z., Yianneskis, M. and Ducci, A. (2009) 'On the interaction of trailing and macro-instability vortices in a stirred vessel-enhanced energy levels and improved mixing potential', *Chemical Engineering Research and Design*, 87(4), pp. 412–420.

doi: 10.1016/j.cherd.2008.12.019.

Doulgerakis, Z., Yianneskis, M. and Ducci, A. (2011) ‘On the manifestation and nature of macroinstabilities in stirred vessels’, *AIChE Journal*, 57(11), pp. 2941–2954. doi: 10.1002/aic.

Ducci, A. and Yianneskis, M. (2007) ‘Vortex tracking and mixing enhancement in stirred processes’, *AIChE Journal*, 53(2), pp. 305–315.

van Eikenhorst, G., Thomassen, Y. E., van der Pol, L. A. and Bakker, W. A. M. (2014) ‘Assessment of mass transfer and mixing in rigid lab-scale disposable bioreactors at low power input levels’, *Biotechnology Progress*, 30(6), pp. 1269–1276. doi: 10.1002/btpr.1981.

Elias, C. B., Desai, R. B., Patole, M. S., Joshi, J. B. and Mashelkar, R. A. (1995) ‘Turbulent shear stress-effect on mammalian cell culture and measurement using laser doppler anemometer’, *Chemical Engineering Science*, 50(15), pp. 2431–2440. doi: 10.1016/0009-2509(95)00084-I.

Escudié, R., Bouyer, D. and Liné, A. (2004) ‘Characterization of trailing vortices generated by a Rushton turbine’, *AIChE Journal*, 50(1), pp. 75–86. doi: 10.1002/aic.10007.

Escudié, R. and Liné, A. (2003) ‘Experimental analysis of hydrodynamics in a radially agitated tank’, *AIChE Journal*, 49(3), pp. 585–603. doi: 10.1002/aic.690490306.

Fernandes, A. M., Fernandes, T. G., Diogo, M. M., da Silva, C. L., Henrique, D. and Cabral, J. M. S. (2007) ‘Mouse embryonic stem cell expansion in a microcarrier-based stirred culture system’, *Journal of Biotechnology*, 132, pp. 227–236. doi: 10.1016/j.jbiotec.2007.05.031.

Fernandes, A. M., Marinho, P. A. N., Sartore, R. C., Paulsen, B. S., Mariante, R. M., Castilho, L. R. and Rehen, S. K. (2009) ‘Successful scale-up of human embryonic stem cell production in a stirred microcarrier culture system’, *Brazilian Journal of Medical and Biological Research*, 42(6), pp. 515–522. doi: 10.1590/s0100-879x2009000600007.

Gabriele, A., Nienow, A. W. and Simmons, M. J. H. (2009) ‘Use of angle resolved PIV to estimate local specific energy dissipation rates for up- and down-pumping pitched blade agitators in a stirred tank’, *Chemical Engineering Science*, 64(1), pp. 126–143. doi: 10.1016/j.ces.2008.09.018.

Ge, D., Liu, X., Li, L., Wu, J., Tu, Q., Shi, Y. and Chen, H. (2009) ‘Chemical and physical stimuli induce cardiomyocyte differentiation from stem cells’, *Biochemical and Biophysical Research Communications*, 381(3), pp. 317–321. doi: 10.1016/j.bbrc.2009.01.173.

GE Healthcare Life Sciences (2013) *Microcarrier Cell Culture: Principles and Methods*.

Geuss, L. R. and Suggs, L. J. (2013) ‘Making cardiomyocytes: how mechanical stimulation can influence differentiation of pluripotent stem cells.’, *Biotechnology progress*, 29(5), pp. 1089–96. doi: 10.1002/btpr.1794.

Go, A. S. *et al.* (2014) *Heart disease and stroke statistics-2014 update: a report from the American Heart Association., Circulation*. doi: 10.1161/01.cir.0000441139.02102.80.

Grein, T. A., Leber, J., Blumenstock, M., Petry, F., Weidner, T., Salzig, D. and Czermak, P. (2016) ‘Multiphase mixing characteristics in a microcarrier-based stirred tank bioreactor suitable for human mesenchymal stem cell expansion’, *Process Biochemistry*, 51(9), pp. 1109–1119. doi: 10.1016/j.procbio.2016.05.010.

Gwak, S. J., Bhang, S. H., Kim, I. K., Kim, S. S., Cho, S. W., Jeon, O., Yoo, K. J., Putnam, A. J. and Kim, B. S. (2008) ‘The effect of cyclic strain on embryonic stem cell-derived cardiomyocytes.’, *Biomaterials*, 29(7), pp. 844–56. doi: 10.1016/j.biomaterials.2007.10.050.

Hall, J. F., Barigou, M., Simmons, M. J. H. and Stitt, E. H. (2004) ‘Mixing in unbaffled high-throughput experimentation reactors’, *Industrial and Engineering Chemistry Research*, 43(15), pp. 4149–4158. doi: 10.1021/ie049872q.

Hall, J. F., Barigou, M., Simmons, M. J. H. and Stitt, E. H. (2005) ‘Comparative study of different mixing strategies in small high throughput experimentation reactors’, *Chemical Engineering Science*, 60, pp. 2355–2368. doi: 10.1016/j.ces.2004.10.045.

Hamilton, D. W., Maul, T. M. and Vorp, D. A. (2004) ‘Characterization of the response of bone marrow-derived progenitor cells to cyclic strain: implications for vascular tissue-engineering applications.’, *Tissue engineering*, 10(3–4), pp. 361–369. doi: 10.1089/107632704323061726.

Haubner, B. J., Schuetz, T. and Penninger, J. M. (2018) ‘Cardiac regeneration in a

newborn: what does this mean for future cardiac repair research?', *Expert Review of Cardiovascular Therapy*, 16(3), pp. 155–157. doi: 10.1080/14779072.2018.1438268.

Heathman, T. R. J. (2015) *Developing a process control strategy for the consistent and scalable manufacture of human mesenchymal stem cells*.

van Heeswijk, M., Nijhuis, J. G. and Hollanders, H. M. (1990) 'Fetal heart rate in early pregnancy.', *Early human development*, 22, pp. 151–156. doi: 10.1016/0378-3782(90)90181-H.

Heidenreich, P. A., Trogdon, J. G., Khavjou, O. A., Butler, J., Dracup, K., Ezekowitz, M. D., Finkelstein, E. A., Hong, Y., Johnston, S. C., Khera, A., Lloyd-Jones, D. M., Nelson, S. A., Nichol, G., Orenstein, D., Wilson, P. W. F. and Woo, Y. J. (2011) 'Forecasting the future of cardiovascular disease in the United States: A policy statement from the American Heart Association', *Circulation*, 123, pp. 933–944. doi: 10.1161/CIR.0b013e31820a55f5.

Heo, J. S. and Lee, J. C. (2011) 'β-catenin mediates cyclic strain-stimulated cardiomyogenesis in mouse embryonic stem cells through ROS-dependent and integrin-mediated PI3K/Akt pathways', *Journal of Cellular Biochemistry*, 112, pp. 1880–1889. doi: 10.1002/jcb.23108.

Hockey, R. M. and Nouri, J. M. (1996) 'Turbulent flow in a baffled vessel stirred by a 60° pitched blade impeller', *Chemical Engineering Science*, 51(19), pp. 4405–4421. doi: 10.1016/0009-2509(96)00267-9.

Ibrahim, S., Jasnin, S. N., Wong, S. D. and Baker, I. F. (2012) 'Zwieterings equation for the suspension of porous particles and the use of curved blade impellers', *International Journal of Chemical Engineering*, 2012, pp. 1–13. doi: 10.1155/2012/749760.

Ibrahim, S. and Nienow, A. W. (1996) 'Particle suspension in the turbulent regime: The effect of impeller type and impeller/vessel configuration', *Trans IChemE Part A, Chem Eng Res Des*, 74, pp. 679–688.

Ibrahim, S. and Nienow, A. W. (2004) 'Suspension of microcarriers for cell culture with axial flow impellers', *Chemical Engineering Research and Design*, 82(9), pp. 1082–1088. doi: 10.1205/cerd.82.9.1082.44161.

Illi, B., Scopece, A., Nanni, S., Farsetti, A., Morgante, L., Biglioli, P., Capogrossi, M. C. and Gaetano, C. (2005) 'Epigenetic histone modification and cardiovascular lineage

programming in mouse embryonic stem cells exposed to laminar shear stress', *Circulation Research*, 96, pp. 501–508. doi: 10.1161/01.RES.0000159181.06379.63.

Ismadi, M., Gupta, P., Fouras, A., Verma, P., Jadhav, S., Bellare, J. and Hourigan, K. (2014) 'Flow characterization of a spinner flask for induced pluripotent stem cell culture application.', *PloS one*, 9(10), pp. 1–11. doi: 10.1371/journal.pone.0106493.

Itskovitz-eldor, J., Schuldiner, M., Karsenti, D., Eden, A., Amit, M., Soreq, H. and Benvenisty, N. (2000) 'Differentiation of human embryonic stem cells into embryoid bodies comprising the three embryonic germ layers', *Molecular Medicine*, 6, pp. 88–95. Available at: http://www.ncbi.nlm.nih.gov/pubmed/10859025.

Jeong, J. and Hussain, F. (1995) 'On the identification of a vortex', *Journal of Fluid Mechanics*, 285, pp. 69–94. doi: 10.1017/S0022112095000462.

Kaiser, S. C., Eibl, R. and Eible, D. (2011) 'Engineering characteristics of a single-use stirred bioreactor at bench-scale: The Mobius CellReady 3L bioreactor as a case study', *Engineering in Life Sciences*, 11(4), pp. 359–368. doi: 10.1002/elsc.201000171.

Kasat, G. R. and Pandit, A. B. (2008) 'Mixing time studies in multiple impeller agitated reactors', *The Canadian Journal of Chemical Engineering*, 82(5), pp. 892–904. doi: 10.1002/cjce.5450820504.

Kattman, S. J., Witty, A. D., Gagliardi, M., Dubois, N. C., Niapour, M., Hotta, A., Ellis, J. and Keller, G. (2011) 'Stage-specific optimization of activin/nodal and BMP signaling promotes cardiac differentiation of mouse and human pluripotent stem cell lines', *Cell Stem Cell*, 8, pp. 228–240. doi: 10.1016/j.stem.2010.12.008.

Kehat, I., Kenyagin-Karsenti, D., Snir, M., Segev, H., Amit, M., Gepstein, A., Livne, E., Binah, O., Itskovitz-Eldor, J. and Gepstein, L. (2001) 'Human embryonic stem cells can differentiate into myocytes with structural and functional properties of cardiomyocytes', *J Clin Invest*, 108, pp. 407–414. doi: 10.1172/JCI12131.

Kehoe, D. E., Jing, D., Lock, L. T. and Tzanakakis, E. S. (2010) 'Scalable stirred-suspension bioreactor culture of human pluripotent stem cells.', *Tissue engineering. Part A*, 16, pp. 405–421. doi: 10.1089/ten.tea.2009.0454.

Keung, A. J., Healy, K. E., Kumar, S. and Schaffer, D. V. (2010) 'Biophysics and dynamics of natural and engineered stem cell microenvironments', *Wiley Interdisciplinary Reviews: Systems Biology and Medicine*, pp. 49–64. doi:

10.1002/wsbm.46.

Keung, W., Boheler, K. R. and Li, R. a (2014) ‘Developmental cues for the maturation of metabolic, electrophysiological and calcium handling properties of human pluripotent stem cell-derived cardiomyocytes.’, *Stem cell research & therapy*, 5(1), p. 17. doi: 10.1186/scrt406.

Khopkar, A., Aubin, J., Rubio-Atoche, C., Xuereb, C., Le Sauze, N., Bertrand, J. and Ranade, V. V. (2004) ‘Flow Generated by Radial Flow Impellers : PIV Measurements and CFD Simulations’, *International Journal of Chemical Reactor Engineering*, 2, pp. 1–17. doi: 10.2202/1542-6580.1146.

Kreke, M. R., Huckle, W. R. and Goldstein, A. S. (2005) ‘Fluid flow stimulates expression of osteopontin and bone sialoprotein by bone marrow stromal cells in a temporally dependent manner’, *Bone*, 36, pp. 1047–1055. doi: 10.1016/j.bone.2005.03.008.

Kresta, S. M. and Wood, P. E. (1993) ‘The flow field produced by a pitched blade turbine: Characterization of the turbulence and estimation of the dissipation rate’, *Chemical Engineering Science*, 48(10), pp. 1761–1774. doi: 10.1016/0009-2509(93)80346-R.

Kreutzer, J., Ikonen, L., Hirvonen, J., Pekkanen-Mattila, M., Aalto-Setälä, K. and Kallio, P. (2014) ‘Pneumatic cell stretching system for cardiac differentiation and culture.’, *Medical engineering & physics*, 36(4), pp. 496–501. doi: 10.1016/j.medengphy.2013.09.008.

van Laake, L. W., Passier, R., Doevendans, P. A. and Mummery, C. L. (2008) ‘Human embryonic stem cell-derived cardiomyocytes and cardiac repair in rodents’, *Circulation Research*, 102, pp. 1008–1010. doi: 10.1161/CIRCRESAHA.108.175505.

Laflamme, M. A. *et al.* (2007) ‘Cardiomyocytes derived from human embryonic stem cells in pro-survival factors enhance function of infarcted rat hearts.’, *Nature biotechnology*, 25(9), pp. 1015–24. doi: 10.1038/nbt1327.

Lam, A. T. L., Chen, A. K. L., Li, J., Birch, W. R., Reuveny, S. and Oh, S. K. W. (2014) ‘Conjoint propagation and differentiation of human embryonic stem cells to cardiomyocytes in a defined microcarrier spinner culture.’, *Stem cell research & therapy*, 5(5), p. 110. doi: 10.1186/scrt498.

Langheinrich, C. and Nienow, A. W. (1999) ‘Control of pH in large-scale, free suspension animal cell bioreactors: Alkali addition and pH excursions’, *Biotechnology and Bioengineering*, 66(3), pp. 171–179. doi: 10.1002/(SICI)1097-0290(1999)66:3<171::AID-BIT5>3.0.CO;2-T.

Lara, A. R., Galindo, E., Ramirez, O. T. and Palomares, L. A. (2006) ‘Living with heterogeneities in bioreactors’, *Molecular Biotechnology*, 34(3), pp. 355–381. doi: 10.1385/mb:34:3:355.

Lau, J. (2013) *The combined effect of mechanical and chemical stimulation on the differentiation of induced pluripotent stem cells into cardiomyocytes*.

Lecina, M., Ting, S., Choo, A., Reuveny, S. and Oh, S. (2010) ‘Scalable platform for human embryonic stem cell differentiation to cardiomyocytes in suspended microcarrier cultures.’, *Tissue engineering. Part C, Methods*, 16, pp. 1609–1619. doi: 10.1089/ten.tec.2010.0104.

Lee, K. C. and Yianneskis, M. (1997) ‘A liquid crystal thermographic technique for the measurement of mixing characteristics in stirred vessels’, *Chemical Engineering Research and Design*, 75(8), pp. 746–754. doi: 10.1205/026387697524416.

Lee, K. C. and Yianneskis, M. (1998) ‘Turbulence properties of the impeller stream of a Rushton turbine’, *AIChE Journal*, 44(1), pp. 13–24.

Leor, J., Gerecht, S., Cohen, S., Miller, L., Holbova, R., Ziskind, A., Shachar, M., Feinberg, M. S., Guetta, E. and Itskovitz-Eldor, J. (2007) ‘Human embryonic stem cell transplantation to repair the infarcted myocardium.’, *Heart (British Cardiac Society)*, 93, pp. 1278–1284. doi: 10.1136/hrt.2006.093161.

Li, Q., Rycaj, K., Chen, X. and Tang, D. G. (2016) ‘Cancer stem cells and cell size: A causal link?’, *Semin Cancer Biol.*, 35, pp. 191–199. doi: 10.1016/j.semcancer.2015.07.002.Cancer.

Lian, X., Hsiao, C., Wilson, G., Zhu, K., Hazeltine, L. B., Azarin, S. M., Raval, K. K., Zhang, J., Kamp, T. J. and Palecek, S. P. (2012) ‘Robust cardiomyocyte differentiation from human pluripotent stem cells via temporal modulation of canonical Wnt signaling.’, *Proceedings of the National Academy of Sciences of the United States of America*, 109, pp. E1848-57. doi: 10.1073/pnas.1200250109.

Liepe, F., Sperling, R. and Jembere, S. (1998) *Rührwerke – Theoretische Grundlagen*,

Auslegung und Bewertung, Eigenverlag FH Anhalt, Köthen.

Liu, S., Ruban, L., Wang, Y., Zhou, Y. and Nesbeth, D. N. (2017) 'Establishing elements of a synthetic biology platform for Vaccinia virus production: BioBrick™ design, serum-free virus production and microcarrier-based cultivation of CV-1 cells', *Heliyon*. Elsevier Ltd., 3(2), p. e00238. doi: 10.1016/j.heliyon.2017.e00238.

Ma, J., Guo, L., Fiene, S. J., Anson, B. D., Thomson, J. a, Kamp, T. J., Kolaja, K. L., Swanson, B. J. and January, C. T. (2011) 'High purity human-induced pluripotent stem cell-derived cardiomyocytes: electrophysiological properties of action potentials and ionic currents.', *American journal of physiology. Heart and circulatory physiology*, 301, pp. H2006-17. doi: 10.1152/ajpheart.00694.2011.

Madhuri, P. S., Moukthika, B. S., Sumanth, N., Vinusha, K. S. and Ganduri, V. S. R. K. (2016) 'Effects of agitation and aeration in mixing time determination for viscous suspensions using double indicator system', *Research Journal of Pharmacy and Technology*, 9(11), pp. 1971–1977. doi: 10.5958/0974-360X.2016.00403.0.

Maul, T. M., Chew, D. W., Nieponice, A. and Vorp, D. a (2011) 'Mechanical stimuli differentially control stem cell behavior: morphology, proliferation, and differentiation.', *Biomechanics and modeling in mechanobiology*, 10(6), pp. 939–53. doi: 10.1007/s10237-010-0285-8.

Melton, L. A., Lipp, C. W., Spradling, R. W. and Paulson, K. A. (2002) 'DISMT - Determination of mixing time through color changes', *Chemical Engineering Communications*, 189(3), pp. 322–338. doi: 10.1080/00986440212077.

Menasche, P., Vanneaux, V., Hagege, A., Bel, A., Cholley, B., Cacciapuoti, I., Parouchev, A., Benhamouda, N., Tachdjian, G., Tosca, L., Trouvin, J. H., Fabreguettes, J. R., Bellamy, V., Guillemain, R., Suberbielle, C., Tartour, E., Desnos, M. and Larghero, J. (2015) 'Human embryonic stem cell-derived cardiac progenitors for severe heart failure treatment: First clinical case report', *European Heart Journal*, 36(30), pp. 2011–2017. doi: 10.1093/eurheartj/ehv189.

Metzner, A. B. and Otto, R. E. (1957) 'Agitation of non-Newtonian fluids', *AIChE Journal*, 3, pp. 3–10. doi: 10.1002/aic.690030103.

Micheletti, M., Nikiforaki, L., Lee, K. C. and Yianneskis, M. (2003) 'Particle concentration and mixing characteristics of moderate-to-dense solid-liquid suspensions', *Industrial & Engineering Chemistry Research*, 42(24), pp. 6236–6249.

doi: Doi 10.1021/Ie0303799.

Mihic, A., Li, J., Miyagi, Y., Gagliardi, M., Li, S.-H., Zu, J., Weisel, R. D., Keller, G. and Li, R.-K. (2014) 'The effect of cyclic stretch on maturation and 3D tissue formation of human embryonic stem cell-derived cardiomyocytes.', *Biomaterials*, 35(9), pp. 2798–808. doi: 10.1016/j.biomaterials.2013.12.052.

Mogi, A., Takei, S., Shimizu, H. and Miura, H. (2013) 'Effects of fluid dynamic forces created by rotary orbital suspension culture on cardiomyogenic differentiation of human embryonic stem cells', *Journal of Medical and Biological Engineering*, 34(2), pp. 101–108. doi: 10.5405/jmbe.1356.

Montante, G., Bakker, A., Paglianti, A. and Magelli, F. (2006) 'Effect of the shaft eccentricity on the hydrodynamics of unbaffled stirred tanks', *Chemical Engineering Science*, 61(9), pp. 2807–2814. doi: 10.1016/j.ces.2005.09.021.

Müller, W. (1985) 'Untersuchung von homogenisiervorgängen in nicht- Newtonschen flüssigkeiten mit einem neuen bildanalytischen verfahren', *TU Dortmund. VDI-Forschungsber*, 3, p. 103. doi: 10.1002/bit.20358.

Mummery, C., Ward-van Oostwaard, D., Doevendans, P., Spijker, R., van den Brink, S., Hassink, R., van der Heyden, M., Opthof, T., Pera, M., de la Riviere, A. B., Passier, R. and Tertoolen, L. (2003) 'Differentiation of human embryonic stem cells to cardiomyocytes: role of coculture with visceral endoderm-like cells.', *Circulation*, 107(21), pp. 2733–40. doi: 10.1161/01.CIR.0000068356.38592.68.

Murphy, S. L., Xu, J. and Kochanek, K. D. (2013) 'Deaths: final data for 2010.', *National vital statistics reports : from the Centers for Disease Control and Prevention, National Center for Health Statistics, National Vital Statistics System*, 61, pp. 1–117. doi: May 8, 2013.

Niebruegge, S., Nehring, A., Bär, H., Schroeder, M., Zweigerdt, R. and Lehmann, J. (2008) 'Cardiomyocyte production in mass suspension culture: embryonic stem cells as a source for great amounts of functional cardiomyocytes.', *Tissue engineering. Part A*, 14(10), pp. 1591–601. doi: 10.1089/ten.tea.2007.0247.

Nienow, A. W. (1997) 'The suspension of solid particles', *Mixing in the Process Industries*, pp. 364–393.

Nienow, A. W., Coopman, K., Heathman, T. R. J., Rafiq, Q. A. and Hewitt, C. J.

(2016a) ‘Bioreactor engineering fundamentals for stem cell manufacturing’, in *Stem Cell Manufacturing*, pp. 43–75. doi: 10.1016/B978-0-444-63265-4.00003-0.

Nienow, A. W., Hewitt, C. J., Heathman, T. R. J., Glyn, V. A. M., Fonte, G. N., Hanga, M. P., Coopman, K. and Rafiq, Q. A. (2016b) ‘Agitation conditions for the culture and detachment of hMSCs from microcarriers in multiple bioreactor platforms’, *Biochemical Engineering Journal*, 108, pp. 24–29. doi: 10.1016/j.bej.2015.08.003.

Nienow, A. W., Rafiq, Q. A., Heathman, T. R. J., Coopman, K. and Hewitt, C. J. (2016c) ‘Mixing theory for culture and harvest in bioreactors of human mesenchymal stem cells on microcarriers’, *Theoretical Foundations of Chemical Engineering*, 50(6), pp. 895–900. doi: 10.1134/S0040579516060117.

Odeleye, A. O. O., Marsh, D. T. J., Osborne, M. D., Lye, G. J. and Micheletti, M. (2014) ‘On the fluid dynamics of a laboratory scale single-use stirred bioreactor’, *Chemical Engineering Science*, 111, pp. 299–312. doi: 10.1016/j.ces.2014.02.032.

Oh, S. K. W., Chen, A. K., Mok, Y., Chen, X., Lim, U. M., Chin, A., Choo, A. B. H. and Reuveny, S. (2009) ‘Long-term microcarrier suspension cultures of human embryonic stem cells’, *Stem Cell Research*, 2, pp. 219–230. doi: 10.1016/j.scr.2009.02.005.

Olmer, R., Lange, A., Selzer, S., Kasper, C., Haverich, A., Martin, U. and Zweigerdt, R. (2012) ‘Suspension culture of human pluripotent stem cells in controlled, stirred bioreactors’, *Tissue Engineering Part C: Methods*, 18(10), pp. 772–784. doi: 10.1089/ten.tec.2011.0717.

Olmos, E., Loubiere, K., Martin, C., Delaplace, G. and Marc, A. (2015) ‘Critical agitation for microcarrier suspension in orbital shaken bioreactors: Experimental study and dimensional analysis’, *Chemical Engineering Science*, 122, pp. 545–554. doi: 10.1016/j.ces.2014.08.063.

Ozturk, S. S. (1996) ‘Engineering challenges in high density cell culture systems.’, *Cytotechnology*, 22(1–3), pp. 3–16. doi: 10.1007/BF00353919.

Park, J. S., Chu, J. S. F., Cheng, C., Chen, F., Chen, D. and Li, S. (2004) ‘Differential effects of equiaxial and uniaxial strain on mesenchymal stem cells’, *Biotechnology and Bioengineering*, 88, pp. 359–368. doi: 10.1002/bit.20250.

Pesl, M. (2013) *Potential applications of cardiomyocytes differentiated from human*

embryonic stem cells and induced pluripotent stem cells in the diseases of the human heart, Medical Biology PhD Thesis.

Phillips, B. W., Horne, R., Lay, T. S., Rust, W. L., Teck, T. T. and Crook, J. M. (2008) 'Attachment and growth of human embryonic stem cells on microcarriers', *Journal of Biotechnology*, 138, pp. 24–32. doi: 10.1016/j.jbiotec.2008.07.1997.

Pieralisi, I., Rodriguez, G., Micheletti, M., Paglianti, A. and Ducci, A. (2016) 'Microcarriers' suspension and flow dynamics in orbitally shaken bioreactors', *Chemical Engineering Research and Design*, 108, pp. 198–209. doi: 10.1016/j.cherd.2015.11.020.

Porrello, E. R., Mahmoud, A. I., Simpson, E., Hill, J. A., James, A., Olson, E. N. and Sadek, H. A. (2011) 'Transient regeneration potential of the neonatal mouse heart', *Science*, 331(6020), pp. 1078–1080. doi: 10.1126/science.1200708.

Rafiq, Q. A., Coopman, K., Nienow, A. W. and Hewitt, C. J. (2016) 'Systematic microcarrier screening and agitated culture conditions improves human mesenchymal stem cell yield in bioreactors', *Biotechnology Journal*, 11(4), pp. 473–486. doi: 10.1002/biot.201400862.

Ramsay, J., Simmons, M. J. H., Ingram, A. and Stitt, E. H. (2016) 'Mixing of Newtonian and viscoelastic fluids using "butterfly" impellers', *Chemical Engineering Science*, 139, pp. 125–141. doi: 10.1016/j.ces.2015.09.026.

Ranade, V. V., Perrard, M., Le Sauze, N., Xuereb, C. and Bertrand, J. (2001) 'Trailing vortices of Rushton turbine: PIV measurements and CFD simulations with snapshot approach', *Chemical Engineering Research and Design*, 79(1), pp. 3–12. doi: 10.1205/026387601528471.

Rebelo, S. R. P. (2015) *Development of 3D in vitro models for prediction of hepatic metabolism and toxicity*.

Reynolds, W. C. and Hussain, A. K. M. F. (1972) 'The mechanics of an organized wave in turbulent shear flow. Part 3. Theoretical models and comparisons with experiments', *J. Fluid Mech.*, 54, pp. 263–288.

Robertson, B. and Ulbrecht, J. J. (1987) 'Measurement of shear rate on an agitator in a fermentation broth', in , *Biotechnology Processes: Scale-up and Mixing*. New York, NY: American Institute of Chemical Engineers, pp. 72–81.

Rodriguez, G., Anderlei, T., Micheletti, M., Yianneskis, M. and Ducci, A. (2014) 'On the measurement and scaling of mixing time in orbitally shaken bioreactors', *Biochemical Engineering Journal*, 82, pp. 10–21. doi: 10.1016/j.bej.2013.10.021.

Rodriguez, G., Micheletti, M. and Ducci, A. (2018) 'Macro- and micro-scale mixing in a shaken bioreactor for fluids of high viscosity', *Chemical Engineering Research and Design*. Institution of Chemical Engineers, 132(2013), pp. 890–901. doi: 10.1016/j.cherd.2018.01.018.

Rodriguez, G., Pieralisi, I., Anderlei, T., Ducci, A. and Micheletti, M. (2016) 'Appraisal of fluid flow in a shaken bioreactor with conical bottom at different operating conditions', *Chemical Engineering Research and Design*, 108, pp. 186–197. doi: 10.1016/j.cherd.2015.12.012.

Rodriguez, G., Weheliye, W., Anderlei, T., Micheletti, M., Yianneskis, M. and Ducci, A. (2013) 'Mixing time and kinetic energy measurements in a shaken cylindrical bioreactor', *Chemical Engineering Research and Design*. Institution of Chemical Engineers, 91(11), pp. 2084–2097. doi: 10.1016/j.cherd.2013.03.005.

Roger, V. L. *et al.* (2011) 'Heart disease and stroke statistics-2011 update: A report from the American Heart Association', *Circulation*, 123. doi: 10.1161/CIR.0b013e3182009701.

Rutherford, K., Lee, K. C., Mahmoudi, S. M. S. and Yianneskis, M. (1996) 'Hydrodynamic characteristics of dual rushton impeller stirred vessels', *AIChE Journal*, 42(2), pp. 332–346. doi: 10.1002/aic.690420204.

Dos Santos, F., Andrade, P. Z., Eibes, G., da Silva, C. L. and Cabral, J. M. S. (2011) 'Ex vivo expansion of human mesenchymal stem cells on microcarriers.', *Methods in molecular biology*, 698, pp. 189–198. doi: 10.1007/978-1-60761-999-4_15.

Sardeshpande, M. V., Kumar, G., Aditya, T. and Ranade, V. V. (2016) 'Mixing studies in unbaffled stirred tank reactor using electrical resistance tomography', *Flow Measurement and Instrumentation.*, 47, pp. 110–121. doi: 10.1016/j.flowmeasinst.2016.01.003.

Savla, J. J., Nelson, B. C., Perry, C. N. and Adler, E. D. (2014) 'Induced pluripotent stem cells for the study of cardiovascular disease.', *Journal of the American College of Cardiology*, 64(5), pp. 512–9. doi: 10.1016/j.jacc.2014.05.038.

Schäfer, M., Yianneskis, M., Wächter, P. and Durst, F. (1998) ‘Trailing vortices around a 45° pitched-blade impeller’, *AIChE Journal*, 44(6), pp. 1233–1246. doi: 10.1002/aic.690440602.

Schaffer, M., Yu, J., Geneger, B. and Durst (2000) ‘Turbulence Generation by Different Types of Impellers’, in *Proc. of the 10th European Conf.* Delft, The Netherlands.

Schmelter, M., Ateghang, B., Helmig, S., Wartenberg, M. and Sauer, H. (2006) ‘Embryonic stem cells utilize reactive oxygen species as transducers of mechanical strain-induced cardiovascular differentiation.’, *FASEB journal : official publication of the Federation of American Societies for Experimental Biology*, 20(8), pp. 1182–4. doi: 10.1096/fj.05-4723fje.

Schroeder, M., Niebruegge, S., Werner, A., Willbold, E., Burg, M., Ruediger, M., Field, L. J., Lehmann, J. and Zweigerdt, R. (2005) ‘Differentiation and lineage selection of mouse embryonic stem cells in a stirred bench scale bioreactor with automated process control.’, *Biotechnology and bioengineering*, 92(7), pp. 920–33. doi: 10.1002/bit.20668.

Sharp, K. V., Hill, D., Troolin, D., Walters, G. and Lai, W. (2010) ‘Volumetric three-component velocimetry measurements of the turbulent flow around a Rushton turbine’, *Experiments in Fluids*, 48(1), pp. 167–183. doi: 10.1007/s00348-009-0711-9.

Shimko, V. and Claycomb, W. (2008) ‘Effect of mechanical loading on three-dimensional cultures of embryonic stem cell-derived cardiomyocytes.’, *Tissue engineering. Part A*, 14(1), pp. 49–58. doi: 10.1089/ten.2007.0092.

Steiros, K., Bruce, P. J. K., Buxton, O. R. H. and Vassilicos, J. C. (2017) ‘Effect of blade modifications on the torque and flow field of radial impellers in stirred tanks’, *Physical Review Fluids*, 2(9), pp. 1–18. doi: 10.1103/PhysRevFluids.2.094802.

Stoots, C. M. and Calabrese, R. V. (1995) ‘Mean velocity field relative to a Rushton turbine blade’, *AIChE Journal*, 41(1), pp. 1–11. doi: 10.1002/aic.690410102.

Story, A., Jaworski, Z., Simmons, M. and Nowak, E. (2014) ‘PIV measurements of the velocity field of a newtonian fluid in a stirred tank equipped with the PMT type impeller’, *Technical Transactions Chemistry*, 111(2–Ch), pp. 125–134.

Takahashi, K. and Yamanaka, S. (2006) ‘Induction of pluripotent stem cells from mouse embryonic and adult fibroblast cultures by defined factors’, *Cell*, 126, pp. 663–676. doi: 10.1016/j.cell.2006.07.024.

Tamburini, A., Gagliano, G., Micale, G., Brucato, A., Scargiali, F. and Ciofalo, M. (2018) 'Direct numerical simulations of creeping to early turbulent flow in unbaffled and baffled stirred tanks', *Chemical Engineering Science*, 192, pp. 161–175. doi: 10.1016/j.ces.2018.07.023.

Tan, R. K., Eberhard, W. and Büchs, J. (2011) 'Measurement and characterization of mixing time in shake flasks', *Chemical Engineering Science*, 66(3), pp. 440–447. doi: 10.1016/j.ces.2010.11.001.

Teixeira, F. G., Carvalho, M. M., Panchalingam, K. M., Rodrigues, A. J., Mendes-Pinheiro, B., Anjo, S., Manadas, B., Behie, L. A., Sousa, N. and Salgado, A. J. (2017) 'Impact of the secretome of human mesenchymal stem cells on brain structure and animal behavior in a rat model of Parkinson's disease', *Stem Cells Translational Medicine*, 6(2), pp. 634–646. doi: 10.5966/sctm.2016-0071.

Teo, A., Mantalaris, A. and Lim, M. (2012) 'Hydrodynamics and bioprocess considerations in designing bioreactors for cardiac tissue engineering', *Journal of Regenerative Medicine and Tissue Engineering*, 1(1), p. 4. doi: 10.7243/2050-1218-1-4.

Thomson, J. A. (1998) 'Embryonic stem cell lines derived from human blastocysts', *Science*, pp. 1145–1147. doi: 10.1126/science.282.5391.1145.

Ting, S., Chen, A., Reuveny, S. and Oh, S. (2014) 'An intermittent rocking platform for integrated expansion and differentiation of human pluripotent stem cells to cardiomyocytes in suspended microcarrier cultures.', *Stem cell research*, 13(2), pp. 202–13. doi: 10.1016/j.scr.2014.06.002.

Ting, S., Lecina, M., Reuveny, S. and Oh, S. (2012) 'Differentiation of human embryonic stem cells to cardiomyocytes on microcarrier cultures.', *Current Protocols in Stem Cell Biology*, Supplement, p. ID.7.1-ID.7.14. doi: 10.1002/9780470151808.sc01d07s21.

Tonsho, M., Michel, S., Ahmed, Z., Alessandrini, A. and Madsen, J. C. (2014) 'Heart transplantation: challenges facing the field.', *Cold Spring Harbor perspectives in medicine*, 4(a015636), pp. 1–21. doi: 10.1101/cshperspect.a015636.

Van't Riet, K. and Smith, J. M. (1975) 'The trailing vortex system produced by Rushton turbine agitators', *Chemical Engineering Science*, 30(9), pp. 1093–1105. doi: 10.1016/0009-2509(75)87012-6.

Venkat, R. V., Stock, L. R. and Chalmers, J. J. (1996) 'Study of hydrodynamics in microcarrier culture spinner vessels: A particle tracking velocimetry approach', *Biotechnology and Bioengineering*, 49(4), pp. 456–466.

Wan, C., Chung, S. and Kamm, R. D. (2011) 'Differentiation of embryonic stem cells into cardiomyocytes in a compliant microfluidic system.', *Annals of biomedical engineering*, 39(6), pp. 1840–7. doi: 10.1007/s10439-011-0275-8.

Wang, W., Ha, C. H., Jhun, B. S., Wong, C., Jain, M. K. and Jin, Z. (2010) 'Fluid shear stress stimulates phosphorylation-dependent nuclear export of HDAC5 and mediates expression of KLF2 and eNOS', *Blood*, 115(14), pp. 2971–2980. doi: 10.1182/blood-2009-05-224824.

Westerweel, J. and Scarano, F. (2005) 'Universal outlier detection for PIV data', *Experiments in Fluids*, 39(6), pp. 1096–1100. doi: 10.1007/s00348-005-0016-6.

van Wezel, A. L. (1985) 'Monolayer growth systems: homogeneous unit processes', in *Animal Cell Biotechnology*, pp. 265–281. doi: 10.1016/C2009-0-02458-1.

Woziwodzki, S. and Słowiński, J. (2012) 'Power requirements for yield stress fluids in a vessel with forward-reverse rotating impeller', *Procedia Engineering*, 42, pp. 1437–1444. doi: 10.1016/j.proeng.2012.07.537.

Wu, H. and Patterson, G. K. (1989) 'Laser doppler measurements of turbulent flow parameters in a stirred mixer', *Chemical Engineering Science*, 44(10), pp. 2207–2221.

Wu, H., Patterson, G. K. and Van Doorn, M. (1989) 'Distribution of turbulence energy dissipation rates in a Rushton turbine stirred mixer', *Experiments in Fluids*, 8(3–4), pp. 153–160. doi: 10.1007/BF00195789.

Yianneskis, M., Popiolek, Z. and Whitelaw, J. H. (1987) 'An experimental study of the steady and unsteady flow characteristics of stirred reactors', *Journal of Fluid Mechanics*, 175, pp. 537–555. doi: 10.1017/S002211208700051X.

Yoshida, M., Ebina, H., Shirosaki, H., Ishioka, K. and Oiso, K. (2015) 'Liquid flow in impeller swept regions of baffled and unbaffled vessels with a turbine-type agitator', *Brazilian Journal of Chemical Engineering*, 32(4), pp. 865–873. doi: 10.1590/0104-6632.20150324s00003682.

Yu, J., Vodyanik, M. A., Smuga-Otto, K., Antosiewicz-Bourget, J., Frane, J. L., Tian, S., Nie, J., Jonsdottir, G. A., Ruotti, V., Stewart, R., Slukvin, I. I. and Thomson, J. A.

(2007) ‘Induced pluripotent stem cell lines derived from human somatic cells’, *Science*, pp. 1917–1920. doi: 10.1126/science.1151526.

Zandstra, P. W., Bauwens, C. L., Yin, T., Liu, Q., Schiller, H., Zweigerdt, R., Pasumarthi, K. B. S. and Field, L. J. (2003) ‘Scalable production of embryonic stem cell-derived cardiomyocytes’, *Tissue engineering*, 9(4), pp. 767–778.

Zhao, J., Gao, Z. and Bao, Y. (2011a) ‘Effects of the blade shape on the trailing vortices in liquid flow generated by disc turbines’, *Chinese Journal of Chemical Engineering*, 19(2), pp. 232–242. doi: 10.1016/S1004-9541(11)60160-2.

Zhao, T., Zhang, Z. N., Rong, Z. and Xu, Y. (2011b) ‘Immunogenicity of induced pluripotent stem cells.’, *Nature*, 474, pp. 212–215. doi: 10.1038/nature10135.

Zhu, R., Blazeski, A., Poon, E., Costa, K. D., Tung, L. and Boheler, K. R. (2014) ‘Physical developmental cues for the maturation of human pluripotent stem cell-derived cardiomyocytes’, *Stem cell research & therapy*, 5(117), pp. 1–18.

Zhu, W. Z., Xie, Y., Moyes, K. W., Gold, J. D., Askari, B. and Laflamme, M. A. (2010) ‘Neuregulin/ErbB signaling regulates cardiac subtype specification in differentiating human embryonic stem cells.’, *Circulation research*, 107(6), pp. 776–86. doi: 10.1161/circresaha.110.223917.

Zwi, L., Caspi, O., Arbel, G., Huber, I., Gepstein, A., Park, I. H. and Gepstein, L. (2009) ‘Cardiomyocyte differentiation of human induced pluripotent stem cells.’, *Circulation*, 120(15), pp. 1513–23. doi: 10.1161/circulationaha.109.868885.

Zwietering, T. N. (1958) ‘Suspending of solid particles in liquid by agitators’, *Chemical Engineering Science*, 8(3–4), pp. 244–253. doi: 10.1016/0009-2509(58)85031-9.